Journal of
Geophysics

Zeitschrift für
Geophysik

Volume 45 1978/1979

Springer International

Journal of Geophysics – Zeitschrift für Geophysik

This journal was founded by the Deutsche Geophysikalische Gesellschaft on the initiative of L. Mintrop in 1924 as the Zeitschrift für Geophysik and edited by G. Angenheister from Vol. 1–18 (1944). It reappeared in 1954 edited by B. Brockamp from Vol. 19–26 (1960), and edited by W. Dieminger and J. Untiedt from Vol. 27 (1961). After Vol. 40 (1970) the title was changed to Journal of Geophysics – Zeitschrift für Geophysik.

Published: Vols. 19–39 by Physica-Verlag, Würzburg, from Vol. 40 by Springer Berlin, Heidelberg, New York.

Springer-Verlag Berlin Heidelberg New York

Printed in Germany by Universitätsdruckerei H. Stürtz AG Würzburg

Author Index

Subject Index

Journal of Geophysics Zeitschrift für Geophysik

Volume 45 Number 1 1978

Contents

Indexed in Current Contents

Springer International

J. Geophys. — ISSN 0340-062X — JGEOD4 45(1) 1–112 (1978) — December 22, 1978

Journal of Geophysics – Zeitschrift für Geophysik

Edited for the

Deutsche Geophysikalische Gesellschaft

by

W. Dieminger and J. Untiedt

Manuscripts may be addressed to any of the Editors. For addresses see last cover page. Manuscripts should conform with the journal's accepted practice as described in the Instructions to Authors.

The Journal accepts

- Review Articles (invited by the Editors)
- Original Papers
- Short Communications
- Letters to the Editors
- Book Reviews

in the field of Geophysics and Space Physics.

Springer International

Members of the Deutsche Geophysikalische Gesellschaft are entitled to purchase the Journal for their own use at a privilege price of DM 98,— payable with the Membership dues. Orders should be sent to the Society's office at the following address: Binderstr. 22, D-2000 Hamburg 13.

Subscription Information
Volumes 45+46 (4 issues each totalling about 852 pages) will appear in 1979. The price of a volume is DM 143,– or $71.50. Information about obtaining back volumes and microform editions available upon request.

North America. Subscription rate: $152.20, including postage and handling. Subscriptions are entered with prepayment only. Orders should be addressed to: Springer-Verlag New York Inc., Service Center Secaucus, 44 Hartz-Way, Secaucus, N.J. 07094, USA. Tel. (201) 348-4033, Telex 0023-125994.

All Other Countries. Subscription rate: DM 286,–, plus postage and handling. Orders can either be placed with your book-dealer or sent directly to: Springer-Verlag, Heidelberger Platz 3, D-1000 Berlin 33, Tel. (030) 822001, Telex 01-83319.

Offices
Springer-Verlag, Heidelberger Platz 3,
D-1000 Berlin 33, Tel. (030) 822001,
Telex 01-83319.

Springer-Verlag, Journal Production
Department II, Postfach 105280,
D-6900 Heidelberg 1, Tel. (06221) 487-1,
Telex 04-61690.

Springer-Verlag New York Inc.,
175 Fifth Avenue, New York, N.Y. 10010, USA,
Tel. (212) 477-8200, Telex 0023-23223.

Responsible for Advertisements:
G. Sternberg,
Kurfürstendamm 237, D-1000 Berlin 15,
Tel. (030) 8821031, Telex 01-85411.

Printed in Germany by
Universitätsdruckerei H. Stürtz AG, Würzburg

J. Geophys. 45, 1–16, 1978

Journal of Geophysics

Original Investigations

Magnetotelluric Investigation of the Lower Crust and Upper Mantle Beneath Iceland

M. Beblo[1] and A. Björnsson[2]

[1] Institut für Allgemeine und Angewandte Geophysik, Universität München, Theresienstraße 41, D-8000 München 2, Federal Republic of Germany
[2] National Energy Authority, Laugavegur 116, Reykjavik, Iceland

Abstract. Magnetotelluric measurements were made at 12 sites on a 210 km long profile in northern and eastern Iceland. The profile crosses areas of different geological age ranging from Tertiary flood basalt to the presently active zone of rifting and volcanism.

Beneath the investigated area, at a depth of a few km down to about 20 km there exists a 5 km thick layer with low resistivity amounting to 15 Ωm which is imbedded between layers of higher resistivities. The depth to the low resistivity layer increases with increasing distance from the spreading axis.

The low resistivity layer is presumably caused by partial melting at the base of the crust and at the top of the anomalous mantle beneath Iceland. Comparison with laboratory measurements confirms a basaltic composition and a temperature of 1,000–1,100° C of the good conductor, and probably partially molten peridotite in the upper mantle beneath.

Mean temperature gradients in the crust calculated from the magnetotelluric data are in good agreement to surface temperature gradients measured in drill holes.

Key words: Magnetotellurics – Iceland – Electrical structure – Low resistivity layer – Temperature gradient – Partial melting.

1. Introduction

During the summer 1977 a magnetotelluric (MT) field program was performed in north-eastern Iceland.

The purpose of this experiment was to investigate vertical and lateral variations of the electrical resistivity in the lower crust and upper mantle beneath Iceland.

Among the physical properties of the earth's interior, which can be measured on the surface, the electrical resistivity is the parameter most sensitive to

0340-062X/78/0045/0001/$03.20

porosity and fluid content in the upper crust. It also correlates well with temperature and chemical composition in the lower crust and mantle. Hence, in measuring in some detail the resistivity distribution, it is possible to investigate crustal thickness and crustal structure. Magnetotelluric measurements could further give valuable informations on the temperature, composition and dimension of the mantle beneath Iceland. Therefore some of the questions concerning processes on the oceanic ridge system like plate accretion may be answered.

2. Geological Setting

Iceland is one of the few land areas, and certainly the largest one, situated on the Mid-Atlantic-Ridge system. The Mid-Atlantic Ridge, which is considered an

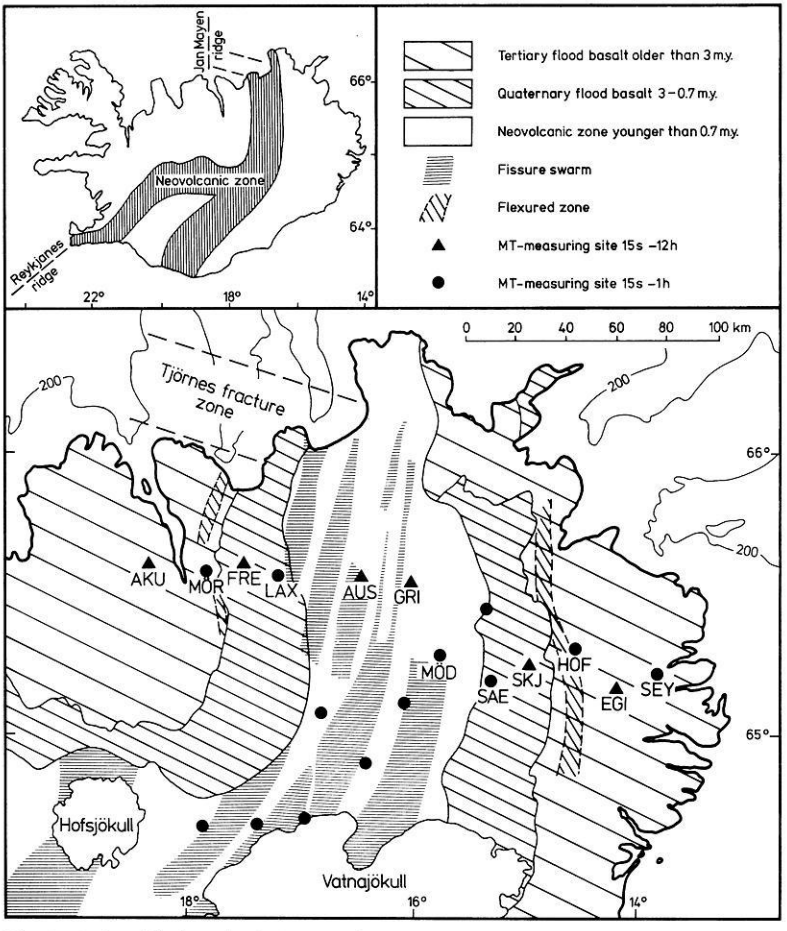

Fig. 1. A simplified geological map of north-eastern Iceland as redrawn from Saemundsson (1974). Triangles are locations of magnetotelluric base sites (period range 15 s–12 h). Filled circles show short period (15 s–1 h) magnetotelluric sites. Only the stations provided with initial letters of site-names are discussed in the present paper

accreting plate boundary of the European and American plates crosses Iceland from south-west to north-east. The surface manifestation of the ridge on land is a tectonically active zone of recent rifting and volcanism, the so called neovolcanic zone. On both sides of the neovolcanic zone there are strips of Quaternary flood basalts followed by Tertiary flood basalts in western and eastern Iceland (see Fig. 1). K/Ar age determinations indicate increasing ages with increasing distance from the active zone (Pálmason and Saemundsson, 1974).

The main features of the geology of north-eastern Iceland have been mapped by Saemundsson (1974). According to his interpretation the neovolcanic zone is characterized by large swarms of north-south trending faults and fissures. The individual swarms are only 5–10 km wide, but several tens of kilometers long. Most of them pass through central volcanos where volcanic activity and high-temperature geothermal fields are concentrated (see Fig. 1).

To the north the neovolcanic zone runs into a complex zone of fractures, the so called Tjörnes fracture zone, which has an east-west direction and joins the ridge system north of Iceland.

Rifting and volcanic activity within the neovolcanic zone in Iceland is mostly confined to the fissure swarms and the associated central volcanos. Major rifting activity is episodic rather than continuous occuring in episodes of a few years with intervals of 100–150 years of quiescence (Björnsson et al., 1977).

3. Previous Geophysical Research in Iceland

A seismic refraction survey of the Icelandic crust was performed by Pálmason (1971). According to his interpretation the upper crust of Iceland consists of a surface layer and two layers of Tertiary flood basalt. These layers are underlain everywhere in the island by a layer with a mean *P*-wave velocity of 6.5 km/s (called layer 3) which is considered to correspond to the oceanic layer 3. This layer is nowhere exposed at the surface and the depth to its upper boundary is usually 3–5 km. In the upper mantle underneath layer 3 there is a layer with a *P*-wave velocity of 7.2 km/s (layer 4). The depth to layer 4 is 8–10 km in the south-west and around 14 km in south-eastern Iceland. No values are available for northern and north-eastern Iceland. If layer 4 is interpreted as the upper mantle it has an anomalously low velocity. This has been explained by a small amount of partial melting. The temperature in this layer should therefore be around 1,000° C, which is in good agreement with values obtained from linear extrapolation of temperature gradients in drill holes which range from 40° C/km in the eastern flood basalt zone to 160° C/km in south-western Iceland (Pálmason, 1973).

The measurements of the time-varying magnetic field were initiated in Iceland by Garland and Ward (1965) and by Hermance and Garland (1968a). They found low resistivities of the order of 10 to 20 Ωm at several sites below a depth of 30 km, which they suggested might be caused by partial melting. They further assumed that the low resitivity layer underlays the entire island rather than just the neovolcanic zone. Magnetotelluric measurements made by Hermance and Garland (1968b) in the northern part of the neovolcanic zone gave similar results for that area.

In further work Hermance and Grillot (1970), Hermance et al. (1972) and Hermance (1973) performed magnetotelluric measurements in order to investigate the electrical structure both of the lower crust and the upper mantle. All these measurements were confined to the neovolcanic zone with special emphasis to its south-western part. Between approximately 2 and 15 km depth they found a conductive layer with a resistivity between 10 and 20 Ωm. Below 10–15 km, at the top of the mantle, the resistivity increases to 40–100 Ωm and shows little variation down to at least 100 km. Hermance (1973) believes that ground water has a considerable effect on the resistivity at depths down to 8–10 km, but below 10 km electronic conduction becomes dominant. Correlating the MT-results with the conductivity of basalt (lower crust) and peridotite (upper mantle) at high temperatures Hermance and Grillot (1974) estimated the temperature at the crust-mantle boundary to be 800–1,200° C. They further estimated the temperature gradient to be about 1° C/km between 15 and 100 km depth.

In further magnetotelluric and geoelectric works in Iceland Hermance et al. (1975), Thayer (1975), and Björnsson (1976) have extended the previous work from within the neovolcanic zone to the older Quaternary and Tertiary flood basalt areas. The aim was to investigate lateral differences in the electrical resistivity of the crust and upper mantle and also to obtain more detailed information on the vertical resistivity distribution, especially around thermal areas. On a regional scale the most significant result of this research is that the resistivity in the upper part of layer 3 at 3–5 km depth is much lower (10–20 Ωm) within the neovolcanic zone than beneath the Quaternary and Tertiary areas (300–1,000 Ωm).

The resistivity below a few tens of km in the mantle beneath Iceland seems to be uniform as reported in previous work. Among these findings there are also indications of differences in the resistivity of the lower crust inside and outside the neovolcanic zone but no detailed information was achieved on that matter.

4. Field Program, Measuring Sites

There were several reasons for performing the magnetotelluric experiment in northern and eastern Iceland:

(1) We intended to determine the temperature in the crust and upper mantle, especially its variations across and along the neovolcanic zone. This can be achieved by the magnetotelluric method since there exists a correlation between temperature and resistivity.

(2) In the part of the country under consideration there is only one neovolcanic zone (running north-south) and the older geological formations seem to be similar and symmetric on both sides of this zone. This means that one could expect a two-dimensional distribution of the electrical conductivity under the area which makes the analysis of MT-measurements on an east-west profile perpendicular to the geological strike much more simple than in the three-dimensional case.

(3) Further more, we planned to investigate possible resistivity changes along the neovolcanic zone from north to south in this area, caused by a proposed mantle plume under the zone in central Iceland (Saedmundsson, 1974).

(4) Long period MT-measurements have never before been made simultaneously at different sites in that part of the country.

(5) Some of the MT-sites were identical with measuring sites of an extensive seismic project (Reykjanes-Ridge-Iceland Seismic Project (RRISP)). The seismic measurements have been carried out in cooperation of Icelandic, German and Soviet geophysical institutions in July 1977. A joint interpretation of the experimental results probably will reduce the number of possible models of the Icelandic crust and upper mantle.

(6) In order to be able to quantitatively consider the influence of the non-uniform inducing magnetic field during night time the profile was orientated approximately perpendicular to the main direction of flow of the polar electrojet.

The major part of the magnetotelluric experiment was done along a 210 km long east-west profile of 12 MT-stations ranging from the Tertiary flood basalt area in the west across the neovolcanic zone to the Tertiary flood basalt area in eastern Iceland. At 6 base-sites on this profile the natural variations of the magnetic and electric field were recorded simultaneously and permanently for 8 weeks (triangles in Fig. 1). The instruments we used were Askania magnetographs for recording the time-variations of the magnetic field, and electrographs (Beblo, 1972) for recording the electric field. The observed period range was 300 s to 12 h.

At all the base-sites, at 6 additional sites on the east-west profile, and at 7 sites on a north-south profile along the neovolcanic zone, MT-measurements were made in the period range 15 s–1 h (filled dots in Fig. 1). A mobile MT-equipment was used consisting of electrograph, fluxgate magnetometer and tape recorder.

The measuring sites, especially the base-sites were installed in geologically homogeneous areas, in order to avoid local distortions of the electric field caused by inhomogeneities of surface resistivities (Beblo, 1974).

In the present paper first results of the magnetotelluric short period measurements (15 s–1 h) on the east-west profile are being presented.

5. The Magnetotelluric Method, Principles of Data Analysis

The electrical resistivity and its distribution within the earth's interior can be determined by observing time-varying magnetic ($\bar{B}$)- and electric ($\bar{E}$) fields at the surface. The depth penetration of the electromagnetic field into the earth depends on the resistivity distribution and the period (T) of the variation. According to the skin-effect, variations of shorter periods ($T < 1{,}000$ s) penetrate only into the uppermost layers (crustal depth). Longer period variations yield informations on the resistivity at greater depth (upper mantle).

5.1. The Impedance Tensor

For the determination of the resistivity-depth-distribution the observed time functions $E(t)$ and $B(t)$ are Fourier-transformed into functions of frequency. The

horizontal and orthogonal components of the electric (E_i, E_j)- and magnetic (B_i, B_j) fields, which are measured at the surface, are combined by a complex transfer function, the impendance tensor $z=(z_{ij})$. The elements of z depend on the resistivity distribution and the orientation of the measuring coordinate system.

$$\begin{pmatrix} E_1 \\ E_2 \end{pmatrix} = \begin{pmatrix} z_{11} & z_{12} \\ z_{21} & z_{22} \end{pmatrix} \cdot \begin{pmatrix} B_1 \\ B_2 \end{pmatrix}$$

SI-units: $\bar{E}$ in V/m, $\bar{B}$ in nT, T in s.
Two parameters, the apparent resistivity $\rho_a(T)$ and the phase difference between the electric and magnetic field $\varphi(T)$ are calculated as functions of period from the impedance tensor.

Interpretation of MT-data in the general three-dimensional case is mathematically complicated and not practicable at the present stage.

In a two-dimensional resistivity distribution the diagonal elements of the impedance tensor disappear if the measured coordinates are parallel or perpendicular to the strike direction of the resistivity anomaly, and there remain the two elements

$$z_{\parallel} = \frac{E_{\parallel}}{B_{\perp}}$$

$$z_{\perp} = \frac{E_{\perp}}{B_{\parallel}}.$$

From these complex functions two different values are obtained for the apparent resistivity ρ_a and two for the phase difference φ:

$$\rho_{a_{\parallel}} = \frac{\mu_0 T}{2\pi} |z_{\parallel}|^2$$
$$\varphi_{\parallel} = \arg(z_{\parallel}) \qquad E\text{-polarization}$$

$$\rho_{a_{\perp}} = \frac{\mu_0 T}{2\pi} |z_{\perp}|^2$$
$$\varphi_{\perp} = -\arg(z_{\perp}) \qquad B\text{-polarization}$$

ρ in Ωm, φ in degrees.
In the case of an one-dimensional resistivity distribution, i.e., if the resistivity varies only with depth, the two values for the apparent resistivity and the two values for the phase become identical.

As Iceland is regularly situated below the polar electrojet the inducing magnetic field may be inhomogeneous. In that case ρ_a and φ depend both on the period T as well as on the spatial dimension, often called wavelength L, of the inducing magnetic field ($\rho_a(L, T)$, $\varphi(L, T)$).

Haak (1978) has made some model calculations to estimate the influence of inhomogeneous source fields on MT-measurements. He found that deviation from the homogeneous case can be neglected for a penetration depth shallower

than the wavelength L. The half-width of the polar electrojet was estimated by Hermance and Garland (1968a) to be about 480 km. This means that the inhomogeneity of the source field in Iceland can be neglected for a penetration depth of less than approximately 100 km. Our present results are calculated from variations with periods shorter than 1 h. Such variations penetrate up to 100 km into the earth. Therefore we neglect effects from inhomogeneous inducing magnetic fields.

Near strong lateral changes in surface resistivity the electromagnetic field is changed considerably. This is for example the case near the ocean shore (ocean effect). It is well known, that for horizontal distances exceeding one or two skin-depths from the boundary the ocean effect can be neglected. Referred to the 200 m depth contour all our MT-stations are further inland by more than this critical distance which justifies our neglection of the ocean effect. Analysing MT-data from south-western Iceland Thayer (1975) arrived at a similar conclusion.

5.2. Polarization and Preference Direction of the Electric Field

The endpoints of the horizontal field-vectors $\bar{E}$ and $\bar{B}$ approximately move along an ellipse during one oscillation period T. The direction of the major axis of the ellipse is called the polarization direction, and the ratio of the major axis to the minor defines the intensity of polarization.

Direction and intensity of polarization of the magnetic source field usually change with time as well as with the period. Direction and intensity of polarization of the induced electric field depend on the magnetic source field but they are also a function of lateral variations of the electric resistivity in the underground near to the measuring site.

If the magnetic source field is randomly polarized and if there exists a preference direction of the polarization of the electric field, the preference direction depends mainly on the resistivity distribution near to the measuring site. If the resistivity distribution in the underground is two-dimensional it is possible to determine the preference direction of the electric field directly from the impedance tensor. For a constant magnetic field polarization direction α_B the tensor-element z_{21} shows a maximum for a certain electric field polarization direction α_E. The angle α_{E_0} where this tensor-element and therefore the electric field direction depends least on the direction of the magnetic field is identical to the preference direction (Kiessling, 1970, published by Haak (1978)). Determining the angle α_{E_0} of the preference direction simultaneously the absolute values of the diagonal elements of the impedance tensor were calculated. The ratio of these elements $|z_{21}/z_{12}|$ is a measure of the inhomogeneity of the electrical resistivity at the corresponding measuring site.

5.3. Model-Calculations

It is well known (Berdichevsky and Dmitriev, 1976) that the B-polarization depends much more on near-surface lateral resistivity variations than on re-

sistivity anomalies at greater depth. In constrast to that case, the *E*-polarization ($\rho_{a_\parallel}$ and $\varphi_\parallel$) is far less affected by local near-surface anomalies and contains more information on the resistivity distribution at greater depth.

Because of the continuity of the electric field component parallel to a lateral resistivity contrast, the $\rho_{a_\parallel}$-values for the *E*-polarization are similar to the ρ_a-values for a plane layered earth. The difference between the *E*-polarization for a two-dimensional resistivity distribution and a one-dimensional case is small if the lateral resistivity gradient is small. From Fig. 2 it is evident that this is the case on our MT-profile in north Iceland. Therefore we have used the $\rho_{a_\parallel}$- and $\varphi_\parallel$-values of the *E*-polarization (not the *B*-polarization) to calculate one-dimensional models of the resistivity distribution with depth at each of the MT-stations.

6. The Magnetotelluric Results

6.1. Preference Direction of the Electric Field

At all the MT-sites along the east-west profile we have calculated the preference direction of the electrical field (α_{E_0}) using the method of Kiessling (1970). An investigation of the inducing magnetic field showed that no dominating preference direction of its polarization exists in the observed period range.

Figure 2 shows the distribution of the preference direction (α_{E_0}) along the profile for the period range of 15 to 300 s. The length of the lines is proportional to the ratio of the tensor elements $|z_{21}/z_{12}|-1$ and is a measure of the intensity of polarization (The lines should be reduced to points for a plane layered or homogeneous earth).

Within the Quaternary flood basalt zone and the neovolcanic zone the short lines indicate small horizontal variations of the resistivity. Strong horizontal variations of resistivity exist at the measuring sites within the Tertiary flood basalt zones. This means that the surface resistivity within the Tertiary flood basalts must be an order of magnitude greater than within the Quaternary and neovolcanic zones. This result is in good agreement with some resistivity (dipole-dipole) measurements made in the area, which show resistivities of the order of hundreds of Ωm at 1–4 km depth in the Tertiary zones, but resistivities well below 100 Ωm in the Quaternary and neovolcanic zones.

The preference direction within the Tertiary zones may be caused by the resistivity distribution of the underground but also by the topography near to the measuring sites.

6.2. Apparent Resistivities and Phase Differences

The impedance tensor has been calculated for all 12 sites on the EW-profil as a function of the angle of rotation. Herefrom we may infer that within the neovolcanic zone and the Quaternary flood basalt zone the tensor has the shape as for a one-dimensional resistivity distribution, whereas within the Tertiary

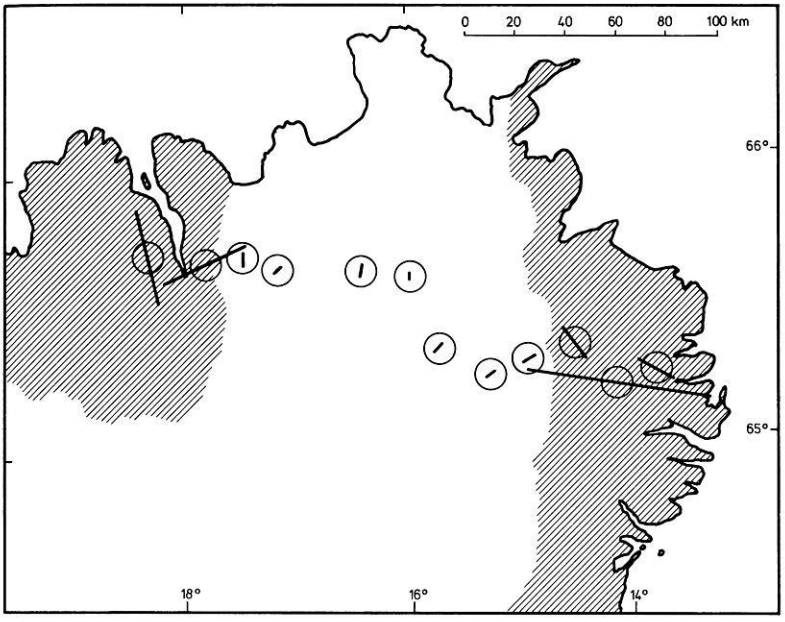

Fig. 2. Preference direction (lines) at each magnetotelluric site of the induced electrical field for the period range 15–300 s. The length of the lines indicates the intensity of polarization and is a measure of the inhomogeneity of the surface resistivity distribution at the sites

flood basalts we see a clear influence from lateral resistivity variations on the impedance tensor. Also from the distribution of the preference direction we may infer an approximately two-dimensional structure of the resistivity, coinciding obviously with the main geological features. Therefore we can discern the fundamental cases of *E*- and *B*-polarization.

Figure 3 shows the calculated values for the apparent resistivities and the phase differences for all the 12 sites, separately for *E*- and *B*-polarization. The phase differences are shown for the *E*-polarization only. The *B*-polarization (that means the component of the electric field perpendicular to the strike direction of the neovolcanic zone) demonstrates clearly strong horizontal resistivity variations. The apparent resistivity changes abruptly at the boundary of the Tertiary zones. The lower resistivity in the center regions can be seen as a trough bordered by higher values.

The *E*-polarization shows the component parallel to the boundary of the neovolcanic zone. The apparent resistivities for this case change continuously at the boundary.

The $\rho_{a_{\parallel}}$-values at the site Hofteigur (HOF) are elevated by a factor 2 or 3 compared to the sites on both sides. It is known (Berktold et al., 1976) that the ρ_a-values may be shifted by local near-surface resistivity anomalies to higher or lower values. The measuring site HOF is situated directly in a highly flexured zone near the border of the Tertiary and Quaternary zones (see Fig. 1) which might cause such an effect. A similar but not as significant shift is observed at

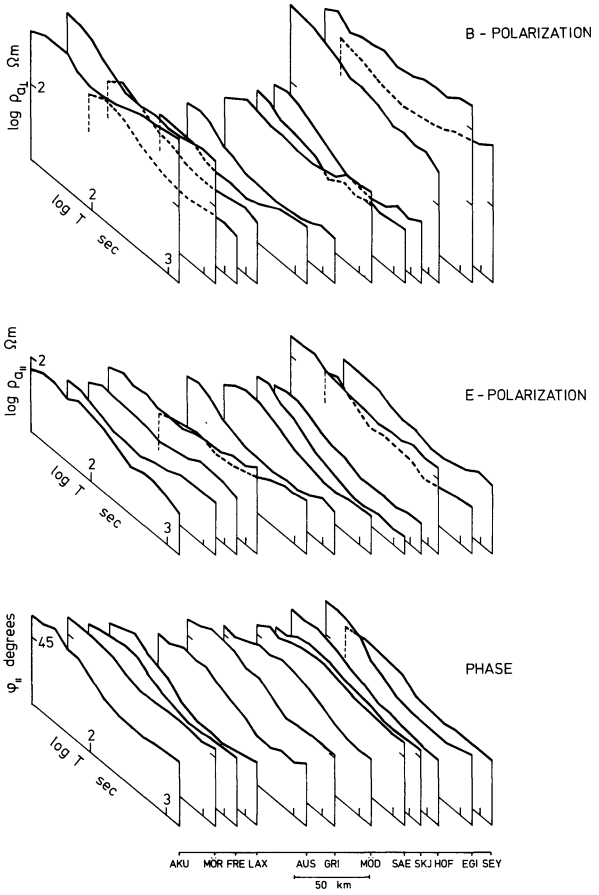

Fig. 3. Apparent resistivities for *E*-polarization $\rho_{a_\parallel}$, *B*-polarization $\rho_{a_\perp}$, and phase difference for *E*-polarization $\varphi_\parallel$ along the whole east-west MT-profile. The values for $\rho_{a_\perp}$ are deplated in the center part of the profile whereas the values for $\rho_{a_\parallel}$ and $\varphi_\parallel$ show similar behaviour across the profile

the sites Laxardalsheidi (LAX) and Saenautavatn (SAE), with ρ_a-values too high, or too low respectively, compared to adjacent sites.

In order to discern the fundamental cases of *E*- and *B*-polarization, we have additionally to consider the continuous or discontinuous behaviour of the apparent resistivities as a major discriminating factor. In AKU these directions seem to be exchanged, possibly caused by local topographic influence.

6.3. Model-Calculations

Because of the weak horizontal variations of the resistivity distribution within the Quaternary and neovolcanic zones we conclude that it is permitted to calculate one-dimensional models (plane layered earth) for the resistivity distribution at the MT-sites.

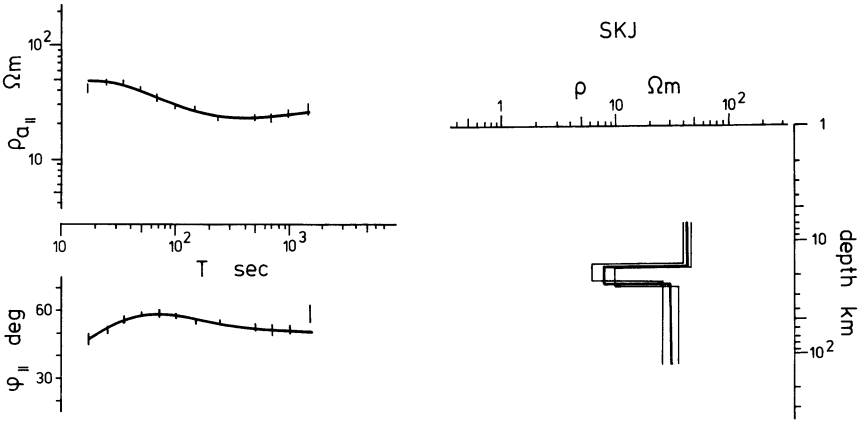

Fig. 4. To the left measured apparent resistivities ρ_a and phases $\varphi_\parallel$ as a function of period T at the site SKJ (Skjöldolfsstadir). The vertical lines are mean square deviations. To the right: a three-layer model with confidence levels computed by the mean square deviation of the measured values. The heavy lines through the measured values are theoretical curves calculated from the model

For calculating the models we used an inversion method given by Schmucker (1974). In all cases a good fit between the measured and calculated resistivities and phases was obtained for three-layer models. Models consisting of more than three layers did not show considerable improvement in the analyzed period range.

Figure 4 shows the measured values of resistivities and phases at the site Skjöldolfsstadir (SKJ), compared to the calculated curves and the corresponding three-layer model.

The absolute resistivity values in each layer obtained by the model calculations are different from site to site along the profile (see Fig. 5). This is probably caused by near-surface local anomalies which either tend to increase or decrease the resistivity values as a whole in all the measured period range. To a lesser extent this effect also affects the depth determinations. In spite of this uncertainty caused by resistivity variations at the surface the computed models are very similar at all MT-sites, showing only three distinct layers except the site AUS.

At approximately 8–15 km depth the mean resistivity is rather high, 50–100 Ωm. The second layer is only about 5 km thick and has a low resisitivity of 10–20 Ωm. The third layer has a resisitivity of 50–100 Ωm down to at least 100 km depth.

The most significant result of this model calculations is the good conducting layer, which appears beneath all the sites on the profile. The depth to the upper boundary of this layer increases with increasing distance from the neovolcanic zone. The depth is 13–14 km near the boundaries of the neovolcanic zone but 18–20 km in the Tertiary region. At the site Austaribrekka (AUS), the only MT-station within the center part of the active zone, the well conducting layer approaches the surface even by 1–2 km. This is clearly shown in Fig. 5.

The greatest deviation of computed phase values from measured values is observed for the longest periods (see Fig. 4). The measured phases increase with

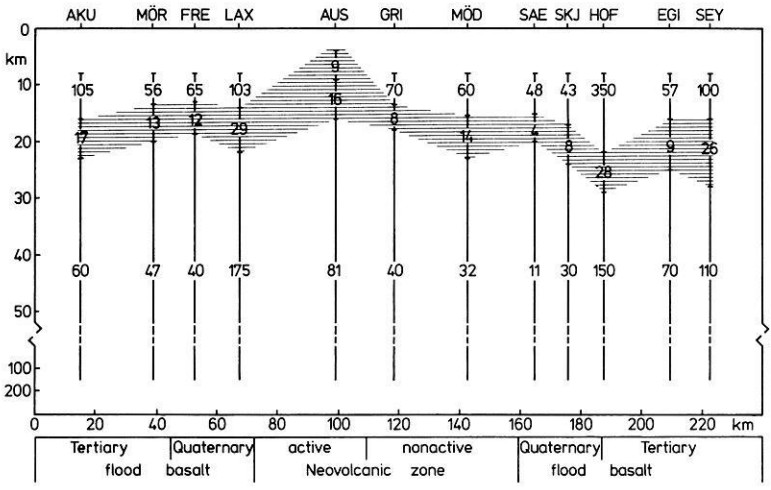

Fig. 5. Three-layer models along the east-west MT-profile calculated from apparent resistivities and phases of the *E*-polarization case. The hatched area is a low resistivity layer near the crust-mantle interface approaching the surface inside the neovolcanic zone. The numbers indicate resistivities in Ωm

increasing period. This behaviour indicates the existence of an additional low resistivity layer at great depth. From model calculations with four layers we have estimated the depth to this layer to be in the range of 200–300 km. This deep low resistivity layer can not be seen in the apparent resistivity. For that purpose the largest analysed periods of 1 h are too short. We hope to be able to delineate this deep low resistivity layer in a later stage having analysed the MT-data with periods up to approximately 12 h.

7. Discussion

In the MT-results the Quaternary and neovolcanic zones are clearly seen as an anomaly with lower electric resistivity than the Tertiary areas on both sides. This is evident both from the preference direction of the induced electric field as well as from the lowered apparent resistivity curves for the *B*-polarization in the central part of the measured profile. This behaviour must result from a zone of low resistivity underlaying the Quaternary and neovolcanic zones at shallow depth in the upper crust, probably 2–5 km. As the shortest measured periods in the MT-experiment were about 15 s the minimal skin-depth is by far too large to obtain detailed informations on this near-surface low resistivity zone. The MT-results show this low resistivity zone only as a marginal effect caused by its influence on the electric field. This result is supported by dipole-dipole measurements. At depths between 2–5 km the bulk rock resistivity is mainly controlled by ionic conduction in the pore fluid and hence by the porosity of the rocks. According to Saemundsson (1974) the Tertiary lava pile in north-eastern Iceland may be up to 4 million years older than the adjoining Quaternary and

neovolcanic zones. Saemundsson has further found (personal communication), that the Quaternary lava pile contents much more sedimentary layers and is less alterated than the Tertiary lava pile. This could cause an abrupt change in porosity and hence in resistivity at the boundaries of the Tertiary and Quaternary flood basalt zones in this part of the country. An increase in porosity from 1 to 3% would decrease the resistivity by one order of magnitude (Björnsson, 1976). It is noticable that no significant lateral change in resistivity is observed at the boundaries of the Quaternary and neovolcanic zones which indicates that no major change in porosity or temperature occurs at this geological contact.

The most significant result of the present MT-experiment is the existence of the low resistivity layer which can be traced along the whole east-west profile at a depth of 10–22 km, increasing in depth with increasing distance from the center of the neovolcanic zone. Only at the site AUS, which is located within the active part of the neovolcanic zone this layer approaches the surface with a minimum depth of 1–2 km.

The low resistivity layer is very likely somehow correlated to the crust-mantle boundary. The increasing depth with increasing distance from the spreading axis can be explained by a thickening of the crust with increasing age. Beneath Iceland Zverev et al. (1978) have found that focal depths of earthquakes increase from a few km down to 20–30 km on a 80 km long profile starting near our MT-site AUS running to the north-west. The depth to the base of the crust i.e., the interface of the seismic layers 3 and 4 is not known in northern and eastern Iceland. In south-eastern Iceland this interface is at a depth of around 14 km, and in the south-west it is at about 10 km (Pálmason, 1971). These depths are comparable with the depth determined by the MT-method, so it is very likely that the low resistivity layer characterises the crust-mantle interface beneath Iceland. If this conclusion is true, the magnetotelluric method can be used in a simple and time saving way to map in detail the lower boundary of the crust in Iceland.

The mean resistivity of the good conductor is about 15 Ωm. At shallower depth in the crust ionic conduction in pore fluids is dominating. Therefore, the good conducting layer within the active part of the neovolcanic zone at the site AUS, probably consists of several zones of different conductivity mechanism at different depths. The measured period range of 15 s–1 h is not adequate to obtain any detailed informations on the resistivity distribution at 0–5 km depth beneath the site AUS and hence the nature of this part of the low resistivity layer will not be discussed further in this paper.

At a depth below 10 km ionic conduction in pore fluids very probably plays a minor role, compared to electronic conduction in the solid rock itself or to conduction in a partial melt. It should therefore be possible to put some constraints on the temperature conditions and material composition at this depth by comparing the measured resistivity values to laboratory measurements of conductivity of different rocks at high temperatures and pressures.

A great number of workers have made laboratory measurements on electrical conductivity as a function of temperature and pressure for different crustal and upper mantle materials (see, for example, Parkhomenko (1967), Khitarov et

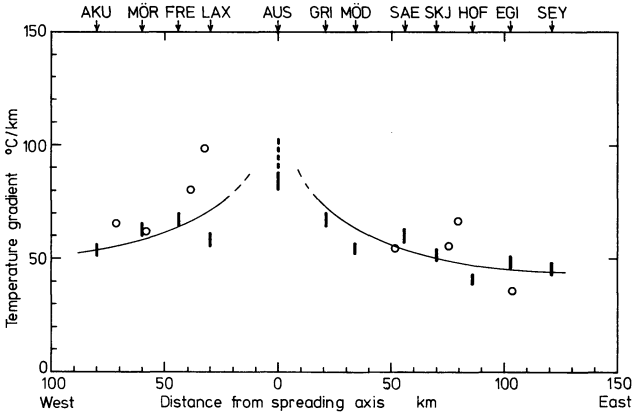

Fig. 6. Temperature gradient as a function of distance from the spreading axis in north-eastern Iceland. The vertical bars show the mean temperature gradient obtained from magnetotelluric measurements at the different sites assuming a temperature range of 1,000–1,100° C in the low resistivity layer beneath the MT-profile. Open circles are surface temperature gradients measured in shallow drill holes

al. (1970), Bondarenko (1972), Presnall et al. (1972)). All the results scatter considerably and seem to depend strongly on laboratory conditions and the measuring technique. Nevertheless the laboratory investigations on dry basalt samples yield temperatures in the range of 800–1,200° C for a resistivity of 15 Ωm, with a resonably good mean value around 1,000–1,100° C. Hence, assuming a basaltic composition of the low resistivity layer at 12–20 km depth the temperature in that layer must be about 1,000–1,100° C. This is in good agreement with the results of Hermance and Grillot (1970) obtained in south-western Iceland. According to some of the laboratory measurements partial melt starts occuring in this temperature range and then the resistivity can be lowered one or two orders of magnitude. The anomalous mantle beneath Iceland very probably consists of partially molten peridotite. If partial melting has reached a sufficient volume fraction the fluid phase and the volatile components will tend to rise to the top of the mantle and form a layer of high melt fraction at the base of the crust. It seems therefore plausible to explain the existence of the low resistivity layer as a thin zone of partial melt at the lower boundary of the crust. No exact information on the volume fraction of the melt phase can be obtained, because the resistivity strongly depends on the shape and liquid bridging of the melt pockets (Waff, 1974), but according to Shankland and Waff (1977) the melt fraction has to be at least 10% to obtain 15 Ωm in the temperature range of 1,000–1,100° C. The increased resistivity in the upper mantle below the good conductor is in good agreement with most of the laboratory measurements, which show that the resistivity of peridotite is aproximately an order of magnitude higher than that of basalt at the same temperature.

Assuming a constant temperature of 1,000–1,100° C in the center part of the low resistivity layer we have calculated the mean temperature gradient in the Icelandic crust below the whole MT-profile by dividing the temperature by the depth of the layer which is shown in Fig. 5. The results are shown in Fig. 6. The

mean temperature gradient decreases with increasing distance from the spreading zone. The obtained value for the center station AUS is uncertain because of uncertain depth determination, but may be around 100° C/km. In east Iceland the calculated gradient is around 50° C/km and in the central part of north Iceland about 60° C/km. Figure 6 also shows surface-temperature gradients measured in shallow drillholes in north and east Iceland from Palmason (1973), and some new data from the files of the National Energy Authority of Iceland.

A relatively good correlation seems to exist between the surface gradients and the mean crustal temperature gradients calculated from the MT-measurements. This demonstrates the possibility to estimate temperatures in the deep Icelandic crust in an economic and time saving way from MT-soundings, especially in places where the surface gradient is disturbed by circulating near-surface ground water. In south Iceland Palmason (1973) has found a similar distribution of the surface temperature gradient but with much higher values across the western part of the active zone. On the other hand the eastern branch of the zone does not show any anomaly in the surface temperature gradient. He explains his observations as a consequence of different ages of the west and east branches of the neovolcanic zone (Saemundsson, 1974).

According to the present data it can be assumed that the low resistivity layer exists beneath the whole of Iceland at different depths. A wide spread partially molten layer at the crust-mantle interface can have an important tectonic implication as pointed out by Anderson and Sammis (1970). Especially beneath Iceland where this layer is at relatively shallow depth it can explain the mobility of the crust in the active spreading zones and the instability of these zones within the crust.

Acknowledgements. This work has been carried out by members of the Institut für Allgemeine und Angewandte Geophysik der Ludwig-Maximilians-Universität München, Federal Republic of Germany, and the National Energy Authority, Orkustofnun, Reykjavik, Iceland. We are grateful to Professor Dr. G. Angenheister, München, and Dr. G. Pálmason, Reykjavik, for their interest and support, as well as to Professor Dr. W. Kertz, Braunschweig, for providing us with cross-country vehicle. We have to thank especially Dr. A. Berktold and Dr. V. Haak for their personal engagement in the field work and discussions, the latter one also for allowing us to use his computer programs. We thank Mr. K. Árnasson and Dr. K. Kemmerle for their help during field measurements and interpretation. The model-calculations have been done at the Leibniz-Rechenzentrum der Bayerischen Akademie der Wissenschaften. The financial support of the Deutsche Forschungsgemeinschaft and of the Deutscher Akademischer Austauschdienst is thankfully acknowledged.

References

Anderson, D.L., Sammis, C.: Partial melting in the upper mantle. Phys. Earth Planet. Inter. **3**, 41–50, 1970

Beblo, M.: A transportable battery-operated electrograph for permanent recording of the induced electric field of the earth. J. Geophys. **38**, 133–143, 1972

Beblo, M.: Die elektrische Leitfähigkeit unter den Ostalpen, abgeleitet aus magnetotellurischen Messungen längs eines Profiles vom Alpennordrand bis zu den Hohen Tauern. Diss. Fak. Geowiss. Univ. München 1974

Berdichevsky, M.N., Dimitriev, V.J.: Basic principles of interpreation of magnetotelluric sounding curves. In: Geoelectric and geothermal studies, A. Adam, ed.: pp. 165–221. Budapest: Akadémiai Kiadó 1976

Berktold, A., Beblo, M., Kemmerle, K.: On the distribution of the electrical conductivity below the Eastern Alps. Geol. Rundschau **65**, 715–732, 1976

Björnsson, A.: Electrical resistivity of layer 3 in the Icelandic crust. In: Greinar V. pp. 7–23, Reykjavik: Societas Scientiarum Islandica 1976

Björnsson, A., Saemundsson, K., Einarsson, P., Tryggvason, E., Grönvold, K.: Current rifting episode in north Iceland. Nature **266**, 318–323, 1977

Bondarenko, A.T., Galdin, N.Y.: On the physicomechanical and electrical properties of basalts at high pressures and temperatures. Izv. Earth Phys. **5**, 28–40, 1972

Garland, G.D., Ward, J.: Magnetic variation measurements in Iceland. Nature **205**, 269–270, 1965

Haak, V.: Interpretations-Verfahren für die Magnetotellurik unter besonderer Berücksichtigung lateral variierender elektrischer Leitfähigkeit im Erdinnern und eines räumlich inhomogenen induzierenden Magnetfelds. München: Bayerische Akademie der Wissenschaften 1978

Hermance, J.F.: An electrical model for the sub-Icelandic crust. Geophysics **38**, 3–13, 1973

Hermance, J.F., Garland, G.D.: Deep electrical structure under Iceland. J. Geophys. Res. **73**, 3797–3800, 1968a

Hermance, J.F., Garland, G.D.: Magnetotelluric deepsounding experiments in Iceland. Earth Planet. Sci. Lett. **4**, 469–474, 1968b

Hermance, J.F., Grillot, L.R.: Correlation of magnetotelluric, seismic and temperature data from southwest Iceland. J. Geophys. Res. **75**, 6582–6591, 1970

Hermance, J.F., Grillot, L.R.: Constraints on temperatures beneath Iceland from magnetotelluric data. Phys. Earth Planet. Inter. **8**, 1–12, 1974

Hermance, J.F., Nur, A., Björnsson, S.: Electrical properties of basalt: relation of laboratory to in situ measurements. J. Geophys. Res. **77**, 1424–1429, 1972

Hermance, J.F., Thayer, R.E., Björnsson, A.: The telluric-magnetotelluric method in the regional assessment of geothermal potential. In: Proceedings, Second United Nations Symp. on the development and use of geothermal resources, San Francisco, pp. 1037–1048. Berkeley-San Francisco: Lawrence Berkeley Lab., Univ. of California 1975

Kiessling, W.: Untersuchung der Variationen des erdelektrischen und erdmagnetischen Feldes im Oberpfälzer Wald zur Bestimmung der elektrischen Leitfähigkeit in größeren Tiefen mit der Methode der Magnetotellurik. Dipl.-Arbeit, Inst. Angew. Geophys. Univ. München 1970

Kitharov, N.I., Slutskiy, A.B., Pugin, A.V.: Electrical conductivity of basalts at high T-P and phase transitions under upper mantle conditions. Phys. Earth Planet. Inter. **3**, 334–342, 1970

Pálmason, G.: Crustal structure of Iceland from explosion seismology. Rit XL, Reykjavik: Societas Scientiarum Islandica, pp. 187, 1971

Pálmason, G.: Kinematics and heat flow in a volcanic rift zone with application to Iceland. Geophys. J. **33**, 451–481, 1973

Pálmason, G., Saemundsson, K.: Iceland in the relation to the Mid-Atlantic Ridge. Ann. Rev. Earth Planet. Sci. **2**, 25–50, 1974

Parkhomenko, E.I.: Electrical properties of rocks. New York: Plenum 1967

Presnall, D.C., Simmons, C.L., Porath, H.: Changes in electrical conductivity of a synthetic basalt during melting. J. Geophys. Res. **77**, 5665–5672, 1972

Saemundsson, K.: Evolution of the axial rifting zone in northern Iceland and the Tjörnes fracture zone. Bull. Geol. Soc. Am. **85**, 495–504, 1974

Schmucker, U.: Erdmagnetische Tiefensondierung mit langperiodischen Variationen. In: Protokoll DFG-Kolloquium Erdmagn. Tiefensond, A. Berktold, ed.: pp. 313–342, Grafrath-München: 1974

Shankland, T.J., Waff, H.S.: Partial melting and electrical conductivity anomalies in the upper mantle. J. Geophys. Res. **82**, 5409–5417, 1977

Thayer, R.E.: Telluric-magnetotelluric investigations of regional geothermal processes in Iceland. Ph. D. thesis, Providence: Dept. Geological Sciences, Brown University 1975

Waff, S.H.: Theoretical considerations of electrical conductivity in a partially molten mantle and implications for geothermometry. J. Geophys. Res. **79**, 4003–4010, 1974

Zverev, S.M., Boldyrev, S.A., Bourmin, V.Yu, Mironova, V.I.: Weak earthquakes in the northern part of the rift zone of Iceland. J. Geophys. **44**, 283–296, 1978

Received June 29, 1978/Accepted October 30, 1978

J. Geophys. 45, 17–28, 1978

Journal of Geophysics

Damped and Constrained Least Squares Method With Application to Gravity Interpretation

J.L. Vigneresse

Centre Armoricain d'Etude Structurale des Socles, Universite de Rennes I, Avenue du Général Leclerc, F-35042 Rennes Cedex, France

Abstract. Many geophysical problems are solved through linear system inversion techniques. Optimization routines are the usual schemes and among them the least-squares method is the most common. Some refinements as matrix decomposition, elimination of insignificant eigenvalues are considered and tapering of small eigenvalues is proposed. The introduction of an upper and a lower limit for the solution vector is presented. This reduces the usual instability encountered when using classical least squares techniques.

An application to gravity profile inversion shows how this method can be used as an intermediate between the direct problem (model construction) and the inverse problem (search for ideal bodies).

Key words: Constrained least squares – Inverse problems – Gravity.

I. Introduction

Provided an appropriate choice of the parameters, a lot of geophysical problems may be reduced to a linear combination of relationships between the measurements b of physical quantities and a set of unknown parameters x. The problem is to solve the linear system

$$Ax=b \tag{1}$$

in order to find the solution vector x representing the unknown parameters x_j. Since the number m of observation points b_i does not need to be equal to the number n of the different physical parameters to be determinated, the system $Ax=b$ must be solved using an approximation theory. A good solution is

$$b'=b+e\ Ax \tag{2}$$

with e being the residuals between computed and observed values. The problem is then to reduce the values of the residuals, that is to say to minimize the

0340-062X/78/0045/0017/$02.40

quantity $\|Ax-b\|$. Several criteria are available, dealing mainly with the power used to calculate the norm. Some of them have been examined in a previous paper (Vigneresse, 1977). Here only least-squares approximations are presented.

2. Theory

2.1. Classical Least Squares

Resolution of the system can be obtained by the usual Gauss method. Normal equations can be written

$$A^T Ax = A^T b. \tag{3}$$

The solution is given by

$$x = (A^T A)^{-1} A^T b. \tag{4}$$

Troubles arise from the computation of the inverse of $A^T A$. Instabilities occur when the A matrix is badly conditioned, since the condition number of $A^T A$ is the square of the condition number of A. This may cause serious problems during the inversion (Anderssen, 1969).

2.2. Matrix Decomposition and Damped Least Squares

Lanczos (1961) proposed an improvement by using an eigenvalues-eigenvectors decomposition of the matrix

$$A = USV^T. \tag{5}$$

Solution is now obtained by

$$x = VS^{-1} U^T b. \tag{6}$$

U and V are orthogonal matrices whose columns are the eigenvectors associated with the columns and rows of A respectively. S is in this case a diagonal matrix, the elements of which are the eigenvalues of the full rank matrix. If degeneracy occurs some eigenvalues are equal to zero. In the numerical application, the existence of small eigenvalues comes from irrelevant and unimportant parameters.

It can be desirable to keep these low eigenvalues during the inversion for instance when the effects of several parameters are very similar and are hardly distinguishable from the data. (Levenberg, 1944; Marquardt, 1963, 1970). The method is also known as ridge regression (Hoerl and Kennard, 1970).

The normal Eq. (3) are modified to

$$(A^T A + \Theta I) x = A^T b \tag{7}$$

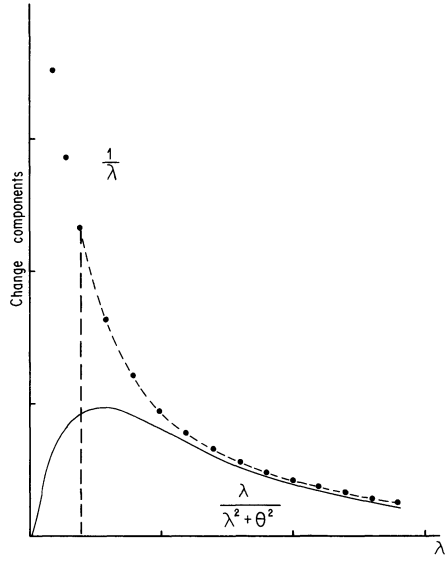

Fig. 1. Eigenvalue spectrum obtained by using classical least squares inversion ($1/\lambda$, dots), threshold value (broken line) and damped least squares as described in present paper ($\lambda/\lambda^2 + \Theta^2$), solid line)

where Θ is a diagonal matrix with positive elements. When using the same type of matrix decomposition as previously (5) the normal equations are written

$$(VS^2U^T + \Theta I)x = VSU^Tb \tag{8}$$

and a solution is

$$x = V|(S^2 + \Theta^2 I)^{-1}S|U^Tb. \tag{9}$$

The effect has been the introduction of a perturbation factor Θ^2 which tapers the spectrum of the eingenvalues (Fig. 1). A scheme of calculations is provided in Table 1.

The choice of a convenient value for Θ is essential. A good estimate is given by weighting the residuals by one over the variances of the observations (Crosson, 1976). This leads to a normally distributed random variable with unit variance. Aki and Lee (1976) use a weight inversely proportional to the variance, namely the ratio of the variance of the data over the variance of the estimated solution. The same choice had been proposed by Franklin (1970) in the method of the stochastic inverse.

2.3. Constrained Least Squares Approximation

In spite of these improvements, the least-squares problem does not have unique solution in the overdetermined case, and the solution may be optimum only in the mathematical sense, i.e.: it can be physically out of range even if the criterion of minimizing the sum of squares of the residuals is fully satisfied. From a geophysical point of view, it would be better to choose a solution within an average range of physically meaningful values.

Table 1. Scheme of resolution of overdetermined system through classical and improved least squares minimization

	System $Ax = b$	
	CLASSICAL LEAST SQUARES	LEVENBERG – MARQUARDT DECOMPOSITION
Minimization of	$(Ax-b)^T(Ax-b)$	$(Ax-b)^T(Ax-b)+\theta^2 x^T x$
Normal équations	$A^T A\ x = A^T b$	$(A^T A+\theta^2 I)\ x = A^T b$
Solution	$x = (A^T A)^{-1} A^T b$	$x = (A^T A+\theta^2 I)^{-1} A^T b$
MATRIX DECOMPOSITION		
	$A = U S V^T$	$A = U S V^T$
Normal équations	$V S^2 U^T x = V S U^T b$	$(V S^2 U^T+\theta^2 I)x = V S U^T b$
Solutions	$x = V S^{-1} U^T b$	$x = V\{(S^2+\theta^2 I)^{-1} S\} U^T b$
	$S^{-1} = \begin{vmatrix} 1/\lambda_1 & & 0 \\ & 1/\lambda_2 & \\ 0 & & 1/\lambda_n \end{vmatrix}$	$(S^2+\theta^2 I)^{-1} S = \begin{vmatrix} \frac{\lambda_1}{\lambda_1^2+\theta^2} & & \\ & \frac{\lambda_2}{\lambda_2^2+\theta^2} & \\ & & \frac{\lambda_n}{\lambda_n^2+\theta^2} \end{vmatrix}$

(a) *Theory*. The introduction of such limits for the solutions can be formulated as the following Constrained Least-Squares problem (CLS problem):

$$\text{Minimize } \|Ax-b\| \text{ subject to } Cx>d \tag{10}$$

with the $m \times n$ matrix A, equivalent to the above notation, and the $p \times n$ matrix C of the relations between the constraints vector d and the solution vector x.

Two particular cases of this problem are evident:

$$\text{Problem LDP (Least Distance Programming): Minimize } \|x\| \text{ subject to } Cx>d \tag{11}$$

$$\text{Problems NNLS (Non Negative Least Squares) Minimize } \|Ax-b\| \text{ subject to } x>0. \tag{12}$$

An algorithm for NNLS problem has been dealt with, and solved, in linear and non-linear programming. Basic theorems are found in the original paper by Kuhn and Tucker (1951) and in books dealing with optimization (Laurent, 1972; Fiacco and McCormick, 1968). Applications and practical use have been developed by Lawson and Hanson (1974), and by Gill and Murray (1974).

Kuhn and Tucker (1951) solved the CLS problem by introducing slack or surplus variables (r) in order to reduce the inequalities in $Cx>d$ to the equalities $Cx-r=d$ with the condition $x, r>0$. The problem of minimizing $\|Ax-b\|$ can be treated using the objective function $\phi=\frac{1}{2}\|Ax-b\|^2$. Saddle-point theory applied to ϕ then provides a set of necessary conditions. Kuhn and Tucker (1951) derived from it what they referred to as "constraint qualification", which places very important restrictive conditions on the nature of the set of feasible solutions in the vicinity of the computed solution x^+. It requires that the negative gradient vector of ϕ at x^+ must be expressed as a non-negative linear

combination of outward pointing normals to the constraint hyperplanes on which x^+ lies. That is to say, that it lies in the convex cone based at the point x^+ and generated by the outward pointing normals. More recent works on functional analysis have developed this point and stress the optimization problem through the intersection of cones of displacement (Laurent, 1972).

For the CLS problem, a solution is then characterized by the following conditions (Lawson and Hanson, 1974): An n vector x^+ is a solution of the CLS problem if and only if there exists an m vector y and a partitioning of the integers 1 to m into subsets E (equality) and S (slack) such that

$$\begin{aligned} &C^T y = A^T(Ax-b) \\ &r_i = 0; \quad y_i > 0 \quad i \varepsilon E \\ &r_i > 0; \quad y_i = 0 \quad i \varepsilon S \quad \text{where } r = Cx-d. \end{aligned} \tag{13}$$

The quantity $-|A^T(Ax-b)|$ is then the negative gradient of the objective function $\phi = \|Ax-b\|^2$ and the lines of $(-C^T)$ represent outward pointing normals to the constraint hyperplanes.

If the NNLS problem may be solved, the point is now to reduce the CLS problem to the NNLS problem. This is done in two steps: reduction of the CLS problem to the LPD problem, and then change of the LDP problem to the NNLS problem.

(b) *Practice.* The reduction is carried out with the help of matrix decompositions as described in the first part of the present paper. An advantage of this procedure is a single singular-values analysis in the first step of the computation.

The first step is done through a change of basis for the vector x. The matrix decomposition which leads to $A = USV^T$ Eq. (5) can be written

$$|A| = |U_1 U_2| \begin{vmatrix} S & 0 \\ 0 & 0 \end{vmatrix} \begin{vmatrix} V_1^T \\ V_2^T \end{vmatrix}. \tag{14}$$

Then by a change of variables $x = V_1 y$, the problem of minimizing the quantity $\|Ax-b\|$ reduces to:

$$\begin{aligned} &\text{minimize } \phi = \|b-Ax\|^2 = \|-Sy+b_1\| + \|b_2\| \\ &\text{with} \quad b_1 = U_1^T b \\ &\qquad\quad b_2 = U_2^T b \end{aligned} \tag{15}$$

A further change of variables $z = Sy - b_1$ reduces the function to

$$\phi = \|z\|^2 + \|b_2\|^2. \tag{16}$$

The problem is now reduced to the LDP problem, except for the additive constant $\|b_2\|^2$:

$$\begin{aligned} &\text{Minimize } \|z\| \text{ subject to } \hat{C}z > \hat{d} \\ &\text{with} \qquad \hat{C} = CV_1 S^{-1} \\ &\qquad\quad \hat{d} = d - CV_1 S^{-1} b_1. \end{aligned} \tag{19}$$

The second step is the transformation from the LDP to the NNLS problem. This can be done through the following change: compute a vector u solving the NNLS conditions:

$$\text{Minimize } \|Eu-f\| \text{ subject to } u>o \tag{18}$$

$$\text{with } E=\begin{vmatrix}\hat{C}^T\\ \hat{d}^T\end{vmatrix} \quad \begin{array}{l}\text{and } f \text{ an } n+1 \text{ vector with all elements}\\ \text{equal to zero except } (n+1)\text{th.}\end{array}$$

The gradient vector of the objective function $\frac{1}{2}\|z\|^2$ in the LDP is simply z. The Kuhn-Tucker conditions require z to be expressible as a nonlinear combination of the row of $\hat{C}^T$. Then z is expressed as

$$z=\hat{C}^T u\|r\|^{-2} \quad \text{with} \quad \|r\|^2=r^T r=r^T\|Eu-f\|. \tag{19}$$

3. Application to Gravity Data

Gravity profile interpretation may be aided through linear system inversion techniques. Two-dimensional density distributions can be selected to represent geological structures. The gravitational attraction due to simple sources represented by polygons is easily calculated by the now classical formula of Talwani et al. (1959). Since the formula is linear with respect to density, a linear system of equations can be constructed yielding a theoretical gravity value at any point. Provided that observed gravity values are available at these points, density contrasts can be adjusted in order to minimize the residuals between observed and computed values of the field.

The assumed structure which underlies the gravity anomaly is divided into several cells by an automatic partitioning or by a more elaborate method which can incorporate results from previous geophysical surveys. Each cells is then represented by a regular polygon.

The gravitational attraction of a k-sided polygon is given by

$$g=2G\rho\sum_{l=1}^{k} Y_l. \tag{20}$$

Where G is the universal gravitational constant and ρ the density. Y_l is the kernel function for one side and is a function of x_l, z_l, corners of the polygon.

The problem reduces to a linear system like Eq. (1) with the solution vector $b=g_i$ the gravity measurements, the unknown vector $x=\rho_j$ the density contrast, and the matrix $A=aij$, represents the gravitational attraction of the j^{th} prism at the i^{th} point of observation. Details of constructing this system may be found in a previous paper (Vigneresse, 1977).

4. Discussion

The inverse problem in gravity interpetation has already been examined by these techniques. To date, several papers have been published, each using different criteria for the optimization of the residuals.

In a first stage, most of the authors have assumed density contrasts and adjusted vertical coordinates of the bodies by means of either iterative processes (Tanner, 1967; Qureshi and Mula, 1971) or least-squares methods (Corbato, 1965). Later, methods with better convergence have been developed through least-squares techniques and generalized inversion (Braile et al., 1974; Philips, 1974; Jupp and Vozoff, 1975). The problem of stability has been partially solved by the Backus and Gilbert (1967, 1968) method (Green, 1975) and by ridge regression (Inmann, 1975). Different criteria for norm minimization have been proposed (Claerbout and Muir, 1973) and compared with each other (Vigneresse, 1977). As far as errors in the data affect the solution, the problem is better solved with the introduction of a damping factor in the least-squares approximation (Crosson, 1976; Aki and Lee, 1976) or using covariance matrix techniques (Jackson, 1976; Burkhard and Jackson, 1976).

From the point of view of the very recent development of the inverse problem (Parker, 1975, 1977; Sabatier, 1977a and b), the method described above may certainly be considered as "old fashionned". The fact is that Parker's philosophy of determining all solutions acceptable for the problem is very reasonable. Unfortunately, this is very time consuming (Sabatier, 1977a). Another point is the basic assumption of a homogenous structure underlying all these methods. Any geologist will have serious criticisms about this. These are the main reasons why the present method has been developed.

When inverting real data, both oscillations and smoothing effects occur but they may be used in order to approach a "better" solution. A solution remains to be found in which the density contrasts are limited within a physically acceptable range, taking into account the other available data for the structure. In that sense the method can be viewed as a compromise between an arbitrary search through model calculations (direct method) and a mathematical inverse problem (automatic adjustements of depth parameters).

The method has been tested with several synthetic models. In all cases the inversion was done in a very short time and gave the previously assumed density contrasts.

In order to simplify the procedure, the same test has been done for several runs in the computer with different initial parameters. An ideal structure had been computed by the usual Talwani et al. (1959) method. It seemed interesting to take the same test model as used by Braile et al. (1974) in order to compare the accuracy (Fig. 2).

Furthermore a test has been made by introducing random noise in the synthetic data. The noise level was progressively raised in order to observe the failing of the method. Up to a noise level of approximatively 20%, the results are within an acceptable range. In fact this follows from the implicit supplementary constraints which result from the location of the geometrical parameters of the model. If a set of cells has exactly the shape of the test model then inversion can be done up to high noise levels. When the division into cells does not approximate the model exactly, however, some differences are found during the least-squares inversion. With respect to the depth, a lower bottom for the structure causes the density contrasts to oscillate while they are smoothed when the top to the structure is higher than that of the model. Such troubles are

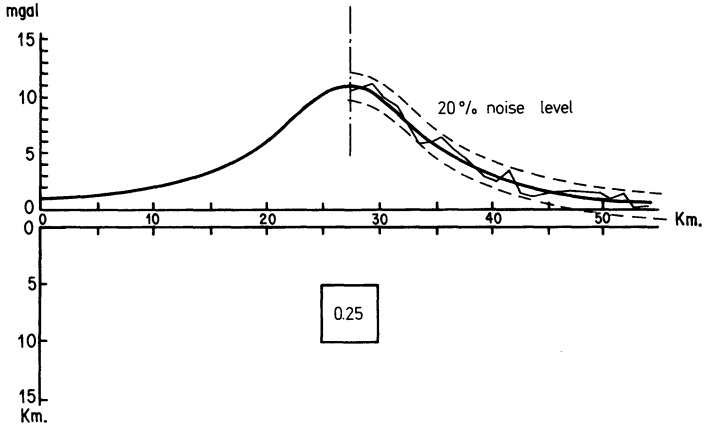

Fig. 2. Test model in the present paper. On the right hand side noise has been added with a noise level of 20%

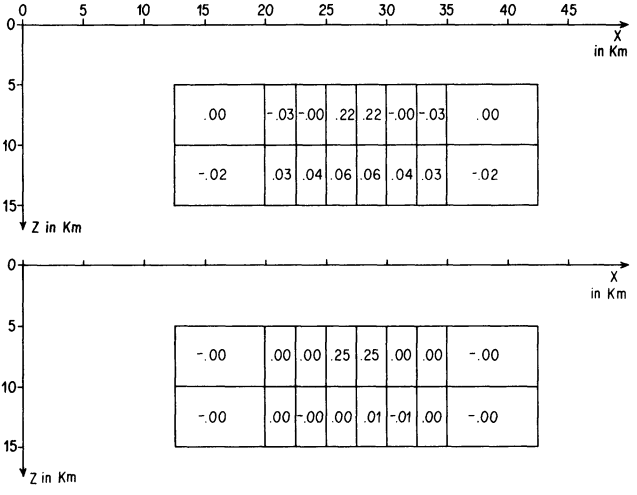

Fig. 3. Test model anomaly inversion. (*a*) damped least squares method; (*b*) constrained least squares method. Upper bound was 1.00 g/cm^3 and lower bound -1.00 g/cm^3

nearly always found during least-squares inversion, but the introduction of constraints reduces the amplitude of the variations. Smoothed values occur only when the structure is higher than the source, which is probably due to the equivalent-layer theorem. Lateral displacement of the cells may affect the result, though in fact only the edges of the structure are affected. If a cell comprises part of the model as well as the host rock, a density contrast which combines their respective densities will be assigned by the procedure. If one cell overlaps the model, then it will be given a density contrast result of a combination of both density contrasts of the model and surrounding structures. The introduc-

tion of constraints upon the solution vector severely reduces the instability during the inversion. An exemple is presented in Fig. 3. The test model anomaly is inverted using both techniques of damped least squares and constrained least squares. The cell structure chosen fits the cell shape, but its lateral extension is less than the length of the profile. This results in a long wavelength instability which manifests itself in an ill conditioning of the coefficient matrix (Vigneresse, 1977). In the damped case, the computer tries to fill the lower cells in order to deal with the long wavelengths. The result is shown in Fig. 3a. The constrained inversion was done using a density contrast of $+1$ and $-1\,g/cm^3$ as upper and lower bounds, respectively. The instability is reduced as one can see in Fig. 3b. The introduction of constraints into the solution results in the construction of a convex hull into which all feasible solutions for the problem fall. In that sense the problem can be viewed as a convex rather than a linear problem (Sabatier, 1977a).

5. Applications

The present method has been developed for a specific geological problem. For a long time, geologists have been interested in the determination of the shape of the roots (bottom) of batholiths.

Gravity data can assist in this problem by calculating the shape of a batholith. This has been done by several authors using different methods. The main point is still unsolved because of a dogmatic assignment of the density contrast; it is generally assumed that the structure is homogenous and does not show variations in its physical parameters. Though it is quite easy to estimate the density contrasts existing at the outcrops, only assumptions are available for depths as great as some ten kilometers as inferred by several authors. Therefore, the determination of the structure, from a continuity in their density contrasts could be a less biased approach to the problem of plutonic roots.

Data are taken from the gravimetric anomaly map of Brittany, western France. Plutons are well known in this area; they consist of leucogranitic rocks dated from 310 m.y. (Cogné, 1974). They are easily recognisable on the Bouguer anomaly map as they are delineated by negative anomalies of some -25 mgal. Density contrast measurements have been carried out on their material (Weber, 1972); an average value for the granite is $2.61\,g/cm^3$ while the palaeozoic formations into which they intruded have a mean density value of $2.69\,g/cm^3$; this results in a gravity contrast of $-0.08\,g/cm^3$ between the granite and surrounding rocks. A profile has been constructed across the Guehenno massif (Fig. 4). Constraints have been placed upon the solution vector. Density constrast is allowed to vary within the range $-0.12\,g/cm^3$ and $+0.05\,g/cm^3$. Inversion has been carried out through the above methods. Results have been compared with other automatic inversion processes (Tanner, 1967; Qureshi and Mula, 1971) (Fig. 5).

A few comments can be made on the results; since the decomposition into cells has been very crude. The decomposition presented shows a similar shape to that of the other methods. It results from several trials with more general

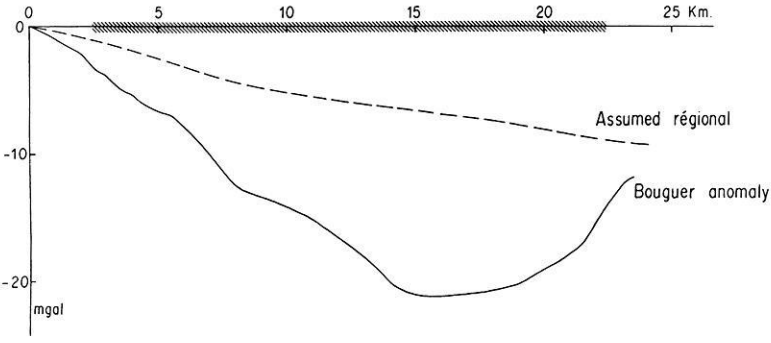

Fig. 4. Bouguer anomaly profile over a granitic pluton. Outcrops are indicated with hatches and measured surface density shown

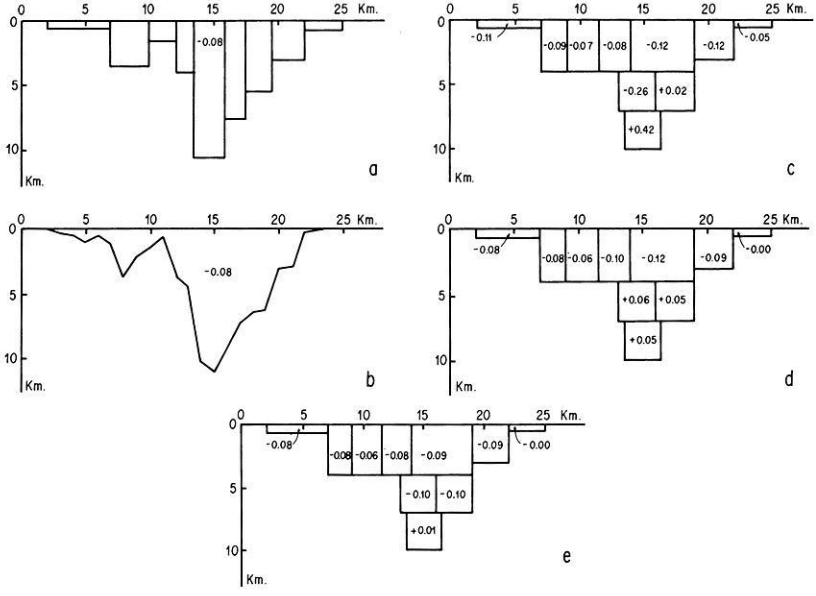

Fig. 5. Diagram showing the results of different methods of inverting gravity data. (*a*) Tanner's (1967) method; (*b*) Qureshi and Mula's (1971) method; (*c*) the classical least squares inversion; (*d*) a damped least squares inversion using Levenberg Marquardt's algorithm; (*e*) results from the constrained least squares optimization. Constraints have been choosen as -0.12 g/cm^3 and $+0.05$ g/cm

divisions. After two runs, convergence of the results leads to this structure. A first comment is the similarity of the results between all the three methods concerning the shape of the batholith. No problem is encountered here. However a significant difference occurs with respect to the depth of structure. Classical inversion methods for a structure having constant density throughout the body (i.e., homogeneity in its density contrast) indicate a greater depth for the root than the one computed through our inverse method. But the density contrasts

calculated by our method change with depth, thus, the batholith may be homogeneous from the point of view of the petrologist, but not for geophysicist. This may result from a density contrast between the body and the host rock which changes gradually from the surface (at the outcrop) to deeper levels in the upper crust.

Conclusions

A method has been developed which solves the gravimetric inverse problem by a linear least-squares approximation. Refinements to the classical method of matrix decomposition have been incorporated. The principal feature is the tapering of the eigenvalue spectrum, avoiding the effect of redundancy in the data. A supplementary and powerful condition is used assigning the convexity to the solution. Assuming that other available data allows a restricted range for the density contrasts, the solution is constrained to lie within that range. The introduction of such constraints during the computation severely stabilizes the method of matrix inversion and allows reasonable solution with limited time consumption. Tests upon synthetic models are significant even when noise is introduced into the data. When used upon real data the method shows good performances compared to other iterative methods of gravity interpretation.

Acknowledgments. This work has been done while the author benefited from a grant from the C.N.R.S. during his stay at the Centre Armoricain d'Etude Structurale des Socles (LP 004661) at Rennes. The author wishes to thank Dr. J.P. Lefort and Dr. J.P. Gerárd for their advice and encouragement and Dr. R. van der Voo for critically reading the manuscript.

References

Aki, K., Lee, W.H.K.: Determination of three-dimensional velocity anomalies under a seismic array using first *P* arrival times from local earthquakes – 1 – A homogeneous initial model. J. Geophys. Res. **81**, 4381–4399, 1976

Anderssen, R.S.: On the solution of certain overdetermined systems of linear equations that raise in geophysics. J. Geophys. Res. **74**, 1045–1051, 1969

Backus, G., Gilbert, F.: Numerical applications of a formalism for geophysical inverse problems. Geophys. J. Roy. Astron. Soc. **13**, 247–276, 1967

Backus, G., Gilbert, F.: The resolving power of gross earth data. Geophys. J. Roy. Astron. Soc. **16**, 169–205, 1968

Braile, L.W., Keller, G.R., Peeples, W.J.: Inversion of gravity data for two-dimensional density distributions. J. Geophys. Res. **79**, 2017–2021, 1974

Burkhard, N., Jackson, D.D.: Applications of stabilized linear inverse theory to gravity data. J. Geophys. Res. **81**, 1513–1518, 1976

Clearbout, J.F., Muir, F.: Robust modeling with erractic data. Geophysics **38**, 826–844, 1973

Cogné, J.: Le massif armoricain. In: Géologie de la France. J. Debelmas, ed.: Doin, 105–161, 1974

Corbato, C.E.: A least squares procedure for gravity interpretation. Geophysics **30**, 228–233, 1965

Crosson, R.S.: Crustal modeling of earthquake data. 1. Simultaneous least squares estimation of hypocenter and velocity parameters. J. Geophys. Res. **81**, 3036–3046, 1976

Fiacco, A.V., McCormick, G.P.: Non linear Programming: Sequential Unconstrained Minimization Techniques. New York: J. Willey and Sons 1968

Franklin, J.N.: Well-posed stochastic extensions of ill-posed linear problems. J. Math. Anal. Appl. **31**, 682–716, 1971

Gill, P.E., Murray, W.: Numerical Methods for constrained optimization. 284 pp. New York: Academic Press 1974

Green, W.R.: Inversion of gravity profiles by use of a Backus Gilbert approach. Geophysics **40**, 763–772, 1975

Hoerl, A.E., Kennard, R.W.: Ridge regression: Biased estimation for non orthogonal problems and applications to non orthogonal problems. Technometrics **12**, 55–82, 1970

Inmann, J.R.: Resistivity inversion with ridge regression. Geophysics **40**, 798–817, 1975

Jackson, D.D.: Most squares inversion. J. Geophys. Res. **81**, 1027–1030, 1976

Jupp, D.L.B., Vozoff, K.: Stable iterative methods for the inversion of geophysical data. Geophys. J. Roy. Astron. Soc. **42**, 957–976, 1975

Kuhn, H.W., Tucker, A.W.: Non linear Programming. In: Proceedings of the 2nd Berkeley symp. on Math. Stat. and, Prob., J. Neyman, ed.: Univ. of Calif. Press 481–492, 1951

Lanczos, C.: Linear differential operators. Van Nostrand 564 pp., 1961

Laurent, P.L.: Approximation et optimization. Hermann ed., Paris 531 pp., 1972

Lawson, C.L., Hanson, R.J.: Solving least squares problems. Prentice Hall 340 pp., 1974

Levenberg, G.: A method for the solution of certain non linear problems in least squares. Quart. Appl. Math. **2**, 164–168, 1944

Marquardt, D.W.: An algorithm for least squares estimation of non linear parameters. J. Soc. Indus. Appl. Math. **11**, 431–441, 1963

Marquardt, D.W.: Generalized inverse ridge regression, biased linear estimation and non linear estimation. Technometrics **12**, 591–612, 1970

Parker, R.L.: Theory of ideal bodies for gravity interpretation. Geophys. J. Roy. Astron. Soc. **42**, 315–334, 1975

Parker, R.L.: Understanding inverse theory. Ann. Rev. Earth. Planet. Sci. **5**, 35–64, 1977

Philips, R.J.: Techniques in Doppler gravity inversion. J. Geophys. Res. **79**, 2027–2036, 1974

Qureshi, I.R., Mula, H.G.: Two dimensional mass distributions from gravity anomalies: a computer method. Geophys. Prospect. **19**, 180–191, 1971

Sabatier, P.C.: Positivity constraints in linear inverse problem-I, General Theory. Geophys. J. Roy. Astron. Soc. **48**, 415–442, 1977a

Sabatier, P.C.: Positivity constraints in linear inverse problem-II, Applications. Geophys. J. Roy. Astron. Soc. **48**, 443–469, 1977b

Talwani, M., Worzel, J.L., Landismann, M.: Rapid gravity computations for two-dimensional bodies with applications to the Mendocino fracture zone. J. Geophys. Res. **64**, 49–59, 1959

Tanner, J.G.: An automated method of gravity interpetation. Geophys. J. Roy. Astron. Soc. **13**, 339–347, 1967

Vigneresse, J.L.: Linear inverse problem in gravity profile interpretation. J. Geophys. **43**, 193–213, 1977

Weber, C.C.: Le socle antétriasique sous la partie sud du bassin de Paris d'après les données géophysiques. Bull. B.R.G.M., II, 3 & 4, 219–343, 1972

Received December 12, 1977/Revised version July 21, 1978

J. Geophys. 45, 29–33, 1978

Journal of Geophysics

Reappraisal of Palaeomagnetism of the Colli Euganei and Monti Lessini Volcanics (Italy)*

J.E.T. Channell[1], V. De Zanche[2], and R. Sedea[2]

[1] Institut für Geophysik, ETH-Hönggerberg, CH-8093 Zurich, Switzerland
[2] Istituto di Geologia dell'Università, I-35100 Padova, Italy

Abstract. New information on the age of the volcanics from Colli Euganei and Monti Lessini shows that the division made by Soffel (1972, 1974, 1975a) of palaeomagnetic directions from the two areas into Eocene and Oligocene groups is not valid. The difference in mean direction of these groups was thought to indicate a rotation of this part of northern Italy of 50° during the intervening time period. This rotation can not be substantiated.

Key words: Palaeomagnetism – Age of Volcanism – Rotation of Italy.

1. Introduction

Soffel (1972, 1974, 1975a and b) has carried out palaeomagnetic studies of the volcanic rocks of Colli Euganei and Monti Lessini. The principle tectonic conclusion from these studies was that this part of northern Italy rotated relative to Europe by about 50° between Late Eocene and Middle Oligocene. Both at Colli Euganei and at Monte Lessini the characteristic remanence directions were divided into two groups one of which was associated with an Oligocene eruptive cycle and the other with an older Eocene cycle. This division could not be made solely on the basis of radiometric and palaeontological ages. A more or less arbitrary value of declination was chosen which divided the data into two groups within the loose constraint of the available dating. The difference between the mean directions of these two groups ($\sim 50°$) was interpreted as indicating an anticlockwise rotation of this magnitude between the eruption of the two cycles.

2. Colli Euganei

The first eruptions in the Colli Euganei have a Late Eocene age and are represented solely by basalts and basaltic breccias which are intercalated with marls allowing precise palaeontological dating (Dieni and Proto-Decima, 1963;

* Contribution No. 221, Institut für Geophysik, ETH Zürich

0340-062X/78/0045/0029/$01.00

De Vecchi and Sedea, 1974; Massari et al., 1976). This type of volcanism only occurred during Late Eocene.

On the other hand, the rhyolitic, trachytic and latitic rocks from this district tend to be intrusive and are dated radiometrically (Borsi et al., 1969) and palaeontologically (Dieni and Proto-Decima, 1970) as Early-Middle Oligocene.

The genetic evolution of the Tertiary magmatism of western Veneto is considered to represent a classic province of intercontinental rifting (De Vecchi et al., 1974, 1976).

The mid-Late Eocene age attributed by Soffel (1974) to most of the differentiated rocks of the eastern part of the Colli Euganei is not consistent with the stratigraphic, palaeontological and petrogenetic evidence. The data indicate that the magmatism of Colli Euganei occurred in the following order: basalts, rhyolites then trachytes, and finally latites. The latites certainly occurred after the rhyolites but it is more difficult to confirm their relationship with the trachytes. The basalts are the only magmatic product in the Euganei which can be attributed to the Upper Eocene. This is demonstrated both by radiometric dating (Borsi et al., 1969) as well as micropalaeontology, the zones *Globorotalia cerroazulensis cerroazulensis* and *G. cerroazulensis cocoaensis* (Toumarkine and Bolli, 1975) being commonly associated with the basalts.

The differentiated products (rhyolites, trachytes, latites) are Middle-Early Oligocene in age. This is based on micropalaeontological and radiometric dating and on their stratigraphic relationship with the Middle Eocene/Lower Oligocene Euganei marls. In the western part of the region, Soffel (1974) attributed most of the sampled differentiated igneous rocks to the middle-Late Eocene. Evidence from these localities for a younger age is available:

(a) The rhyolitic breccias of Monte Nuovo have been shown by radiometric dating to have an age of 33 ± 1 m.y. (Borsi et al., 1969).

(b) The latite breccias of Monte Croce (site 10) can be assigned, according to Dieni and Proto-Decima (1970), to the *Globigerina tapuriensis* zone (Blow, 1969) of the Early Oligocene. The rhyolitic breccia of Monte Ceva is associated with the same palaeontological zone.

(c) The trachytic body of Monte Alto (site 12) is stratigraphically above and cuts rhyolitic breccias dated palaeontologically as Early Oligocene.

(d) The rhyolites of Monte Cimisella (site 13) cut marls of Early Oligocene age.

(e) The trachytes of Monte Lonzina (site 23) cut marls of Late Eocene age (zone *Globorotalia cerroazulensis cerroazulensis* of Toumarkine and Bolli, 1975) and were erupted after the rhyolite of Monte Brusà (called M. Lonzina by Borsi et al., 1969) which has been dated as Oligocene (33 ± 1 m.y.).

(f) Sites 3, 5, 16 were located at M. Castello di Calaone, M. Orsara and M. Rua. At all three of these localities the differentiated igneous rocks post-date marls and basaltic products of Late Eocene age.

(g) In the case of the differentiated rocks from sites 5, 22, 24 and 25, there is no direct evidence as to their age because the Tertiary sedimentary cover is lacking, and no radiometric ages are available. The connection of these sites with the central part of the Colli Euganei volcanic complex is obscured by alluvium.

The samples collected by Soffel (1972, 1974) from the Colli Euganei region were all reported to be rhyolites (=liparites), trachytes, or latites (=andesites). They are therefore *all* due to the younger Oligocene eruptive cycle. The sampling sites cannot be divided into two groups on the basis of age. Therefore the two mean directions have no meaning and the supposed 50° rotation of this part of Italy in Eocene/Oligocene cannot be substantiated.

Soffel (1974) has presented some conclusive arguments for the primary nature of the magnetization of these volcanics and secondary magnetizations do not appear to have caused the observed scatter of site mean directions. At most localities it is not possible to see the relationship between the igneous rocks and the original horizontal and the lack of good tectonic control may explain the dispersion of site mean directions.

3. Monti Lessini

In the case of Monti Lessini, Soffel (1975a) also divided his palaeomagnetic mean directions into two groups, one of which was considered to be Early-Middle Oligocene and the other Middle-Late Eocene. Again, this division could not be made solely on the basis of age determinations and an arbitrary declination value of 180° was used as a dividing line. Re-examination of the ages of the basalts of Monti Lessini indicates that the age of certain of Soffel's palaeomagnetic sites must be revised.

(a) Site 14: the age of these volcanics near Marosticano is Oligocene (Piccoli, 1967) with very rare occurrences of Paleocene volcanoclastics (Dal Prá and Medizza, 1965).

(b) Site 2 and 33: the age of these volcanics from Monti Berici is Late-Middle Eocene rather than Oligocene as they are overlain by Upper Eocene biocalcarenites. The same age is also apparent for the basalts (sites 22 and 23) of southern Trentino (Castellarin, 1966).

(c) Most of Soffel's palaeomagnetic samples came from the central-eastern part of Monti Lessini, where the basalts are largely Middle Eocene, with some Early Eocene and Paleocene occurrences. Dykes and lava plugs of Eocene or Oligocene age are also frequent. We consider that certain of these sites (no. 3, 4, 10, 27, 31), which were attributed by Soffel to the Oligocene, are Middle Eocene in age. The Middle Eocene rifting produced maximum thicknesses of volcanics in the valleys of T. Alpone, T. Chiampo and T. Agno (Piccoli, 1966; De Zanche and Conterno, 1972). Site 10 is immediately beneath the limestones of Roncá which contain *Nummulites brongniarti* (Uppermost Middle Eocene). The samples from sites 3, 4, and 27 are found between the Roncá limestones and limestones containing *Nummulites fabianii* of Late Eocene age. The samples from localities 31/1 and 31/2 are intercalated with the limestones of S. Giovanni Ilarione which contain *Nummilites millecaput* of Lutetian age, and with the Roncá limestones.

The remanence directions from Monti Lessini are plotted in Figure 1a showing the age according to Soffel (1975a). The difference in the mean declinations of the two groups (Fig. 1a) was considered to indicate a 50° anticlockwise

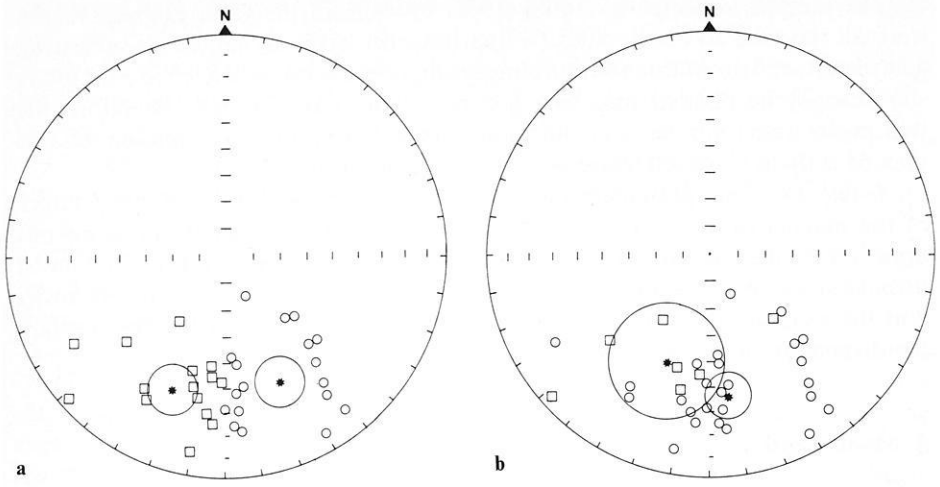

Fig. 1 a and b. Site mean directions from Monti Lessini (Soffel, 1975a) showing the Eocene (circles) and Oligocene sites (squares) according to Soffel (**a**) and according to this paper, based on latest information (**b**). The stars represent the means for the Eocene and Oligocene sites, and circular approximations to α_{95} are shown. All inclinations are negative

rotation of this part of Italy during the time interval between the two volcanic cycles. Our re-classification of these ages (Fig. 1 b) illustrates that the difference between the Eocene and Oligocene mean directions is, in fact, not well-defined. As in the case of Colli Euganei, the data from Monti Lessini do not provide evidence for any rotation during this time interval.

Acknowledgements. This work has been financially supported by the Centro di Studio per i Problemi dell'Orogeno delle Alpi Orientali – C.N.R. – Padova. We thank W. Lowrie, F. Heller, and R. Van der Voo for their comments.

References

Blow, W.H.: Late Middle Eocene to Recent planktonic foraminiferal biostratigraphy. Proc. I Intern. Conf. plankt. microfossils **1**, 199–422, 1969

Borsi, S., Ferrara, G., Piccoli, G.: Determinazione col metodo K/Ar dell'età delle eruzioni euganee. Rend. Soc. Ital. Mineral. Petrol. **25**, 27–34, 1969

Castellarin, A.: Carta geologica della zona tra l'Adige e il Sarca a Sud del Bondone (Trentino). Litografia Artistica Cartografica, Firenze, 1966

Dal Prà, A., Medizza, F.: Manifestazioni vulcaniche paleoceniche nella zona di Laverda sulle colline tra Thiene e Bassano (Vicenza). Atti Accad. Naz. Lincei, Rend. Cl. Sc. Fis. Mat. Nat. **39**, 106–112, 1965

DeVecchi, Gp., Gregnanin, A., Piccirillo, E.M.: Le rocce eruttive dei Colli Euganei. Chimismo, nomenclatura e considerazioni petrogenetiche. Mem. Ist. Geol. Min. Univ. Padova **30**, 1–25, 1974

DeVecchi, Gp., Gregnanin, A., Piccirillo, E.M.: Aspetti petrogenetici del vulcanesimo terziario veneto. Mem. Ist. Geol. Min. Univ. Padova **30**, 1–32, 1976

DeVecchi, Gp., Sedea, R.: Sui basalti eocenici dei Colli Euganei. Mem. Ist. Geol. Min. Univ. Padova **31**, 1–26, 1974

De Zanche, V., Conterno, T.: Contributo alla conoscenza geologica dell' orizzonte eocenico di Roncá nel Veronese e nel Vicentino. Mem. Acc. Patav. Sc. Lett. Arti, Cl. Sc. Mat. Nat. **84**, 287–295, 1972

Dieni, I., Proto Decima, F.: Eruzioni sottomarine con lave a cuscini nell'Eocene superiore dei Colli Euganei. Mem. Acc. Patav. Sc. Lett. Arti, Cl. Sc. Mat. Nat. **74**, 161–170, 1963

Dieni, I., Proto Decima, F.: Documentazione paleontologica dell'età oligocenica inferiore del vulcanismo euganeo. Mem. Acc. Patav. Sc. Lett. Arti, Cl. Sc. Mat. Nat. **77**, 321–360, 1970

Massari, F., Medizza, F., Sedea, R.: L'evoluzione geologica dell'area euganea tra il Giurese superiore e l'Oligocene inferiore. In Piccoli et al. 1976. Mem. Ist. Geol. Miner. Univ. Padova **30**, 174–197, 1976

Piccoli, G.: Studio geologico del vulcanismo paleogenico veneto. Mem. Ist. Geol. Min. Univ. Padova **26**, 1–100, 1966

Piccoli, G.: Illustrazione della carta geologica del Marosticano occidentale fra Thiene a la valle del torrente Laverda nel Vicentino. Mem. Ist. Geol. Miner. Un. Padova **26**, 1–14, 1967

Soffel, H.: Anticlockwise rotation of Italy between the Eocene and Miocene: paleomagnetic evidence from the Colli Euganei, Italy. Earth Planet. Sci. Lett. **17**, 207–210, 1972

Soffel, H.: Palaeomagnetism and rock magnetism of the Colli Euganei volcanites and the rotation of Northern Italy between Eocene and Oligocene. Boll. Geofis. Teor. Appl. **16** (64), 333–355, 1974

Soffel, H.: The palaeomagnetism of age dated tertiary volcanites of the Monti Lessini (Northern Italy) and its implications to the rotation of Northern Italy. J. Geophys. **41**, 385–400, 1975a

Soffel, H.: Rock magnetism of the Monti Lessini and Monti Berici volcanites and age of volcanism deduced from the Heirtzler polarity time scale. J. Geophys. **41**, 401–411, 1975b

Toumarkine, M., Bolli, H.M.: Foraminifères planctoniques de l'Eocène Moyen et Supérieur de la Coupe de Possagno. In: Monografia Micropaleontologica sul Paleocene e l'Eocene di Possagno, Provincia di Treviso, Italia. H.M. Bolli, ed. Schweiz. Palaeont. Abh. **97**, 69–83, 1975

Received June 20, 1978 / Accepted September 25, 1978

J. Geophys. 45, 35–39, 1978

Journal of Geophysics

Reinterpretation of Palaeomagnetism of the Colli Euganei and Monti Lessini (Italy)

H. Soffel

Institut für Allgemeine und Angewandte Geophysik, Universität München, Theresienstraße 41, D-8000 München 2, Germany

Abstract. New information on the age of the volcanics from the Colli Euganei and Monti Lessini (Northern Italy) collected by Channell et al. (1978) show that the divisions made by Soffel (1972, 1974, 1975a) of palaeomagnetic directions from the two areas into Eocene and Oligocene groups had to be modified. From the data of both sampling areas alone an anticlockwise rotation of the area between Eocene and Oligocene can no longer be clearly demonstrated. However, a combination of the predominantly Oligocene data from the Colli Euganei with the predominently Eocene data from the Monti Lessini as well as their comparison with corresponding palaeomagnetic data from Stable Europe brings enough statistical evidence for an anticlockwise rotation of the area of at least 20–30° between Upper Eocene and Lower to Middle Oligocene.

Key words: Palaeomagnetism – Age of Volcanism – Rotation of Italy.

1. Introduction

Channell, De Zanche and Sedea (1978) have presented valuable new information about the ages of many volcanic units which have been studied with respect to their palaeomagnetic and rock magnetic properties by Soffel (1972, 1974) in the Colli Euganei and later (Soffel, 1975a and b) in the Monti Lessini in Northern Italy. In the area of the Colli Euganei with two cycles of volcanic activities (one in Eocene, a second in Oligocene) Soffel (1972, 1974) interpreted an extremely non-Fisherian distribution of remanence directions ($225.5° > D > 122.3°$) in terms of two groups of remanence directions setting a dividing line at about $D = 180°$. All volcanic units (some of them with radiometric ages around 33 m.y.) with a declination $D > 180°$ were classified as Oligocene, all with $D < 180°$ as Eocene. A declination difference of about 50° was found between the two groups.

With this working hypothesis, additional sampling was made in the nearby Monti Lessini, where many volcanics of Eocene age crop out, some of them

0340-062X/78/0045/0035/$01.00

radiometrically dated as around 47 m.y. old. Also in this region an extremely non-Fisherian distribution of remanence directions was found ($239.9° > D > 131.9°$). Like in the Colli Euganei, two groups of remanence directions were postulated setting again the dividing line at about $D = 180°$. All radiometrically dated volcanic units of Eocene age and others which could be classified as Eocene from the available geological maps had in general declinations smaller than 180°. Some of the volcanites with $D > 180°$ could clearly be identified as Oligocene. However, some units could not attributed to one of the two age groups because of lack of detailed geological information available at that time.

The ages of some volcanic units from both sampling areas are still uncertain, even after the study of Channell et al. (1978). In order to avoid further confusion, their palaeomagnetic data have been left out from the following discussion.

Simply because of lack of a sufficient number of unambiguous Eocene remanence directions in the Colli Euganei area, I agree with Channell et al. (1978) and their statement, that "a 50° anticlockwise rotation of the area between Eocene and Oligocene can no more be substantiated". However, this does not devalue the remanence directions of the "clearly" Oligocene volcanic units of the Colli Euganei for any further comparison with the remanence directions of "clearly" Eocene volcanics from the Monti Lessini and with corresponding palaeomagnetic data from Stable Europe. "Clearly" in this context means that the critical revision of the ages of volcanism by Channell et al. (1978) is fully accepted at the moment, although, as has been mentioned previously, it may be difficult in some places to state whether a certain volcanic unit is still uppermost Late Eocene or already youngest Lower Oligocene from biostratigraphy or purely petrological evidence alone.

2. Reinterpretation of the Palaeomagnetic Data

Figure 1a shows the mean remanence directions of the "clearly" Oligocene volcanic units of the Colli Euganei (C) and Monti Lessini (M). The numbers refer to the site numbers in the corresponding papers (Soffel, 1972, 1974, 1975a). There is a fairly well and closely grouped Fisherian distribution of Oligocene remanence directions from both sampling areas with the following mean (open square): $N = 17$, $R = 16.43$, $D = 200.2°$, $I = -52.5°$, $k = 28.3$, $\alpha_{95} = 6.4°$. This group is surrounded by 8 "satellite" remanence directions, which are in general about 30° apart from the marginal directions of the closer group. The mean also including these 8 remanence directions is (open diamond): $N = 25$, $R = 22.16$, $D = 189.5°$, $I = -46.7°$, $k = 8.5$, $\alpha_{95} = 9.6°$. It must be noted here that the inclusion of the 8 "satellite" remanence directions reduces the precision parameter k from 28.3 (an average value of k for a group of volcanic rocks of the same age) to a very low value of only 8.5. This may be due to lack of sufficient tectonic control implying undetected tilts up to about 60°. The absence of almost any tilts in the Monti Lessini area and the presence of only small tilts in the Colli Euganei call this in question. Eventually older (Eocene) ages may be the reason for the directions with D around 150°, although part of them

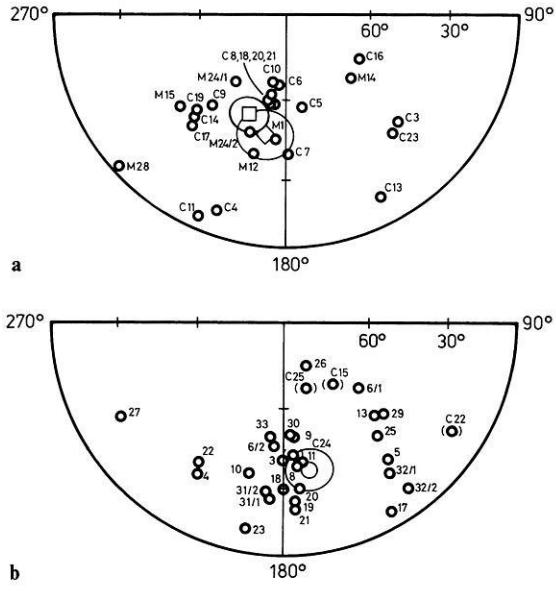

Fig. 1 a and b. Site mean directions of stable remanence of the Colli Euganei **(C)** and Monti Lessini **(M)** area. Only reversed directions are shown. Numbers refer to site numbers. The circles of 95% confidence are also shown. **a** Oligocene directions. Mean of all sites: open diamond. Mean of the closely grouped directions: open square. **b** Eocene directions. Mean of all sites from the Monti Lessini, excluding M27 and those in brackets of uncertain age from the Colli Euganei: open circle

were classified as "clearly". Oligocene by Channell et al. (1978). Some intermediate geomagnetic field directions may also contribute to the scatter of the 8 "satellite" remanence directions.

Figure 1 b shows the mean remanence directions of the "clearly" Eocene volcanic units. They come entirely from the Monti Lessini (M) area. Numbers refer to the site numbers according to Soffel (1975 a). The remanence directions of 4 sites from the Colli Euganei (C15, C22, C24, C25) are also plotted in brackets. There is no direct evidence for their age according to Channell et al. (1978). They have been regarded as Eocene by Soffel (1972, 1974). Considering only the data from the Monti Lessini (discarding M27 because of too large deviation from the remaining group) the following mean is obtained and plotted in Figure 1 b as an open circle: $N=26$, $R=23.89$, $D=169.9°$, $I=-36.7°$, $k=11.8$, $\alpha_{95}=8.0°$. Including also M27 we get the following mean: $N=27$, $R=24.38$, $D=172.5°$, $I=-36.9°$, $k=9.9$, $\alpha_{95}=8.6°$. An exclusion of one site out of 27 sites, which reduces the precision parameter k by about 20%, seems to be justified. Tentatively including besides M27 also the 4 directions of the eventually Late Eocene sites from the Colli Euganei yields the following mean: $N=31$, $R=27.77$, $D=169.8°$, $I=-38.8°$, $k=9.3$, $\alpha_{95}=8.3°$. All three means for Eocene differ only by less than 3°. Site numbers M5, M6/1, M6/2, M8, M9, and M12 have radiometric ages of around 47 m.y. (see Soffel, 1975 a). Their mean is: $N=6$, $R=5.76$, $D=163.2°$, $I=-44.0°$, $k=20.7$, $\alpha_{95}=15.0°$. This also indicates that the mean Eocene remanence direction is situated rather in the second than in the third quadrant.

Figure 2 shows the mean of the closely grouped (open square) Oligocene directions. The Oligocene mean including also the 8 "satellite" directions is plotted as open diamond. The open circle is the mean Eocene direction (excluding

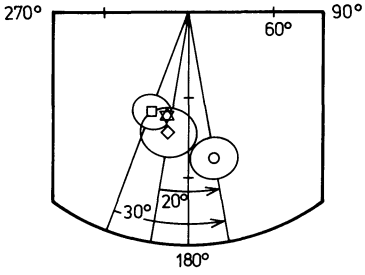

Fig. 2. Means of the Oligocene (open square and diamond) and Eocene (open circle) directions. For details see text and caption of Fig. 1. Open star: expected remanence direction for Lower Tertiary in the sampling area (see text). The amounts of anticlockwise rotation are indicated

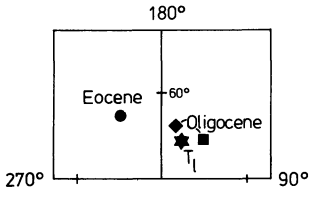

Fig. 3. Pole positions. Star: mean pole position for Lower Tertiary (T_1) after McElhinny (1973). Diamond: Oligocene (all). Square: Oligocene (closely grouped). Circle: Eocene

M27). The corresponding circles of 95% confidence are also shown. In order to test the significance of the difference between the means for Oligocene and Eocene the *F*-test after Watson (1956) was applied yielding the following values:

(a) Oligocene, closely grouped directions: $N_1=17$, $R_1=16.43$. Eocene: $N_2=26$, $R_2=23.89$. Total of both groups: $N=43$, $R=39.29$. *F*-ratio: 15.76. Critical value for the 95% confidence level: 3.20 and for the 99% confidence level: 5.15.

(b) Oligocene, including the 8 "satellite" directions: $N_1=25$, $R_1=22.16$. Eocene: $N_2=26$, $R_2=23.89$. Total of both groups: $N=51$, $R=45.50$. *F*-ratio: 4.79. Critical value for the 95% confidence level: 3.18 and for the 99% confidence level: 5.05.

According the McElhinny (1973) the mean pole position for Lower Tertiary (T_1) of Stable Europe is: $\lambda'=151°$ E, $\varphi'=75°$ N (see Fig. 3, star). For the mean sampling locality ($\lambda=11.4°$ E, $\varphi=45.4°$ N) the expected remanence direction is: $D=191.6°, I=-52.8°$, which is also plotted in Figure 2 has an open star. This value is in agreement within the limits of error with what has been measured for the Lower to Middle Oligocene in the Colli Euganei and Monti Lessini area. Yet its declination is at least 20° different from the Late Eocene value.

The pole positions are shown in Fig. 3 using the same (closed) symbols as for the remanence directions in Fig. 2. Star ($\lambda'=151°$ E, $\varphi'=75°$ N): Lower Tertiary of Stable Europe according to McElhinny (1973). Square ($\lambda'=133.8°$ E, $\varphi'=70.2°$ N): Oligocene, closely grouped data alone. Diamond ($\lambda'=164.8°$ E, $\varphi'=71.0°$ N): Oligocene, all data. Circle: ($\lambda'=213.1°$ E, $\varphi'=63.7°$ N): Eocene.

According to the standard criteria in palaeomagnetism, especially regarding the statistical evidence for the difference between the mean remanence directions of the "clearly" Oligocene and Eocene groups, the statement of Channell et al. (1978), that "a 50° anticlockwise rotation of this part of Northern Italy can not be substantiated" has to be modified. There seems to be sufficient statistical

evidence that an anticlockwise rotation within the short time interval between Late Eocene and Lower to Middle Oligocene of 20–30° took place. The uncertainties of some ages, which tend to bring the two groups of data together thus reducing the difference of the means and increasing their internal scatter favour an even larger amount of rotation between Eocene and Oligocene.

Acknowledgement. The author is indepted to Dr. Channell (Zürich) and his colleagues from the Geological Institute of the University of Padova for critically reviewing the ages of volcanism in the Colli Euganei and Monti Lessini. The helpful remarks and suggestions of Professor Dr. G. Angenheister, Dr. A. Schult and Dr. N. Petersen are kindly acknowledged.

References

Channell, J.E.T., De Zanche, V., Sedea, R.: Reappraisal of Palaeomagnetism of the Colli Euganei and Monti Lessini (Italy). J. Geophys. **45**, 29–33, 1978

McElhinny, W.M.: Palaeomagnetism and Plate Tectonics. p. 206. Cambridge: The University Press 1973

Soffel, H.: Anticlockwise rotation of Italy between Eocene and Miocene: palaeomagnetic evidence from the Colli Euganei, Italy. Earth Planet. Sci. Lett. **17**, 207–210, 1972

Soffel, H.: Palaeomagnetism and rock magnetism of the Colli Euganei volcanites and the rotation of Northern Italy between Eocene and Oligocene. Boll. Geofis. Teor. Appl. **16** (64), 333–355, 1974

Soffel, H.: The palaeomagnetism of age dated Tertiary volcanites of the Monti Lessini (Northern Italy) and its implication to the rotation of Northern Italy. J. Geophys. **41**, 385–400, 1975a

Soffel, H.: Rock magnetism of the Monti Lessini and Monte Berici volcanites and age of volcanism deduced from the Heirtzler polarity time scale. J. Geophys. **41**, 401–411, 1975b

Watson, G.S.: Analysis of dispersion on a sphere. Monthly Notices Roy. Astron. Soc. Geophys. Suppl. **7**, 153–159, 1956

Received August 4, 1978 / Accepted September 25, 1978

J. Geophys. 45, 41–65, 1978

Journal of Geophysics

Observations of the Initial Development of an Auroral and Magnetic Substorm at Magnetic Midnight

J. Untiedt[1], R. Pellinen[2], F. Küppers[1], H.J. Opgenoorth[1], W.D. Pelster[1], W. Baumjohann[1], H. Ranta[3], J. Kangas[4], P. Czechowsky[5], and W.J. Heikkila[6]

[1] Institut für Geophysik der Universität Münster, Gievenbecker Weg 61, D-4400 Münster, Federal Republic of Germany

[2] Division of Geomagnetism, Finnish Meteorological Institute, Vuorikatu 24, Bos 503, SF-00100 Helsinki 10, Finland

[3] Geophysical Observatory, SF-99600 Sodankylä, Finland

[4] Dept. of Physics, University of Oulu, Linnanmaa, SF-90100 Oulu 10, Finland

[5] Max-Planck-Institut für Aeronomie, Postfach 20, D-3411 Katlenburg-Lindau 3, Federal Republic of Germany

[6] Center for Space Sciences, University of Texas at Dallas, Richardson, Texas 75080, USA

Abstract. On April 6, 1975 a rather well isolated magnetic substorm began with a sharp onset at 2122 UT one hour after a clear southward turning of the interplanetary magnetic field. We report on results of observations obtained with meridian chains of magnetometers, all sky cameras, riometers, and short period pulsation magnetometers, plus additional stations and equipment, one hour before and a few minutes around the onset of a substorm at magnetic midnight within the Scandinavian area.

The time interval before onset was mainly characterized by an auroral arc which drifted southward in parallel with a westward electrojet and with a bay-like weak absorption region. The arc being located above the northern half of the electrojet showed intermittent local distortions, including a mature spiral, which in each case was accompanied by local pi B type magnetic pulsations. The spiral enclosed a region of upward directed field-aligned current as inferred from local distortions of the magnetic field at ground. Possibly the electrojet was due to a large-scale westward electric field, with the intensity of the corresponding field-aligned currents amounting to values of the order of 1 Akm^{-2} at the time when auroral distortions first appeared.

At substorm onset, the westerly part of the midnight auroral breakup region seems to have been observed by our all-sky cameras. This region was also characterized by strong cosmic noise absorption; it was surrounded by an anticlockwise (if viewed from above) differential equivalent current vector circulation, which indicates that the breakup occurred below a region of intense upward field-aligned currents switched on during substorm onset. Such a conclusion seems to be supported by our simultaneous radio wave backscatter amplitude and Doppler shift observations.

Key words: Auroral substorm – Magnetic substorm – Growth phase – Auroral electrojet – Auroral loops.

0340-062X/78/0045/0041/$05.00

1. Introduction

Numerous papers have been written on the magnetospheric substorm based on results of satellite, rocket, balloon, and ground based observations. The general pattern of the substorm both on the global and on the magnetospheric scale seems to be rather well known, and has been described in several monographs and review articles (e.g., Akasofu, 1968, 1977; Rostoker, 1972; Russell and McPherron, 1973). However, because of limited observation facilities there are many details of the picture for which an accurate description both in space and time is still impossible. Also, the physical relationship between the different phenomena occurring at the same time is rather unclear, in many cases. Near the earth this is especially true for the very limited area of the auroral oval close to magnetic midnight where the breakup phase of the auroral substorm usually occurs. Our present paper reports on ground based observations of different types made under this area when it was situated over Northern Scandinavia on April 6, 1975, one hour before and during the early expansion phase of a rather isolated substorm.

The instruments from which data have been used in our study include meridian chains of all-sky cameras, of magnetometers, and of riometers. Among others, additional data were available from a radio-wave backscatter facility measuring both signal intensity and Doppler shift, and from several pulsation magnetometers.

Originally, the event was selected because of its remarkably large steplike magnetic D disturbance occurring at the time and near the location of the auroral breakup. Later, it was found that the one hour interval before this magnetic onset, possibly constituting a substorm growth phase (McPherron, 1970), also exhibited interesting relationships between the local magnetic and auroral phenomena.

2. Instruments

Within this section we give a short description of the main instruments from which data have been used in the present study. The location and other details of each instrument may be taken from Fig. 1 or from Table 1.

The five all-sky cameras set up by the Finnish Meteorological Institute approximately in a north-south chain are of a new design (Hyppönen et al., 1974), with digital time display accurate to the nearest second. The 16 mm colour film is processed to ASA rating 1000, permitting an exposure time of 2 s. Radioactive sources were used to activate calibration surfaces visible on each photograph, for calibrations within both the red and green parts of the spectrum. During the time interval considered in this study the stations were run at the rate of one frame per minute, with the one exception of Ivalo. There, due to a fortunate malfunction, the camera operated at eight frames per minute just around the time of the auroral breakup.

In order to compare the locations of aurorae relative to other observed phenomena, structures like arcs, spirals etc. have been digitized, rectified, and

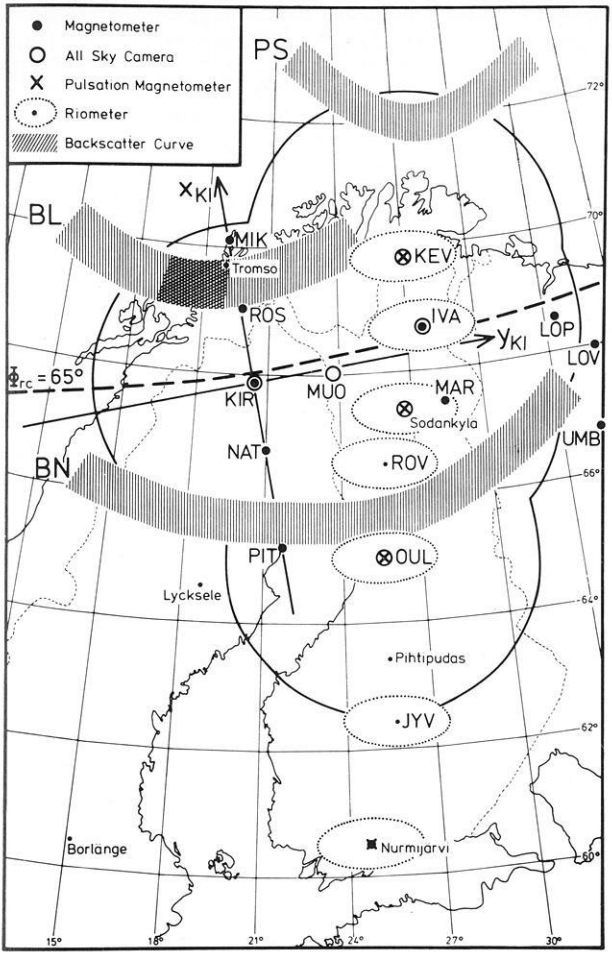

Fig. 1. Map of stations situated within Scandinavian area. Observational coverage through all-sky cameras is indicated by a solid curve (as defined by 70° elevation angle and 110 km height); corresponding coverage of each riometer is represented by a dotted curve. Backscatter curves: PS: transmitter at Pihtipudas, receiver at Sodankylä; BL and BN: transmitter at Borlänge, receiver at Lycksele and Nurmijärvi, respectively. Crosshatched part of curve BL corresponds to narrow beam receiver. The x_{KI}, y_{KI} coordinate system which is being used widely within this study, is also shown. The broken line denoted by $\phi_{rc}=65°$ represents a curve of constant revised corrected geomagnetic latitude. For more explanation see text

mapped assuming a height of 100 km (Boyd et al., 1971). If possible, lower borders of aurorae were used during the digitization process. In most cases, the same auroral structure was digitized from photographs of several cameras and the results were compared after mapping. Generally the mapped structures coincided within about 20 km, with the exception of weak aurorae or structures recorded at low elevation angles.

For the present study, magnetograms were available from the first five stations of the University of Münster magnetometer array that has been installed

Table 1. Permanent or temporary stations from which data have been used, mainly, in the present study

Station	Symbol	Geograph. Coord.		RCGL[a]	Type of instrument[b] and running institution[c] (in brackets)		
Ny Alesund	NYA	78.9°N	11.9°E	75.9°	M(AOT)		
Bear Island	B4	74.5	19.0	71.3	M(AOT)		
Mikkelvik	MIK	70.1	19.0	67.1	M(UM)		
Rostadalen	ROS	69.0	19.7	66.0	M(UM)		
Kiruna	KIR	67.8	20.4	64.8	M(UM)	ASC(KGI)	
Nattavara	NAT	66.8	21.0	63.7	M(UM)		
Pitea	PIT	65.2	21.6	62.2	M(UM)		
Kevo	KEV	69.8	27.0	66.2		ASC(FMI)	R, P
Ivalvo	IVA	68.6	27.5	65.0	M(TUB)	ASC(FMI)	R
Muonio	MUO	68.0	23.6	64.8		ASC(FMI)	
Sodankylä	SO	67.4	26.6	63.9		ASC(FMI)	R, P
Martii	MAR	67.5	28.3	63.9	M(TUB)		
Rovaniemi	ROV	66.6	25.8	63.2			R
Oulu	OUL	65.1	25.5	61.8		ASC(FMI)	R, P
Jyväskylä	JYV	62.4	25.7	59.0			R
Nurmijärvi	NU	60.5	24.6	57.0	M(FMI)		R, P
Loparskaya	LOP	68.6	33.3	64.7	M(PGIA)		
Lovozero	LOV	68.0	35.0	64.1	M(PGIA)		
Umba	UMB	66.7	34.5	62.9	M(PGIA)		

[a] Revised Corrected Geomagnetic Latitude (Gustafsson, 1970)
[b] M: magnetometer; ASC all-sky camera; R: riometer; P: pulsation magnetometer
[c] If not explained unambiguously within text;
FMI: Finnish Meterorological Institute; UM: University at Münster; TUB: Technical University at Braunschweig; KGI: Kiruna Geophysical Institute; PGIA: Polar Geophysical Institute at Apatity; AOT: Auroral Observatory at Tromsö

stepwise in 1974–1976 for groundbased observations during the International Magnetospheric Study (IMS, 1976–1979) in Scandinavia (Küppers et al., 1979). The instruments are improved versions of the Gough-Reitzel magnetometer (Gough and Reitzel, 1967). They yield analog records with 1–2 nT or 2% of amplitude accuracy, and better than 10 s time resolution and accuracy. The five stations are located on a straight profile oriented perpendicularly to the line of constant revised corrected geomagnetic latitude (Gustafsson, 1970) that is intersected at Kiruna.

In addition to these five stations, magnetograms from several nearby magnetic observatories or temporarily installed magnetic stations have been used (cf. Table 1). The latter are two stations equipped with flux-gate magnetometers and digital recording that are being operated by H. Maurer, Technical University of Braunschweig, and three stations with analog recording run by the Polar Geophysical Institute at Apatity on the Kola peninsula (USSR). The time accuracy of these additional magnetic data was about 1 min due to a clock malfunction or reading errors within copies, respectively.

A north-south chain of seven 27.6 MHz riometers was operated by the Geophysical Observatory at Sodankylä on a routine basis. Four additional

riometers of frequencies 20 MHz, 40 MHz, and 50 MHz were operated at Sodankylä. The data were recorded with a chart speed of 60 mm/h, allowing one minute time resolution.

Observation of radio aurora is another method by which disturbances in the polar E-region may be studied, although the mechanism by which the scattering irregularities are generated is not yet understood completely (Egeland, 1976). During the substorm under consideration, signals recorded by three bistatic CW – backscatter equipments supplemented the other observations. One transmitter was operated at Borlänge (Fig. 1) at a frequency of 145 MHz. Its backscattered signals were received at Lycksele and Nurmijärvi. Another transmitter (97 MHz) was located at Pihtipudas, with a receiving station being operated at Sodankylä. The corresponding three backscatter regions within the ionospheric E-region are quite confined in latitude due to aspect angle dependence. They are rather evenly distributed over Northern Scandinavia (Fig. 1). It was important for our study that the station at Lycksele operated by the Max-Planck-Institut für Aeronomie, Lindau/Harz, was equipped with two receiving antennas of different beam widths. The half power beam width of receiver A mounted to 37 degrees, whereas that of receiver B was only 10 degrees. For receiver B this resulted in a backscatter volume also correspondingly confined in longitude, and located a little southwest of Tromsö (Fig. 1). Furthermore, both receivers were able to record the mean Doppler shift of the backscattered signal.

Magnetic pulsation recordings were available from four permanent stations in Finland. They are run by the University of Oulu and the Geophysical Observatories at Sodankylä and Nurmijärvi, and are equipped with induction coil magnetometers that are most sensitive between 0.1 Hz and 1 Hz. The time resolution is better than half a minute.

3. Observations

General Situation

The substorm under consideration occurred on April 6, 1975 between 20 and 23 UT when northern Scandinavia was located under the midnight sector of the auroral oval. Near the center of this region, e.g., at Ivalo (IVA, Fig. 1) corrected geomagnetic midnight was at 2120 UT (Whalen, 1970). The substorm seems to have been isolated rather well. As demonstrated by Figure 2 the well-known magnetic observatories along the auroral zone, as well as midnight-sector low latitude stations, exhibited only small shifts or fluctuations within the horizontal components between 18 and 20 UT. The shifts may partly be due to the late recovery phase of another though weaker substorm period that started between 14 and 15 UT. The magnetic quietness between the two substorms is also indicated by the absence of any Pi 2 activity between 16 and 21 UT at middle European observatories which were located within the evening sector during this time (H. Voelker, pers. comm.).

Simultaneously, the interplanetary magnetic field showed the following characteristics according to observations by the satellite IMP-J which was located

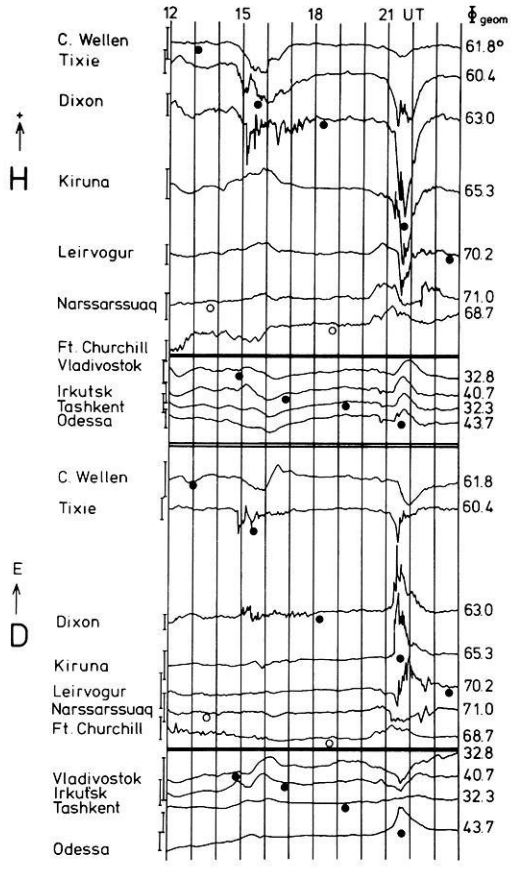

Fig. 2. Variations of horizontal components along the northern hemisphere auroral zone and at four stations from the southern part of the USSR on April 6, 1975. Scale bars correspond to 50 nT for the four low latitude stations, and to 200 nT otherwise. Magnetic midnight and midday (after Whalen, 1970) are denoted by full and open circles, respectively

at the point (-0.6, -21.5, 18.8) as measured in geocentric solar magnetospheric coordinates (Russell, 1971): Between 1800 and 2016 UT the field was northward with the exception of two short southward excursions at 1904 and 1920 UT, with a duration of about 2 min each. There are data gaps around 2000 and 2010 UT each lasting for about 5 min. At 2016 UT a sharp change to the southward direction occurred. This direction persisted until 2133 UT when the field gradually became northward and essentially stayed in this way for the next 2 h (J. Vette, pers. comm.).

The general character of the substorm as observed over the Scandinavian region is shown by the magnetograms in Figure 3. Here, the horizontal field is represented by its components A and B. They are defined as being parallel to the x_{KI} axis and the y_{KI} axis, respectively, that are shown in Fig. 1. This cartesian system has been introduced by Küppers et al. (1979). It is applicable only within a limited region, because projection onto a tangential plane is the basic assumption. The adopted plane is tangent to the globe at Kiruna. At this point the x_{KI} or A direction is chosen as to be orthogonal to the line of constant revised corrected geomagnetic latitude (Fig. 1). The A variations

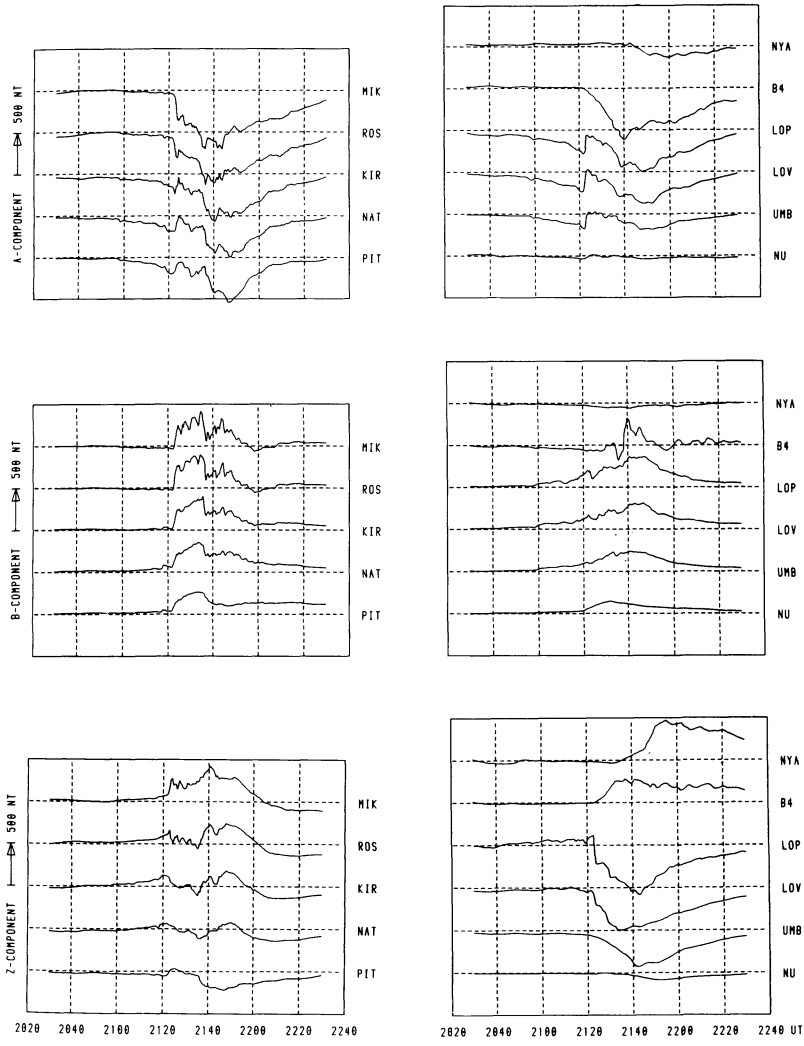

Fig. 3. Magnetic variations on April 6, 1975 at selected stations within and around the Scandinavian area. Stations B4 and NYA (see Table 1) are not shown within Figure 1. A and B denote horizontal components parallel to x_{KI} and y_{KI} axis (shown in Fig. 1), respectively. Z positive downwards. Horizontal lines corresponding to undisturbed levels

generally are rather similar to the usual *H* variations, and the same similarity exists between B and D.

In Fig. 3, magnetograms to the left are from the University of Münster chain and those to the right from islands north of Scandinavia, from the Kola peninsula to the east, and from southern Finland (cf. Fig. 1 and Table 1). Before 2040 UT the traces are close to the quiet time level which for each station and component is represented by the horizontal broken line.

As judged from the A and Z traces in Fig. 3, the substorm is governed by a broad westward electrojet. It flows above and northward of our region

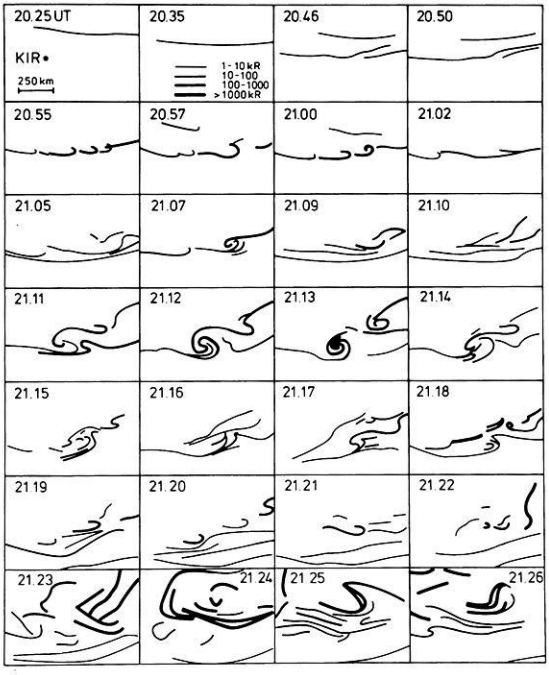

Fig. 4. Montage of maps showing position of linear auroral forms above northern Scandinavia at different moments on April 6, 1975. Results of analysis of digitized and rectified data from several all-sky cameras (see text). x_{KI} axis is oriented upwards, y_{KI} axis to the right (cf. Fig. 1). Position of Kiruna ($x_{KI}=y_{KI}=O$) is shown on the first map, intensity scale on second map

and reaches its maximum strength corresponding to a magnetic 500 nT disturbance at ground around 2145 UT, i.e., around local magnetic midnight. The same electrojet is evident in the H traces from Narssarssuaq (Greenland) and Leirvogur (Iceland) to the west and from the stations along the northern coast of the Soviet Union, to the east (cf. Fig. 2). The magnetic observatories at lower latitudes within the midnight sector see a typical bay disturbance most pronounced in the D component which changes sign at around 02 MLT (Fig. 2). The latter fact indicates that the central meridian of a Birkeland type ionospheric-magnetopheric current system (e.g., according to Meng and Akasofu, 1969) capable to explain these main substorm characteristics probably is located 2 h eastward from our region.

The onset of the main substorm phase occurred at about 2122 UT as indicated by the high and low latitude magnetograms (Fig. 2 and 3) which show strong inflections of all components at this time, and by Pi 2 activity as observed in middle and northern Europe. We concentrate our present study on the preceding hour and on the few minutes around this onset.

Figure 4 gives a synopsis of the auroral activity over northern Scandinavia throughout this time interval. Fair weather conditions permitted good observations from twilight at around 1940 UT on, when a faint arc was located about 70 km north of our northernmost all sky camera station Kevo. Later this arc, and also intermittently appearing additional arcs, underwent different intensifications and foldings until between 2122 and 2123 UT the breakup occurred. Throughout most of the time auroral arcs travelled southward and structures to the east.

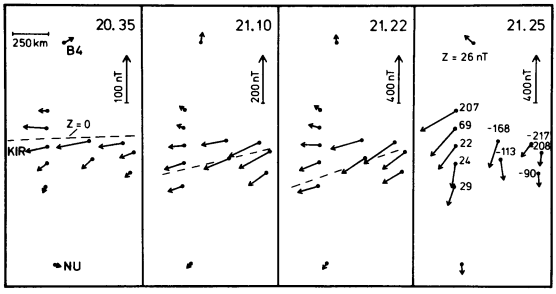

Fig. 5. Equivalent current vectors at selected moments (UT) within and around Scandinavia. Orientation of axes as in Figure 4. Position of three magnetic stations is indicated on first map. Numbers on fourth map give Z values (nT). Broken lines indicate curve where Z = 0 (estimated from Z values observed at stations). Note different magnetic scales

A corresponding synopsis of the magnetic field development within about the same region is given by Figure 5 which shows equivalent current vectors, i.e., horizontal magnetic disturbance vectors rotated 90 degrees clockwise if viewed from above. The equivalent current flow changes slowly from a westward direction (as defined within the x_{KI}, y_{KI} system) towards a more southwestern flow until 2122 UT when a sudden deflection occurs towards a southern direction at the time of the main onset (cf. flow pattern at 2125 UT). As indicated by the different scale marks within Figure 5, the intensity of the currents increases by a factor of 4 between 2035 and 2122 UT but remains of the same order of magnitude over the magnetic onset.

Pre-Onset Period (2025-2122 UT)

During the one hour preceding the onset the magnetograms from the high latitude stations around the globe (some of which are illustrated in Fig. 2) indicate increasing eastward equivalent current flow (see H components from Narssarssuaq and Leirvogur) if westward from our region, i.e., if the stations are located in the afternoon and evening sector, and vice versa. The evening sector eastward flow extends into the polar cap according to the magnetogram (not shown) from Upernavik (western Greenland). At midlatitudes in the midnight sector (e.g., Odessa in Fig. 2) increasing D components indicate increasing southward flow during the same time interval.

These magnetic observations point to a high-latitude equivalent current system of the twin-vortex mode including two electrojets, as described for example by Troshichev et al. (1974). It may be assumed that this system is mainly due to magnetospheric convection starting to increase at the time of southward turning of the interplanetary magnetic field, as mentioned above. The southward and eastward auroral motions observed over Scandinavia fit into this picture (Vorobjev et al., 1976).

The average southward motion of the southernmost arc between 2025 and 2120 UT (Fig. 4) amounts to 120 ms^{-1}. Because we are close to magnetic midnight where the auroral oval is east-west aligned this motion may directly indicate an expansion of the oval. On the other hand, southward velocities of this magnitude are regularly observed for individual auroral forms independent of the oval behaviour at this time of the day (Snyder and Akasofu, 1972; Vorobjev

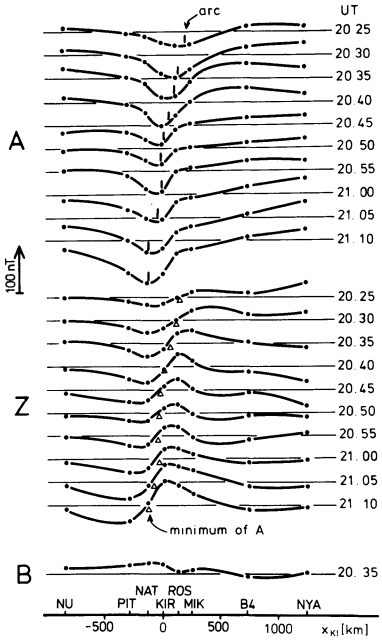

Fig. 6. Latitude profiles of different magnetic components at selected equidistant moments well before substorm onset (auroral breakup). Horizontal lines correspond to undisturbed levels. The position of the southernmost auroral arc is indicated at the A profiles, position of A minimum likewise indicated at Z profiles. Only one B latitude profile shown, as an example

et al., 1975). It should be mentioned that Lassen et al. (1977) who recently performed a case study partly similar to the present one, have found a southward drift of the preexpansive phase arc after the southward turning of the interplanetary magnetic field in the evening sector only, but not around midnight.

The westward or southwestward equivalent current flow observed over Scandinavia before 2122 UT mainly consists of a rather narrow electrojet, according to the latitude profiles of A and Z shown by Figure 6. The current is centered a little south of the southernmost (and for most of the time solely observed) auroral arc (cf. vertical bars within A latitude profiles), and remarkably follows its southward motion. Some spatial relationship between auroral arcs as observed by the ISIS 2 satellite and eastward and westward electrojets (generally of a larger width than in our case) has already been studied by Wallis et al. (1976), but here we are able to show that electrojet and arc travel with about the same southward speed. As will be discussed below this holds even for the case when the speed undergoes temporal variations.

According to the B latitude profiles, of which only one typical example is shown in Figure 6, the electrojet is not of a two-dimensional nature. This is also evident from Figure 5. For the time interval under consideration, the magnetic observations may be modelled by a Birkeland type current loop consisting of a homogeneous ionospheric electrojet of finite length with corresponding up- and down-flowing field aligned currents at its ends, according to the method described and applied extensively by Kisabeth (1972; see also Kisabeth and Rostoker, 1977). If we compare our latitude profiles with those given by Kisabeth (1972) for different model Birkeland current loops we may draw the conclusion that we are under the western half of the electrojet and that as a first approxima-

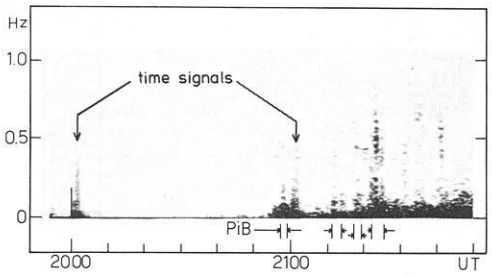

Fig. 7. Spectrogram of short period magnetic pulsation activity at Sodankylä on April 6, 1975. Pi B events are denoted

tion end effects and the effects of the field-aligned currents may be neglected within A and Z components. That we are still far enough from the ends of the electrojet follows from the fact that the total variation within the B profiles is considerably smaller than the total variation within the corresponding Z profiles.

The development of auroral activity will now be described a little more in detail (cf. Fig. 4). In addition to the main arc which had intensified and narrowed showing slight distortion for the first time, at 2046 UT a second faint arc became visible about 120 km to the north but disappeared after a few minutes. At about 2054 UT the main arc intensified and simultaneously developed into a chain of hook-like folds that travelled towards the east with a velocity of 1–2 km s^{-1}. At the same time the first Pi B event (impulsive broadband Pi burst, see Heacock, 1967) of this night was detected by the short-period pulsation magnetometers at Sodankylä and also, with smaller amplitudes, at Oulu and Nurmijärvi (cf. spectrogram from Sodankylä as shown in Fig. 7). Around the time of this auroral disturbance which persisted only for 8 min, the magnetic A latitude profiles (Fig. 6) became more asymmetrical by exhibiting stronger gradients at the northern border of the electrojet region than at the southern one. Corresponding deformations (a more pronounced northern maximum) are to be seen in the Z profiles.

At 2107 UT a short-lived spiral-like structure appeared over the eastern part of our region followed by wavy or hook-like weak disturbances. By 2110 UT all auroral activity had reduced to several faint arcs. Immediately thereafter, an intense well-defined stationary auroral spiral (Davis and Hallinan, 1976) developed. It showed an anticlockwise winding-up (if viewed from above) of former rectilinear structures. This sense of rotation is always observed for spirals (Davis and Hallinan, 1976) and is due to a magnetic shear caused by a concentration of upward field-aligned currents according to the theory proposed by Hallinan (1976).

During the few minutes of spiral formation, which culminated at 2113 UT, some slight distortion of the equivalent current distributions occurred. These distributions were otherwise similar to the example shown in Fig. 5 for 2110 UT. In order to see if this distortion might be ascribed directly to the auroral spiral the difference of the equivalent current vectors between 2110 and 2113 UT has been mapped in Figure 8. This method is analogous to the use of differential latitude profiles of magnetic components introduced by Kisabeth (1972). Figure 8 clearly shows that over the time interval of spiral growth an equivalent

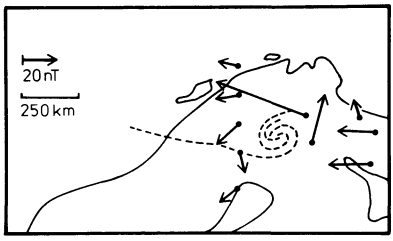

Fig. 8. Position of auroral spiral (dotted) at 2113 UT, and differential equivalent current vectors calculated for the time difference 2110 and 2113 UT (i.e., currents being added over this interval)

current pattern is being added to the formerly existing one that exhibits an anticlockwise current circulation around the spiral center. Such an equivalent current loop will be generated (Fukushima, 1971) if a vertical upward directed field-aligned line current is escaping from a laterally homogeneous or rotationally symmetric ionosphere. The field-aligned current would be fed by radially inward directed Pedersen currents (cf. Fig. 15 below) that compensate its magnetic field below the ionosphere. Therefore, only the magnetic field of the circular Hall currents will be detectable at the ground.

Accordingly, our observations seem to indicate that during spiral formation there is a local addition or concentration of upward field-aligned current, as predicted by the theory of Hallinan (1976). Similar conclusions have been drawn by Wescott et al. (1975) from the results of a barium plasma injection experiment.

Like the auroral activity at 2055 UT the beginning of spiral development was accompanied by a Pi burst at 2111 UT (Fig. 7). Another Pi B appeared at 2116 UT when the last auroral intensification before breakup began. Again, hook-like folds travelled rapidly towards east. Simultaneously, the first Pi 2 event was recorded at middle European magnetic observatories (e.g., Wingst and Göttingen).

At the same time an onset of weak backscattering of radio waves from auroral structures was noticed at Sodankylä (corresponding to the backscatter region PS in Fig. 1), but probably not at Lycksele (region BL) and undoubtedly not at Nurmijärvi (region BN). Afterwards, at 2119 UT a nearly total fading of backscatter intensity occurred, as well as in auroral activity. According to all-sky photographs, the northern sky became especially dark, in agreement with the pre-breakup observations reported by Snyder and Aksofu (1972). Auroral fading seems to be a phenomenon regularly occurring before breakup as has been reported and discussed by Pellinen and Heikkila (1978).

During the time before breakup and main substorm onset, the riometers from the Finnish chain had already indicated some weak absorption (Fig. 9) which started around 2030 UT above Ivalo (and possibly above Kevo where heavy fluctuations all the time impeded interpretation of the data) and later and more gradually above Sodankylä, Rovaniemi and Oulu. A southward shift or expansion of the absorption region can be inferred from Figure 9 yielding a speed of 100–200 ms^{-1}. According to Hargreaves et al. (1975) who like others (Pytte et al., 1976) regularly observed this phenomenon, the pre-onset bay-like equatorward moving absorption activity is indicative of inward convection of energetic plasma in the magnetosphere and should be regarded as evidence

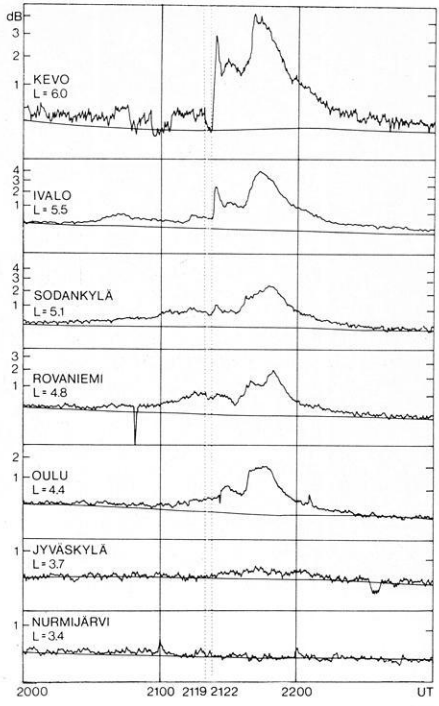

Fig. 9. Cosmic noise absorption as recorded by the Finnish riometer meridian chain on April 6, 1975. Undisturbed levels are indicated

for a substorm growth phase. Note that in our case the absorption region drift is of the same direction and magnitude as the average drift observed simultaneously for the southernmost auroral arc and the westward electrojet within the same region (cf. Fig. 6, or Fig. 12a and b, below).

Around 2113 UT the absorption was slightly increased above Ivalo and probably above Sodankylä, possibly in relation to the spiral formation which has been discussed above. Between 2119 and 2122 UT (i.e., just before substorm onset and auroral breakup), the absorption decreased clearly above Sodankylä and Rovaniemi and most strongly above Kevo. This phenomenon is well known especially from balloon-borne X-ray measurements (Pytte and Trefall, 1972; Pytte et al., 1976).

Auroral Breakup and Magnetic Onset

After the last auroral fading mentioned, an intensive hooklike structure developed rather far to the west (a little south of Kiruna) at 2119:30 UT (cf. Fig. 4). For almost 2 min it was nearly the only auroral form to be seen (Fig. 10). It travelled rapidly towards the east with an increasing velocity up to 3 km s^{-1} until at 2121:43 its motion was suddenly stopped. Eight seconds later the structure had become partly wound up anticlockwise into a somewhat rayed spiral. It then dissolved rapidly, and developed into a rather intense north-south-aligned linear form above the Kola peninsula. This was accompanied by the appearance

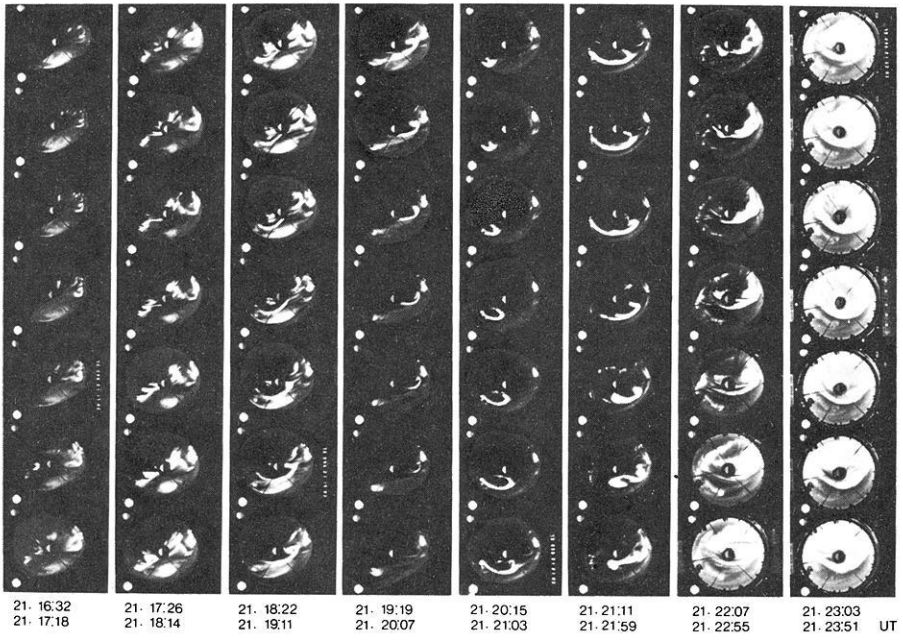

Fig. 10. All-sky camera records from the station Ivalo for a time interval a few minutes before and around auroral breakup. Below each row time of uppermost and lowest frame is indicated. Geographic north is upwards, east is to the right

of rayed auroral forms in the northwest of the region under observation. At 2122:31 UT all the formerly existing forms intensified extremely, and at 2122:51 UT nearly the whole sky of the northern part of the region was covered with bright aurorae (Fig. 10). We may conclude that the auroral breakup occurred at about 2122:30 UT above northern Scandinavia.

During the breakup, the equivalent current system over Scandinavia changed drastically into a broad south-westward directed flow (Fig. 5, cf. current system at 2125 UT). The magnetic onset at our northernmost stations was extremely sharp, especially in the D- or B-components (cf. Fig. 3), and occurred between 2122:00 and 2122:10 UT.

This magnetic onset was accompanied by an intense Pi B event observed especially at Kevo and Sodankylä (and possibly preceded by another weaker event one minute earlier) (cf. Fig. 7), and by a clear Pi 2 event at middle European magnetic observatories (e.g., Wingst and Göttingen). As may be seen from Figure 2 the onset occurred at the beginning of worldwide substorm activity. The magnetograms from observatories to the east (Dixon, Cape Cheluskin) possibly indicate an onset 1–2 min earlier.

Note that at our stations in and near Scandinavia the magnetic behaviour is quite different (Fig. 3). Whereas at the western stations (profile between MIK and PIT) B is especially affected by the onset, the eastern stations show the main changes in A and Z. If we neglect the observations within the Scandinavian region the observations to the east on the nightside of the northern

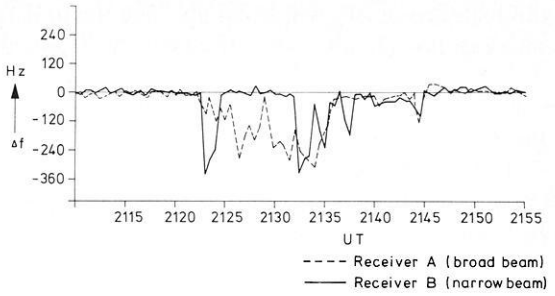

Fig. 11. Mean Doppler shift as a function of time as recorded by auroral radio wave backscatter receivers at Lycksele (cf. Fig. 1 for corresponding backscatter regions, denoted there by letters BL)

hemisphere probably indicate the switching on of an additional westward auroral electrojet of large longitudinal extent with corresponding field-aligned currents at the ends. The central meridian of this Birkeland type current system (cf. Kisabeth 1972) probably was located at about 03 MLT according to the magnetograms from the southern part of the Soviet Union (partly shown in Fig. 2), i.e., eastward from Scandinavia (00 MLT).

Simultaneously with the auroral breakup and the magnetic onset the Finnish riometers indicate a sharp onset of >40 keV electron precipitation above Kevo and Ivalo (Fig. 9). It is also observable at Tromsö and, though being a little more gradual and less intense, at Kiruna. At Kevo the maximum absorption difference amounts to 3.3 dB. Stations to the north and west of Scandinavia recorded only smooth delayed increases in absorption after the breakup. Eastward of Finland the strong absorption started before the observed breakup, showing a typical morningside behaviour with slow increase in absorption and delayed maxima (3 dB at Dixon Island at 2130 UT). On the dayside in Alaska small absorption started around 2040 UT, reaching 1 dB at around 2100 UT; after that the absorption decreased gradually.

As regards the radio wave backscatter receiver stations, Nurmijärvi (corresponding to the backscatter region BN in Fig. 1) received no signal. Sodankylä (region PS) showed a small precursor at 2118 UT followed by a fade, and then a sharp onset of a very strong signal at 2121:30 UT. At Lycksele (backscatter region BL) receivers A and B both recorded strong signals and negative Doppler shift from 2122 UT on, but with important differences (Fig. 11). Whereas receiver A (broad beam) showed a very gradual increase in signal amplitude and negative Doppler shift, both amplitude and shift at receiver B (narrow beam) appeared in a steplike fashion half a minute later and persisted for only 2 min. This means that backscattering was not uniformly distributed over the whole backscatter region belonging to receiver A, but was concentrated mostly to the part near Tromsö (crosshatched part of region BL in Fig. 1). The difference of the onset times indicates a westward propagation of the backscattering irregularities after the breakup over Kevo.

4. Discussion and Conclusions

Our further discussion will be concentrated upon the observed relationship between the early electrojet development and the accompanying auroral activity including spiral formation, and upon the phenomena at the time and around

the location of auroral breakup. The auroral fading which we observed before breakup has already been discussed by Pellinen and Heikkila (1978).

Pre-Onset Westward Electrojet System

Often it has been assumed that the northern and southern borders of an auroral electrojet are given by the locations of the extrema of Z as observed on the ground along a meridian chain of magnetometers (e.g., Wallis et al., 1976). This is correct for a broad electrojet. On the other hand, if the width becomes small as compared to the height h of the current, the north-south distance 2s between the minimum and maximum of Z approaches the value 2h. For a homogeneous sheet current of finite width 2w the relation $s=(w^2+h^2)^{1/2}$ holds, and the height-integrated current intensity J may be calculated from the values of the two Z extrema or from the H (or A) extremum value. Of course, it has to be assumed that internal contributions to the observed magnetic field at the ground are negligible. The smallness of such contributions has been verified for Scandinavia for slowly varying electrojets like the present one (U. Mersmann and K. Lange, priv. comm.). Also it is necessary that we are located far enough from the eastern ends of the electrojet. As was mentioned above, according to the small B variations before breakup this condition seems to be fulfilled in our case.

Accordingly, position (from the Z=O locations), width 2w (assuming h= 100 km), and height-integrated current intensity J have been calculated from the Z and A latitude profiles that are shown in Figure 6. The results are represented in Figure 12 (parts a and b), together with the location of the observed arcs above our meridian chain of magnetometers. With one exception, the southernmost arc is located within the northern half of the electrojet all the time. As was mentioned already, the electrojet and the southernmost arc travel southward in parallel. Note especially the slowing down or even interruption of the southward motion of both electrojet and auroral arc which occurs at 2050 UT. A common southward velocity averaged over 15 min has been calculated for the electrojet and for the southernmost arc. The results are also shown in Fig. 12b, both as a velocity and as an equivalent westward electric field E_{eq} (defined as the field which would give the observed motion if it were due to an $\mathbf{E}\times\mathbf{B}$ drift).

At the beginning of our interval E_{eq} is constant whereas J increases steadily. It seems as if the minimum of J occurring at 2050 UT is related to the deep decrease of E_{eq} at this time. Indeed, the quotient J/E_{eq} here called Σ_{eff} (effective height-integrated conductivity) and delineated in Figure 12c is steadily increasing all the time up to 2055 UT.

The question may be asked why the first hook-like distortions of the auroral arc (Sect. 3 and Fig. 4) appeared at 2055 UT. Apparently, no one of the three electrojet parameters 2w, J, and E_{eq} exhibits any peculiarity at this time, whereas Σ_{eff} shows a sharp maximum possibly indicating an extremum of height-integrated conductivities and therefore of particle precipitation over the 200 km wide latitudinal electrojet range.

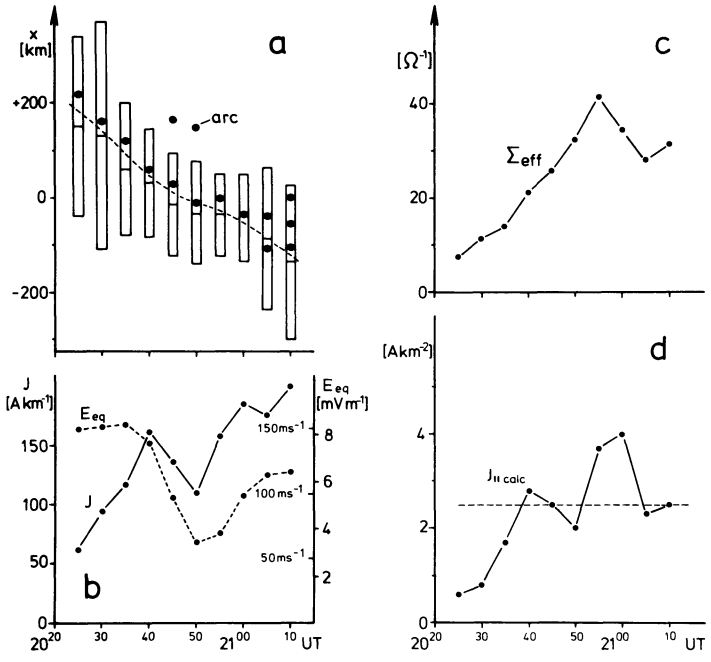

Fig. 12a–d. Different parameters derived from observations of pre-onset electrojet (Fig. 6) and auroral arcs, as functions of time. **a** Width 2w and position (vertical bars) of equivalent homogeneous ionospheric sheet current, and position of arcs (dots). **b** Intensity J of sheet current and smoothed southward velocity (scale to the right) of electrojet and southernmost arc, expressed as an equivalent westward electric field Σ_{eq} (according to $\mathbf{v}=\mathbf{E}\times\mathbf{B}/B^2$). **c** $\Sigma_{eff}=J/E_{eq}$. **d** $j_{\parallel calc}=\Sigma_H\Sigma_P^{-1}\,J\ w^{-1}$ as an order-of-magnitude estimate of the field-aligned current intensity, under the assumption of model B1 from Figure 13. The broken line indicates Hallinan's (1976) critical value, for comparison

On the other hand, it seems to be probable that the observed hook-like distortions constitute the beginning of spiral formation which requires a certain critical intensity of upward field-aligned currents, according to the theory developed by Hallinan (1976). Therefore, it may be useful to try to estimate at least by an order of magnitude calculation the field-aligned current directions and intensities from the above derived electrojet parameters.

There are two basic mechanisms by which an electrojet at high latitudes may be generated (Boström, 1964, 1977): The first mechanism (Fig. 13, part A) regards the magnetosphere as a current or voltage generator. According to this model the field-aligned current within two vertical parallel sheets above the borders of the electrojet or the voltage between these two sheets are given. The two antiparallel field-aligned sheet currents are closed via Pedersen currents within the ionosphere. The corresponding Hall current constitutes the electrojet. For a westward electrojet (our case) the field-aligned currents above its northern border flow downward.

In the second mechanism (Fig. 13, parts B) that part of the magnetosphere which is connected to the central part of the electrojet (i.e., the part in the middle between its eastern and western ends) along the magnetic field lines

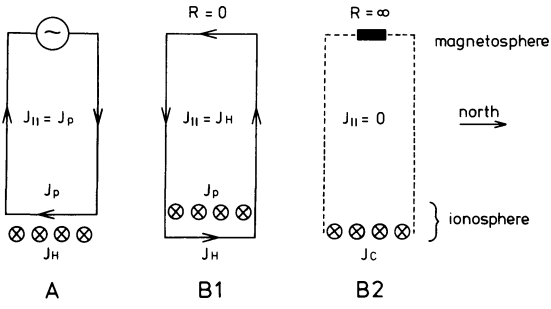

Fig. 13. Three mechanisms by which a westward polar electrojet (crossed circles) may be generated. In Model A the magnetosphere acts as a generator, the ionospheric electric field (southward) is limited to the electrojet region. Models B imply a large-scale westward ionospheric electric field. J_P Pedersen current, J_H Hall current, J_C Cowling current, $J_{||}$ field-aligned current

acts as a load. The source of the electrojet is a large-scale ionospheric electric field $\mathbf{E}_0$ – generally generated by large-scale magnetospheric processes – which meets a local channel of higher conductivity. Because the current has to be source-free, eventually electric space charges will accumulate at the boundaries of the well conducting channel. Depending on the circumstances the electrojet may consist mainly of Hall or of Pedersen currents. Of critical importance are the horizontal direction of $\mathbf{E}_0$, the resistance R of the magnetospheric load between the two current sheets, and the contrast of conductivities outside and inside the channel.

The observed southward motion of the electrojet and of the accompanying arc suggests that a large-scale ionospheric electric field $\mathbf{E}_0$ with a westward component equal to E_{eq} (Fig. 12b; see Kelley et al. (1971) for justification of this latter assumption) was present, indeed. According to Mozer (1971), a westward electric field of the order of 10 mVm^{-1} typically appears during the hour preceding a substorm onset around magnetic midnight. For that reason, we consider first the consequences of applying the second mechanism to our case.

According to the magnetic A-component latitude profiles shown in Figure 6 the electrojet clearly stands out above the background to the north and south where the ionospheric currents generally seem to be rather small. We assume therefore, that the conductivities outside the electrojet region may be neglected. This excludes the possibility that the north-south component of $\mathbf{E}_0$, if present, was of any importance for electrojet generation because due to the non-divergence of currents the corresponding Pedersen currents – and therefore the Hall currents also – would have been negligible within the conductivity channel.

The westward component of $\mathbf{E}_0$ renders an upward directed field-aligned sheet current of intensity $J_{\parallel}=(\Sigma_H/\Sigma_p)J$ above the northern border of the electrojet if the resistance of the mentioned magnetospheric load is assumed to be negligible (case B1 in Fig. 13). Here, Σ_H and Σ_P denote the height-integrated Hall and Pedersen conductivity, respectively, and J means the derived electrojet current density as shown in Figure 12b. In this case, the electrojet is a pure Pedersen current, and Σ_{eff} (Fig. 12c) has to be interpreted as Σ_P. If, on the other hand, the magnetospheric resistance is assumed to be infinitely large, the field-aligned currents are suppressed completely, and the electrjet is a Cowling current with $\Sigma_{eff}=\Sigma_P+\Sigma_H^2\Sigma_P^{-1}$(case B2 in Fig. 13).

In reality, $J_\parallel$ will be distributed over a horizontal north-south range of the order of w (see Fig. 12a). This gives a field-aligned current density of the order of $j_{\parallel calc} = J_\parallel / w$. Under the assumption that model B1 (Fig. 13) holds, this quantity is equal to the values shown in Figure 12d if a value of 2 is inserted for the ratio Σ_H/Σ_P as indicated by results given by Evans et al. (1977), De La Beaujardiere et al. (1977), and Horwitz et al. (1978). It seems remarkable that the above-mentioned first hook-like auroral distortions appear at the time (2055–2100 UT, see Fig. 4) when our calculated values of field-aligned current density (Fig. 12d) for the first time substantially surpass the critical value 2.5 A km^{-2} given by Hallinan (1976). On the other hand, it seems to be unacceptable to interpret the Σ_{eff}-values as shown in Figure 12c correspondingly as height-integrated Pedersen conductivities, because outside auroral arcs Σ_P generally is of the order of only 10 Ω^{-1} (Horwitz et al., 1978). We conclude therefore, that it seems to be possible to interpret our electrojet observations within the framework of model B (Fig. 13), but only if at least some part of the field-aligned current is suppressed by finite magnetospheric resistance.

Rocket experiments (see, for example, Anderson and Vondrak, 1975; Casserly, 1977) and theoretical considerations (Sato, 1978; for example) have shown that an auroral arc is connected to a quite local (north-south range a few tens of kilometers) system of field-aligned currents and one or two electrojets. The upward directed field-aligned current flows above the arc, and it is the intensity of this current which seems to be critical for the development of auroral spirals (Hallinan, 1976). As Sato (1978) has pointed out the local arc current system may develop under quite different circumstances (different directions of $\mathbf{E}_0$, for example). We conclude therefore, that in our case not only a mixture between the models B1 and B2 (Fig. 13) is capable of explaining the observations of electrojet growth and spiral formation. Model A or a pure model B2 may be considered as well.

Model A yields downward field-aligned currents above the northern half of the electrojet (Fig. 13), i.e., within the region where upward current is necessary for explanation of the observed spiral formation. As may be seen from Figure 13, the order of magnitude of this downward current would amount to (Σ_P/Σ_H)J w^{-1} and would therefore be smaller than the values shown in Figure 12d by a factor of 4 (if again $\Sigma_H/\Sigma_P = 2$ is assumed). This background of downward currents of intensities well below Hallinan's (1976) critical value all the time would probably not impede spiral growth if the local mechanism of arc formation proposed by Sato (1978) is going on which seems to render upward currents above the arc of the order of 10 A km^{-2} in cases like the present one.

Auroral Breakup Current System

The second item which we intend to discuss more thoroughly is the electric current system around the time of the observed auroral breakup and of the strong absorption event (2122 UT, cf. Figs. 4, 9 and 10). The Scandinavian magnetograms (Fig. 3) suggest that an additional current system had been switched

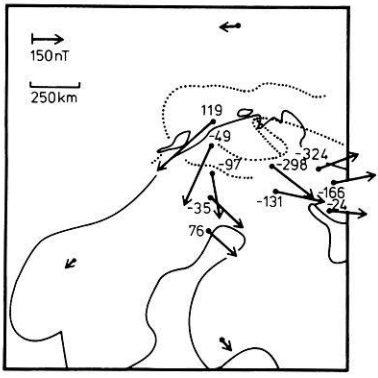

Fig. 14. Main auroral structures (dotted) immediately after breakup at 2125 UT, and differential equivalent current vectors calculated for the time difference 2122 and 2125 UT (cf. Fig. 8). Numbers indicate corresponding Z differences (in nT)

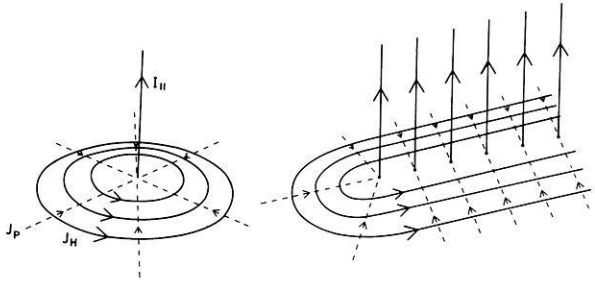

Fig. 15. Schematic view of a current system (right) which may be able to explain the pattern of equivalent current vectors shown within Figure 13. It is composed of elementary systems (Fukushima, 1971) as shown to the left. J_P and J_H denote the Pedersen and Hall currents, respectively

on very abruptly, at this time. Assuming that the preexisting current system (Fig. 5, system at 2122 UT) had remained constant we get the additional (differential) equivalent current vectors shown in Figure 14. These vectors seem to encircle the region where the auroral breakup and the strong absorption event have been observed, i.e., the region of most intense particle precipitation. The differential equivalent current vectors suggest that this was a region of intense upward field-aligned current according to the already mentioned model of Fukushima (1971), shown schematically in Figure 15 (left part). On the other hand the Z variations from our easternmost stations (cf. Fig. 3, and Z values given in Fig. 14) indicate that the differential equivalent current system may be rather elongated towards the east, and that accordingly the field-aligned current would be more similar to a current ribbon (Fig. 15, right part) with its western boundary above Scandinavia, than to a line current.

Figure 14 in connection with Figure 15 indicates that during breakup strong southward Hall currents, i.e., strong northward E-region electron drifts are generated only in the longitudinally confined region near Tromsö (magnetic stations MIK and ROS, cf. Fig. 1). Qualitatively at least this is in accordance with the negative Doppler shifts (Fig. 11) observed at Lycksele from the backscatter region denoted by letters BL in Figure 1. Furthermore, the amazing

differences (see above) between the large amplitude and Doppler shift (Fig. 11) recorded by the narrow beam receiver A (cf. small crosshatched backscatter region near Tromsö in Fig. 1) and the much smaller shift recorded by the broad beam receiver B between 2122 and 2124 UT may be due to this longitudinal confinement of strong electron drifts. If we assume that the electron drift vector was not too far from being parallel to the line of sight of the backscatter transmitter – receiver system, we may deduce an eastward electric field with a strength of 15 mV m^{-1} from the – 250 Hz Doppler shift observed by receiver B, for the region near our magnetic stations ROS and MIK. On the other hand, the 300 nT change recorded in the D component at these two stations between 2122 and 2124 UT indicates a height-integrated southward Hall current density of 0.5 Am^{-1} (calculated from the formula for an infinite current sheet). Because of the lateral inhomogeneity of the current system (which also justifies the neglect of internal field contributions) this will be an underestimate. The ratio of the two quantities gives a height-integrated Hall conductivity of about 50 Ω^{-1} for this region which seems to be quite realistic (Brekke et al., 1974; De La Beaujardiere et al., 1977).

Our magnetic observations during the auroral breakup show some similarity to the observations reported by Kisabeth and Rostoker (1973) for the case of a westward travelling surge passing their meridian chain of stations. This regards especially the large disturbances in the D component. On the other hand, our optical observations indicate essentially a local auroral breakup, and not passing of a preexisting auroral form. Furthermore, the traces on our magnetic records show a sharply defined (within less than 10 s) inflection, instead of a more gradual increase which has to be expected if a stationary overhead current system is approaching the station with constant and reasonable velocity.

Kisabeth and Rostoker (1973) have interpreted their observations by a north – south shear in the ionospheric part of a Birkeland current loop (Fig. 9 within their paper). Probably this would be an alternative interpretation in our case. The main difference seems to be that their model does not include local field-aligned currents. On the other hand, in another paper Rostoker (1974) has envisaged a single field-aligned current jumping to a new position during the substorm expansion phase, in the midnight region. This model comes nearer to our interpretation.

5. Summary

Our observations made shortly (1–0 h) before magnetic midnight between the time of the southward turning of the interplanetary magnetic field (2016 UT) and substorm onset (2122 UT) may be summarized in the following way:

1. A westward electrojet with generally increasing intensity appeared over northern Scandinavia. It may be modelled by a homogeneous sheet current of finite width. The corresponding sheet current density reached values near 200 A km^{-1} well before onset, whereas the width varied in a nonmonotonous way between 200 and 400 km.

2. An auroral arc, intermittently accompanied by parallel arcs to the north, was situated above the northern half of the electrojet.

3. Both electrojet and arc moved southward in parallel, with an average (2025–2110 UT) speed of 120 ms^{-1}. Around 2050 UT both electrojet and arc nearly discontinued their motion, intermittently.

4. Our riometers indicated weak ionospheric absorption above the same region at this time. The absorption region also moved towards south, with an estimated speed of 100–200 ms^{-1}.

5. From 2055 UT on, the arc was intermittently distorted with increasing intensity. The first distortions were shaped in a hook-like fashion, later on a mature spiral developed.

6. The first distortions appeared at a time when the field-aligned current intensity, estimated from the derived electrojet parameters by an order-of-magnitude calculation, reached values of the order of 1 A km^{-2}.

7. Nearby short period pulsation magnetometers indicated Pi B activity whenever the auroral arc was distorted.

8. During the few minutes of spiral growth and at the same location, an additional pattern of radially directed magnetic disturbance vectors at the ground appeared. This observation seems to indicate rather directly that the spiral enclosed a local region of upward directed field-aligned current.

9. At the time (2116 UT) of the last auroral intensification and distortion before the magnetic onset and the auroral breakup, in addition to the mentioned Pi B activity a first Pi 2 event was recorded in middle Europe, and weak auroral backscattering of radio waves occurred above northern Scandinavia.

As regards the southward drift of the auroral arc, the electrojet, and the absorption region, our observations seem to supplement results published by Pytte et al. (1976).

We think that it has to remain an open question whether our observations support the concept of the growth phase (McPherron, 1970). Perhaps the substorm under discussion was not isolated well enough. However, we must emphasize that nearly all the different ground-signatures which are thought to be evidence for a growth phase (McPherron, 1970; McPherron et al., 1973; Kokubun and Iijima, 1975; Vorobjev et al., 1976; Mozer, 1971; Hargreaves et al., 1975) have been observed by us and have been shown to be closely related.

About our results regarding the auroral breakup, which was observed exactly at magnetic midnight, the following may be stated:

1. The magnetic observations are interpreted by us by a model in which at the time and at the location of the breakup a current system is added to the preexisting electrojet which implies strong upward directed field-aligned current flow above the breakup region and a corresponding ionospheric Hall current circulation around it.

2. This interpretation seems to be supported by the fact that at the time of auroral breakup strong radio wave auroral backscatter signals with a large negative Doppler shift of frequency were received only from a small region, quite confined in longitude, immediately to the west of the breakup region, which was also a region of strong ionospheric absorption as indicated by the riometer observations. Furthermore, the value of the observed Doppler shift

is in accordance with the observed magnitude of the magnetic east-west disturbance at ground, if a reasonable value of the height-integrated Hall conductivity is assumed.

Acknowledgements. Our magnetic observations have been performed in cooperation with the Department of Plasma Physics of the Royal Institute of Technology at Stockholm, with the Kiruna Geophysical Institute, and with the Auroral Observatory at Tromsö. There, we got much help and scientific advice especially from Dr. R. Boström, Dr. G. Gustafsson, and Mr. St. Berger. For providing additional magnetic data, our thanks are due to Mr. H. Maurer from the Technical University of Braunschweig, Dr. G.A. Loginov from the Polar Geophysical Institute at Apatity, Mr. St. Berger from the Auroral Observatory at Tromsö, Dr. C. Sucksdorff from the Finnish Meteorological Institute, and to the World Data Center C1 at Copenhagen. Similarly, we are obliged to Dr. G. Gustafsson from the Kiruna Geophysical Institute for placing all-sky-camera records at our disposal. We wish to thank Dr. J. Vette from the Satellite Situation Center (SSC) at Goddard Space Flight Center, Greenbelt, Maryland, for providing data on the interplanetary magnetic field, and Dr. H. Voelker from the University of Göttingen who kindly sent us information on Pi 2 activity. We are also indebted to Dr. J. Kisabeth, Edmonton, for critical and very helpful comments during preparation of this paper, and to Dr. A. Jones, Münster, for critically reading the text.

The University of Münster part of this work has been supported financially by the Deutsche Forschungsgemeinschaft. One of us (W.J.H.) acknowledges support from the National Science Foundation.

References

Akasofu, S.-I.: Polar and magnetospheric substorms, Dordrecht: D. Reidel Publ. Comp. 1968

Akasofu, S.-I.: Physics of magnetospheric substorms. Dordrecht-Boston: D. Reidel Publ. Comp. 1977

Anderson, H.R., Vondrak, R.R.: Observations of Birkeland currents at auroral latitudes. Rev. Geophys. Space Phys. **13**, 243–262, 1975

Boström, R.: A model of the auroral electrojets, J. Geophys. Res. **69**, 4983–4999, 1964

Boström, R.: Current systems in the magnetosphere and ionosphere. In: Radar probing of the auroral plasma, A. Brekke, ed.: Proc. EISCAT Summer School, Tromsö, Norway June 5–13, 1975, Universitetsforlaget, Tromsö-Oslo-Bergen, 1977

Boyd, J.S., Belon, A.E., Romick, G.J.: Latitude and time variations in precipitated electron energy inferred from measurements of auroral heights. J. Geophys. Res. **76**, 7694–7700, 1971

Brekke, A., Doupnik, J.R., Banks, P.M.: Incoherent scatter measurements of *E*-region conductivities and currents in the auroral zone. J. Geophys. Res. **79**, 3773–3790, 1974

Casserly, R.T., Jr.: Observation of a structured auroral field-aligned current system. J. Geophys. Res. **82**, 155–163, 1977

Davis, T.N., Hallinan, T.J.: Auroral spirals, 1. Observations. J. Geophys. Res. **81**, 3953–3958, 1976

De La Beaujardiere, O., Vondrak, R., Baron, M.: Radar observations of electric fields and currents associated with auroral arcs. J. Geophys. Res. **82**, 5051–5062, 1977

Egeland, A.: Formation and movements of ionospheric irregularities in the auroral *E*-region. In: Radio systems and the ionosphere, AGARD Conference Proc. No. 173, W.T. Blackband, ed.: pp. 32-1–32-15, Adv. Group for Aerospace Res. and Development, Neuilly Sur Seine, 1976

Evans, D.S., Maynard, N.C., Trøim, J., Jacobsen, T., Egeland, A.: Auroral vector electric field and particle comparisons, 2. Electrodynamics of an arc. J. Geophys. Res. **82**, 2235–2249, 1977

Fukushima, N.: Electric current systems for polar substorms and their magnetic effect below and above the ionosphere. Radio Sci. **6**, 269–275, 1971

Gough, D.I., Reitzel, J.S.: A portable three-component magnetic variometer. J. Geomag. Geoelectr. **19**, 203–215, 1967

Gustafsson, G.: A revised corrected geomagnetic coordinate system. Ark. Geofys. **5**, 595–617, 1970

Hallinan, T.J.: Auroral spirals, 2. Theory. J. Geophys. Res. **81**, 3959–3965, 1976

Hargreaves, J.K., Chivers, H.J.A., Axford, W.I.: The development of the substorm in auroral radio absorption. Planet. Space Sci. **23**, 905–911, 1975

Heacock, R.R.: Two subtypes of type Pi micropulsations. J. Geophys. Res. **72**, 3905–3917, 1967

Horwitz, J.L., Doupnik, J.R., Banks, P.M.: Chatanika radar observations of the latitudinal distributions of auroral zone electric fields, conductivities, and currents. J. Geophys. Res. **83**, 1463–1481, 1978

Hyppönen, M., Pellinen, R., Sucksdorff, C., Torniainen, R.: Digital all-sky camera, Techn. Rept. No. 9, Finnish Meteorol. Inst., 1974

Kelley, M.C., Starr, J.A., Mozer, F.S.: Relationship between magnetospheric electric fields and the motion of auroral forms. J. Geophys. Res. **76**, 5269–5277, 1971

Kisabeth, J.L.: The dynamical development of the polar electrojets, PhD thesis, University of Alberta, Edmonton, 1972

Kisabeth, J.L., Rostoker, G.: Current flow in auroral loops and surges inferred from ground-based magnetic observations. J. Geophys. Res. **78**, 5573–5584, 1973

Kisabeth, J.L., Rostoker, G.: Modelling of three-dimensional current systems associated with magnetospheric substorms. Geophys. J. Roy. Astron. Soc. **49**, 655–683, 1977

Kokubun, S., Iijima, T.: Time-sequence of polar magnetic substorms. Planet. Space Sci. **23**, 1483–1494, 1975

Küppers, F., Untiedt, J., Baumjohann, W., Lange, K.: A two-dimensional magnetometer array for ground-based observation of auroral zone electric currents during the IMS. J. Geophys. **45**, in press, 1979

Lassen, K., Sharber, J.R., Winningham, J.D.: The development of auroral and geomagnetic substorm activity after a southward turning of the interplanetary magnetic field following several hours of magnetic calm. J. Geophys. Res. **82**, 5031–5050, 1977

McPherron, R.L.: Growth phase of magnetospheric substorms. J. Geophys. Res. **75**, 5592–5599, 1970

McPherron, R.L., Russell, C.T., Aubry, M.P.: Satellite studies of magnetospheric substorms on August 15, 1968, 9. Phenomenological model for substorms. J. Geophys. Res. **78**, 3131–3149, 1973

Meng, C.-I., Akasofu, S.-I.: A study of polar magnetic substorms, 2. Three-dimensional current system. J. Geophys. Res. **74**, 4035–4053, 1969

Mozer, F.S.: Origin and effects of electric fields during isolated magnetospheric substorms. J. Geophys. Res. **76**, 7595–7608, 1971

Pellinen, R.J., Heikkila, W.J.: Observations of auroral fading before breakup (accepted for publication) J. Geophys. Res., 1978

Pytte, T., Trefall, H.: Auroral-zone electron precipitation events observed before and at the onset of negative magnetic bays. J. Atmos. Terr. Phys. **34**, 315–337, 1972

Pytte, T., Trefall, H., Kremser, G., Jalonen, L., Riedler, W.: On the morphology of energetic ($\geqq$30 keV) electron precipitation during the growth phase of magnetospheric substorms. J. Atmos. Terr. Phys. **38**, 739–755, 1976

Rostoker, G.: Polar magnetic substorms. Rev. Geophys. Space Phys. **10**, 157–211, 1972

Rostoker, G.: Current flow in the magnetosphere during magnetospheric substorms. J. Geophys. Res. **79**, 1994–1998, 1974

Russell, C.T.: Geophysical coordinate transformations. Cosmic Electrodyn. **2**, 184–196, 1971

Russell, C.T., McPherron, R.L.: The magnetotail and substorms. Space Sci. Rev. **15**, 205–266, 1973

Sato, T.: A theory of quiet auroral arcs. J. Geophys. Res. **83**, 1042–1048, 1978

Snyder, A.L., Akasofu, S.-I.: Observations of the auroral oval by the Alaskan meridian chain of stations. J. Geophys. Res. **77**, 3419–3430, 1972

Troshichev, O.A., Kuznetsov, B.M., Pudovkin, M.I.: The current systems of the magnetic substorm growth and explosive phases. Planet. Space Sci. **22**, 1403–1412, 1974

Vorobjev, V.G., Gustafsson, G., Starkov, G.V., Feldstein, Y.I., Shevnina, N.F.: Dynamics of day and night aurora during substorms. Planet. Space Sci. **23**, 269–278, 1975

Vorobjev, V.G., Starkov, G.V., Feldstein, Y.I.: The auroral oval during the substorm development. Planet. Space Sci. **24**, 955–965, 1976

Wallis, D.D., Anger, C.D., Rostoker, G.: The spatial relationship of auroral electrojets and visible aurora in the evening sector. J. Geophys. Res. **81**, 2857–2869, 1976

Wescott, E.M., Stenbaek-Nielsen, H.C., Davis, T.N., Murcray, W.B., Peek, H.M., Bottoms, P.J.: The L=6.6 Oosik barium plasma injection experiment and magnetic storm of March 7, 1972. J. Geophys. Res. **80**, 951–967, 1975

Whalen, J.A.: Auroral oval plotter and nomograph for determining corrected geomagnetic local time, latitude, and longitude for high latitudes in the northern hemisphere, Environmental Res. Papers, No. 327, Air Force Cambridge Res. Lab., Bedford, Mass., 1970

Received July 14, 1978 / Accepted September 14, 1978

J. Geophys. 45, 67–80, 1978

Journal of Geophysics

Ionospheric Observation of Gravity-Waves Associated With Hurricane Eloise

R.J. Hung and J.P. Kuo

The University of Alabama in Huntsville, Huntsville, Alabama 35807, U.S.A.

Abstract. An experiment conducted by using a continuous wave-spectrum high frequency radio wave Doppler sounder array with three sites and nine transmitters (each site with three transmitters) was carried out to observe the coupling of energy between the troposphere and the ionosphere during the period of Hurricane Eloise. The analysis of the Doppler sounder records indicated that gravity waves were detected when the eye wall of Hurricane Eloise was located at the Gulf of Mexico. A group ray tracing has been used in an attempt to locate the sources of these waves. Wave sources are located along the storm track and near the storm center. The wave excitation mechanism is discussed.

Key words: Hurricanes – Gravity waves – Ionosphere.

1. Introduction

In the past decade, observations made by Georges (1968), Baker and Davies (1969), Davies and Jones (1972), Georges (1973), Hung et al. (1975), Smith and Hung (1975), and Hung and Smith (1977a; 1977b) show a correlation between ionospheric wave-like disturbances and severe weather activity. A recent study of Hung et al. (1978a, 1978b) and Hung and Smith (1978a, 1978b) indicated a close correlation of atmospheric gravity waves and tornado activity. The present study reveals the correlation of gravity waves observed in ionospheric height and the activity of Hurricane Eloise.

The correlation of the atmospheric acoustic-gravity waves and severe storms has been investigated in the past twenty years. Tepper (1950, 1954) proposed that the pressure jump lines effectively lifted the lowest layers of the atmosphere and appeared to initiate squall line development in convectively unstable air. Matsumoto and Akiyama (1969); Matsumoto and Tsuneoka (1969); and Matsumoto et al. (1967a, 1967b) contended that acoustic-gravity waves were responsible for a pulsating tendency of winter and summer convective storms in Western

0340-062X/78/0045/0067/$02.80

Japan. Recently Uccellini (1975) proposed that acoustic-gravity waves are an important mechanism for the initiation of severe convective storms. He also suggested that the study of acoustic-gravity waves could reveal the development of thunderstorms.

It is also suggested that the spiral bands of hurricans and typhoons behave like gravity waves. Tepper (1958) and Abdullah (1966) hypothesized that the bands are gravity waves similar to pressure jumps. Based on numerical simulation, Kurihara (1976) shows that a spiral band of tropical cyclone, which propagates outward, can grow in the presence of the horizontal shear of the basic azimuthal flow. The horizontal wavelength of the band is 200 km, and the characteristics of waves behave like gravity modes.

Gravity waves are also important in understanding the behavior of ionospheric irregularities (Hines, 1960). The ionospheric irregularities known as TID's (traveling ionospheric disturbances) observed by Munro (1950, 1958) have been identified as gravity waves in the form of the fluctuations of ionization in the F region (e.g., Rishbeth and Garriot, 1969). TID's, in general, can be divided into two categories, large scale TID's and medium scale TID's based on the characteristics of wave propagation (e.g., Kato, 1976). The large scale TID's have been identified to be the production of Joule heating and of Ampere mechanical force at the auroral zone during magnetic substorms (e.g., Chimonas and Hines, 1970; Testud, 1970). Medium scale TID's have been observed more often than large scale TID's and may be excited by various sources including meteorological severe storm activity and magnetic disturbances. The discussion of the characteristics of gravity waves in lower and upper atmospheres are given by Gossard and Hooke (1975), and we are limiting ourselves to examine the gravity waves associated with severe storms, in particular, hurricanes in this study.

The observation of atmospheric gravity waves (medium scale TID's) associated with severe storms at the ionospheric height is possible when severe thunderstorms with tops (radar heights) in excess of about 12 km occurred within a radius of several hundred kilometers of the ionospheric reflection points (Georges, 1976; Prasad et al., 1975), or only when intense updrafts of clouds penetrate the tropopause. A similar idea was proposed by Saunders (1962), that the convection regions imbedded in the stratiform anvil of the thunderstorms are clearly the overshooting convective cells which penetrate the tropopause. Observations of the hurricane eye wall by radar echoes made by Malkus (1960) also indicate that the eye wall cloud penetrate well above the tropopause. By taking photographs from a U-2 airplane flying over the thunderstorms, Vonnegut et al. (1966) also showed that convective overshooting turrets rose above the anvil cloud and penetrated the tropopause. This may suggest that the penetration of the intense updrafts of convection through the tropopause could be the mechanism of wave generation. In other words, the process of convective overshooting associated with severe thunderstorms (which in turn is associated with tornadoes) or with the wallclouds of hurricanes is responsible for the generation of atmospheric acoustic-gravity waves. Recent observations made by ATS satellites (Fjuita, 1974) and Skylab (Black, 1977) also endorse the correlation of the growth and collapse of convective overshoot-

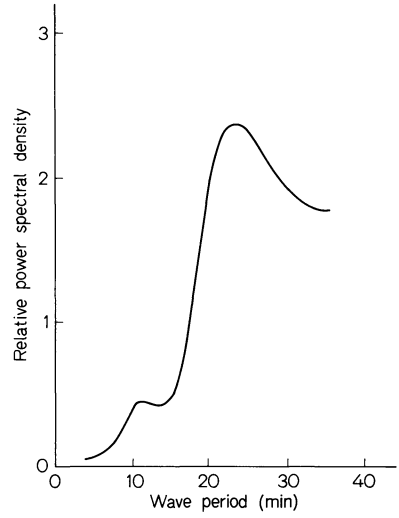

Fig. 1. Power spectral density of waves from Muscle Shoals, Alabama to Huntsville, Alabama at 0200–0340 UT, 9–23–1975

ing turrets associated with severe storms and the generation of gravity waves.

In the present study, we are particularly interested in the investigation of hurricane-associated acoustic-gravity waves which were observed on ground-based ionospheric sounding records as perturbations in electron densities at ionospheric heights. We have employed a continuous wave-spectrum high frequency radio wave Doppler sounder array to observe ionospheric disturbances during the activity of Hurricane Eloise which was located at the Gulf of Mexico on September 23, 1975. The evidence for the coupling of energy from the troposphere into the ionosphere has come from observations of electron density fluctuations which appear as changes of phase and frequency of the ionospherically reflected radio waves.

The results of the coupling between the troposphere and the ionosphere through the upward propagation of gravity waves during the time period of hurricane activity are discussed. The probable errors in computed trajectories of the observed waves will be discussed in Sections 2 and 4.

2. Experiments and Data Analysis

Our Doppler array system consists of three sites with nine field transmitters operating at 4.0125, 4.759 and 5.734 MHz. These sites are located in Northern Alabama and the Tennessee Valley area. A detailed description of the geographical locations and array systems have been given by Hung et al. (1978a) and Hung and Smith (1978a). The propagation characteristics of atmospheric gravity waves can be observed from electron density fluctuations in the ionosphere.

During the time periods of the Hurricane Eloise activity on September 22–23, 1975, wave-like fluctuations were observed at F-region ionospheric heights with wavelengths on the order of 100 km. These observed traveling ionospheric distur-

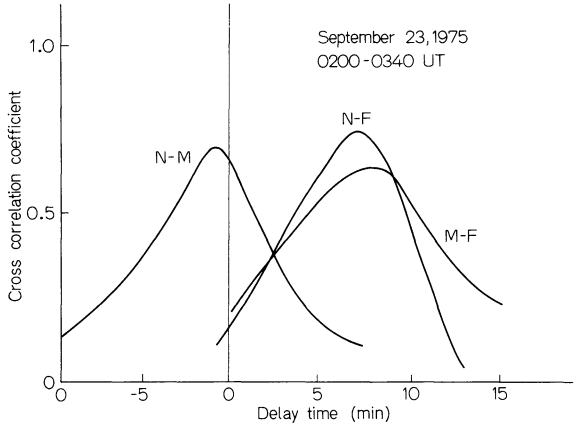

Fig. 2. Cross correlograms at time period 0200–0340 UT, 9–23–1975

bances (TID's) associated with hurricanes belong to medium scale TID's in contrast with large scale TID's associated with geomagnetic activity initiated at the auroral zone (Kato, 1976).

Doppler records observed were subjected to power spectral density analysis and cross-correlation analysis. As an example, Figure 1 shows power spectral density of the ionospheric disturbances from the transmitters at Muscle Shoals, Alabama to the receivers at Huntsville, Alabama, at the observation time 0200–0340 UT, September 23, 1975. The wave period of the disturbances during this time period of observation is 23 min.

The amplitude of the gravity waves is inversely proportional to the square root of the density of the medium (Davies and Jones, 1972). The observed amplitude of the gravity waves associated with severe storms also depends upon the distance from the location of the wave source to the point of the wave observation. The amplitude of waves associated with different types of severe storms, such as severe thunderstorms, tornadoes, and/or hurricanes are all in the order of 0.1 to 0.5 Hz of frequency shift measured at F-2 region ionospheric heights.

As usual, the horizontal phase velocity of the disturbances can be computed from cross-correlograms (detailed description see Hung et al., 1978a). Figures 2 and 3 show cross-correlograms during the time interval 0200–0340 and 0500–0730 UT, September 23, 1975. The accuracy of the determination of the azimuthal angle of wave propagation is within $\pm 5°$, and the horizontal phase velocity is within ± 8 percent of deviation in this set up.

In this experiment, the following characteristics of waves were observed: (1) in the time period 0200–0340 UT, gravity-waves with wave periods of 23 min, azimuthal angle of wave vector 353°, and horizontal phase speed 160 m/s were observed; and (2) in the time period 0500–0730 UT, gravity waves with wave periods of 23 min, azimuthal angle of the wave vector 344°, and horizontal phase speed of 195 m/s were detected.

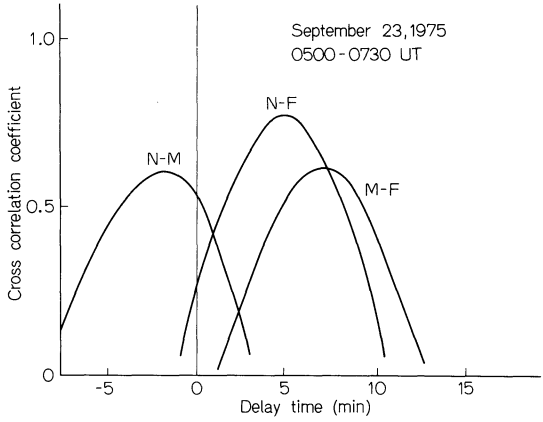

Fig. 3. Cross correlograms at time period 0500–0730 UT, 9–23–1975

3. Reverse Ray Tracing

Theoretical discussions of group rays of atmospheric gravity waves have been carried out by Bretherton (1966), Jones (1969), Cowling et al. (1971) and Bertin et al. (1975). These discussions suggest that the geometrical optics approximation seems valid for the ray propagation of gravity waves if the distance from the source to the point of observation is much longer than the wavelength of the gravity waves. This is approximately true for our case. The wave propagated is assumed to be locally plane so that a local dispersion relation of atmospheric gravity waves, proposed by Hines (1960), is satisfied. Ray tracing, thus, could be carried out by following the group velocity direction in a wind-stratified model atmosphere.

The propagation of wave energy in a lossless transparent medium follows the direction of the group velocity (e.g., Yeh and Liu, 1972). This direction is termed ray direction. In general, in an anisotropic medium the ray direction is different from that of the wave vector. The reverse ray tracing computation is the integration of group velocity with respect to time domain from the ionospheric reflection point back down to the tropopause using the wave period, wavelength, and azimuthal direction of wave propagation obtained from the observational data, the initial vertical wave vector computed from the dispersion relation and appropriate atmospheric parameters. The effect of wind was taken into account by considering the time-space transformation given by the Galilean transformations of displacement vector, time, Doppler-shift of wave frequency, and wave vector. The detailed description of group ray tracing computation has been given in another article (Hung and Smith, 1978a).

In the present paper, the neutral wind is treated as constant in each slab of the atmosphere considered. The values of atmospheric parameters for each altitude are calculated from the U.S. Standard Atmosphere (1962). The profiles of the neutral winds are established using data from the following two sources:

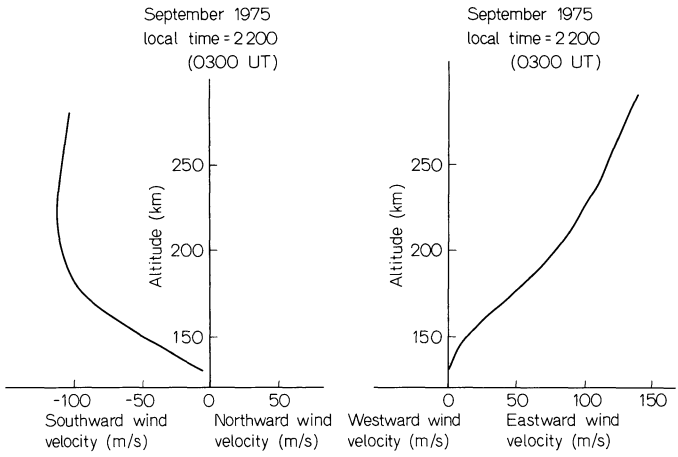

Fig. 4. Computed vertical wind profiles of meridional and zonal components at 2200 local time (0300 UT), September 1975

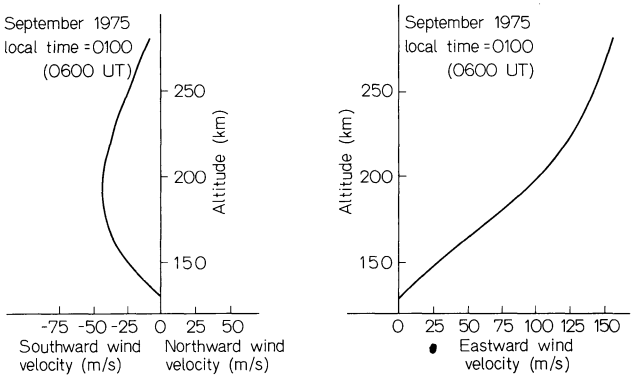

Fig. 5. Computed vertical wind profiles of meridional and zonal components at 0100 local time (0600 UT), September 1975

(1) wind profiles above 100 km altitude are computed from the atmospheric wind model proposed by Kohl and King (1967); (2) at an altitude below 90 km, wind profiles are obtained from meteorological rocketsonde data at Cape Kennedy, Florida.

Figure 4 shows two computed vertical wind profiles from the Kohl and King Model (1967) for zonal component and meridional component at 2200 local time (0300 UT), September 1975. Figure 5 indicates two similar computed vertical wind profiles from the Kohl and King Model (1967) at 0100 local time (0600 UT), September 1975. The observed vertical wind profiles of meridional and zonal components from the meteorological rocketsonde data at 1426 UT, September 23, 1975, at Cape Kennedy, Florida are given in Figure 6.

The wind model proposed by Kohl and King (1967), however, started with

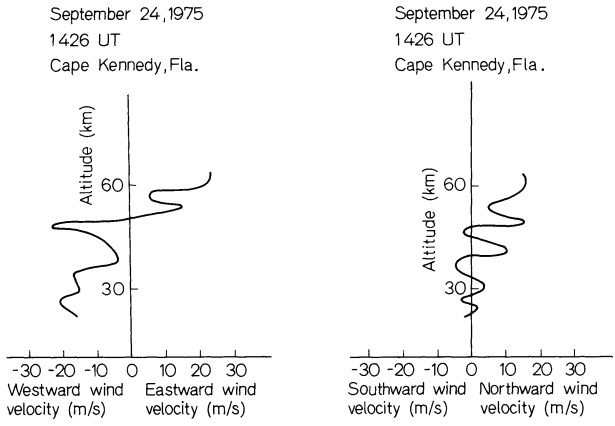

Fig. 6. Observed vertical wind profiles of meridional and zonal components at 1426 UT, 9–24–1975, Cape Kennedy, Florida

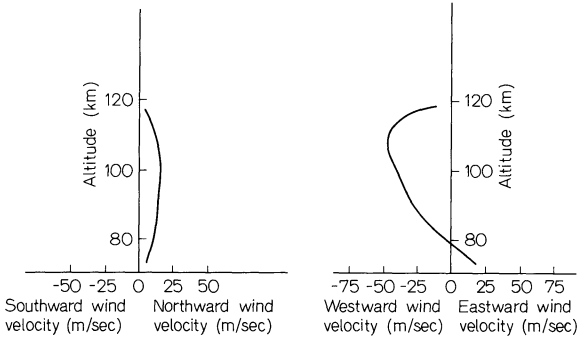

Fig. 7. Wind profiles from altitudes of 70 to 120 km based on 25 sodium cloud experiments from Wallops Island during the summer time

an artificial boundary condition for which the wind velocity is equal to zero at altitude 120 km. To make up this discrepancy, wind profiles based on 25 sodium cloud experiments from Wallops Island (see West et al., 1977), from altitudes of 70 to 120 km as illustrated in Figure 7, were used and faired into meteorological rocketsonde data from Cape Kennedy and computed thermospheric one based on Kohl and King's model. These wind profiles were also checked with the four dimensional wind model (Justus et al., 1974a, 1974b) used by NASA for spacecraft design purposes.

4. Sources of Waves

The reverse ray tracing is started at an altitude of ionospheric reflection height with a frequency of 4.0125 MHz and continues as long as the calculation is

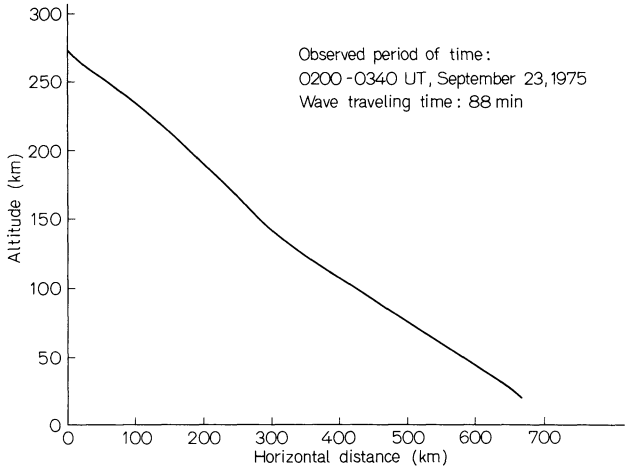

Fig. 8. Trajectory of the computed reverse group ray path for the waves at time periods 0200–0340 UT, 9–23–1975

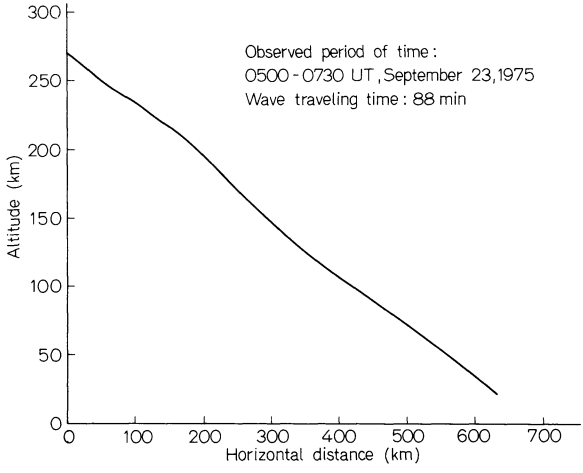

Fig. 9. Trajectory of the computed reverse group ray path for the waves at time period 0500–0730 UT, 9–23–1975

possible to a lower limit of 10 km altitude or the altitude of tropopause. For the purpose of the present study the geographic location of the point at which the calculation is terminated is referred to as the probable source. The probable source of acoustic-gravity waves are then checked with the actual physical features, which is the meteorological observation of storm track of Hurricane Eloise.

It is interesting to review the historical development of Hurricane Eloise. Eloise moved off the coast of Africa as a weak disturbance on September 6, 1975. It then followed a steady westward path across the Atlantic becoming

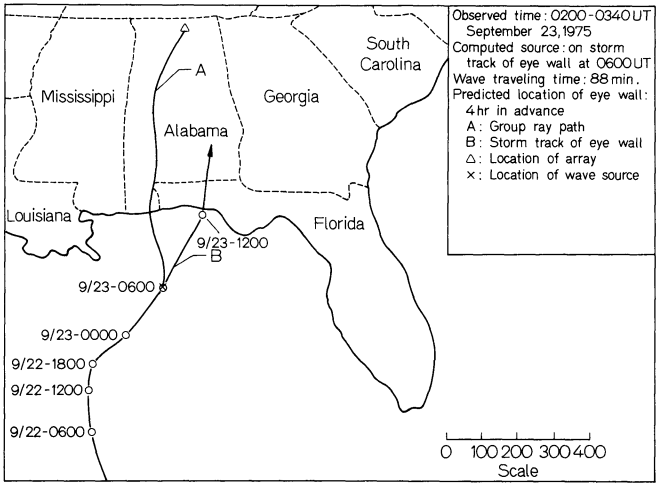

Fig. 10. Geographical map of the trajectory of computed source of waves at time period 0200–0340 UT, 9–23–1975

a tropical depression 600 km east of the Leeward Island on September 13, was named a tropical storm and subsequently a hurricane north of Puerto Rico on the 16th. The westward track carried the center or eye over eastern Cuba and as it moved out over the water, Eloise became a tropical storm once again. After crossing the northeastern tip of the Yucatan Penisula, Eloise turned northward into the Gulf of Mexico on the 21st reaching hurricane force once more on the morning of the 22nd. By that evening, Eloise turned rather abruptly northeastward towards the Florida coastline.

Figure 8 shows trajectory of the computer reverse ray path for the waves observed during time period 0200–0340 UT, September 23, 1975, in terms of height against horizontal distance. Figure 9 shows another trajectory of the computer reverse ray path observed during the time period 0500–0730 UT, September 23, 1975 for the similar profile. Again the group ray paths in the horizontal distance are projected in the map to show the geographical location of the probable sources of waves.

Figure 10 shows the horizontal ray path and the geographical location of the probable source of the wave which was detected in the ionospheric height with receivers at Huntsville, Alabama, at 0200–0340 UT, September 23, 1975. The computed location of the wave source is located right on the storm track of the eye wall at 0600 UT, September 23, 1975. The calculated traveling time of this wave from the probable source to the receiver at Huntsville, Alabama was 88 min. Thus, in this particular case, the location of the wave source was along the storm track and about 90 km distance from the storm center or 4 h in advance of the location of the eye wall.

Figure 11 presents another geographical location of the probable source of the wave which was observed at 0500–0730 UT, September 23, 1975. In this case, the computed probable source of the wave is located right on the

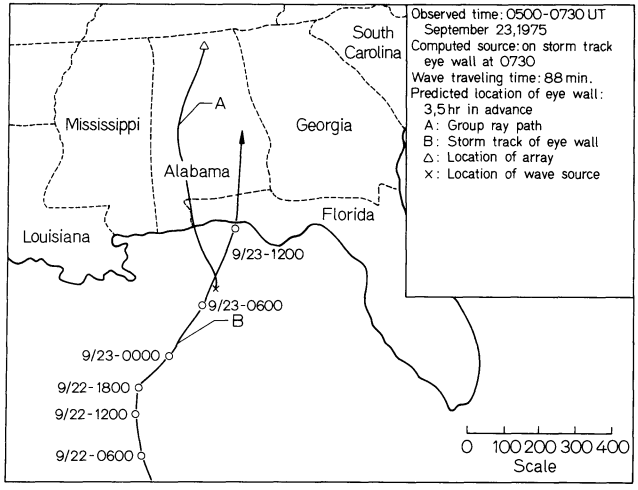

Fig. 11. Geographical map of the trajectory of computed source of waves at time period 0500–0730 UT, 9–23–1975

storm track of the eye wall at 0730 UT, September 23, 1975. The calculated traveling time of this wave from the probable source to the receiver at Huntsville, Alabama was also 88 min. Thus, the wave source was located along the storm track of Hurricane Eloise, and about 80 km distance from the storm center or approximately 3.5 h in advance of the location of the eye wall.

The determination of probable errors or ranges in the reverse ray tracing computation due to the accuracy of the determining of the azimuthal angle of wave propagation and horizontal phase velocity are rather standard. However, it is not easy to determine the errors due to the uncertainty of the wind profiles, in particular, the lacking of real time measurements of the thermosphere part of wind profiles. Hung and Smith (1978a) has estimated the probable errors caused by double the wind velocity, reduce the wind velocity to half, rotate 90° the direction of wind velocity counterclockwise, and rotated 180° the direction of the wind velocity for horizontal distance around 400 km and found that, even under the situation as mentioned, the probable errors are within ± 12 km per 100 km of the horizontal distance. The total probable errors can be estimated based on more than twenty cases of reverse ray tracing computations, compared with physical features of storm data, that the computed probable errors are less than ± 20 km per 100 km of the horizontal distance of ray tracing in our cases. If the probable errors less than ± 20 km per 100 km of the horizontal distance is taken into account, the location of the probable sources of waves was around the outer layer of the wall cloud and 70 to 150 km distance from the storm center. This result agrees with outward propagating gravity waves in the numerical model developed by Kurihara (1976) in which the gravity waves excited around the inner layer of the wall cloud propagate inward with a higher damping rate and the gravity waves developed

around the outer layer of the wall cloud propagate outward with a low damping rate.

In addition to the work by Georges (1976), Prasad et al. (1975), Saunders (1962), and Malkus (1960), Vonnegut et al. (1966) using photographs from a U-2 airplane flying over the thunderstorms, showed that convective overshooting turrets rose above the anvil cloud and penetrated the tropopause. This may suggest that the penetration of intense updrafts through the tropopause could be the wave generation mechanisms. Recent Skylab observations (Black, 1977) based on stereophotographs taken from tropical storm Ellen also indicated the overshooting turrets above the tropopause in the wall clouds.

From a fluid dynamics point of view, Lighthill (1952, 1954, 1962, and 1967), Townsend (1968, 1969), and Deardorff et al. (1969) show that gravity waves can be generated by tongues of turbulence penetrating above the turbulent convective zone. This suggests that the overshooting and ensuing collapse of the convective turrets may be responsible for the generation of the atmospheric acoustic-gravity waves. Recently, Shenk (1974) made extensive observations of strong convective cells of severe storms using geosynchronous satellite data and U-2 photographs. When the results of Shenk's analysis are used in the model proposed by Lighthill (1952, 1954, 1962, and 1967), waves with the same periods as those waves associated with severe storms observed by the Doppler array are excited (Hung and Smith, 1977b). Furthermore, by using relative cloud heights of hurricane wall clouds based on photographic enhancement techniques computed from Skylab photographs (Black, 1977) and the growth rate of turrets estimated by Fujita (1974), in Lighthill's model, the wave period in the range of 20 to 25 min associated with hurricanes in the present observation can be generated. The detailed description of the wave generation mechanism will be published in subsequent papers.

George (1960) reported that hurricanes tend to move toward the location where the K-instability index[1] is a maximum with a higher index being related to a higher moisture content and a higher temperature. Results of this study seem to indicate that this is the location of the source of the waves. The possibility of using a combination of these facts as a prediction technique will be the subject of future investigations. This study suggests that the analysis of ionospheric Doppler sounder observations of gravity associated with hurricanes, together with the study of the growth and collapse of convective overshooting turrets based on satellite photographs, can contribute to the understanding of the dynamical behavior of hurricanes.

Acknowledgment. The authors are indebted to R.E. Smith of NASA/Marshall Space Flight Center for the discussions concerning this study. They also appreciate the support of present research from the National Science Foundation and the U.S. Army Research Office through Grant NSF/ATM75-15706.

[1] Definition of K index is

K = (850-mb temp − 500-mb temp) + (850-mb dewpoint) − (700-mb dewpoint depression)

which has been widely used by meteorologist to predict severe weather (George, 1960)

References

Abdullah, A.J.: The spiral bands of a hurricane: A possible dynamic explanation. J. Atmos. Sci. **23**, 367–375, 1966

Baker, D.M., Davies, K.: F2-region acoustic waves from severe weather, J. Atmos. Terr. Phys. **31**, 1345–1352, 1969

Bertin, F., Testud, J., Kersley, L.: Medium scale gravity waves in the ionospheric F-region and their possible origin in weather disturbances. Planet. Space Sci. **23**, 493–507, 1975

Black, P.G.: Some aspects of tropical storm structure revealed by handheld-camera photographs from space, in Skylab Explores the Earth, ed. by V.R. Wilmarth, NASA SP-380, pp. 417–461, 1977

Bretherton, F.P.: The propagation of groups of internal gravity-waves in a shear flow. Quant. J. Roy. Meteor. Soc. **92**, 466–480, 1966

Chimonas, G., Hines, C.O.: Atmospheric gravity waves launched by auroral currents. Planet. Space Sci. **18**, 565–582, 1970

Cowling, D.H., Webb, H.D., Yeh, K.C.: Group rays of internal gravity waves in a wind stratified atmosphere. J. Geophys. Res. **76**, 213–220, 1971

Davies, K., Jones, J.E.: Ionospheric disturbances produced by severe thunderstorms, NOAA Professional Paper 6, U.S. Dept. of Commerce, NOAA, Rockville, Md., pp. 47, 1972

Deardorff, J.W., Willis, G.E., Lilly, D.K.: Laboratory investigation of non-steady penetrative convection. J. Fluid Mech. **35**, 7–31, 1969

Fujita, T.T.: Overshooting thunderheads observed from ATS and Learjet. NASA CR-13859T, 1974

George, J.J.: Weather Forecasting for Aeronautics, pp. 673. New York: Academic Press 1960

Georges, T.M.: Short-period ionsopheric oscillations associated with severe weather, Proc. Symp. Acoustic-Gravity Waves in the Atmosphere, Govt. Printing Office, Washington, D.C., pp. 171–178, 1968

Georges, T.M.: Infrasound from convective storms: Examining the evidence. Rev. Geophys. Space Phys. **11**, 571–594, 1973

Georges, T.M.: Infrasound from convective storms, Part II: A critique of source candidates, NOAA Tech. Rep. ERL 380-WPL49, pp. 59, 1976

Gossard, E.E., Hooke, W.H.: Waves in the Atmosphere-Atmospheric Infrasound and Gravity Waves, Their Generation and Propagation, pp. 456. Netherland: Elsevier Scientific Publ. Co. 1975

Hines, C.O.: Internal atmospheric gravity waves at ionospheric heights, Can. J. Phys. **38**, 1441–1481, 1960

Hung, R.J., Phan, T., Smith, R.E.: Observation of gravity waves during the extreme tornado outbreak of April 3, 1974, J. Atmos. Terr. Phys. 1978a (in press)

Hung, R.J., Phan, T., Smith, R.E.: Ionospheric Doppler sounder as remote sensing for detection and prediction of severe storms. AIAA Paper, No. 78–250, 1–6, 1978; also AIAA Journal, **16**, 763–766, 1978b

Hung, R.J., Smith, R.E.: Observation of upper atmospheric disturbances caused by hurricanes and tropical storms. Space Res. **17**, 205–210, 1977a

Hung, R.J., Smith, R.E.: Study of stratospheric-ionospheric coupling during time periods of thunderstorms and tornadic storms. Space Res. **17**, 210–216, 1977b

Hung, R.J., Smith, R.E.: Ray tracing of gravity waves as a possible warning system for tornadic storms and hurricanes. J. Appl. Meteorol. **17**, 3–11, 1978a

Hung, R.J., Smith, R.E.: Dynamics of severe storms through the study of thermospheric-tropospheric coupling. J. Geomag. Geoelectr., 1978b (in press)

Hung, R.J., Smith, R.E., West, G.S., Henson, B.B.: Detection of upper atmospheric disturbances in Northern Alabama during extreme tornado outbreak of April 3, 1974, Ninth Conference on Severe Local Storms, Amer. Meteor. Soc., Boston, Mass., pp. 294–300, 1975

Jones, W.L.: Ray tracing of internal gravity waves. J. Geophys. Res. **74**, 2028–2033, 1969

Justus, C.G., Woodrum, A.W., Roper, R.G., Smith, O.E.: Four-D Global Reference Atmosphere Technical Description, Part I, pp. 106, NASA TM-X-64871, 1974a

Justus, C.G., Woodrum, A.W., Roper, R.G., Smith, O.E.: Four-D Global Reference Atmosphere Technical Description, Part II, pp. 206, NASA TM-X-64872, 1974b

Kato, S.: Thermospheric Waves—a Review. J. Geomag. Geolectr. **28**, 189–206, 1976

Kohl, H., King, J.W.: Atmospheric winds between 100 and 700 km and their effects on the ionosphere. J. Atmos. Terr. Phys. **29**, 1045–1062, 1967

Kurihara, Y.: On the development of spiral bands in a tropical cyclone. J. Atmos. Sci. **33**, 940–958, 1976

Lighthill, M.J.: On sound generated aerodynamically, I. General theory. Proc. Roy. Soc. A **211**, 564–587, 1952

Lighthill, M.J.: On sound generated aerodynamically, II. Turbulence as a source of sound. Proc. Roy. Soc. A **222**, 1–32, 1954

Lighthill, M.J.: Sound generated aerodynamically. Proc. Roy. Soc. A **267**, 147–182, 1962

Lighthill, M.J.: Prediction on the velocity field coming from acoustic noise and a generalized turbulence in a layer overlaying a convectively unstable atmospheric region. I.A.U. Symposium **28**, 429–469, 1967

Malkus, J.S.: Recent developments in studies of penetrative convection and the application to hurricane cumulonimbus towers. Cumulus Dynamics, pp. 65–84. New York: Pergamon Press 1960

Matsumoto, S., Akiyama, T.: Some characteristic features of the heavy rainfalls observed over the Western Japan on July 9, 1967, Part I: Mesoscele structure and short period pulsation. J. Meteorol. Soc. Japan **47**, 255–266, 1969

Matsumoto, S., Ninomiya, K., Akiyama, T.: A synoptic and dynamic study on the three-dimensional structure of mesoscale disturbances observed in the vicinity of a cold vortex center. J. Meteorol. Soc. Japan **45**, 64–81, 1967a

Matsumoto, S., Ninomiya, K., Akiyama, T.: Cumulus activities in relation to the mesoscale convergence field. J. Meteorol. Soc. Japan **45**, 292–304, 1967b

Matsumoto, S., Tsuneoka, Y.: Some characteristic features of the heavy rainfalls observed over the Western Japan on July 9, 1967, Part II: Displacement and life cycles of mesoscale rainfall cells. J. Meteorol. Soc. Japan **47**, 267–278, 1969

Munro, G.H.: Traveling disturbances in the ionosphere. Proc. Roy. Soc. (London) **A202**, 208–223, 1950

Munro, G.H.: Traveling ionospheric disturbances in the F region. Australian J. Phys. **11**, 91–112, 1958

Prasad, S.S., Schneck, L.J., Davies, K.: Ionospheric disturbances by severe tropospheric weather storms. J. Atmos. Terr. Phys. **37**, 1357–1363, 1975

Rishbeth, H., Garriot, O.K.: Introduction to Ionospheric Physics, pp. 331. New York: Academic Press 1969

Saunders, P.M.: Penetrative convection in stably stratified fluids. Tellus **14**, 177–194, 1962

Shenk, W.E.: Cloud top height variability of strong convective cells. J. Appl. Meteorol. **13**, 917–922, 1974

Smith, R.E., Hung, R.J.: Observation of severe weather activities by Doppler sounder array. J. Appl. Meteorol. **14**, 1611–1615, 1975

Tepper, M.: A proposed mechanism of squall lines: the pressure jump. J. Meteorol. **7**, 21–29, 1950

Tepper, M.: Pressure jump lines in Midwestern United States, January–August 1951. Research Paper No. 37, pp. 70, U.S. Weather Bureau, Washington, D.C., 1954

Tepper, M.: A theoretical model for hurricane radar bands. Preprints Seventh Weather Radar Conf., Miami, Amer. Meteor. Soc., K56–65, 1958

Testud, J.: Gravity waves during magnetic substorms. J. Atmos. Terr. Phys. **32**, 1793–1805, 1970

Townsend, A.A.: Internal waves produced by a convective layer. J. Fluid Mech. **24**, 307–319, 1966

Townsend, A.A.: Excitation of internal waves in a stably-stratified atmosphere with considerable wind-shear. J. Fluid Mech. **32**, 145–171, 1968

Uccellini, L.W.: A case study of apparent gravity waves initiation of severe convective storms. Mon. Wea. Rev. **103**, 497–513, 1975

United States Committee on Extension to the Standard Atmosphere: U.S. Standard Atmosphere 1962, pp. 278, U.S. Govt. Printing Office, Washington, D.C., 1962

Vonnegut, B., Moore, C.B., Espinola, R.P., Blau, H.H., Jr.: Electric potential gradients above thunderstorms. J. Atmos. Sci. **23**, 764–770, 1966

West, G.S., Wright, J.J., Euler, H.C.: Space and Planetary Environment Criteria Guideline for Use in Space Vehicle Development, 1977 Revision, pp. 450, NASA Tech. Memo. 78119, 1977

Yeh, K.C., Liu, C.H.: The Theory of Ionospheric Waves, pp. 467. New York: Academic Press 1972

Received February 13, 1978 / Revised version June 28, 1978

J. Geophys. 45, 81–90, 1978

Journal of Geophysics

On the Annual Wave of Hemispheric Geomagnetic Activity

D. Damaske

Institut für Geophysikalische Wissenschaften, Freie Universität Berlin,
Rheinbabenallee 49, 1000 Berlin 33

Abstract. A harmonic analysis of geomagnetic indices *Kn* and *Ks* introduced by Mayaud (1967) yields a persistent annual wave in hemispheric activity with a maximum near the summer *solstice* (northern hemisphere) or the winter *solstice* (southern hemisphere). It shows up with nearly the same phase for each of the five northern (or three southern) longitude sectors on which the deduction of the hemispheric indices is based. The results are in accordance with expectation derived from a modified hemispheric modulation function as suggested by the annual amplitude variation of the diurnal UT wave. Apparent discrepancies in the corresponding results for the linear equivalent amplitudes *an* and *as* are shown to be due to an increased amplitude scattering together with a residual of an incompletely eliminated *planetary* 12-month wave in activity *sequences*.

Key words: Geomagnetic activity – Annual wave.

1. Introduction

The most prominent periodicities in the terrestrial modulation of geomagnetic activity are the well-known semi-annual wave and the universal time (UT) variation. Both effects are determined by the varying angle β between the direction of the solar wind flow and the earth's dipole axis. The existence of a UT variation and the terrestrial origin of the semi-annual wave have first been stated by Bartels (1925, 1928, 1932) realizing that the dates of maximum activity are in favour of the equinoxes rather than of the dates where the earth reaches maximum heliographic latitude, thus indicating a purely terrestrial characteristic.

As a daily pendant of the semi-annual wave the UT variation for certain observatories shows a diurnal component for the solstices and a semi-diurnal component for the equinoxes (McIntosh, 1959). The existence of such universal waves was further established by synchronization of appropriate geomagnetic indices (Mayaud, 1967, 1970) and by the harmonic analysis method (Meyer,

0340-062X/78/0045/0081/$02.00

1973, 1974) yielding results in the same form as expected from a modulation function governed by the square-sine of the solar wind angle β. This concept holds true also for the annual amplitude modulation of the diurnal and semi-diurnal waves in geomagnetic activity as far as the earth as a whole is concerned (Damaske, 1976, 1977).

However, when treating separately northern and southern hemispheres the amplitude of the diurnal UT wave turns out to be systematically shifted towards higher (smaller) values in the respective meteorological winter (summer) half-year. The effect has quantitatively been detected from a 14-year series of hemispheric quasi-logarithmic indices *Kn* and *Ks* (Damaske, 1976, 1977) as well as from the corresponding linear indices *an* and *as* (Damaske, 1978). It can fully be accounted for by adding a constant angle β_0 to the time-dependent angle β, with opposite sign on both hemispheres. If such an alteration is really effective, the modified modulation function requires – besides the 6-month wave – the existence of an additional 12-month wave in hemispheric activity itself, due to the asymmetry between summer and winter half-years. The phase of the annual wave in activity modulation is again opposite on both hemispheres corresponding to a maximum at the respective meteorological summer *solstice*. In fact, from hemispheric daily indices *C9n* and *C9s*, i.e., ten-step quasi-logarithmic character figures derived from daily means of *an* and *as* by the same conversion table as yields *C9* from *ap* (Bartels, 1957; see also Siebert, 1971; Damaske, 1977), a significant annual wave has been obtained with phase and amplitude being in full accordance with expectation from the annual modulation of the diurnal UT wave and the modified modulation function $\sin^2(\beta+\beta_0)$. For a detailed description including deductions of all formulas see Damaske, 1976, 1977.

If the disclosed concept of a hemispheric modification of geomagnetic activity modulation is correct, the additional annual wave should appear also in the separate sector values of *K* from which (after latitude standardization) the indices *an* and *as* are calculated (Mayaud, 1968). Its amplitude is expected to be of the same order of magnitude for each of the five northern sectors and the three southern sectors as well, while the phase is being reversed on both hemispheres.

The average annual variation for each separate sector using the sector values after transformation into equivalent amplitudes has been calculated by Mayaud (1977) with data from 1959 to 1974. In addition to the planetary activity modulation following the square-sine of the angle β which he refers to as the McIntosh effect, Mayaud (1977) interprets the results by two other components. The first component has its maximum during the summer solstice of each hemisphere and is assumed to be caused by additional activity, especially in the *H*-component, around 15 h LT. This should give rise to a longitude-dependent amplitude variation being largest on the meridian of the geomagnetic pole in each hemisphere. The second component would correspond to a larger activity around local midnight during the winter solstice than during the summer solstice. This interpretation allows also for the anomalous phase reversal of the annual wave which Mayaud finds for the South American sector. It is the purpose of the present investigation to check by actual harmonic analysis the sectorial data

with respect to amplitude and phase behaviour of the respective annual wave, aiming at a better understanding of the origin of the hemispheric annual wave.

2. Results of Harmonic Analysis

Although the synchronization method is an approved and useful tool for the detection of real periodicities, classical harmonic analysis offers a more accurate investigation of amplitudes and phases of the various periodic components. At the same time it permits to calculate the probable error for each single harmonic, thus allowing a clear judgement of reality through an unobjectionable test of significance.

For the analysis of geophysical time-series with respect to yearly periodicities, i.e., annual waves and semi-annual waves or even higher harmonics, the fundamental interval is the period of one year. Usually the analysis is based on the 12 monthly mean values per year. However, for problems of geomagnetic activity, because of its recurrence tendency, it is more reasonable to start from 27-day means, instead. This leads to the methods of harmonic sequence analysis (Meyer, 1973), where the fundamental interval is two years giving annual and semi-annual waves as the second or fourth harmonic, respectively.

The results for the annual wave in 27-day means of sectorial K-values, obtained from the eight biannual periods from 1959/60 till 1973/74, are shown in Fig. 1 for all eight sectors. Especially marked on the dial are the days of summer solstice (June 22) and winter solstice (December 22). The amplitude scale is given in units of K. The probable error circle, defined by an exceeding probability of 50% for the unknown "true" value (Bartels, 1932; see also Meyer, 1974) is approximately the same for each vector and, therefore, is presented only once around the origin. The phase reversal between northern and southern hemispheres, as derived from the modified modulation function $\sin^2(\beta+\beta_0)$, is immediately apparent by the nearly opposite directions of the five northern sector vectors $N_i (i=1,2,3,4,5)$ and the three southern sector vectors $S_j (j=6,7,8)$. The ratio between the vector amplitude and the radius of the probable error circle exceeds for most of them the 2.92 limit (corresponding to a 0.27% exceeding probability) for a definite statistical significance. Only the results for the central Siberian sector N_2 and the South American sector S_8, when being judged separately, do not yet meet these rather pretentious demands for significance. Nevertheless, since the directions of the vectors are again in full accordance with expectancy for the respective hemisphere, their reality need not be doubted, thus indicating the existence of an annual wave on both hemispheres over the entire longitude range. The theoretical dates of the annual wave maximum as deduced from the modified modulation fuction $\sin^2(\beta+\beta_0)$ are the two solstices. The observed phase for the northern hemisphere corresponds to a maximum early in July, whereas in the southern hemisphere the calculated annual maximum lies at about the middle of December.

In spite of the relatively large probable error circles of the single vectors, a superimposed systematic amplitude variation, especially for the northern hemisphere, cannot be excluded from the present results. If such an effect really exists,

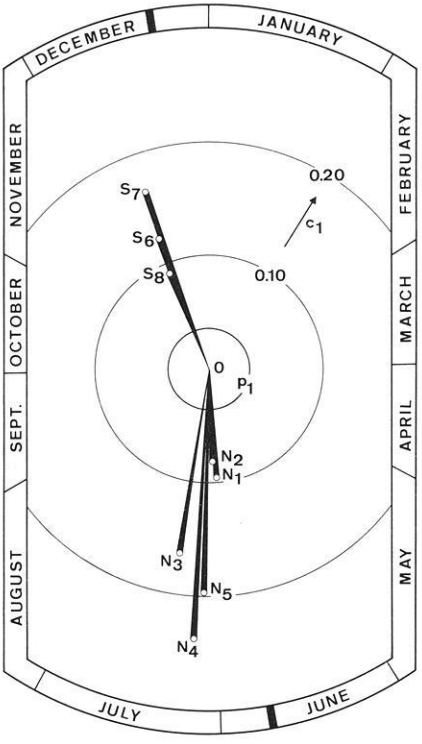

Fig. 1. Harmonic dial for the annual wave in quasi-logarithmic indices K (years 1959–1974) for eight northern and southern longitude sectors. The northern sectors cover the areas as follows: N_1: the western coast of the Pacific Ocean; N_2: central Siberia; N_3: Europe; N_4: the western coast of the Atlantic Ocean; N_5: the eastern coast of the Pacific Ocean. The vectors for the southern hemisphere refer to: S_6: Australia; S_7: the western part of the Indian Ocean; S_8: South America. The amplitude scale is given in units of K, p_1 denotes the probable error. Marked black on the dial are the two solstices

it would imply a longitudinal dependence of the sectorial annual wave amplitude. Such a longitudinal amplitude modulation might well be described in connection with the asymmetry of the polar oval which, on the other hand, is certainly associated with fields and processes in the magnetospheric tail.

To further investigate the small but apparently systematic phase deviations from the theoretical value, the scattering of the results for the annual wave has been compared with the one of the corresponding results for the well-known semi-annual wave calculated from the same eight double-years from 1959 to 1974 (Fig. 2). The notation of the eight vectors is the same as before. The amplitudes are again given in units of K with the (average) probable error circle about the origin of the dial. All vectors except the one for the sector S_8 independently reveal statistical significance. But as for the annual wave, the phase of the vector S_8 leaves no doubt on the real existence of a semi-annual wave also in the South American sector. Moreover, the phases of all eight vectors closely correspond to the expected days of maxima, i.e., the equinoxes. The good agreement among the results for the sectorial semi-annual waves is also demonstrated by the relatively small amplitude scattering. The average amplitude amounts to about two-thirds of the one for the annual wave. (Note that the scale in Fig. 2 is enhanced by a factor of two as compared with Fig. 1). Within the scope of statistical accuracy this ratio agrees with the theoretical ratio of 0.53 deduced from a value of $\beta_0 = \pm 11°$ (Damaske, 1976, 1977).

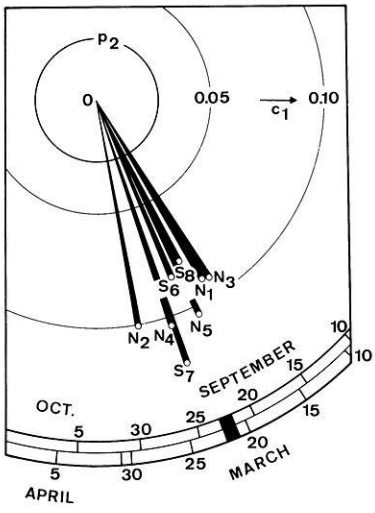

Fig. 2. Harmonic dial for the semi-annual wave in quasi-logarithmic indices K (years 1959–1974) for the same longitude sectors as for the annual wave in Fig. 1. The amplitude scale is again given in units of K. The theoretical times of wave maxima are the equinoxes

The close correspondence of the average semi-annual wave phase with expectation from theory makes it necessary to look for a physical interpretation of the perceptible phase deviation of the average annual wave. A harmonic analysis carried out with altered boundaries of the fundamental interval and leading to quantitatively the same results, ensures that the effect cannot be caused by any superimposed non-cyclic variation. Fig. 3 shows that the systematic deflection of the annual wave vectors toward the left-hand side of the harmonic dial is also present in the results obtained from the hemispheric daily character figures *C9n* and *C9s*. The vector N for the northern hemisphere indicates a wave maximum in the first decade of July. For the southern hemisphere (vector S) the date of wave maximum precedes the theoretical time at the winter solistice by approximately the same amount. The pure hemispheric wave, which is clearly present in both vectors, can be obtained by making use of the known phase reversal between the vectors for the two hemispheres. Reversing the sign for one of them, e.g., the vector S, yields the average true hemisphere annual wave N-S, while any other systematic components are reduced. In fact, the phase of the vector N-S corresponds to a wave maximum only three days after the solstices. Substracting this real hemispheric annual wave from either vector N or S gives the total average vector $N+S$. Though still being statistically insignificant, it may well indicate the presence of another (systematic) annual component, now with equal phase in both hemispheres.

Such a planetary annual wave can also be perceived in other type of data, e.g., means of *Ap* (Siebert, 1971; see also Meyer, 1973). It is especially well pronounced in the years 1959–63, i.e., during the declining branch of the solar cycle 19. As has been shown by Meyer (1972, 1973), it is primarily present in recurrent *sequences* of activity (i.e., sequences of daily values at intervals of 27 days), with arbitrarily alternating phase corresponding to a wave maximum at either one of the equinoxes. Hence, it is partially averaged out when monthly or 27-day means are being analysed. The same morphology of an annual plane-

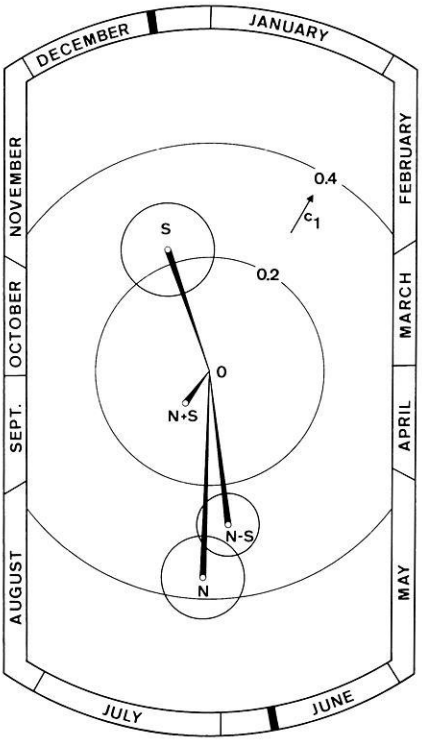

Fig. 3. Annual wave in 27-day means of hemispheric daily character figures *C9n* (northern hemisphere, vector *N*) and *C9s* (southern hemisphere, vector *S*) from the years 1959–74. $N-S$ represents the average annual wave after elimination of the north/south phase reversal; $N+S$ is the total average without taking into account the phase reversal. The circle about the end-point of a vector denotes the probable error

tary wave in geomagnetic activity (with a maximum either in spring or fall) has been found by Berthelier (1976) on the basis of 6 years of indices *Am* and *AE*, and which is attributed to the alternate polarity of the interplanetary magnetic field.

A harmonic analysis of 27-day means of planetary daily character figures *C9m* (derived correspondingly from the three-hourly *am*) for the years 1959–1974 yields a quantitatively similar average result (Fig. 4, vector *M*) as has been obtained for the total average from both hemispheres (vector $N+S$ in Fig. 3). On inspection of the single results for double years which are spread preferably into two opposite directions of the harmonic dial centered at about the dial sectors for March and September (Fig. 4), it is evident that the planetary annual wave has not yet been averaged out completely, even for a full solar cycle. This finding makes it sure that the perceptible deflection of the hemispheric annual wave vectors (*N* and *S* in Fig. 3) into the same direction of the harmonic dial is indeed due to a non-vanishing residual of the planetary annual wave in recurrent activity sequences. The reality of this residual is further supported by the distinct conservation tendency for the single results in Fig. 4. The prevailing phase of the sequential annual wave clearly corresponds to an autumnal maximum throughout the years 1959–1966, then changing sign to a predominating spring maximum until at least 1974.

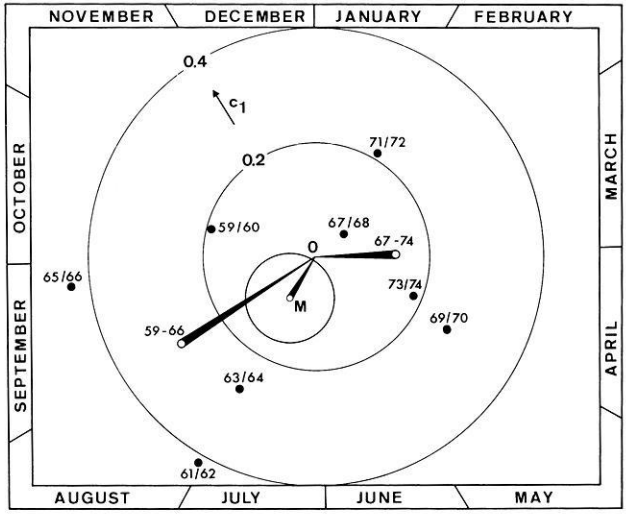

Fig. 4. 12-month wave in 27-day means of the planetary daily character figure *C9m*, for each single double-year from 1959/60 to 1973/74 and for all years (vector *M*). Shown are also the group averages for the years 1959–1966 and 1967–1974

The use of quasi-logarithmic indices implies that the amplitudes of the harmonic components are less sensitive to the general activity level than the results based on linear indices (Meyer, 1973). For the geomagnetic indices *am*, *an*, and *as* the specific amplitude dependence of the diurnal and semi-diurnal UT waves has been set forth in detail by Damaske (1978). As the activity level is primarily governed by sources outside the magnetosphere, it should equally influence the results for each of the eight sectors when equivalent amplitudes instead of quasi-logarithmic indices are analysed. In particular, the planetary 12-month wave in single activity sequences should likewise affect the characteristics of the hemispheric annual wave.

A harmonic analysis of 27-day means of sectorial equivalent amplitudes derived from the sectorial *K*-values by the original conversion table of Mayaud (1968), again for the years 1959–1974, yields essentially the same results for the annual wave (Fig. 5) as from the quasi-logarithmic indices. Only the amplitude scattering is noticeably larger, as expected from the above considerations. And also the deflection of the vectors toward the left-hand side of the dial is somewhat more impressed than for the corresponding results in Fig. 1, thereby affecting especially the vectors with smaller amplitudes. On account of the probable error circle and, in addition, regarding the single vector direction in comparison with the direction of the others, the vectors N_1 and N_2 as well as S_8 in Fig. 5 have no statistical significance at all and thus on no account may give rise to any peculiar interpretation.

For a special investigation of the vector S_8 for the South American sector, Fig. 6 shows once more the single results for the eight double-years from 1959–1974. The clear distribution of the vectors into two opposite dial sections as well as the two group averages for 1959–1966 and 1967–1974 in connection

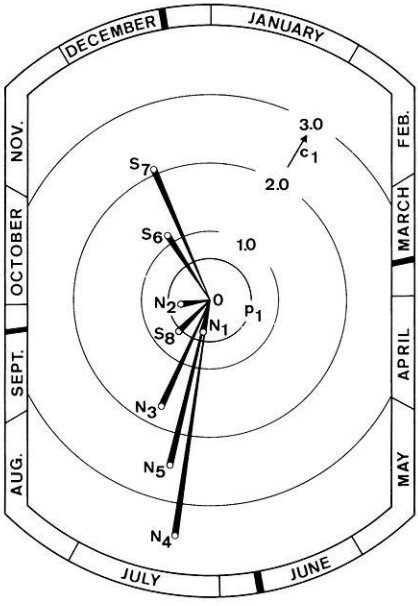

Fig. 5. Same as Fig. 1, but for the annual wave in equivalent amplitudes. In addition to the solstices, the two equinoxes are also marked as black bars on the dial

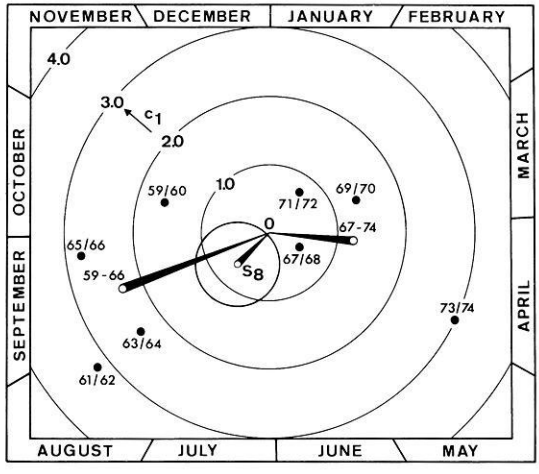

Fig. 6. Same as Fig. 4, but for the annual wave in the equivalent amplitudes for the South American sector only. The total average vector S_8 is identical to the vector S_8 in Fig. 5

with the conservation tendency, make it evident that the vector S_8 as a total average must again be traced back to a non-vanishing residual of the planetary 12-month wave in activity sequences. There is no other systematic annual component detectable in the available data, much less a significant phase reversal, i.e., an annual wave with a maximum at the June solstice.

3. Conclusions

A persistent annual wave in hemispheric magnetic activity, calculated from quasi-logarithmic *K*-indices with data from 1959 to 1974, clearly exists for all eight longitude sectors, in accordance with the modified modulation function $\sin^2(\beta+\beta_0)$ deduced from the annual amplitude modulation of the diurnal UT wave. In particular, the north/south phase reversal of the hemispheric annual wave is definitely present over the entire longitude range. Apparent discrepancies in the corresponding results from equivalent amplitudes *a*, especially for the South American sector, are mainly due to a larger amplitude scattering, although a superimposed systematic amplitude modulation cannot be excluded from the present results. In addition, a small residual of the *planetary* 12-month wave in recurrent activity *sequences* found by Meyer (1972, 1973) leads to a systematic phase deflection (relative to the predicted phase) of the calculated hemispheric annual wave. As long as the statistical error for the sectorial annual wave vector is not reduced considerably, the deviations of any single sector result should not give rise to the suggestion of additional mechanisms for an interpretation of the whole hemispheric annual wave.

The comparison between the annual results from (linear) equivalent amplitudes and quasi-longarithmic indices anew illustrates the advantage of the latter measure for the analysis of geomagnetic activity modulation with regard to the study of solar-terrestrial relationships. Modulation amplitudes calculated from quasi-logarithmic values are in general much less affected, if at all, by the level of activity, therefore, yielding the more accurate results because of a smaller scattering. Hence, if not investigating specifically the effect of a varying activity level, preference should be given to quasi-logarithmic measures. Their advantage is again demonstrated for the annual wave in the hemispheric daily character figures *C9n* and *C9s* with all characteristics being in quantitative agreement with expectation from the modified modulation function $\sin^2(\beta \pm 11°)$.

Acknowledgements. It should like to express my thanks to Professor J. Meyer for a number of fruitful discussions and helpful comments during the preparation of this paper.

References

Bartels, J.: Eine universelle Tagesperiode der erdmagnetischen Aktivität. Meteor. Z. **42**, 147–152, 1925

Bartels, J.: Periodische Variationen, Aktivität. In: Handb. d. Experimentalphysik. Bd. XXV/1, W. Wien and F. Harms, eds.: pp. 658–665. Leipzig: Akad. Verlagsges. 1928

Bartels, J.: Terrestrial-magnetic activity and its relations to solar phenomena. Terr. Mag. Atm. El. **37**, 1–52, 1932, (reprinted by Carnegie Institution of Washington 1959)

Bartels, J.: The geomagnetic measures for the time-variations of solar corpuscular radiation, described for use in correlation studies in other geophysical fields. Annals of the IGY, **4**, 227–236, 1957

Berthelier, A.: Influence of the polarity of the interplanetary magnetic field on the annual and the diurnal variations of magnetic activity. J. Geophys. Res. **81**, 4546–4552, 1976

Damaske, D.: Der Weltzeitgang der erdmagnetischen Aktivität als magnetosphärischer Modulationseffekt. Geophys. Abh., Inst. Geophys., Freie Universität Berlin, Heft 5, Berlin: Reimer 1976

Damaske, D.: Magnetospheric modulation of geomagnetic activity, I. Harmonic analysis of quasi-logarithmic indices *Km*, *Kn*, and *Ks*. Ann. Géophys. **33**, 461–478, 1977; – II. Harmonic analysis of linear indices *am*, *an*, and *as*. Ann. Géophys. **34**, 461–478, 1978

Mayaud, P.N.: Calcul préliminaire d'indices *Km*, *Kn* et *Ks* ou *am*, *an* et *as*, mesures de l'activité magnétique à l'échelle mondiale et dans les hémisphères Nord et Sud. Ann. Géophys. **23**, 585–617, 1967

Mayaud, P.N.: Indices *Kn*, *Ks* et *Km* 1964–1967. Editions du C.N.R.S., Paris 1968

Mayaud, P.N.: Sur quelques propriétés de l'activité magnétique, déduites de l'analyse d'une série de neuf années des indices *Kn*, *Ks* et *Km*; II. Les diverses composantes "temps universel" dans chaque hémisphère, de la variation journalière de l'activité. Ann. Géophys. **26**, 313–336, 1970

Mayaud, P.N.: Analyse d'une série centenaire d'indices d'activité magnétique; IV. Les diverses composantes de l'onde annuelle aux latitudes subaurorales. Ann. Géophys. **33**, 479–501, 1977

McIntosh, D.H.: On the annual variation of magnetic disturbance. Phil. Trans. Roy. Soc. London, Ser. A **251**, 525–552, 1959

Meyer, J.: A 12-month wave in geomagnetic activity. J. Geophys. Res. **77**, 3566–3574, 1972

Meyer, J.: Zur Modulation der erdmagnetischen Aktivität. Geophys. Abh., Inst. Geophys., Freie Universität Berlin, Heft 3, Berlin: Reimer 1973

Meyer, J.: Harmonic analysis of geomagnetic indices *Km*. Ann. Géophys. **30**, 503–509, 1974

Siebert, M.: Solarer Wind und Halbjahreswelle der erdmagnetischen Aktivität. Z. Geophys. **36**, 41–56, 1970

Siebert, M.: Maßzahlen der erdmagnetischen Aktivität. In: Encyclopedia of Physics, Vol. XLIX/3, K. Rawer, ed.: pp. 206–275, Berlin, Heidelberg, New York: Springer 1971

Received February 13, 1978; Revised version June 28, 1978

J. Geophys. 45, 91 – 100, 1978

Journal of Geophysics

Solar Electron Fluxes, Increased Geomagnetic Activity and Ionospheric Absorption Following Selected Flares

F. Märcz

Geodetical and Geophysical Research Institute of the Hungarian Academy of Sciences, H-9401 Sopron POB 5, Hungary

Abstract. Investigations on the after-effect in ionospheric absorption following selected solar flares are presented for the interval 1966–1969. By a superposed epoch analysis a significant after-effect was detected in night absorption data at 245 kHz on the circuit Kalundborg/Denmark – Kühlungsborn/GDR by using days of important flares (CFI = 9–16) with intense electron fluxes (> 40 keV) as key days. Further analyses have revealed some specific details, namely that the most outstanding after-effects are related to central-zone flares (30° E-30° W) of high importance, even when the associated electron fluxes were lower than in case of outer-zone 30°–90° W-flares of similar importance. An inverse test has implicitly confirmed these results, and has also proved that not all of the intense geomagnetic disturbances are followed by a significant after-effect.

Key words: Solar flares – Comprehensive Flare Index (CFI) – Flare position – Flare-associated electrons – Geomagnetic activity – Lower ionosphere – Absorption after-effect.

1. Introduction

Enhanced electron densities in the lower ionosphere (particularly in the D-region) result in increased absorption of reflected radio waves. The anomalous increase of absorption in winter-time may be attributed to electron enhancements of "meteorological" type as it was first suggested by Dieminger (1952). The after-effect, i.e., another type of increase of radio wave absorption at mid-latitudes following certain geomagnetic storms has been attributed to energetic electrons (> 50 keV) precipitating from the earth's outer radiation belt into the lower ionosphere (e.g., Lauter and Knuth, 1967).

A recent study (Märcz and Verö, 1977) has found some connections between after-effects in ionospheric absorption and Pc 1-type micropulsations. The latter results are in agreement with explanations invoking the resonant scattering

0340-062X/78/0045/0091/$02.00

by ELF waves as a reasonable mechanism responsible for the precipitation of energetic electrons at mid-latitudes (e.g., Spjeldvik and Thorne, 1975).

The connection between electron precipitation and increased ionization in the D-region has also been verified by coordinated experiments using satellite measurements of electron fluxes and ground-based partial reflection data obtained at Ottawa (Larsen et al., 1976).

In our earlier studies (Märcz, 1971, 1973) – devoted to the latitude dependence of the after-effect in ionospheric absorption as well as to the role of the frequency differences of radio waves used – the superposed epoch analyses of absorption data were carried out by selecting key days on the basis of high geomagnetic activity. This had been a common procedure, also applied in other investigations (e.g., Bourne and Hewitt, 1968) studying the phenomenon on a statistical basis. The superposed epoch method has also been used in the present study, key days, however, were selected according to other criteria. Some additional aspects were considered, too.

As first step of these analyses days of occurrence of certain solar flare events have been chosen as key days and expected variations have been traced both in geomagnetic activity and in absorption during the post-flare period. We intended to check whether any differences in the solar source of the magnetic activity would be reflected in the appearance, or in any other parameters of the absorption after-effect. Two main factors have been considered:

(a) The importance of the flare regarding both its electromagnetic and particle radiation

(b) the position of the flare on the Sun's visible disk.

Investigations carried out according to these aspects, as well as their results will be presented in the following sections.

2. Solar Flares and Associated Electron Fluxes

Dodson and Hedeman (1971) have elaborated a system to characterize the flare on the basis of the associated electromagnetic radiation. Their Comprehensive Flare Index (CFI) is equal to the sum of five components:

$$\mathrm{CFI} = A + B + C + D + E$$

where, A = importance of ionizing radiation as indicated by the accompanying Short Wave Fadeout (SWF), or other SIDs (scale 1–3),

B = importance of H_α flare (scale 1–3),

C = characteristic of the log of ~ 10 cm flux in units of 10^{-22} W m^{-2} Hz^{-1},

D = dynamic spectrum events: type II = 1, continuum = 2, type IV = 3,

E = characteristic of the log of ~ 200 MHZ flux in units of 10^{-22} W m^{-2} Hz^{-1}.

The CFI can reach about 15–17 for flares which are outstanding in all aspects of electromagnetic flare radiation. The flare-associated increase of ionizing electromagnetic radiation (directly affecting the ionosphere) is taken into account by the A-component.

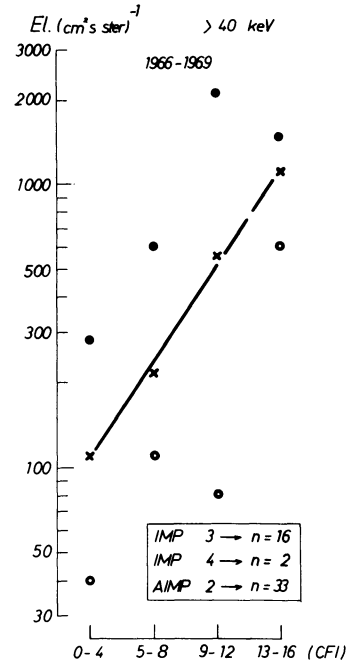

Fig. 1. Median values (crosses) of flare-associated electron (>40 keV) fluxes (cm^2s ster)$^{-1}$ measured by IMP-3, IMP-4 and AIMP-2 satellites during 1966–1969 as a function of Dodson-Hedeman indices (CFI). The appropriate lower quartiles (circles), upper quartiles (dots) and number of observations (n) by the individual satellites are also indicated

During solar flares, however, the Sun is also a source of increased particle streams of different energies. Švestka and Simon (1975) compiled a catalog of solar particle events for the interval 1955–1969. Their particle data for the second half of the sixties were mainly measured on spacecrafts beyond the magnetosphere. The data coverage of this part of the catalog is sufficiently complete due to the improved instrumentation of IMP satellites. Thus, in our investigations we have used the data from 1966 to 1969.

For the forthcoming analyses the selection of suitable key days was based on the following main condition: a flare should be taken into account only if in addition to the increased electromagnetic flare radiation (experienced by different ground-based flare monitoring) the associated particles had also been observed on spacecraft at the near-earth space. In order to have a possible homogeneous material only those events containing also electrons of >40 keV energies were chosen. The CFI-index of the flare, i.e., the importance of the associated electromagnetic radiation was also taken into account, as follows. The electron fluxes selected from the catalog were grouped according to the CFI-value of the corresponding flare. Four flare groups with the given ranges of CFI have been established:

Group 1: CFI= 0–4, weakly active (9),
Group 2: CFI= 5–8, moderately active (21),
Group 3: CFI= 9–12, quite active (17),
Group 4: CFI=13–16, highly active (4).

The values in brackets give the number of flares in the individual groups – in cases of available electron flux data – for the interval 1966–1969. Finally, median values of the appropriately grouped flux data have been determined, they are presented as a function of CFI in Figure 1.

The median values of electron fluxes (>40 keV) lie approximately on a straight line. (The broken line towards high CFI-values indicates the scarcity of cases). Thus there is a logarithmic increase of electron fluxes with increasing flare-associated electromagnetic radiation characterized by CFI. (To represent the scatter of individual data, the upper and lower quartiles are given for each group by dots and circles, respectively, in Fig. 1, where the number of flux data from each satellite is also noted).

Figure 1 yields a rough estimation of flare-associated electron fluxes (>40 keV) on the basis of CFI-indices. Taking into account this empirical connection, the key days of the forthcoming analyses can be selected according to the CFI-values, and by setting appropriate CFI-ranges the dependence of the absorption after-effect on the flare importance can be traced.

3. Geomagnetic Activity and Ionospheric Absorption Following Solar Flare Events

3.1. Dependence on Flare Importance

The particle effects can be detected more easily in the night absorption data, since electron precipitation more frequently occurs in the midnight sector of the auroral oval. Furthermore, the influence of the Sun's electromagnetic radiation on absorption vanishes after sunset, thus mixed effects can be restrained when using night data. Therefore our analyses have also been based on night-time ionospheric absorption data (Geophysikalische Meßreihen, Kühlungsborn, 1966–67, and HHI Geophysikalische Beobachtungsergebnisse, 1968–69). The ΣKp-values (Geomagnetic Planetary Indices, Göttingen, 1966–69) were applied to characterize geomagnetic activity. In order to investigate the dependence on flare importance, the data covering the interval 1966–69 were arranged into two sets, and two independent superposed epoch analysis were carried out.

First, days of weakly and moderately active solar flares (CFI = 0–8) with associated electron fluxes were chosen as key days (0-days). In the left part of Figure 2, the lower curve shows the changes in geomagnetic activity on and around the selected key days. On the average the maximum activity occurs on the third day following the flare. It surpasses the reference level by about 30%. In case of the ionospheric night absorption (upper curve) the mean departures from the appropriate monthly medians are small and they fluctuate around the reference level, i.e., do not show a significant effect.

There is, however, a drastic change in the picture when days with solar flares qualified as quite active and highly active (cf. Section 2) are set as key days in the superposed epoch analysis. (These solar flares of CFI = 9–16 were associated with intense electron fluxes. During the intervals after key days further smaller flares only occasionally occurred, but they were not accompanied by electron fluxes). In the right part of Figure 2 the peak of geomagnetic activity appears again on the third day following the selected flare events. The ΣKp-

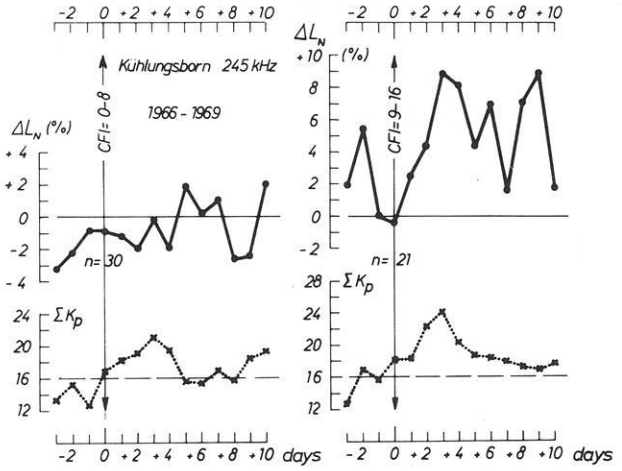

Fig. 2. Mean departures of ionospheric night absorption (245 kHz, Kühlungsborn: $\varphi_{geogr.} = 54°03'N$, $\lambda_{geogr.} = 11°46'E$; GDR) from the corresponding monthly medians given in percentages (dots with full lines) around key days (O) selected on the basis of solar flares associated with electron fluxes (>40 keV); as well as changes of the ΣKp mean values (crosses with dotted lines). Horizontal broken line indicates the ΣKp-average for the interval 1966–1969. *In the left part*: the solar flares ($n=30$) were weakly, or moderately active (CFI=0–8) and were associated with small electron fluxes. *In the right part*: the solar flares ($n=21$) were quite active, or highly active (CFI=9–16) and were associated with intense electron fluxes

average is about 50% higher than the reference value. A simultaneous maximum in ionospheric absorption corresponds to the "primary storm effect". A few days later, the geomagnetic activity approaches its normal level, but the ionospheric night absorption remains above normal. This can be interpreted as an after-effect most likely caused by particle precipitation (Lauter and Knuth, 1967). It should be mentioned, however, that increased concentrations of NO^+ (at the expense of hydrated ions) could also be observed in the D-region during a certain post-magnetic storm period in winter (Aikin et al., 1977). Thus composition changes might occasionally contribute to the post-storm increase of electron density, although electron precipitation should be regarded as the dominant factor.

The confidence of the latter results was checked by a χ^2-test. As null hypothesis it was assumed that the number of positive and negative departures from the median is equal. The observed distribution of absorption departures determined for all intervals following the key days (between days "+1" and "+10") have been checked against this null hypothesis by the χ^2-test. The positive departures for the ionospheric night absorption (245 kHz) in the right part of Figure 2 proved to be significant at the 99% confidence level.

3.2. Dependence on Flare Position

A connection of the great magnetic storms with the longitudinal position of the intense flares on the visible solar disk has been known since several decades

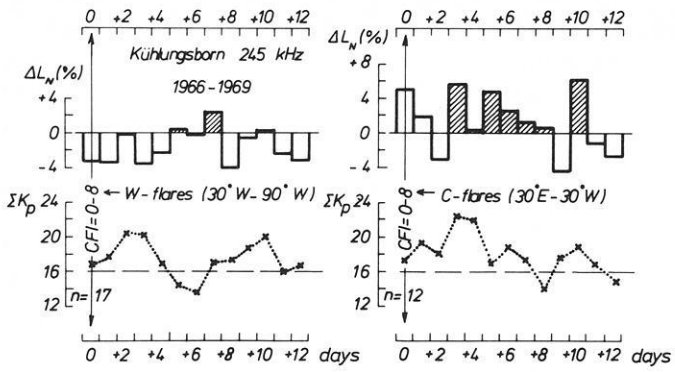

Fig. 3. Mean departures of the ionospheric night absorption from the corresponding monthly medians (in percentages) on and following days with flares of lower importance (CFI = 0–8). Shaded columns indicate the period with primary storm effect and after-effect. Changes of the ΣK_p mean values are shown by crosses with dotted lines. *In the left part*: the solar flares were located in the western outer-zone on the visible solar disk (30°W–90°W). *In the right part*: the solar flares were located in the central-zone on the visible solar disk (30°E–30°W)

(e.g., Newton, 1944). The association has been found to be much closer in case of central-zone flares than in case of outer-zone flares.

The analyses to be presented in this section intended to clarify whether a dependence of magnetic activity on flare position would be transferred into certain changes of the absorption after-effect. Therefore, magnetic and absorption data investigated in the previous section were additionally grouped on the basis of the longitudinal position of flares. Flare position has been depicted in relation to the Sun's central meridian, wherein three zones (east, central and west) have been distinguished. Each zone covers a longitude range of 60°. Consequently, the flares are denoted within the zones as

90° E to 30° E: E-flares
30° E to 30° W: C-flares
30° W to 90° W: W-flares.

According to this classification, the 51 flare events used for setting key days in the previous section (cf., Fig. 2), have included only 2 E-flares, but 20 C-flares and 29 W-flares. Excluding the two E-flares, the absorption and magnetic data analyzed in Section 3.1 were divided into two subsets (central, or west). This was separately done for flares of lower (CFI = 0–8) and of higher (CFI = 9–16) importance.

The results of superposed epoch analyses carried out with these four groups of data are presented in Figure 3 (for CFI = 0–8) and Figure 4 (for CFI = 9–16). C-flares of lower importance can be followed by a rather moderate absorption increase, while no effect occurs in case of the corresponding W-flares, as shown in Figure 3. It becomes obvious that central-zone flares of high importance (Fig. 4) – associated with high geomagnetic activity – play the major role in the significant absorption after-effect found in the right part of Figure 2 (As proved

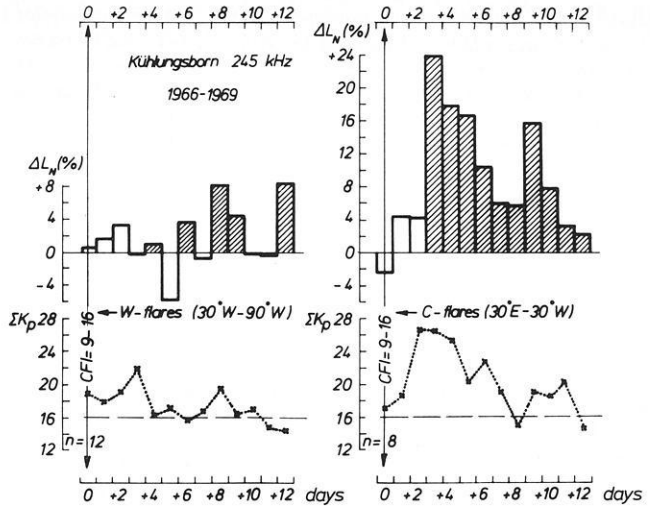

Fig. 4. Same as Figure 3, but for flares of higher importance (CFI = 9–16)

by a χ^2-test, the positive departures in the right part of Fig. 4 are only significant at the 90% confidence level, this, however is conceivable because of the smaller number of data, $n = 8$, compared with those in the right part of Fig. 2).

4. Summary and Discussion

Before summarizing the results of this study and presenting additional ones some basic ideas should be advanced. We accept that the absorption after-effect can be attributed to excess ionization which is most likely caused ba particle precipitation following the enhanced geomagnetic activity, as found by earlier investigations (e.g., Lauter and Knuth, 1967). Furthermore, for the interpretation of our results we also would like to use the considerations about the mechanism of electron precipitation (e.g., Spjeldvik and Thorne, 1975) including the radial diffusion of electrons towards lower L-values after an appropriately intense geomagnetic disturbance, as well as wave-particle interactions. As regards the solar flare electrons (> 50 keV) it is known that they can enter the magnetosphere along connected (interplanetary and geomagnetic) field lines and appear in the tail of the magnetosphere with little delay after the flare (Anderson, 1970).

The present analyses have provided some informations on the flare-associated characteristics of the absorption after-effect, as additional factors with respect to the solar source of both the particles and the magnetic activity have also been taken into account.

Following important flares (CFI = 9–16) a significant absorption after-effect has been shown in the right part of Figure 2 (On the basis of earlier experiences this result could have been expected in advance.) Actually, more complex analyses have also revealed that the characteristics of the absorption after-effect depend – besides the flare importance – on flare position as well (Figs. 3 and 4). In case of C-flares, e.g., the after-effect is preceded by a primary storm

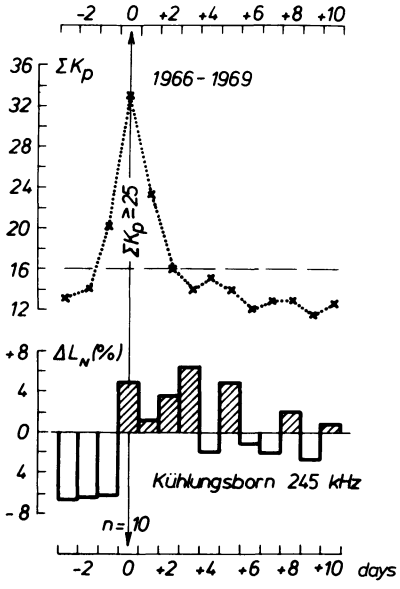

Fig. 5. The ΣK_p mean values on and around selected geomagnetic disturbances (crosses with dotted lines), and mean departures of the ionospheric night absorption from the corresponding monthly medians in percentages. Shaded columns indicate the period with primary storm effect and after-effect

effect. Furthermore, it appears that the major magnetic disturbances attached to central-zone flares (and especially to the important ones) result in the most effective particle precipitation which consequently causes a significant after-effect in ionospheric absorption. (Important W-flares – CFI = 9–16 – are followed by a rather moderate after-effect). Thus in case of central-zone flares, we can suggest a certain proportionality in the sequence of processes, namely between those originating from the solar source and the terminal ones causing the effect in the lower ionosphere.

The latter results seem to be in contradiction with some earlier findings which have indicated that particle precipitation is not always connected to the major geomagnetic disturbances (Lauter and Knuth, 1967; Märcz, 1973). As the following test should confirm both versions might be true, depending on different circumstances.

The test is based on key days chosen from the same 1966–1969 interval, for their selection, however, a geomagnetic criterion was prescribed: $\Sigma \mathrm{Kp} \geqq 25$. Additionally, in order to have an independent test, days with particle events of the catalog of Švestka and Simon (1975) were excluded. Altogether 10 major magnetic disturbances have fulfilled the selection criteria. Mean departures of the ionospheric absorption (245 kHz) from the corresponding monthly median are shown on and around the selected key days in the lower part of Figure 5. For the rather moderate after-effect the following explanation can be given. Seven out of the ten selected magnetic disturbances were preceded by corresponding solar flares of importances of Sb, 1b, 3b, or 2n (according to the dual-importance scheme adopted by the International Astronomical Union). In any case, only two flares out of them were located in the central-zone of the solar disk and all remaining ones were observed in the outer-zones. Thus, the results

Table 1. Classification of flare-associated electron fluxes (>40 keV) observed on spacecrafts between 1966 and 1969. (The flux data were selected from the catalog of Švestka and Simon, 1975)

Flare position	90° E–30° E East-flare	30° E–30° W Central-flare	30° W–90° W West-flare	Flare importance
Number of cases	1	12	17	CFI = 0–8
El. (cm^2 s ster)$^{-1}$ median value	(600)	200	160	
Number of cases	1	8	12	CFI = 9–16
El. (cm^2 s ster)$^{-1}$ median value	(100)	325	1750	

of the test implicitly hint at the outstanding role of the central-zone flares in the after-effect. In addition, the results have shown that the intense magnetic disturbances are not always followed by a significant absorption after-effect. Certainly, this also occurred in cases included in the test as the increased magnetic activity was connected with outer-zone flares.

Finally, Table 1 presents some parameters of the 51 flares with electron fluxes (>40 keV) investigated in the previous sections. Both flare position and flare importance have been taken into account for the classification. The scarcity of observed electron fluxes in case of E-flares is due to the general spiral structure of the interplanetary magnetic field which guides the flare particles. Consequently, electrons emitted from the eastern outer-zone on the solar disk have only a little chance to encounter the earth. The opposite is true for the western outer-zone flares, what is confirmed by the corresponding number of cases in Table 1. Median values of electron fluxes connected with important flares (CFI = 9–16) are rather different; they depend on the flare position as shown in Table 1. After all, although the fluxes were more intense in case of W-flares than in case of C-flares, the geomagnetic activity was higher and the absorption after-effect more significant following C-flares (cf. Fig. 4). This stresses again the clear relationship between events connected with central-zone flares and the investigated effect.

References

Aikin, A.C., Goldberg, R.A., Jones, W., Kane, J.A.: Observations of the mid-latitude lower ionosphere in winter. J. Geophys. Res. **82**, 1869–1875, 1977

Anderson, K.A.: Entry of solar cosmic rays into the Earth's magnetosphere. In: Particles and Fields in the Magnetosphere, B.M. McCormac, ed.: pp. 3–17. Dordrecht-Holland: D. Reidel Publishing Comp. 1970

Bourne, I.A., Hewitt, L.W.: The dependence of ionospheric absorption of MF radio waves at mid-latitudes on planetary magnetic activity. J. Atmos. Terr. Phys. **30**, 1381–1395, 1968

Dieminger, W.: Über die Ursache der exzessiven Absorption in der Ionosphäre an Wintertagen. J. Atmos. Terr. Phys. **2**, 340–349, 1952

Dodson, H.W., Hedeman, E.R.: An experimental Comprehensive Flare Index and its derivation for "major" flares, 1955–1969. WDC-A Report UAG-14, NOAA, Boulder, 1971

Geomagnetic Planetary Indices, Göttingen, 1966–1969

Geophysikalische Meßreihen, Kühlungsborn, 1966–1967

HHI Geophysikalische Beobachtungsergebnisse, 1968–1969

Larsen, T.R., Reagan, J.B., Imhof, W.L., Montbriand, L.E., Belrose, J.S.: A coordinated study of energetic electron precipitation and D-region eletron concentrations over Ottawa during disturbed conditions. J. Geophys. Res. **81**, 2200–2212, 1976

Lauter, E.A., Knuth, R.: Precipitation of high energy particles into the upper atmosphere at medium latitudes after magnetic storms. J. Atmos. Terr. Phys. **29**, 411–417, 1967

Märcz, F.: Ionospheric absorption and geomagnetic activity. Acta Geod. Geoph. Mont. Hung. **6**, 83–93, 1971

Märcz, F.: Further studies on ionospheric absorption and geomagnetic activity. Acta Geod. Geoph. Mont. Hung. **8**, 297–311, 1973

Märcz, F., Verö, J.: Ionospheric absorption and Pc l-type micropulsations following enhanced geomagnetic activity. J. Atmos. Terr. Phys. **39**, 295–302, 1977

Newton, H.W.: Solar flares and magnetic storms. Monthly Notices Roy. Astron. Soc. **103**, 244, 1944

Spjeldvik, W.N., Thorne, R.M.: The cause of storm after effects in the middle latitude D-region. J. Atmos. Terr. Phys. **37**, 777–795, 1975

Švestka, Z., Simon, P.: Catalog of solar particle events 1955–1969. Astrophysics and Space Science Library 49, Dordrecht-Holland, Boston-USA.: D.Reidel Publishing Comp. 1975

Received April 27, 1978 / Accepted July 26, 1978

J. Geophys. 45, 101–106, 1978

Journal of Geophysics

The *H* Amplitude of Sudden Commencements of Magnetic Storms at Sabhawala (Dehra Dun)

A.R. Jain* and N.S. Sastri

Indian Institute of Geomagnetism, Colaba, Bombay 400 005, India

Abstract. The storm sudden commencement (SSC) amplitude in H is invariably much larger at Sabhawala, in Northern India, than at the neighbouring low-latitude stations. Examination of ten-year data shows that the ratio of the amplitude at Sabhawala to that at Alibag is persistently higher than unity, on an average about 1.5, both during day and night. The abrupt increase in amplitude from the nearest station, Jaipur, to Sabhawala indicates that neither ionospheric nor magnetospheric currents are directly responsible for the enhancement of the amplitude at Sabhawala. Considering the behaviour of SSC amplitudes in the three components, H, Z, and D at Sabhawala, subsurface electrical conductivity is shown to be the most likely source and the direction of anomalous induced current is determined to be westward. The high conductivity regions may possibly be following the trend of the Himalayas.

Key words: Sudden commencements of magnetic storms – Induced currents – Electrical conductivity anomalies.

The sudden commencement of a magnetic storm, SSC, appears at mid- and low-latitude stations as a sudden increase in the geomagnetic horizontal component, H. Individual SSCs observed simultaneously at different stations all over the world show a considerable local time inequality. A systematic change in the shape of SSCs exists with geographic longitude at higher latitudes, though the shape is more or less the same for any event in low latitudes (Obayashi and Jacobs, 1957). Of the six Indian magnetic observatories with over a decade of data collection, three are in the equatorial electrojet belt and two are at

* *Present address:* Radio Science Division, National Physical Laboratory, Hillside Road, New Delhi 110012, India

0340-062X/78/0045/0101/$01.20

Table 1. Location of the Indian Observatories and Mean SSC(H)

Station	Geographic		Dipole		Dip	Mean SSC(H) in nT	
	Latitude	Longitude	Latitude	Longitude		Day-time	Night-time
Trivandrum	8°29′N	76°57′E	1.2°S	146.4°	−0.9°	44±4	27±2
Kodaikanal	10°14′N	77°28′E	0.6°N	147.1°	3.0°	39±5[a]	33±3[a]
Annamalainagar	11°22′N	79°41′E	1.4°N	149.4°	5.4°	44±4	34±3
Hyderabad	17°25′N	78°33′E	7.6°N	148.9°	20.7°	28±2	30±3
Alibag	18°38′N	72°52′E	9.5°N	143.6°	24.3°	27±2	29±3
Ujjain	23°11′N	75°47′E	13.5°N	147.0°	32.7°	–	–
Jaipur	26°55′N	75°48′E	17.3°N	147.4°	39.4°	–	–
Sabhawala	30°22′N	77°48′E	20.8°N	149.8°	48.2°	36±3	46±4

[a] For Kodaikanal, the day-time events are 23 and the night-time events are 27 only, due to non-availability of published data for the years 1968 and 1969 and also because only prominent events are reported in the Bulletins of this observatory

low latitudes; the sixth is the northernmost observatory in the country, situated near Dehra Dun in the Himalayan foothills. Two magnetic observatories were recently started between Alibag and Sabhawala. The locations of these observatories, which are within a narrow (about 7°) longitudinal range, are given in Table 1. The Table also contains the average amplitude in H of about 40 day-time and 50 night-time SSC events, generally recorded at all the six older observatories during the period 1964–1973.

The amplitude at low-latitude stations from Hyderabad to Sabhawala is expected to be nearly constant. But, surprisingly, SSC(H) at Sabhawala is large compared to that at Alibag and Hyderabad. During the night-time, SSC(H) is comparable from Trivandrum to Alibag. But, at Sabhawala, it remains large, and even larger than the day-time amplitude; however, the difference between the day and night amplitudes is not statistically significant.

Mean SSC(H) at different stations, normalized with respect to the amplitude registered at Alibag, is shown in Fig. 1 a as a function of dipole latitude, separately for the day- and night-time events. Mean of SSC(Z) − SSC amplitude in the vertical component Z − is also similarly plotted in Fig. 1 b. The wellknown day-time enhancement of SSC(H) in the electrojet belt (Sugiura, 1953 and others), evident in Table 1, is clearly seen in Fig. 1 a, as also the persistence of the high ratio at Sabhawala. While the former is attributed to the enhancement of the equatorial electrojet at the time of SSC (Jacobs and Watanabe, 1963; Rastogi, 1976), the latter cannot be attributed to the currents in the ionospheric *E*-layer because persistently high values of SSC(H) are observed both during the day and the night.

Mean amplitudes of five SSC events recorded at Ujjain and Jaipur between May and December, 1975, as well as the mean values for the same events for Trivandrum, Annamalainagar, Alibag and Sabhawala, are also plotted in

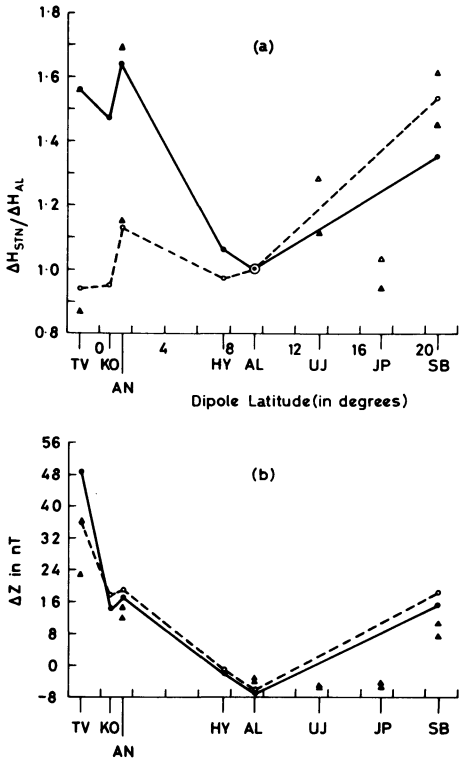

Fig. 1 a and b. Plot, over dipole latitude, of **(a)** the ratio of sudden commencement, SSC, amplitude in the horizontal component at a station, ΔH_{STN}, to the corresponding amplitude at Alibag, ΔH_{AL}, and **(b)** the mean SSC amplitude in the vertical component, ΔZ. Day-time and night-time events are separately shown: Full circles and solid line for day-time events and open circles and broken line for night-time events. Mean values for the five recent events are shown by full triangles and open triangles for the day-time and night-time events respectively. (*TV*: Trivandrum; *KO*: Kodaikanal; *AN*: Annamalainagar; *HY*: Hyderabad; *AL*: Alibag; *UJ*: Ujjain; *JP*: Jaipur; *SB*: Sabhawala)

Fig. 1, normalized SSC(H) in (a) and only SSC(Z) in (b). Figure 1 a shows a sharp increase in the ratio from Jaipur to Sabhawala and the variation over the latitudes is not smooth. This is not expected if the amplitude variation were mainly due to magnetospheric currents.

In contrast to the normalised SSC(H) curve in Fig. 1 a, there is little difference between day- and nigh-time variations of SSC amplitude in Z with latitude. The influence of the overhead currents on SSC(Z) is therefore slight. As seen from the mean values for the five recent events in Fig. 1 b, mean SSC(Z) from Alibag to Jaipur remains the same, whereas there is an abrupt increase at Sabhawala. Such anomalous differences in SSC(Z) at neighbouring stations are commonly attributed to variations in the distribution of sub-surface electrical conductivity (Rikitake, 1966). SSC amplitudes in Z as large as those at Sabhawala are observed at the equatorial stations, Annamalainagar, Kodaikanal, and Trivandrum. The anomalously large variations at different periods at these equatorial stations are under investigation at present and some preliminary results have been reported (for example, Srivastava et al., 1975 and References therein). Rajagopal et al. (1976) have attributed the anomalous Z variations at Annamalainagar and Trivandrum to the complex nature of the subsurface electrical conductivity and also channelling of induced currents through the Palk Straits, a shallow channel separating the tip of the Indian Peninsula from the

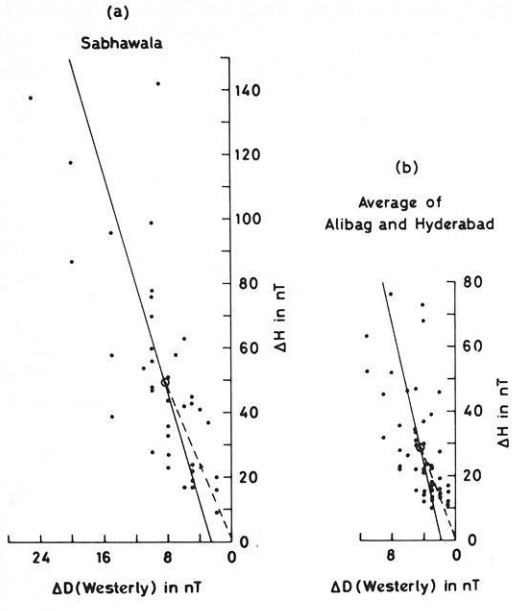

Fig. 2. a and b. Plot of night-time sudden commencement, SSC, amplitude in the horizontal component, ΔH, against the corresponding amplitude in declination, ΔD, **(a)** at Sabhawala and **(b)** average of the corresponding amplitudes at Alibag and Hyderabad. Solid line is the regression line of ΔD on ΔH and the broken line indicates the mean horizontal vector

island of Sri Lanka. A similar explanation may also be valid for large SSC(Z) at Kodaikanal since it is in the same peninsular region. Sabhawala, however, is about 1,600 km inland from any coast and is not affected by the same processes.

The departure of SSC amplitudes in H and Z at Sabhawala from the expected values at low to mid-latitudes is noticeable when these are compared to the corresponding amplitudes at Alibag and Hyderabad. Normally SSC(Z) at low latitudes is expected to be small in the absence of induced subsurface currents. Since SSC(Z) at Alibag as well as Hyderabad is small, the induced anomalous part in SSC(H) and declinational component, SSC(D), may reasonably be assumed to be small and hence the amplitude of SSC at these stations can be considered normal. A plot of SSC(H) against SSC(D) at Sabhawala for all the night-time events is given in Fig. 2a. Taking an average of the amplitudes at Alibag and Hyderabad, a similar plot of the average SSC(H) against average SSC(D) for the night-time events is shown in Fig. 2b. Regression line of SSC(D) on SSC(H) as well as the mean horizontal vector is shown in both the diagrams. The two plots are similar, with almost the same slope for the regression line. The mean vector at Sabhawala is, however, considerably larger in magnitude than the mean vector in Fig. 2b. This indicates that induced part exists in both SSC(H) and SSC(D) at Sabhawala.

SSC amplitude is measured as deviation from pre-storm level. In any component the average of SSC amplitudes at the two stations, Alibag and Hyderabad, may reasonably be taken as the normal amplitude. The difference, for any event, between this average and the corresponding amplitude at Sabhawala is assumed to be the anomalous induced part. In the case of Z, the total amplitude is taken to be anomalous since the average of SSC(Z) at Alibag

Table 2. Induction coefficients in the three components

Coefficient	H	Z	D
A	0.6 ± 0.1	0.5 ± 0.1	-0.1 ± 0.03
B	-0.2 ± 0.5	-0.5 ± 0.3	0.2 ± 0.2

and Hyderabad is small (≈ 0) and is not correlated with the anomalous part at Sabhawala in any of the three components. If X_n represents the normal part of component X, as observed at Alibag and Hyderabad, the anomalous part at Sabhawala, $X_a = X - X_n$. Then, using the equation (Schmucker, 1970):

$$X_a = A_x H_n + B_x D_n + \varepsilon_x$$

where ε_x is the uncorrelated part, A's and B's are evaluated for each of the components H, Z, and D. These together with their standard errors are given in Table 2.

The sign for B's is opposite to that of A's because the change in declination is westerly when SSC occurs. A_H and A_Z are comparable within error limits. This suggests that, at Sabhawala, the induced part of SSC(H) is considerably large. A_D, though small, is statistically significant. The horizontal disturbance vector determined from the anomalous parts of H and D is about 10° west of north, almost the same as the direction of the mean vector in Fig. 2. This indicates that the subsurface induced currents may be flowing westwards about 10° south of west (Schmucker, 1969). A_Z and B_Z determine the induction vector and its direction, determined by $\tan^{-1}(B_Z/A_Z)$ measured clockwise from south, indicates the direction of current concentration (Untiedt, 1970). It varies between about 10° and 60° east of south; this wide variation is due to the large standard error of B_Z.

The results suggest the existence of an anomalous induced part in all the three components of the SSC amplitude at Sabhawala which is situated in the Himalayan foothills. The anomalous induced currents are indicated to flow approximately from east to west and the current concentration, in a good east-west conductor, is to the south-east of Sabhawala. Schmucker (1969) made a detailed study of the conductivity anomaly with special reference to Andes and inferred that anomalous induced currents are channelled into a high conductivity zone which follows the general trend of the mountain range. The Himalayas have a similar geological history to that of the Andes. Therefore, it is likely that regions of high subsurface conductivity, where the induced currents flow, may follow the trend of the Himalayan mountain range. However, a systematic magnetic array study in the neighbourhood of Sabhawala is required to determine the depth and extent of the conductive feature.

Acknowledgements. We thank the Director, Geodetic and Research Branch, Survey of India, Dehra Dun, for sending us data of five most recent SSC events. We also thank Professor B.N. Bhargava, Director, Indian Institute of Geomagnetism, for going through the manuscript and our colleagues, Dr. B.P. Singh, Miss N. Nityananda, and Dr. R. Rajaram, for many helpful discussions.

References

Jacobs, J.A., Watanabe, T.: The equatorial enhancement of sudden commencements of geomagnetic storms. J. Atmos. Terr. Phys. **25**, 267–279, 1963

Obayashi, T., Jacobs, J.A.: Sudden commencements of magnetic storms and atmospheric dynamo action. J. Geophys. Res. **62,** 589–616, 1957

Rajagopal, A.S., Nityananda, N., Singh, B.P.: Variations in Z during magnetic storms at Alibag, Annamalainagar & Trivandrum. Indian J. Radio Space Phys. **5**, 50–54, 1976

Rastogi, R.G.: Equatorial E region electric field changes associated with a geomagnetic storm sudden commencement. J. Geophys. Res. **81**, 687–689, 1976

Rikitake, T.: Electromagnetism and the earth's interior. Amsterdam: Elsevier Publishing Company 1966

Schmucker, U.: Conductivity anomalies, with special reference to the Andes. In: Application of modern physics to the earth and planetary interiors, S.K. Runcorn, ed.: pp. 125–138. New York: Inter Science 1969

Schmucher, U.: Anomalies of geomagnetic variations in the southern United States. Bull. Scripps Institution of Oceanography, Univ. of Calif., San Diego **13**, 165 pp., 1970

Srivastava, B.J.: Geomagnetic induction studies in India. Proc. Symp. Equatorial Geomagnetic Phenomena, IIG, Bombay, 15–16 May, 1975, 173–184, 1975

Sugiura, M.: The solar diurnal variation in the amplitude of sudden commencements of magnetic storms at the geomagnetic equator. J. Geophys. Res. **58**, 558–559, 1953

Untiedt, J.: Conductivity anomalies in central and southern Europe. J. Geomag. Geoelectr. **22**, 131–149, 1970

Received January 14, 1977 / Accepted September 25, 1978

J. Geophys. 45, 107–109, 1978

Journal of Geophysics

Short Communication

Crustal Structure of the Reykjanes Ridge at 63° N Derived From Seismic Measurements

M. Snoek and S. Goldflam

Institut für Geophysik, Bundesstr. 55, D-2000 Hamburg 13, Federal Republic of Germany

Key words: Reykjanes ridge – Refraction seismics – Crustal structure

In 1976 the Institute of Geophysics of the University of Hamburg performed seismic measurements as part of a Presite Survey program for DSDP/IPOD LEG 49. Due to bad weather conditions only one split profile of about 60 km was obtained, at Site 409. The shots were recorded on F.S. Meteor by means of one moored telemetric buoy developed in the IfG Hamburg; one Ocean-Bottom-Hydrophone (OBH) was deployed. For the experiment explosives between 5 and 50 kg GEOSIT were fired at an average spacing of 0.820 km.

All seismograms were digitized, a 25 Hz lowpass filter was applied. For the calculation of ray path the time terms were corrected to sealevel. Differences in the intercept times between observed and calculated travel times made it necessary to introduce a thin sediment layer. Knowing the depth of the ocean floor from continuous echoprofilings, we calculated a set of possible sediment

Table 1. Structure section and interpretation

Depth (km)	Velocity (kms^{-1})	
	1.48	water
0.8		
	1.56	sediments
1.0		
	4.30	vesicular basalts
2.0		
	5.35	fresh basalts
3.5		
	6.59	gabbro, metabasites
6.8		
	7.86	mantle material

0340-062X/78/0045/0107/$01.00

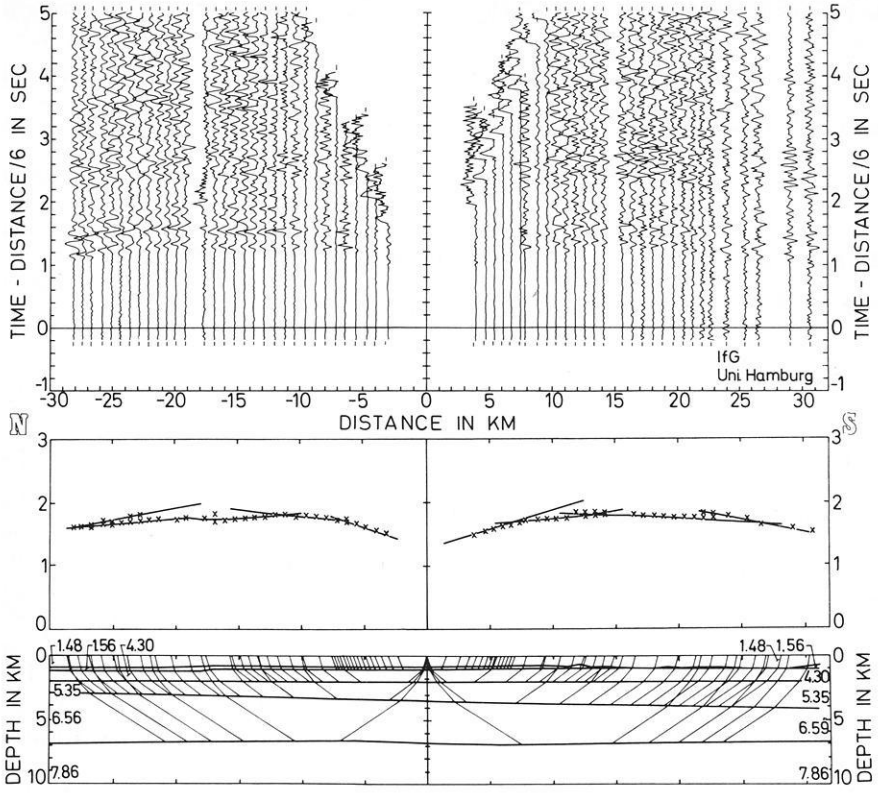

Fig. 1. *Upper part:* seismogram section in reduced time scale t-(x)/6. *Middle:* observed insets (crosses) and calculated travel times. *Lower part:* crustal section with calculated ray paths, *P*-wave velocities are given in kms^{-1}

velocities and thicknesses. The chosen velocity (see Table 1) is in good agreement with the velocity measurements in the sediments of Site 409 (Sharman, 1978).

Local dips as well as true velocities of the overlaying layer were taken into account to calculate configuration and true velocities of the underlaying layer. The boundaries of the layers were shifted vertically until observed and calculated travel time had the same value. Due to good fits an additional correction of travel times for local undulations of the layers was not necessary. Our final model is to be seen in Table 1 and Figure 1. Layer boundaries are almost horizontal except for the interface layer 2/3, where there is a slight rise in direction of Iceland.

Interpretation

We introduced a calculated sediment layer with a *P*-wave velocity of 1.56 km/s and a thickness of 0.190 km below the OBH. Drilling results gave evidence

of an 81.5 m thick sediment layer with measured velocity of 1.57 km/s, the oldest aged late Pliocene. A thin sediment coverage with rapid variation in thickness as indicated by reflection profiles is consistent with the tectonic nature of an active ridge crest. The sediments are underlain by basaltic rocks with measured compressional wave velocities of 3.7–5.75 km/s (Sharman, 1978). We distinguish two refractors with *P*-wave velocities of 4.30 and 5.35 km/s, interpreted as vesicular to fresh basalts, thus corresponding to layer 2A and 2B (Houtz and Ewing, 1976). The next deeper refractor with a velocity of 6.59 km/s is interpreted as layer 3, associated with gabbros and metabasites, frequently dredged and drilled from the oceanic crust (Peterson et al., 1974). The mean *P*-wave velocity of layer 3 according to Christensen and Salisbury (1975), is 6.73 ± 0.19 km/s and the thickness is about 3 km for a young crust, i.e., younger than 2 my.

Our deepest refractor with a value of 7.86 km/s for the *P*-wave is considered to be the crust-mantle boundary. Depth and velocity of this refractor as well as the thickness of layer 3 suggest an interpretation as upper mantle velocity. In comparison to the other existing refraction seismic results of the Reykjanes Ridge and the Reykjanes Peninsula (Talwani et al., 1971; Björnson et al., 1972), this value is high, but we think our calculation and interpretation is well backed by the good quality of the seismograms.

Acknowledgement. We wish to express our thanks to captain and crew of F.S. Meteor for their help, D. Voppel and H. Closs for their support, the German Science Association DFG for the financial aid and shooting and IfG crew for their untiring work.

References

Björnson, S., Arnorson, S., Tomasson, J.: Economic evaluation of Reykjanes Thermal Brine Area. Am. Ass. Petrol. Geol. Bull. **56**, 2380–2391, 1972

Christensen, N., Salisbury, M.: Structure and constitution of the lower oceanic crust. Rev. Geophys. Space Phys. **13**, 57–86, 1975

Houtz, R., Ewing, J.: Upper crustal structure as a function of plate age. J. Geophys. Res. **81**, 2490–2498, 1976

Peterson, J., Fox, J., Schreiber, E.: Newfoundland ophiolites and the geology of the oceanic layer. Nature **247**, 194–196, 1974

Sharman, G.: Seismic velocity measurements of DSDP LEG 49, Initial Reports of DSDP, LEG 49 (in press) 1978

Talwani, M., Windisch, C., Langseth, M.: Reykjanes Ridge Crest: A detailed geophysical study. J. Geophys. Res. **76**, 473–517, 1971

Received July 24, 1978 / Revised version September 21, 1978

J. Geophys. 45, 111–112, 1978

Journal of Geophysics

Book Review

W.H. Munk, G.J.F. MacDonald: The Rotation of the Earth. A Geophysical Discussion. Cambridge, London, New York, Melbourne: Cambridge University Press. First published 1960, reprinted with corrections 1975. 323 pages, 57 figures. £ 6.80 net in UK.

Nachdem wir die Zeit nicht mehr an der rotierenden Erde, sondern an Atomuhren ablesen, dienen astronomische Zeit- und Polhöhenbestimmungen der Messung der Rotationsschwankungen als Indikator geophysikalischer Prozesse auf und in der Erde: "In our subject the Earth is a geophysical laboratory, not a timekeeper". Damit ist "The Rotation of the Earth", erstmals 1960 erschienen und 1975 praktisch unverändert neu gedruckt, in weiten Teilen auch heute noch aktuell. Ob sich der Wert dieses Standardwerkes durch Einarbeitung neuer Daten wesentlich verändert hätte, ist eine müßige Frage. Immerhin haben die Verfasser einige Folgerungen aus der damals noch nicht geborenen Plattentektonik vorweggenommen, indem sie aus der Vorstellung einer "turbulence of continents", einer statistisch verteilten Relativbewegung von 21 Blöcken, Wirkungen auf Chandler wobble und Tageslänge abgeschätzt haben. Das Ergebnis ist interessant: Diese Bewegungen sind für die dekadischen Schwankungen der Tageslänge nicht verantwortlich zu machen, weil dabei 260mal größere Polverlagerungen resultieren würden, die nicht beobachtet werden. Das Gleiche gilt für den Effekt von Erdbeben auf die Variationen des Chandler wobbles, der um 4 Größenordnungen zu klein ist. Neuere Daten, wie Spektren der Rotationsschwankungen und der erdmagnetischen Säkularvariation, bestätigen nur, was sich den Verfassern aus älterem Material an Zusammenhängen andeutete.

Wie der Untertitel sagt, handelt es sich um eine geophysikalische Diskussion, die allerdings auf sehr solidem Fundament ruht. Mit diesem muß sich der Leser zunächst vertraut machen. Es ist kaum zu vermeiden, das Buch von vorn gründlich zu lesen, ein etwas mühsamer Einstieg, der sich jedoch lohnt. Die ihrer Natur nach komplexen, anschaulich kaum faßbaren Zusammenhänge zwischen Pollage, Wobble, dem Deformationsverhalten des Erdkörpers (Love-Zahlen), Schwankungen der Tageslänge, den verursachenden Anregungsfaktoren (Gezeiten, Luftmassenbewegungen, Meeresströmungen, Änderungen der Trägheitsmomente durch Eis, Grundwasser usw.) sind in einer mathematisch eleganten, an Durchsichtigkeit kaum zu übertreffenden Darstellungsweise behandelt. Alle erreichbaren Denkansätze zur Deutung der beobachteten Rotations- und Polhöhenschwankungen werden besprochen und damit der Rahmen fixiert, in dem sich auch künftige Überlegungen vollziehen müssen, wenn ad hoc-Spekulationen vermieden werden sollen. Insbesondere die dekadischen Schwankungen der Tageslänge fordern angesichts ihrer großen Amplitude und relativ hohen Frequenz die Geophysik heute wie vor 18 Jahren heraus. Pollage, Chandler wobble und Rotationsschwankungen sind über die Anregungsfunktionen gekoppelt, wodurch über die Natur der verursachenden Vorgänge, wie z.B. Abschmelzen von Eismassen, Aussagen möglich sind: "The pole of rotation is a remarkably sensitive indicator of the source of melted water". So bleibt ferner zur Erklärung der dekadischen Rotationsschwankungen nach heutigem Wissen allein eine elektromagnetische Kopplung zwischen Mantel und turbulenten Bewegungen im Kern übrig: "... we have found the faintest of hints in the magnetic data that motions in the core are associated with the twentieth century wiggle"; mehr konnten die Verfasser 1960 nicht sagen. Heute könnte lediglich das Wort „faintest" gestrichen werden.

Das Buch ist in 12 Kapitel eingeteilt. Die ersten 6 Kapitel behandeln die mathematisch-physikalischen Grundlagen der Präzession, Nutation und Polhöhenschwankungen, ferner die fundamentalen Gleichungen (Euler, Liouville), Bezugssysteme, Deformationen, Love-Zahlen und Lösungen der

Liouville-Gleichung. Die zweite Hälfte des Buches ist den Beobachtungen von Breite und Tageslänge, den kurzperiodischen Rotationsschwankungen, dem Chandler wobble, den säkularen und dekadischen Variationen der Rotation gewidmet, wobei alle denkbaren Ursachen ausführlich besprochen und in ihren Wirkungen quantitativ abgeschätzt werden. Bemerkenswert ist, daß die nicht auf Gezeitenbremsung beruhenden Variationen auf eine *Abnahme* der Tageslänge seit 2000 Jahren hindeuten, und daß die kurzperiodischen (dekadischen) Fluktuationen der Tageslänge von gleicher Größenordnung sind wie die Variation seit der Zeit der Ägypter. Aber: "A remarcable feature ist that the astronomical observations prior to 1800 show no trace of these short-period fluctuations. Indeed, these constitute an enigmatic phenomenon". Dies gilt auch heute, 18 Jahre seit dem Erstdruck.

Das letzte Kapitel „Geological Variations" läßt den zeitlichen Abstand allerdings fühlbar werden. Plattentektonik, Paläomagnetik und Satellitenbeobachtungen würden viele der hier behandelten Fragen, wie z.B. Polwanderung, in ganz anderem Lichte erscheinen lassen.

Trotzdem muß man froh sein, daß dieses Standardwerk durch den Neudruck wieder verfügbar wurde. Freude macht übrigens auch der exzellente Stil des Textes, ein Musterbeispiel für die besondere Eignung der englischen Sprache zur kurzen und prägnanten Formulierung wissenschaftlicher Sachverhalte. Und schließlich kommt auch der Humor nicht zu kurz. Man lese u.a. die Fußnote S. 56/57, die mit der Feststellung schließt: "... After seventy years, the government in Washington still refuses to recognize the existence of the equatorial bulge". Die Vorgeschichte kann daselbst nachgelesen werden.

K. Strobach, Stuttgart

J. Geophys. 45, 113–117, 1979

Journal of Geophysics

Original Investigations

Electron Density in the South Atlantic Anomaly Region

M. Noor Sheikh*, K. Rawer, and E. Neske

Fraunhofer-Institut für physikalische Weltraumforschung, Heidenhofstraße 8, D-7800 Freiburg
Federal Republic of Germany

Abstract. Since an increased particle flux was found in a well-defined region in the South Atlantic, AEROS-B electron density measurements of August 1974 were checked for a similar effect. During daylight no particular influence could be found, for quiet as well as for disturbed conditions. During night the Atlantic longitude sector shows greater electron densities, but there is no well-defined disturbance area as found for the particle flux.

Key words: Ionosphere – South atlantic anomaly.

The aeronomy satellites Aeros-A and -B were both Sun-synchronous in polar orbits covering a height range between about 220 and 800 km (Lämmerzahl and Bauer, 1974). The instrumentation comprised an EUV-spectrometer, a retarding potential analyzer and an impedance probe, both for plasma diagnostics, and two mass-spectrometers, one of which analyzed natural ions and neutrals alternatively. On the night side the EUV spectrometer recorded keV electrons. A remarkable increase of this corpuscular radiation was found to occur in the South-Atlantic, centered at about 30° S, 320° E (Knoll et al., 1977). The extension of this phenomenon was approximately by 15° in latitude and 30° in longitude on either side.

Since there are no ionosonde stations in this oceanic region, we found it worthwhile to look for corresponding features of the thermal plasma population in the data obtained in August 1974 with the impedance probe (Neske and Kist, 1974) aboard the satellite Aeros-B. At low and middle latitudes the local time at the satellite was almost constant at 3h30 on the night side and 15h30 at the day side. To show typical results for day time we present days no 213 (1 August) and 215 (3 August). 1 August was magnetically quiet with Kp-values 1 and 2. A sudden commencement occurred at noon UT on 2 August starting a magnetic disturbance which reached its maximum ($Kp=6^+$) at the end of 3 August. Thus day 215 was during a developing disturbance.

* *Present address:* Department of Electrical Engineering University of Engineering & Technology, Lahore, Pakistan

0340-062X/79/0045/0113/$01.00

Since the upper ionosphere has a longitude effect, mainly due to the magnetic field, the question arises with which latitudes the South-Atlantic data should be compared at other longitudes. The same problem occurred in the past when world-wide mapping of the peak electron density was asked for. In 1967, to this end, the Comité Consultatif International des Radiocommunications (C.C.I.R.) adopted a particular coordinate proposed by Rawer (1963). This "modified dip" coordinate (abbreviated to "modip" μ) is defined by

$$\tan \mu = I/\sqrt{\cos \varphi}$$

where φ is geographic latitude and I magnetic inclination (as measured in radians): Modip essentially equals dip in the equatorial region but comes to geographic latitude near the (geographic) poles.

Using this coordinate let us first consider the sunlit hemisphere, around 15h30 LT. Figures 1 and 2 show the electron density curves measured during different satellite passes. The general density increase towards North is due to the satellite orbit: On these days the apogee was between 72° and 76° S (geographic) so that the perigee occurred on the night hemisphere at high northern latitude. In the range presented in both Figures the satellite was going down towards the peak altitude of the ionosphere, which was reached around 80° N (geographic). The curves of Figs. 1 and 2 are therefore oblique cuts in height and latitude (modip).

In order to correct for the effect of variable satellite height, we should transform the measured data to a fixed altitude. This can be done with a standard profile as reference. We took as such a model established (mainly with ALOUETTE data) by Bent and Llewellyn (1970), which uses as independent variables; magnetic latitude, solar activity, but also peak density and altitude, these latter being deduced from the C.C.I.R. numerical maps. Taking the relative change with height from the model, observed densities at a given altitude can be transformed to another altitude (Noor Sheikh et al., 1978). In such a way, Fig. 3 was obtained from Fig. 1 for an altitude of 700 km, in the modip angle range $-40°$ to $-20°$ (where the South Atlantic anomaly occurs). No important differences in electron density are seen between the different passes except that pass 247 at longitude 262 E has the steepest gradient. Pass 244 which had a longitude of 333°, just in the anomaly, shows no particularity. Thus, a remarkable anomaly effect on the electron density does not occur during a quiet day.

On the disturbed day 215 we meet a totally different situation. Figure 2 shows that depending on the development of the disturbance, there was a drastic increase of electron density in the equatorial belt (so-called positive perturbation). This increase was, however, not seen at all longitudes, only in the far East (145° and 97°) and in Europe/Africa (2°), not in the near East (49°) and in the Atlantic (315°). This could reveal a development in time of the disturbance, but it is also known that increased ionization can occur in isolated longitudinal shells. In any case there is no specific effect occurring at Atlantic longitudes only.

We conclude that no appreciable anomaly effect could be found in daytime, neither for quiet nor for disturbed conditions.

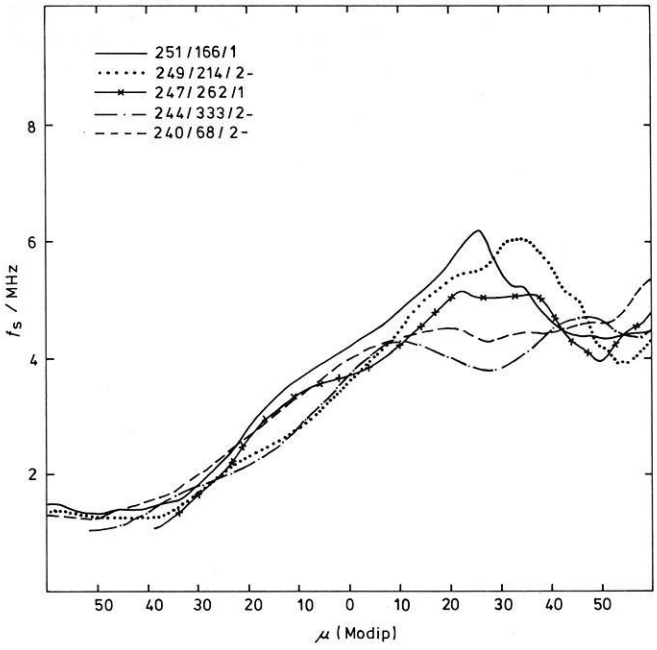

Fig. 1. Local plasma frequency fs (proportional to square root of electron density) as measured during daytime at the satellite, as a function of the "modified dip angle" μ (given in degrees, abbreviated by "Modip"; for explanation see text). Day 213, 1974 – quiet. Parameters: orbit no./nod longitude/Kp value

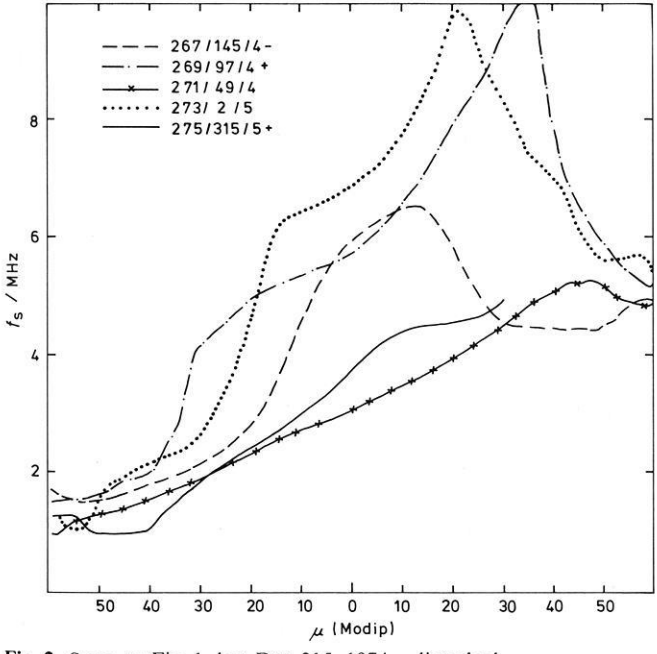

Fig. 2. Same as Fig. 1, but Day 215, 1974 – disturbed

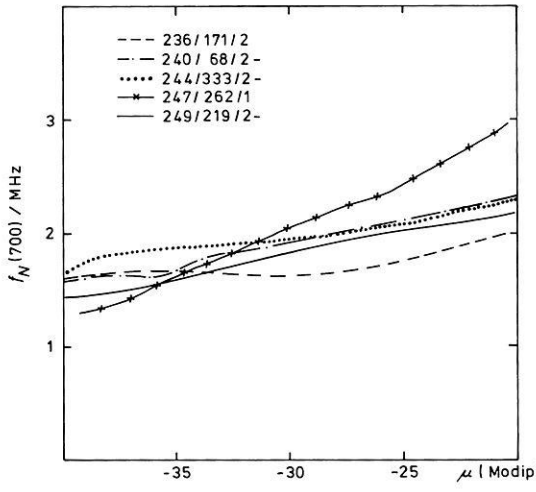

Fig. 3. Virtual plasma frequency during daytime at 700 km (above the South Atlantic) deduced from in situ measurements. Day: 213, 1974 – quiet

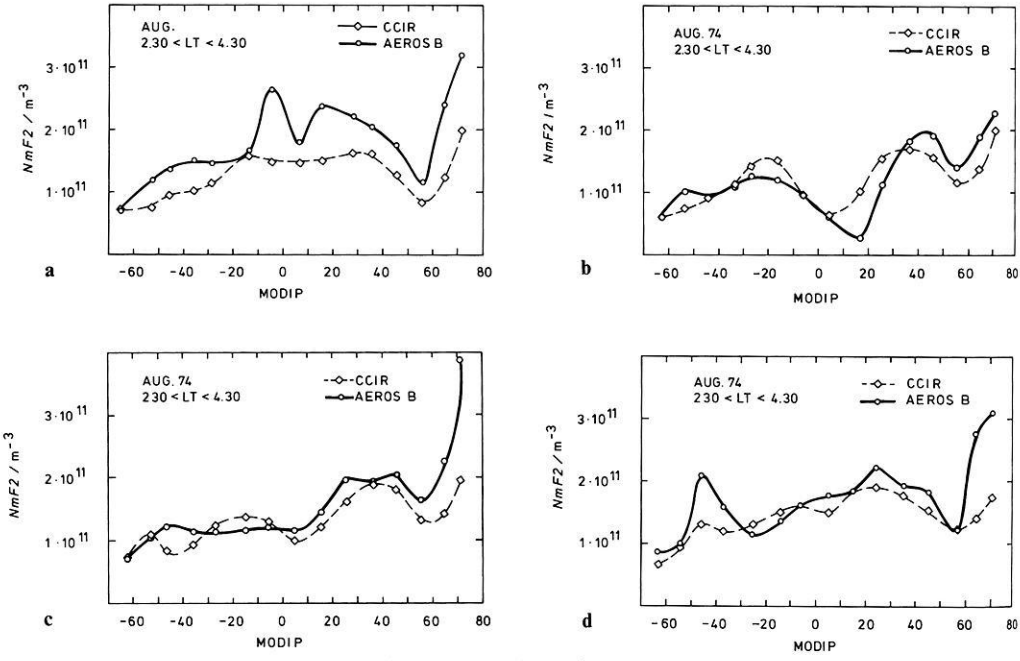

Fig. 4a–d. Peak electron densities (*full curves*) deduced from Aeros-B measurements (averages for August, 1974), at night, for the following selected longitude ranges: **a** America, **b** Atlantic, **c** Eurasia, **d** Pacific. *Broken curves:* C.C.I.R. prediction for comparison

At night the satellite was slightly above peak altitude in the South Atlantic zone. After reduction to peak altitude our data allowed to establish typical monthly median variations for different longitude ranges. Modip was again used as coordinate in Fig. 4. The absolute density values are highest in the American longitude zone, but it is difficult to identify a particular effect in

the South Atlantic. An interesting point is the bifurcation near the dip equator, which is a typical low latitude day-time phenomenon. This occurs only at American longitudes as reported by Knudsen and Sharp (1968). The phenomenon might be related with the excentricity of the terrestrial magnetic field but, if so, is not centered in the South Atlantic but more a general feature of this longitude.

Discussions and Conclusions

Gledhill (1976) has summarized electron density measurements in the anomalous region. Some workers find a minimum and others a maximum at the location of the lowest magnetic field intensity on a given L-shell. As a possible explanation, two competing processes were proposed, namely ionization by the precipitated electrons tending to increase foF2 and heating of the atmosphere tending to reduce it by increased recombination. Our measurements show no remarkable enhancement in the South Atlantic region at altitudes around 700 km during daytime. At somewhat lower altitudes at night the American longitude zone has increased electron density, without a particular enhancement above the Southern Atlantic. It may be that the idea of a "conjugate F-region enhancement" (Pike et al., 1968) could give an explanation. At any case the well-defined zone of the corpuscular anomaly (Knoll et al., 1977) is not privileged in electron density.

References

Bent, R.B., Llewellyn, S.K.: Description of the 1965–1971 ionospheric model in the definite orbit determination system (DODS). Melbourne (Fa.), U.S.A.: DBA Systems 1970

Comité Consultatif International des Radiocommunications (C.C.I.R.): Atlas of Ionospheric Characteristics (Report 340). Genève: Union Internationale des Télécommunications 1967

Gledhill, J.A.: Aeronomic Effects in the South Atlantic Anomaly. Rev. Geophys. Space Phys. **14**, 173–187, 1976

Knoll, G., Holzer, K., Schmidtke, G.: Spatial Shift of the South Atlantic Anomaly. J. Geophys. Res. **82**, 5281–5282, 1977

Knudsen, W.C., Sharp, G.W.: F2-region Electron Concentration Enhancement from Inner Radiation Belt Particles. J. Geophys. Res. **73**, 6275–6283, 1968

Lämmerzahl, P., Bauer, S.J.: The AEROS Mission. J. Geophys. **40**, 571–576, 1974

Neske, E., Kist, R.: Impedance Probe. The AEROS-B Electron Density Experiment. J. Geophys. **40**, 593–600, 1974

Noor Sheikh, M., Neske, E., Rawer, K., Rebstock, C.: Comparison of Peak Electron Densities of the F2-Layer Derived from in situ Measurements with CCIR Predictions. Telecomm. J. **45**, 225–227, 1978

Pike, C.P., Herman, J.R., Gassmann, G.J.: Conjugate F-Region Enhancement Related to the South Atlantic Magnetic Anomaly. Radio Sci. **3**, 680–687, 1968

Rawer, K.: Propagation of Decameter Waves (HF-band). In: Meteorological and Astronimical influences on Radio Wave Propagation, B. Landmark, ed.: pp. 221–250. New York: Pergamon Press 1963

Received June 19, 1978; Accepted January 12, 1979

J. Geophys. 45, 119–128, 1979

Journal of Geophysics

Inversion of Satellite Magnetic Anomaly Data

M. A. Mayhew

Geophysics Branch, NASA Goddard Space Flight Center, Greenbelt, Maryland 20771, USA

Abstract. A method of finding a first approximation to a crustal magnetization distribution from inversion of satellite magnetic anomaly data is described. Magnetization is expressed as a Fourier series in a segment of spherical shell. Input to this procedure is an equivalent source representation of the observed anomaly field. Instability of the inversion occurs when high frequency noise is present in the input data, or when the series is carried to an excessively high wave number. Preliminary results are given for the United States and adjacent areas.

Key words: Magnetic anomalies – Crustal magnetization – Equivalent source.

Introduction

The polar-orbiting satellites OGO 2, 4, and 6 collected total-field magnetic data at elevations above 400 km. A preliminary anomaly data set was created by selecting data with minimal external field effects, and by subtracting a 13th degree spherical harmonic representation of the core field fit to this data subset. Regan et al. (1975) published a 1°-average representation of the anomaly field for a strip around the world between 50° N and 50° S, and described the data reduction procedures.

This paper is a review of a simple method for finding a first approximation to a crustal magnetization distribution which will produce a field which reproduces the measured satellite field. The term "crust" is used loosely to mean a layer bounded by the Earth's surface and the Curie isotherm, and may or may not correspond to the petrologic crust in a given area.

Modeling the Anomaly Field

The anomaly data set is contaminated by noise of three main kinds: (1) instrument noise, (2) local current effects, and (3) very long wavelength effects

0340-062X/79/0045/0119/$02.00

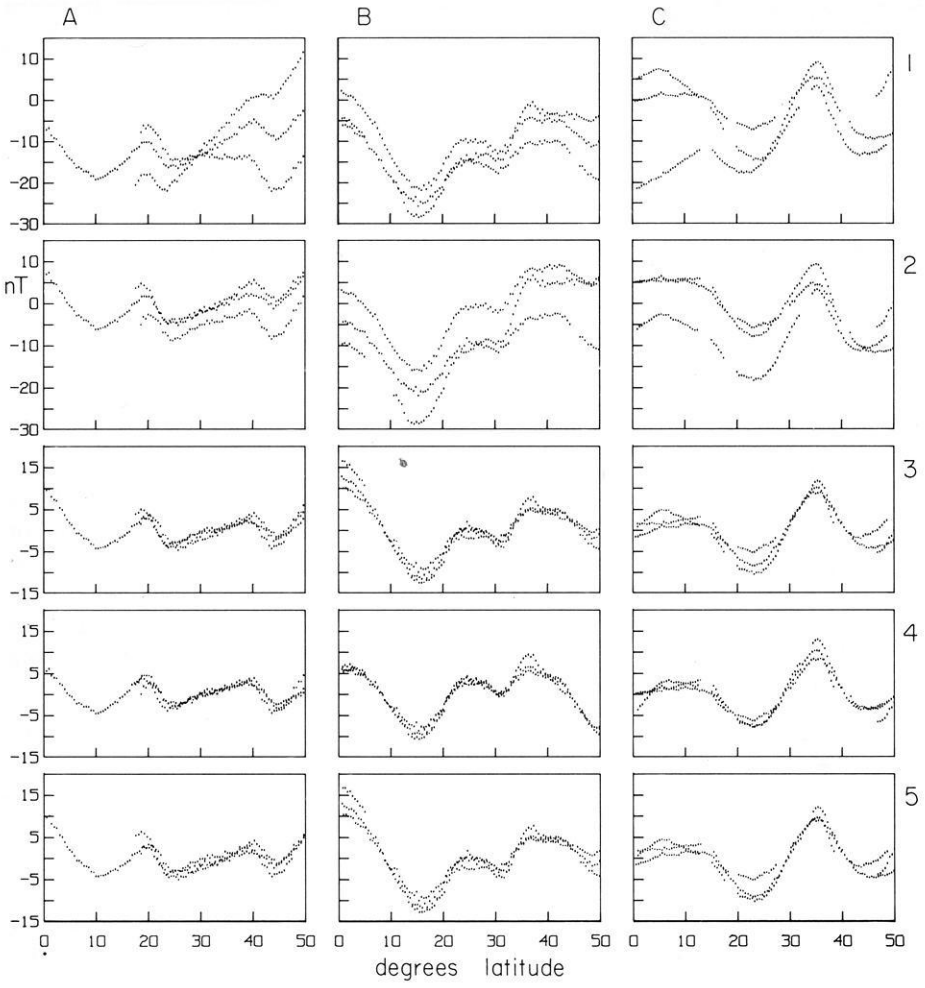

Fig. 1. Satellite magnetic anomaly profiles; locations shown in Figure 2. Row 1, raw anomaly data. Rows 2–5, anomalies with corrections described in text. Ordinate units are nT

due to magnetospheric ring currents. The third effect has been described by Langel and Sweeney (1971). Cain and Davis (1973) modeled this effect as a first zonal harmonic, which they fit to individual satellite passes between 50° N and 50° S geomagnetic. Figure 1 is three groups of three passes in profile form; the tracks are shown in Fig. 2. Within each group the satellite elevations are similar, and thus the profiles should be similar. The raw anomaly data is shown in row 1; clearly, residual long wavelength effects are present in the individual profiles. Row 2 is "ring-corrected" data. The correction generally improves the internal agreement, but a substantial residual remains, and some further correction is needed. This residual is partly responsible for the north-south elongation of anomaly contours, reflecting the satellite tracks, in the world map of Regan et al.

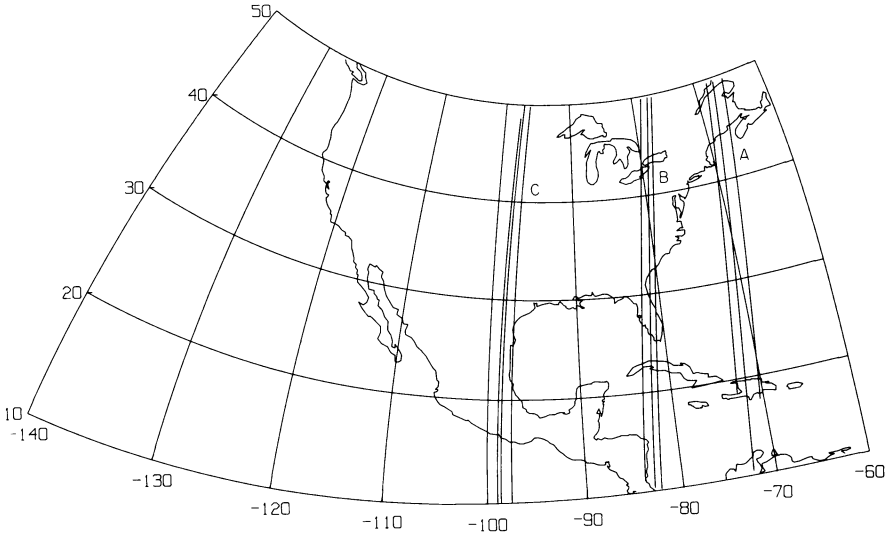

Fig. 2. Location of profiles shown in Fig. 1

(1975). The result is effective high frequency noise in the east-west direction. In rows 3 and 4 linear and quadratic functions, respectively, have been fit to the individual profiles and subtracted. In row 5, a first zonal harmonic term has been fit only over the latitude range shown. The internal agreement is greatly improved in each case, but seems slightly better for the quadratic fit; therefore, a quadratic function was fit to and subtracted from each profile used in the computations described below.

The data is distributed through a considerable elevation range, but we would like to be able to represent the field at an arbitrary constant elevation. For this reason, and to average out instrumental and transient current effects, the anomaly field was modeled by an equivalent source procedure. This consisted of setting out an array of dipoles at the Earth's surface in a 4° latitude-longitude grid, and determining a set of moments for the dipoles which would generate an artificial field which would make a least-squares best fit to the data; the mathematics is outlined in the Appendix. The dipoles were oriented along the direction of the main field, although simply to model the field this direction is not critical. The input data was limited to the elevation range 400–550 km. The fit of the computed field to the data is to a standard deviation of about 1 nT. Once the dipole moments are determined, the field can be computed at any elevation; a computation at 450 km is shown in Fig. 3. Fig. 4 shows the fit of observed and computed fields for an arbitrary selection of profiles running between 10° N and 50° N in the area of Fig. 3.

The input field to the inversion procedure outlined below must be smooth. Since the equivalent source field fills this requirement, it, rather than the raw anomaly data, was so used.

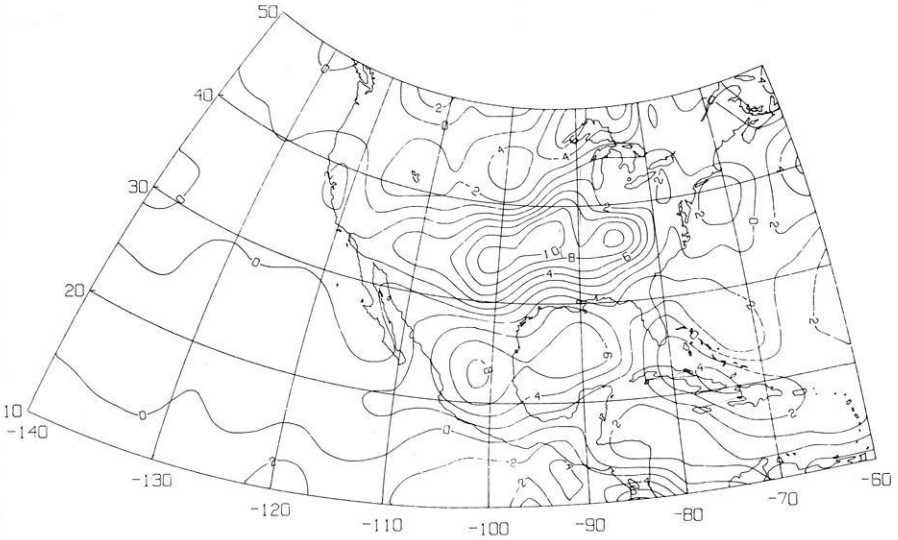

Fig. 3. Equivalent source anomaly field computed at 450 km elevation. Units are nT

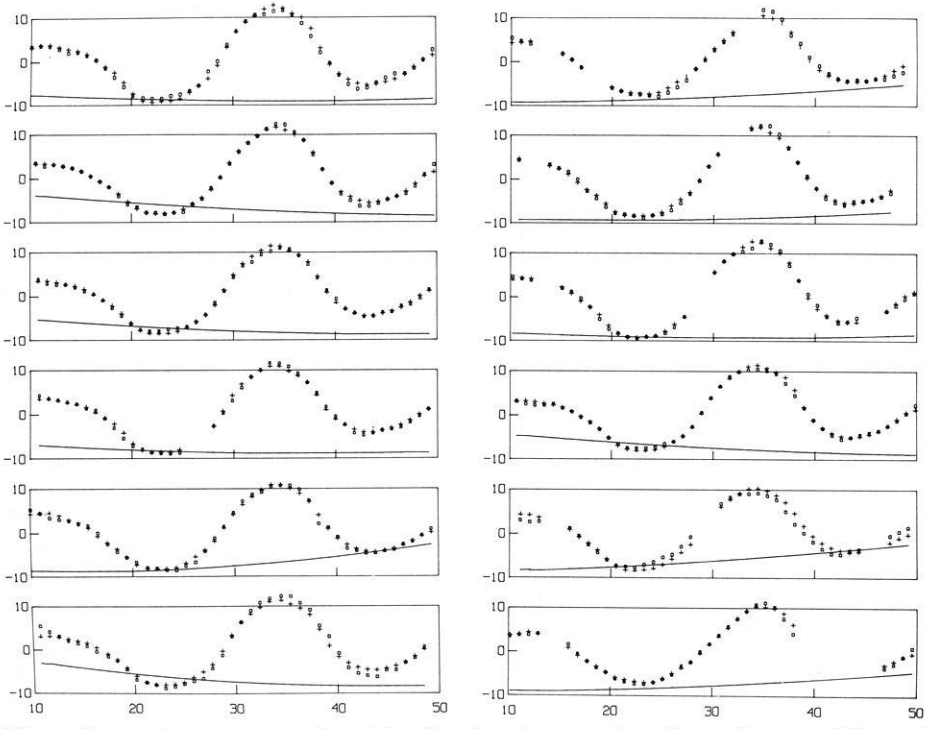

Fig. 4. Corrected measurements for arbitrarily selected group of profiles in the area of Figure 3 (*circles*) and computed values (*pluses*). Abcissa scale is degrees latitude as in Fig. 1. Ordinate scale for anomaly profiles is nT. Solid line is satellite elevation scaled from 400 to 700 km over the ordinate range

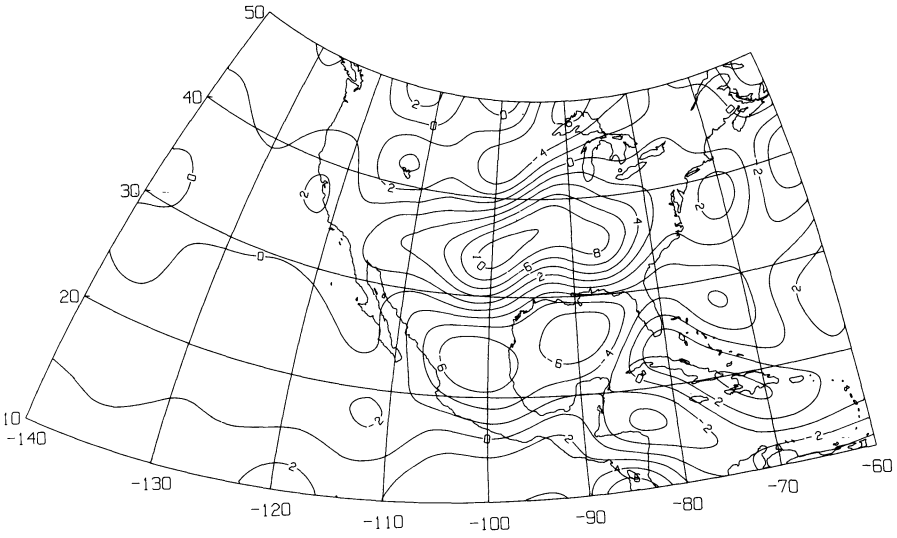

Fig. 5. Anomaly field at 450 km computed from magnetization distribution of Fig. 6. Units are nT

Magnetization Distribution

The set of magnetic moments determined in the equivalent source computation vary irregularly, and have no particular physical significance. One approach to developing a physically meaningful model of the magnetic source distribution is to seek a continuous distribution of magnetization in a layer of constant thickness which will give rise to a field which closely fits the input field. The result is a first approximation to gross magnetization variations in the magnetic crust. The procedure is similar to that for the equivalent source computations described above, but with two essential differences. First, the sources are 2° blocks 40 km thick, rather than dipoles. An approximate source function was developed for the anomaly due to such spherical prisms (see Appendix). Second, rather than allowing the moments of the sources to vary independently, their magnetizations were specified by the value of a double Fourier series in latitude and longitude having terms of the form

$$A_{ij} \cdot (\cos, \sin)(2\pi ix/X) \cdot (\cos, \sin)(2\pi jy/Y). \tag{1}$$

The unknown parameters in the least-squares formulation are then the constants of the series, rather than the magnetic moments of individual sources. Map areas 40° by 40° were treated individually. The equivalent source field, tapered to zero

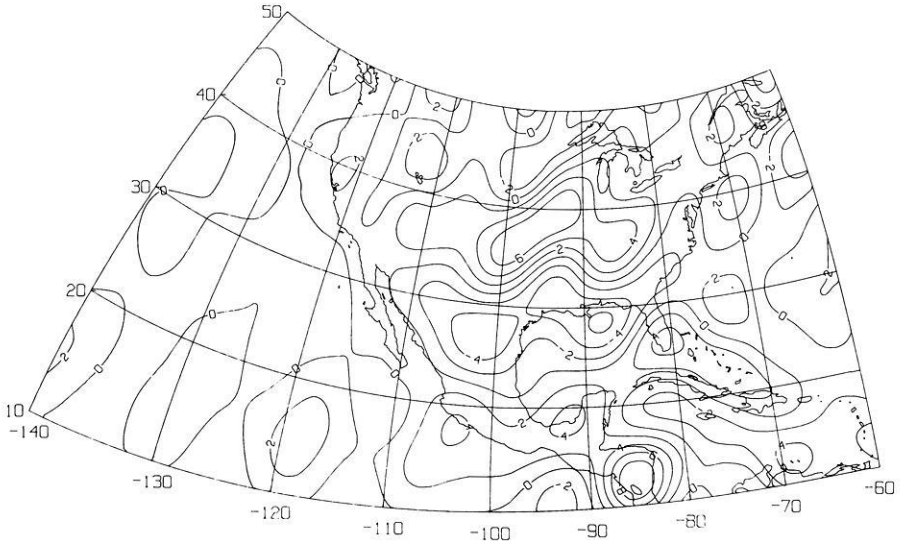

Fig. 6. Magnetization distribution from data of Fig. 3. Units are 10^{-1} Am^{-1}

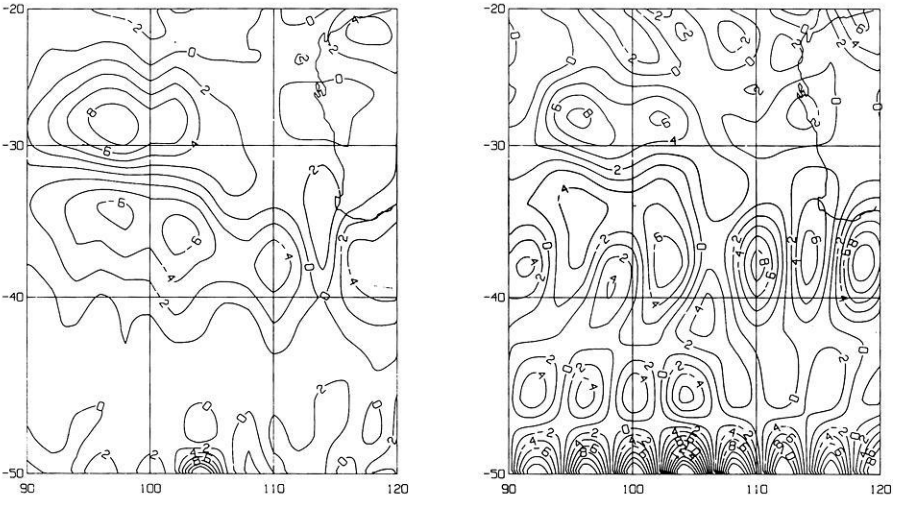

Fig. 7. 1° average anomaly data (*left*) and magnetization distribution (*right*) from inversion of this data. Units are nT (*left*) and 10^{-1} Am^{-1} (right)

4° beyond each map border, was used for input. The Fourier series was expressed within the extended area; thus, in expression (1) above $X = Y = 48°$.

Once the series parameters are determined, the field can be computed at arbitrary elevation. The result at 450 km is shown in Fig. 5, which is to be compared with Fig. 3. The magnetization distribution itself is shown in Fig. 6.

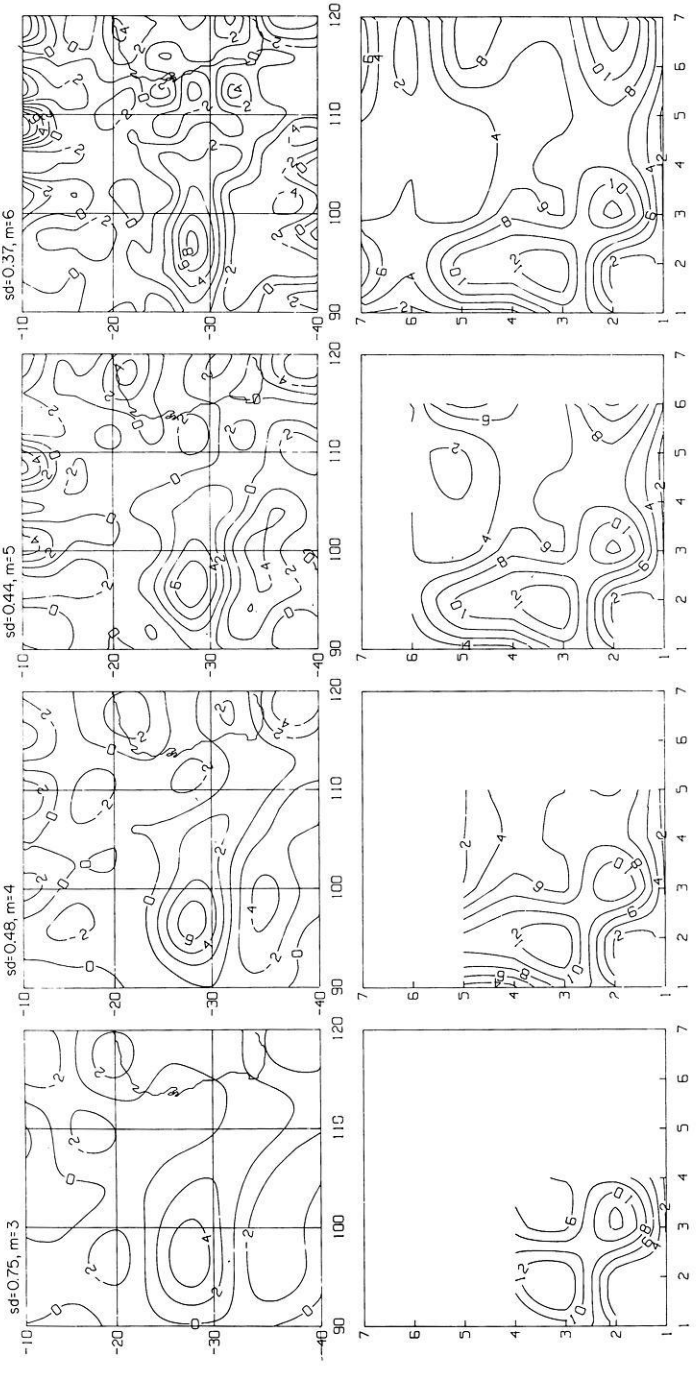

Fig. 8. Magnetization distributions and corresponding amplitude spectra for maximum wave number $m=3$, 4, 5, and 6. Scale shown is wave number plus one. Units are $10^{-1}\,\mathrm{Am}^{-1}$. sd is the standard deviation of the fit between observed anomaly field and that computed from the magnetization distributions

There is a particular advantage to having the data so high above the sources. An individual source block has very nearly the same anomaly as a block twice the thickness and half the magnetization; thus, one can readily convert the model of magnetization variation in a layer of constant thickness to variations in a layer of variable thickness where there is independent evidence on the thickness of the magnetic crust.

Sources of Instability

High frequency components of the field tend to be strongly amplified on inversion. Two examples of difficulties of this type are discussed below.

The map on the left in Fig. 7, a test area in the Indian Ocean, was made by averaging corrected data within the elevation range 400–550 km over 1° squares; average data generally contains high frequency noise contamination. The southern part of the map is in high magnetic latitudes, and external field noise is present along the southern border. The map on the right is the result of an inversion in which these components have evidently been exaggerated, producing a characteristic cell-like structure.

Figure 8 shows a second kind of problem. There is an obvious question of how large the maximum wave number in the Fourier representation of magnetization can be. Figure 8 shows the results of computations for maximum wave number 3, 4, 5 and 6. An equivalent source representation of the anomaly field computed at 450 km over a 2° grid was used as input. The maps in the top row are the magnetization results; shown below are the corresponding amplitude spectra. Note that while the low frequency part of the spectrum does not change very much, for $m=5$ and 6 increasing energy is entering the high frequency part. Apparently spurious effects appear in the corresponding magnetization maps. It would seem, then, that for an area this size the maximum appropriate wave number is 4, despite the fact that the fit of input to computed values continues to improve with expanding series, as indicated by the standard deviation values. The result suggests the limits of source resolution with this method. $m=4$ corresponds to a minimum wavelength of roughly twice the elevation of the data. The results of Fig. 6 were computed for $m=5$, which corresponds to about the same minimum wavelength because the map area is larger.

Acknowledgements. This work was done as part of the NASA-U.S. Geological Survey program for interpretation of satellite magnetic data. W.M. Davis of USGS has been largely responsible for preparation of the data set used in this study. The author was supported by a Research Associateship from the National Academy of Sciences.

Appendix

Equivalent Source Field

We seek an expression for the potential of a dipole located at a point j on the Earth's surface at some external measurement point i. Specify the coordinates as (r_j, θ_j, ϕ_j) and (r_i, θ_i, ϕ_i) where r is

radial distance, θ is colatitude, and ϕ is longitude east.

$$V_{ij} = -\bar{m}_j \cdot \nabla \frac{1}{l_{ij}},$$

where l_{ij} is the distance between i and j.

$$l_{ij}^2 = r_j^2 + r_i^2 - 2 r_j r_i \cos\zeta_{ij},$$

where ζ_{ij} is the central angle between i and j, and

$$\cos\zeta_{ij} = \cos\theta_j \cos\theta_i + \sin\theta_j \sin\theta_i \cos(\phi_i - \phi_j).$$

The components of $\bar{m}_j$ are

$$(m_j \sin I, m_j \cos I \cos D, m_j \cos I \sin D),$$

where I and D are inclination and declination of the dipole, taken to be that of the main field vector at the dipole.

Differentiation and substitution yields

$$V_{ij} = m_j((r_j - r_i A)\sin I + r_i B \cos I \cos D - r_i C \cos I \sin D)/l_{ij}^3,$$

where

$$A = \cos\theta_j \cos\theta_i + \sin\theta_j \sin\theta_i \cos(\phi_i - \phi_j)$$
$$B = \sin\theta_j \cos\theta_i - \cos\theta_j \sin\theta_i \cos(\phi_i - \phi_j)$$
$$C = \sin\theta_i \sin(\phi_i - \phi_j).$$

The gradient of V_{ij} in the total field direction is the anomaly in the total field, expressed as $m_j G_{ij}$, where G_{ij} is the pure geometrical part of the anomaly.

The anomaly due to all the dipoles is

$$F_i = \sum_j m_j G_{ij}.$$

Using a procedure outlined by Cain et al. (1967), we determine a set of values for the m_j which will minimize the square residuals between observed and computed F over all points i.

Field due to Spherical Prism of Elemental Area

Proceeding from the dipole result, we write down an expression for the potential of a volume element.

$$dV_{ij} = \frac{1}{l_{ij}^3}(J_r(r_j - r_i A) + J_\theta r_i B - J_\phi r_i C) r_j^2 \sin\theta_j \, d\theta_j \, d\phi_j \, dr_j,$$

where (J_r, J_θ, J_ϕ) is the magnetization vector.

Then integrating in the r direction, and replacing the infinitesimal angles by small finite angles gives the potential of a spherical prism of elemental area,

$$\Delta V_{ij} = J_r \sin\theta_j \Delta\theta_j \Delta\phi_j \int_{R_1}^{R_2} \frac{r_j^3}{l_{ij}^3} dr_j$$
$$+ (-J_r r_i A + J_\theta r_i B - J_\phi r_i C)\sin\theta_j \Delta\theta_j \Delta\phi_j \int_{R_1}^{R_2} \frac{r_j^2}{l_{ij}^3} dr_j,$$

where $(R_2 - R_1) = 40\,\text{km}$, the approximate "crustal" thickness used in this paper. Experiments with

computations have shown that the $\Delta\theta$ and $\Delta\phi$ can be taken to be 2° in the above expression, and still give an excellent approximation to the field of a prism with finite angular dimensions.

The integrals above are given by Gradshteyn and Ryzhik (1965); the expressions are fairly lengthy, and are not reproduced here.

References

Cain, J.C., Hendricks, S.J., Langel, R.A., Hudson, W.V.: A Proposed Model for the International Geomagnetic Reference Field – 1965: J. Geomag. Geoelectr. **19**, 335–355, 1967

Cain, J.C., Davis, W.M.: Low Latitude Variations of the Magnetic Field: In: Symposium on Low Level Satellite Surveys, J.C. Cain, ed.: pp. 67–87. Internat'l. Assoc. of Geomagnetism and Aeronomy, Paris, 1973

Gradshteyn, I.S., Ryzhik, I.M.: Table of Integrals. Series and Products, A. Jeffrey, ed. p. 83. New York: Academic Press 1965

Langel, R.A., Sweeney, R.E.: Asymmetric Ring Current at Twilight Local Time: J. Geophys. Res. **76**, 4420–4427, 1971

Regan, R.D., Cain, J.C., Davis, W.M.: A Global Magnetic Anomaly Map: J. Geophys. Res. **80**, 794–802, 1975

Received October 25, 1977; Accepted December 4, 1978

J. Geophys. 45, 129–145, 1979

Journal of Geophysics

The Effect of Earth Structure on Radial Oscillations

C. Wang[1]*, J.R. Cleary[1], and R.S. Anderssen[2]

[1] Research School of Earth Sciences, Australian National University, Canberra, A.C.T. 2600, Australia
[2] Computing Research Group, Australian National University, Canberra, A.C.T. 2600, Australia

Abstract. Quasi-periodic variations observed in the spacings between successive eigenfrequencies of radial oscillations and of spheroidal oscillations of PKIKP type are produced by the inner and outer core discontinuities and by the transition zone in the upper mantle. The individual effects of these regions have been separated by modelling experiments. The inner and outer core boundaries cause persistent oscillations in the eigenfrequency spacings, having periods (with respect to overtone number) of about 5.5 and 2.4 respectively. The oscillation produced by the upper mantle transition zone has a period of about 8. A discontinuous upper mantle causes a persistent oscillation of this kind, while that produced by a continuous upper mantle decays with increasing overtone number. In principle, differences between continuous and discontinuous upper mantle models are detectable in the currently observable eigenfrequency range. The analysis shows that the extent of presently available data is insufficient to determine structure at the core boundaries within adequate limits.

Key words: Radial oscillations – Earth structure – Eigenfrequency spacing.

1. Introduction

Anderssen, Cleary and Dziewonski (1975) have shown that the observed periods of the Earth's free oscillation modes ${}_nS_0$ and ${}_nS_1$ exhibit an oscillatory behaviour consistent with the existence of a solotone effect (cf. McNabb et al., 1976). They attributed this behaviour to the presence of the core discontinuities, but did not explore the extent to which the observed periods of these modes contain information about the detail of the discontinuities.

* *Present address:* Institute of Earth Sciences, Academia Sinica, P.O. Box 23–59, Taipei, Taiwan, R.O.C.

0340-062X/79/0045/0129/$03.40

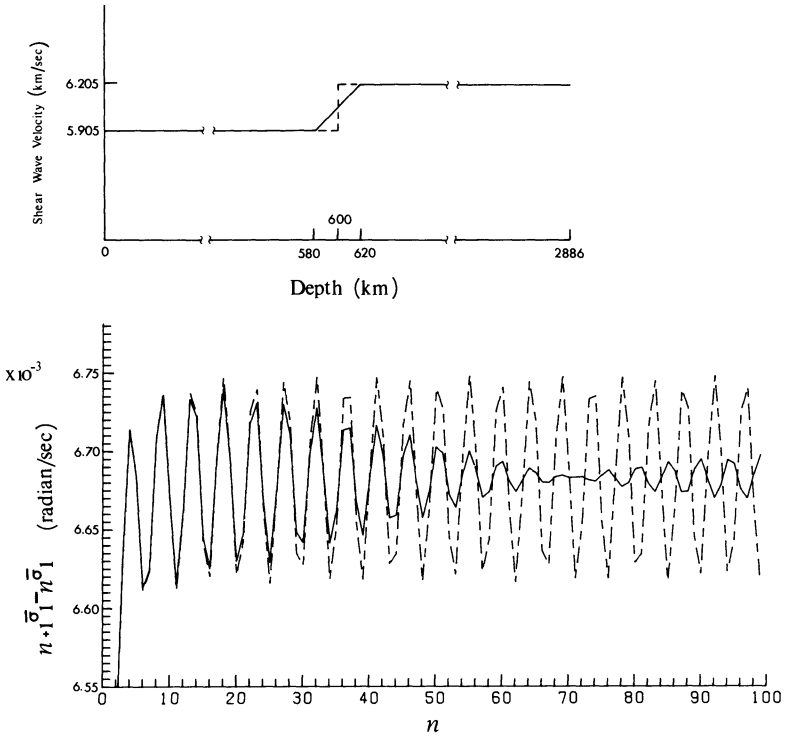

Fig. 1. Comparison between amplitudes of the solotone oscillations corresponding to a discontinuity *(dashed line)* and to a transition layer *(solid line)*, respectively, at 600 km depth (where ${}_n\bar{\sigma}_1$ is a torsional eigenfrequency)

It is clear from observations of short-period reflections from the core-mantle and inner-outer core boundaries that the changes in elastic properties at both boundaries are abrupt. On the other hand, little is known at present about lateral variations in the radii of the boundaries, although there has been speculation about variations of both short and long wave length in the radius of the core-mantle boundary (cf. Hide and Horai, 1968; Hales and Roberts, 1970; Haddon, 1972; Chang and Cleary, 1978). If such variations were present, it would be expected that the globally-averaging properties of spheroidal and radial oscillations would result in observed periods similar to those of a spherically symmetric Earth with transition regions at the core boundaries.

Transition regions in the Earth are important structural features, but their effect on the Earth's free oscillations has not yet been examined in sufficient detail. However, at least for torsional oscillations, it is clear that in this case the solotone effect is modified such that its amplitude decreases with increasing overtone number. This is a consequence of the fact that the amplitudes of waves reflected from transitions of finite width decrease as the frequency of the incident wave increases (cf. Wolf, 1937). This point is illustrated in Fig. 1.

Since (Anderssen et al., 1975) the differential equation for radial free oscillations can be written as a Sturm-Liouville system of the type examined by

McNabb et al. (1975), the above results should remain valid for radial oscillations. Anderssen et al. (1975) showed that the spacings between observed radial (and, for $l=1$, spheroidal) eigenfrequencies of successive overtone numbers contain an oscillatory component. In this paper the effects of the core-mantle (C/M) and inner-outer core (I/O) boundaries, and of the crust and upper mantle structure, on radial oscillations are studied, in order to confirm that results for torsional free oscillations are applicable to radial oscillations, and to provide a general basis for further Earth modelling.

Anderssen et al. (1975) also showed, in their Fig. 1, that the spacings between observed normal modes and between the corresponding eigenfrequencies of model 1066A or 1066B (Gilbert and Dziewonski, 1975) have some minor differences. We have examined the sensitivity of these differences to changes in the structure of the core boundaries, and the possibility of obtaining further information of the Earth's structure from the observed radial normal modes.

We restrict attention to radial oscillations, since they correspond to vertical PKIKP rays with no P/SV conversion at interfaces. The results show that each of the structural regions considered produces an oscillation of a particular period in the spacings between eigenfrequencies of successive overtone numbers. The period is determined by the location of the region, whereas the amplitude of the oscillation is closely related to the velocity and density contrast across the region and decreases at a rate related to its width.

2. Terminology

2.1. ${}_n\bar{\gamma}_l$ Curves

The effect of Earth structure on free oscillations is exhibited in the spacing of eigenfrequencies. Therefore, any parameter which depends on the overtone eigenfrequency spacing will reflect the effect of Earth structure. For fixed angular order number l, one such parameter is ${}_n\bar{\gamma}_l(\kappa)=\pi/[{}_{n+1}\sigma_l(\kappa)-{}_n\sigma_l(\kappa)]$, where ${}_n\sigma_l(\kappa)$ are the eigenfrequencies of any of the $(ScS)_H$, $(ScS)_V$, PKIKP, and J_V sequences (Anderssen et al., 1975; Gilbert, 1975). This parameter was first used by Anderssen, Cleary and Dziewonski (1975) and has the advantage that, when l is small, the baseline for the ${}_n\bar{\gamma}_l(\kappa)-n$ curve yields a reliable estimate of the radial travel time for PKIKP waves (from oscillations of PKIKP type, such as radial oscillations) or for S waves between the surface and the core-mantle boundary (from oscillations of SH or SV type, such as torsional free oscillations). Since we are dealing here mainly with free oscillations equivalent to PKIKP waves, for brevity we simply use ${}_n\bar{\gamma}_l$ for ${}_n\bar{\gamma}_l$ (PKIKP) and ${}_n\sigma_l$ for ${}_n\sigma_l$ (PKIKP) except where otherwise stated. It should be noted that the parameter ${}_n\bar{\gamma}_l$ differs slightly from the parameter ${}_n\gamma_l$ defined by Anderssen and Cleary (1974), which also yields a valid estimate of radial travel times.

In order to examine the effect of Earth structure on ${}_n\bar{\gamma}_l$, its values are normally plotted as a function of n. This paper is concerned mainly with the effects on ${}_n\bar{\gamma}_l$ of discontinuities and transition layers. These effects occur as oscillations in the ${}_n\bar{\gamma}_l$ curves, which are described in terms of *amplitude* (in units of

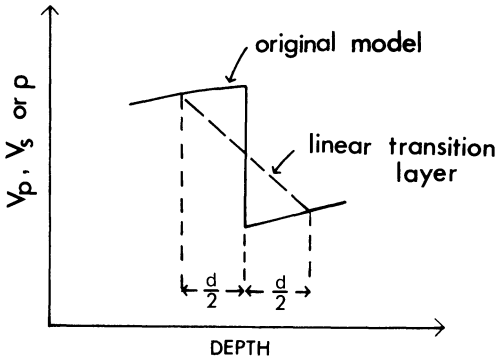

Fig. 2. Diagram showing how a discontinuity in a parameter is replaced by a linear transition layer

seconds) and *frequency* (in cycles per unit n) or *period* (in units of n, i.e. dimensionless).

2.2. *Magnitudes of Discontinuities and Transition Layers*

We define a *transition layer* as a spherically symmetric region of limited thickness in the Earth's interior, in which the density and the compressional and shear wave velocities are monotone functions of depth. It is clear that a discontinuity is the limiting case where a transition layer has zero thickness. In order to be consistent with normal terminology, however, we will restrict the term 'transition layer' to regions of finite thickness.

The radial oscillations are equivalent to vertically incident PKIKP waves. If the results for torsional eigenfrequencies are applicable to radial oscillations, the amplitude of the oscillation in the ${}_n\bar{\gamma}_0$ curve caused by a discontinuity is related to the reflection coefficient for these waves at the discontinuity, which in turn is related to the *magnitude* of the discontinuity which is defined as the *absolute value of the reflection coefficient for vertically incident P waves*, i.e.,

$$|\rho^+\alpha^+ - \rho^-\alpha^-|/(\rho^+\alpha^+ + \rho^-\alpha^-) \tag{1}$$

where (ρ^+, α^+) and (ρ^-, α^-) are pairs of density and P wave velocity on opposite sides of the discontinuity. This can be generalized to the case of a transition layer. Since the reflection coefficient for these waves at a transition layer is closely related to the contrast in the acoustic impedance (product of density and velocity) at the two ends of the transition layer (cf. Wolf, 1937), we define the magnitude of a transition layer to be (1), where (ρ^+, α^+) and (ρ^-, α^-) denote the pairs of density and P wave velocity values at the two ends of the transition layer.

Let $R(\omega, d)$ denote the absolute value of the reflection coefficient for waves of angular frequency ω normally incident at a transition layer with thickness d. Then $R(\omega, d)$ approaches (1) as ω approaches zero, and, generally speaking, $R(\omega, d)$ decreases as ω increases. The rate of decrease is closely associated with d: the larger d, the more rapid the decrease in $R(\omega, d)$ (cf. Wolf, 1937). This

implies that, for waves with wavelengths much greater than d, the transition layer can be treated as a discontinuity, while the reflection of waves with wavelengths much smaller than d at the transition layer is negligible.

3. Effects of Core Boundaries

The effects of the I/O and C/M boundaries will be studied by systematic replacement of either or both of the I/O and C/M discontinuities by linear transition layers as shown in Fig. 2.

3.1. Earth Models Used

Models 1066A (Fig. 3A; Gilbert and Dziewonski, 1975) and HOMO (with homogeneous mantle, outer core and inner core; Fig. 3B), and a set of models derived from them by systematic replacement of either or both the I/O and C/M discontinuities by linear transition layers, are used in this section.

Model 1066A is continuous except at the crust-mantle, I/O and C/M boundaries, where the discontinuities in density and elastic wave velocities are large. It has been confirmed by numerical experiments that, compared to the effects of the core boundaries, the effect of the crust-mantle discontinuity on the radial oscillations is negligible for 1066A. It is therefore not necessary to take its existence into account. For convenience the Earth models derived from 1066A are referred to as ACxIy, where ACxIy contains a linear transition layer ACx of thickness x at the C/M boundary and a linear transition layer AIy of thickness y at the I/O boundary. Model AC0I0 corresponds to 1066A. Some other examples of ACxIy are shown in Fig. 3A. Although it is known from the observations of short period reflections such as PcP and PKIKP that the changes in elastic properties at both core boundaries are quite abrupt, for the purposes of this investigation models with transition layers of several hundred km at the core boundaries have been included.

The simple model HOMO was constructed from model PEM (Dziewonski et al., 1975) by taking the average values of density, P and S wave velocities for the mantle (including the crust), the outer core and the inner core, in the sense that total mass and the P and S wave radial travel times are preserved. The models derived from HOMO are referred to as HCxIy, where HCxIy, like ACxIy, is a model with a C/M transition layer of thickness x and an I/O transition layer of thickness y.

3.2. Results

Our results show that the ${}_n\bar{\gamma}_o$ curves for models 1066A and HOMO contain, for high overtone numbers (say, $n > 20$), two distinct oscillations with periods of 5.5 and 2.4, which are produced by the I/O and C/M discontinuities respectively. If either of the discontinuities is replaced by a linear transition layer, the amplitude

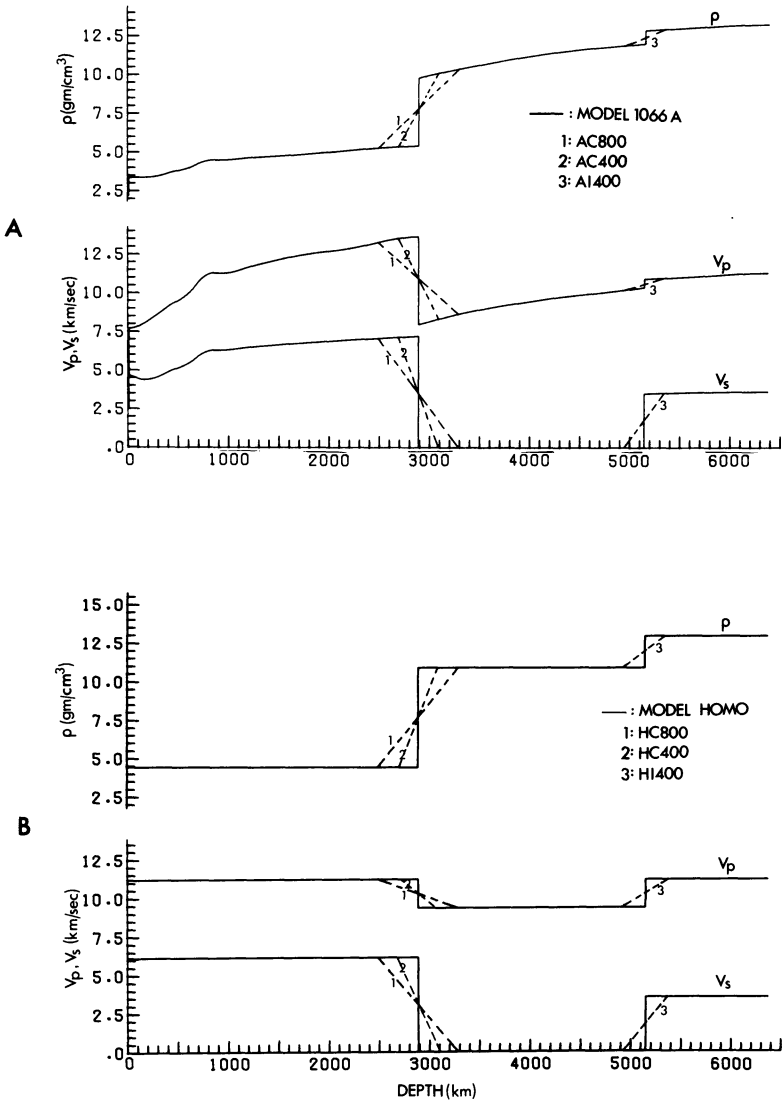

Fig. 3A and B. Models 1066A **(A)** and HOMO **(B)** and some other models ACxIy and HCxIy derived from them. See text for descriptions of ACxIy and HCxIy

of the corresponding oscillation decreases as the overtone number n increases. The rate of the decrease is closely related to the thickness of the transition layer: the thicker the transition layer, the more rapid the amplitude decrease. This is related to the above-mentioned property that, for a fixed value of d, $R(\omega, d)$ decreases as ω increases. We now discuss separately the effects at the core boundaries.

3.2.1 Effect of a Discontinuity or Transition Layer at the I/O Boundary. Figures 4 and 5 show the ${}_n\bar{\gamma}_o$ curves constructed from ACxIy and HCxIy, respectively, with

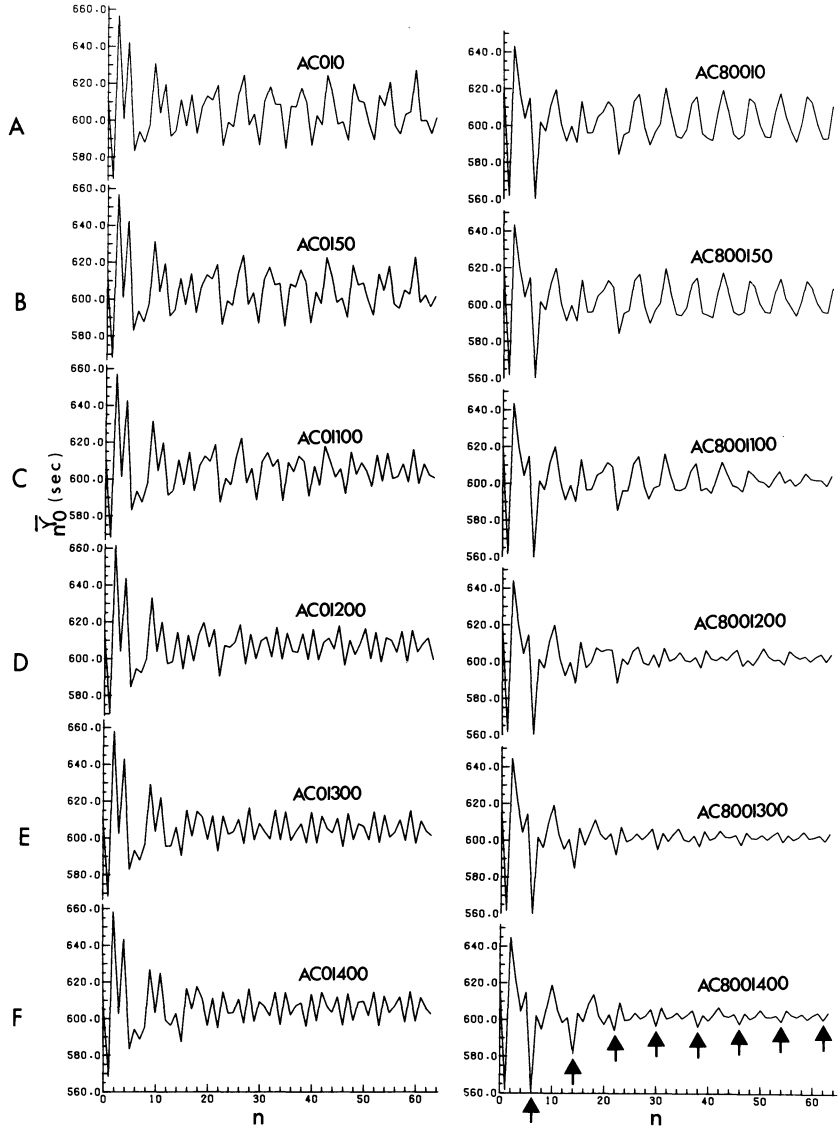

Fig. 4A–F. $_n\bar{\gamma}_o - n$ curves constructed from ACxIy with varying y and fixed x values of 0 km *(left column)* and 800 km *(right column)*

varying thickness y. The $_n\bar{\gamma}_o$ curves in the right-hand column of each figure contain, for $n \geqq 20$, an oscillation with period 5.5. Except for small n, these curves have a negligibly small C/M boundary effect, because the C/M discontinuity has been replaced by an 800 km transition layer. They are much simpler than those in the left-hand columns, where the discontinuity has been retained.

In both Figs. 4 and 5, when $y \neq 0$ the amplitude of the oscillation with period 5.5 in the $_n\bar{\gamma}_o$ curve decreases with increasing n, and the rate of the decrease is closely associated with the value of y. In addition, there is a close agreement in behaviour, as y increases, between the corresponding curves in Figs. 4 and 5. For

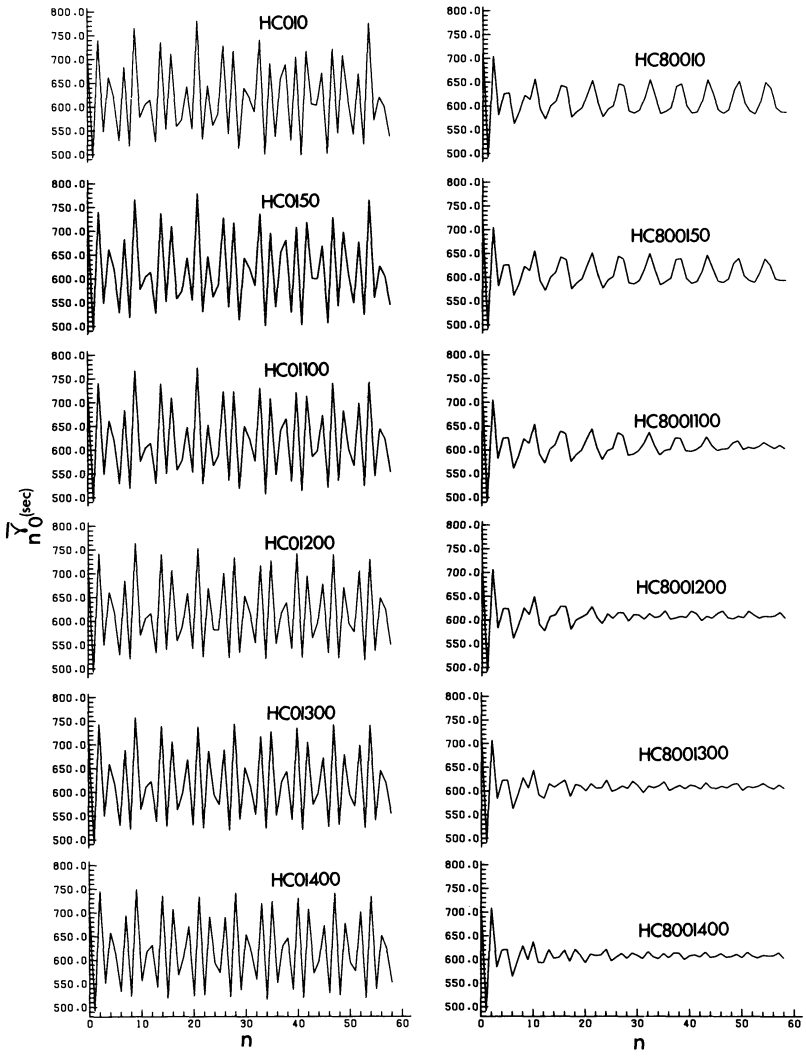

Fig. 5A–F. ${}_n\bar{\gamma}_o - n$ curves constructed from HCxIy with varying y and fixed x values of 9 km *(left column)* and 800 km *(right column)*

$y \geqq 200$ km, the decrease in the amplitude of the oscillation is restricted to the range $0 \leqq n \leqq 20$, except for a slowly-decreasing ripple (with a period of about 8) in Fig. 4, which is produced by the transition zone in the upper mantle of 1066A.

It is therefore clear that the oscillation in Figs. 4A and 5A having a period of 5.5 arises from the I/O discontinuity. It follows that the oscillation having a period of 2.4 in the left-hand columns of Figs. 4 and 5 is produced by the C/M discontinuity, since in both 1066A and HOMO the only two dominant structural features which can cause large amplitude oscillations in the ${}_n\bar{\gamma}_o$ curves are the I/O and C/M discontinuities.

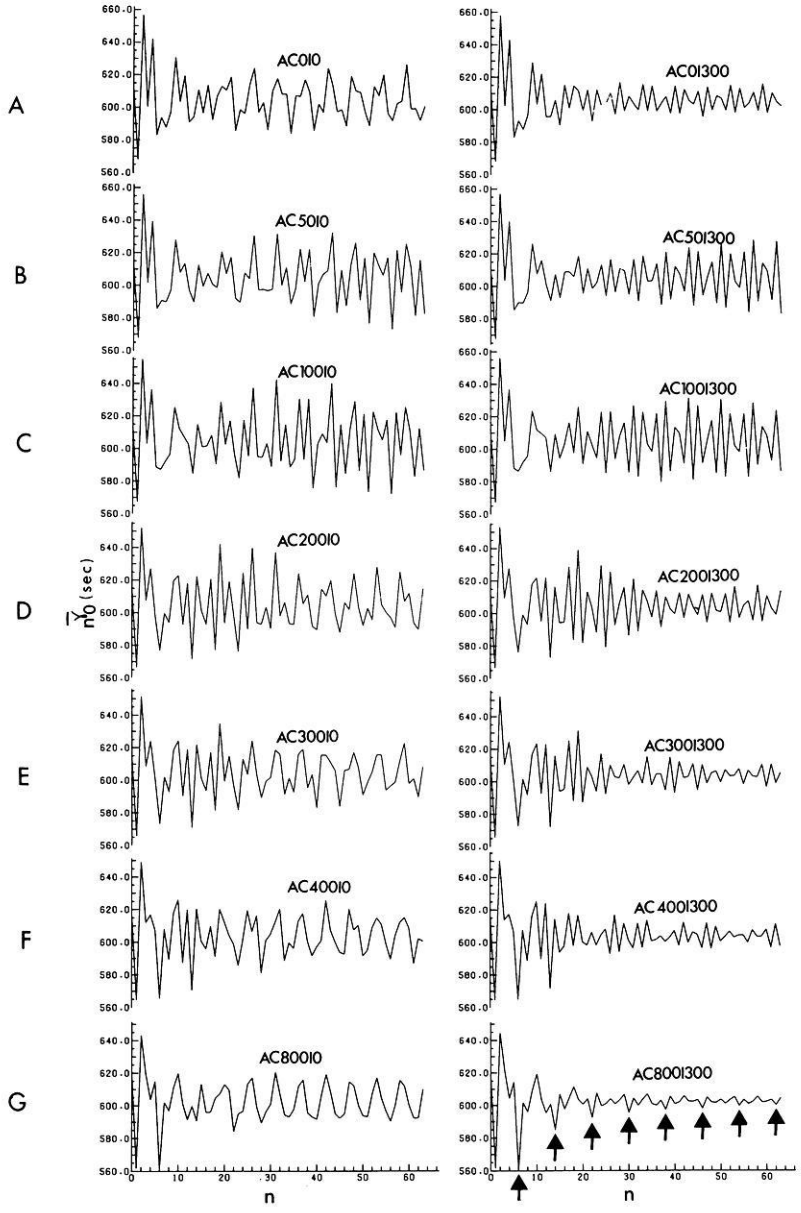

Fig. 6A–G. $_n\bar{\gamma}_o - n$ curves constructed from ACxIy with varying x and fixed y values of 0 km *(left column)* and 300 km *(right column)*

3.2.2. Effect of a Discontinuity or Transition Layer at the C/M Boundary. Figures 6 and 7 show $_n\bar{\gamma}_o$ curves contructed from models ACxIy and HCxIy, respectively, with varying x values. The effect of the I/O boundary on the $_n\bar{\gamma}_o$ curves in the right columns of Figs. 6 and 7 is greatly reduced when n is large, since it is replaced by a 300 km thick transition layer. For $n \geqq 20$, these $_n\bar{\gamma}_o$ curves contain

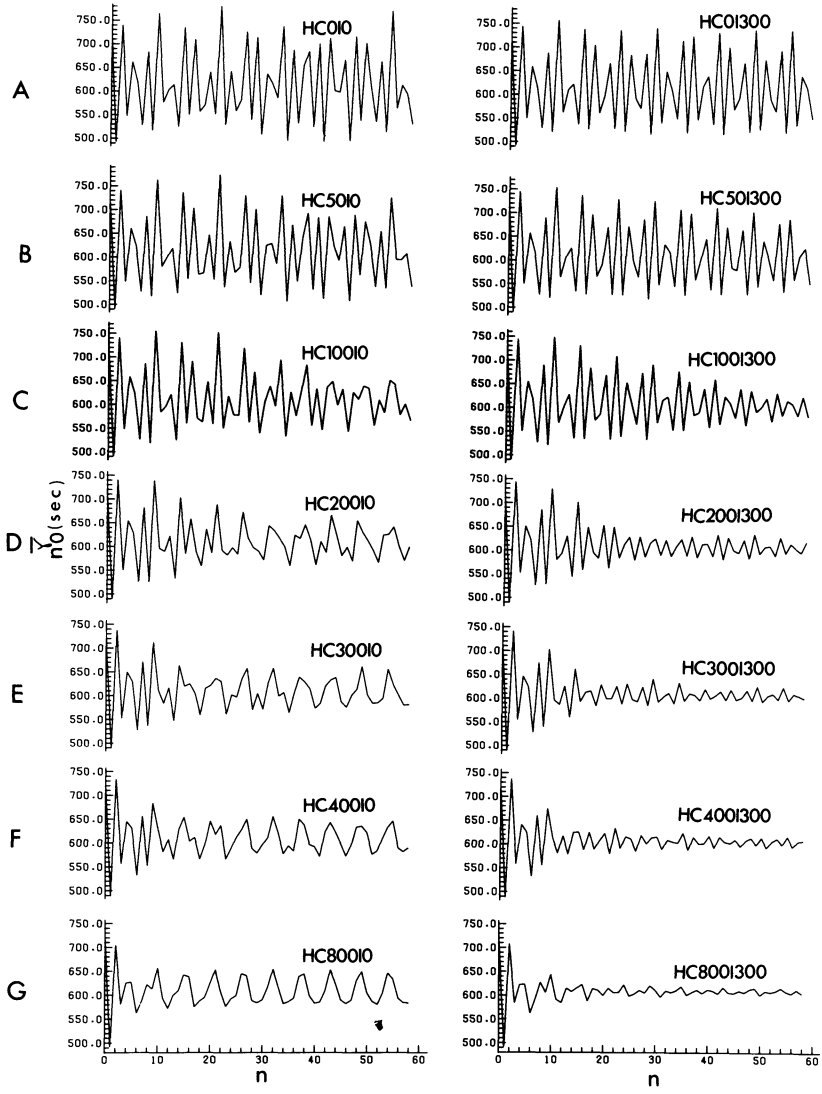

Fig. 7A–G. $_n\bar{y}_o - n$ curves constructed from HCxIy with varying x and fixed y values of 0 km *(left column)* and 300 km *(right column)*

an oscillation with period 2.4. As the C/M transition layer is extended to 800 km, the amplitude of this oscillation is significantly reduced. It can therefore be identified as the effect of the C/M transition layer.

As x increases, the change in the form of the $_n\bar{y}_o$ curves is more complex for ACxIy than for HCxIy. The character of the change common to both 1066A and HOMO is: when $x=0$ (i.e., the C/M boundary is a discontinuity), the oscillation with period 2.4 is persistent (cf. Figs. 6A and 7A), whereas when $x \neq 0$ (i.e., the C/M boundary is a transition layer), the amplitude of this oscillation

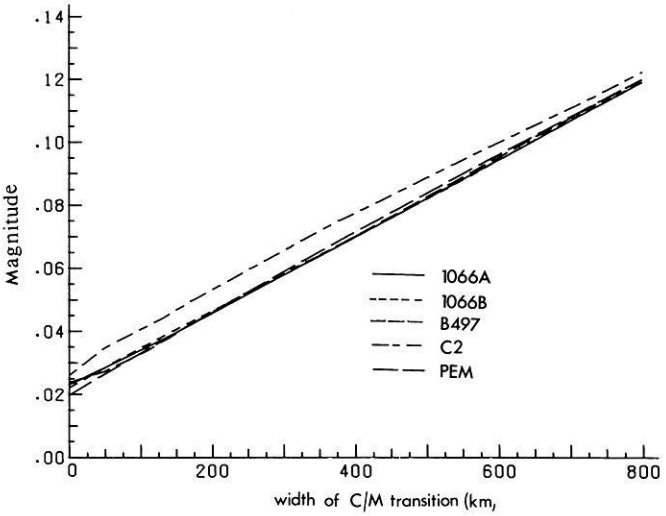

Fig. 8. The dependence of the magnitude of the C/M transition layer on the thickness of the layer for different Earth models

decreases with increasing n (cf. Figs. 6D through 6G and 7B through 7G). The rate of decrease is closely related to the vaue of x.

In addition, the character of the change for ACxIy has the following two properties: (i) The amplitude of the oscillation with period 2.4 increases with increasing x (cf. the right-hand curves of Fig. 6B through D for the range $10 \leqq n \leqq 30$). This increase corresponds to an increase in the magnitude of the C/M transition layer when x is increased. Such an increase in magnitude will occur for most existing Earth models. The dependence of this magnitude on x is shown in Fig. 8 for models 1066A, 1066B (Gilbert and Dziewonski, 1975), B497 (Dziewonski and Gilbert, 1973, Appendix Al), PEM (Dziewonski et al., 1975) and C2 (Anderson and Hart, 1976). (ii) The amplitude of the oscillation with period 2.4 increases with increasing n for certain values of x; in particular, for $n > 10$ when $x = 50$ km, and for $10 < n < 45$ when $x = 100$ km. Its connection with any special characteristic of the C/M boundary is unknown.

Because of (i) and (ii), the decrease (with n) of the amplitude of the oscillation with period 2.4 is much slower for ACxIy than for HCxIy.

4. Effect of the Crust and Upper Mantle Structure

From Sect. 3 it follows that a discontinuity or a transition layer will produce in the ${}_n\bar{\gamma}_o$ curve an oscillation with a particular frequency determined by its position. The oscillation produced by a discontinuity is persistent, whereas the amplitude of the oscillation produced by a transition layer decreases with n at a rate closely related to the thickness of the transition layer. In this section the effect of crust and upper mantle structure on the ${}_n\bar{\gamma}_o$ curve will be discussed based on this conclusion.

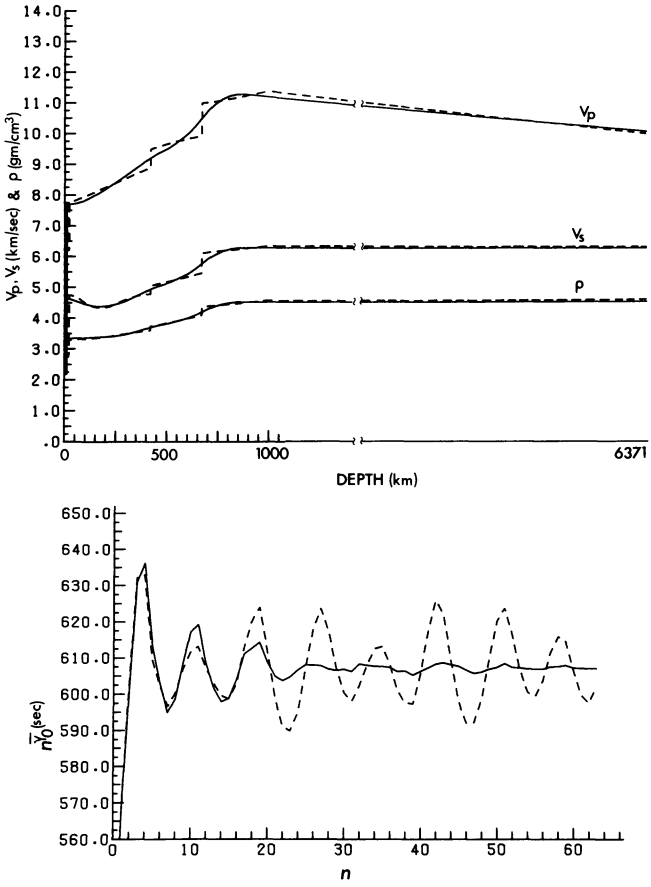

Fig. 9. Comparison of the effect of the continuous upper mantle of 1066A *(solid line)* and that of the discontinuous one of 1066B *(dashed line)* on the ${}_n\bar{\gamma}_o - n$ curves. The models used are derived in a way such that the radial P wave travel times from the core-mantle discontinuity to the Earth's center are kept the same as 1066A and 1066B respectively

The upper mantle (extending from the base of the crust to a depth of about 1000 km) is the region where the density and P and S wave velocities are most complicated and where the existing Earth models differ most. These Earth models can be divided into two classes: those containing a discontinuous upper mantle, which generates a persistent oscillation in the ${}_n\bar{\gamma}_o$ curve, and those containing a continuous upper mantle, which generates an oscillation with decreasing amplitude. To illustrate, the effect of the continuous upper mantle of 1066A and that of the discontinuous upper mantle of 1066B are compared in Fig. 9. The ${}_n\bar{\gamma}_o$ curves for models 1066A and 1066B (constructed from the same set of geophysical data) are also compared in Fig. 10.

The oscillation corresponding to the upper mantle structure has a period of 8 (approximately). Except for discontinuities, the effect of upper mantle structure on the ${}_n\bar{\gamma}_o$ curve is mainly restricted to $n \leqq 20$ (Fig. 9). Therefore, for $n > 20$, the

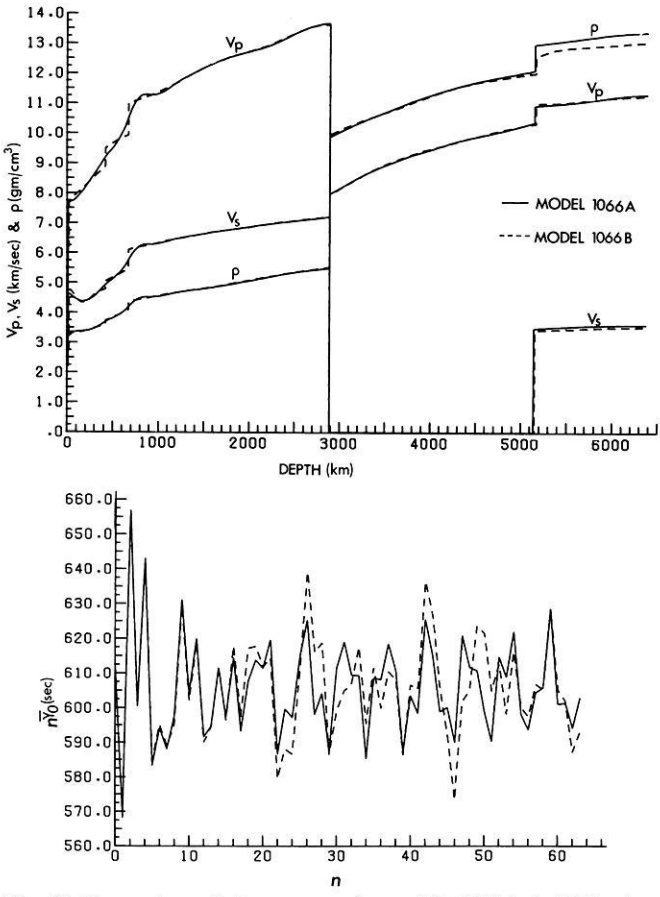

Fig. 10. Comparison of ${}_n\bar{T}_o - n$ curves for models 1066A *(solid line)* and 1066B *(dashed line)*

oscillation only corresponds to the upper mantle discontinuities and rapid transition layers. For example, the slowly-decreasing ripples marked by arrows in Figs. 4 and 6 arise from the transition region in the upper mantle. Since the discontinuities and rapid transition layers generate oscillations with similar periods, their individual properties cannot be separated. Thus the effects of the 421 km and 671 km discontinuities in model 1066B combine to form an oscillation with period 8 (Figs. 9 and 10).

For torsional oscillations, it has been shown in Wang (1978, Ch. 6) that the amplitude of the solotone effect corresponding to a discontinuity in the upper mantle or crust is proportional to $k_1 \sin(t_1 \pi/\alpha)$ while the period of the solotone effect is α/t_1, where k_1 is the reflection coefficient at the discontinuity for normally incident SH waves, and t_1 and α are the shear wave radial travel times from the Earth's surface to the discontinuity and the core-mantle boundary respectively. Numerical experimentation has indicated that this result can be extended to radial oscillations. Thus the oscillation generated by a discontinuity

or transition layer in the upper mantle or crust will have a period z_0/z_1 and an amplitude closely associated with the product of the magnitude of the discontinuity or transition layer and $\sin(z_1\pi/z_0)$, where z_1 and z_0 are the P wave radial travel times from the Earth's surface to the discontinuity or transition layer and the Earth's center respectively. Therefore, as a discontinuity or a transition layer in the upper mantle is moved toward the surface of a model Earth, the oscillation in the ${}_n\bar{\gamma}_o$ curve corresponding to it becomes smaller in amplitude and longer in period.

Accordingly, an oscillation corresponding to a discontinuity or transition layer in the crust will have very long period and a very small amplitude, since z_1/z_0 will be very small. In particular, for a discontinuity at a depth less than 40 km and with a magnitude less than 0.5, the corresponding oscillation will have a peak-to-peak amplitude less than 10 s.

It follows from the above that although the dominant effects in ${}_n\bar{\gamma}_o$ curves from radial oscillations of PKIKP type are produced by the C/M and I/O discontinuities (as indicated by Anderssen et al., 1975), it may be possible to separate out upper mantle effects on the basis of period. In particular, it can be seen in Fig. 9 that there is a significant difference in ${}_n\bar{\gamma}_o$ between continuous and discontinuous models at about $n=10$, which is within the presently observable range. As shown in Fig. 10, this difference has been compensated for in Models 1066A and 1066B. The result nevertheless shows that the effect of the upper mantle is in principle separable from the data at comparatively small values of n.

5. Comparison Between Observed and Synthetic Data

Figure 11B shows the differences between ${}_n\bar{\gamma}_o$ values for model 1066A (Curve 1) and for observed free oscillation data (designated by '$\times$'). It can be seen that 1066A fits the observed ${}_n\bar{\gamma}_o$ values well for $n\leqq 2$ and that, in general, when n increases, the fit becomes worse. This trend indicates that the differences in ${}_n\bar{\gamma}_o$ values could be reduced by changing the parameter values concerning discontinuities and/or rapid transitions in the model.

Shown in Fig. 11A (Curves 2 and 3) are two perturbed models of 1066A which fit, except for ${}_5\bar{\gamma}_o$, the observed ${}_n\bar{\gamma}_o$ values better than 1066A. Figure 11 confirms that the radial normal mode data for small overtone numbers cannot distinguish an Earth model with discontinuous core boundaries from an Earth model with continuous ones. Although the perturbed models are not realistic, the results show that the differences between ${}_n\bar{\gamma}_o$ values derived from observed data and eigenfrequencies of 1066A are sensitive to the changes in parameter values defining the core boundaries, and indicate that if sufficiently refined normal mode data, including high overtone numbers, can be obtained, the Earth model can be improved significantly.

Figure 11B also shows the error ranges (designated by triangles) of the observed ${}_n\bar{\gamma}_o$ values, based on the observation errors listed by Gilbert and Dziewonski (1975). It is clear from these that, in addition to data of higher overtone number, a refinement of the present data is required for satisfactory constraint on the Earth's fine structure.

If lateral variations in the radius of the C/M boundary exist, as suggested, for example, by Hide and Horai (1968), then because of the averaging properties of

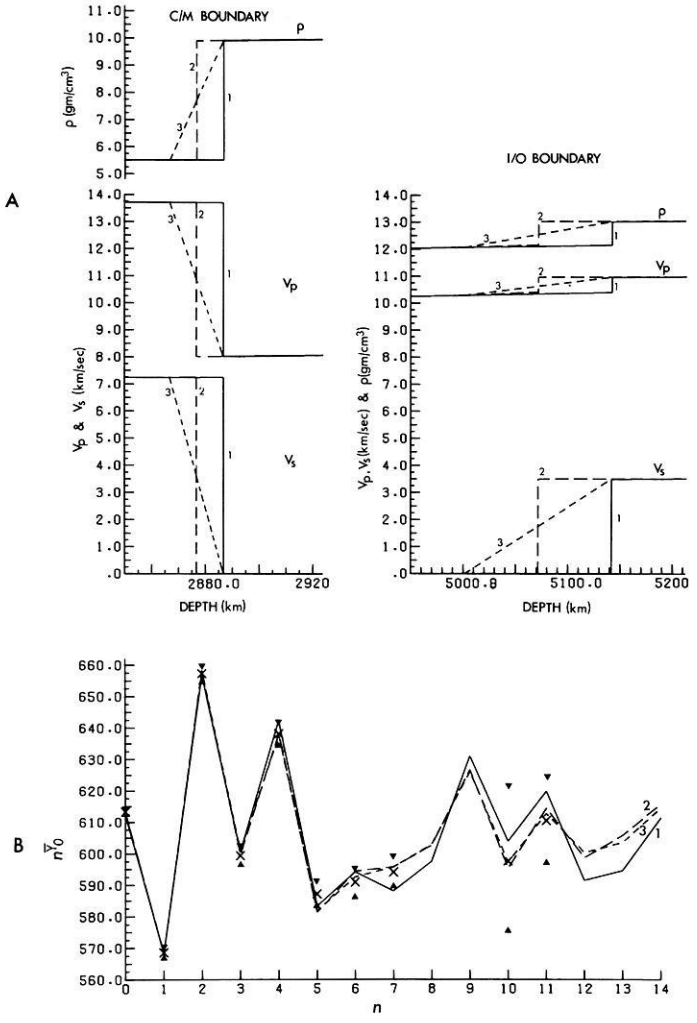

Fig. 11 A and B. Error ranges *(designated by triangles)* and comparison of observed ${}_n\bar{\gamma}_o$ values *(designated by '×')* and those constructed from 1066A *(curve 1)* and two perturbed models of 1066A *(curves 2 and 3)*. One perturbed model is derived from 1066A by shifting the C/M and I/O discontinuities toward the Earth's surface by 10 and 70 km respectively, and the other by replacing the discontinuities by 20 and 140 km thick transition layers in the way shown

free oscillations, the effect of these variations would be similar to that of a transition layer at the boundary. It follows from the above results that such variations would not be detectable by the present radial oscillation data.

6. Conclusions

The above results may be summarized as follows:

(1) A ${}_n\bar{\gamma}_o$ curve comprises a baseline component whose value is determined by the P wave radial travel time from the surface to the centre of the Earth, and

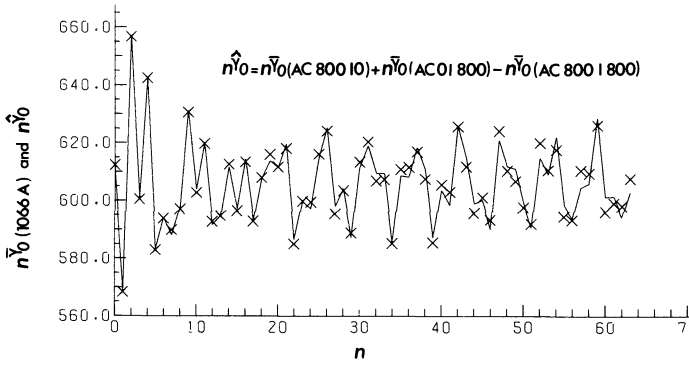

Fig. 12. Comparision of ${}_n\bar{\gamma}_o$(1066A) *(solid line)* and $[{}_n\bar{\gamma}_o(\mathrm{AC800I0}) + {}_n\bar{\gamma}_o(\mathrm{AC0I800}) - {}_n\bar{\gamma}_o(\mathrm{AC800I800})]$ *(designated by '×')* values

an oscillatory component which reflects the structure in the Earth's interior, including gradual slopes, transition layers and discontinuities.

(2) The effect of a discontinuity on the ${}_n\bar{\gamma}_o$ curve is seen as a persistent oscillation, while the effect of a transition layer is seen as an oscillation whose amplitude decreases with n at a rate closely associated with the thickness of the layer. The amplitude of the oscillation is closely related to the magnitude of the discontinuity or transition layer, while the period is related to its position. A consequence of this is that the effects of gradual slopes on the ${}_n\bar{\gamma}_o$ curve are limited to small overtone numbers (say $n \leqq 20$) only.

(3) It is known from the observation of short period waves that the I/O and C/M boundaries are discontinuities or very rapid transition layers of large magnitudes, therefore their effects on the Earth's radial oscillations are persistent or almost persistent oscillations in the ${}_n\bar{\gamma}_o$ curve having periods of about 5.5 and 2.4 respectively. Except for very rapid transition layers or discontinuities, the effect of upper mantle structure is mostly restricted to $n \leqq 20$. The oscillation corresponding to the structure of the upper mantle has a period of about 8. The effect of crustal structure on the radial oscillations is seen as an oscillation of very long period and very small amplitude (less than 10s from peak-to-peak).

(4) As a consequence of the above, the oscillations of very small n (say, $n<5$) in the ${}_n\bar{\gamma}_o$ curve are a composite effect of all the Earth's interior structures (gradual slopes, transition layers and discontinuities), i.e., they reflect the overall spherically symmetric structure of the Earth. When n increases, the oscillations tend to reflect local structures such as very rapid transitions and discontinuities, i.e., their effects are proportionally greater. When $n>20$, the oscillations are mostly the effects of these very rapid transition layers and discontinuities.

(5) The exact manner in which the effects of all the structural features of the Earth on the radial free oscillations are composed still requires a detailed study. By neglecting the minor effects and the interference among the effects of major structural features, however, we can represent the overall composite effect of the Earth's structure as the sum of all the individual oscillations in the ${}_n\bar{\gamma}_o$ curve. Figure 12 shows the comparison of ${}_n\bar{\gamma}_o$ (1066A) (solid line) and $[{}_n\bar{\gamma}_o(\mathrm{AC800I0})$

$+{}_n\bar{\gamma}_o(\text{AC0I800}) - {}_n\bar{\gamma}_o(\text{AC800I800})]$ (designated by '×') structures, where ${}_n\bar{\gamma}_o(\kappa)$ is the ${}_n\bar{\gamma}_o$ value for model κ.

(6) A comparison between observed and synthetic ${}_n\bar{\gamma}_o$ values confirms that the radial normal mode data for small overtone number cannot distinguish a continuous Earth model from a discontinuous one. Because of the large error ranges of the observed ${}_n\bar{\gamma}_o$ values and the nature of free oscillations of low overtone number, information about the fine structure of the Earth and lateral variations in the radius of the C/M boundary cannot be detected by the present radial oscillation data.

Acknowledgements. We wish to thank Professor Freeman Gilbert of the Scripps Institution of Oceanography, University of California at San Diego for making his computer program MODE available to us.

References

Anderson, D.L., Hart, R.S.: An Earth model based on free oscillations and body waves. J. Geophys. Res. **81**, 1461–1475, 1976

Anderssen, R.S., Cleary, J.R.: Asymptotic structure in torsional free oscillations of the Earth-I. Overtone structure. Geophys. J. Roy. Astron. Soc. **39**, 241–268, 1974

Anderssen, R.S., Cleary, J.R., Dziewonski, A.M.: Asymptotic structure in eigenfrequencies of spheroidal normal models of the Earth. Geophys. J. Roy. Astron. Soc. **43**, 1001–1006, 1975

Chang, A.C., Cleary, J.R.: Precursors to PKKP. Bull. Seism. Soc. Am. **68**, 1059–1079, 1978

Dziewonski, A.M., Gilbert, F.: Observations of normal modes from 84 recordings of the Alaskan earthquake of 1964 March 28, Part II. Further remarks based on new spheroidal overtone data. Geophys. J. Roy. Astron. Soc. **35**, 401–437, 1973

Dziewonski, A.M., Hales, A.L., Lapwood, E.R.: Parametrically simple Earth models consistent with geophysical data. Phys. Earth. Planet. Inter. **10**, 12–48, 1975

Gilbert, F.: Some asymptotic properties of the normal modes of the Earth. Geophys. J. Roy. Astron. Soc. **43**, 1007–1011, 1975

Gilbert, F., Dziewonski, A.M.: An application of normal mode theory to the retrieval of structural parameters and source mechanisms from seismic spectra. Philos. Trans. Roy. Soc. Lond. [A] **278**, 187–269, 1975

Haddon, R.A.W.: Corrugations on the mantle-core boundary or transition layers between inner and outer cores? Trans. Am. Geophys. Union **53**, 600 (abstract), 1972

Hales, A.L., Roberts, J.L.: Shear velocities in the lower mantle and the radius of the core. Bull. Seism. Soc. Am. **60**, 1427–1436, 1970

Hide, R., Horai, K.: On the topography of the core-mantle interface. Phys. Earth Planet. Inter. **1**, 305–308, 1968

McNabb, A., Anderssen, R.S., Lapwood, E.R.: Asymptotic behavior of the eigenvalues of a Sturm-Liouville system with discontinuous coefficients. J. Math. Anal. Appl. **54**, 741–751, 1976

Wang, C.: Ray-mode duality for SH waves and the effect of Earth structure on free oscillation eigenfrequencies. Ph.D. thesis. Australian National University, 1978

Wolf, A.: The reflection of elastic waves from transition layers of variable velocity. Geophysics **2**, 357–363, 1937

Received November 23, 1978; Accepted February 6, 1979

J. Geophys. 45, 147–158, 1979

Journal of Geophysics

Relationship Between the Seismic Quality Factor Q and the Effective Viscosity η*

R.O. Meissner and U.R. Vetter

Institut für Geophysik der Universität, D-2300 Kiel, Federal Republic of Germany

Abstract. Two very similar relationships are developed for the effective viscosity η and the seismic quality factor Q with regard to the ratio of the solidus temperature T_m to temperature T. This relationship is linear both for log Q and log η and seems to be valid for $0.95 > T/T_m > 0.5$. Within this temperature interval two different creep laws dominate; also two different attenuation mechanisms are observed from a compilation of seismic body wave data and T_m/T values. The transition from the linear Nabarro-Herring creep to power law creep and that from one attenuation mechanism to the other both take place around 0.7 to 0.8 T/T_m. For the above mentioned temperature regime, which covers the lower lithosphere and the asthenosphere, and for body wave frequencies around 1 to 10 Hz the following linear relationship between $\ln \eta$ and $\ln Q$ is tentatively established:

$$\ln \eta = 4.4 \ln Q + 22 \quad \text{(for } \eta \text{ given in poise)}.$$

Activation energies for attenuation are only about 23% of those for creep.

Key words: Seismic quality factor – Attenuation – Effective viscosity – Activation energies.

1. Introduction

The seismic quality factor Q and the effective viscosity η are governed by different physical processes. At first glance there seems to be little hope of finding a relationship between them. Scattering effects dominate in the near surface area, especially in sediments, and hence Q is strongly frequency dependent, increasing for decreasing frequencies (McDonal et al., 1958; Lütjen, 1978). Although geometrical scattering is not related to the anelastic properties of the medium but rather to certain boundary conditions, its effect cannot be removed from seismic attenuation measurements. The effective viscosity in near surface areas down to the middle or lower crust is also influenced by boundary

* Publ.-No. 169 from the Institut für Geophysik, D-2300 Kiel, Federal Republic of Germany

0340-062X/79/0045/0147/$02.40

conditions: An especially low viscosity associated with fault zones determines the viscosity values in all areas where faults are present (Meissner, 1978; Vetter and Meissner, 1979). Effective fault zone viscosities as low as 10^{14} poise have been calculated for the upper few hundred meters of the crust whereas Q-values between 5 and 25 are found in young sediments at shallow depths (Meissner, 1965). It seems, however, that Q-values in the upper crust are connected with microcracks and are more a bulk property of the whole rock assemblage than are the η-values, but information on this subject is scarce. Estimates of η are derived from temperature models (Meissner and Vetter, 1976) and from the uplift of salt domes and diapirs (Hunsche, 1977). Calculations of Q are based on measurements of the attenuation of body waves (Sutton et al., 1967; Barazangi and Isacks, 1971) and surface waves (Hart et al., 1967; Solomon et al., 1972).

Calculation of η for the whole lithosphere and the asthenosphere can be obtained using the temperature method, postglacial uplift data (Walcott, 1973; Crittenden, 1967; Brennen, 1974), and the movement of plates (Meissner and Vetter, 1976), while amplitude decay spectra of free oscillations in addition to the surface wave and body wave data are used for an estimation of Q in the whole earth (Sailor and Dziewonski, 1978). Figure 1 shows a summary of η- and Q-values versus depth with a smooth curve between data of the authors mentioned above. This figure provides information only on the general behavior of η and Q and certainly can not be used for detailed considerations. It is important to note, however, that Q and η both increase in the upper crust and decrease down to the asthenosphere.

The present study is mainly concerned with the relation between η and Q in the lower lithosphere and asthenosphere with some extrapolations to the middle and lower mantle. The area under consideration covers mainly the temperature range between about $0.95\,T_m > T > 0.5\,T_m$ (with T_m = solidus temperature), though some extrapolations to lower and higher T-values will be made. Also the considered frequency range Δf is small; most body wave data cover the range between 1 and 10 Hz. From theoretical studies (Jackson and Anderson, 1970; Anderson and Hart, 1978; Goetze, 1977) it seems that Q in this $\Delta T - \Delta f$ field is dominated by a grain-boundary relaxation mechanism with an exponential relation to T_m/T. A similar exponential relation has been established for η (Weertman, 1970; Kohlstedt and Goetze, 1974; Kohlstedt et al., 1976; Mercier et al., 1977; among others). Physically, steady state creep may consist of grain boundary diffusion (Coble, 1963) or of a dislocation glide mechanism (Weertman, 1970) – the so called power law creep. The possible relevance of both creep laws for conditions in the lithosphere and asthenosphere has been investigated by Weertman and Weertman (1975), Meissner and Vetter (1976), and Vetter and Meissner (1977). It seems that the likelihood that a close relation between Q and η might exist is greatest in the above mentioned high temperature field where grain boundary processes dominate.

2. Derivation of Formulas for η and Q in the High Temperature Field

As shown by Weertman (1970), Kohlstedt et al. (1976) and others, creep properties of igneous rocks are governed by the general creep equation

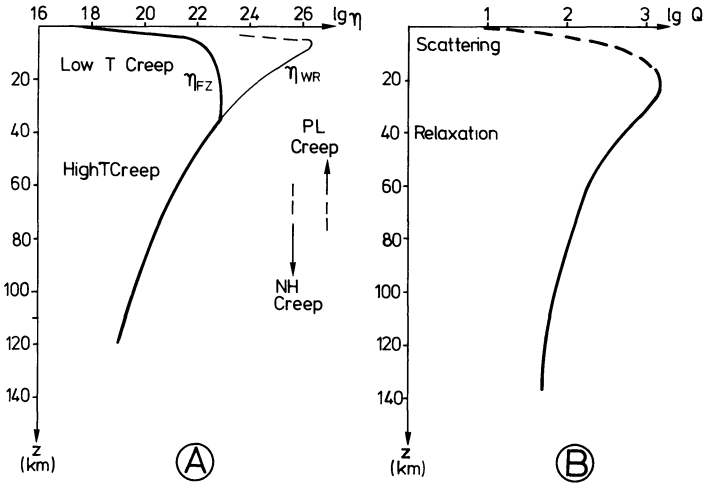

Fig. 1. **A** General behavior of η versus depth; **B** General behavior of Q versus depth in the lithosphere/asthenosphere after various authors (see text). η_{FZ}: effective fracture zone viscosity. η_{WR}: effective whole rock viscosity. PL: Power creep law and NH: Nabarro-Herring creep law = high T creep. Q-data from body wave investigations

$$\dot{\varepsilon} = C_n \sigma^n \exp - [(U + p\,V)/RT] \tag{1}$$

with

C_n = creep constant — $\dot{\varepsilon}$ = creep rate
σ = stress — p = pressure
n = exponent of the creep law (1...3)
U = activation energy — V = activation volume
R = gas constant — T = absolute temperature.

Weertman (1970) has shown that a good approximation of (1) is

$$\dot{\varepsilon} = C_n \sigma^n \exp(-g^* T_m/T) \tag{2}$$

with g^* = constant [about 29 for olivine after Kohlstedt and Goetze (1974)]

T_m = melting temperature (solidus).

Introducing the effective viscosity

$$\eta \approx \sigma/\dot{\varepsilon} \tag{3}$$

and inserting (2) into (3) one obtains

$$\ln \eta = g^* T_m/T - \ln C_n - \ln \sigma^{n-1}. \tag{4}$$

(η always in poise).

If mass transport takes place by general diffusional processes (Nabarro-Herring creep) or along grain boundaries by means of grain-boundary diffusion

(Coble creep) the exponent n will be equal to 1 or at least near 1 (Langdon, 1970). Hence, (4) may be written as,

$$\ln \eta_{NH} = g^* T_m/T - \ln C_1 \quad \text{for } n=1 \tag{5}$$

i.e., η_{NH} does not depend on stress or creep rate. Dislocation glide mechanisms, as thoroughly investigated by Weertman (1970), Kohlstedt and Goetze (1974), and Carter (1976), may also be derived from (4) using $n=3$. For $\dot{\varepsilon}=$const. one obtains after inserting $\sigma \approx \eta \dot{\varepsilon}$

$$\ln \eta_{PL} = 1/3\, g^* T_m/T - 1/3 \ln C_3 - 2/3 \ln \dot{\varepsilon}. \tag{6}$$

In the following it will be shown that formulas like (4), (5), and (6) can also be obtained by assuming a similar grainboundary relaxation process as postulated by Anderson and Hart (1978) and O'Connell and Budiansky (1978). The relaxation time for the inelastic relaxation after a small displacement is

$$\tau = \tau_0 \exp[(\tilde{U} + p\,\tilde{V})/RT] \tag{7}$$

with $\tilde{U}$ and $\tilde{V}$ = activation energy and volume respectively for small scale displacements – as, for instance, caused by the passing of a seismic wave.

τ_0 = characteristic time which according to Anderson and Hart (1978) should be related to the atomic jump frequency. $\tilde{U}$ and $\tilde{V}$ are certainly not identical with U and V of Eq. (1) and may be considerably smaller. From (7), a similar approximation as that of (2) gives

$$\tau = \tau_0 \exp(g_Q T_m/T). \quad \text{For } g_Q \text{ see (14).} \tag{8}$$

The introduction of the general Debye equation for Q gives

$$Q = (c_0/\Delta c) \cdot (1+\omega^2 \tau^2)/\omega \tau \tag{9}$$

with

c_0 = low frequency elastic wave velocity
Δc = difference between low and high frequency wave velocity
ω = angular frequency.

We apply a high frequency approximation and obtain

$$Q = (c_0/\Delta c)\, \omega \tau \quad \text{for } \omega^2 \tau^2 \gg 1. \tag{10}$$

As τ appears to be in the range of 10 to 100 s (Anderson and Hart, 1978) the approximation of (10) seems to be valid for frequencies larger than 0.1 Hz, i.e., certainly for body wave data from explosions and small earthquakes.

Inserting (8) into (10) one obtains

$$\ln Q = g_Q (T_m/T) + \ln(c_0/\Delta c) + \ln(\omega \tau_0). \tag{11}$$

This equation is of the same form as (4), (5), and (6). It describes the strong dependence of Q on the ratio of T_m/T which is similar to that of η. Equation (11) also contains a direct relationship between Q and ω which generally appears in

theoretical derivations (Knopoff, 1964) as well as in some experimental studies (Goetze, 1977). This relationship is hard to understand in view of the large amount of seismic field observations which are consistent with a frequency independent Q (Anderson and Hart, 1978). Recent experimental work of Berckhemer and his coworkers (personal communication) shows (as the earlier experiments of Gordon and Davis (1968)) that Q at high temperature may be independent of frequency over at least 2 decades. We suggest an inverse relationship between ω and τ_0 and will mention this problem later again.

In order to compare both η and Q with values of T_m/T, as needed for a later calculation of activation energies, we define the gradient g_ν of the logarithm of η as a partial derivative from (5), (6), and (11):

$$g_1 = \frac{\partial(\ln \eta)}{\partial(T_m/T)} = g^* \tag{12}$$

for NH creep and PL creep with constant σ

$$g_2 = \frac{\partial(\ln \eta)}{\partial(T_m/T)} = 1/3\, g^* \tag{13}$$

for PL creep with constant $\dot{\varepsilon}$ and with $n=3$

$$g_3 = \frac{\partial(\ln Q)}{\partial(T_m/T)} = g_Q \tag{14}$$

with g_Q between 0.07 and 0.23 g^* as will be shown in the next section.

In general, the Eqs. (5), (6), and (11) can be used to derive a relation between η and Q. Solving (11) for T_m/T and inserting T_m/T into (5) and (6), gives

$$\ln \eta = (g^*/g_Q) \ln Q - (g^*/g_Q) \ln(c_0/\Delta c) - (g^*/g_Q) \ln(\omega \tau_0) - \ln C_1 \tag{15}$$

for NH creep and

$$\ln \eta = 1/3(g^*/g_Q) \ln Q - 1/3(g^*/g_Q) \ln(c_0/\Delta c) - 1/3(g^*/g_Q) \ln(\omega \tau_0) - 1/3 \ln C_3 - 2/3 \ln \dot{\varepsilon} \quad (\text{for } \eta \text{ in poise}) \tag{16}$$

for Pl creep with $n=3$. While g^* is rather well known from experiments of steady state creep processes and seems to be in agreement with in situ observations, g_Q has not yet been determined.

3. Comparisons Between Q and η From Field Observations

Figure 2A gives some well known relations between η and T_m/T resp. T/T_m. Effective viscosities were calculated on the basis of the rheological constants of olivine (Kohlstedt and Goetze, 1974), which is supposed to be the main constituent of mantle material. T- and T_m-values of an oceanic mantle have been used for this figure as in Vetter (1978). These values are in good agreement with

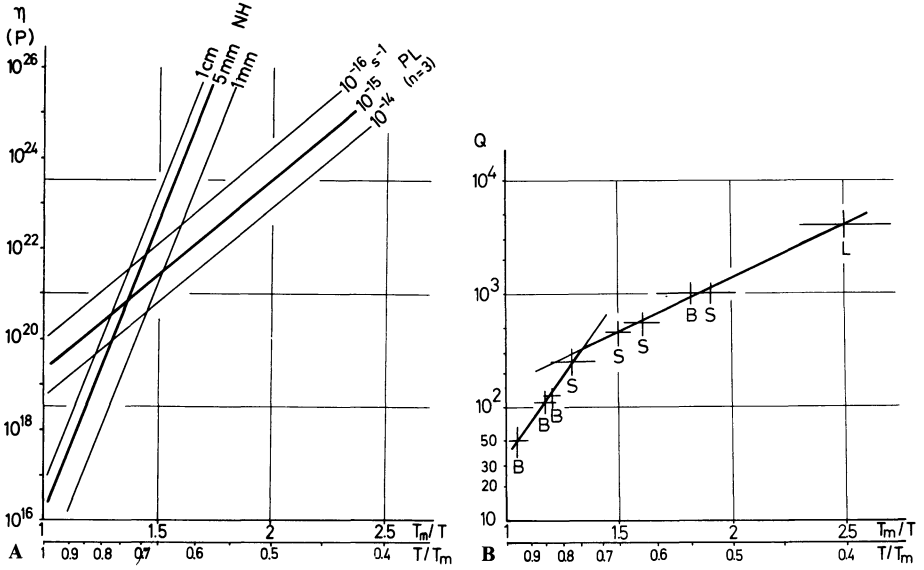

Fig. 2. **A** Effective viscosities according to Nabarro-Herring (*NH*) and power law (*PL*) creep for different grain sizes and creep rates as a function of the ratio of solidus (T_m) to temperature (T). For global relations a grain size of 5 mm and a mean creep rate of $\dot{\varepsilon}=10^{-15}\,s^{-1}$ is used. [For details see Vetter and Meissner (1978)]. **B** Q-values as a function of T_m/T resp. T/T_m. *B*: Barazangi and Isacks (1971); *S*: Sutton et al. (1967); *L*: Latham et al. (1970) (size of crosses-measure for the variance). T_m = dry pyrolite solidus (after Stocker and Ashby, 1975)

temperature models as well as viscosity values from other methods such as uplift data and plate movements. The creep process which operates with the lowest effective viscosity will always dominate about the other one. An average grain size of about 5 mm and a viscosity of 10^{21} poise were found to prevail in the continental shield asthenosphere [for details see Meissner and Vetter (1976), and Vetter and Meissner (1977)]. The transition from *NH* to *PL* creep occurs at about 1 bar and at T/T_m between 0.7 and 0.8, depending on grain size and creep rate $\dot{\varepsilon}$. We presume, based on our former work, that the power law creep in the upper part of a fast moving oceanic asthenosphere may follow the curve of $\dot{\varepsilon}=10^{-14}\,s^{-1}$ which grades into the lithosphere with $\dot{\varepsilon}\approx 10^{-15}$ and $10^{-16}\,s^{-1}$. Accordingly, the viscosity-values for lower T/T_m have to be taken from those $\dot{\varepsilon}$-curves if a special area is considered. On the other hand, an average of $\dot{\varepsilon}=10^{-15}\,s^{-1}$ will be used for obtaining an average η for *PL* creep on a global scale. A grain size of 5 mm will be used for *NH* creep in accordance with our former work.

Figure 2B shows the observed relations between Q and T_m/T. Q-values from body wave data (Sutton et al., 1967; Barazangi and Isacks, 1971; Anderson and Kovach, 1964) were considered more reliable than those derived from surface wave inversion. They can more easily be located with respect to depth and position and can therefore better be related to the temperature regime. The lunar value is from Latham et al. (1970). The relation of Q to the T_m/T regime

was made for a depth of 100 ± 50 km, mostly relying to the P_n-wave or direct P-wave data at these depths. The T_m/T-values in various heat flow provinces were estimated from those of Vetter and Meissner (1976) for terrestrial data and Meissner (1975) for the lunar data point. We are aware of the fact that the lunar data point may not be representative for terrestrial material because of the high vacuum and the total absence of any traces of water. We have added it, though, to the terrestrial data because of the petrological similarity between the terrestrial and the lunar mantle and our belief that possibly Q and η might be equally influenced by the strange lunar environment.

As seen from Fig. 2B, it is not possible to combine the data points by a straight line in the semilog diagram. Two straight lines, considered as extreme values in the higher and lower temperature field, have been plotted with gradients of $\partial(\ln Q)/\partial(T_m/T) = 6.6$ and 2.2, respectively. The transition between the two gradients, like that between the two creep laws, is between 0.7 and 0.8 T_m. The two straight line approximations can be expressed as

$$\lg Q = 0.94\, T_m/T + 1.25 \quad \text{for } T/T_m < 0.7 \tag{17}$$

and

$$\lg Q = 2.87\, T_m/T - 1.17 \quad \text{for } T/T_m > 0.8. \tag{18}$$

A detailed comparison between η and T_m/T as well as between Q and T_m/T may be obtained by a cross section through a well known subduction zone. We combine recent microearthquake observations of Hasegawa et al. (1978), which clearly show a double planed structure in the descending Pacific plate near Japan, with a temperature model of Toksöz et al. (1971). Figure 3A shows Hasegawa's results which were obtained by taking into account the velocity structure of the descending plate and its vicinity. Figure 3B gives the temperature model of Toksöz et al. (1971) with some modifications in the back arc area where an observed heat flow of more than 2 HFU was used as a basis to modify the temperature model. Figure 4 is obtained by transforming the temperature curves into T/T_m-curves and superimposing them onto Fig. 3A. The coincidence between the double plane earthquake structure and the isoline $T/T_m = 0.6$ ($T_m/T = 1.67$) is really striking. Earthquakes only occur within an area with $T/T_m \lesssim 0.6$. This value had previously been considered to be the lower limit of T/T_m where enough stress for a subsequent stress release by quakes can accumulate (Meissner, 1978; Vetter and Meissner, in preparation). The temperature relation of $T/T_m = 0.6$ corresponds to whole rock viscosities of $\eta \approx 10^{23}$ poise. Lower viscosities do not allow the build-up of significant stresses because the whole material creeps. In fact, no quakes occur outside the double plane structure where whole rock viscosities are below 10^{23} poise with the exception of an anomalous area in the upper right side of the figure where apparently a new slab of cold material is formed which has not been incorporated into the thermal model.

Very rigid and highly viscous zones should not show quakes either if they are surrounded by a less viscous material. In fact, only very few quakes are observed in the very interior of the subduced plate inside the two earthquake belts, which may be considered as two "fault zones" with a slightly reduced effective fault

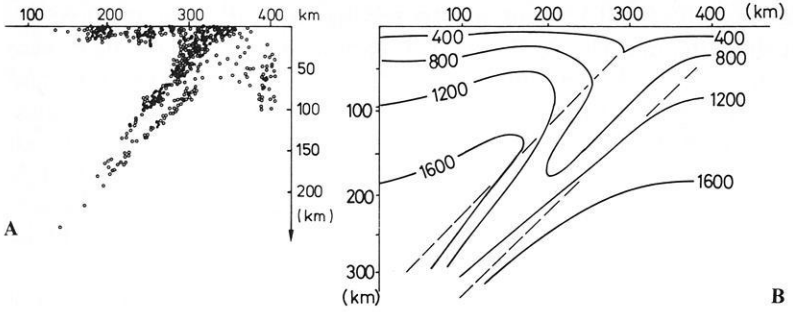

Fig. 3. A Microearthquakes as determined by recent array studies under the Japanese Islands (Hasegawa et al., 1978). **B** Thermal model for a descending plate in a subduction area with $v_{sub} = 8$ cm/y; adiabatic compression, conduction, phase changes, strain heating, and back arc spreading are taken into account. Temperatures in °C. [After Toksöz et al. (1971), modified in the back arc area]

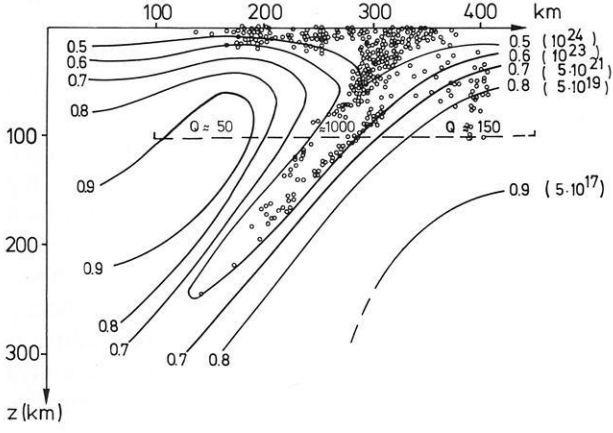

Fig. 4. T/T_m-values as calculated from Toksöz's et al. (1971) model related to Hasegawa's et al. (1978) microearthquake distribution. *Numbers in brackets* are viscosity values in poise calculated for *PL*-creep ($\dot{\varepsilon} = 10^{-14} \ldots 10^{-16}\,s^{-1}$) and for *NH*-creep (grain size 5 mm). Quakes in the *upper right* hand side of the figure possibly show a new onset of subduction not contained in the thermal model

zone viscosity. Quakes in the high viscosity area between the "fault zones" are scarce because high fracture stresses tend to translate all stresses to the next "weaker" zones, zones which apparently are be double planed "master faults".

The good agreement between viscosity and seismicity in this example seems to be a solid basis to relate the η- to the Q-values. Adopting the Q-model of Barazangi and Isacks (1971), Fig. 5 shows the smooth η-curve together with the average Q-values from P body waves for a depth of 100 km. There is certainly a close relationship between both parameters.

Finally, Fig. 6 summarizes all available Q-values and shows their relation to η. This figure was obtained by converting the data of Figs. 2A and B into a

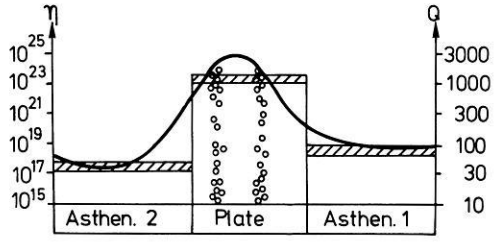

Fig. 5. η and Q in a cross section through the subduction area at a depth of approximately 100 km. *open dots:* zone of quakes inside the descending plate; *Asthen. 1:* "normal" oceanic asthenosphere; *Asthen. 2:* asthenosphere in the back arc area hatched bars = average Q-values of Barazangi and Isacks (1971); η-curve from values of Fig. 4

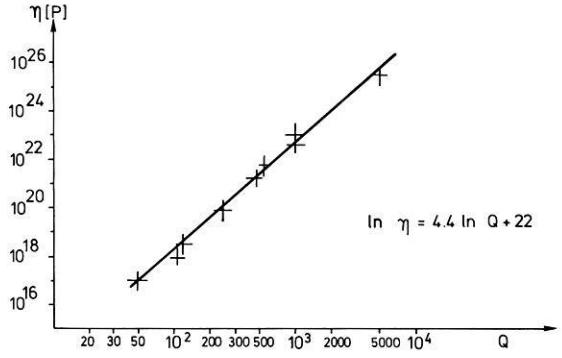

Fig. 6. General relation between η and Q as obtained from the data of Fig. 2A and B

combined log-log diagram. As the two gradients in Fig. 2A and those of Fig. 2B both differ by a factor of about 3 and change at about the same value of T/T_m it was not surprising to us to observe a rather well established linear relationship between $\log \eta$ and $\log Q$:

$$\lg \eta = 4.4 \log Q + 9.6 \tag{19}$$

and

$$\ln \eta = 4.4 \ln Q + 22 \quad \text{(for } \eta \text{ in poise).} \tag{20}$$

This means that apparently different values of g_Q are related to the different creep laws, i.e., NH-creep with $g_1 = g^* = 29$ is connected with $g_Q^{(1)} = 6.6$ and *PL*-creep ($n=3$) with $g_2 = 1/3\, g^* = 29/3$ is connected with $g_Q^{(2)} = 2.2$ ($= 6.6/3$). As mentioned before, an average value of $\dot{\varepsilon} = 10^{-15}\,\mathrm{s}^{-1}$ was used for the calculation of η.

4. Discussion

As seen from Figs. 2B and 6, the error bars are rather large. As mentioned before, the values of the 2 different gradients $\partial(\ln Q)/\partial(T_m/T)$ should be consid-

ered as extremes or asymptotic values. Also, the gradient of $\partial(\ln \eta)/\partial(T_m/T)$ should be understood as asymptotic; further, as mentioned before, the dependence of η on $\dot{\varepsilon}$ causes uncertainties in η because of the uncertain values of $\dot{\varepsilon}$. In another approach we have tried to calculate η for different depths by assuming a systematic change of $\dot{\varepsilon}$ from the asthenosphere into the lithosphere. In doing so we arrive at smaller gradients for $\partial(\ln \eta)/\partial(\ln Q)$. However, as $\dot{\varepsilon}$ on a global scale is hard to define and because all creep experiments as the basis for the calculation of creep constants are performed at constant $\dot{\varepsilon}$-values, we preferred to present the general relation between Q and η for a constant $\dot{\varepsilon}$. We have also compared our results with those of Anderson and O'Connell (1967) who gave a constant ratio of η/Q of about $4 \cdot 10^{19}$ poise. As seen from Fig. 6, our ratio η/Q is about 10^{16} poise for $Q = 50$–100 and 10^{20} for a Q around 1000.

The linear relation between $\ln Q$ and $\ln \eta$ is certainly hard to understand in view of the small stresses associated with wave transmission and the stress dependent different creep processes which are related to grain boundary diffusion or power law dislocation glide mechanisms. This means that not only does the creep mechanism change between 0.7 and 0.8 T_m, but also the relaxation mechanism responsible for Q changes its character at these temperatures. Apparently only small stresses can build up in the range of $T/T_m > 0.8$, where creep is not dependent on creep rate or stress. In contrast, at $T/T_m < 0.7$ the lithosphere generally exhibits some stress, $\sigma > 1$ bar, which may be released in earthquakes if the temperature drops a little more and more stress is built-up.

Regarding the activation energies, a value of 125 kcal/mol (for olivine) corresponding to $g^* = 29$ is found for NH creep, while an "effective activation energy" of only $125/3 = 41.7$ kcal/mol is found for PL creep (because of $g = g^*/3$). The activation energy at higher temperatures is 28.3 for the attenuation process; at slightly lower temperatures it is 9.44 kcal/mol. Certainly, the transmission of an elastic wave does not activate as many atoms or grain-boundaries as does a steady state creep process; however, at higher temperatures a larger number of particles is apparently activated.

So far, a dependence of Q on the frequency of waves has not yet been proved by field observations. Many authors present convincing evidence that these data are consistent with Q being independent of frequency at least between 1 and 60 s (Anderson and Hart, 1978). Equation (11) however contains a frequency term. Several authors, among them Lomnitz (1957) and Kanamori and Anderson (1977), try to avoid this dilemma by assuming a whole spectrum of relaxation times, the superposition of them then giving a quasi frequency independent Q. While this may be an interesting approach for deriving Q-values for different depths, compositions, and densities, it fails to explain the Q-values of the lower lithosphere and asthenosphere where olivine certainly dominates. The only way to remove the dependence of frequency from Eq. (11) is to assume that the term $\omega \tau_0$ is constant. This means that τ_0 must be proportional to $1/\omega$. Its value may be obtained by comparing (11) with (17) and (18). It is about $2.3 \cdot 10^{-4}$ s for a 10 Hz frequency and $T/T_m < 0.7$ and about $1.4 \cdot 10^{-4}$ s for 10 Hz and $T/T_m > 0.8$. This means that τ_0 certainly is too large to be related directly to the atomic jump frequency and therefore seems to describe a more general relaxation upon very small stresses. The higher the frequency, the lower is τ_0.

5. Conclusion

It has been shown by a simple theoretical approach that the parameters Q and η can be expressed by a very similar exponential relationship with regard to the ratio of the solidus temperature T_m to temperature T, at least for body wave frequencies larger than about 1 Hz and for $0.95 > T/T_m > 0.5$. The attenuation seems to obey two different laws, one at higher and one at lower temperatures; as such there is a strong similarity in this behavior to that of creep in that there are also two dominating processes, the Nabarro-Herring or Newtonian linear creep law in a small stress-high temperature regime and the power law dislocation glide mechanism at slightly lower temperatures. Effective activation energies for seismic attenuation seem to be only 23% of that of steady state creep. Both creep and attenuation exhibit lower effective activation energies for lower temperatures. The change of effective activation energies for both creep and attenuation to about a third of that for high temperature values takes place between 0.8 and 0.7 T_m. From this, a linear relationship between $\lg Q$ and $\lg \eta$ has tentatively been established. It agrees with field observations of high frequency body waves and known creep processes in the earth's asthenosphere. The relation is substantiated by more evidence than were those of Anderson and O'Connell (1967) or Meissner (1975) but will certainly be subject to revision when more data become available. Moreover, other relations definitely exist in the upper lithosphere especially for sediments, and possibly also for the middle and deeper part of the mantle, where phase transitions change the structure of minerals. It should, however, be mentioned that data from surface wave and free oscillation inversions and those from viscosity estimations may well agree with the empirical relation presented in this study.

Acknowledgement. When presenting our paper at the EGS-ESC meeting in Strasbourg in September 1978 we noticed that Berckhemer and his coworkers had found quite a similar relationship between Q and η, based on experimental high temperature studies in Frankfurt. Subsequent discussions helped us considerably in developing our arguments. We thank Dr. A. Binder for critically reading the manuscript.

References

Anderson, D.L., Hart, R.S.: Attenuation models of the earth. Phys. Earth Planet. Inter. **16**, 289–306, 1978

Anderson, D.L., Kovach, R.L.: Attenuation in the mantle and rigidity of the core from multiply reflected core phases. Proc. Natl. Acad. Sci. U.S.A. **51**, 168–172, 1964

Anderson, D.L., O'Connell, R.: Viscosity of the earth. Geophys. J.R. Astron. Soc. **14**, 287–295, 1967

Barazangi, M., Isacks, B.: Lateral variation of seismic wave attenuation in the upper mantle above the inclined earthquake zone of the Tonga Island Arc: deep anomaly in the upper mantle. J. Geophys. Res. **76**, 8493–8516, 1971

Brennen, C.: Isostatic recovery and the strain rate dependent viscosity of the earth's mantle. J. Geophys. Res. **79**, 3993–4001, 1974

Carter, N.L.: Steady state flow of rocks. Rev. Geophys. Space Phys. **14**, 301–360, 1976

Coble, R.L.: A model for boundary diffusion controlled creep in polycrystalline materials. J. Appl. Phys. **36**, 1679–1682, 1963

Crittenden, M.D. Jr.: Viscosity and finite strength of the mantle as determined from water and ice loads. Geophys. J.R. Astron. Soc. **14**, 261–279, 1967

Goetze, C.: Bounds on the subsolidus attenuation for four rock types at simultaneous high temperature and pressure. Tectonophysics **42**, T1–T5, 1977
Gordon, R.B., Davis, L.A.: Velocity and attenuation of seismic waves in imperfectly elastic rock. J. Geophys. Res. **73**, 3917–3935, 1968
Hart, R.S., Anderson, D.L., Kanamori, H.: Shear velocity and density of an attenuating earth. Earth Planet. Sci. Lett. **32**, 25–34, 1967
Hasegawa, A., Umino, N., Takagi, A.: Double-planed structure of the deep seismic zone in the NE Japan arc. Tectonophysics, **47**, 43–58, 1978
Hunsche, U.: Modellrechnungen zur Entstehung von Salzstockfamilien. Diss. Math.-Naturwiss. Fakultät, Techn. Univ. Braunschweig, 1977
Jackson, D.D., Anderson, D.L.: Physical mechanism of seismic wave attenuation. Rev. Geophys. Space Phys. **8**, 1–63, 1970
Kanamori, H., Anderson, D.L.: Importance of physical dispersion in surface wave and free oscillation problems. Rev. Geophys. Space Phys. **15**, 105–112, 1977
Knopoff, L.: Q. Rev. Geophys. Space Phys. **2**, 625–661, 1964
Kohlstedt, D.L., Goetze, C.: Low-stress high-temperature creep in olivine single crystals. J. Geophys. Res. **79**, 2045–2051, 1974
Kohlstedt, D.L., Goetze, C., Durham, W.B.: Experimental deformation of single crystal olivine with application to flow in the mantle. In: Physics and Chemistry of Minerals and Rocks, R.G. Strens, ed.; 35–50. New York: J. Wiley & Sons 1976
Langdon, T.G.: Grain boundary sliding as a deformation mechanism during creep. Phil. Mag. **22**, 689–700, 1970
Latham, G., Ewing, M., Dorman, J., Press, F., Toksöz, N., Sutton, G., Meissner, R., Duennebier, F., Nakamura, Y., Kovach, R., and Yates. M.: Seismic data from man-made impacts on the moon. Science **167** (3958), 620–626, 1970
Lomnitz, C.: Linear dissipation in solids. J. Appl. Phys. **57**, 201–205, 1957
Lütjen, H.: Feldversuche zur Bestimmung des Amplitudenabfalls im Nahbereich zweier seismischer Quellen. Dipl.-Arbeit Inst. f. Geophysik, Universität Kiel, 1978
McDonal, F.J., Angona, F.A., Mills, R.L., Sengbush, R.L., Nostrand, R.G. Van, White, J.E.: Attenuation of shear and compressional waves in Pierre shale. Geophysics **23**, 421–439, 1958
Meissner, R.O.: *P*- and *SV*-waves from uphole shooting. Geophys. Prospect. **XIII**, 433–459, 1965
Meissner, R.O.: Lunar viscosity as obtained from the selenotherms. The Moon **12**, 179–191, 1975
Meissner, R.O.: Viscosity and creep processes in the lithosphere. In: Eustasy, Isostasy, and Uplift, A. Mörner, ed. New York: J. Wiley & Sons, 1979 (in press)
Meissner, R.O., Vetter, U.R.: Isostatic and dynamic processes and their relation to viscosity. Tectonophysics **35**, 137–148, 1976
O'Connell, R.J., Budiansky, B.: Measure of dissipation in viscoelastic media. Geophys. Res. Lett. **5**, 5–8, 1978
Solomon, S.C.: Seismic wave attenuation and partial melting in the upper mantle of N America. J. Geophys. Res. **77**, 1483–1502, 1972
Stocker, R.L., Ashby, M.F.: On the rheology of the upper mantle. Rev. Geophys. Space Phys. **11**, 391–426, 1973
Sutton, G.H., Mitronovas, W., Pomeroy, P.W.: Short-period seismic energy radiation patterns from underground nuclear explosions and small-magnitude earthquakes. Bull. Seism. Soc. Am. **57**, 249–267, 1967
Toksöz, M.N., Minear, J.W., Julian, B.R.: Temperature field and geophysical effects of the downgoing slab. J. Geophys. Res. **76**, 1113–1138, 1971
Vetter, U.R.: Stress and viscosity in the asthenosphere. J. Geophys. **44**, 231–244, 1978
Vetter, U.R., Meissner, R.O.: Creep in geodynamic processes. Tectonophysics **42**, 37–54, 1977
Walcott, R.J.: Structure of the earth from glacio-isostatic rebound. Ann. Rev. Earth Planet. Sci. **1**, 15–37, 1973
Weertman, J.: The creep strength of the earth's mantle. Rev. Geophys. Space Phys. **8**, 145–168, 1970
Weertman, J., Weertman, J.R.: High temperature creep of rock and mantle viscosity. Ann. Rev. Earth Planet. Sci. **3**, 293–315, 1975

Received November 13, 1978; Accepted January 13, 1979

J. Geophys. 45, 159–170, 1979

Journal of Geophysics

The Wave Field Associated With a Fine Structured Moho in Continents and Oceans

I.P. Kosminskaya and N.K. Kapustian

Institute of Physics of the Earth, Academy of Sciences of the USSR, Moscow, USSR

Abstract. The crust-mantle transition zone in continents and oceans is regarded as a complex block-layered structure. The case of blocks of small dimension may be described by a thin-layered zone with random distribution of its seismic parameters. Such structure accounts for continuous and well correlated subcritical reflections whose amplitudes are 3–4 times higher than those of a first order velocity discontinuity. The reflectivity from the random zone is practically independent of frequency above 10 Hz. If the dimensions of the blocks are large the subcritical reflections may be correlated as discontinuous branches of the travel-time curve with various amplitudes on them.

Key words: Crust-mantle transition – Thinlayered zone – Spectra – Reflectivity – Travel-time and amplitude-distance curves.

During the past decade great attention was paid to the investigation of the fine structure of the Moho-boundary beneath continents. In some regions the crust-mantle transition may be strongly layered and can be represented by thinlayered zones (Fuchs, 1970; Fuchs and Müller, 1971; Berzon et al., 1975; Davydova et al., 1972; Pavlenkova, 1973). It was shown that dynamic analysis (amplitudes, spectra, wave form) of reflections in the sub-critical area is most efficient for the study of the structure of thinlayered zones.

Until recently deep seismic sounding (DSS) studies in oceans have been based on frequencies of about 5 Hz, i.e., on wave lengths comparable with the total thickness of the oceanic crust. The wave field was observed in critical and overcritical areas. All these factors hindered the investigation of the thinlayering of the oceanic crust and upper mantle. The utilization of airgun sources in marine DSS studies now makes it possible to expand the frequency band (20–30 Hz) and to obtain better correlations: this is important for the detection of subcritical reflections in the second arrivals. The statistical analysis of data obtained from airguns and shots shows considerably thinner layering of both the upper and the lower parts of the oceanic crust (Kosminskaya and Kapustian,

0340-062X/79/0045/0159/$02.40

1975). The use of airguns in marine studies enables us to investigate the thinlayering of the oceanic crust and especially the crustmantle transition. This is important for the study of the processes of formation and development of the oceanic crust.

In continents the structure of the crust-mantle thinlayered transition was generally supposed to be horizontally continuous. Such models accounted for those peculiarities of the wave correlation which could not be explained by simple first order discontinuities or gradiental transition zones. Nevertheless it is difficult to imagine such stability of individual layers within the transition zone over horizontal distance of dozens of kilometers. The assumption of variable layer parameters is more realistic. Investigations of the discontinuous wave correlation or the dashed character of the crustal wave field will show the complex micro- and macro-block-layering of the crust: thus it may be possible to study the complex block-layered crust-mantle transition. Hence it is important to assess the chances for the detection of thinlayering and micro-blocked structure of the Mohorovičič zone and to develop the DSS method in continents and oceans appropriately.

Theory tells us that reflection dynamics depend not only on the structure at the reflection point but on the properties of the media in the vicinity of this point, limited by the effective section of the ray tube[1]. The linear dimension of this effective section is proportional to $\sqrt{\lambda L}$, where λ is the wave length and L is the ray length, i.e., the dimension is transformed in terms of the boundary depth and epicentral distance. In continents the linear dimension of this area is about 10 km for the reflection from the Moho (depth 40 km) observed at a distance of about 10 km from the source (Davydova et al., 1972). This dimension of the ray tube for the oceanic crust (Moho-depth 10 km) is about 3 km and increases with epicentral distance from the shotpoint. Such calculations make it possible to divide the supposed block-layering of the Moho into two types:

(1) micro-block-layering; i.e., the horizontal dimensions of the blocks are less than the whole reflectivity area;

(2) macro-block-layering, i.e., the transition zone consists of blocks of the same dimension as the reflectivity area. The layering structure is stable within an individual block.

The case of micro-block-layering is represented by a thinlayered zone with a random distribution of its seismic parameters. It is possible to imagine such a structure as a mixture of small lenses whose velocity and thickness are derived from a normal distribution. The computational methods for such media were developed in seismic prospecting (Berzon et al., 1973), and were discussed in the paper by Davydova et al. (1972) for the continental DSS data for the subcritical area.

Here we investigate such thinlayered zones not only for continents but also oceans and discuss dynamics for all distance ranges – subcritical, critical and overcritical – to choose the optimal frequency and distance ranges for observation of blockthinlayered zones.

---

[1] The effective section of the ray tube is the area obtained from the intersection of the ray tube and the boundary or the part of the boundary within the ray tube

The random layered zone structure is determined by the random parameters of the layers: thickness $h_n (1 \leqq n \leqq N)$, P- and S-wave velocities $V_{p,n}$; $V_{s,n}$ and densities ρ_n. We consider the normal law of layer parameters distribution. It is possible to construct a random vector $\vec{\beta}$ with coordinates equal to the layer parameters

$$\beta_{4n} = V_{p,n}; \quad \beta_{4n+1} = V_{s,n}; \quad \beta_{4n+2} = h_n; \quad \beta_{4n+3} = \rho_n.$$

In the case of the incident plane P-wave pulse

$$F_p(t) = \frac{1}{2\pi} \int_{-\infty}^{+\infty} S(\omega) e^{i\omega t} d\omega,$$

where $S(\omega)$ is its spectrum, the P-reflection from a thinlayered zone will be as follows

$$F_{pp}(t) = \frac{1}{2\pi} \int_{-\infty}^{+\infty} S(\omega) \eta_0(\omega) e^{i\omega t} d\omega,$$

where $\eta_0(\omega)$ is the reflectivity for this zone. It is calculated by the well-known reflectivity matrix method (Ratnikova and Levshin, 1967; Fuchs, 1968). In the case of a random thinlayered zone, the random reflection for the wide incident wave conditions will be as follows

$$f(t, \vec{\beta}) = \frac{1}{2\pi} \int_{-\infty}^{+\infty} S(\omega) \eta(\omega, \vec{\beta}) e^{i\omega t} d\omega,$$

where $\eta(\omega, \vec{\beta})$ is the reflectivity for random zone and random function of frequency ω and

$$M[f(t, \vec{\beta})] = \frac{1}{2\pi} \int_{-\infty}^{+\infty} S(\omega) M[\eta(\omega, \vec{\beta})] e^{i\omega t} d\omega.$$

We calculated $M[\eta(\omega, \vec{\beta})]$ for $L = 30$ realizations. Each individual realization was a thinlayered zone whose parameters were an individual realization of vector $\vec{\beta}$. The reflectivity for each individual realization has been calculated and after that the reflectivity for the random zone was obtained by the formulas:

$$M[\eta(\omega_\kappa, \vec{\beta})] = \frac{1}{L} \sum_{l=1}^{L} \eta(\omega_\kappa, \vec{\beta}_l);$$

$$M[|\eta(\omega_\kappa, \vec{\beta})|] = \frac{1}{L} \sum_{l=1}^{L} |\eta(\omega_\kappa, \vec{\beta}_l)|.$$

In this paper the thinlayered random zone is regarded as a model of the Moho in continents and oceans. The mean velocity in the random zone (8.2 km/s) is approximately equal to the value in upper mantle (8.0 km/s) and differs greatly from the value in the crust (7.0 km/s). The dynamics for such a structure is calculated in subcritical, critical and overcritical areas and is

compared with the computations for individual relaizations and an equivalent layer (the layer whose parameters are equal to the mean values for the random zone $V_p = 8.2$ km/s; $h = 1.1$ km).

Figure 1 represents the depth-velocity models (Fig. 1C), the cross-section (Fig. 1B) of the micro-block-layered M-boundary and the dynamic travel-time curve[2] for the M-reflection $P_{\text{refl}}^{8.0}$ (Fig. 1A). In the case of 30 realizations the dimension of each micro-block (the block which layer thickness and velocity are stable) has to be approximately 100 m for oceanic and 300 m for continental crust. The reflection from such a structure will be correlated continuously and its amplitude near the shot point will be 3–4 times greater than those for the equivalent layer.

The frequency characteristics of the micro-block-layered M-boundary reflection are shown in Fig. 2. The amplitude spectra of the reflected wave (reflectivity) depend on the epicentral distance and frequency. The sets of spectra may be divided into 3 zones: subcritical, critical and overcritical.

In the subcritical zone (from 2 to 70 km in continental DSS studies 0.5 to 20 km in oceans) the amplitude spectra increase approximately linearly with frequency up to 5 Hz. Within the higher frequency band spectra oscillate slightly (15%) around the average value independent of the frequency and decrease as distance increases.

In the critical zone (70–150 km in continents, 20–40 km in oceans) spectra increase with frequency, the fastest increase being up to 10 Hz. The location of the critical point in this area is moved towards smaller distances for higher frequencies. This phenomenon is known (Červeny and Ravindra, 1971) to be determined by the relationship between the wave length and the thickness of the layer. This fact should be taken into account in the choosing of the optimum frequency and distance ranges in the modern critical-angle-reflection studies in oceans.

In the overcritical zone (greater than 150 km in continents, 40 km in oceans) the amplitude spectra are practically independent of frequency. Thus overcritical reflections are not suitable for the determination of fine structure.

Figure 3 shows the comparison of the spectra for a random zone, an equivalent layer, individual realizations and a simple first order boundary in the subcritical (Fig. 3B), critical (Fig. 3C) and overcritical (Fig. 3D) zones. In subcritical and critical zones spectra of individual realizations are of the complex resonance form with alternation of sharp maximum and minimum. The spectrum of the equivalent layer is of a sine form oscillating around the reflectivity for a first order discontinuity. In the overcritical zone spectra for all M-boundary models are practically independent on frequency. Curves 2 and 3 (Fig. 3) show that the spectra of individual thinlayered zones (zones whose structure are stable within the profile) vary greatly with epicentral distance. Such a phenomenon shows the difficulty in comparing spectra obtained at different distances to determine a boundary model. Spectra for a micro-block layered M-boundary (curve 1, Fig. 3) are not of a resonance form and are stable within the profile in contrast to the case of individual realizations.

---

[2] The dynamic travel-time curve is a combination of an amplitude distance curve and a travel-time curve. The amplitudes are plotted above the travel-time curve

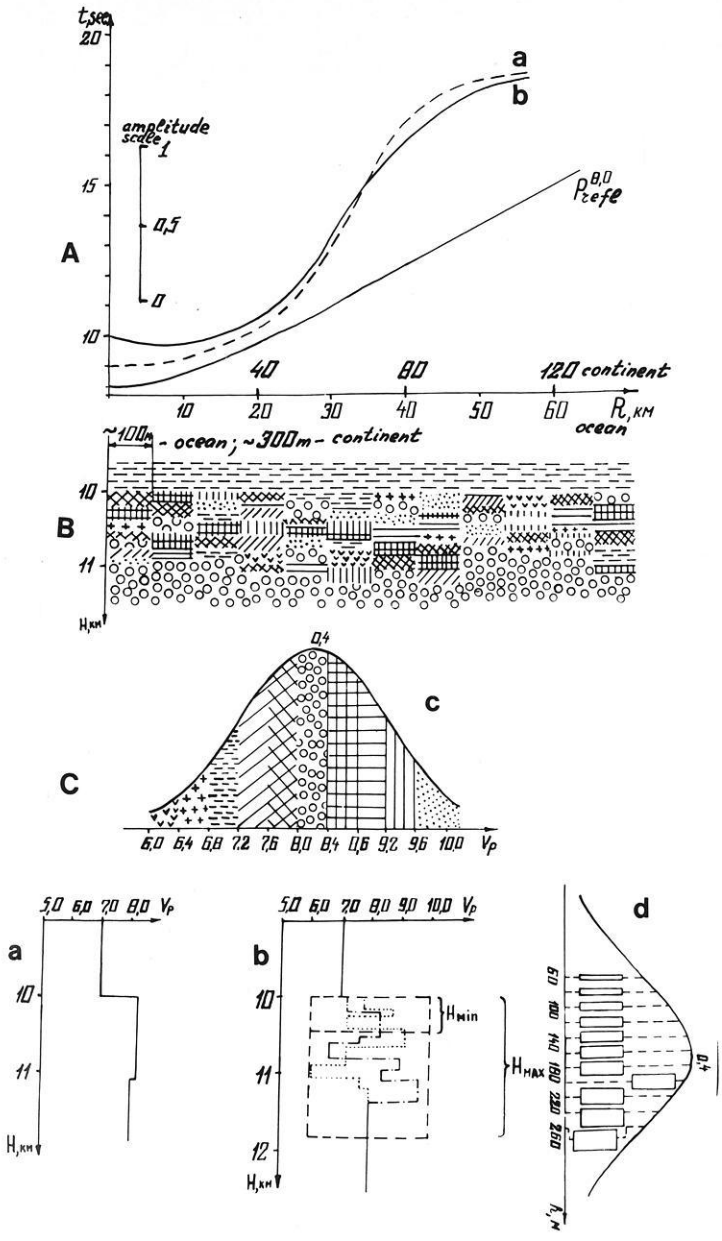

Fig. 1A–C. Dynamic travel-time curve (**A**), cross-section (**B**) and velocity-depth models (**C**) of the micro-block-layered structure of the M-boundary in continents and oceans: *a* equivalent layer, *b* random zone; *c* velocity and *d* thickness distribution in the individual layers of random zone

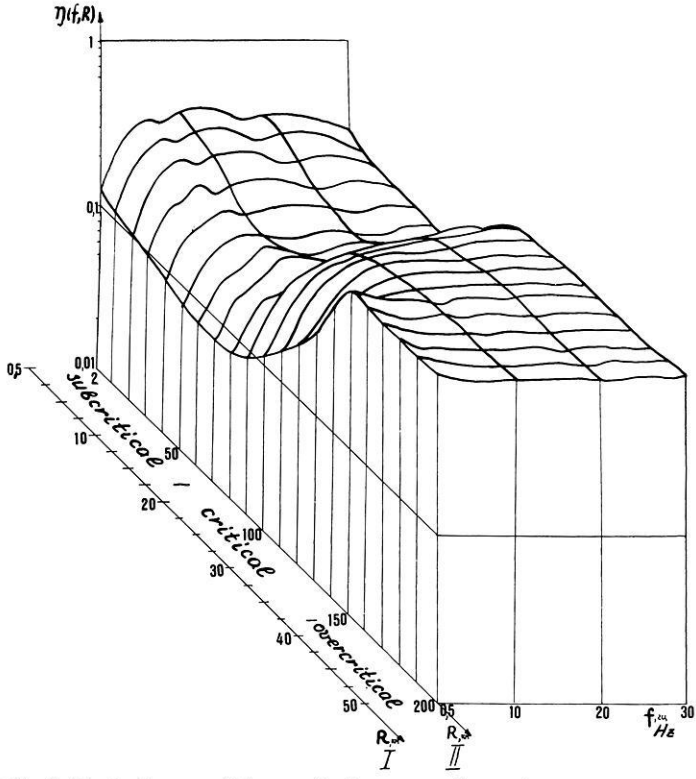

Fig. 2. Block-diagram of the amplitude spectra of a random zone in oceans (*scale I*) and continents (*scale II*)

In Fig. 4 the dependence of reflectivity on epicentral distance studies are shown at 10 Hz (DSS studies in continents) and 30 Hz (airgun studies in oceans) for the same M-boundary models as in Fig. 3. For individual realizations the curves in Fig. 4 correspond to the amplitude-distance curves obtained with a narrow band-width pulse. Such pulses are typical of non-explosive sources: airguns, sparkers, etc. In this case subcritical and overcritical reflections may be characterized by great variation in amplitudes and by interruptions of the phase correlation. Interruption in wave correlation may also occur in the case of stable thinlayered zones due to amplitudes falling below the noise level (in Fig. 4 the noise is dashed). Therefore if the source pulse is of narrow band-width form such interruption of subcritical reflections can be observed even if the structure of the thinlayered zone is horizontally homogeneous and stable.The reflections from a micro-block-layered M-boundary (curve 1, Fig. 4) are stable within the whole profile and frequency band. The amplitudes in the subcritical area are 3–4 times higher than those of a first order discontinuity or the equivalent layer.

In Fig. 5 the change of wave form with epicentral distance for reflections from a random zone and from an individual realization is shown. The pulse has a wide-band width with the main frequency 10 Hz. Figure 4 shows the energy redistribution towards the first phases: the wave pattern becomes relatively

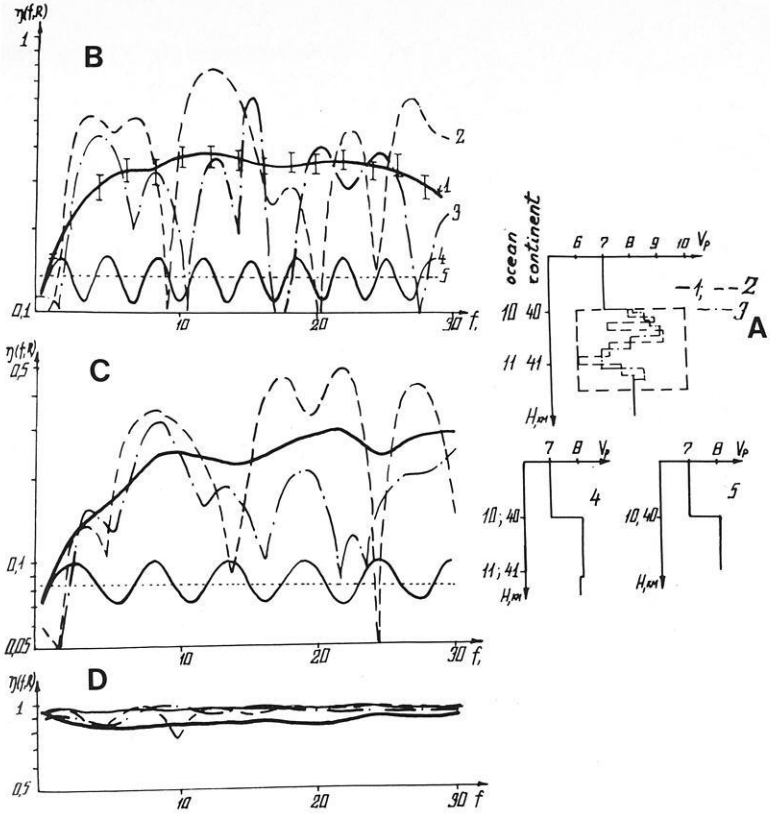

Fig. 3A–D. M-boundary models (**A**) and their spectra in subcritical (**B**), critical (**C**) and overcritical (**D**) areas: *1* random zone; *2*, *3* its individual realizations, *4* equivalent layer, *5* first order discontinuity. In *curve 1* (Fig. 3B) the dispersion level $3\sigma/\sqrt{L}$ is shown

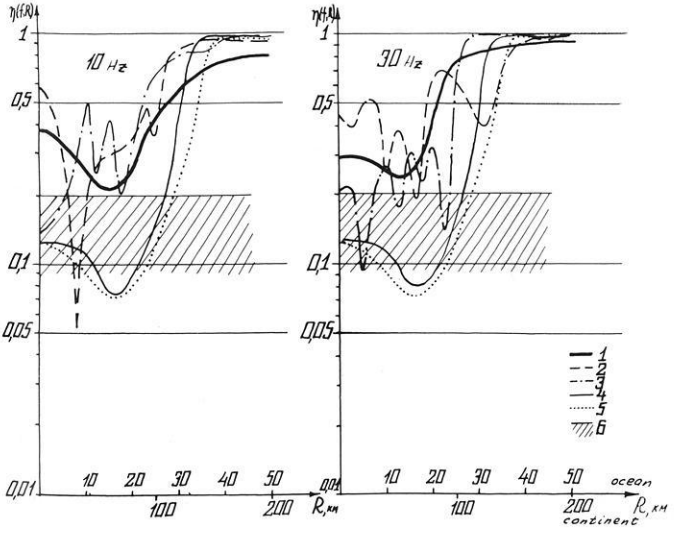

Fig. 4. The dependence of reflectivity at frequency components at 10 Hz and 30 Hz and on the epicentral distance for M-boundary models: *1* random zone; *2*, *3* its individual realizations, *4* equivalent layer, *5* first order discontinuity (models see in Fig. 3); *6* possible level of the second arrivals

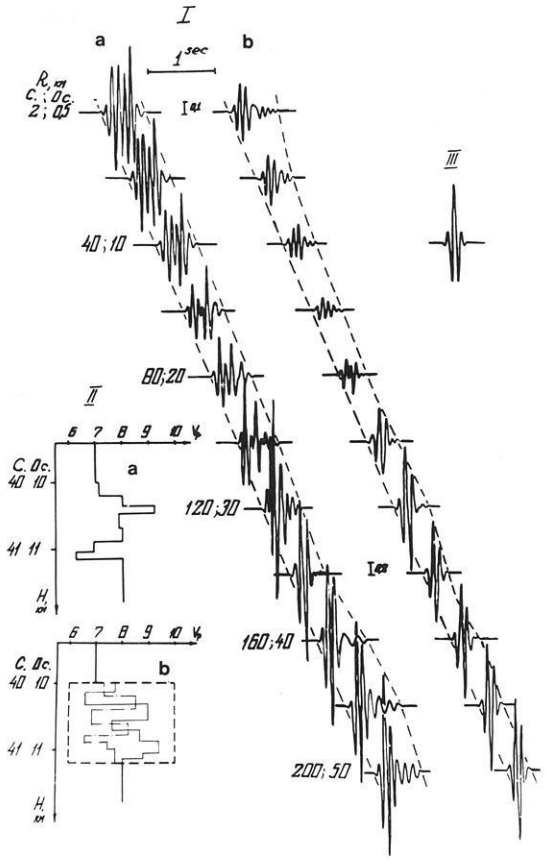

Fig. 5. The synthetic seismograms (*I*) for the reflections of M-boundary models (*II*): *a* individual realization and *b* random zone. (*III*) Incident pulse

shorter. It may be noticed that near the shot point the length of the reflection is 2–3 times greater than those of the incident pulse: this fact should be considered when interpreting data obtained at these distances using non-explosive sources. Analysis of the change in wave pattern shows that in the case of a thinlayered zone that is stable within the profile, and using a wide-band pulse, the wave form is very unstable and phase correlation is difficult. If the transition zone is micro-block-layered the wave pattern will change weakly with distance and it will be possible to correlate individual phases.

The investigation of the dynamics of micro-block-layering reflections shows that such M-boundary structure gives strong and well-correlated subcritical reflections with nonresonance spectra. Up to now absorption (i.e., the frequency selectivity of the media) has not been taken into account. If one includes the influence of absorption and ray divergence it will be easier to compare the theoretical results with experimental data so as to adopt the best observational methods.

In Fig. 6A the block-diagram of amplitude spectra with absorption for $Q = 400$ (see Berzon et al., 1975) and ray divergence, $\frac{1}{R}$, is shown for micro-block-

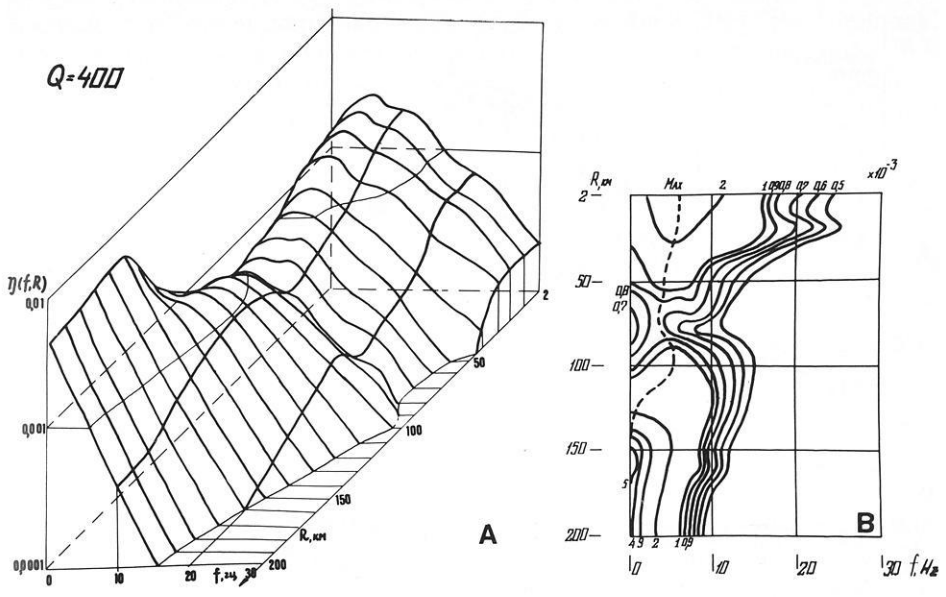

Fig. 6A and B. Block-diagram of amplitude spectra (**A**) with absorption $Q = 400$ and ray divergency 1/R for the reflection from random M-zone in continents. (**B**) The spectrum field for this surface

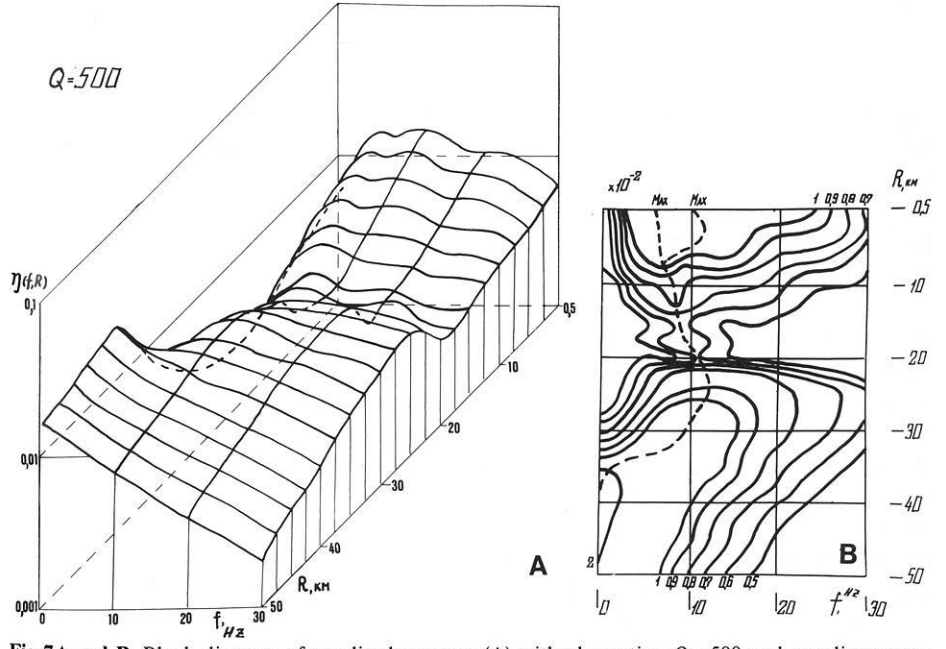

Fig. 7A and B. Block-diagram of amplitude spectra (**A**) with absorption $Q = 500$ and ray divergency 1/R for the reflection from random M-zone in oceans. (**B**) The spectrum field for this surface

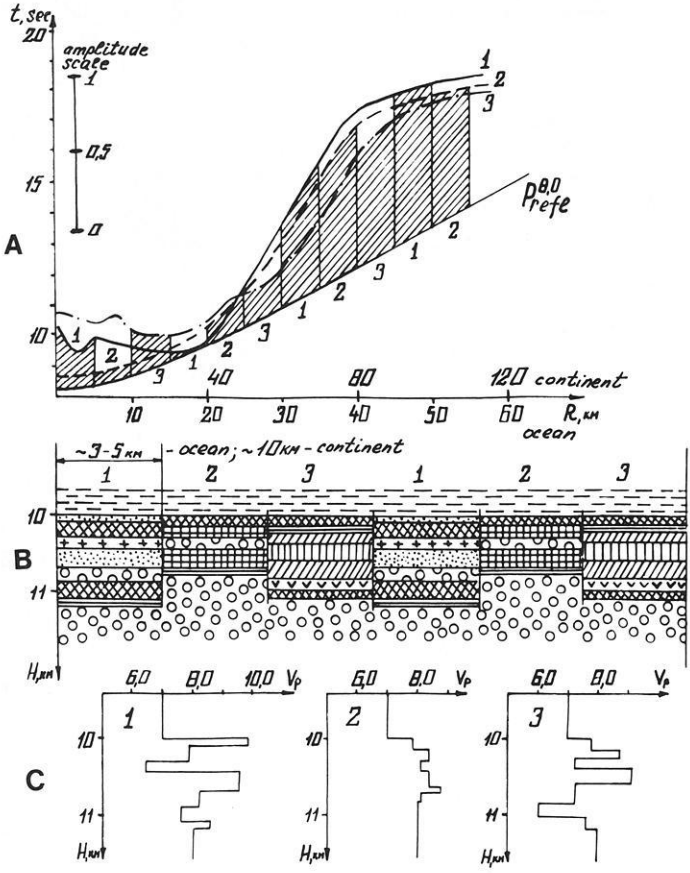

Fig. 8A–C. Dynamic travel-time curve (**A**), cross-section (**B**) and depth-velocity models (**C**) for macro-block-layered M-boundary in continent and ocean consisted of the altering of blocks 1, 2, 3

layered M-boundary in a continent. Figure 6B represents the spectrum field for this surface: the pulse spectrum was not considered, corresponding to the case of a wideband source or receiver. Figure 6 makes it clear that the amplitude spectra of a reflection acquires more sharp resonance due to the effect of absorption. The maximum of the spectrum occurs at 5 Hz in the sub-critical and critical zone and at the lowest frequencies of the incident pulse in the overcritical zone. Movement of the spectrum maximum shown in Fig. 6B corresponds to the changing of the main frequency that can be observed in records. It is evident that the visible frequency becomes lower in the overcritical zone as compared to those in subcritical ones. Such a peculiarity is due to the frequency features of the micro-block-layering of M-boundary and not to the interference of head and reflected waves in the critical zone.

It is clear from Fig. 6B that frequencies up to 10 Hz are the best ones to investigate micro-block-layering of the M-boundary in continental DSS studies. The utilization of higher frequencies even near the shot point will lead to a

decrease in reflection amplitude. If the frequency is about 20 Hz the amplitude will decrease 3 times as compared to its maximum value near the shot point and therefore it will be more difficult to correlate reflections in the second arrivals.

In Fig. 7 the block-diagram of amplitude spectrum and spectrum field for a micro-block-layered M-boundary in oceans are represented. We assume $Q = 500$. As one can see from Fig. 7 the important peculiarity of reflection correlation is the great changes of visible frequency on records. The visible frequency increases from 6 Hz to about 12 Hz towards the critical zone and in subcritical regions decreases to the lowest frequency of the incident pulse.

Figure 7 shows that the best frequencies to investigate such structures in oceans are those of about 5–10 Hz. These frequencies are essential in marine DSS studies due to the difficulty of subcritical reflection correlation among the direct and multiple water wave arrivals. The utilization of airgun sources with frequencies 20–30 Hz decreases the possible amplitude level by a factor of 1.5–2 in the subcritical zone. In the critical zone the use of highfrequency sources (20–30 Hz) also decreases the possible amplitude by a factor of up to 2. This should be taken into account in considering the best frequency band for critical-angle-reflection-studies in oceans.

Now we come to the analyses of the wave field reflected from macro-block layered M-boundary in continents and oceans. The cross-section of such structure with altering of blocks containing thinlayered zones of types 1, 2, 3 is shown in Fig. 8. The dynamic travel-time curve (Fig. 8A) consists of pieces of dynamic travel-time curves for the individual blocks. As one can see from Fig. 8 the subcritical and nearcritical areas are rather informative for the investigation of fine M-boundary structure whereas the overcritical reflections are not in fact sensitive to such structure. The reflections may be characterized by both large pieces of interruptions of wave correlation (with dimension about the horizontal dimension of a block) and phase correlation discontinuities. In the first case the reflections from blocks with reflectivity lower than the level of second arrivals can not be seen. The phase correlation interruptions and the amplitude variations are connected with the reflectivity properties within the individual blocks (see the above-mentioned dynamic analysis of individual realizations). The branches of reflection correlation may be both equal and smaller or greater (see for example the nearcritical area) than the horizontal dimension of a block.

The representation of the M-boundary by thinlayered zones consisting of blocks of different dimensions accounts for the important dynamic and kinematic peculiarities of M-reflections.

References

Berzon, I.S., Kaz, S.A., Kostenich, V.I., Ratnikova, L.I.: The reflected and transmitted waves for the random thinlayered zones (in Russian). In: Seismic waves in thinlayered media, p. 221. Moscow-Leningrad: Nauka 1973

Berzon, I.S., Veizman, P.S., Kapustian, N.K.: The results of thinlayered Mohorovičič boundary model construction (in Russian). Izvestia Academy of Sciences USSR, ser. Physics of the Earth **2**, 25–36, 1975

Červený, V., Ravindra, R.: Theory of seismic head waves. University of Toronto Press, 1971
Davydova, N.I., Kosminskaya, I.P., Kapustian, N.K., Michota, G.G.: Models of the Earth's crust and M-boundary. Z. Geophys. **38**, 369–393, 1972
Fuchs, K.: Das Reflexions- und Transmissionsvermögen eines geschichteten Mediums mit beliebiger Tiefen-Verteilung der elastischen Moduln und der Dichte für schrägen Einfall ebener Wellen. Z. Geophys. **34**, 389–413, 1968
Fuchs, K.: On the determination of velocity depth distribution of elastic waves from the dynamic characteristics of the reflected wave field. Z. Geophys. **36**, 531–548, 1970
Fuchs, K., Müller, G.: Computation of synthetic seismograms with the reflectivity method and comparison with observations. Geophys. J. Roy. Astron. Soc. **23**, 417–433, 1971
Kosminskaya, I.P., Kapustian, N.K.: The generalized seismic model of the typical oceanic crust (in Russian). Izvestia Academy of Science USSR, ser. Physics of the Earth, **2**, 37–49, 1975.
Pavlenkova, N.I.: Wave fields and Earth's crustal model, Naukova Dumka (in Russian), 219, 1973
Ratnikova, L.I., Levshin, A.L.: The calculation of spectra for thinlayered media. Izvestia Academy of Science USSR, ser. Physics of the Earth (in Russian), **2**, 41–53, 1967

Received September 22, 1976; Revised Version June 22, 1978

J. Geophys. 45, 171 – 182, 1979

Journal of Geophysics

Tidal Triggering of Earthquakes in the Swabian Jura?

D. Young[1] and W. Zürn[2]

[1] Department of Geodesy and Geophysics, University of Cambridge, Madingley Rise, Madingley Road, Cambridge CB3 OEZ, Great Britain
[2] Geowissenschaftliches Gemeinschaftsobservatorium Schiltach, Universität Karlsruhe, D-7500 Karlsruhe, Federal Republic of Germany

Abstract. Several statistical tests were used to investigate the possibility that the earthquakes in the Swabian Jura are triggered by the tidal stress in the earth. The results provide weak evidence that the earthquakes tend to occur when the tidal shear stress on the fault plane in the direction supporting the tectonic stress is greatest. A comparison of some of the statistical methods available for investigating tidal triggering effects is made.

Key words: Tidal triggering – Earthquake statistics – Swabian Jura.

1. Introduction

There have been many studies of the hypothesis that the times of occurrence of earthquakes are influenced by the periodic tidal stresses in the Earth. These have generally indicated the existence of such an effect only when they have separated the catalogue of earthquakes into small geographical regions, over which the earthquake mechanism may be reasonably expected to be fairly constant, for example Klein (1976), or when the orientation of the fault plane and slip vector of each earthquake has been taken into account in calculating the effective tidal stress, as in Heaton (1975). This is to be expected, since in an analysis which involves earthquakes of various mechanisms without allowing for these variations, a tidal effect is liable to be masked by the differences in the time dependences of the tidal forces acting in different directions.

An earthquake catalogue of 259 earthquakes from the Swabian Jura, in southern Germany, was felt to be particularly suitable for a study of this type because the fault plane mechanisms are very well known and show remarkable consistency. The opportunity was taken to apply to this one data set several of the statistical tests used previously in various studies, so that their results might be compared.

0340-062X/79/0045/0171/$02.40

2. The Catalogue

The catalogue contained earthquakes in the region between latitudes 47°57′ N and 48°32′ N and between longitudes 8°26′ E and 9°28′ E which occurred between 1900 and 1976 inclusive. They ranged in local magnitude from 2.0 to 6.3 and in depth from 1 km to 15 km. Their origin times are given in the appendix.

All the fault plane solutions which have been carried out on these earthquakes (Schneider, 1968, 1971) show a strike slip mechanism with nearly vertical nodal planes lying roughly north-south and east-west, with the compressive axis in the NW-SE direction. The variance of the nodal plane directions is very small, being only about 5°. There is good evidence that the north-south plane is in fact the fault plane: this is indicated by observations of slickensides at the surface, the extension of isoseismic contours in the north-south direction, aftershock distribution, and by detailed studies of the focal mechanism (Schick, 1968). For this study the north-south striking plane was assumed to be the fault plane, and in this case the sense of the strike-slip motion is left lateral.

3. A Model for Tidal Triggering

In order to apply statistical tests to the data a model for the process under consideration must be formulated. A simple but reasonable physical model is that fracture occurs on the fault plane when the shear stress applied to it exceeds the cohesive strength of the fault, which may depend upon the normal stress on the fault plane. The applied stress will consist of the unknown accumulating tectonic stress upon which is superimposed the stress due to the solid earth tides. Whilst the stresses due to the tides are much smaller than the tectonic stresses normally expected, they vary rapidly, the major constituents having diurnal and semidiurnal periods, and so on this simple model may be expected to trigger the occurrence of earthquakes, provided that the rate of increase of tectonic stress immediately prior to an earthquake is relatively small. This model suggests that aftershocks are less likely to be tidally triggered than main shocks occurring after a period of quiescence, since at times when the crust is in a disturbed state the rates of change of parameters other than the tidal strains will be greatest. Different authors have adopted different approaches: Heaton (1975) used only main shocks, whereas Shlien (1972) specifically analysed an aftershock sequence. In view of the small size of the sample and the lack of a suitable criterion for identifying aftershocks, we have chosen to include all the recorded events.

On the basis of these ideas, two quantities were taken as being of interest: the tidal shear strain on a vertical plane of strike N 10° E (close to the mean of the fault plane solution orientations), and the tidal linear strain (extension) normal to this plane. The first of these quantities is proportional to the tidal shear stress on the fault plane; the second quantity is closely related to the tidal normal stress on the plane and might be expected to influence the strength of the fault.

For this fault, the tidal normal extension as a function of time has a predominantly 24 h period and is approximately in phase with the diurnal part of the local gravitational potential, whereas the shear strain is a mixture of components varying both diurnally and semidiurnally in quadrature with the components of the local gravitational potential. In both cases intermodulation of the lunar and solar components of the tide produces variations in amplitude over periods of about two weeks.

The theoretical solid earth strain tide was calculated using a program by Berger (Bilham et al., 1972). This program calculates the linear horizontal tidal extension at a given position and orientation. The shear strain on the fault is merely half the difference between the extensions in two directions at 45° on either side of the fault. Ocean load tides were not taken into account, but Beavan (1976) has calculated ocean load tidal strains at Schiltach, latitude 48°17′ N, longitude 8°21′ E, some 50 km from the main earthquake region, and shown that their contribution to the total theoretical tidal strains is small. The ocean loading correction makes a difference of less than 10° to the phase of the theoretical M2 tide at Schiltach, a result supported by measurements, so it seems reasonable to neglect ocean load tides for our purpose.

The theoretical earth tide is calculated for a laterally homogeneous, isotropic earth model. However, local inhomogeneities near the fault will modify the effective strain in its vicinity so that the real strain at a point will differ from the calculated strain (Bilham et al., 1974). Since there is no means of allowing for this effect, the theoretical strain must be used; but if the inhomogeneities present are on a scale small compared with the size of the fault plane, the theoretical strain field will be representative of the average strain over the fault.

4. Tests of the Triggering Hypothesis

The suggestion that these earthquakes may be tidally triggered is here tested using standard methods, the comparison of which we believe to be important. The techniques of Sect. 4.1 have been chosen because they deal directly with the information available on the amplitudes of the tidal strains at the times of the earthquakes, and being "non-parametric" tests do not involve assumptions about the distributions of these amplitudes, nor do they require the grouping of the observations into bins. Those of Sect. 4.2 have been more commonly applied in the past and are simpler in application, but deal less directly with the data in requiring the definition of a "phase" of the tide for each earthquake. In Sect. 5 we give the results of a study of the cross-correlation of the earthquake origin times with the tidal strain functions in order to obtain a qualitative comparison of this method with the others.

4.1. Tests on the Distribution of Strain Magnitudes at Origin Times

Following Shudde and Barr (1977) we tested the null hypothesis that the distribution of the tidal strains at the origin times of the earthquakes may have arisen

by random sampling of the tidal strain curve. To do this, it is necessary to obtain a reference distribution, which may be formed by sampling the theoretical tidal strain curve at a large number of random times. The number of random samples must be sufficiently large that they serve to define the underlying distribution. If the number of random samples is not made considerably larger than the number of earthquakes, a difference between the two distributions could be due to random fluctuations in the artificially generated distribution resulting from the sampling process rather than to an effect associated with the distribution corresponding to the real earthquakes. We used 10,000 samples for these tests.

Pseudo-random numbers were generated using the linear congruential generator

$$y_{i+1} \equiv 41475557\, y_i \pmod{2^{28}}$$

where y_i is the i th number to be generated. Dieter (1971) indicates that this generator is of high quality. Random times uniformly distributed through the period of the catalogue were generated by a linear transformation from the numbers y_i and the tidal strains calculated for the random times exactly as for the real earthquakes. The histogram of the strains thus obtained was taken as the reference distribution against which the histogram of the strains at the times of the real earthquakes could be compared.

Figure 1 shows the histograms and cumulative distribution functions formed by these procedures, and it may be seen that the distribution of normal tidal strain calculated for the real earthquake origin times appears to differ little from the corresponding distribution for randomly generated events, but that in the case of the shear strain the difference is greater.

The significance of this difference was assessed using two tests: the Kolmogorov-Smirnov test and the Wilcoxon-Mann-Whitney test (Siegel, 1956), which make no assumptions concerning the form of the distributions in question. The Kolmogorov-Smirnov test uses as its statistic the largest difference between the two cumulative distribution functions; this is the largest vertical gap between the curve for the real earthquakes and the curve for randomly generated events in Fig. 1c or d and may be written as

$$\text{Max}\,|F(x)-G(x)|$$

where $F(x)$ is the fraction of real earthquakes which occurred when the strain under consideration (normal or shear) was less than or equal to x, $G(x)$ is the fraction of randomly generated times at which the strain was less than or equal to x, and the maximum is taken over all values of x. The Wilcoxon-Mann-Whitney test uses the sum of the ranks of the observations from one of the distributions when the observations making up both distributions are all ranked together; this is related to the sum of the number of observations from one distribution which are less than each of the observations in the other distribution. Both tests are simple to apply, and the sampling distributions of the statistics, which give the probability associated with a particular value of the statistic calculated, are well known. (See, for example, Massey, 1951

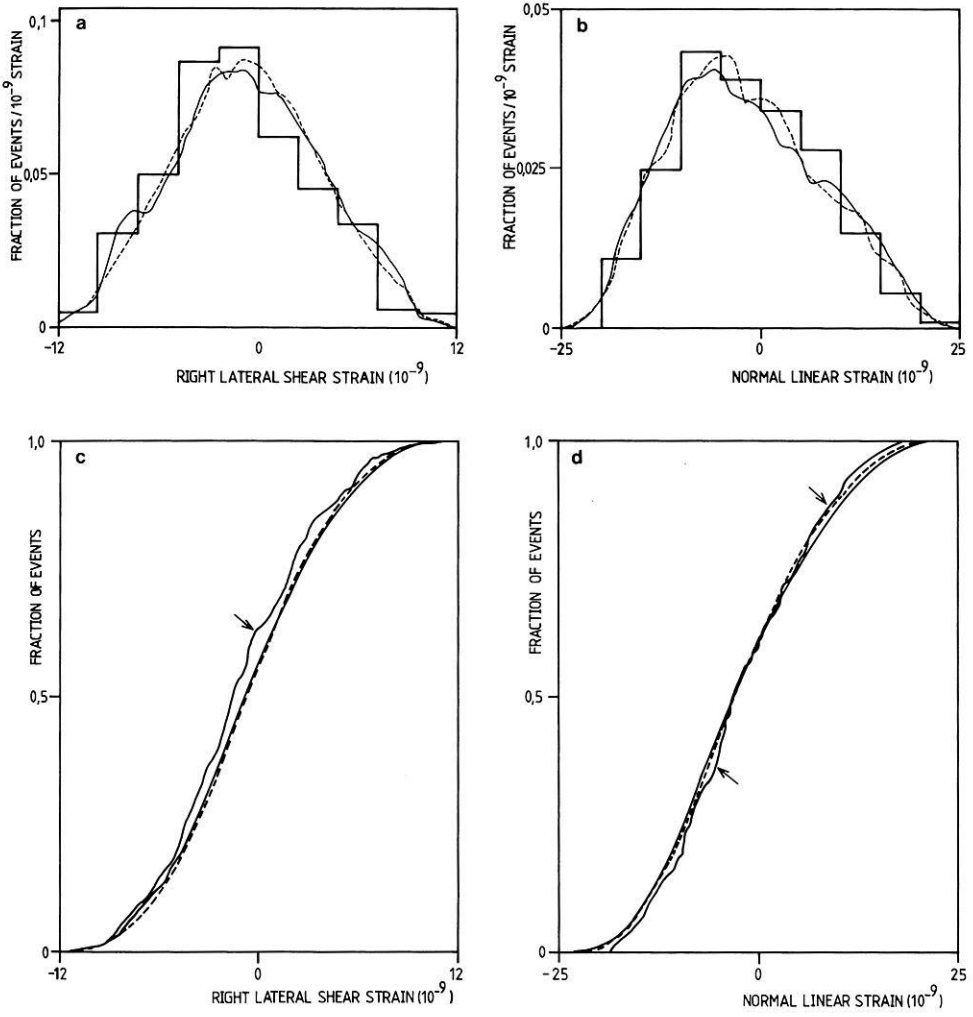

Fig. 1 a and b. Histograms of shear and normal strains on the fault. *Stepped line:* for the earthquake origin times. *Continuous curve:* for random events clustered round the origin times. *Broken curve:* for random events uniformly distributed in time. **c and d** Cumulative distribution functions of shear and normal strains. *Arrowed curve:* for earthquake origin times. *Unmarked continuous curve:* for clustered random events. *Broken curve:* for uniformly distributed random events

and Mann and Whitney, 1947; Siegel, 1956 gives other references.) One-tailed tests are appropriate since the alternative hypotheses are directional: that is, if there is triggering the origin times will be displaced towards times when the left lateral shear strain or the normal extension is greatest, rather than towards either of the possible extremes of these quantities. Application of these tests leads to the significance levels shown in Table 1; these are the probabilities under the null hypothesis of the statistic calculated taking on a more extreme value than that actually found for the data.

Table 1. Significance levels

Test used	Strain component	
	Shear	Normal
Wilcoxon-Mann-Whitney	0.015	>0.1
Kolmogorov-Smirnov	0.025	>0.1
Schuster	0.14	0.62

It is necessary to consider in addition the effect of the existence of aftershock sequences on the results of the above tests, since it is possible that clustering of the earthquakes in time will result in a different distribution of the tidal strain amplitudes from that generated by a uniform distribution of earthquakes in time, even when there is no influence of the tidal strain in either case. It is not necessary to omit all aftershocks since an earthquake occurring only a few hours after the previous one occurs at a very different value of the strain, but the possibility of an effect must be investigated. Sets of 10,000 random times, clustered in a way approximating the clustering of the origin times, were therefore generated and the distributions of strain amplitudes calculated. These sets of times were drawn from a set of overlapping Gaussian distributions, each of which was centred on an origin time, so that the probability of sampling the tidal strain curve was greater close to the times when the real earthquakes had occurred. By choosing the standard deviation of the Gaussian distributions appropriately, the basic clustering in time of the real earthquakes is preserved in the reference set of times, but the latter will still sample the tidal strain curve randomly with respect to the short term variations to form the reference distribution of strains. Taking, on this basis, 25 h as a suitable value for the standard deviation leads to the distributions displayed in Fig. 1, from which it may be seen that they differ little from the distribution of strains obtained from uniformly distributed random times. This indicates that the departure of the distribution of shear strains at the origin times from that of shear strains at uniformly distributed random times cannot be attributed merely to clustering of the origin times. Indeed, if the distribution of shear strains at the clustered random times is taken as the reference distribution in the Wilcoxon-Mann-Whitney and Kolmogorov-Smirnov tests applied as above, significance levels of 0.022 and 0.031 respectively are found, differing little from the significance levels obtained using the uniformly distributed random times. Whilst the reference distribution is now no longer strictly independent of the data, these significance levels are nevertheless still the probabilities associated with the null hypothesis that the distribution of shear strains at origin times arose from random sampling of the distribution obtained by the procedure described above. It was noted that the reference distributions of strains seemed insensitive to the method used to produce them: those shown in Fig. 1, those formed by clustering the times with a 50 h Gaussian, and those formed by sampling at regular intervals of time (provided the interval was not a tidal period) all fall very close together.

4.2. Tests on the Distribution of Tidal Phases

Knopoff (1964), Shlien (1971), Heaton (1975), and Klein (1976) all use tests based on the relationship of the time of occurrence of an earthquake to the times of the preceding and succeeding extrema in the curve of the chosen tidal function. Thus a tidal "phase" for the time of an event may be defined, for example, by taking the length of time from the maximum of the tidal strain curve immediately preceding the event to the maximum immediately following it as the local "period" of the tide, and dividing the length of time from the preceding maximum to the event by this period. The result is usually multiplied by 360° or 2π for convenience. This method makes no use of the value of the tidal strain (or other function) at the time of the event, using the tidal calculations only to determine the times of adjacent extrema, and has the disadvantage that as the amplitude of a tidal function will often differ greatly between adjacent maxima, the phase may be determined by a comparatively insignificant peak in the tidal curve. The advantage of the method is that under the null hypothesis the distribution of such phases is uniform across the interval chosen to represent a full period, and so is immediately available for comparison with the observed distribution. This is in contrast to the situation with regard to the strain amplitudes, when the distribution under the null hypothesis had to be ascertained by the random sampling methods of Sect. 4.1.

Figure 2 shows the histograms, plotted as rose diagrams, of the tidal phases defined by reference to the maxima nearest to the earthquake origin time in the shear and normal strain curves. A tendency for the earthquakes to occur around the times of greatest left lateral shear strain on the fault is discernable, but no such effect can be seen for the normal strain. The statistical test customarily used to examine the significance of the departure of such a distribution from uniformity was first proposed by Schuster (1897) and is clearly described by Heaton (1975) and Shlien (1971). Essentially, the phase for each earthquake is taken as the angle of a unit vector in two dimensions with respect to an

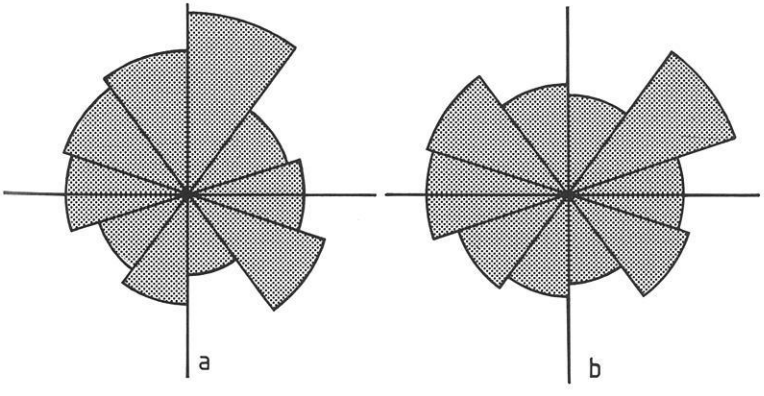

Fig. 2a and b. Histograms of phases at earthquake origin times of **a** left lateral shear strain; **b** normal linear strain. Phase increases clockwise from the top axis, which corresponds to maximum strain. The lengths of the axes are equal to the radius of a sector containing 40 events

axis; the statistic calculated for the distribution is the magnitude of the vector sum of all such vectors. Under the null hypothesis the unit vectors will perform a random walk in two dimensions, and the probability that the resultant vector will then have a magnitude greater than or equal to R is $\exp(-R^2/N)$, when there are N earthquakes.

The probabilities obtained for the distributions of phases with respect to the normal and shear strains are given in Table 1.

4.3. Interpretation of Significance Levels

The various significance levels we have calculated cannot easily be combined into a single significance level for the rejection of the null hypothesis. It is reasonable to interpret the results from the Wilcoxon-Mann-Whitney tests and the Kolmogorov-Smirnov tests as simply corroborating one another, in that they looked at differences between the same pairs of distributions, and to omit from consideration the results of tests on the distribution of phases since this test appears to be rather weak. However, we performed tests of the null hypothesis using two distinct alternative hypotheses, one involving the shear strain and the other the normal extension at the fault. Thus the probability under the null hypothesis that one of the results should reach a particular significance level is increased: clearly repeated trials of even a true null hypothesis will yield a "significant" result sooner or later by chance. If the two trials were independent then the significance levels could be combined by a standard technique such as that of Fisher (1970, pp. 99–100); but since the shear strain and normal extension are related to one another through the tidal potential this is not possible. This difficulty becomes acute when even more tidal functions are used, as is apparent in the study by Shudde and Barr (1977) where significance levels for fourteen tidal functions are calculated. Although several of these are very small, and would be deemed highly significant if taken alone, Shudde and Barr attribute them to random fluctuations under the null hypothesis, and conclude that they provide no evidence for tidal triggering.

We do not therefore attempt to give an overall significance level for a trial of the null hypothesis, but present the separate significance levels as the best indication of the ability of this data to reveal a tidal triggering effect.

5. Cross Correlation of Earthquake Times and Tides

Knopoff (1964) calculated the cross correlation function of the time sequence of southern Californian earthquakes with the tidal acceleration, treating the earthquakes as a series of delta functions in time. This cross correlation is given by

$$C(\tau)=\int \sum_{n=1}^{N} (t-t_n) f(t-\tau)\, dt = \sum_{n=1}^{N} f(t_n-\tau)$$

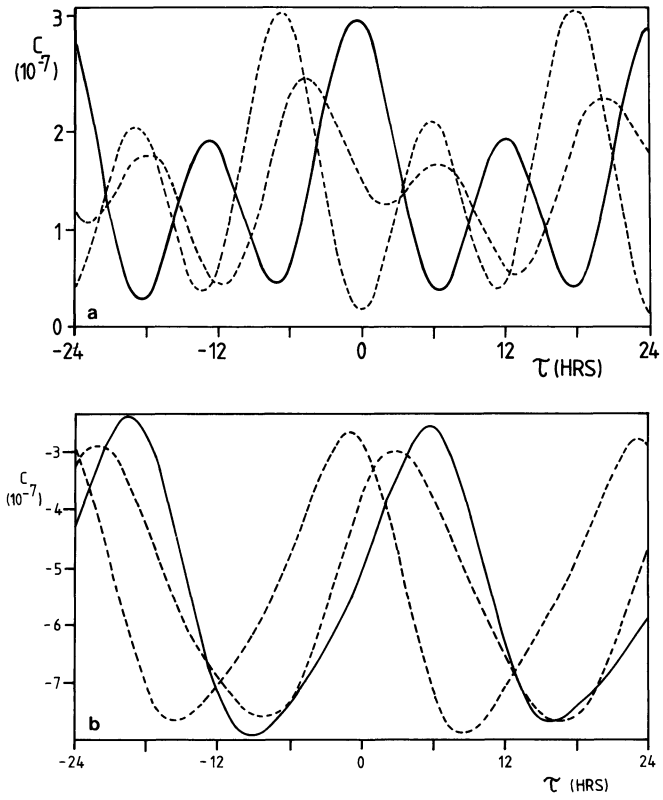

Fig. 3a and b. The cross correlation function for **a** left lateral shear strain; **b** normal linear strain. *Continuous curves:* earthquake origin times. *Broken curves.* times obtained by adding random numbers to the origin times

where $f(t)$ is the tidal function of interest and the N earthquakes occurred at the times t_n. This calculation was repeated for the Swabian Jura earthquakes, using for f the tidal normal and shear strains. The results are shown in Fig. 3, together with the cross correlations calculated for sets of 259 random times for comparison. The random times were generated in this case by the formula

$$r_n = t_n + 48a_n - 24$$

where r_n is the n th random time in hours and a_n is a pseudo-random number uniformly distributed between 0.0 and 1.0 produced as described in Sect. 4.1 above.

In neither the case of the shear strain nor that of the normal strain are the peaks in the cross correlation function larger for the times of the real earthquakes than for the sets of random times. Such a result provides no evidence for a tidal triggering effect; however, it is of interest that the peak of the correlation for the shear strain does occur at exactly zero lag. The statistical

significance of such correlations is difficult to assess quantitatively. The cross correlation technique would be useful for demonstrating phase lags between a variable associated with triggering and the origin times, but this comparison shows that a much stronger effect or a much larger data set is necessary before it can be applied with confidence. We think that the methods of Sect. 4.1 are a more sensitive way to test the null hypothesis.

6. Discussion

Assuming that adequate allowance has been made for the clustering in time of the earthquakes, statistical tests based on the distributions of the strains at the times of earthquakes provide weak evidence that the origin times of the earthquakes in the Swabian Jura are not independent of the tidal shear strain. There is no evidence of any influence of the tidal normal extension. The implication for the simple model we have used is that the effect of change, due to the tidal normal extension, in the cohesive force preventing relative movement across the fault is small compared to the effect of tidal enhancement of the tectonic shear stress on the fault. Heaton's (1975) results also indicate that the shear stress plays the predominant role in any tidal effect, although the correlation he observes is not present in the shallow strike-slip earthquakes amongst his sample, and Klein (1976) explains many of his results by tidally enhanced shear on fault planes.

Statistical tests carried out on the distribution of the strains at the origin times of the earthquakes appear to be more sensitive in detecting a tidal effect than tests on the distribution of tidal phases. This is presumably because the strains at the actual times of the earthquakes are taken into account in the former kind of test. However, if an effect is accepted, analysis in the time rather than in the strain domain gives more information about the relationship of the earthquake times to features of the tidal strain curve, and both the histogram of phases and the cross correlation function may be useful in this respect.

On the basis of the significance levels obtained we cannot conclude that tidal triggering has been demonstrated; merely that the results are indicative that an effect may be present. Indeed, the tidal effect for earthquakes of this type appears to be too weak to be clearly demonstrable in a catalogue of this size and it would be most desirable to extend the catalogue in time rather than in space. However, when a catalogue from a larger geographical region is used, it is important that attention be paid to the details of the fault plane solutions. It is also essential that statistical tests be carried out only on the basis of a definite physical model in order to avoid the effects of multiple alternative hypotheses.

Acknowledgements. The authors are indebted to Dr. Rolf Schick for supplying the earthquake catalogue and for helpful discussions. We thank Drs. Paul Davis, Karl Fuchs, Geof King, Leon Knopoff, Gerhard Müller, and Michael Shimshoni for critically reading the manuscript. DSY is very grateful to Professor H. Mälzer for providing the opportunity to work at Schiltach observa-

tory, and was in receipt of a postgraduate award from the Natural Environment Research Council at the time the work was carried out.

Appendix

Times of occurrence of Swabian Jura earthquakes Origin times given as year (minus 1900), month, day, hour (GMT) and minute.

00	1	27	1	44	02	10	3	20	45	02	10	9	14	38	11	9	6	4	21
11	11	16	21	25	11	11	23	1	59	11	11	28	17	38	11	12	12	5	8
12	1	17	4	39	12	1	17	5	12	12	1	18	21	6	12	1	18	21	19
12	1	19	1	00	12	1	19	5	46	12	1	26	00	00	12	2	3	3	40
12	2	5	3	46	12	5	4	16	48	12	9	27	18	9	12	12	31	17	44
13	7	20	12	6	13	7	20	12	6	14	2	2	15	35	14	2	8	21	51
14	8	25	6	49	14	10	14	19	8	15	3	20	11	41	15	6	13	14	15
15	6	13	14	20	16	2	13	11	58	16	4	15	16	8	24	12	11	16	33
24	12	12	7	21	25	10	13	19	42	27	12	16	10	44	28	8	30	20	11
31	12	11	20	45	31	12	22	2	48	33	2	21	15	45	33	2	26	3	7
33	3	1	2	13	33	6	4	19	49	33	10	10	20	55	33	10	10	21	00
33	12	30	2	43	34	1	1	14	26	34	3	17	2	9	34	3	24	2	48
36	2	18	21	3	36	2	21	17	22	36	4	19	22	21	37	6	17	9	57
38	8	2	4	11	39	3	1	11	33	39	10	11	17	43	40	8	6	15	18
42	7	17	10	26	42	7	30	21	50	42	12	3	2	14	43	2	4	9	18
43	2	17	11	2	43	4	21	8	34	43	4	25	11	35	43	5	2	1	8
43	5	28	00	24	43	6	1	13	53	43	6	14	21	39	43	6	24	19	43
43	7	4	4	37	43	7	14	4	16	43	8	23	3	00	43	9	14	3	27
43	9	16	5	27	43	9	16	17	19	43	9	17	6	47	43	9	18	10	15
43	10	12	9	2	43	10	13	11	22	43	10	13	23	24	43	10	17	2	30
43	10	22	10	41	43	12	12	13	32	43	12	27	18	50	43	12	27	18	57
43	12	27	19	46	43	12	27	19	53	43	12	28	3	36	44	1	5	19	6
44	1	6	5	10	44	1	9	5	26	44	1	9	18	5	44	1	13	2	17
44	1	21	21	16	44	1	22	20	29	44	1	23	14	14	44	1	27	19	40
44	1	30	16	7	44	2	8	12	34	44	2	9	12	2	44	4	25	6	5
44	5	25	16	33	44	5	29	8	51	44	8	17	3	39	44	8	17	4	39
44	10	26	20	44	45	3	27	00	54	46	10	5	00	29	46	10	5	00	33
46	12	1	2	37	47	4	14	21	30	47	6	28	11	13	47	9	14	20	5
48	1	27	3	17	48	8	6	2	40	48	9	19	13	31	49	3	7	20	48
49	7	8	13	53	49	8	22	20	7	49	9	15	00	26	49	11	6	7	49
50	1	1	00	20	50	1	20	23	50	50	1	27	5	30	50	4	13	12	37
50	5	24	14	27	50	7	11	3	6	51	10	18	19	57	52	7	10	16	12
54	4	4	18	39	55	4	11	11	47	55	4	11	13	23	55	6	26	18	57
55	6	26	19	28	55	6	26	19	48	55	6	30	23	12	55	7	2	18	9
55	7	29	11	12	55	8	20	5	20	55	10	21	20	40	55	11	17	21	48
56	1	4	14	2	56	1	5	7	44	56	1	8	4	18	56	8	1	9	40
56	8	1	15	14	56	8	9	11	35	57	4	30	00	49	57	5	25	22	2
57	8	28	9	8	57	8	28	11	45	57	8	29	3	45	57	9	23	11	20
57	9	24	19	52	57	9	28	21	39	57	12	8	5	54	58	2	27	6	16
58	11	5	12	24	59	1	13	11	33	59	3	18	23	21	59	7	9	9	24
59	7	9	16	37	60	3	28	2	52	60	4	5	4	25	60	12	16	14	23
61	3	23	15	42	61	4	18	3	9	61	4	19	00	16	61	4	19	7	57
61	5	11	23	11	62	1	21	6	49	62	4	8	20	51	62	4	9	00	14
62	7	3	00	59	66	4	7	8	8	69	2	26	1	28	69	3	1	20	27
69	3	1	20	31	69	3	9	6	58	69	6	6	5	27	69	6	23	00	54
69	9	22	23	45	69	9	29	21	59	70	1	22	15	22	70	1	22	15	42
70	1	22	16	14	70	1	22	16	32	70	1	22	17	3	70	1	22	17	39
70	1	22	17	54	70	1	22	18	41	70	1	23	3	52	70	1	23	7	10
70	1	23	7	51	70	1	23	15	47	70	1	23	20	10	70	1	24	4	16

70	1	24	7	43	70	1	24	17	14	70	1	24	21	14	70	1	26	11	23
70	1	27	4	17	70	1	29	14	59	70	2	1	10	12	70	2	1	16	28
70	2	13	14	53	70	2	13	17	8	70	2	15	1	8	70	2	16	10	38
70	2	20	13	9	70	3	21	20	40	70	4	10	20	19	70	5	25	17	45
70	5	29	7	28	70	5	30	16	38	70	5	31	8	11	70	12	10	8	27
70	12	11	2	7	71	1	15	2	55	71	1	27	9	16	71	4	29	4	35
71	5	19	17	30	71	6	8	2	22	71	9	22	18	35	71	11	19	3	3
72	5	17	8	13	72	5	18	8	11	72	10	17	11	1	73	5	6	8	18
73	6	14	5	55	73	10	19	9	16	74	2	21	20	59	74	2	22	11	8
74	2	23	00	27	74	2	25	4	3	74	5	12	19	48	74	6	24	00	23
74	10	16	3	42	74	11	11	00	41	74	11	14	17	9	74	12	1	20	39
74	12	27	8	28	75	1	25	23	52	75	6	2	19	5	75	7	17	22	37
75	7	18	21	34	76	2	18	12	58	76	3	6	7	11	76	9	1	13	30
76	9	15	23	39	76	9	16	00	6	76	9	16	22	49	76	9	18	11	10
76	9	19	12	31	76	9	21	8	42	76	9	23	11	2	76	9	28	7	25
76	9	29	18	5	76	9	30	16	45	76	10	31	17	36					

References

Beavan, R.: Earth strain: ocean loading and analysis. PhD dissertation, University of Cambridge 1976

Bilham, R., Evans, R., King, G., Lawson, A., McKenzie, D.: Earth strain tides observed in Yorkshire, England, with a simple wire strainmeter. Geophys. J. **29**, 473–485, 1972

Bilham, R., King, G., McKenzie, D.: Inhomogeneous tidal strains in Queensbury tunnel, Yorkshire. Geophys. J. **37**, 217–226, 1974

Dieter, U.: Pseudo-random numbers: the exact distribution of pairs. Math. Comp. **25**, 855–883, 1971

Fisher, R.: Statistical methods for research workers, 14th ed. Edinburgh: Oliver & Boyd 1970

Heaton, T.: Tidal triggering of earthquakes. Geophys. J. **43**, 307–326, 1975

Klein, F.: Earthquake swarms and the semidiurnal solid earth tide. Geophys. J. **45**, 245–295, 1976

Knopoff, L.: Earth tides as a triggering mechanism for earthquakes. Bull. Seism. Soc. Am. **54**, 1865–1870, 1964

Mann, H., Whitney, D.: A test of whether one of two random variables is stochastically larger than the other. Ann. Math. Stat. **18**, 50–59, 1947

Massey, F., Jr.: The Kolmogorov-Smirnov test for goodness of fit. J. Amer. Statist. Ass. **46**, 68–78, 1951

Schick, R.: Untersuchungen über die Bruchausdehnung und Bruchgeschwindigkeit bei Erdbeben mit kleinen Magnituden ($M < 4$). Z. Geophys. **34**, 267–286, 1968

Schneider, G.: Erdbeben und Tektonik in Südwest-Deutschland. Tectonophysics. **5**, 459–511, 1968

Schneider, G.: Seismizität und Seismotektonik der Schwäbischen Alb. Stuttgart: Ferdinand Enke Verlag 1971

Schuster, A.: On lunar and solar periodicities of earthquakes. Proc. Roy. Soc. **61**, 455–465, 1897

Shlien, S.: Earthquake tide correlation. Geophys. J. **28**, 27–34, 1972

Shudde, R., Barr, D.: An analysis of earthquake frequency data. Bull. Seism. Soc. Am. **67**, 1379–1386, 1977

Siegel, S.: Nonparametric statistics for the behavioural sciences, international student edition. Tokyo: McGraw-Hill Kogakusha 1956

Received June 22, 1978; Accepted January 31, 1979

J. Geophys. 45, 183–198, 1979

Journal of Geophysics

Theoretical Investigations on Acoustic Remote Sensing of Ocean Surface Waves

H.-H. Essen

Institut für Geophysik, Universität Hamburg,
D-2000 Hamburg 13, Bundesstraße 55, Federal Republic of Germany

Abstract. Some aspects of acoustic remote sensing in the ocean are discussed with application to surface waves. Bragg scattering is assumed for the physical mechanism of modulating the acoustic carrier. The frequencies necessary for that mechanism are in the range of some 100 Hz. It is shown that the variance spectrum of the modulated slowly varying acoustic amplitude is the appropriate quantity for deriving the relevant statistical properties of surface waves. For remote sensing the relationship between the measured acoustic and unknown surface-wave spectrum is described by a transfer function. Theoretical transfer functions are computed for CW (continuous wave) measurements over long ranges in shallow water. A mode- and a ray-propagation model are considered and the numerical results are compared. The transfer function depends strongly on the angular distribution of surface waves, which usually is unknown. If, on the other hand, both the 1-dimensional acoustic and waveheight spectrum are measured simultaneously these values can be used to determine the angular-distribution function. The necessary assumptions for this method are discussed and a simple model is presented which allows the application of matrix inversion.

Key words: Underwater acoustic – Remote sensing – Ocean-surface waves.

1. Introduction

In the last ten years the interest of oceanographers in remote-sensing methods has increased. Especially the technique of radar backscatter from the rough sea surface has been developed. The mechanism involved is Bragg scattering which presumes a matching of radio wavelengths to surface wavelengths. For example, HF radio waves are scattered by long ocean waves and the backscattered signal yields information on the 2-dimensional wave-height spectrum as well as near-surface currents (Tyler et al., 1974; Barrick et al., 1977).

0340-062X/79/0045/0183/$03.20

Due to the strong attenuation of radio waves within sea water only acoustic waves are appropriate for remote sensing of the inner ocean. A possible mechanism of coupling oceanic motions to acoustic waves is again Bragg scattering. Considering e.g. the problem of measuring surface waves by means of sound scattering the wavelength matching then requires low acoustic frequencies.

Contrary to the radar technique forward scattering is considered, i.e., source and receiver are at separate positions. Due to the long duration of acoustic echos, especially in shallow water, backscatter methods are not applicable.

In the present paper results of theoretical investigations on acoustic remote sensing in the ocean are reported. The acoustic measurement system consists of a bottom-mounted source and a receiver. A low-frequency continuous wave (CW) is transmitted over a fixed range in the ocean and is modulated in amplitude and phase by the water motions. Observations show that the modulation frequencies correspond to the frequencies of oceanic motions, e.g. surface waves, internal waves, tides, etc. (Clark and Kronengold, 1974; Essen et al., 1978). While the first cited paper considers the influence of long-period motions, the second one investigates the remote sensing of surface waves, which also is the topic of the following chapters.

In Chapter 2 the theory of acoustic scattering from a rough sea surface is outlined in the limit of Bragg scattering. The surface-wave heights are random variables and thus the Doppler-shifted portion of the received signal is random as well. This aspect is considered in Chapter 3. An acoustic spectrum is defined which may be related to the variance spectrum of surface wave heights by a transfer function. The transfer function itself depends on the geometry of the acoustic propagation. For shallow water and low frequencies the sound field is best represented by normal modes. In Chapter 4 numerical results for the transfer function are shown where both mode- and ray-models are used. It turns out that the results become the same if the number of trapped modes is 8 or more.

A further result is that the transfer function strongly depends on the angular distribution of surface waves. This undesired property for the determination of the 1-dimensional wave-height spectrum from acoustic measurements may be used on the other hand for estimating the angular distribution. For this purpose both the acoustic and the 1-dimensional wave height spectrum must be measured and it has to be assumed that the angular distribution function does not depend on frequency, at least within a certain interval. In Chapter 5 a technique is presented to compute the surface-wave angular distribution from the measured transfer function by a matrix inversion.

2. Scattering Mechanism

The influence of the sea surface is treated in the limit of weak wave-wave interaction, or Bragg scattering. The rough surface may be compared with a moving grate. Considering an incoming plane acoustic wave the outgoing field includes a number of scattered Doppler-shifted waves beside the specular reflected one. The technique for handling this problem mathematically is perturbation expansion, which will be briefly outlined according to Essen (1974).

The sea surface may be described by the temporally varying deviations from a mean plane ($x_3=0$),

$$x_3=\zeta(x_1, x_2, t) \tag{1}$$

which are suitably presented by a Fourier sum of plane waves,

$$\zeta=\sum_{\boldsymbol{\kappa}} Z_{\boldsymbol{\kappa}} \exp\{i(\boldsymbol{\kappa}\boldsymbol{x}-\sigma t)\}+\text{c.c.} \tag{2}$$

$Z_{\boldsymbol{\kappa}}$ = complex Fourier amplitude
$\boldsymbol{\kappa}=(\kappa_1, \kappa_2)$ = horizontal wavenumber vector
σ = circular frequency

Since a real notation is needed for later computations the complex conjugated solution (c.c.) is added. Within this paper the validity of the deep-water dispersion relation is assumed,

$$\sigma^2=g\kappa. \tag{3}$$

The boundary condition for a sound wave at a pressure-free surface is,

$$p=0 \quad \text{at} \quad x_3=\zeta \tag{4}$$

and a Taylor expansion at the undisturbed surface yields,

$$p+\frac{\partial p}{\partial x_3}\cdot\zeta+---=0 \quad \text{at} \quad x_3=0. \tag{5}$$

Acoustic propagation may be presented by modes or rays. In both cases the scattered sound field is obtained from a perturbation expansion,

$$p=p^{(1)}+p^{(2)}+--- \tag{6}$$

with,

$$|p^{(1)}|\gg|p^{(2)}|\gg---.$$

From Eqs. (5)–(6) the boundary conditions of 1. and 2. order become,

$$p^{(1)}=0 \quad \text{at} \quad x_3=0 \tag{7}$$

$$p^{(2)}=-\frac{\partial p^{(1)}}{\partial x_3}\cdot\zeta \quad \text{at} \quad x_3=0 \tag{8}$$

where formally ζ is of 1. perturbation order.

Inhomogeneities within the water may be neglected and the wave equation is undisturbed in all perturbation orders,

$$\frac{\partial^2 p^{(l)}}{\partial t^2}-c_W^2\frac{\partial^2 p^{(l)}}{\partial x_i\,\partial x_i}=0 \qquad (i=1, 2, 3) \tag{9}$$

with, $l=1, 2, \ldots$, and, c_W = sound velocity of water.

The first-order plane-wave solution satisfying the wave equation and the boundary condition is,

$$p^{(1)} = P_0 \exp\{i(\boldsymbol{k}\boldsymbol{x} + k_3 x_3 - \omega_0 t)\} + \text{c.c.} \\ - P_0 \exp\{i(\boldsymbol{k}\boldsymbol{x} - k_3 x_3 - \omega_0 t)\} + \text{c.c.} \tag{10}$$

$$\boldsymbol{k} = (k_1, k_2), \quad k_3 = \sqrt{\frac{\omega_0^2}{c_W^2} - k^2} = \text{ wave number of the incident plane wave}$$

$$\frac{\omega_0}{2\pi} = \text{ source frequency.}$$

This solution includes the incident and the specular reflected wave. By inserting (2) and (10), the second order boundary condition (8) and the wave Eq. (9) yield the solution,

$$p^{(2)} = -2i \sum_{\substack{\boldsymbol{\kappa} \\ s = \pm 1}} k_3 P_0 Z_{\boldsymbol{\kappa}}^s \exp\{i(\boldsymbol{k}_s \boldsymbol{x} + k_{s3} x_3 - (\omega_0 + s\sigma) t\} + \text{c.c.} \tag{11}$$

$$Z_{\boldsymbol{\kappa}}^+ = Z_{\boldsymbol{\kappa}}, \quad Z_{\boldsymbol{\kappa}}^- = Z_{\boldsymbol{\kappa}}^*$$

$$\boldsymbol{k}_s = \boldsymbol{k} + s\boldsymbol{\kappa}, \quad k_{s3} \approx \sqrt{\frac{\omega_0^2}{c_W^2} - k_s^2} \quad (\text{as } \sigma \ll \omega_0).$$

Apparently, each Fourier component $\boldsymbol{\kappa}$ of the surface-wave field produces two scattered acoustic waves which are Doppler-shifted by $\pm\sigma$ from the carrier frequency ω_0.

The perturbation condition (2.6) requires,

$$k_3 |\zeta| \ll 1. \tag{12}$$

Considering a 200 Hz acoustic wave at 45° incidence angle one obtains for 1 m peak-to-trough wave height, $k_3 |\zeta| \approx 0.2$. This example illustrates the validity of the theory.

3. Continuous-Wave (CW) Source and Fixed-Range Propagation

If the theoretical considerations about scattering are applied to acoustic measurements in the ocean, the experimental configuration and the random nature of surface waves must be considered. In this paper we will refer to measurements carried out with a low-frequency source, where a CW signal is transmitted over a fixed range in the ocean. Usually source and receiver are placed at the bottom of the sea. Due to water motions the acoustic pressure is modulated in amplitude and phase,

$$p(t) = A(t)\cos[\omega_0 t - \Phi(t)]$$
$$= X(t)\cos(\omega_0 t) + Y(t)\sin(\omega_0 t) \tag{13}$$

with,

$$X(t) = A(t)\cos\Phi(t), \qquad Y(t) = A(t)\sin\Phi(t).$$

Following the Bragg-scattering theory the received signal consists of a superposition of first order coherent and second order Doppler-shifted waves. Beside these contributions the oceanic noise must be included,

$$p(t) = p_0(t) + p_s(t) + p_N(t). \tag{14}$$

The coherent portion may be written as,

$$p_0(t) = A_0(t)\cos(\omega_0 t - \Phi_0) \tag{15}$$

with,

$A_0, \Phi_0 =$ constant.

The contribution from scattered waves is modulated in amplitude and phase by the motion of surface waves.

$$p_s(t) = A_s(t)\cos[\omega_0 t - \Phi_s(t)]$$
$$= X_s(t)\cos(\omega_0 t) + Y_s(t)\sin(\omega_0 t). \tag{16}$$

Due to the randomness of surface waves p_s is a random variable. To a good approximation the surface waveheight ζ is a homogeneous, stationary Gaussian process. Thus the Fourier coefficients $Z_{\boldsymbol{\kappa}}$ in (2) are independent Gaussian variables with, cf. Kinsman (1965)

$$\langle Z_{\boldsymbol{\kappa}} \rangle = 0$$
$$\langle Z_{\boldsymbol{\kappa}} Z_{\boldsymbol{\kappa}'} \rangle = 0, \qquad \langle Z_{\boldsymbol{\kappa}} Z^*_{\boldsymbol{\kappa}'} \rangle = 0 \quad \text{if} \quad \boldsymbol{\kappa} \neq \boldsymbol{\kappa}' \tag{17}$$

and,

$$\langle \zeta^2 \rangle = 2\sum_{\boldsymbol{\kappa}} \langle |Z_{\boldsymbol{\kappa}}|^2 \rangle = \iint E_G(\boldsymbol{\kappa})\, d\boldsymbol{\kappa}.$$

The cornered parentheses denote ensemble-mean values. Considering now the second-order solution (11) the single components of the scattered field turn out to be proportional to the Gaussian variable $Z_{\boldsymbol{\kappa}}$. Decomposing the components into $\cos(\omega_0 t)$- and $\sin(\omega_0 t)$-portions, these are uncorrelated as a result of (17). The received acoustic signal is a superposition of all scattered wave components reaching the hydrophone from different directions. Thus if ζ is a zero-mean Gaussian variable it follows that X_s and Y_s are uncorrelated zero-mean Gaussian variables with equal variance,

$$\langle X_s \rangle = \langle Y_s \rangle = 0, \qquad \langle X_s Y_s \rangle = 0$$
$$\langle X_s^2 \rangle = \langle Y_s^2 \rangle = \int F_s(\sigma)\, d\sigma. \tag{18}$$

$F_s(\sigma) =$ variance spectrum of scattered waves.

Here the circular frequency is denoted by σ in order to distinguish the low oceanic frequencies (σ) from the high acoustic frequencies (ω).

Before recording the received signal on tape it is filtered by a small bandpass centered at the carrier frequency ω_0. Due to the Fourier expansion,

$$p_N(t) = \sum_{n=1}^{\infty} \{\alpha_n \cos(\omega_n t) + \beta_n \sin(\omega_n t)\} \tag{19}$$

the noise contribution may be written

$$p_N(t) = X_N(t) \cos(\omega_0 t) + Y_N(t) \sin(\omega_0 t) \tag{20}$$

with,

$$X_N(t) = \sum_{n=1}^{\infty} \{\alpha_n \cos[(\omega_n - \omega_0) t] + \beta_n \sin[(\omega_n - \omega_0) t]\},$$

$$Y_N(t) = \sum_{n=1}^{\infty} \{\beta_n \cos[(\omega_n - \omega_0) t] - \alpha_n \sin[(\omega_n - \omega_0) t]\}.$$

It should be pointed out that, as a result of bandpass filtering, $X_N(t)$ and $Y_N(t)$ are slowly varying as compared with the carrier signal. Furthermore it may be shown [cf. Rice (1954)] that if $p_N(t)$ is a Gaussian process with zero mean then $X_N(t)$ and $Y_N(t)$ are uncorrelated zero-mean Gaussian processes with equal variance,

$$\begin{aligned} &\langle X_N \rangle = \langle Y_N \rangle = 0, \quad \langle X_N Y_N \rangle = 0 \\ &\langle X_N^2 \rangle = \langle Y_N^2 \rangle = \int F_N(\sigma)\, d\sigma \end{aligned} \tag{21}$$

with,

$$\sigma = \omega - \omega_0.$$

For our investigations only the variance spectra of $X_s(t)$ and $Y_s(t)$ from the scattered acoustic waves are of interest. In order to compute these spectra the received (bandpass-filtered) signal is demodulated by multiplying with $\cos(\omega_0 t)$ or $\sin(\omega_0 t)$ and by averaging over an acoustic period. On the basis of (14)–(16) and (19) one obtains,

$$\begin{aligned} X(t) &= 2\overline{p(t) \cos(\omega_0 t)} = A_0 \cos \Phi_0 + X_s(t) + X_N(t) \\ Y(t) &= 2\overline{p(t) \sin(\omega_0 t)} = A_0 \sin \Phi_0 + Y_s(t) + Y_N(t). \end{aligned} \tag{22}$$

This result implies that $X_{S,N}(t)$ and $Y_{S,N}(t)$ are slowly varying during an acoustic period.

For surface waves only frequencies up to 0.5 Hz are considered here, which correspond to a frequency band of $(\omega_0/2\pi \pm 0.5)$ Hz. Within this small band the noise may be assumed to be white,

$$F_N(\sigma) = \text{const.} \tag{23}$$

For convenience the acoustic spectrum is defined by,

$$\tfrac{1}{2}(\langle X^2\rangle+\langle Y^2\rangle)=\int F_A(\sigma)\,d\sigma. \tag{24}$$

It may be expected that the scattered acoustic signal is uncorrelated with oceanic noise. Therefore $F_A(\sigma)$ defined by (24) becomes, cf. (18), (21), and (22),

$$F_A(\sigma)=\tfrac{1}{2}A_0^2\,\delta(\sigma)+F_S(\sigma)+F_N(\sigma). \tag{25}$$

The coherent waves only contribute at zero frequency. The contribution of noise may be estimated by the frequency-independent portions within the observed spectra.

4. Transfer Functions

The acoustic measurements yield the 1-dimensional variance spectrum $F_A(\sigma)$ as defined by (24). For describing the ocean surface a 2-dimensional spectrum is needed, such as the directional waveheight spectrum $E_G(\boldsymbol{\kappa})$ introduced by (17). The aim now is to derive the relation between these spectra. Considering only second-order scattered waves it may be concluded from the foregoing considerations that a surface wave of frequency σ yields a contribution to the scattered variance spectrum $F_S(\sigma)$ at the same frequency. Thus the desired relation will be,

$$F_s(\sigma)=\int \tilde{T}(\sigma,\alpha)\,\tilde{E}_G(\sigma,\alpha)\,d\alpha \tag{26}$$

with,

$$\boldsymbol{\kappa}=(\kappa\cos\alpha,\ \kappa\sin\alpha).$$

$$\tilde{E}_G(\sigma,\alpha)=\kappa\frac{d\kappa}{d\sigma}E_G(\boldsymbol{\kappa}).$$

For comparing the measured spectrum $F_A(\sigma)$ with the theoretical $F_S(\sigma)$ the noise contribution must be estimated, cf. (25).

The directional dependence of surface waves can be separated from the 2-dimensional spectrum according to,

$$\tilde{E}_G(\sigma,\alpha)=F_G(\sigma)\cdot S_G(\sigma,\alpha) \tag{27}$$

where

$$\int_{-\pi}^{\pi} S_G(\sigma,\alpha)\,d\alpha=1.$$

Inserting (27) into (26) one obtains,

$$F_S(\sigma)=T(\sigma)\cdot F_G(\sigma) \tag{28}$$

with,

$$T(\sigma)=\int_{-\pi}^{\pi}\tilde{T}(\sigma,\alpha)\,S_G(\sigma,\alpha)\,d\alpha.$$

With this equation the inversion, that is the determination of the surface-waveheight spectrum from the measured acoustic spectrum becomes trivial, as $T(\sigma)$ is known from theory. On the other hand, only the 1-dimensional frequency spectrum may be estimated, and no information is obtained on the directional distribution of surface waves. The angular distribution function $S_G(\sigma, \alpha)$ must be even known for computing the transfer function $T(\sigma)$. This restriction will be discussed again at the end of this chapter.

The transfer function will now be computed for long-range propagation, which means that the distance between source and receiver is assumed to be large compared to the water depth, and that the sound waves undergo many bounces at the sea surface and the bottom.

Sound propagation can be described by modes or rays. For low-frequency shallow-water propagation the mode representation is more appropriate. We will consider both, modes and rays, and compare the computed transfer functions.

Mode Propagation

We assume a water layer of constant depth overlying a homogeneous sedimentary halfspace, which may be treated as a fluid. This simple model has been shown to yield good agreement between computed and observed mode characteristics such as depth dependence of the amplitudes and group velocities of the single modes.

The first-order acoustic wave field is generated by a CW point source located at $(r=0, x_3=d)$ within the water layer, cf. Fig. 1. Thus the wave equation within first order becomes,

$$\frac{1}{c_W^2}\frac{\partial^2 p^{(1)}}{\partial t^2}-\frac{\partial^2 p^{(1)}}{\partial x_i\,\partial x_i}=Q\,\delta(x_1)\,\delta(x_2)\,\delta(x_3-d)\cos(\omega_0 t) \tag{29}$$

where $Q=$ source strength,
while the second-order Eq. (9) remains unchanged. Additional to the boundary conditions (7), (8) at the surface and to the wave Eqs. (9) or (29) the boundary conditions at the sea floor and the wave equation within the sedimentary halfspace must be considered. They are undisturbed in all perturbation orders.

At a fluid-fluid interface continuity of pressure and of the normal component of particle velocity are required,

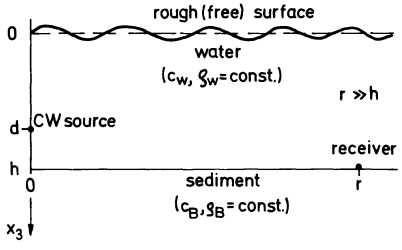

Fig. 1. Geometry of sound propagation in shallow water (2-layer fluid-fluid model)

$$\left.\begin{matrix} p^{(l)} \\ u_3^{(l)} \end{matrix}\right\} \text{ continuous at } x_3 = h \qquad (l = 1, 2, \ldots) \tag{30}$$

with,

$$\rho \frac{\partial u_3^{(l)}}{\partial t} + \frac{\partial p^{(l)}}{\partial x_3} = 0 \qquad \rho = \rho_W, \rho_B$$

= density of water layer and bottom respectively.

The wave equation for the sedimentary sea floor is

$$\frac{\partial^2 p^{(l)}}{\partial t^2} - c_B^2 \frac{\partial^2 p^{(l)}}{\partial x_i \partial x_i} = 0 \qquad \text{for } x_3 > h \tag{31}$$

c_B = sound velocity of the sea bottom.

With (29)–(31) the first-order far-field solution becomes.

$$p^{(1)}(r, x_3, t) = \sum_{n=1}^{N} r^{-\frac{1}{2}} A_n \varphi_n(x_3) \exp\{i(k_n r - \omega_0 t)\} + \text{c.c.} \tag{32}$$

with,

$$r = \sqrt{x_1^2 + x_2^2} \gg h$$

$$A_n = \frac{Q \varphi_n(d) \exp\left(i \frac{\pi}{4}\right)}{4 \rho_W \sqrt{2\pi k_n} \int_0^\infty \frac{1}{\rho} \varphi_n^2 \, dx_3}.$$

The mode functions $\varphi_n(x_3)$ and horizontal wavenumbers k_n are solutions of an eigenvalue problem. A detailed derivation of (32) is given by Kuperman and Ingenito (1977).

The acoustic field (32) only includes a finite number of trapped modes, i.e., waves which are totally reflected at the sea bottom. The continuum of leaking modes may be neglected as, due to multiple reflections, nearly all energy is transferred to the infinitely deep sea floor for long-range propagation.

To find the second-order solution, the first-order solution (32) and the representation of the surface wave-heigth (2) are inserted into the boundary condition (8) at the sea surface. Beside this the second-order wave equations of the water layer (9) and of the sedimentary halfspace (31), and the boundary conditions at the water-sediment interface (30) must be fulfilled.

For long-range propagation we only are interested in the trapped-mode portion of the solution, which becomes nonstationary (= resonant) if the scattered wavenumber and frequency satisfy the dispersion relation of trapped modes,

$$\begin{aligned} \boldsymbol{k}_s &= \boldsymbol{k}_n + s\boldsymbol{\kappa} \\ \omega_m &= \omega_0 + s\sigma \end{aligned} \qquad (s = \pm 1). \tag{33}$$

This means that ω_m ist the frequency of the mode m at the wavenumber k_s. The solution in the vicinity of the resonant branches is,

$$p^{(2)} = \sum_{\substack{\boldsymbol{k}_s \\ s=\pm 1}} r^{-\frac{1}{2}} A_n Z_{\boldsymbol{\kappa}}^s \{D_s \varphi_m(x_3) q_s(t) + \psi_s(x_3)\} \cdot \exp\{i(\boldsymbol{k}_s \boldsymbol{x} - (\omega_0 + s\sigma)t\} + \text{c.c.} \tag{34}$$

with,

$$D_s = \frac{\varphi_n'(0)\,\varphi_m'(0)}{\rho_W e_m}, \qquad e_m = \int_0^\infty \frac{1}{\rho c^2}\,\varphi_m^2\,dx_3$$

$$q_s(t) = \frac{1-\exp\{i(\omega_0 + s\sigma - \omega_m)t\}}{(\omega_0 + s\sigma)^2 - \omega_m^2}$$

where,

$$\omega_0 + s\sigma > 0 \quad \text{as} \quad \sigma \ll \omega_0.$$

At a fixed point, e.g., at the position of the receiver, the scattered field of course is stationary, but the temporal increase of the solution (34) has to be regarded along the wave path and describes the transfer of energy.

Asymptotically one obtains,

$$\lim_{t\to\infty} \frac{d}{dt} |q_s(t)|^2 = \frac{\pi}{2\omega_m^2}\,\delta(\omega_0 + s\sigma - \omega_m) \tag{35}$$

with,

$$\frac{d}{dt} = v_m \frac{\partial}{\partial r_s} \qquad (r_s \text{ parallel to } \boldsymbol{k}_s)$$

$$v_m = \frac{d\omega_m}{dk_s} \qquad \text{group velocity.}$$

We are interested in the variance spectra of X_S and Y_S from,

$$p^{(2)} = X_S \cos(\omega_0 t) + Y_S \sin(\omega_0 t). \tag{36}$$

Due to the interference pattern of the scattered modes φ_m the functions X_S and Y_S depend on the vertical coordinate x_3. It is therefore meaningful to consider the vertical average of the variance spectra.

Making use of the orthogonality of the eigenfunctions we define,

$$\frac{\rho_W c_W^2}{2h} \int_0^\infty \frac{1}{\rho c^2} (\langle X_s^2 \rangle + \langle Y_s^2 \rangle)\,dx_3 = \sum_{\boldsymbol{k}_s,\, m} E_{\boldsymbol{k}_s}^m \tag{37}$$

with,

$$\frac{\partial E_{\boldsymbol{k}_s}^m}{\partial r_s} = \frac{\pi}{2 r v_m} \sum_{\substack{n \\ s=\pm 1}} |A_n|^2 \langle |Z_{\boldsymbol{\kappa}}|^2 \rangle |D_s|^2 \frac{\rho_W c_W^2}{h} e_m\,\delta(\omega_0 + s\sigma - \omega_m).$$

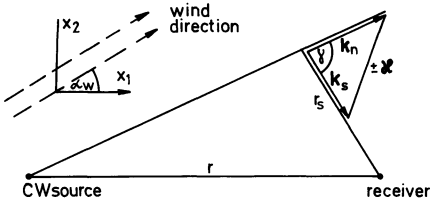

Fig. 2. Geometry of the scattering paths. $k_s = k_n + s\kappa$ ($s = \pm 1$); k: horizontal acoustic wavenumber; κ: wavenumber of surface waves

By taking care of the geometry of the scattering problem shown in Fig. 2 the integration may be carried out. Instead of discret wavenumbers a continuous notation is used and a relation between the two-dimensional acoustic and waveheight spectra is obtained. Because the measurements give only the one-dimensional acoustic spectrum, we integrate over all directions of incoming waves. The result is,

$$F_s(\sigma) = \int_{-\pi}^{\pi} \tilde{T}(\sigma, \alpha)\, E_G(\sigma, \alpha)\, d\alpha \tag{38}$$

with,

$$\tilde{T}(\sigma, \alpha) = \frac{\pi \rho_W c_W^2}{2h} \sum_{\substack{n, m \\ s = \pm 1}} \frac{e_m}{v_m^2 \omega_0^2} |A_n|^2 |D_s|^2 \frac{1}{k_n \sin^2 \gamma}.$$

More detailed investigations on wave-wave interaction are given by Hasselmann (1967), and the problem of acoustic scattering at the sea surface in shallow water is treated by Essen and Hasselmann (1970).

Ray Representation

Rays in comparison with modes stand for a further simplification of sound-propagation theory, which is obtained by neglecting the interference of up- and downwards travelling waves in the ocean. Rays are a suitable representation for a deep ocean, where adjacent modes become very close, and the (horizontal) wavenumber may be considered as a continuous variable.

The transfer function may be computed by intensity considerations. This procedure includes three steps:

(a) Determination of the radiated (1. order) intensity at each point of the sea surface: Again an isotropic point source of constant frequency is assumed [cf. (29)], and the horizontal distance from the source should be large compared with the water depth.

(b) Computation of the scattered (2. order) intensity: This can be done in dependence on the 1. order intensity with help of (11).

(c) Summarizing the intensities of all waves reaching the receiver from the different horizontal and vertical directions. The geometry is the same as in Fig. 2. As for the mode computations only the 1. and 2. order solutions are considered, which are totally reflected at the sea floor.

With the assumptions (17) about the surface-wave statistics one obtains,

$$\tilde{T}(\sigma, \alpha)=\frac{\omega_0^2 Q^2}{8\pi^2 h^2 c_W^2} \sum_{s=\pm 1} \iint \frac{\sin \vartheta_a \operatorname{tg} \vartheta_a \sin \vartheta_s \operatorname{tg} \vartheta_s}{\sin^2 \gamma} d\vartheta_a \, d\vartheta_s$$

with,

$$k_a=\frac{\omega_0}{c_W} \cos \vartheta_a; \quad k_s=\frac{\omega_s}{c_W} \cos \vartheta_s$$

$$\boldsymbol{k}_s=\boldsymbol{k}_a+s\boldsymbol{\kappa}, \quad \omega_s=\omega_0+s\sigma \approx \omega_0 \quad (s=\pm 1). \tag{39}$$

This result does not depend on the vertical positions of source and receiver, as may be understood by the outlined way of computation. In the limit of many (dense) modes the mode transfer function (38) must approach the ray transfer function (39). The summations over n and s are replaced by integrations with respect to ϑ_a and ϑ_s. Furthermore the phase change for sea-floor reflection is not considered in ray computations and (39) is obtained from (38) by assuming $\rho_B=\infty$.

Numerical Results

Before presenting computed transfer functions some general statements should be made. The equations (38), (39) show that there is no dependence on the distance between source and receiver. This surprising result follows from the geometry of the scattering problem.

The water depth is of influence on the mode transfer function as the ratio of acoustic wavelength and water depth determines the number of trapped modes.

In order to simplify the presentation of the numerical results a dimensionless transfer function is defined by [cf. (28)]

$$\Gamma(\sigma)=\frac{8\pi^2 h^2 c_W^2}{\omega_0^2 Q^2} \int_{-\pi}^{\pi} \tilde{T}(\sigma, \alpha) S_G(\sigma, \alpha) \, d\alpha. \tag{40}$$

Figure 3 shows transfer functions for continuous wavenumbers (rays) at the carrier frequencies of 200 and 400 Hz. A very strong influence of the surface-wave directions is found. Higher carrier frequencies yield a shift of the curves to higher frequencies.

It should be mentioned that the ray transfer function becomes infinite at $\gamma=\pi/2$, which refers to infinitely distant scattering points. For the frequencies regarded in our computations these points are excluded, i.e. $0 \leqq \gamma < \pi/2$.

Considering the mode-transfer function (38) it turns out that it exists of a sequence of (integrable) singularities, which result from scattering points on the straight line between source and receiver ($\gamma=0$). It is convenient to define a smoothed transfer function,

$$\Gamma_M(\sigma)=\frac{1}{2\Delta\sigma} \int_{\sigma-\Delta\sigma}^{\sigma+\Delta\sigma} \Gamma(\sigma) \, d\sigma \tag{41}$$

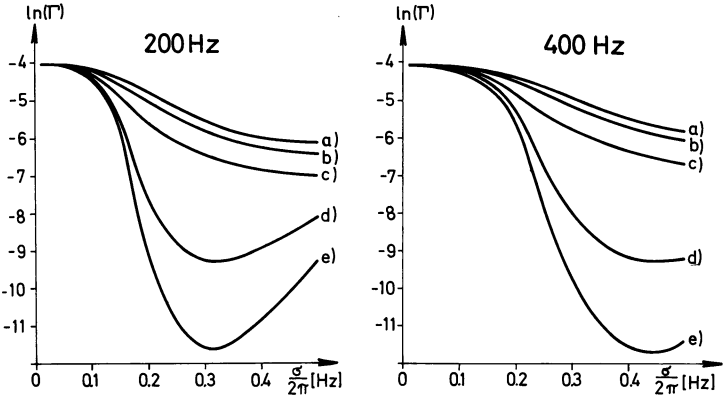

Fig. 3. Theoretical transfer functions for a ray-propagation model. CW frequencies: 200 and 400 Hz; angular-distribution functions:

$$S_G(\sigma, \alpha) = \begin{cases} \frac{1}{\pi} \hat{S}(\hat{\alpha}) & \text{for } |\hat{\alpha}| \leqq \frac{\pi}{2} \\ 0 & \text{else} \end{cases}$$

with, $\hat{\alpha} = \alpha - \alpha_W$. α_W = mean surface-wave (or wind) direction

$\hat{S}(\hat{\alpha}) = (a)\ \frac{8}{3}\cos^4\hat{\alpha}$, $(b)\ 2\cos^2\hat{\alpha}$, with, $\alpha_W = \frac{\pi}{2}$, $(c)\ \hat{\alpha}$, with, α_W = arbitrary, $(d)\ 2\cos^2\hat{\alpha}$, $(e)\ \frac{8}{3}\cos^4\hat{\alpha}$, with, $\alpha_W = 0$

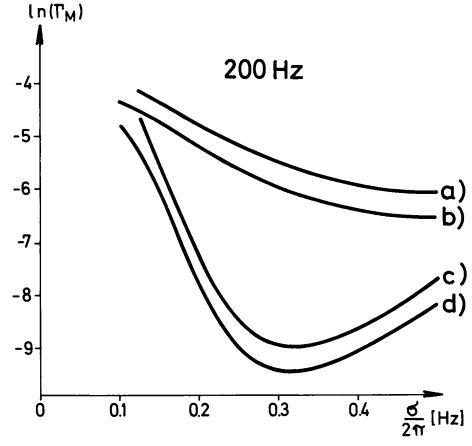

Fig. 4. Theoretical transfer functions for a mode-propagation model. CW frequency: 200 Hz; angular-distribution function:

$$S_G(\sigma, \alpha) = \begin{cases} \frac{2}{\pi} \cos(\alpha - \alpha_W) & \text{for } |\alpha - \alpha_W| \leqq \frac{\pi}{2} \\ 0 & \text{else} \end{cases}$$

water depths and mean surface-wave (or wind) directions:

$(a)\ h = 20$ m, $(b)\ h = 60$ m, with, $\alpha_W = \frac{\pi}{2}$

$(c)\ h = 20$ m, $(d)\ h = 60$ m, with, $\alpha_W = 0$;

sea-floor parameters: $c_B = 1.15 \cdot c_W$, $\rho_B = 1.9 \cdot \rho_W$

with,

$$\Delta\sigma \ll \sigma.$$

In Fig. 4 computed $\Gamma_M(\sigma)$ are shown for a carrier frequency of 200 Hz and a $\cos^2$ distribution of surface-wave directions. The water depths are 20 and 60 m, which correspond to 3 and 8 trapped modes, respectively. The low-frequency cutoff of the curves is determined by the smoothness of the function (41). For about 8 modes and

more the ray-transfer function can be used. This was verified for a number of different acoustic carrier frequencies and surface-wave direction functions.

The inverse problem, i.e., the problem to determine the 1-dimensional waveheight spectrum from the measured acoustic spectrum, requires the knowledge of the angular distribution of the surface waves. Of course this is a very crucial restriction, since the measurement of the surface-wave angular-distribution is much more difficult than the measurement of wave height. On the other hand, with the knowledge of the mean surface-wave direction and an empirical angular distribution function such as $\cos^{2\beta}(1 \leqq \beta \leqq 2)$ one may get a satisfactory estimate of the surface-wave spectrum from acoustic measurements.

The dependence of the transfer function on the surface-wave directions allows the determination of the angular distribution, provided that certain assumptions can be made. This will be discussed in the last chapter.

5. Determination of Surface-Wave Height Directions

Within several experiments in the North Sea, performed by the Institute of Geophysics in Hamburg, the acoustic and wave height spectra have been measured simultaneously, and from these data experimental transfer functions may be obtained. We will investigate the possibility of determining the directional distribution of surface waves from these data. For this purpose it must be assumed that he angular distribution S_G, cf. (27) does not depend on frequency within a certain interval,

$$S_G(\sigma, \alpha) = S_G(\alpha) \quad \text{for} \quad \sigma_\mu \leqq \sigma \leqq \sigma_0 \tag{42}$$

where,

$$\frac{\sigma_0 - \sigma_\mu}{2\pi} \approx 0.1 \text{ Hz}$$

and that the transfer function was measured for N frequencies of this interval,

$$T_n = T(\sigma_n) \quad (n = 1, \ldots, N) \tag{43}$$

with,

$$\sigma_\mu \leqq \sigma_n \leqq \sigma_0 \quad \text{(data)}.$$

The problem is now to invert the following relation, cf. (28)

$$T_n = \int_{-\pi}^{\pi} \tilde{T}(\sigma_n, \alpha)\, S_G(\alpha)\, d\alpha \tag{44}$$

where $\tilde{T}(\sigma, \alpha)$ is known from the theory presented in the preceeding chapter.

A reasonable method of inversion is a least-squares fit. In order to make use of the matrix inversion method as presented by Jackson (1972), the continuous distribution function is approximated by a number of discret steps,

$$S_G(\alpha) + S_G(\alpha + \pi) = S_m \quad \text{for} \quad (m-1) \cdot \Delta\alpha - \frac{\pi}{2} \leqq \alpha \leqq m \cdot \Delta\alpha - \frac{\pi}{2} \tag{45}$$

with,

$$\Delta\alpha=\frac{\pi}{M}\ (m=1, \ldots, M) \qquad \text{(model)}.$$

Ocean surface waves travelling in opposite directions yield the same contribution to the transfer function. This ambiguity has been taken into consideration by defining S_m in (45).

With (45) the inversion problem (44) becomes,

$$T_n=\sum_{m=1}^{M} G_{nm}\cdot S_m \tag{46}$$

with,

$$G_{nm}=\int_{(m-1)\cdot\Delta\alpha-\frac{\pi}{2}}^{m\cdot\Delta\alpha-\frac{\pi}{2}} \tilde{T}(\sigma_n, \alpha)\, d\alpha.$$

The data T_n depend linearly on the model parameter S_m. We assume that the number of data exceeds the number of model parameters,

$$N>M. \tag{47}$$

Following Jackson (1972) we consider the coupled eigenvalue problem,

$$\begin{aligned} G\,v &= \lambda\mu \\ G^T u &= \lambda v \end{aligned} \tag{48}$$

where G is the $n\times m$ matrix defined by (46), and u and v are eigenvectors with n or m components, respectively. The nonzero eigenvalues are computed and ranked in decreasing order of magnitude.

$$\lambda_1^2\geqq\lambda_2^2\geqq\ldots\geqq\lambda_p^2>0 \tag{49}$$

with,

$$p\leqq M<N.$$

The generalized (Lanczos) inverse of G is defined by,

$$H=V\Lambda^{-1}U^T \tag{50}$$

where U and V are the $n\times p$ and $m\times p$ eigenvector matrices, respectively, and Λ is the diagonal $p\times p$ matrix of the nonzero eigenvalues. It can be shown that H is a least-aquares inverse.

In order to test the method, angular distribution functions have been computed for artificial data. In Fig. 5 an example is shown, where the data correspond to a $\cos^2$ angular distribution with two different main directions. The number of data is $N=11$ from the frequency interval 0.1–0.2 Hz, and the number of model parameters is $M=5$ or $M=7$. The number of nonzero eigenvalues is M, but the higher eigenvalues become very small. It is useful to construct the inverse H out of

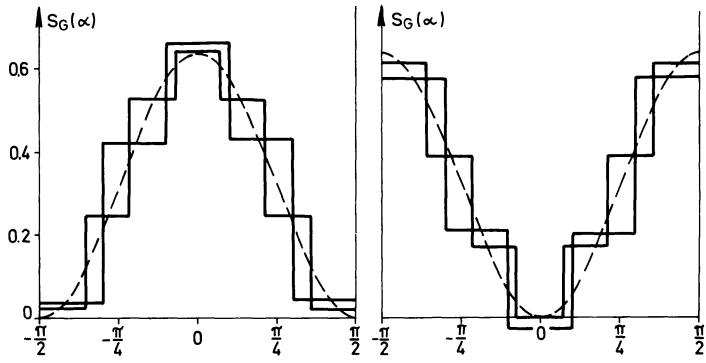

Fig. 5. Angular-distribution functions computed by matrix inversion from theoretical "data". CW frequency: 200 Hz; N = 11 data, i.e., computed values of the transfer function at equidistant frequencies between 0.1 and 0,2 Hz and for continuous angular-distribution functions *(dashed lines)*; M = 5,7 model parameters, respectively

eigenvectors only, that correspond to the p largest eigenvalues, which are in our example, $p=3$ for $M=5$, and $p=5$ for $M=7$.

As may be expected for artificial data the steps of the model angular distribution S_m fit the continuous $\cos^2$ distribution quite well. Measured data and an estimation of errors will be presented in a later paper.

Acknowledgements. This research was supported by the "Sonderforschungsbereich 94, Meeresforschung Hamburg".

References

Barrick, D.E., Evans, H.W., Weber, B.L.: Ocean surface currents mapped by Radar, Science **198**, 138–144, 1977

Clark, J.G., Kronengold, M.: Long-period fluctuations of CW signals in deep and shallow water. J. Acoust. Soc. Am. **56**, 1071–1083, 1974

Essen, H.-H.: Wave-facet interaction model applied to acoustic scattering from a rough sea surface, Acustica **31**, 107–113, 1974

Essen, H.-H., Hasselmann, K.: Scattering of low-frequency sound in the ocean, Z. Geophys. **36**, 655–678, 1970

Essen, H.-H., Schirmer, F., Siebert, J.: Measurements of ocean surface-waves with an acoustic range. Dt. hydrogr. Z. **31**, 7–15, 1978

Hasselmann, K.: Nonlinear interactions treated by the methods of theoretical physics (with application to the generation of waves by wind). Proc. Roy. Soc. A **299**, 77–100, 1967

Jackson, D.D.: Interpretation of inaccurate, insufficient and inconsistent data. Geophys. J.R. Astron. Soc. **28**, 97–109, 1972

Kinsman, B.: Wind waves – their generation and propagation on the ocean surface. Prentice-Hall, Englewood Cliffs, 1965

Kuperman, W.A., Ingenito, F.: Attenuation of the coherent component of sound propagating in shallow water with rough boundaries. J. Acoust. Soc. Am. **61**, 1178–1187, 1977

Rice, S.O.: Mathematical analysis of random noise, from Wax: Selected papers on noise and stochastic processes. Dover, New York 1954

Tyler, G.L., Teague, C.C., Stewart, R.H., Peterson, A.M., Munk, W.H., Joy, J.W.: Wave directional spectra from synthetic aperture observations of radio scatter. Deep-Sea Res. **21**, 989–1016, 1974

Received July 31, 1978; Accepted January 12, 1979

J. Geophys. 45, 199–207, 1979

Journal of Geophysics

A Comparison of Results of Geothermal and Magnetotelluric Investigations in Northwestern Germany

K. Knödel[1], W. Losecke[1], and J. Wohlenberg[2]

[1] Bundesanstalt für Geowissenschaften und Rohstoffe, Postfach 510153, D-3000 Hannover 51, Federal Republic of Germany

[2] Niedersächsisches Landesamt für Bodenforschung, Postfach 510153, D-3000 Hannover 51, Federal Republic of Germany

Abstract. The results of a regional magnetotelluric survey carried out during exploration for new energy resources in the northwestern part of the Federal Republic of Germany were used to make maps of the average electric resistivity of the sediments between the earth's surface and the Zechstein base as well as of the sediments between the Zechstein base and the top of the basement. Structures striking E-W were dominant in these maps.

Furthermore, anomalies occur with a strike of NE-SW to NNE-SSW. A region of very low resistivities of pre-Zechstein layers striking E-W at the southern margin of the North German Basin is of special interest. Maps of the average resistivity are compared with temperature maps of subsurface levels at 2000 m and 3000 m depths in Northwestern Germany. There is a remarkable correspondence between zones of low resistivity and regions of significantly elevated temperatures. The possible origins of both anomalies are discussed.

Key words: Geothermics – Magnetotellurics – North German Basin – Temperature distribution – Conductivity distribution – Prepermian.

Introduction

Geothermal and magnetotelluric studies have been carried out during exploration for new energy resources in North-western Germany since 1975. Investigations to establish a temperature atlas for the Federal Republic of Germany were sponsored by the Federal Ministry of Research and Technology (BMFT) (Wohlenberg, 1978). This project was executed by the Niedersächsisches Landesamt für Bodenforschung (NLfB). Object of the investigations was the mapping of potential geothermal resources in the subsurface of the Federal Republic. Temperature data were taken from (1) drilling reports from the oil industry, (2) temperature logs recorded in

0340-062X/79/0045/0199/$01.80

boreholes and mines, and (3) calculated temperature-depth functions based on heatflow and thermal conductivity data.

Temperature maps based on these data were plotted for the subsurface of the Federal Republic of Germany.

At the same time, the BMFT and the LEP (Landes-Entwicklungs-Plan) funded large-scale magnetotelluric experiments to investigate the size and structure of the sedimentary basin of NW Germany with special interest in more detailed information on the pre-Zechstein strata. This work was carried out by the BGR (Federal Institute for Geosciences and Natural Resources). The magnetotelluric investigation can be divided into three parts: (1) computer controlled digital recording of the electric and magnetic field components (time series); (2) analysis of the time series by extensive data processing (sounding graphs); (3) construction of a model of the subsurface structure from the sounding graphs combining model computation and geological information.

This paper presents the results of both investigations and discusses the possible common origin of the temperature and electric resistivity anomalies.

Geothermal Investigations

Temperature data for the construction of the temperature maps were collected from more than 4,800 drill holes out of a total of 16,000 bore holes. The geographical distribution of these data is not uniform throughout the area of the Federal Republic of Germany. Only the oil-bearing sedimentary basins have a high density of boreholes, i.e., a high information density. For the region under consideration, namely the sedimentary basin of northwestern Germany, temperature data was obtained from more than 3,770 drill holes. In addition, the NLfB took high quality temperature logs in 26 deep drill holes. Temperature-depth curves could be calculated from 8 heat-flow measurements. The quality of the data taken from the drilling reports is uncertain. Therefore, a statistical treatment was applied to all of the data. Temperature-depth curves were calculated on the basis of all the available temperature data from within areal elements of 12×12 km, taken from the 1:25,000 topographical map grid. The so produced temperature maps for several depth levels were smoothed applying a two dimensional moving average over nine elements. On the basis of these refined charts, isothermal maps were constructed for depths of 100 m, 250 m, 500 m, 1,000 m, 1,500 m, 2,000 m, and 3,000 m (Wohlenberg, 1978).

A map of temperatures at a depth of 2,000 m is shown in Fig. 1. Differences of more than 20° C occur at this level. A region of remarkably elevated temperatures stretches from the Netherlands through the area of Hannover to the Flechtinger Hills. Temperatures are significantly lower to the north and south of this region. Less pronounced anomalies striking NE-SW and NNE-SSW appear in the northern and southern part of the region shown in Fig. 1.

A similar pattern of anomalies is shown in Fig. 2 for the 3,000 m level. Temperature differences of more than 30° C are observed at this level. The higher temperatures appear along the southern margin of the North German

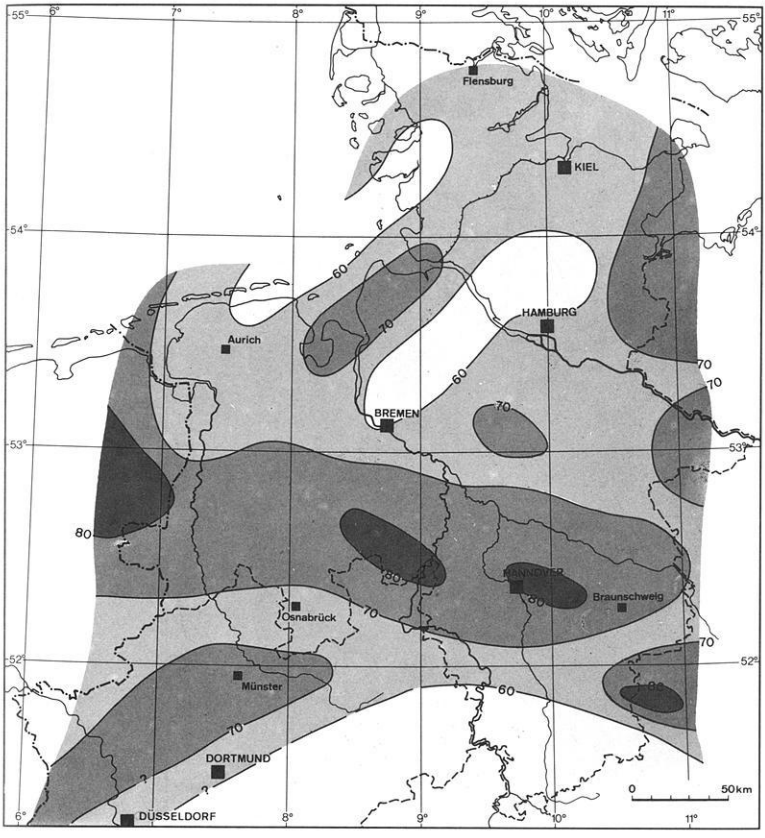

Fig. 1. Isoline map of temperatures at a depth of 2,000 m in the northern part of the Federal Republic of Germany (Wohlenberg, 1978); in °C

Basin, similar to what was observed in Fig. 1 for the 2,000 m level. The E-W striking anomaly obviously becomes more significants with increasing depth.

Magnetotelluric Investigations

The interpretation of the magnetotelluric observations is based on tensor rotated curves of apparent resistivity (ρ_{12}, ρ_{21}) and phase (φ_{12}, φ_{21}), rotation angle of the principal axes and skewness in the period range 0.2 to 2,048 s. For cases in which both the curves of apparent resistivity and both the phase curves did not deviate too much from each other a single new curve of apparent resistivity $\bar{\rho}$ and also a single curve of phase $\bar{\varphi}$ was calculated as follows:

$$\bar{\rho}_\kappa = \sqrt{\rho_{12}(T_\kappa) \cdot \rho_{21}(T_\kappa)}, \qquad \bar{\varphi}_\kappa = \tfrac{1}{2}[\varphi_{12}(T_\kappa) + \varphi_{21}(T_\kappa)]$$

$$T_\kappa = \text{period} \qquad \kappa = 1, 2, 3 \ldots$$

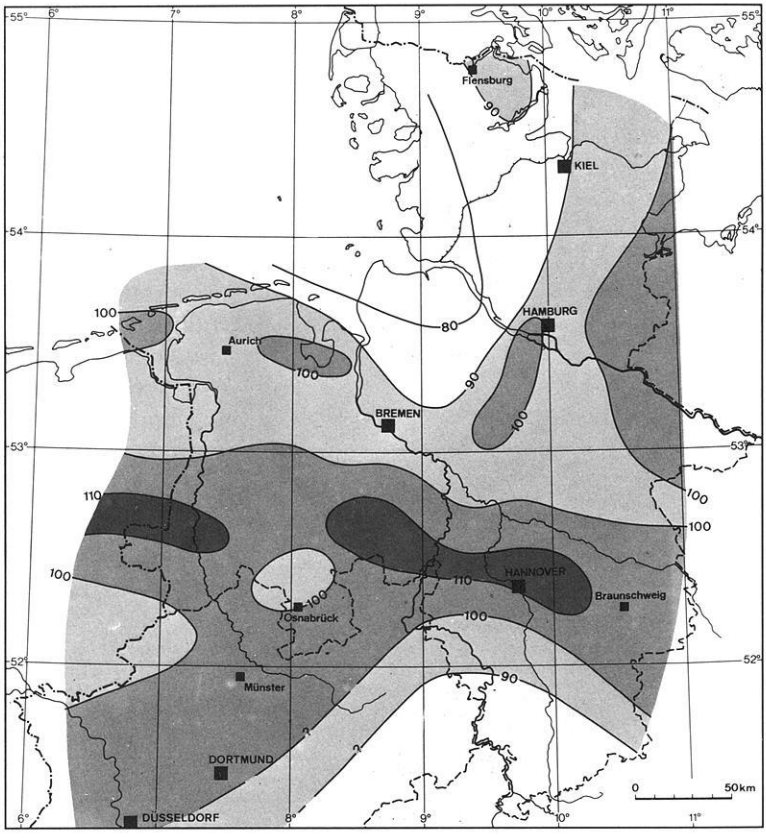

Fig. 2. Isoline map of temperatures at a depth of 3,000 m in the northern part of the Federal Republic of Germany (Wohlenberg, 1978); in °C

For interpretation in a first step, a horizontal layer inversion according to Bostick (1976) resulted in an approximative resistivity-depth curve for each observation point. In a second step, a correlation of maxima and minima of these resistivity-depth functions between the neighbouring points was successful, and first horizontal layer models were constructed. From these models it was possible to derive number, thickness, and approximate resistivity values of the layers down to the high resistivity magnetotelluric basement. An improved second model was constructed using the horizontal layer inversion according to Marquardt-Müller (Müller, 1977).

As a characterizing parameter for the subsurface below each observation point, the integrated conductivity S is of special interest. S is not very sensitive to changes in the model. It is defined for a series of highly conductive layers above a high resistivity basement:

$$S = \sum_{i=1}^{n-1} \frac{h_i}{\rho_i} \tag{1}$$

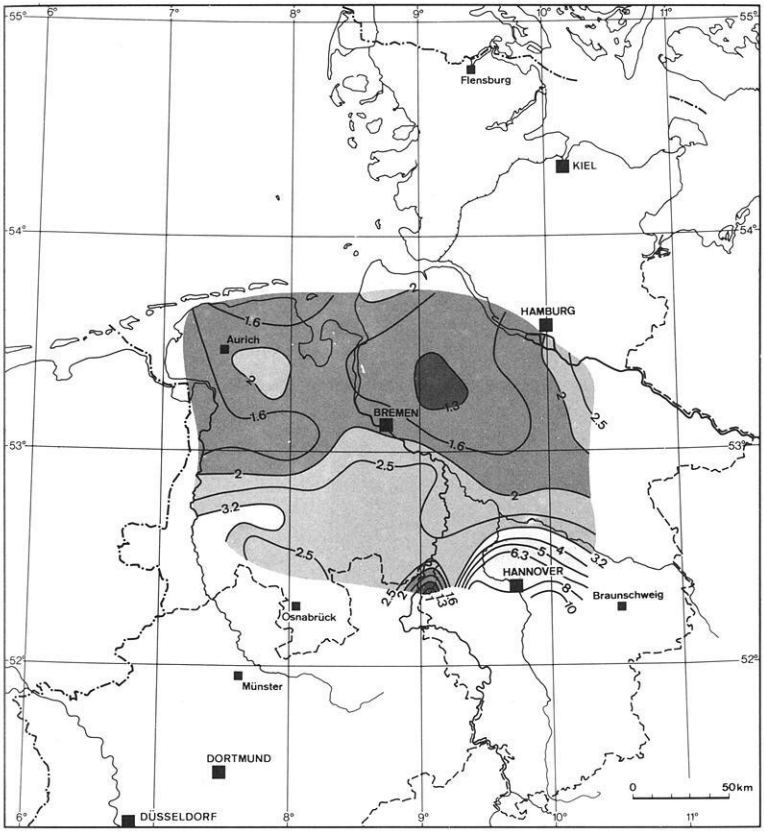

Fig. 3. Isoline map of electric resistivity ρ_m (ohm·m) in the post-Zechstein formations in the northwestern Germany constructed from magnetotelluric data (Knödel et al., 1978)

where h_i = thickness of the layers,
ρ_i = resistivity,
$n-1$ = number of layers above the basement,
n_m = number of layers above the Zechstein base,
n_p = number of layers between the Zechstein base and, the basement, i.e., $n_m+n_p=n-1$.

In addition, the following relationships are valid:

$$h=\sum_{i=1}^{n-1} h_i=\bar{\rho}\cdot S \tag{2}$$

where $\bar{\rho}$ = average resistivity.

Since S behaves additive, the integrated conductivities can be defined for parts of the series as well:

$$S_g=S_m+S_p=\sum_{i=1}^{nm}\frac{h_i}{\rho_i}+\sum_{i=nm+1}^{n-1}\frac{h_i}{\rho_i}. \tag{3}$$

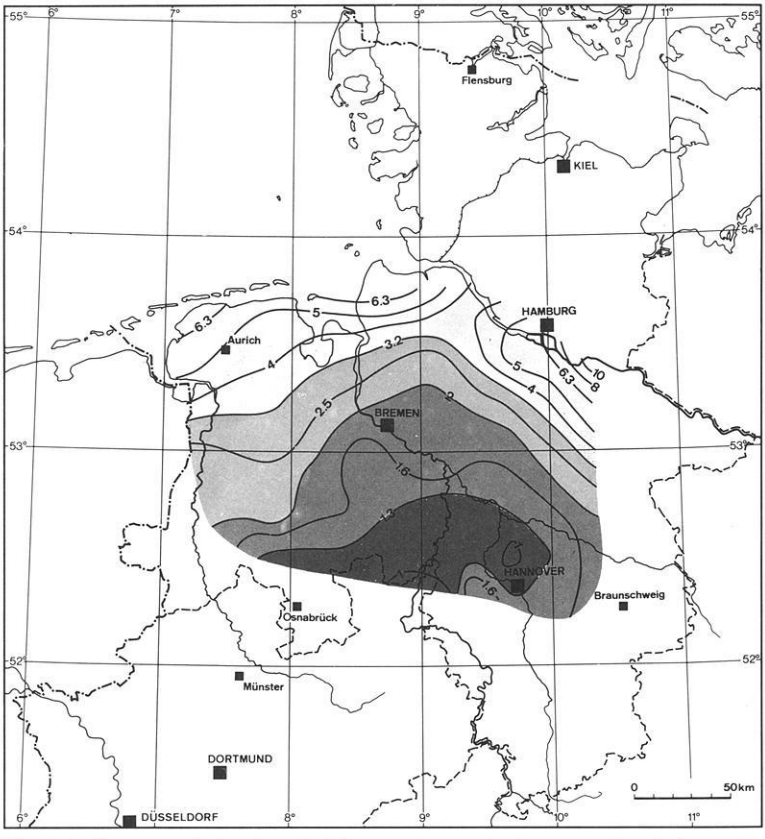

Fig. 4. Isoline map of electric resistivity ρ_p (ohm · m) in the pre-Zechstein formations in northwestern Germany constructed from magnetotelluric data (Knödel et al., 1978)

The S-values can be calculated from results of the horizontal layer inversion at any observation point. The average resistivities ρ_m and ρ_p for the layers above and below the Zechstein base can be determined from S_m, S_p, and the corresponding thicknesses (for the distribution of the depth of the Zechstein base see International Map of Natural Gas Fields in Europe, Bundesanstalt für Geowissenschaften und Rohstoffe, Hannover 1972). The thickness of the layers from the Zechstein base down to the basement is changing from 7 km in the southern part to 11 km in the northern part of the region under consideration (for further information see Losecke et al., in press).

Figure 3 shows an isoline map of the average resistivities ρ_m above the Zechstein base. The isolines were derived from observations at approximately 50 stations arranged on a rectangular grid of about 40 km between points.

Figure 4 shows an isoline map of the average resistivities ρ_p for the layers between the Zechstein base and the basement. The ρ values vary in both maps from 1 to 10 Ωm.

The great difference in the pattern of isolines for ρ_m and ρ_p (Figs. 3 and 4, respectively) is remarkable. While for the post-Zechstein layers the lower

resistivities appear in the more northern parts of the region under discussion, the pre-Zechstein pattern is just the reverse, the low resistivity values appear in the southern parts. The very low resistivity values ρ_m near the Weser west of Hannover are an exception. Structures with an E-W strike are prominent in Figs. 3 and 4. Besides these, there are structures with a NE-SW to NNE-SSW strike. Of special interest is a region of very low resistivities on the southern margin of the North German Basin (pre-Zechstein).

Discussion of Results

1. Extrapolating the temperature field presented in Figs. 1 and 2 for pre-Zechstein layers and assuming only electrolytic conduction, temperature controlled differences of not more than 20% of the mean value can be expected for the average resistivity ρ_p. Under these conditions the observed pattern of the resistivity ρ_p (Fig. 4) can be explained by variations of the temperature field to only a small amount ($<20\%$).

2. The attempt to explain the pattern of resistivity ρ_p by variations in the facies is not satisfactory. There is at present no indication of such an extensive facies difference. Moreover, the attempt to correlate the temperature pattern with facies changes leads to a contradiction of the results of the magnetotelluric investigations, because a simultaneous increase in electric and thermal conductivity would be required, which is very unlikely.

3. The assumption of several thin layers of highly concentrated semiconductive or metallic minerals (e.g., pyrite or graphite) could explain the resistivity (ρ_p) pattern. Such high concentrations of conductive minerals over large areas are unknown.

4. Another explanation for the observed anomalies in the parameters ρ_p and T is possible: the regions with the lowest resistivities and elevated temperatures coincide with a region of tectonic activity, namely the basin of Lower Saxony (see Fig. 5) (Boigk, 1968; Stadler and Teichmüller, 1971). The boundaries of the basin to the north and the east are formed by the Pompeckj swell, to the south by the Rhenish Massif along old fault zones. The E-W striking basin crosses the Mediterranian-Mjösen lineament. Two independent tectonic events determined the present shape of the Saxonian basin. Tectonic shear strains during the Upper Jurassic caused the subsidence of a broad crustal strip and the intrusion of magmatic matter. The thickness of the Upper Jurassic and Lower Cretaceous sediments reached 3,000–4,000 m, depending on the amount of subsidence.

An orogenic phase during the Upper Cretaceous caused an uplift of the basin of approximately 1,000 m. During this phase, the inner part of the Lower Saxonian Basin was subjected to intensive block faulting with thrusting along the northern and southern margins. According to Boigk (1968), the possible origin of these dynamic processes are vertical movements within subsaliniferous and/or still deeper crustal layers. Seismic studies by Polskov et al. (1976) in the North German-Polish basin east of Lower Saxony under discussion have shown that extensive fault zones exist across the entire crust. Phases of repeated tectonic activity occured along these geologically unstable zones during all the

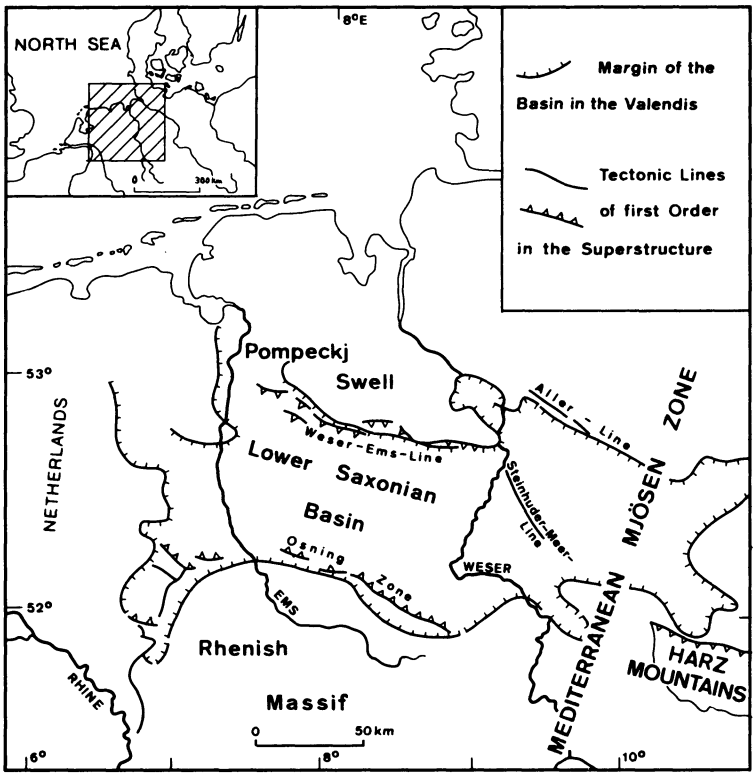

Fig. 5. The geologic and tectonic macro-structure of northern Germany according to Boigk (1968)

times and in Precambrian created E-W striking fault systems were reactivated and extended by different dynamic processes (Lauterbach and Lauterbach, 1973).

These continuous tectonic activities probably not only produced numerous fault systems, but also increased the crack porosity. Particularly the pre-Zechstein sedimentary layers were subjected to phases of uplift and subsidence during the Jurassic and Cretaceous.

The crack porosity still exists even under effective pressures of more than 3 kbars (Hurtig et al., 1972). Since the water filling the pore volume reduces the effective pressure, fracture porosities can be expected for the whole Palaeozoic formation. It may be remarked within this context, that within several deep drillings at depths larger than 5 km porosities of more than 5 % have been found for Palaeozoic formations. In many cases the pore space was filled by water.

This model easily explains the pattern of resistivity ρ_p of the pre-Zechstein sedimentary layers by electrolytic conductivity in a medium with regional differences in fracture porosities. The high temperatures at the 2,000 m and 3,000 m levels are then caused by heat convection processes along the unstable zones described above. Hurtig et al. (1975) have discussed connections between geoelectromagnetic and geothermal anomalies on the one hand and fault zones on the other hand.

Acknowledgements. The authors thank the Ministry of Lower Saxony, the Federal Ministry of Research and Technology and the project management of the energy research branch of KFA Jülich for their support.

References

Boigk, H.: Gedanken zur Entwicklung des Niedersächsischen Tektogens. Geol. Jb. **85**, 861–900, 1968

Bostick, F.X.: A simple almost exact method of MT analysis. Workshop on Electrical Methods in Geothermal Exploration. 4.–7. 11. 76 Snowbird (Utah)

Hurtig, E., Burde, B., Löhning, W.: Zur Bedeutung der Crackporosity (Rißporosität) bei Messungen unter hydrostatischem Druck. In: Physikalische Parameter und seismische Geschwindigkeiten, Symposium im Zentralinstitut für Physik des Erdkörpers (ZIPE), 50–61, Potsdam 1972

Hurtig, E., Oesberg, R.-P., Ritter, E., Grünthal, G., Jacobs, F.: Studies of the Crustal Structure in the Northern Part of Central Europe. Gerlands Beitr. Geophys. **84**, 317–325, 1975

Knödel, K., Losecke, W., Müller, W.: Detailauswertung magnetotellurischer Vermessungen tiefer Stockwerke in Norddeutschland für Rückschlüsse auf mögliche erdölgeologisch interessante Strukturen. Abschlußbericht zum BMFT-Projekt ET 3214, Hannover 1978

Losecke, W., Knödel, K., Müller, W.: The conductivity Distribution in the North German Sedimentary Basin Derived from Widely Spaced Areal Magnetotelluric Measurements. Geophys. J.R. Astron. Soc. (in press)

Lauterbach, R., Lauterbach, J.: Zur Rolle der Bruchsysteme in Ost-West-Richtung. In: Stockwerkbau und Felderteilung, Symposium im Zentralinstitut für Physik des Erdkörpers (ZIPE), 617–621, Potsdam 1973

Müller, W.: Inversion by simultaneous fitting of apparent resistivity and phase angle. Acta Geodaet. Geophys. Montanist. Acad. Sci. Hung. **12**, 215–222, 1977

Polskov, M.K., Pomeranceva, I.V., Mozzenko, A.N., Lange, W., Nowak, W.-E., Heckeler, V.: Die deutsch-sowjetische Zusammenarbeit bei der Erforschung des Tiefenbaus der Erdkruste im Nordteil der DDR. Z. geol. Wiss. **4**, 113–123, 1976

Stadler, G., Teichmüller, R.: Zusammenfassender Überblick über die Entwicklung des Bramscher Massivs und des Niedersächsischen Tektogens. Fortschr. Geol. Rheinld. u. Westf. **18**, 547–564, 1971

Wohlenberg, J.: Das Temperaturfeld im Untergrund der Bundesrepublik Deutschland. Geol. Jb. 1978 (in press)

Received September 5, 1978; Accepted February 12, 1979

J. Geophys. 45, 209–218, 1979

Journal of Geophysics

Effect of the Coastline Configuration of South Indian and Sri Lanka Regions on the Induced Field at Short Period

M. Takeda and H. Maeda*

Geophysical Institute, Kyoto University, Kyoto 606, Japan

Abstract. Deformation of induced currents by the Palk Strait and the coasts of India and Sri Lanka (Ceylon) is studied by data analysis and model calculation in the cases of SSC's and bay disturbances at night. In the model calculation a thin flat layer model in which only contrast of conductivity due to the distribution of land and depth of sea is taken into account is used, the inducing field is assumed to be parallel to the geomagnetic axis, and the effect of self induction is included. It is found that the anomalous distribution of geomagnetic SSC's or bays in the South Indian region during the nighttime could be explained, at least qualitatively, by abnormal current patterns caused by the Palk Strait and the coasts of India and Sri Lanka. It is also found that a large phase lag is expected in the induced field especially in the D and Z components at shorter periods, as an effect of self induction.

Key words: Geomagnetism – Induction – Palk strait.

1. Introduction

It was often pointed out that geomagnetic variations observed on the ground are much affected by oceans. In a previous research note (Takeda and Maeda, 1978) we have suggested the possibility that anomalously large amplitudes in the horizontal component of SSC's at Annamalainagar in India may be resulted from a concentration of induced currents at the Palk Strait. Also, Nityananda et al. (1977) has recently examined mean direction of "anomalous" horizontal variations of SSC's and bays at Annamalainagar and Trivandrum, and mentioned that the reason of this anomalies may be caused by the induced currents along the coastline and through the Palk strait. In this paper, we first show that not only SSC's but also bays have abnormally large horizontal amplitude at Annamalainagar in the nighttime, and then by model calculations by taking a

* Also at the Data Analysis Center for Geomagnetism and Spacemagnetism, Faculty of Science, Kyoto University

0340-062X/79/0045/0209/$02.00

self-induction term into account, we attempt to explain this anomaly in terms of induced currents in the sea around the Indian Peninsula and through the Palk Strait.

2. Data Analysis

In a previous note (Takeda and Maeda, 1978) we studied the amplitude distribution of H component of nighttime SSC's in the equatorial zone of American, Pacific and Indian regions, suggesting different effects of induced currents in the Earth. In the Pacific region the distribution is rather uniform because of uniform induced currents. However, in the Indian region a quite different distribution is seen, and we suggested that the anomaly of this kind may be caused by induced currents in the Palk Strait.

In order to examine the anomaly in the Indian region, we have analysed the H component of bays during the IGY, 1957–1958, in the nighttime, but an apparent anti-equatorial enhancement is also seen in bays as well as SSC's. Furthermore, as is shown by Nityananda et al. (1977) and Singh et al. (1977), the amplitude of Z component observed at Annamalainagar and Trivandrum at night is so large (equal or more than the H component) that it cannot be explained without considering a current-density gradient in the Earth.

3. Method of Calculation

The method of calculation in this study is based on the theory of electromagnetic induction within a non-uniform thin plane sheet conductor. It was established by Price (1949) and applied to actual problems by Sasai (1968) and Honkura (1972).

Assuming that the inducing field is parallel to the geomagnetic axis, we can put the potential of this field as

$$We = A_0 \exp(i\omega t + \lambda z) \sin(\lambda x) \tag{1}$$

where ω is equal to the angular frequency of the inducing field, z the upward distance measured from the Earth's surface, x the northward distance measured from the geomagnetic equator, A_0 is a constant and we assumed it to be unity, and $1/\lambda$ is defined as the wavelength. Considering that the space of the inducing field is about as large as that of the Earth, $1/\lambda$ could be put to the Earth's radius, though the value of λ does not much effect on the results. Then we can write the induced current function Ψ_0 in a conductor (sea) having uniform depth as

$$\Psi_0 = 2(1-\alpha i)/(1+\alpha^2) \exp(i\omega t) \sin(\lambda x) \tag{2}$$

where $\alpha = 2\lambda\rho_0/(\omega\mu)$, $\rho_0 = 1/(\sigma_0 D_S)$, σ_0 is the conductivity of the sea water which is supposed to be 4 S/m ($=4$ mho/m), D_S is the assumed uniform sea depth, and μ is the permeability ($4\pi\times10^{-7}$ H/m). And the total current function Ψ may be written as

$$\Psi = \Psi_0 + \psi \tag{3}$$

where ψ is regarded as a current function due to anomalous (or additional) current distribution.

The equation to be solved thus becomes

$$\rho \Delta \psi + \nabla \rho \cdot \nabla \psi = -(\rho - \rho_0) \Delta \Psi_0 - \nabla(\rho - \rho_0) \cdot \nabla \Psi_0 + \mu \frac{\partial z^*}{\partial t} \tag{4}$$

where ρ is inverse of the integrated conductivity. If we define the equivalent sea depth D, it can be written as $1/(\sigma_0 D)$. Z^* is the vertically downward component of the magnetic field generated by the current function ψ, and written by Biot-Savart's law as

$$Z^*(0,0) = \frac{1}{4\pi} \int_0^{2\pi} \int_0^{\infty} \frac{1}{r} \frac{\partial \psi}{\partial r} \, dr \, d\theta = -\frac{1}{4\pi} \int_0^{2\pi} \int_0^{\infty} \frac{\psi(r,\theta) - \psi(0,0)}{r^2} \, dr \, d\theta \tag{5}$$

where (r, θ) is the polar coordinate originated at a point the value at which we require. Substituting (2) and (5) into (4), we obtain an equation which contains ψ only. Thus, solving this equation by the relaxation method, we can get the value of ψ as a function of place. Once we get ψ and so Ψ, using the relation between magnetic potential by the inducing currents W and current function Ψ

$$W = \Psi/2 \tag{6}$$

the magnetic fields (H, northward; D, eastward; Z, downward component) by the induced current are obtained as follows:

$$H = -\frac{\partial W}{\partial \kappa} = -\frac{1}{2} \frac{\partial \Psi}{\partial \kappa}$$

$$D = -\frac{\partial W}{\partial y} = -\frac{1}{2} \frac{\partial \Psi}{\partial y}$$

$$Z = -\frac{1}{4\pi} \int_0^{2\pi} \int_0^{\infty} \frac{\Psi(r,\theta) - \Psi(0,0)}{r^2} \, dr \, d\theta = -\frac{1}{4\pi} \int_0^{2\pi} \int_0^{\infty} \frac{\psi(r,\theta) - \psi(0,0)}{r^2} \, dr \, d\theta \tag{7}$$

where (r, θ) is the same coordinate as in Eq. (5).

In the actual calculation, D_S is taken to be 2000 m, the mesh interval to be 15 Km, and a 1200 Km square mesh putting the Palk Strait near the center of the square is adopted. The isobaths in the Indian ocean are shown in Fig. 1, together with three magnetic observatories (Annamalainagar, Kodaikanal, and Trivandrum). Using this map, the equivalent sea depths are determined as follows: In the sea region deeper than 2000 m, D is taken to be 2000 m, in the region of depth between 1000 m and 2000 m, D to be 1500 m, and in the region between 200 m and 1000 m, D to be 600 m. In the land region $D(=D_0)$ is assumed to be 10 m at first and 100 m in the next. When D_0 is taken to be 10 m, D in the region of depth between 0 m and 200 m is taken to be 100 m, and when $D_0 = 100$ m it is taken to be 200 m. As for the boundary condition, ψ is put to be 0 at the sides of the largest mesh square, and this is equivalent to the assumption

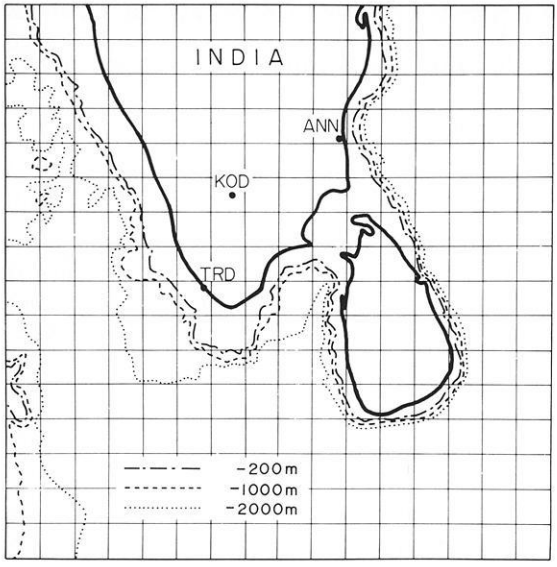

Fig. 1. Distribution of the Indian magnetic observatories (Annamalainagar, Kodaikanal, and Trivandrum) and the isobaths (-200 m, -1000 m, and -2000 m) in the Indian ocean

that the indiced (westward) current is not disturbed outside of this mesh, and current density is constant on the west or east side.

In the calculation of the self induction term [Eq. (5)], we summed the terms up to the points at a distance of five times (75 Km) of mesh intervals. Assuming that the additional current function decreases and tends to zero as inversely propotional to the distances, we express the remaining terms by integral. So the form of self induction term used in the actual calculation is as follows:

$$Z^*(i,j) = -\sum_{\substack{k,\,l=-5 \\ k^2+l^2\neq 0}}^{5} \frac{\psi(i+k,j+l)-\psi(i,j)}{4\pi(k^2+l^2)^{3/2}\,d} - \frac{1}{4\pi}\int_0^{2\pi}\int_{d_r}^{\infty} \frac{\psi_m \times \dfrac{d}{r} - \psi(i,j)}{r^2}\,dr$$

$$= -\sum_{\substack{k,\,l=-5 \\ k^2+l^2\neq 0}}^{5} \frac{\psi(i+k,j+l)-\psi(i,j)}{4\pi(k^2+l^2)^{3/2}\,d} - \frac{\psi_m}{4d_r} + \frac{\psi(i,j)}{2d_r} \tag{8}$$

where d is the mesh interval (15 Km), d_r is the radius of a circle (105 Km) which has the same area as the eleven mesh interval square, and ψ_m is the mean of ψ on the sides of it. Other methods, such as using only first term of Eq. (8) or summing from $k, l = -10$ up to 10, were studied, but they did not give so much different results. However, in the calculation of the induction of 1 min period, the self induction term cannot be neglected. If we do not take this term into account, the effect of the inhomogeneity of conductivity is overestimated, but in the imaginary part (phase shift) it is underestimated. Calculations were made for two inducing geomagnetic fields, one has a 1 min period that may correspond to SSC's, and the other has a 60 min period to bays.

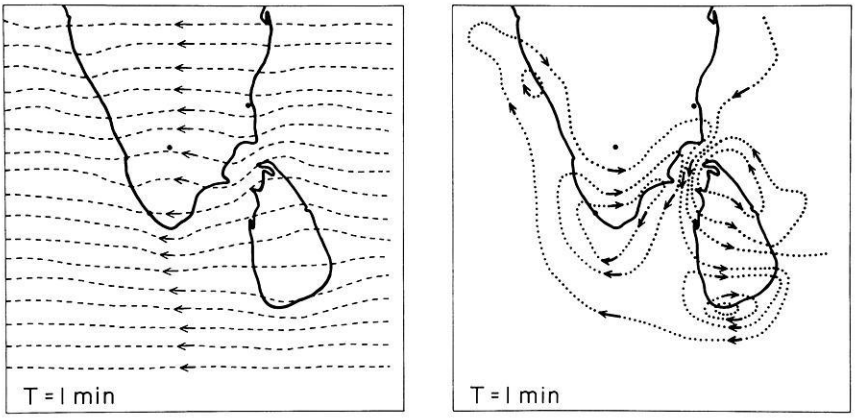

Fig. 2. Streamlines of the total induced currents for the inducing field of 1 min period (*left*) and those of the additional part (*right*). When the inducing field changes by 1 nT, the current flowing between the adjacent lines is 100 A in the left and 25 A in the right

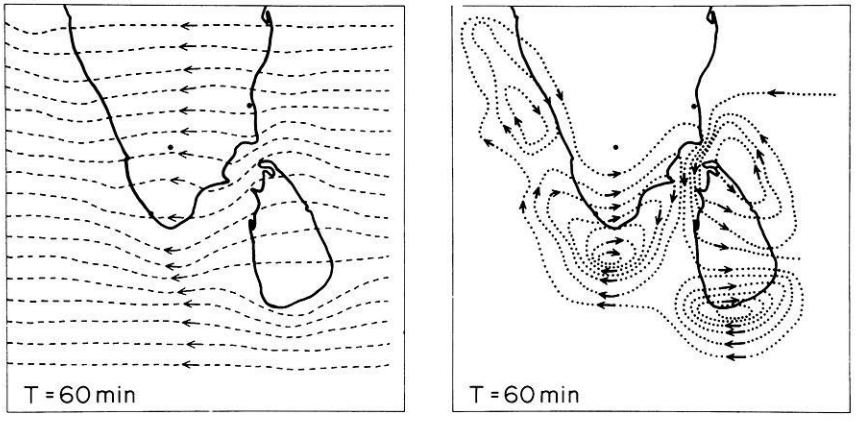

Fig. 3. Streamlines of the total induced currents for the inducing field of 60 min period (*left*) and those of the additional part (*right*). When the inducing field changes by 1 nT the current flowing between the adjacent lines is 100 A in the left and 25 A in the right

4. Results and Discussion

The total current patterns in the case of $D_0 = 10$ m are shown on the left-hand side of Fig. 2 (for 1 min) and Fig. 3 (for 60 min). It is generally seen that the streamlines are influenced by the distribution of Indian Peninsula and Sri Lanka. In order to see more clearly the deformation of induced currents, the additional current parts are shown on the right-hand side of Figs. 2 and 3. It is clearly seen that the induced currents are much distorted along the coasts of India and Sri Lanka, especially in regions of the south of India and Sri Lanka and in the Palk Strait. These kinds of deformation are usually called "peninsula effect" and "strait effect", respectively.

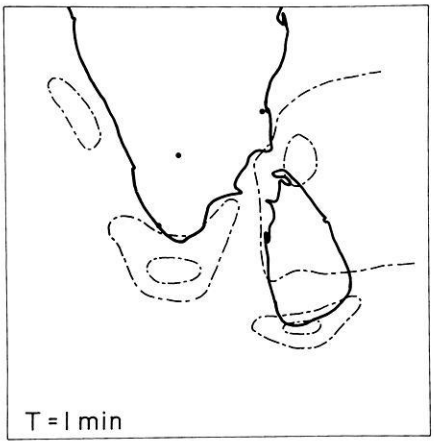

Fig. 4. Streamlines of the imaginary part of induced current function for the inducing field of 1 min period. When the inducing field changes by 1 nT, the current flowing between the adjacent lines is 25 A

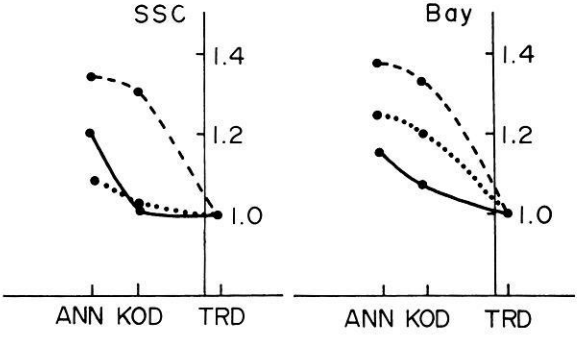

Fig. 5. Distribution of the observed (*full lines*) and calculated (*broken lines* for $D_0 = 10$ m and *dotted lines* for $D_0 = 100$ m) amplitudes of SSC's (*left*) and bays (*right*)

Figure 4 shows the distribution of the imaginary part of the current function for 1 min period, and this result means that the induced current shows a phase shift from the inducing field because of self induction. This phase shift can be regarded as the total phase shift, because in the uniform state the imaginary part is very small (α times the real part, where α is 3×10^{-4} for 1 min period and 0.018 for 60 min period). Such a phase shift by the additional current was very small for the 60 min period and so we did not show here.

Since the result of these distorted currents can be observed as geomagnetic variations, we have calculated the magnetic effect of the inducing and induced currents. Figure 5 shows the distribution of observed (full line) and calculated (broken or dotted lines) amplitudes of H-component for SSC's (left) and bays (right) at Annamalainagar, Kodaikanal, and Trivandrum normalized at Trivandrum. In this figure the broken lines are for the case of $D_0 = 10$ m, and the dotted line for the case of $D_0 = 100$ m. The ratio calculated for $D_0 = 10$ m is larger than the observed one at both Kodaikanal and Annamalainagar, and that for $D_0 = 100$ m is nearly equal at Kodaikanal and smaller at Annanalainagar for SSC's. But they are both larger for bays.

One of the most difficult problems in calculation of this kind would be the estimation of the conductivity of land. If we suppose that the land conductivity is 5×10^{-3} times the sea conductivity, the assumption of $D_0 = 10$ m means that the current induced in the sea does not sink so deep and flows horizontally in the land, whereas that of $D_0 = 100$ m means that it spreads in the land about ten times deeper than in the sea. As is seen in Fig. 5 the observed ratio is almost between the results for these two D_0 values, so that for SSC's the spreading of induced currents in the land would be between one and ten times the assumed sea depth if other assumption are justified.

The distribution of calculated magnetic effects is shown in Fig. 6a–c for the components of H, D, and Z respectively, in the case of $D = 10$ m. The real part is shown on the left-hand side, and the imaginary part on the right-hand side. The dot-dash lines represent the contour of undisturbed values for real H component, and of zero values for the others. As will be expected from the distribution of induced currents, the magnetic effects are much deformed along the coasts of India and Sri Lanka and around the Palk Strait, resulting in abnormal geomagnetic variations at Trivandrum and Annamalainagar. As for the Z component, the calculated and observed Z/H ratios for SSC's are shown in Table 1. From this table it can be seen that at Annamalainagar the assumption of $D_0 = 10$ m is good, but at Trivandrum and Kodaikanal the result of $D_0 = 100$ m is better. It might result from the scale of current concentration. That is, at Annamalainagar the currents which contribute to Z flow mainly in the Palk Strait, but at Trivandrum and Kodaikanal they flow beyond the tip of the Indian Peninsula, and scale of the former is smaller than that of the latter. If we consider that some distance is necessary for the induced currents to spread and sink into the land, this is natural. Of course especially at Trivandrum the agreement between the observed and calculated values is not so good even in the case of $D_0 = 100$ m. This might be due to the step-like conductivity configuration that we used in the present calculation, or due to the boundary condition we used. For example, a conductivity configuration of larger scale such as inferred by Rikitake (1967) might have to be considered for the determination of boundary condition. For the D component, the calculated and observed D/H ratios for SSC's are shown in Table 2. Observed D/H ratios are generally smaller than the calculated ones. This may be attributed to the inducing field. For example, if the inducing field is not parallel to the geomagnetic axis but tilted by about six degrees, it has D component one tenth as large as H component, and so the calculated result for $D_0 = 10$ m agrees better with the observed one. In fact, Nityananda et al. (1977) show that D/H ratio of SSC's in the nighttime is negative at Alibag and Hyderabad, too.

Furthermore, as a result of self induction term, the imaginary part is not small and so it cannot be neglected, especially for the inducing field of short period. For the H component the imaginary part is relatively small, but for the D and Z components it is rather large, because the "normal" field has large H component but no D component and small Z component. Therefore, a large phase lag is expected in the D and Z components. This tendendy is emphasized when the resistivity gradient is comparatively small, because in this case the third term on the right-hand side of Eq. (4) is more effective compared with the

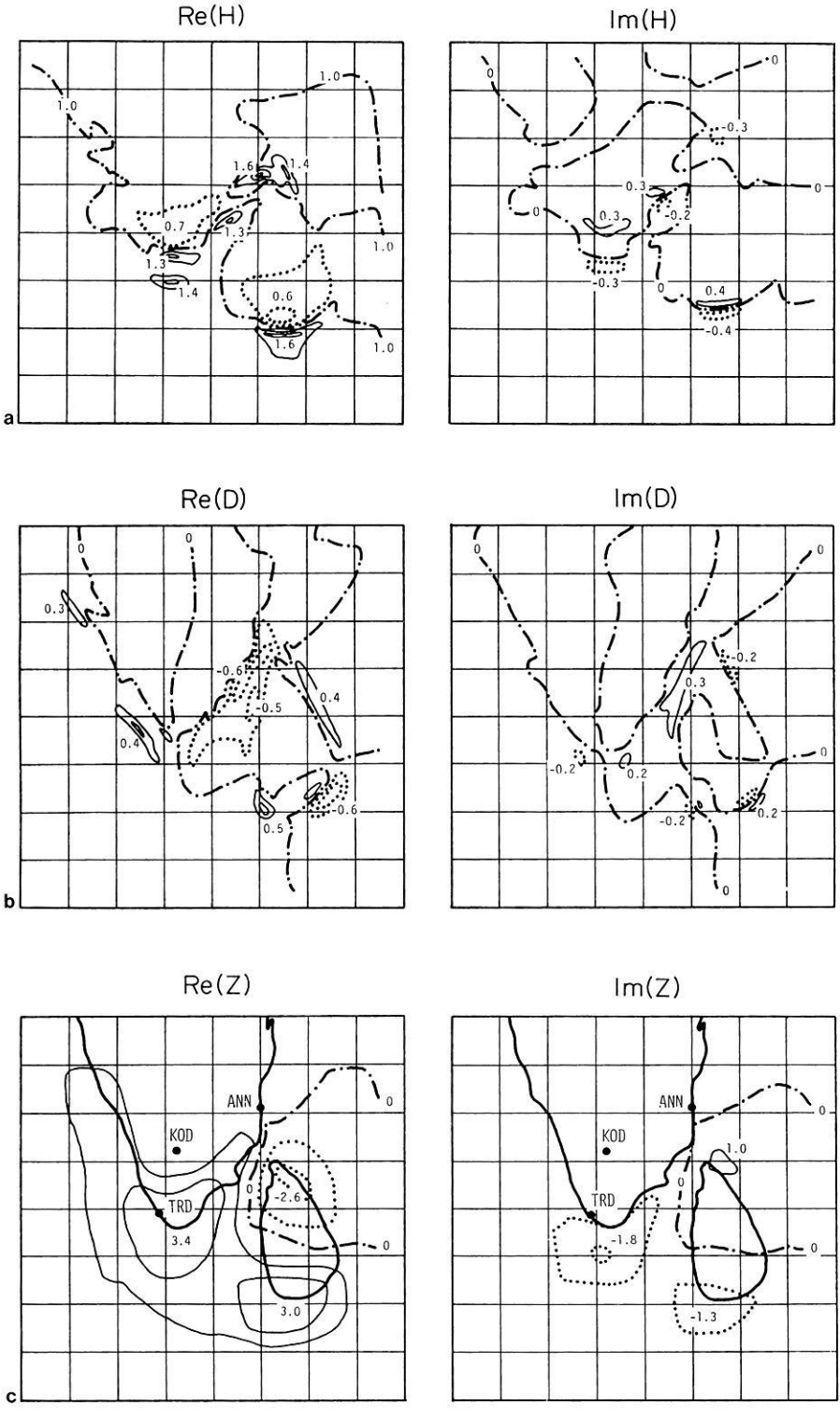
Re(H)
Im(H)
a
Re(D)
Im(D)
b
Re(Z)
Im(Z)
ANN
KOD
TRD
c

Table 1. Observed and calculated values of Z/H in the case of $T=1$ min. Observed values of Z/H are obtained by Singh et al. (1977)

Stations	Annamalainagar	Kodaikanal	Trivandrum
Observed values (SSC's at night)	0.43	0.44	1.26
Calculated values ($T=1$ min)			
$D_0=10$ m	0.43	0.57	4.73
$D_0=100$ m	0.05	0.48	1.72

Table 2. Observed and calculated values of D/H in the case of $T=1$ min. Observed values of D/H are obtained by Nityananda et al. (1977)

Stations	Annamalainagar	Kodaikanal	Trivandrum
Observed values (SSC's at night)	−0.30	−0.18	0.11
Calculated values ($T=1$ min)			
$D_0=10$ m	−0.21	−0.04	0.25
$D_0=100$ m	−0.07	−0.02	0.11

first and second terms. So, the phase lag is larger in the case of $D_0=100$ m than $D_0=10$ m. If these phase lags really exist, they could be observed in geomagnetic pulsations more easily than in SSC's or bays, and so the observation of this kind might help to reveal the spreading rate of the induced current. Anyway, more dense network observations in this region (along India-Sri Lanka line including the Palk Strait) would be important to make clear the conductivity configuration there.

Acknowledgements. We ackowledge Miss T. Obata for assistance in preparing the manuscripts. The data used in this study were obtained from the World Data Center C2 for Geomagnetism, and the numerical analyses were made by using facilities at the Data Analysis Center for Geomagnetism and Spacemagnetism and also at the Data Processing Center of Kyoto University.

References

Honkura, Y.: Geomagnetic variation anomaly on Miyake-jima Island. J. Geomag. Geoelect. **23**, 307–333, 1972

Nityananda, N., Agarwal, A.K., Singh, B.P.: Induction at short periods in the horizontal field variations in the Indian Peninsula. Phys. Earth Planet. Inter. **15**, P5–P9, 1977

Fig. 6a–c. Distribution of the ratios of the induced magnetic field [H (*a*), D (*b*) and Z (*c*) components] to the inducing field of 1 min period for the real (*left*) and imaginary (*right*) parts, where the imaginary parts indicate the phase lag of the induced field from the inducing field. *Dot-dash lines* represent the standard values (i.e., 1 for real H component and 0 for the other components), *thin solid lines* the larger values and *dotted lines* the smaller values. *Thick solid lines* in (*c*) represent the coastline. Values in this figure except for the standard values represent the maximum or minimum values

Price, A.T.: The induction of electric current in non-uniform thin sheets and shells. Quart. J. Mech. Appl. Math. **2**, 283–310, 1949

Rikitake, T.: Electromagnetic induction within non-uniform plane and spherical sheets. Bull. Earthq. Res. Inst. **45**, 1229–1294, 1967

Sasai, Y.: Spacial dependence of short period geomagnetic fluctuations on Oshima Island (2). Bull. Earthq. Res. Inst. **46**, 907–926, 1968

Singh, B.P., Nityananda, N., Agarwal, A.K.: Induced magnetic variations in the Indian Peninsula, Acta Geodaet. Geophys. Montanist. Acad. Sci. Hung. **12**, 65–72, 1977

Takeda, M., Maeda, H.: Note on geomagnetic variations in the equatorial zone. J. Geomag. Geoelect. **30**, 121–123, 1978

Received May 2, 1978; Accepted February 3, 1979

J. Geophys. 45, 219–221, 1979

Journal of Geophysics

Short Communication

Correction of Graphs Concerning the Chapman-Ferraro Image Method

O.M. Burkard[1] and H. Rucker[2]

[1] Institut für Meteorologie und Geophysik, Universität Graz, Austria
[2] Institut für Weltraumforschung, Österr. Akademie der Wissenschaften, Austria

Key words: Chapman-Ferraro image method – Correction of current system graph – Correction of $\vec{B}$-field structure graph.

The basic investigations concerning the interaction between the solar wind particles and the geomagnetic field were done by Chapman and Ferraro (1931). Unfortunately they published some wrong graphs on the current system and on the resulting magnetic field line structure, which are reproduced subsequently by several authors in the literature.

The concept of the Chapman-Ferraro image method initially was invented by Maxwell (1881, 1954), who analysed the physical processes arising in the case of a relative motion between a magnetic pole and a conductive sheet. The sudden introduction of a magnetic system (e.g., the earth's dipole field) and the relative motion between it and a conductive sheet (e.g., the foremost front of the approaching solar wind particles) will generate currents within the sheet. As Chapman and Ferraro (l.c.) pointed out, *the electric field lines are the lines of intersection of the sheet with the equipotential surfaces of the magnetic field.* In spite of their correct equations the graph of the Chapman-Ferraro-currents within the sheet is wrong (Fig. 1 a), which is reproduced by Chapman and Bartels (1940), Chamberlain (1958), Chapman (1964) and certainly in other papers, too.

The exact definition on the electric field lines (as mentioned above) leads to our calculated Fig. 1 b and differs from the wrong current line picture known in the literature in the way that the big semiaxis of the oval field lines is parallel to the y – axis and not parallel to the x – axis. The electric field has a positive maximum value at the point (0, 0, 0), two points with $\vec{E}=0$ and two further points beyond those with $\vec{E}=0$ with the coordinates ($\pm z/\sqrt{3/2}$, 0, 0) with a negative maximum value (z means the dipole's distance to the sheet).

0340-062X/79/0045/0219/$01.00

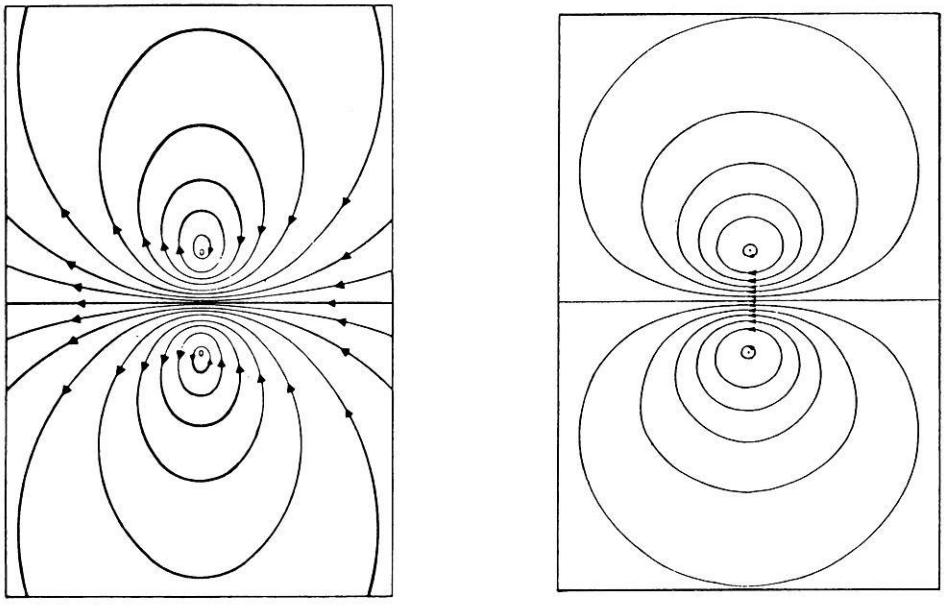

Fig. 1. The wrong and corrected graphs of the electric field line pattern

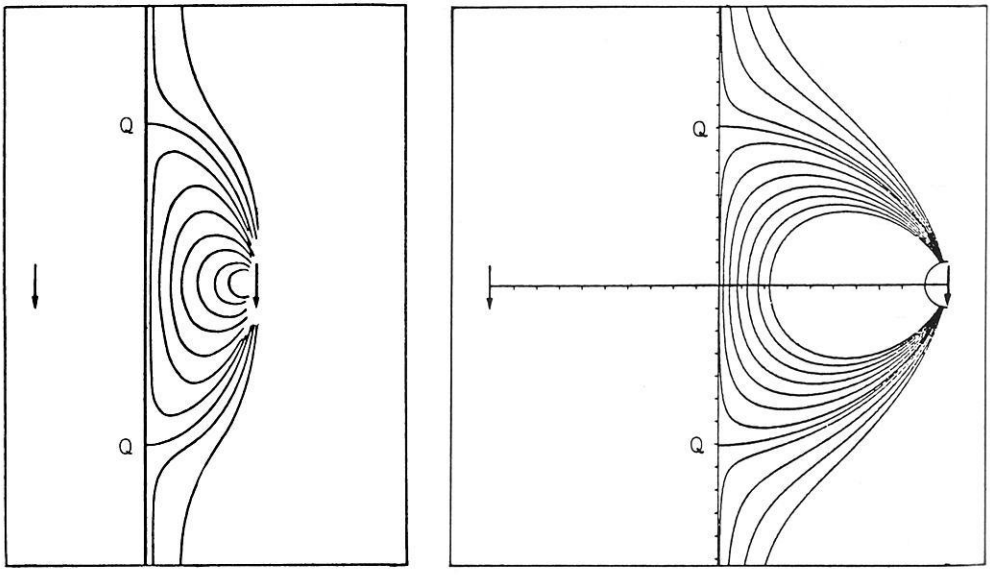

Fig. 2. The wrong and corrected graphs of the magnetic field line pattern

The current system excited in the sheet produces a magnetic effect, which can be represented by two image dipoles in both the half-spaces before and behind the sheet. The superposition of the earth's dipole field and the sheet's magnetic field led to the first impression of the internal magnetospheric $\vec{B}$-field structure. But again the magnetic field line structure in the paper of Chapman and Ferraro (l.c.) (Fig. 2a) is not correct. The field lines of the total magnetic field penetrate perpendicularly the current sheet at the points $\vec{E}=0$ with the coordinates $(\pm z/\sqrt{2}, 0, 0)$. In Fig. 2b one can see the correct relation between the dipole's distance z (standardized to unity) and the position of the point Q. In the case of total magnetic shielding one special magnetic field line ends perpendicularly at the sheet at the point Q, which is a point of zero-$\vec{E}$ and zero-$\vec{B}$.

Of course the magnetospheric boundary physics is explained in many new investigations, but some of them are applied to the Chapman-Ferraro-image method and this fact required a correction of the corresponding graphs.

References

Chamberlain, J.W.: Theories of Aurora, Adv. Geophys. **4**, 165, 1958

Chapman, S.: Solar Plasma, Geomagnetism and Aurora, Gordon and Breach, p. 54, 1964

Chapman, S., Bartels, J.: Geomagnetism, pp. 860–861. Oxford: Clarendon Press, 1940

Chapman, S., Ferraro, V.C.A.: A New Theory of Magnetic Storms. Terr. Magn. Atmos. Electr. **36**, pp. 177, 179, 1931

Maxwell, J.C.: A Treatise on Electricity and Megnetism, Oxford: Clarendon Press, 1881, Dover Publication, Inc., 1954

Received November 24, 1978; Accepted November 30, 1978

J. Geophys. 45, 223–229, 1979

Journal of Geophysics

Letter to the Editor

On the Difference Between Polarisation and Coherence

A. G. Jones

Institut für Geophysik, Gievenbecker Weg 61, D-4400 Münster, Federal Republic of Germany

Key words: Polarisation analysis – Coherence.

1. Introduction

In the analysis of plane waves – for example in optics or magnetic studies – it is of primary interest to determine the polarisation parameters of the signal from its measured components. Several methods have been presented to deal with this problem in both two- and three-dimensions (Fowler et al., 1967; McPherron et al., 1972; Means, 1972; Samson, 1973; Kodera et al., 1977) but in this letter the remarks are restricted to the two-dimensional case – they are equally valid however in three-dimensions. It should be noted that many workers have applied the techniques of these authors to analyse their own data (for example Paulson, 1968; Rankin and Reddy, 1972; Arthur et al., 1976; Jones, 1977; Kodera et al., 1977; Samson, 1977) and have shown the superiority of these forms of frequency domain analyses to the time domain hodogram.

However, it has occurred to the author that there is not a widespread appreciation of the (somewhat) subtle difference between the definitions of polarisation and coherence. It is the purpose of this letter to show that the distinction between polarised and unpolarised parts is not necessarily consistent with that between coherent and incoherent parts.

2. Basic Theory

The basic theory of polarisation analysis is well treated by Born and Wolf (1964) and is repeated in Fowler et al. (1967). For consistency this paper will follow the notation of Fowler et al. (1967) as far as possible. Any wave field can be characterised by examining the coherence (or cross-spectral) matrix of that field given by

0340-062X/79/0045/0223/$01.40

$$J(\omega)=\begin{bmatrix} J_{xx}(\omega) & J_{xy}(\omega) \\ J_{yx}(\omega) & J_{yy}(\omega) \end{bmatrix} \tag{1}$$

where $J_{ab}(\omega)=\frac{1}{T}\langle A^*(\omega)\,B(\omega)\rangle$

and the x and y subscripts refer to orthogonal components of the signal. From this matrix, the following parameters can be determined

$\det[J]$ = determinant of J
$\mathrm{Tr}[J]$ = trace (or intensity) of J
$\tan\beta$ = ratio of minor to major axis of the polarisation ellipse,
  $\beta>0$ implies right-handed polarisation
  $\beta=0$ implies linear polarisation
  $\beta<0$ implies left-handed polarisation
θ = direction of the major axis of the ellipse (clockwise round from the x-axis)
γ^2_{xy} = coherence between the two components
R = ratio of polarised power to total power.

All real signals consist (or can be resolved to consist) of three parts, a completely polarised signal, a completely unpolarised signal and a random noise contribution. These three will be considered separately.

(*a*) *Completely Polarised Signal*

For a *strictly* monochromatic signal, with cross-spectral matrix $[P]$, it can easily be shown that (Born and Wolf, 1964)

$$\det[P]=0 \tag{2a}$$

$$\mathrm{Tr}[P]=P_{xx}+P_{yy} \tag{2b}$$

$$\sin 2\beta=\frac{2\,\mathrm{Im}(P_{xy})}{P_{xx}+P_{yy}} \tag{2c}$$

$$\tan 2\theta=\frac{2\,\mathrm{Re}(P_{xy})}{P_{xx}-P_{yy}} \tag{2d}$$

$$\gamma^2_{xy}=1 \tag{2e}$$

$$R=1 \tag{2f}$$

(*b*) *Completely Unpolarised Signal*

Similarly, for a completely unpolarised signal with cross-spectral matrix $[U]$ (Born and Wolf, 1964)

$$U_{xy} = U_{yx} = 0 \cdot \tag{3a}$$

$$U_{xx} = U_{yy} \quad (= D \text{ in notation of Fowler et al., 1967}) \tag{3b}$$

$$\gamma_{xy}^2 = 0 \tag{3c}$$

$$\det[U] = D^2 \tag{3d}$$

$$\mathrm{Tr}[U] = 2D \tag{3e}$$

$$R = 0. \tag{3f}$$

(*c*) *Random Noise Signal*

For two random noise series, x and y, with cross-spectral matrix $[N]$,

$$N_{xy} = N_{yx} = 0 \quad \text{(Jones, 1977)} \tag{4a}$$

$$\gamma_{xy}^2 = 0 \tag{4b}$$

$$\det[J] = N_{xx} N_{yy} \tag{4c}$$

$$\mathrm{Tr}[J] = N_{xx} + N_{yy} \tag{4d}$$

There is no requirement for $N_{xx} = N_{yy}$ and most data contain unequal noise contributions on each channel. Thus $N_{xx} \neq N_{yy}$ and Born and Wolf (1964) show that the noise exhibits a degree of polarisation (R_r) given by

$$R_r = \frac{N_{xx} - N_{yy}}{N_{xx} + N_{yy}}. \tag{4e}$$

It should be noted that the polarised part of the noise represents a linear polarisation, which is along the x-axis for $R_r > 0$ or along the y-axis for $R_r < 0$.

3. Signal Analysis

Any quasi-monochromatic wave may be regarded as the sum of a completely polarised wave $[P]$ and a completely unpolarised wave $[U]$, which are independent of each other, and this representation is unique

$$J = P + U. \tag{5}$$

Also if several *independent* waves are propagated in the same direction, they superpose and the *total* polarisation matrix $[P_t]$ is given by the summation of the individual matrices $[P_1]$, $[P_2]$, etc.

$$P_t = P_1 + P_2 + \ldots \tag{6}$$

and similarly for $[U_t]$.

(*a*) *Uncontaminated Signal*

If the data are uncontaminated by noise, then they consist of only two parts, a completely polarised signal $[P]$ and a completely unpolarised signal $[U]$ such that,

$$J=\begin{bmatrix}P_{xx} & P_{xy}\\ P_{yx} & P_{yy}\end{bmatrix}+\begin{bmatrix}D & 0\\ 0 & D\end{bmatrix} \tag{7}$$

and $D=\frac{1}{2}\mathrm{Tr}\,[J]-\frac{1}{2}(\mathrm{Tr}^2\,[J]-4\det[J])^{1/2}$

i.e., the characteristic root (or eigenvalue) of the coherence matrix. The polarisation parameters R, θ, β are given by

$$R = \left(1-\frac{4\det[J]}{\mathrm{Tr}^2\,[J]}\right)^{1/2} \tag{8a}$$

$$\tan 2\theta=\frac{2\,\mathrm{Re}\,(J_{xy})}{J_{xx}-J_{yy}} \tag{8b}$$

$$\sin 2\beta=\frac{2\,\mathrm{Im}\,(J_{xy})}{[(J_{xx}-J_{yy})^2+4J_{xy}J_{yx}]^{1/2}}. \tag{8c}$$

These three polarisation parameters – R, θ and β – it should be noted, are *rotational invariants* (see below).

(*b*) *Signal Contaminated by Noise*

When there are noise components in the data, N_{xx} and N_{yy}, then the data are represented by a separation into completely polarised signal $[P]$, completely unpolarised signal $[U]$ and noise $[N]$ such that

$$J=\begin{bmatrix}P_{xx} & P_{xy}\\ P_{yx} & P_{yy}\end{bmatrix}+\begin{bmatrix}D & 0\\ 0 & D\end{bmatrix}+\begin{bmatrix}N_{xx} & 0\\ 0 & N_{yy}\end{bmatrix}. \tag{9}$$

For the unique decomposition of this form however a full a priori knowledge of the noise terms (matrix $[N]$) is required.

From Sect. 2a–c it is obvious that the *coherent* part of the data is given by $[P]$ whilst the *incoherent* part is given by $[U]+[N]$, i.e.,

$$\text{coherent part} = \begin{bmatrix}P_{xx} & P_{xy}\\ P_{yx} & P_{yy}\end{bmatrix} \tag{10a}$$

$$\text{incoherent part} = \begin{bmatrix}D+N_{xx} & 0\\ 0 & D+N_{yy}\end{bmatrix}. \tag{10b}$$

But from the discussion in 2c it is apparent that, unless the noise contributions on the orthogonal components are equal ($N_{xx}=N_{yy}$), the noise matrix is separable into a polarised part $[N_p]$ and an unpolarised part $[N_u]$. Thus

$$N = N_p + N_u \tag{11a}$$

$$= \begin{bmatrix} \frac{2R_r N_{xx}}{1+R_r} & 0 \\ 0 & 0 \end{bmatrix} + \begin{bmatrix} \frac{1-R_r}{1+R_r} N_{xx} & 0 \\ 0 & N_{yy} \end{bmatrix} \tag{11b}$$

(assuming $R_r > 0$, i.e., $N_{xx} > N_{yy}$)

and the *total* polarised matrix $[P_t]$ is given by

$$P_t = P + N_p \tag{12a}$$

(i.e., total polarised part)

$$= \begin{bmatrix} P_{xx} + \frac{2R_r}{1+R_r} N_{xx} & P_{xy} \\ P_{yx} & P_{yy} \end{bmatrix}, \tag{12b}$$

whilst the *total* unpolarised matrix $[U_t]$ is

$$U_t = U + N_u \tag{13a}$$

(i.e., total unpolarised part)

$$= \begin{bmatrix} D + \frac{1-R_r}{1+R_r} N_{xx} & 0 \\ 0 & D + N_{yy} \end{bmatrix}. \tag{13b}$$

From Eqs. (10), (12), and (13) it is seen that the *coherent* part equals the *polarised* part, if *and only if*, $R_r = 0$ (i.e., $N_{xx} = N_{yy}$, the noise contributions on both components are of equal magnitude).

Hence θ, derived from Eq. (8b) will be biassed towards the x-axis for $R_r > 0$, and towards the y-axis for $R_r < 0$. Similarly R, from equation 8a, will be always overestimated for $R_r \neq 0$ (since the geometric mean of any two positive numbers cannot exceed their arithmetic mean) whilst $\tan\beta$ – the ellipticity – will be overestimated for $P_{xx} > P_{yy}$ with $R_r < 0$ and for $P_{xx} < P_{yy}$ with $R_r > 0$, and underestimated for $P_{xx} > P_{yy}$ with $R_r > 0$ and for $P_{xx} < P_{yy}$ with $R_r < 0$.

4. Rotation and Coherence

Rotation of matrix J by angle ϕ results in J' from

$$J' = C J C^t \tag{14}$$

where C is the clockwise Cartesian rotation matrix given by

$$C = \begin{bmatrix} \cos\phi & \sin\phi \\ -\sin\phi & \cos\phi \end{bmatrix}$$

and C^t is the transpose of C. The polarisation parameters in the new co-ordinate system (R', θ', β') are related to the original parameters by

$$R' = R$$
$$\theta' = \theta - \phi$$

and

$$\beta' = \beta,$$

hence are *rotational invariants.*

However, the coherence function, γ^2_{xy}, between the two components, defined as

$$\gamma^2_{xy} = \frac{|J_{xy}|^2}{J_{xx}\, J_{yy}} \tag{15}$$

is a function of rotation. From Eq. (8a) for R, and the definition of γ^2_{xy} [Eq. (15)], it can easily be shown that the two are inter-related by

$$1 - R^2 = \frac{4 J_{xx} J_{yy}}{(J_{xx} + J_{yy})^2}(1 - \gamma^2_{xy}) \tag{16}$$

and hence

$$R^2 \geqq \gamma^2_{xy} \tag{17}$$

The equality holds when $4J_{xx}J_{yy} = (J_{xx} + J_{yy})^2$, which can only be true for $J_{xx} = J_{yy}$.

Expanding Eq. (14) and equating the terms for J'_{xx} and J'_{yy} gives the angle required for maximising γ^2_{xy} as

$$\tan 2\phi_m = \frac{J_{yy} - J_{xx}}{J_{xy} + J_{yx}}. \tag{18}$$

At angle ϕ_m, the following are true

$$R^2 = \gamma^2_{xy}$$
$$\theta' = \pi/4.$$

Such a rotation does not affect the separation of the coherence matrix into polarised and unpolarised parts (as indicated by the rotational invariance of the polarisation parameters) but *does* affect the separation into coherent and incoherent parts, by maximising the former with respect to the latter (as indicated by γ^2_{xy} maximum).

Finally, the author would like to add that strong caution is advised when interpreting the estimated value of coherence due to the inherent bias associated with the estimation itself (see Jones, 1977).

References

Arthur, C.W., McPherron, R.L., Means, J.D.: A comparative study of three techniques of using the spectral matrix in wave analysis. Radio Sci. **11**, 833–845, 1976

Born, J., Wolf, E.: Principles of Optics. New York: Macmillan 1964
Fowler, R.A., Kotick, B.J., Elliot, R.D.: Polarization analysis of naturally and artificially induced geomagnetic micropulsations. J. Geophys. Res. **72**, 2871–2883, 1967
Jones, A.G.: Geomagnetic Induction Studies in Southern Scotland, Ph. D. thesis, Univ. of Edinburgh, 1977
Kodera, K., Gendrin, R., Villedary, C. de: Complex Representation of a Polarised Signal and Its Application to the Analysis of ULF Waves, J. Geophys. Res. **82**(7), 1245–1255, 1977
McPherron, R.L., Russell, C.T., Coleman, P.J., Jr.: Fluctuating magnetic fields in the magnetosphere, 2, ULF waves. Space Sci. Rev. **13**, 411–454, 1972
Means, J.D.: Use of the three-dimensional covariance matrix in analyzing the polarization properties of plane waves. J. Geophys. Res. **77**, 5551–5559, 1972
Paulson, K.V.: The Polarisation and Spectral Characteristics of some High-Latitude Irregular Geomagnetic Micropulsations. Ann. Geophys. **24**, 1–6, 1968
Rankin, D., Reddy, I.K.: Effect of Geo-electric structure on the Polarisation Characteristics of Geomagnetic Micropulsations. J. Geophys. Res. **77**, 1286–1291, 1972
Samson, J.C.: Descriptions of the polarization states of vector processes: Applications to ULF magnetic fields. Geophys. J. Roy. Astron. Soc. **34**, 403–419, 1973
Samson, J.C.: Matrix and Stokes vector representations of detectors for polarized waveforms: Theory, with some applications to teleseismic waves, Geophys. J. Roy. Astron. Soc. **51**, 583–603, 1977

Received November 7, 1978; Accepted February 2, 1979

J. Geophys. 45, 231, 1979

Journal of Geophysics

Addendum

J. Geophys. 44, 545–555, 1978:

Palaeosecular Variation Studies of the Brunhes Epoch in the Volcanic Province of the East-Eifel, Germany

H. Kohnen and H. Westkämper

Institute of Geophysics, University Münster, Gievenbecker Weg 61, 4400 Münster, Federal Republic of Germany

In Figure 2, page 547, are two ^{14}C-ages (Schmincke, personal communication). For a correct interpretation, the following comments have to be given:

1. Eiterkopf II

Three ^{14}C-age determinations (M.A. Gey, 1977, personal communication) have been carried out on charcoal samples from three tuff beds between overlying loess and underlying scoria cones yielding concordant ages of 11,000 to 14,000 y. B.P., much younger than the overlying Würm loess. Therefore, the underlying lavas can be much older.

2. Plaidter Hummerich

A minimum ^{14}C-age of 44,000 years (upper limit of the method) was obtained (M.A. Gey, 1977, personal communication) from charcoal samples of tuffs underlying the Plaidter Hummerich lavas. This volcano and the underlying Kollert volcano can therefore be appreciably older than 44,000 y. B.P.

H. Kohnen, Münster

Received November 21, 1978; Accepted January 25, 1979

J. Geophys. 45, 233, 1979

Journal of Geophysics

Book Review

Max Wyss (ed.): Earthquake Prediction and Rock Mechanics, Contributions to Current Research in Geophysics. Vol. 1. Basel – Stuttgart: Birkhäuser 1975. 330 Seiten. Gebunden DM 78,–. ISBN 3-7643-0809-5

Die Reihe "Contributions to Current Research in Geophysics" bringt Originalarbeiten aus einem jeweils eng umrissenen Teilgebiet der Geophysik in Buchform heraus. Der erste Band befaßt sich mit dem Themenkomplex Erdbebenvorhersage und Gesteinsmechanik. Der Herausgeber, Professor Max Wyss (Univ. of Colorado/USA), der selbst internationales Ansehen auf dem Gebiet der Erdbebenvorhersage genießt, hat in diesem Band 28 Originalpublikationen zusammengestellt, die sich mit folgenden Themen befassen:

- Feldmessungen vor einem Erdbeben
- Labormessungen von Materialeigenschaften
- Modellvorstellungen zur Erklärung von Erdbeben-Vorwarneffekten.

Die Verfasser arbeiten vorwiegend an Instituten in den USA, es sind aber auch einige Beiträge aus der UdSSR, aus Japan und Westdeutschland enthalten.

Der Band enthält – wie es leider bei solchen Sammlungen von Originalveröffentlichungen üblich ist – keine verbindenden Texte zwischen den einzelnen Arbeiten oder zwischen größeren Themengruppen. Besonders stört es aber, daß auch kein einführendes Vorwort existiert.

In der obigen Reihe ist inzwischen als Nr. 6 ein weiterer Band zu ähnlichen Fragen unter dem Titel "Rock Friction and Earthquake Prediction" erschienen. **R. Vees, Clausthal-Zellerfeld**

Sixth Annual Meeting of the European Geophysical Society

Vienna, Austria, September 11-14, 1979

Call for Papers

Deadline for Abstracts
June 1, 1979

The European Geophysical Society (EGS) will hold its Sixth Annual Meeting at the Technical University of Vienna (TU Wien) September 11-14, 1979. The meeting will be devoted to all areas embraced by the EGS:

- Solid Earth
- Hydrosphere
- Atmosphere
- Magnetosphere
- Interplanetary Space, Moon, and Planets

The meeting will have an open character, thus providing an interdisciplinary forum in Europe for all scientists working in the above fields. It will be devoted to the special symposia as well as to sessions on the basis of the abstracts submitted. In this way the European Geophysical Community can define itself and shape its own meeting. 'The Council of the EGS' especially invites papers giving latest results, including reports by students on their thesis work. Poster sessions can also be arranged.

For further information: Sixth EGS Meeting, c/o Institut für Meteorologie und Geophysik, Universität Wien, Hohe Warte 38, A-1190 Wien, Austria. Tel.: (0222) 36 44 53-237.

J. Geophys. 45, 235–257, 1979

Journal of Geophysics

Original Investigations

Partial Self-Reversal of Natural Remanent Magnetization of an Historical Lava Flow of Mt. Etna (Sicily)*

F. Heller[1], H. Markert[2], and E. Schmidbauer[3]

[1] Institut für Geophysik, ETH Zürich, CH-8093 Zürich, Switzerland
[2] Physikalisches Institut, Universität Bayreuth, D-8580 Bayreuth, Federal Republic of Germany
[3] Institut für Allgemeine und Angewandte Geophysik, Universität München, D-8000 München 2, Federal Republic of Germany

Abstract. Three historical lava flows of Mt. Etna (Sicily) have been sampled. Various rock magnetic parameters as well as microchemical and Mössbauer characteristics have been investigated. The natural remanent magnetization (NRM) of one lava flow shows partial self-reversal upon heat treatment. As two different magnetic phases have been identified in this flow, it is suggested that negative magnetostatic interaction causes the observed self-reversal of NRM.

Key words: Rock magnetism – Continental basalts – NRM – Self-reversal.

1. Introduction

The discovery of reversed polarity of natural remanent magnetization (NRM) of rocks was one of the early findings in palaeomagnetism. Reversals of the geomagnetic field or self-reversal mechanisms such as those suggested by Néel (1955) may cause the reversed polarities of NRM observed in the course of many palaeomagnetic investigations. Nowadays field reversals are generally accepted to be responsible for the vast majority of reversed NRM directions. Nevertheless some examples of self-reversal of NRM have been reported: for instance the self-reversing Haruna dacite (Nagata et al., 1952), certain oceanic basalts studied by Ozima and Ozima (1967) and Sasajima and Nishida (1974) and more recently a fragment of continental basalt investigated by Schult (1976). Furthermore it has been shown by several authors (Havard and Lewis, 1965; Creer et al., 1970; Creer and Petersen, 1969) investigating continental basalts which contain titanium-rich homogeneous titanomagnetites that an artificial thermoremanent magnetization (TRM) produced during moderate heat treatment in the laboratory can acquire self-reversal or at least partial self-reversal characteristics at room temperature.

* Institut für Geophysik, ETH Zürich, Contribution no. 240

0340-062X/79/0045/0235/$04.60

Self-reversals can be classified into three categories according to different physical mechanisms: (1) A one-constituent model in which the direction of spontaneous magnetization J_s changes sign at a certain temperature. This behaviour is found in Néel's *P*- or *N*-type ferrimagnets because of the different temperature dependence of the antiparallel sublattice magnetizations. (2) A two-constituent model in which exchange interaction across the boundary of two magnetic phases plays the essential role. This is thought to be the mechanism in the self-reversing compositional range of the ilmenite-haematite solid solution series (Hoffmann, 1975). (3) A two-constituent model in which magnetostatic interaction between two phases leads to complete or partial self-reversal of remanence. This mechanism has been invoked for the TRM reversal found by Creer et al. (1970).

There is also a type of apparent partial self-reversal which was detected in experiments on oxidized titanomagnetite by Petherbridge et al. (1974) and Rahman and Parry (1975). This type has been interpreted theoretically by Stephenson (1975) in terms of screening of the magnetization of a high Curie point phase by a surrounding host material with lower Curie temperature.

This paper deals with observations on partial self-reversal of natural remanent magnetization found in recent lavas of Mt. Etna. Continuous thermal demagnetization of NRM, field dependence of TRM and IRM, $J_s(T)$ behaviour, microprobe analysis and Mössbauer studies together with routine palaeomagnetic investigations have been carried out in order to investigate the reversal mechanism of these basalts.

2. Sampling Sites, Ore Microscopic Observations and Fundamental Rockmagnetic Data

Three historical lava flows of Mt. Etna originating from the eruptions in 1329, 1669, and 1971 have been sampled. The lava flow of 1329 was drilled near Stazzo (geogr. coord.: Lat. 37°35′ N, Long. 15°11′ E) where the flow now dips into the Mediterranean sea. Samples were taken along a vertical profile of 2 m depth from the top surface of the flow. The samples of the 1669 eruption were drilled in a quarry about 1 km to the west of Nicolosi (geogr. coord.: Lat. 37°36′ N, Long. 15°00′ E). This quarry is situated closely to the former eruption point of the flow. Two profiles A and B on either side of the quarry were drilled, profile A reaching a depth of about 3 m from the top of the lava surface. The specimens of the 1971 lava were obtained from two roughly oriented hand samples taken along the road about 1 km to the north of Fornazzo (geogr. coord.: Lat. 37°44′ N, Long. 15°05′ E).

Microscopic observation reveals a fairly uniform magnetic ore mineralogy throughout the three lavas. The only highly reflecting mineral to be found is titanomagnetite of various grain sizes. The titanomagnetites of the 1329 and 1971 lavas are optically homogeneous (oxidation class I according to Ade-Hall et al., 1968) showing only in very rare cases oxidation features along cracks in the larger grains; a few grains appear to be strongly oxidized and may be titanohaematite. The visible grain size distribution is different in both lavas. The 1971 lava contains two fractions: a very high percentage of the grains

consist of euhedral to subeuhedral, sharply edged small grains whose size reaches up to 5 μm. A smaller fraction of larger grains usually covers a size distribution between 250 μm and 500 μm. They are rounded or even corroded. The smaller grains of the 1329 lava have a size frequency maximum around 20 μm and very small grains below 5 μm diameter are very seldom. In the 1669 lava homogeneous titanomagnetites also prevail, but about 5 percent of the ore grains have a bluish-grey tint which is seen in high magnification observation to be caused by granulation of the surface. This indicates partial oxidation to titanomaghemite and perhaps further to Ti-poor magnetite (see Sect. 4.2). The grain size distribution has a frequency maximum between 20 μm and 50 μm. Larger grains are also observed with size and appearance like in the other two flows.

Some fundamental rock magnetic data of the 1329 and 1669 lavas, such as initial susceptibility and the direction and intensity of NRM before and after AF-cleaning, are given in Fig. 1 and Table 1. The variation of these parameters with depth along the drilled sections has been plotted in Fig. 1 together

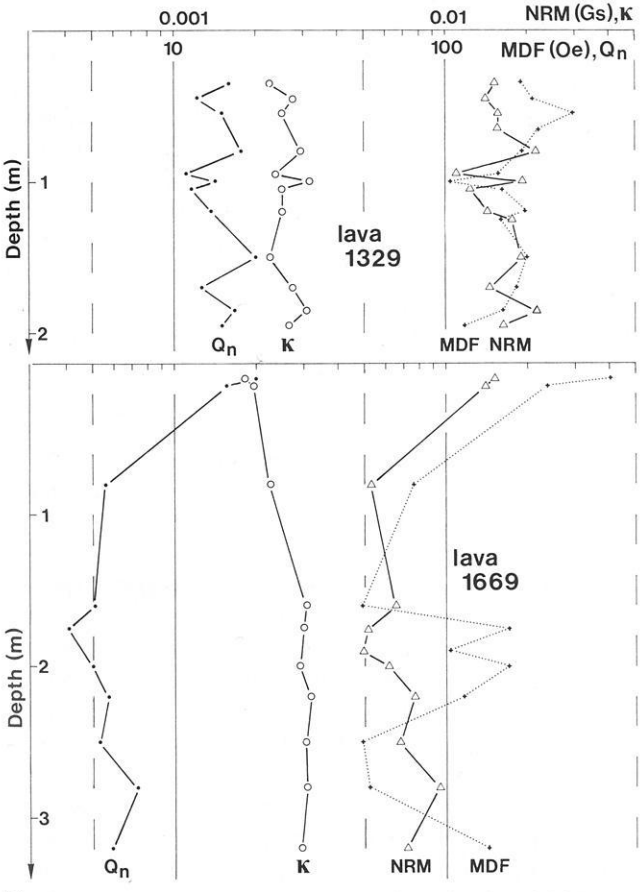

Fig. 1. Semilogarithmic plot of NRM before cleaning, initial susceptibility κ, median destructive field MDF and Koenigsberger ratio Q_n as a function of distance from the top surface of the lavas 1329 and 1669

Table 1. NRM mean directions and intensities before (D_o, I_o, NRM_o) and after optimum AF cleaning (D_{opt}, I_{opt}) with intensity standard deviation (σ) and 95% circle of confidence (α_{95}) of the lava flows 1329 and 1669. n = number of samples, κ = mean initial susceptibility, Q_n = Koenigsberger factor mean

Lava flow	n	NRM_o (Gs)	σ (%)	D_o	I_o	α_{95}	D_{opt}	I_{opt}	α_{95}	κ (emu)	σ (%)	Q_n
1329	15	1.66E-02	±28	106.3	76.5	9.5	2.2	64.5	2.5	2.59E-03	±14	15.2
1669	16	7.48E-03	±42	12.9	29.9	25.0	359.4	57.7	4.2	2.68E-03	±17	6.6

with the variation of the Koenigsberger ratio Q_n and the median destructive field MDF which denotes the AF peak amplitude necessary to reduce the NRM intensity to 50% of its initial value.

In contrast to the findings of Tanguy (1970) the distribution of NRM directions before AF cleaning is appreciably scattered (Fig. 2). This is especially true for the lava flow 1669 which according to Tanguy should display extremely low NRM scatter. The different NRM scatter results possibly from a difference in the technique of sample extraction. Tanguy took oriented hand samples without any drilling and cutting. He measured his rock fragments using Thellier's (1967) big sample spinner magnetometer. Our samples always were drilled and cut into cylindrical specimen shape. Although we have used different equipment (electrical and gasoline powered machines) for that purpose, nearly all specimens possess secondary magnetization components. Magnetic stray fields eventually originating from electrical apparatus have been measured. They are smaller than the Earth's magnetic field and probably do not produce the observed secondary magnetization. Perhaps mechanical forces applied during the drilling and cutting procedure may change the magnetostrictive strain energy of the samples in the presence of the geomagnetic field. Thus a soft secondary magnetization having an arbitrary direction with respect to the present Earth's field may have been acquired.

The secondary magnetization components can be erased by AF-cleaning (optimum fields vary between 120 Oe and 240 Oe) so that well grouped NRM mean directions are obtained in the lava flows (Table 1). Nevertheless the cleaned NRM directions of the lava 1669 still show a systematic scatter (cf. Fig. 2). Samples taken from profile *A* differ significantly in inclination from samples taken from profile *B* at the other side of the quarry. Mechanically unstable tuffs and ashes underly the flow and may be responsible for later attitude changes and post-magnetization displacement of certain parts of the outcrop. Our mean directions of 1329 and 1669 (Table 1) differ slightly from Tanguy's (1970) values. They fit only marginally to the secular variation curves for Sicily published so far (Chevallier, 1925; Tanguy, 1970) which however are based on uncleaned NRM results.

The within site scatter of NRM intensity, initial susceptibility κ, Koenigsberger ratio and MDF values, as demonstrated in Table 1 and Fig. 1, is small for the lava originating from 1329. On the other hand these parameters clearly show a strong dependence on the position within the section in the 1669 basalt flow. Here the two uppermost samples have high initial NRM intensity (com-

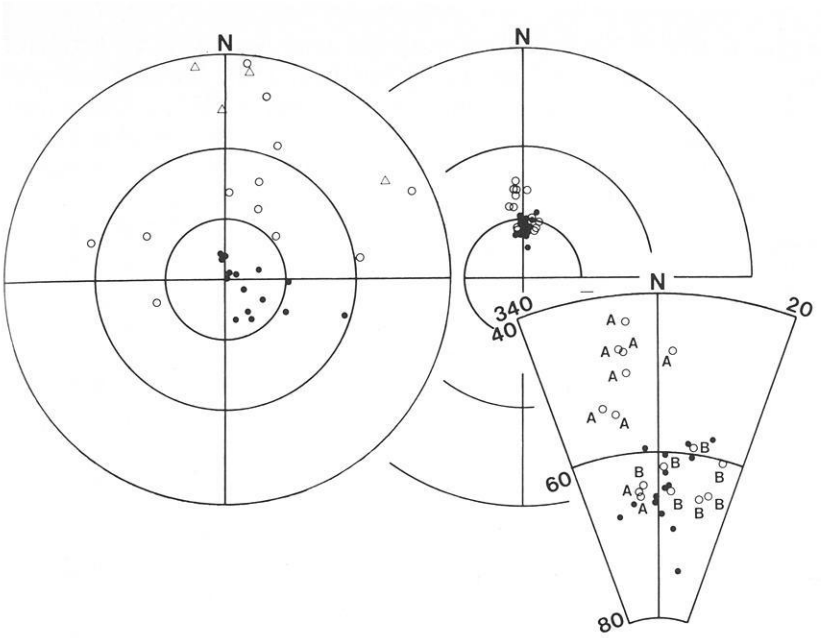

Fig. 2. Equal area projection of NRM directions before (*left side*) and after optimum AF cleaning (*right side*). *Triangles* indicate projection on upper hemisphere, *circles* and *dots* indicate projection on lower hemisphere. *Open symbols* refer to NRM directions of lava 1669, *dots* represent NRM directions of lava 1329. Circles plotted on the enlarged section and denoted with *A* or *B* refer to samples collected from the flow 1669 along profile *A* or *B* respectively

pared to the rest of the section), high MDF values (up to 400 Oe) and slightly reduced susceptibility. This is probably due to oxidation occurring in the uppermost, very porous part of the lava. The main difference between the two sections 1329 and 1669 is given by the lower NRM intensity of the 1669 lava. As susceptibility and visible ore grain size distribution in both profiles are very similar, the NRM difference seems to be quite remarkable and may be caused by partial self-reversal of NRM found in the 1669 basalt (see Sect. 3.1).

3. Thermomagnetic Measurements

3.1. Continuous Thermal Demagnetization of NRM

Heiniger and Heller (1976) developed a magnetometer system which allows spinner magnetometer measurements to be performed throughout a wide temperature range between $-200°$ C and 700° C. The NRM vector can be measured continuously in zero field as a function of temperature down to intensities of about 1×10^{-6} Gs. The continuous thermal demagnetization of Mt. Etna basalts yielded the following results.

At first the original uncleaned NRM of some representative samples taken from the three lavas was investigated (Fig. 3). The resulting vector plots indicate

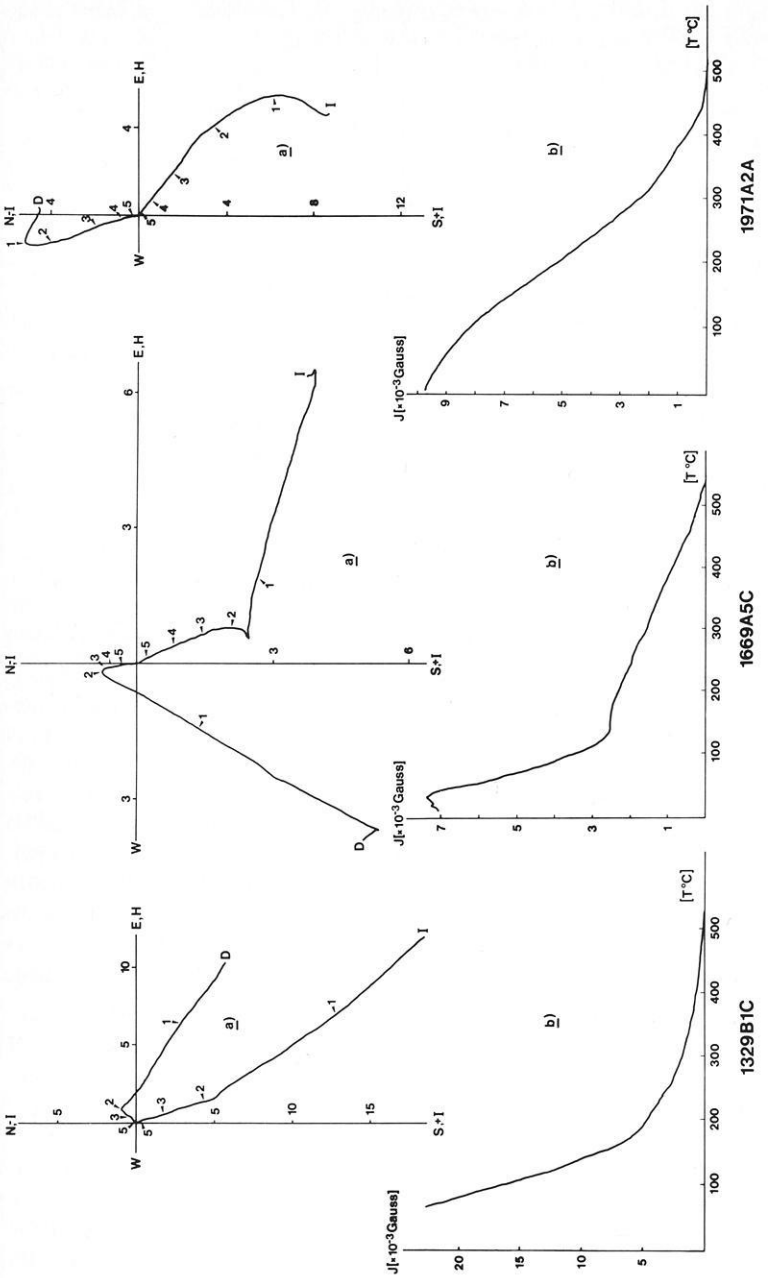

Fig. 3. Continuous thermal demagnetization of NRM of three samples taken from the 1329, 1669, 1971 lavas respectively. The vector diagrams (scale unit: 1 mG) show declination and inclination as function of temperature. The numbers 1–5 along each curve indicate the temperature $T/100°$ C. Heating rate in all experiments: 10° C/min. Thermal demagnetization always done in zero field and under normal air pressure

the presence of rather strong unstable secondary NRM components which are removed between 200° C and 300° C, whereas stable components remain up to temperatures around 500° C. The stable components are aligned parallel to the expected direction of the historical geomagnetic field. They possess northerly declinations and relatively steep inclinations (cf. Fig. 3). The unstable components are up to four times as strong as the stable components residing in phases with high Curie points.

The curves which represent the change of NRM intensity with increasing temperature [($J(T)$-curves], generally show a regular intensity decay. This applies especially to samples originating from the 1329 and 1971 lavas. A conspicuous qualitative difference is observed in the $J(T)$ curves of the 1669 lava, namely the development of a level of constant intensity and even a very slight intensity increase between temperatures of 140° C and 180° C. Secondly the uppermost blocking temperatures of the 1669 samples are distinctly higher (around 550° C) than those of the other two flows (ca. 500° C).

As the secondary NRM components present in our samples obscure the behaviour of the stable components during thermal demagnetization below 200° C to 300° C, some samples from all three basalts were subjected to partial AF demagnetization. The maximum field amplitude (between 60 Oe and 90 Oe) was chosen so that the secondary components just had been removed. After this cleaning procedure the samples were continuously demagnetized by heating in air. Fig. 4 demonstrates the resulting demagnetization plots.

Since any directional changes during heating are absent in all three vector plots, we conclude that secondary components have been successfully removed by the preceding AF cleaning. The NRM intensity curves of 1329 and 1971 samples decrease monotonously with increasing temperature and remanent magnetism with normal polarity, i.e., parallel to the present earth's field disappears at maximum blocking temperatures around 500° C. Up to 200° C the intensity of the 1329 sample is much more rapidly reduced than that of the 1971 sample. The NRM intensity of the 1669 sample shows up to 200° C very unusual behaviour: at first up to about 140° C there is only very little change in intensity, then up to 180° C a sharp intensity increase by ca. 11% which is followed by a continuous intensity loss with increasing temperature. From the corresponding vector plot it can be seen that the intensity increase is caused apparently by a magnetization component which is antiparallel or reversed with respect to the normal magnetization direction at temperatures above 180° C. The highest blocking temperatures are reached at around 550° C.

The 1669 sample appears to be partially self-reversed with a dominant high Curie point magnetization of normal polarity. This partial self-reversal is an intrinsic property of all 1669 samples and can be reestablished by thermal cycling of NRM above and below 200° C in zero field. Prior to the process of thermal cycling, another 1669 sample was cleaned by AC fields to remove secondary NRM components. As can be seen from Fig. 5, the first cooling and reheating cycle in zero field develops a stronger reversed component than the original NRM showed at first. When the original NRM had been acquired, the geomagnetic field was present during the whole cooling process thus acting against the reversal mechanism below 200° C. Also, as we will see later, some chemical

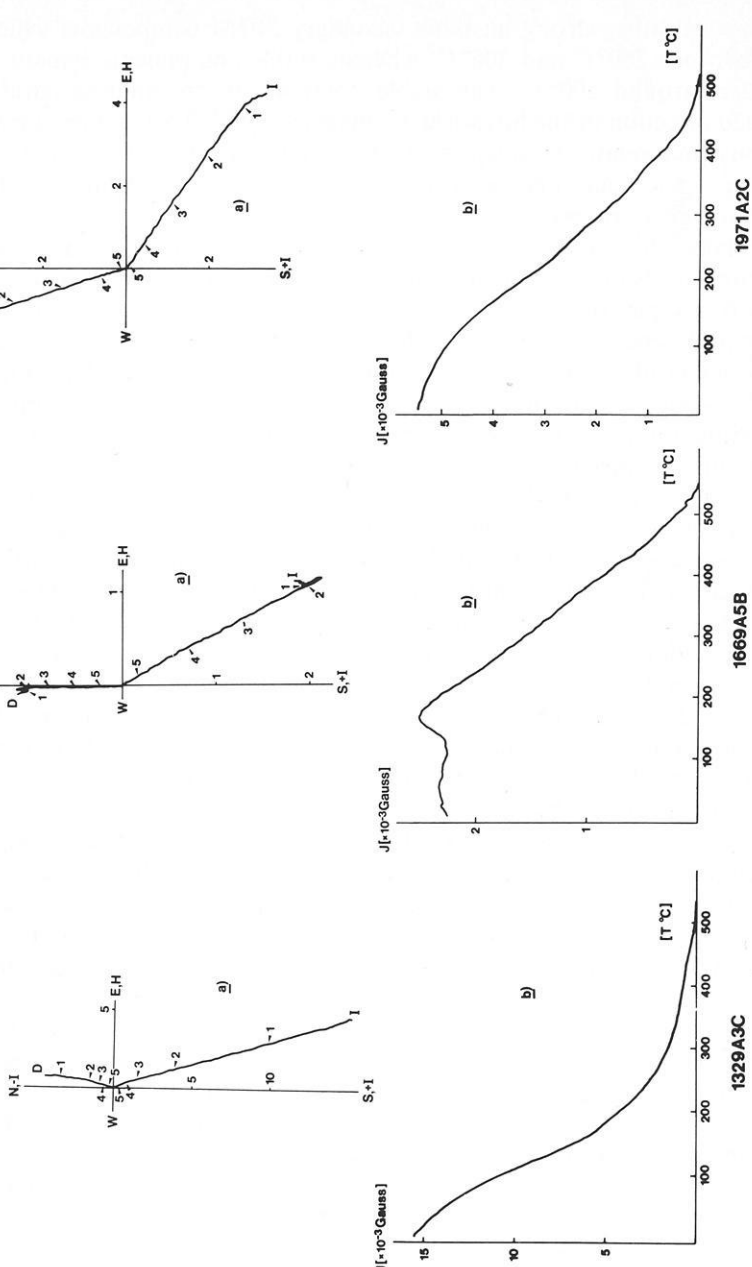

Fig. 4. Continuous thermal demagnetization of *AF* cleaned NRM, the *AC* field amplitude just high enough to remove secondary magnetization components. Scale units and signatures as in Fig. 3

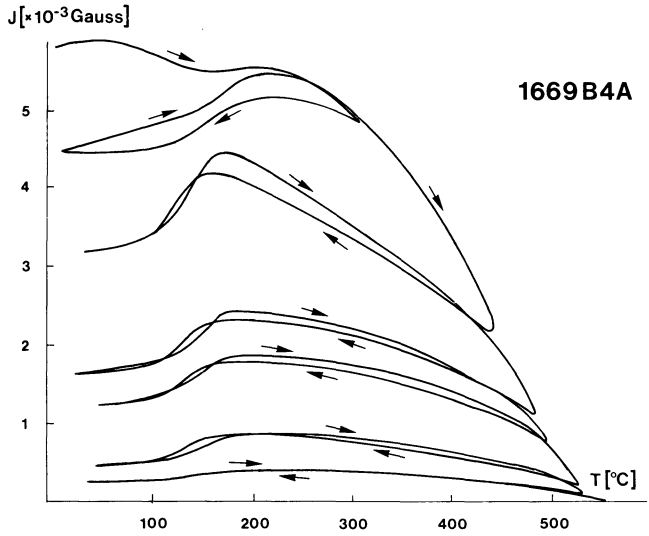

Fig. 5. Repeated heating and cooling cycles (*thermal cycling*) of *AF* cleaned NRM of a 1669 sample which shows partial self-reversal. During each cycle the maximum temperature has been progressively increased

changes may take place during re-heating. They may affect especially any titanomaghemite phases present. Extrapolating the intensity of the higher Curie point component down to room temperature in the second cooling cycle it can be estimated that the intensity of the apparently reversed component comes roughly to one third of the normal component at room temperature. Repeated cycling with progressively increased maximum temperature lowers the absolute intensities of both magnetization components thus suggesting that the reversed component is closely connected to the intensity (and hence the field) of the normal component. An apparent decrease of the lower Curie point by as much as 80° C is also observed. The onset of the reversal gets much more distinct in the second and later cycles where the temperature had been raised above 400° C. Assuming no alteration of the high Curie temperature phase during thermal cycling, it is evident from Fig. 5 that about three quarters of the stable normal NRM are blocked in the temperature interval ranging from 450° C to 550° C.

3.2. Saturation Magnetization

In order to determine type and compositional range of the magnetic phases present in the three lavas, saturation magnetization has been measured as a function of temperature. An automatically recording translation balance has been used. The results obtained by measuring pulverized samples in air (size fraction: 1 mm∅) with an applied field $H=1.7$ kOe have been plotted in Fig. 6.

The magnetization of the 1971 lava is nearly reversible upon heating and cooling and a distinct Curie point is indicated around $T_c=240°$ C. A component

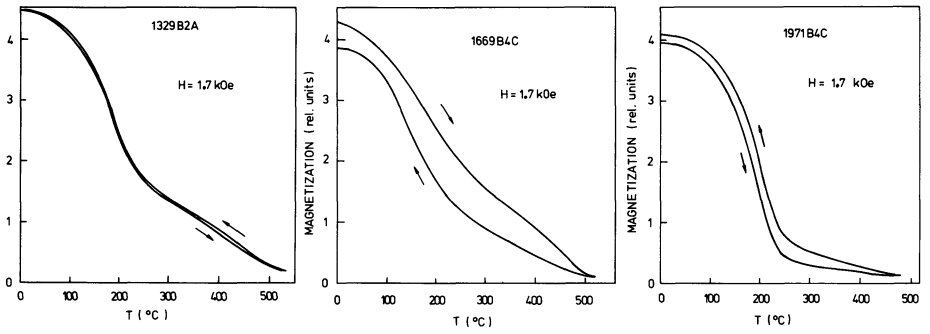

Fig. 6. $J_s(T)$ curves of three basalt samples of Mt. Etna. Applied field $H=1.7$ kOe. Grain size fraction: ca. 1 mm

of minor importance with a higher Curie temperature is faintly seen during heating. It is more strongly pronounced during the cooling cycle. The slightly higher intensity of magnetization upon cooling is probably due to oxidation and production of a Ti-poor magnetite phase with a Curie temperature around $T_c=500°$ C during heat treatment. The $J_s(T)$ curve seems to contradict the monotonic decay of NRM during continuous thermal demagnetization up to $T=500°$ C (Fig. 4). The different behaviour is possibly due to different heating times, since the oxidation process is time dependent.

The $J_s(T)$ curve of the 1329 lava is reversible during heat treatment. Two distinct Curie points can be recognized: the higher one at $T_c=530°$ C and the lower around $T_c=220°$ C. This is in agreement with the decay of NRM during thermal treatment where the major portion of NRM is lost below 200° C (Fig. 4).

The 1669 lava shows a distinct Curie temperature just above 500° C. Upon heating the $J_s(T)$ curve seems to indicate a broad range of lower Curie temperatures between 200° C and 300° C. $J_s(T)$ is not reversible upon cooling – probably due to oxidation of the Ti-richer phases (Ti-maghemite?) –, but the lower Curie temperature range gets more restricted and a second Curie point may be defined around 225° C.

3.3 Low Temperature Susceptibility

According to Syono (1965) the zero-transition temperature ($T_{K=0}$) of the magneto-crystalline anisotropy constant K_1 of stoichiometric titanomagnetites of general composition $x\mathrm{Fe_2TiO_4}\cdot(1-x)\mathrm{Fe_3O_4}$ depends strongly on the titanium concentration x. This is illustrated in Fig. 7 which also shows the relationship between Curie temperature T_c and ulvospinel content for a wide range of titanomagnetites.

At the temperature $T_{K=0}$ the magneto-crystalline anisotropy energy of a multidomain titanomagnetite grain of given Ti- concentration x becomes minimum. The domain wall energy of the grain becomes minimum, too. Thus the domain wall mobility passes through a maximum at $T_{K=0}$ leading to a susceptibility maximum at that temperature.

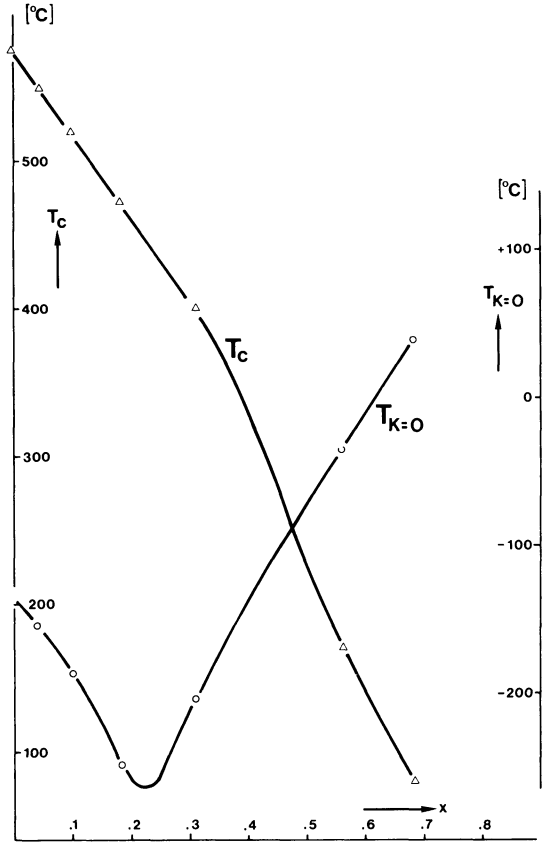

Fig. 7. Curie temperature (T_c) and zero transition temperature ($T_{K=0}$) of the magneto-crystalline anisotropy constant K_1 as a function of composition in the magnetite-ulvospinel solid solution series according to Syono (1965)

If for instance the Ti-content equals $x=0.5$, it follows from Fig. 7 that the Curie temperature amounts to about 225° C, while the anisotropy constant K_1 changes sign at about −83° C. At this temperature the susceptibility passes through a maximum. Therefore throughout a wide compositional range the low temperature dependence of susceptibility can be used to estimate the Ti-content of titanomagnetites. These measurements avoid the danger of oxidation of the material which is always involved in the usual Curie point determination. Figure 7 also shows some practical limitations of the method: (1.) Unambiguous estimates of x can only be obtained for $x>0.4$ since $T_{K=0}$ passes through a minimum at $x=0.22$. (2.) Temperatures below −196° C (liquid nitrogen) can be gained only with special low temperature devices. Thus $T_{K=0}$ of titanomagnetites with composition $0.12 \leqq x \leqq 0.32$ usually cannot be detected.

The $\chi(T)$ measurements below room temperature have been carried out using the Fraunberger resonance bridge described by Markert et al. (1974). At the same time the high frequency losses $\alpha(T)$ which show the same temperature dependence as $\chi(T)$ have been measured. The results for the three lavas are shown in Fig. 8. The overall increase of $\chi(T)$ and $\alpha(T)$ is mainly caused by instrumental drift. The sharpness of the susceptibility and high frequency loss maxima which are superposed in all curves, is conspicuously different for the

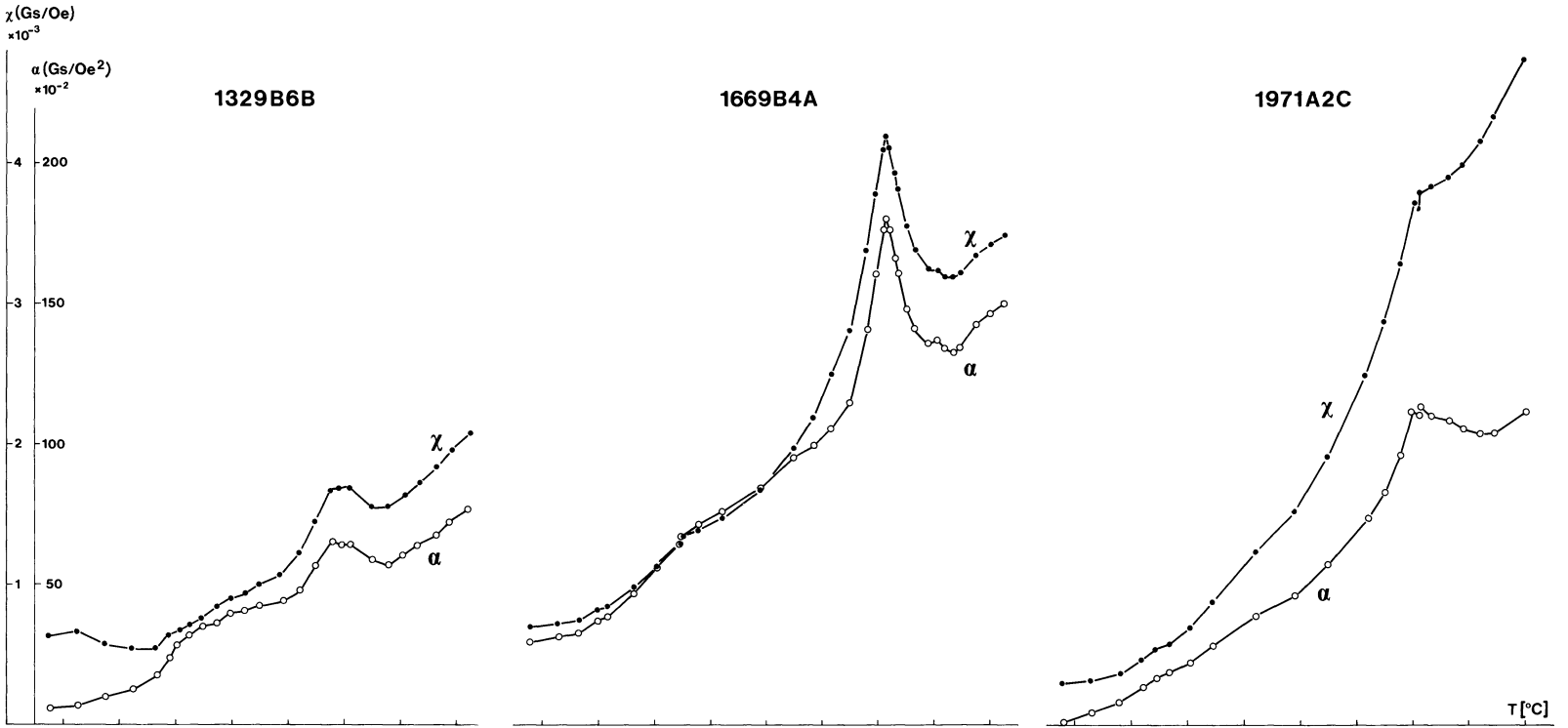

Fig. 8. Low temperature dependence of susceptibility (χ) and high frequency loss (α) in samples taken from the three lava flows

three samples. Only the 1669 sample shows very clear peaks at $T=-45°$ C which may correspond to a very well defined titanomagnetite phase having a Ti-content $x=0.55$. The samples 1329 and 1971 behave as if the titanium concentrations of their Ti-rich magnetite phases are smeared out to some extent. Nevertheless some fairly pronounced peaks can be recognized at $T=-70°$ C corresponding to a composition $x=0.51$ (sample 1329 B6B) and $T=-50°$ C corresponding to $x=0.54$ (sample 1971 A2C). The $\chi(T)$ curves of the lavas originating from 1329 and 1669 have a second, less well developed maximum at lower temperatures. These maxima which are not found in the 1971 lava, indicate the presence of another titanomagnetite phase. The second peak is clearly seen in the 1669 lava around $T=-120°$ C and corresponds to a titanomagnetite with $x=0.43$. The 1329 basalt has a very vaguely indicated second maximum at about $T=-165°$ C which may reflect a phase either with $x=0.36$ or with $x=0.07$.

3.4. Significance of Thermomagnetic Measurements

Out of the three lava flows from Mt. Etna the 1669 lava clearly shows partial self-reversal. The reversed component of NRM is increased by thermal cycling at moderately elevated temperature so that the reversed component makes up to nearly 50% of the normal component. Similar results have been obtained by Creer and Petersen (1969) on laboratory produced TRM of a Rauher Kulm basalt sample. In contrast to the findings of these authors, however, the reversed component of the historical Etna basalt disappears by heating above 200° C and the normal component is held by a phase with a high Curie point around 550° C.

Table 2 summarizes the results of low temperature behaviour of susceptibility and $J_s(T)$ curves including the composition parameter x of stoichiometric titanomagnetites derived by the two methods. Two titanomagnetite phases consistently indicated by both methods are contained in the 1329 lava: the compositions are given with $x=0.51$ and $x=0.07$. For the 1669 basalt the susceptibility curves indicate two phases with $x=0.55$ and $x=0.43$ which may reflect the smeared Curie temperature distributions between 200° C and 300° C in the $J_s(T)$ curves. The higher Curie temperature at $T_c=510°$ C is attributed to a titanomagnetite with $x=0.12$. This phase could not be proved in the $\chi(T)$ curves, since $T_{K=0}$ is below $-170°$ C the lowest temperature which could be achieved during low

Table 2. In the three lavas observed susceptibility maxima ($T_{K=0}$) with corresponding Curie temperature (T_{cs}) and composition parameter x_{cs} according to Syono (1965) and directly measured Curie temperatures (T_{cm}) with corresponding composition parameter x_{cm}

Lava flow	$T_{K=0}$ (° C)	Corresp. x_{cs}	T_{cs} (° C)	T_{cm} (° C)	Corresp. x_{cm}
1329	−70, −165	0.51, 0.36 or 0.07	215, 530	220, 530	0.51, 0.07
1669	−45, −120	0.55, 0.43	185, 305	200–300, 510	0.4–0.5, 0.12
1971	−55	0.52	200	240	0.48

temperature measurements. The composition of the titanomagnetite in the 1971 lava is equally well determined by both methods and gives a mean value of $x=0.50$.

When comparing the results of $J_s(T)$ and $\chi(T)$ measurements it is found that the $\chi(T)$ method, although certainly limited for the determination of titanomagnetite compositions, in many cases may work as an important tool for the rock magnetist. As demonstrated by the 1669 sample the method may be especially helpful when dealing with $J_s(T)$ curves which indicate Curie temperatures apparently not sharply defined.

The different phases in the 1329 and 1669 lavas must be caused by oxidation and exsolution before laboratory heating. Prolonged heat treatment during continuous thermal demagnetization therefore alters only the unoxidized titanomagnetite of the 1971 lava, and maximum blocking temperatures are reached around 500° C although the original Curie temperature was found around 240° C. The macroscopically high porosity of this flow also may favour rapid oxidation during thermal demagnetization. The magnetic phases in the 1329 and 1669 basalts are more stable against heating due to low rock porosity and previous oxidation, thus allowing thermal cycling without major chemical changes. Only the 1669 titanomaghemite phase gets oxidized so that the partial self-reversal becomes more pronounced and shifted to lower temperatures during heat treatment. Petersen and Bleil (1973) have shown that self-reversal in synthetic titanomagnetite occurs at a critical state of oxidation caused by heating in air. This oxidation state seems to have been achieved naturally by the 1669 lava.

4. Microchemical and Mössbauer Analysis

4.1. Microprobe Analysis

Three optically homogeneous titanomagnetite grains of variable size from each lava have been analyzed. Readings were taken along profiles across the polished surface of the grains and analyzed for Fe, Ti, Al, Mg, and Cr. Some of the profiles have been plotted in Fig. 9.

Table 3 contains the average weight percentage of cations analyzed in each grain with the respective standard deviation. Using Gidskehaug's (1975) program the composition parameter x has been calculated assuming stoichiometric titanomagnetite together with the equivalent Curie point T_{cx}. Following Richards et al. (1973) the influence of the 'impurity' cations Al and Mg on depressing the Curie temperature has been taken into account. This Curie point is denoted with $T_{c\delta}$. Also the oxidation parameter z has been evaluated following the method proposed by the latter authors. For the grains which show two measurable Curie points, this has been done by assuming that the chemical analysis reflects the composition of the lower Curie point phase rather than that of the high Curie point phase.

A relatively high 'impurity' content of Al and Mg is recognized in all grains. Thus the estimated Curie point $T_{c\delta}$ of the substituted stoichiometric

Table 3. Microprobe analysis of three titanomagnetite grains of each lava sampled. Elements analyzed: Ti,Fe,Cr,Al,Mg. x=resulting composition parameter in the magnetite-ulvospinel solid solution series. T_{cx}=Curie temperature resulting from x. T_c=Curie temperature depressed by Al and Mg according to Richards et al. (1973). z=oxidation parameter calculated following Richards et al. (1973). n=number of observation points

Flow year	Grain	Size (μm)	n	Ti (wt %)	Fe (wt %)	Cr (wt %)	Al (wt %)	Mg (wt %)	Sum (wt %)	x	T_{cx} (° C)	$T_{c\delta}$ (° C)	z
1329	A3BA	90	10	9.47±0.06	55.71±0.30	0.33±0.06	2.13±0.06	2.42±0.11	70.07±0.33	0.43	264	143	0.4
	A3BB	140	8	9.45±0.30	55.64±0.32	0.36±0.18	2.07±0.16	2.12±0.31	69.64±0.31	0.43	261	147	0.4
	A3BC	150	8	9.01±0.17	56.00±0.10	0.02±0.03	2.39±0.15	2.48±0.20	69.90±0.26	0.41	279	146	0.4
1669	B4BA	600	7	7.62±0.69	56.45±0.47	0.11±0.02	3.27±0.20	2.84±0.54	70.29±0.28	0.34	331	156	0.0, 0.9
	B4BB	200	11	8.04±0.92	56.65±0.48	0.38±0.08	3.08±0.34	1.83±0.21	69.99±0.39	0.37	311	155	0.0, 0.9
	B4BC	120	7	8.77±0.43	56.23±0.28	0.36±0.03	2.91±0.21	1.75±0.11	70.02±0.30	0.40	286	140	0.0, 0.9
1971	A3AA	240	7	7.37±0.35	56.02±0.46	0.06±0.01	3.06±0.13	3.45±0.30	69.95±0.23	0.33	339	166	0.0
	A3AB	100	6	6.70±0.11	56.55±0.18	0.06±0.01	3.18±0.09	3.25±0.12	69.73±0.23	0.30	360	184	0.0
	A3AC	90	7	6.56±0.10	56.45±0.19	0.07±0.03	3.28±0.06	3.27±0.16	69.65±0.25	0.29	364	184	0.0

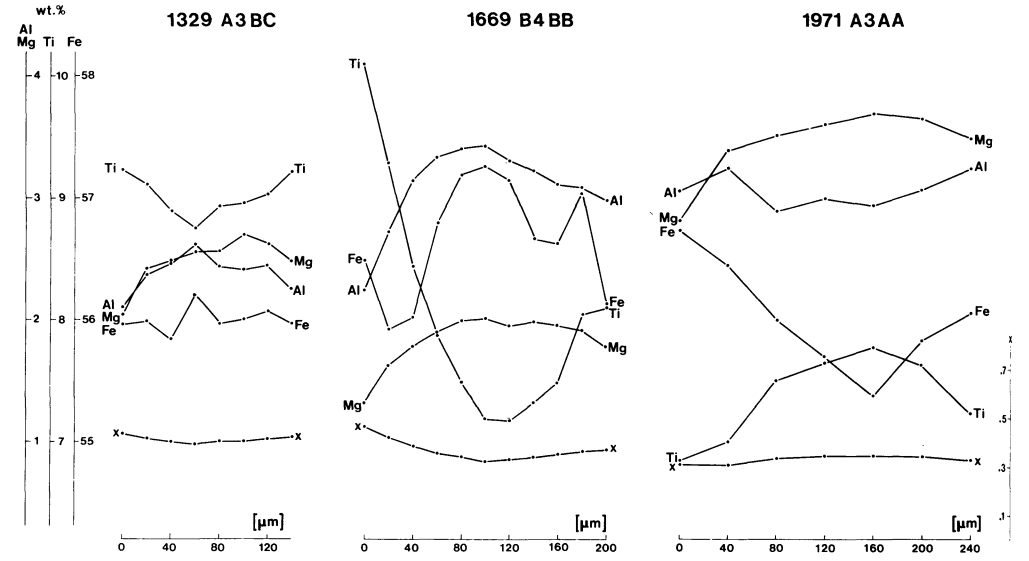

Fig. 9. Microchemical analysis of Fe, Ti, Mg, Al concentration and corresponding x value of the series $x \cdot Fe_2TiO_4(1\text{-}x)Fe_3O_4$ as a function of distance in grains selected from the three lavas. All profiles cross the grains from one margin to the other

titanomagnetite $Fe_{3-x-\delta}$ (Al, Mg) $_\delta Ti_xO_4$ is depressed by up to 180° C compared to T_{cx} of pure titanomagnetite, since δ averages 0.22 for each of both impurity elements. The measured Curie temperatures T_{cm} which range between 200° and 300° C, as well as the Curie temperatures T_{cs} which according to Fig. 7 can be derived from low temperature susceptibility measurements, always fall in between the values which have been calculated for substituted and pure stoichiometric titanomagnetite.

The 1971 lava shows the lowest degree of oxidation (z-parameter $\cong 0.0$) which is indicated by only one measured Curie point and a small difference between $T_{c\delta}$ and T_{cm}. The Ti- content is low and therefore the calculated x value is at $x=0.3$ only; Al and Mg show the highest concentrations of all three lavas. The 1329 lava is fairly oxidized. We have measured two distinct Curie points (Fig. 6) and the oxidation parameter equals $z \cong 0.4$. Most complicated is the situation for the 1669 basalt. The homogeneity of cation distribution of the two mayor elements Ti and Fe as indicated by the standard deviation is definitely less uniform than in the other lavas. The Curie points as measured in the $J_s(T)$ curves seem to be smeared out between 200° C and 300° C. Taking the T_{cs} values as representative for the lower Curie point phases one is forced to conclude that one of these phases is strongly oxidized ($z \cong 0.9$ for $T_{cs}=305°$ C) and the other phase not ($z \cong 0.0$ for $T_{cs}=185°$ C). The high Curie point phase obviously cannot be resolved by microchemical analysis perhaps due to very fine grain size or intergrowth with the titanomaghemite phase.

The inhomogeneous cation distribution in the 1669 titanomagnetite grains is more clearly observed in Fig. 9 and depends on the position in the grains.

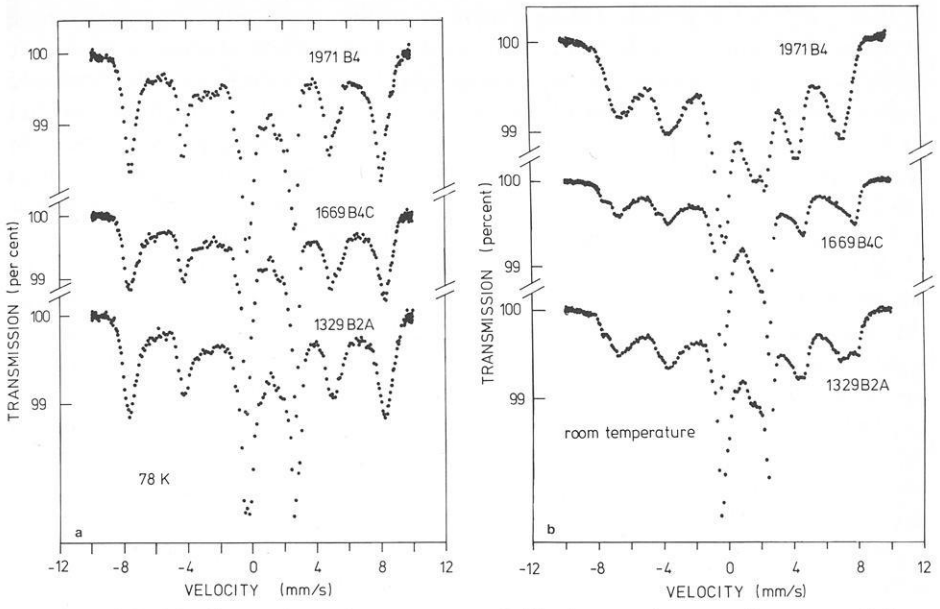

Fig. 10a and b. Mössbauer absorption spectra on Fe^{57} of magnetic ore grains extracted from three basalt samples. **a** Temperature: 78 K. **b** Room temperature

Thus the Ti-content of the 1669 grains increases by about 50% towards the grain margin, whereas Al and Mg increase towards the grain centre where their concentration is about 50% higher than at the margins. For iron the concentration-distance relationship is not so well developed. Looking at the grains of the 1329 lava we find the same relations for the cations analyzed, but not as pronounced as in the former case. The grain which is representative for the 1971 titanomagnetites, shows the opposite concentration-distance relations for Ti and Al, whereas Mg again is enriched towards the grain centre. In general we see that the changes in cation concentration are most pronounced in the 1669 samples.

4.2. Mössbauer Absorption Spectra

Mössbauer absorption spectra on Fe^{57} have been taken at room temperature and $-195°$ C on ore grains extracted from pulverized samples by a bar magnet. A description of the Mössbauer instrumentation will be given elsewhere.

The spectra from the three basalts are presented in Fig. 10. Any information about the ferrimagnetic ore can be deduced merely from the outer parts of the spectra in the positive and negative velocity ranges, as in the centre of the spectra the dominant contribution arises from diamagnetic and/or paramagnetic mineral phases of the rock matrix due to a non complete separation of the ore minerals.

At −195° C, a six-line sub-spectrum is visible from Fig. 10a in all three samples. The inner two lines of each six-line field are contained in the rock matrix contribution of the centre of the spectra. Line broadening and asymmetric lines indicate a superposition of two six-line patterns which might be created by two distinct phases. From the spectra the internal magnetic hyperfine field H_{int} at the site of a Fe nucleus can be derived. The spectra are not well enough resolved to allow a reliable determination of the isomer shift IS and the quadrupole splitting QS [by least squares computer fit (Wertheim, 1964)].

Room temperature absorption spectra (Fig. 10b) reveal more clearly the existence of two overlapping subspectra for the 1669 and 1329 samples, although the lines appear to be broad. The outermost lines of the respective spectra consist of two lines in the negative and positive velocity ranges, whereas in the case of the 1971 sample one broad peak is observed.

$J_s(T)$ curves have shown that the ore grains of 1669 and 1329 exhibit at least two Curie points each, whereas the 1971 sample has one Curie point and, hence one ferrimagnetic phase. These findings are in accordance with the Mössbauer data. We assign the patterns with the larger internal magnetic hyperfine field H_{int} to phases with the higher Curie temperatures. The broad lines reflect the fact that there is a certain range of Curie points. Our assignment accounts also correctly for the intensity relations. $J_s(T)$ and NRM continuous thermal demagnetization curves for 1329 samples show the phase with the lower Curie temperature to be dominant, whereas the phase with the higher Curie temperature seems to prevail in the 1669 basalt.

A ferrimagnetic titanomagnetite phase with a Curie point $T_c > 500°$ C gives, similar to Fe_3O_4, at room temperature a Mössbauer absorption spectrum with the outermost line in the negative velocity range clearly split into two distinct lines. The latter arise from Fe ions on tetrahedral (A) and octahedral (B) sites. Thus two values of H_{int} can be deduced, the lower one arising from the mixture of Fe^{2+} and Fe^{3+} on B-sites of the spinel lattice. This situation appears to exist for the 1669 sample concerning the dominating phase. From the asymmetry of the outermost lines a second phase with a smaller H_{int} can be suggested.

The values of H_{int} taken from the spectra of all samples are listed in Table 4.

Table 4. Magnetic hyperfine field H_{int} deduced from the Mössbauer absorption spectra at 20° C and −195° C; also Curie temperatures T_{cm} given as derived from $J_s(T)$ measurements

Sample	T (°C)	$H_{int} \pm 10$ (kOe)				Remarks
		Phase I	T_{cm} (°C)	Phase II	T_{cm} (°C)	
1971 B4	20	431	240	–	–	one phase
	−195	489		–		
1669 B4C	20	< 450	200–300	454(A)[a], 476(B)[a]	510	more than one phase; dominating phase with higher T_c
	−195	< 490		496		
1329 B2A	20	432	220	485	530	more than one phase; dominating phase with low T_c
	−195	495		495		

[a] A and B indicate A sites and B sites of the spinel lattice

5. Discussion

The three Mt. Etna lava flows sampled show very different magnetic properties. $J_s(T)$ curves, Mössbauer spectra and microchemical analysis indicate the presence of several ferromagnetic phases. The 1971 lava contains a single unoxidized titanomagnetite phase with a low Curie point around $T_c = 240°$ C. This titanomagnetite is homogeneous according to microprobe data. Nevertheless maximum blocking temperatures of 500° C have been obtained upon heating of NRM. This indicates a rapid oxidation and production of remanent magnetization above 240° C which directionally is controlled by the magnetization of the original Ti-magnetite. No partial self-reversal has been found in this flow.

Two distinct Ti-magnetite phases have been detected in the 1329 lava using $J_s(T)$ and Mössbauer techniques. A slightly oxidized intermediate titanomagnetite seems to control the magnetic behaviour of the 1329 samples. A higher Curie point titanomagnetite may be concentrated towards the centre of the ore grains where the Ti-content shows a vaguely defined minimum (Fig. 9). Therefore interaction between the two phases which effects the remanence properties cannot be ruled out. In fact some 1329 samples have been found which show anomalous thermal demagnetization curves of NRM (cf. Heiniger and Heller, 1976), but not to the same extent as all the 1669 samples.

Most difficult is the identification of the ferromagnetic material present in the 1669 lava. The asymmetry of the outermost Mössbauer lines suggests more than one titanomagnetite phase to be present. The $J_s(T)$ curves show a titanomagnetite with $T_c = 510°$ C and a smeared range of Curie temperatures between 200–300° C which may be caused by the two phases with $T_c = 305°$ C and $T_c = 185°$ C indicated by low temperature measurement of $\chi(T)$. After heating the strongly oxidized Ti-maghemite with $T_c = 305°$ C disappears in the $J_s(T)$ curve. This may be one of the reasons why the apparent partial self-reversal gets more pronounced after the first heating cycle and the onset of the reversal is shiftet to lower temperatures (Fig. 5).

The partial self-reversal seems to be bound to some kind of interaction between the (unoxidized) titanomagnetite with $T_c = 185°$ C and the Ti-poor magnetite with $T_c = 510°$ C. These two phases occur within one grain – at least in grain sizes which allow microprobe analysis. In these grains the Ti-poor material which carries the normal NRM component is concentrated towards the grain centre (Fig. 9) and surrounded by a Ti-richer phase. We could not prove, if the geometry of this structure is closed or open. There is some microprobe evidence that the Ti-rich outer shell is not fully closed, at least its thickness varies considerably (cf. Fig. 9).

As mentioned in the introduction, there are several theoretical models to explain the observed reversal in the 1669 lava. We exclude single phase models like Néel's *P*-type, because firstly $J_s(T)$ curves do not indicate this (Fig. 6) and secondly we have Mössbauer and microchemical evidence for two magnetic phases. The two-phase models can be divided into three categories: (1) exchange interaction across phase boundaries, (2) magnetic screening and (3) magnetostatic interaction.

The field and temperature dependence of artificial TRM is one possibility to test which two-phase model might apply to the 1669 lava. Figure 11 shows

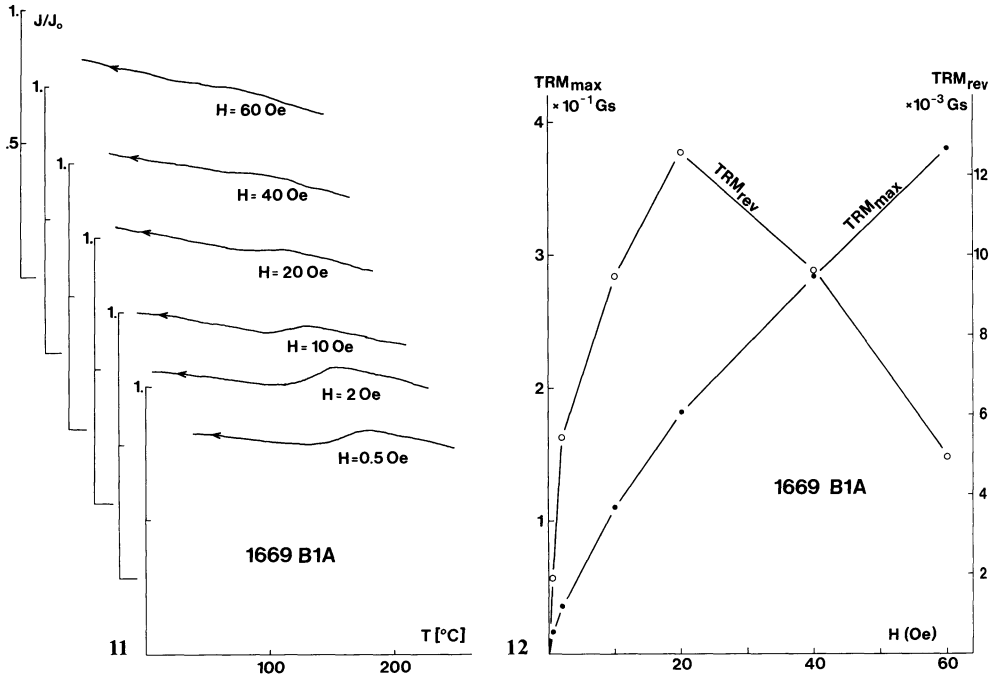

Fig. 11. Cooling cycles of total TRM acquired in dc fields ranging from $H=0.46$ Oe to $H=60$ Oe. TRM has been measured after the sample had been reheated to about 250° C in zero field

Fig. 12. Absolute intensities of total TRM at room temperature (TRM_{max}) and of the reversed TRM component (TRM_{rev}) as a function of the applied field

the resulting assemblage of TRM cooling cycles after the sample had been heated to 600° C and was allowed to cool down to room temperature in various *dc*-fields. The field had been increased step by step after each measuring cycle up to the maximum temperatures (ca. 250° C) indicated in Fig. 11. Clearly the reversal effect becomes reduced with increasing *dc*-field amplitude. Figure 12 indicates the absolute intensities of total TRM after each heating cycle in the applied field together with the absolute amount of the reversed component detected during cooling in zero field. The reversed component increases up to $H_{dc}=20$ Oe and decreases with further increments of the external field so that by extrapolation it would disappear well below 100 Oe.

This field dependency is not to be expected for the exchange interaction model, since the coupling is due to Weiss-Heisenberg forces which result in extremely high interaction fields. Uyeda (1958) found by experiment for the intermediate members of the ilmenite-haematite series interaction fields greater than 500 Oe.

In the model of magnetic screening the magnetization of a high Curie point phase encircled more or less completely by a lower Curie point phase can be shielded magnetically as soon as the lower Curie point is reached upon cooling. Stephen-

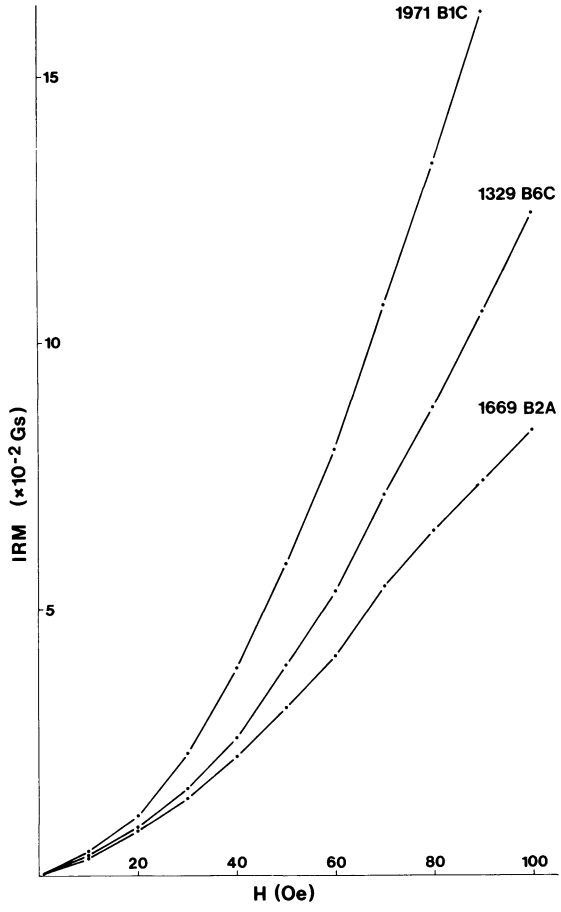

Fig. 13. Isothermal remanence (IRM) acquisition curves of the three lavas of Mt. Etna. Only the 1669 sample shows a distinct inflexion at $H=70$ Oe

son (1975) derived that the screening factor depends only on the relative permeabilities and the demagnetization factors of the two phases. His theory has been backed up experimentally by Rahman and Parry (1975) who found for certain titanomagnetite material a largely field independent screening up to $H_{ex}=$ 135 Oe. Our result is different from their finding and this model does not apply to the 1669 lava, since our partial self-reversal is suppressed certainly below 100 Oe external field.

Therefore magnetostatic interaction remains to explain the partial self-reversal of NRM and laboratory produced TRM in the 1669 Mt. Etna lava. Obviously the negative magnetostatic interaction field reaches a maximum at $H_{ex}=20$ Oe and certainly below 100 Oe the external field overwhelms the negative interaction during TRM acquisition. Negative interaction is also observed during acquisition of isothermal remanence (Fig. 13). The IRM of the 1669 lava sample shows a small inflexion at $H_{ex}=70$ Oe which indicates that this field amplitude is sufficient to suppress the interaction mechanisms.

Certain geometric relations are necessary for the model of negative magnetostatic interaction (for details see Uyeda, 1958, p. 50 ff.). These relations must hold for the majority of ferromagnetic grains in the 1669 lava. We don't know yet the cause for this kind of alignment, but it may be connected to the flow structure or to the asymmetric exsolution of these titanomagnetites indicated by microprobe analysis. Since the 1669 sampling site is very near to the former eruption point, the lava may have cooled down very slowly and some alignment of the ore grains due to viscous flow combined with asymmetric high temperature oxidation may have led to the geometrical conditions necessary for negative magnetostatic interaction. Thus the high Curie point phase developed at temperatures above 500° C and was magnetized parallel to the earth field at the time, whereas the lower Curie point phase(s) at least partly interacted in a negative way with the high Curie point titanomagnetite.

References

Ade-Hall, J.M., Khan, M.A., Dagley, P., Wilson, R.L.: A detailed opaque petrological and magnetic investigation of a single Tertiary lava flow from Skye, Scotland. – I. Iron-titanium oxide petrology. Geophys. J. R. Astron. Soc. **16**, 375–388, 1968

Chevallier, R.: L'aimantation des laves de l'Etna et l'orientation du champ terrestre en Sicile du XIIème au XVIIème siècle, Thèse de Physique, Paris. p. 164, 1925

Creer, K.M., Petersen, N.: Thermochemical magnetization in basalts, Z. Geophys. **35**, 501–516, 1969

Creer, K.M., Petersen, N., Petherbridge, J.: Partial self-reversal of remanent magnetization and anisotropy of viscous magnetization in basalts. Geophys. J. R. Astron. Soc. **21**, 471–483, 1970

Gidskehaug, A.: Method to determine the degree of non-stoichiometry of iron-titanium oxides. Geophys. J. R. Astron. Soc. **41**, 255–269, 1975

Havard, A.D., Lewis, M.: Reversed partial thermomagnetic remanence in natural and synthetic titanomagnetites. Geophys. J. R. Astron. Soc. **10**, 59–68, 1965

Heiniger, Chr., Heller, F.: A high temperature vector magnetometer. Geophys. J. R. Astron. Soc. **44**, 281–287, 1976

Hoffman, K.A.: Cation diffusion processes and self-reversal of thermoremanent magnetization in the ilmenite-haematite solid solution series. Geophys. J. R. Astron. Soc. **41**, 65–80, 1975

Markert, H., Trissl, K.-H., Zimmermann, G.J.: On a high-frequency method for the measurement of susceptibilities and hysteresis losses of rocks and minerals between nitrogen temperature and 700° C. J. Geophys. **40**, 303–328, 1974

Nagata, T., Uyeda, S., Akimoto, S.: Self-reversal of thermo-remanent magnetization of igneous rocks J. Geomagn. Geoelectr. **4**, 22–38, 1952

Néel, L.: Propriétés magnétique des ferrites; ferrimagnétisme et antiferromagnétisme. Ann. Phys. **3**, 137–198, 1948

Néel, L.: Some theoretical aspects of rock magnetism. Adv. Phys. **4**, 191–243, 1955

Ozima, M., Ozima, M.: Self-reversal of remanent magnetization in some dredged submarine basalts. Earth Planet. Sci. Lett. **3**, 213–215, 1967

Petersen, N., Bleil, U.: Self reversal of remanent magnetization in synthetic titanomagnetites. Z. Geophys. **39**, 965–977, 1973

Petherbridge, J., Campbell, A.L., Hauptman, Z.: Magnetic behaviour of some partially unmixed titanomagnetites. Nature **250**, 479–480, 1974

Rahman, A.A., Parry, L.G.: Self shielding of inclusions in titanomagnetite grains. Phys. Earth Planet. Inter. **11**, 139–146, 1975

Richards, J.C.W., O'Donovan, J.B., Hauptman, Z., O'Reilly, W., Creer, K.M.: A magnetic study of titanomagnetite substituted by magnesium and aluminium. Phys. Earth Planet. Inter. **7**, 437–444, 1973

Sasajima, S., Nishida, J.: On the self-reversal of TRM in a highly oxidized submarine basalt. Rock Magnetism Paleogeophys. **2**, 5–9, 1974

Schult, A.: Self-reversal above room temperature due to *N*-type magnetization in basalt. J. Geophys. **42**, 81–84, 1976

Stephenson, A.: The observed moment of a magnetized inclusion of high Curie point within a titanomagnetite particle of lower Curie point. Geophys. J. R. Astron. Soc. **40**, 29–36, 1975

Syono, Y.: Magnetocrystalline anisotropy and magnetostriction of Fe_3O_4–Fe_2TiO_4 series, with special application to rock magnetism. Jpn. J. Geophys. **4**, 71–143, 1965

Tanguy, J.C.: An archaeomagnetic study of Mount Etna: The magnetic direction recorded in lava flows subsequent to the twelfth century. Archaeometry **12**, 115–128, 1970

Thellier, E.: A big sample spinner magnetometer. In: Methods in Palaeomagnetism, D.W. Collinson, K.M. Creer, S.K. Runcorn, eds: pp. 149–154. Amsterdam: Elsevier 1967

Uyeda, S.: Thermo-remanent magnetism as a medium of palaeomagnetism, with special reference to reverse thermo-remanent magnetism. Jpn. J. Geophys. **2**, 1–123, 1958

Wertheim, G.K.: The Mössbauer effect: Principles and applications. New York: Academic Press 1964

Received February 19, 1979; Accepted May 22, 1979

J. Geophys. 45, 259–280, 1979

Journal of Geophysics

Palaeomagnetic Study of the Tertiary Volcanics of Sardinia

J.-B. Edel

Laboratoire de Paléomagnétisme, Institut de Physique du Globe, F-67000 Strasbourg, France

Abstract. A thorough investigation of the Sardinian Oligo-Miocene calc-alkaline volcanics has been carried out in Anglona, Logurodo, Bosano and Sulcis. Standard palaeomagnetic techniques applied to 790 specimens representing 94 sites of ignimbrites, andesites, and tuffites show that the magnetic and palaeomagnetic properties vary with the petrographic nature of the rocks. Thermomagnetic curves in high field as well as thermal and alternating field demagnetization reveal the importance of secondary magnetization, mainly due to regional hydrothermal alteration. Except for the upper ignimbritic layer the directions of characteristic magnetization considered as original TRM are scattered around the mean direction $D=332°$, $I=52°$ with $k=22$.

Key words: Sardinia – Palaeomagnetism – Oligo – Miocene volcanics.

1. Introduction

The geological structure of Sardinia consists essentially of a Palaeozoic basement cut by a Tertiary graben which is oriented NS in the northern part and NW-SE in the southern. This graben is filled by thick and massive volcanic and volcano-sedimentary series (Fig. 1). The volcanism can be subdivided into two cycles. The first, of calc-alkaline type, began at the limit Oligocene-Miocene and ended in the middle Miocene. The second of alkaline type, succeded the middle Miocene marine transgression.

This large volcanic region has attracted several groups of palaeomagnetists, interested in the movements of Sardinia (de Jong et al., 1969, 1973; Bobier and Coulon, 1970; Coulon et al., 1974; Bobier, 1974; Manzoni, 1974, 1975). The diverse palaeomagnetic investigations have generally given comparable results but the ensuing interpretations are rather divergent.

In the Plio-Quaternary alkaline lavas, all authors agree that the directions of the characteristic magnetization are close to the present N direction. In the calc-alkaline lavas, de Jong et al. (1969, 1973) and Manzoni (1974, 1975) found dominent NW directions of magnetization. They explain the transition from NW directions to N directions by an anticlockwise rotation of Sardinia relative

0340-062X/79/0045/0259/$04.40

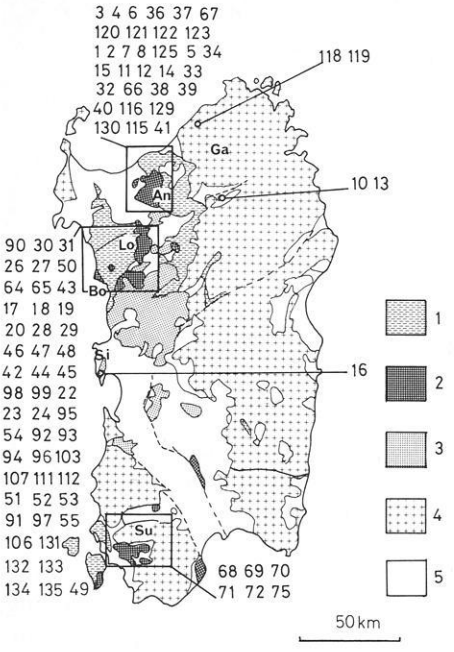

Fig. 1. Geology of Sardinia and location of sampling sites (*numbers*). 1: Tertiary ignimbrites; 2: Tertiary andesites; 3: Plio-quaternary basalts; 4: Palaeozoic basement; 5: sediments; *An*, Anglona; *Ga*, Gallura; *Lo*, Logudoro; *Bo*, Bosano; *Si*, Sinis; *Su*, Sulcis

to Europe. Bobier (Coulon et al., 1974; Bobier, 1974) did not find such NW directions in the lower unit of the calc-alkaline volcanics. Thus he proposed two other solutions. In the first he explains the NW directions by secular variations and anomalous positions of the geomagnetic field during a reversal. The second involves two successive rotations in opposite directions.

To remove this incertainty a thorough investigation of the Sardinian volcanics was required. This study had to deal with the largest stretch of geological time and the widest geographical sampling possible. Preliminary results based on 55 sites were in agreement with the hypothesis of a rotation during the calc-alkaline volcanism (Edel and Lörtscher, 1978). Nevertheless they showed a rather important scatter of the directions. A more detailed investigation, based on a better separation of the different components of the natural remanent magnetization was necessary. In the present paper these results have been refined by measurements of supplementary specimens and enhanced by complete investigations on 39 new sites. To obtain better information on the palaeomagnetic quality of the different rocks, their properties and their behaviour during both alternating field demagnetization and heating up to the Curie temperature, have been measured.

2. Geological Setting and Sampling

In Logurodo and Bosano, Coulon et al. (1974), Coulon (1977) distinguish several series in the calc-alkaline volcanics

– a lower andesitic series, SA1 (or α_1 on the geologic maps 'Alghero' and 'Bonorva'
– a lower ignimbrites series SI1 (τ_1, t_1)
– an upper andesitic series SA2 (α_2)
– the dacites of Cossoïne and M. Frusciu (τ_3)
– the rhyolite of M. Traessu (τ_3)
– an upper ignimbritic series SI2 (τ_2, t_2)

All these units have been sampled for palaeomagnetic studies. Nevertheless it is often not possible to know in which series one is, and the geologic maps include several errors.

In Anglona the geologic map 'Castelsardo' shows three main series
– an andesitic series (α) that Coulon compares to SA2 (personal communication)
– a volcano-sedimentary series (M_1t) consisting of a succession of tuffitic and sedimentary layers and of intercalations of ignimbrites ($M_1\tau$)
– an upper ignimbritic series (τ_2) which is the same in Logudoro and Bosano.

Our sampling concerns α, M_1t and $M_1\tau$.

In Sulcis (SW of Sardinia) the geologic map 'Iglesias' mentions undifferentiated andesites (α) and liparites (τ). Both have been sampled.

In Gallura and near Oschiri the samples of sites 118, 119, 10, 13 have been taken in ignimbrites overlying the granitic basement.

Our study is based on measurements on 790 specimens representing 549 samples and 94 sites. Figure 1 shows the distribution of the sites as follows: 32 sites in Anglona, 51 in Bosano and Logudoro, 6 in Sulcis, 2 in Gallura, 2 near Oschiri and 1 in Sinis. Sites 49 and 16 belong to the Plio-quaternary alkaline volcanics.

The samples of sites 1 to 33 have been broken off in hand samples, oriented with an horizontal plaster cap (geog. N, mag. N) and cut into 43 mm cubes. The samples of the succeeding sites have been drilled and cut into 25 mm cores. Each sample is composed of 2 to 5 specimens.

3. Magnetic Properties of the Calc-Alkaline Volcanics

To study the magnetic properties of the different rocks which compose the calc-alkaline series, we have measured different parameters such as the 'natural remanent magnetization' (NRM), the rate of viscosity (Iv) and the susceptibility (K). The equipment used for measurements consists of a Spinner magnetometer P.A.R. SMI and a Digico magnetometer. Susceptibility is measured in a field of 0.7 mT and 10 kHz with a susceptibility bridge. We consider the results now and discuss them later.

Figure 2 shows the behaviour of the NRM (J), the susceptibility (K) and the Koenigsberger factor (Q) for the three main volcanic rocks, ignimbrites, andesites and tuffites. Each sample is represented by a point. J is weakest for the tuffites. For the lower values, a trend at Q=constant can be observed.

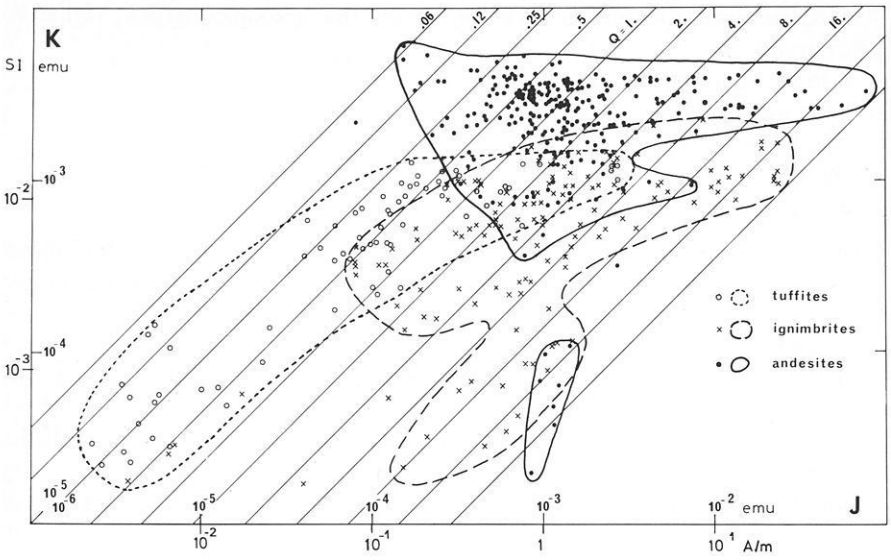

Fig. 2. Intensity of NRM (J), susceptibility (K) and Koenigsberger factor (Q)

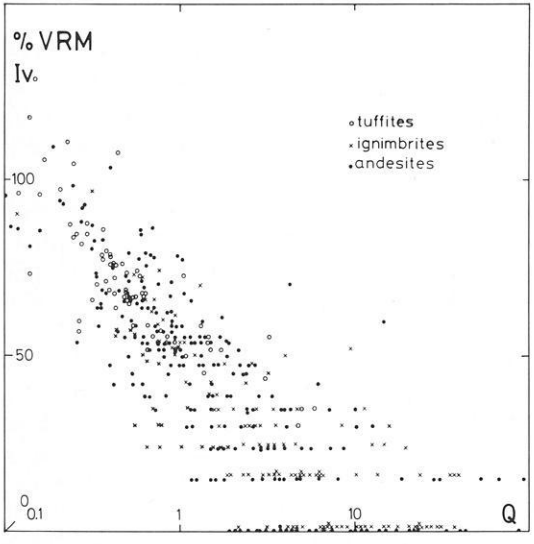

Fig. 3. Viscosity (Iv) and Koenigsberger factor (Q)

This is also visible for the samples at the same site. The behaviour of the andesites is quite different. J varies between 10^{-1} and 10^{-2} A/m but K remains rather constant. This observation can also be made at numerous sites. The greatest density of population corresponds to $J=1$ A/m, $K=3{,}7\ 10^{-2}$, and consequently $Q=0{,}74$. For the ignimbrites the distribution is intermediate. The remanence is comparable with that of the andesites but the susceptibility is gener-

ally weaker. At any one site the trend looks sometimes like that of the tuffites but more often it is also intermediate.

The samples were stored for 3 weeks in a normal laboratory field. After measurement of the NRM, they were inverted and left for about 3 weeks in a reverse laboratory field. The quantity of viscosity if given by:

$$Iv = 100 \times \frac{|\mathbf{M}_1 - \mathbf{M}_2|}{|\mathbf{M}_1 + \mathbf{M}_2|} \%$$

with: $\mathbf{M}_1$ = NRM vector in the normal field position
$\mathbf{M}_2$ = NRM vector in the inverted field position

Figure 3 shows the distribution of the samples in a logarithmic diagram of Iv against Q. The points seem to be scattered about a straight line. Thus, Iv is a function of the type $Iv = a/Q^{\log a}$. The quantity of viscosity decreas Q increases. For $Q > 0.2$, the scatter is least for the tuffites and greatest for the ignimbrites. The scatter increases as Q increases.

4. Magnetic Properties After Alternating Field and Thermal Demagnetizing

Thermomagnetic Curves

Our aim is to assess the magnetization acquired during the cooling of the lavas. Theoretically the coercivity is greater for that magnetization than for secondary magnetization acquired later. Usually, the blocking temperature is also higher for that primary magnetization. Therefore we have tried to eliminate the secondary magnetizations by applying an alternating magnetic field and by heating the samples up to the Curie temperature. Our equipment allows us to reach alternating fields of up to 150 mT. All specimens have been demagnetized. At least one specimen per site has been heated up to 550°–600° C. The alternating field demagnetization for all other specimens has been done at 5 to 15 different field intensities.

Figure 4a shows some examples of the behaviour of the intensity after alternating field demagnetization. Figure 4b gives the variations of the intensity of the remanent magnetization and of the susceptibility after heating at different temperatures and after cooling in null field. Thermomagnetic curves obtained with a horizontal Curie balance (Artzt, 1972) in a high field (0.5 T) complete the study of the magnetization with temperature (Fig. 5).

Typical curves for ignimbrites are given by samples 54211 and 54212 (54:number of the site, 2:number of the sample, 11 and 12:number of the specimens). They shows a strong coercitivity and a blocking temperature higher than 600° C. An intermediate inflection appears on some intensity curves and on some susceptibility curves (53112, 7312). Thermomagnetic curves in high field show often a similar behaviour (Lörtscher, 1976).

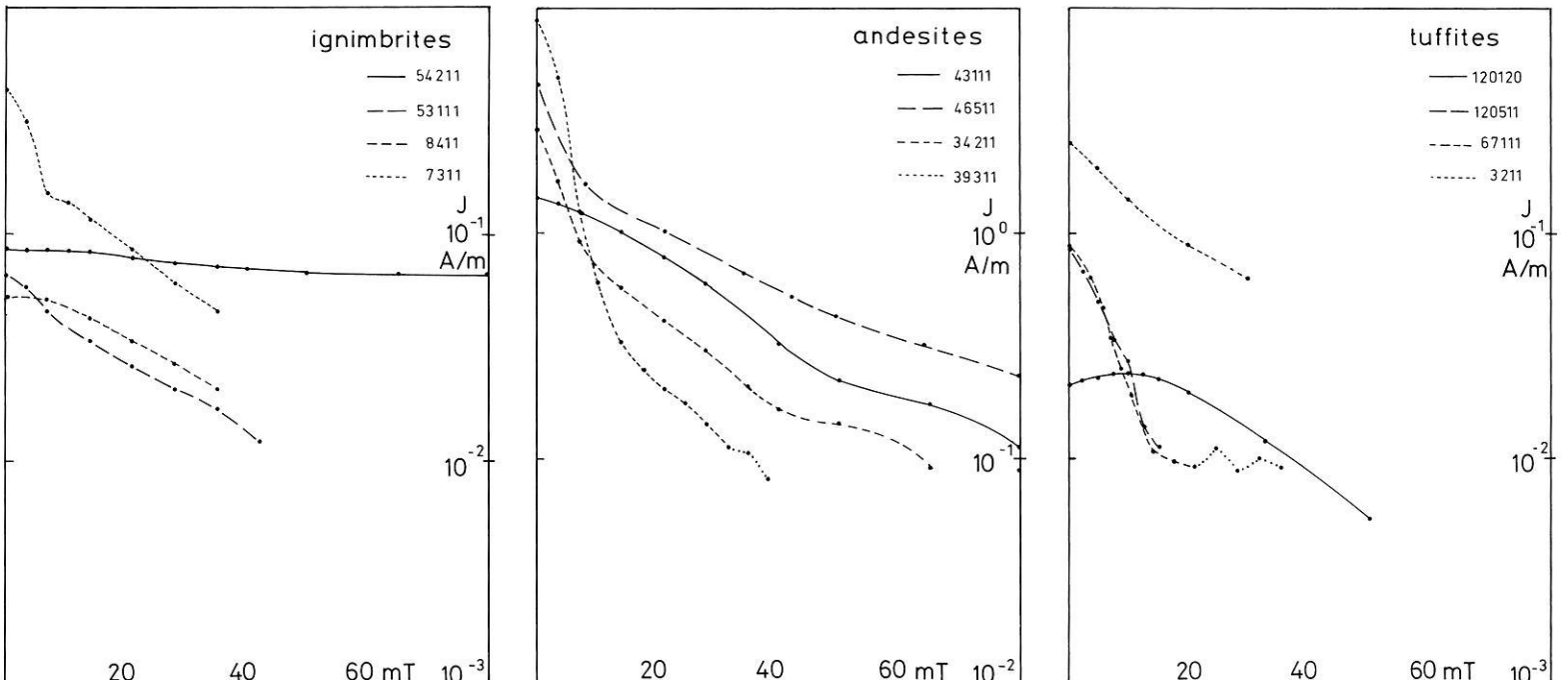

a

Fig. 4a and b. Typical results of: **a** alternating field demagnetization; **b** thermal demagnetization. (.) remanence intensity J, (x) susceptibility K as a function of temperature

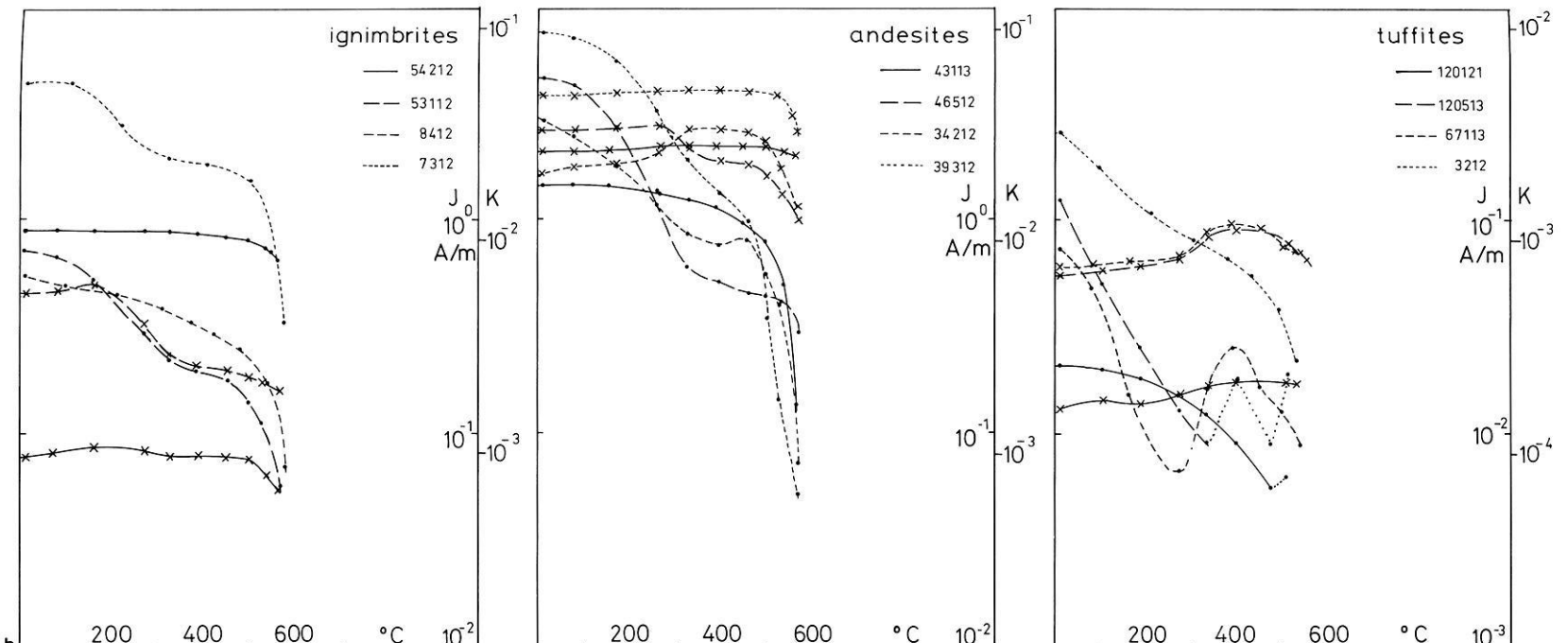
b
ignimbrites
54212
53112
8412
7312
J
K
10^0
A/m
10^{-1}
10^{-2}
10^{-3}
200
400
600
°C
andesites
43113
46512
34212
39312
tuffites
120121
120513
67113
3212
10^{-4}

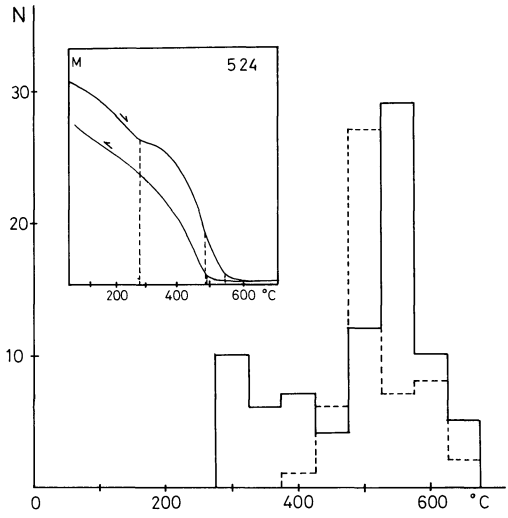

Fig. 5. Curie temperature distribution; *Full line*, heating; *dashed line*, cooling

The andesites show more variable coercivities. Demagnetization was obtained for samples 43111 and 43113 without any problem. The coercivity is strong and the temperature curve is a typical curve for a magnetite poor in titanium. But more often this is not the case. The NRM is mainly due to a secondary magnetization which disappears sometimes rather quickly at 10–20 mT (39311). The intermediate temperature of 300° C appears on many curves: at that temperature the susceptibility can either decrease or increase (46512, 34212).

The tuffites have two types of behaviour. In one, the coercivity is rather strong and after heating the intensity decreases slowly (120120, 120121). In the other, the NRM is essentially due to a magnetization with a weak coercivity. The intensity decreases quickly up to 300° C, then either increases again, or begins to oscillate. At 300° C the susceptibility increases slightly.

5. Components of the Normal Remanent Magnetization

When the coercivity spectra of the different magnetizations which compose the NRM are distinct, it is possible by a judicious demagnetization to separate the directions of the magnetizations. Our demagnetization procedures have yielded several patterns shown as cases (a) and (b) in Fig. 6.

In case (a) which corresponds to the majority of the ignimbrites, the NRM is composed of only a secondary magnetization, which is mainly a very weak viscous magnetization, and a primary magnetization which can be considered to be the characteristic magnetization. That primary vector can either be easily demagnetized (a1) or not (a2) and then directions begin to oscillate. These oscillations are a function of the rock and of the demagnetizing equipment.

In case (b) which is very often that for the andesites and the tuffites, we have obtained three components: the viscous magnetization which rapidly disap-

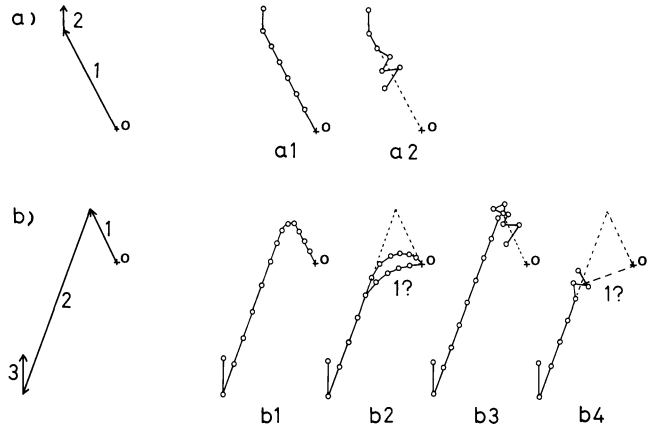

Fig. 6. Components of the NRM (schematic representation). Types of demagnetizations

pears, a secondary and a primary magnetization. In the best case, all components can be separated (b1). Usually the direction of the secondary vector can also be determined. This is not always the case for the primary. When the coercivity spectra overlap, one demagnetizes the primary as well as the secondary magnetization (b2). Many andesites show such a behaviour. Sometimes, especially in the tuffites, the directions begin to oscillate during the demagnetizing of the secondary magnetization (b4), or only at the begining of the demagnetizing of the primary (b3). In cases (b2, b3, b4), the directions obtained after demagnetizing are scattered and the mean direction does not give the direction of the characteristic magnetization. However at a homogenous site the planes defined by the secondary and the primary vectors must intersect along a common line which is the direction of the primary vector (Halls, 1976). This computation has always be done when the demagnetization did not show a clear primary vector such as that in cases (a1 and b1). An example is given by site 55 in Fig. 7.

6. Palaeomagnetic Properties of the Different Calc-Alkaline Volcanics

On many temperature versus intensity of remanence curve (Fig. 4) as well as on the thermomagnetic curves in high field (Fig. 5), we have observed an intermediate Curie temperature of about 300° C. The susceptibility curves also show an inflection at the same temperature. Similar thermomagnetic diagrams have been found for oceanic dredged basalts by Ade-Hall (1964) and Wasilewski (1968). Readman and O'Reilly (1970) obtained analoguous results with synthetic titanomaghemite in a vacuum. Ade-Hall and al. (1971) explain such thermomagnetic behaviour of continental basalts by a regional hydrothermal alteration. This alteration acts in an environment of the zeolite metamorphic facies and produces new magnetic phases.

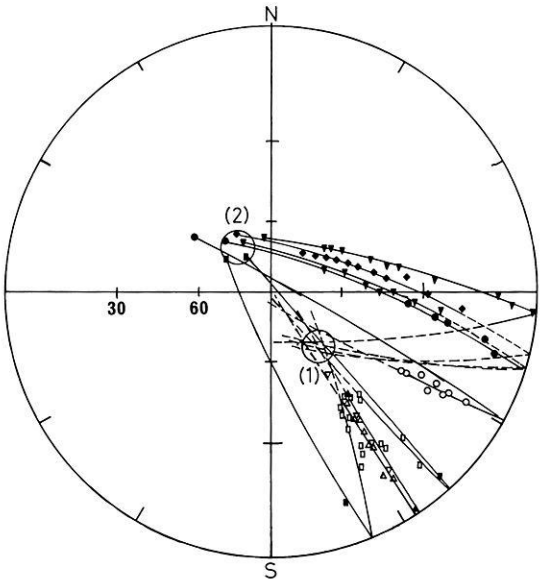

Fig. 7. Example (site 55) of secondary (2) and primary (1) magnetization directions. The primary direction is given by the intersections of the demagnetizing planes. Each symbol represents a specimen

We have observed zeolites on several thin sections of our samples, as has Baque (1974). Thus the hypothesis of Ade-Hall and al. (1971) may also hold for the calc-alkaline rocks of Sardinia. Regional hydrothermal alteration would be the most important creator of secondary magnetizations. However the effects vary with the petrographic nature of the rocks.

In the tuffites one distinguishes two types; those which constitute a good palaeomagnetic material and the others. In the first type the opaque grains are small. They correspond to samples which show a Q=constant trend (Fig. 2). In the case of monodomain grains, remanence and susceptibility are due to the same grains and when the number of grains increases, J and K increase together and Q remains constant. So it is possible that in our case the monodomain grains are dominant. Their demagnetizing curves indicate a great coercivity and a Curie temperature between 500° and 580° C. The demagnetizing process allows the determination of the primary direction. In the second type, which is the more usual, the opaque grains are rather big (0.1 mm). The viscosity is important. The demagnetizing process reveals essentially a secondary magnetization which can be attributed to hydrothermal alteration. The coercivity is weak but at 16 kAm^{-1} (200 Oe) the remanence begins to oscillate and it is often impossible to obtain the primary direction. Similar difficulties arise after heating up to 300° C. Sometimes the demagnetizing curves look like typical (a1) curves. Nevertheless the latter considerations show that the vector would only be composed of a secondary magnetization and the primary would have completely disappeared.

The andesites show many types of behaviour and to discuss how they are distinguished would take to long. Only one distinction can be made: some of the NRM correspond to type (a), others to type (b). The first (samples 43111, 43112 on Fig. 4) do not present any difficulty. The others are more

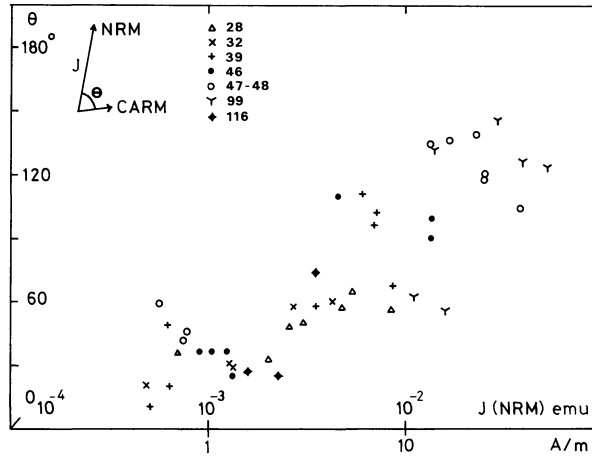

Fig. 8. Intensity of NRM (J) and angle (θ) defined by NRM and CARM

complicated. In Fig. 2 we noted that in a plot of J against K, K remains quite constant. For an intensity of the NRM higher than 1 A/m, we observed a correlation between the intensity J (NRM) and the angle θ defined by NRM and CARM (characteristic magnetization) (Fig. 8): θ increases as J increases. This means that a relatively strong secondary magnetization has been acquired in a reversed field to the TRM field. This is available for sites with normal and reversed polarity. For some specimens one can observe that θ increases with J as well as with the degree of alteration. When the NRM is strong (>1 SI), the viscosity is weak and then the secondary magnetization is probably a chemical. The intermediate Curie temperatures allows us to attribute this chemical magnetization to the hydrothermal alteration. Often the primary direction can be defined, usually by the intersections of the demagnetizating planes. Nevertheless in some cases the secondary magnetization has a Curie temperature of up to 600° C. Such thermomagnetic curves can be explained by deuteric oxidation (Ade-Hall et al., 1971). Then it is often not possible to find a primary direction. As well as for tuffites a demagnetizing curve (a) can be a demagnetizing curve (b) (Fig. 6) for which the TRM has disappeared. So one confound the secondary chemical magnetization with the TRM.

The ignimbrites are by far the best material for palaeomagnetic studies in Sardinia. The weak viscous magnetization disappears quickly. When they exist the secondary magnetizations can be eliminated easily.

7. Directions of the Remanent Magnetizations and Interpretation

All informations on the directions of secondary and primary magnetization are given in Table 1. These directions which have been judged representative for a site are illustrated in Fig. 9.

Table 1. *Site*, site number; *Loc*, topographic maps, 1/25 000e; ×, longitude; *Y*, latitude; *Dip*, direction and dip of max. slope; *d*, method of demagnetizing (Fig. 4); *a*, primary (1) or secondary (2) magnetization; *s*, Fisher statistic (F) or intersect of the demagnetising planes (C); N/N_0, number of samples taken for the mean direction computation (N) and total number of samples (N_0); $\mu/n/n_0$, number of specimens taken for the mean direction computation (μ), number of specimens

Site	Loc.	X	Y	Dip	d	a
3	Castelsardo	8 44 28	40 53 19	0 à 7NO	b1	2 1
4	Castelsardo	8 45 55	40 54 11	5N320	b3a1	2?
6	Castelsardo	8 44 54	40 53 35	10N320	b3a1	2?
36	Castelsardo	8 44 38	40 53 54	15N320	a1	1
37	Castelsardo	8 44 46	40 53 49	15N320	a1	1
67	Castelsardo	8 45 10	40 53 30	7N230	b3b4	2 1 1
120	Castelsardo	8 43 08	40 54 45	10N10	a1b4	2 1 1
121	Castelsardo	8 43 41	40 54 45	10N0	a1b4	2
122	Castelsardo	8 43 41	40 54 45	10N0	b4b3	2 1?
123	Castelsardo	8 43 41	40 54 45	10N20	b4b3	2 1?
124	Castelsardo	8 45 19	40 53 34	5N280	b3b4	2 1 1
126	Castelsardo	8 45 03	40 53 30	5N320	a1b4	2?
127	Castelsardo	8 45 23	40 53 37	5N280	b3	2 1 1
128	Castelsardo	8 45 48	40 53 46	5N260	b4a1	2 1
1	Castelsardo	8 46 10	40 53 51	6N240	b1	2 1
2	Castelsardo	8 46 20	40 53 54	7N265	a1	1
7	Castelsardo	8 46 50	40 54 14	–	b1b2	1
8	Castelsardo	8 46 34	40 54 24	15N170	a1b1	2 1
125	Castelsardo	8 49 43	40 53 37	7N270	a1	1
10	Oschiri	9 06 54	40 42 43	–	a1	1
13	Oschiri	9 07 12	40 43 13	10N250	a1b2	1 1
118	Costa Paradiso			~0	a2	1
119	Costa Paradiso			~0	a2b3	1

which possess the considered magnetization (n), total number of specimens (n_0); D, declination; I, inclination; R, k, α_{95}, Fisher statistic parameters; β, defines the cone in which μ magnetization planes intersect; b, direction taken in account in Fig. 9; *PS*, petrographic and stratigraphic denomination (chapter 2)

s	N/N_0	$\mu/n/n_0$	D	I	R	k	α_{95} β	b	PS
F	5/5	8/8/11	352	58	7,9147	82	6	2	M_1t
F	5/5	8/8/11	328	58	7,9742	272	3	1	
F	4/4	6/7/7	359	57	5,9825	287	4	2?	M_1t
F	3/3	6/6/6	358	54	5,8936	47	10	2?	M_1t
F	5/5	5/5/5	358	48	4,9914	468	4	1	M_1t
F	6/6	6/6/6	353	−14	5,9768	216	5	1	M_1t
F	6/6	8/8/14	298	62	7,7963	34	9	2	M_1t
F	6/6	11/11/14	164	−28	9,8562	9	16		
C	6/6	11/14	143	−56			10	1	
F	7/7	13/13/15	349	50	12,6846	38	7	2	M_1t
F	2/7	2/4/15	106	−56					
C	3/7	3/15	130	−64			5	1	
F	6/6	9/9/9	331	64	8,9485	155	4	2	M_1t
F	5/5	6/6/9	335	60	5,9451	91	7	2	M_1t
F	4/5	6/6/9	353	60	5,9683	158	5	1?	
F	2/3	3/3/5	352	62	2,9925	268	7	2	M_1t
	1/3	1/1/5	7	63					
F	4/6	5/8/9	337	57	4,8682	30	14	2	M_1t
F	5/6	7/7/9	121	−70	6,9760	250	4		
C	6/6	8/9	131	−70			8	1	
F	5/5	5/5/5	5	56	4,9900	402	4	2?	M_1t
F	7/7	9/9/9	349	46	8,8032	41	8	2	M_1t
F	6/7	6/6/9	152	−59	5,8814	42	10		
C	7/7	9/9	159	−60			7	1	
F	6/6	10/11/11	330	54	9,6791	28	9	2	M_1t
C	6/6	9/11	148	−61			5	1	
F	5/5	6/6/6	314	58	5,9824	285	4	2	M_1t
F	5/5	5/6/6	286	53	4,9756	164	6	1	
F	5/5	7/7/7	287	54	6,9921	765	2	1	$M_1\tau$
F	3/3	4/4/4	281	57	3,9369	48	13	1	$M_1\tau$
F	2/5	2/3/6	305	65				2	
F	5/5	6/6/6	281	60	5,9889	452	3	1	$M_1\tau$
F	7/7	7/7/7	166	−31	6,9919	747	2	1	$M_1\tau$
F	6/6	9/10/10	164	−49	8,9674	246	3	1	τ
F	6/6	7/7/7	148	−38	6,9591	147	5		τ
C	6/6	7/7	150	−46			7	1	
F	6/6	6/6/6	144	−44	5,9931	727	2	1	τ
F	6/7	6/6/7	146	−44	5,9847	329	4	1	τ

Table 1 (Continued)

Site	Loc.	X	Y	Dip	d	a
5	Castelsardo	8 44 59	40 53 40	~15N320	a1b1	1
34	Castelsardo	8 44 49	40 53 47	~15N320	a1b1	2 1
15	Castelsardo	8 46 14	40 52 32	–	a1	
11	Castelsardo	8 43 24	40 52 18	–	a1b1b2	2 1
12	Castelsardo	8 43 23	40 52 26	–	a1b1b2	2 1
14	Castelsardo	8 44 30	40 52 57	–	b4	2
33	Nulvi	8 44 34	40 48 06	–	a1b1	1
32	Nulvi	8 47 01	40 46 53	–	b2b1	1?
66	Castelsardo	8 42 34	40 50 05	–	a1	1
38	Sorso	8 40 37	40 45 59	–	b4	2
39	Sorso	8 41 34	40 47 08		b3b4	1
40	Osilo	8 39 38	40 44 00	–	a1b3	2 1
116	Osilo	8 41 43	40 44 15	–	a1b2	1
129	Osilo	8 39 21	40 44 04	–	b2b3b4	2 1?
130	Osilo	8 40 29	40 44 56	–	b2	1? 1?
115	Chiaramonti	8 45 00	40 41 07	–	b1b2b4	1
41	Chiaramonti	8 44 59	40 40 42	–	b3b4	2 1 1
90	Bosa	8 31 40	40 17 28	–	b4	1 1
30	Bosa	8 30 52	40 18 32	–	a1b2	1
31	Bosa	8 30 05	40 18 40	~0	a1b2	1
26	Padria	8 35 11	40 22 05	–	a1	1
27	Padria	8 35 17	40 22 05	–	b1b2	1 1
50	Sindia	8 35 49	40 19 53	–	a2b3	1
63	Romana	8 38 58	40 28 38			
64	Romana	8 39 08	40 28 52	–	a2	1
65	Romana	8 39 58	40 28 24	–	b3b4	1 1
43	Banari	8 39 41	40 33 42	–	a1	1

s	N/N_0	$\mu/n/n_0$	D	I	R	k	α_{95} β	b	PS
F	7/7	8/8/8	356	−17	7,9472	133	5	1	α
F	6/6	7/8/10	4	45	6,8843	52	8	2	α
F	5/6	9/10/10	358	−13	8,9258	108	5	1	
	1/3	2/2/5	331	20					α
	2/3	3/3/5	357	34					
F	2/5	4/5/9	297	48	3,9502	60	12	2	α
F	3/5	4/4/9	330	53	3,9339	45	14	1	
F	4/6	5/5/10	347	41	4,9571	93	8	2	α
F	4/6	5/5/10	332	49	4,9773	177	6	1	
F	5/5	8/9/9	134	− 7	7,9619	184	4	2	α
F	5/5	8/8/8	322	11	7,9764	297	3	1	α
F	5/5	7/7/7	307	67	6,9604	152	5	1	α
F	6/6	9/9/9	123	−17	8,4866	598	2	1	α
F	6/6	8/8/10	358	48	7,9558	159	4	2	α
F	4/9	7/7/14	157	−36	6,9702	201	4		α
C	8/9	12/14	160	−35			8	1	
F	4/6	5/6/15	358	46	4,8163	22	17	2	α
F	5/6	9/10/15	321	55	8,7939	39	8	1	
F	6/7	6/7/7	343	53	5,9892	465	3	1	α
F	3/10	4/5/18	357	62	3,9954	659	4	2	α
F	8/10	12/12/18	316	67	11,8781	90	5	1?	
F	7/7	8/9/9	20	57	7,8026	35	9		α
C	7/7	7/9	8	50			10	1?	
F	6/6	7/7/8	8	47	6,9839	375	3	1	α
F	2/4	2/2/6	354	64			2		α
F	4/4	6/6/6	118	−21	5,6910	16	17		
C	3/4	4/6	155	−53			5	1	
F	5/6	9/12/12	146	−45	8,5469	18	13		α
C	5/6	9/12	148	−66			10	1	
F	6/6	9/9/9	139	−40	8,8844	69	6	1	SA_2
F	5/5	5/5/5	11	80	4,9659	117	7	1	SA_2
F	3/4	3/4/4	174	−41	2,9989	1812	3	1	SA_2
F	4/5	4/5/5	172	−32	3,9604	76	11		SA_2
C	5/5	5/5	182	−47			5	1	
F	5/6	6/8/8	183	−54	5,9805	257	4	1	SA_2 SA_2
F	5/5	7/7/7	172	−56	6,9921	762	2	1	SA_2
F	2/4	4/4/9	100	−68	3,9792	144	8		SA_2
C	4/4	7/9	109	−68			8	1	
F	3/3	5/5	344	55	4,9978	1835	2	1	SA_2

Table 1 (Continued)

Site	Loc.	X	Y	Dip	d	a
17	Capo Marargiu	8 24 20	40 22 34			
18	Capo Marargiu	8 24 29	40 22 06	–	b4	2
19	Capo Marargiu	8 24 42	40 22 00	–	a1	
20	Capo Marargiu	8 25 07	40 21 30	–	b2b3b4	1
21	Capo Marargiu	8 23 33	40 20 20			
28	Capo Marargiu	8 24 00	40 22 11	–	a1b4	1?
29	Capo Marargiu	8 25 18	40 21 19	–	a1b2	1
46	Banari	8 40 02	40 30 25	–	a1	1
47	Romana	8 41 03	40 29 45	–	a1	1
48	Romana	8 41 13	40 29 54	–	b2b3	2 1 1
42	Banari	8 38 17	40 34 08	–	a1	1
44	Banari	8 39 34	40 34 56	–	a2b3	1
45	Banari	8 39 08	40 33 20	–	b3b4	2 1
98	Banari	8 39 43	40 34 42	–	b1b4	2 1 1
99	Banari	8 38 45	40 34 22	–	b3b4	1 1
22	Montresta	8 30 03	40 23 05	–	a1a2	1
23	Montresta	8 29 37	40 23 18	–	b2	1
24	Montresta	8 28 51	40 23 40	–	a2b2	1
95	Montresta	8 28 56	40 23 18	–	a1	1
54	Montresta	8 29 27	40 20 02	17N25	a1a2	1
92	Bosa	8 30 40	40 19 17	20N30	a1	1
93	Bosa	8 30 37	40 20 00	15N15	a1	1
94	Montresta	8 27 54	40 23 44	–	a1b2	1
96	Montresta	8 31 09	40 23 39	510N7080	a1	1
103	Itiri	8 27 38	40 37 13	15N80	a1	1
107	Valverde	8 23 18	40 33 47	0 15N350	a1	1
111	Pedra Ettori	8 23 43	40 26 24	~0	a1	1
112	Pedra Ettori	8 23 43	40 26 24	~0	a1	1
51	Torre Argentina	8 26 16	40 19 23	?	a1	1?

s	N/N_0	$\mu/n/n_0$	D	I	R	k	α_{95} β	b	PS
									SA_1
F	5/5	6/8/8	148	− 3	5,9278	69	8	2	SA_1
F	2/3	4/4/7	353	31	3,9801	151	7		SA_1
	1/3	3/3/7	323	35	2,9931	294	7		
F	5/5	7/7/7	156	−67	6,6712	18	14		SA_1
C	5/5	7/7	190	−62			10	1	SA_1
F	2/6	4/4/10	316	52	3,9012	30	17	1	SA_1
F	4/6	6/6/10	276	28	5,8210	28	13	2	
F	4/4	6/6/6	141	−68	5,9494	99	7	1	SA_1
F	9/9	9/11/11	163	−33	8,9396	132	4	1	SA_1
F	4/4	4/4/4	128	−49	3,9609	77	10	1	SA_1
F	4/4	7/7/7	316	3	6,8720	47	9	2	SA_1
F	4/4	7/7/7	124	−44	6,7191	21	13		
C	4/4	7/7	140	−35			5	1	
F	8/8	10/11/11	340	35	9,9757	372	3	1	SA_1
F	3/3	8/8/8	176	−54	7,9246	93	6	1	SA_1
F	2/8	3/3/11	274	56	1,9976	420	12	2	SA_1
F	5/8	5/6/11	318	52	4,9225	52	11	1	
F	5/5	5/6/7	317	63	4,9617	104	7	2	SA_1
F	3/5	3/3/7	145	−43	2,9973	760	4		
C	5/5	7/7	147	−57			5	1	SA_1
	1/7	1/7/14	343	38					
C	6/7	11/14	345	36			5	1	SA_1
F	4/4	5/5/5	160	−43	4,9978	1886	2	1	SA_1
F	4/4	4/4/4	145	−59	3,9909	331	5	1	SA_1
F	4/4	5/5/5	142	−45	4,9740	154	6	1	SA_1
F	6/6	6/6/6	151	−37	5,9855	346	4	1	SA_1
F	5/6	7/8/8	168	−30	6,9870	464	3	1	SI_1
F	6/6	6/6/7	153	−60	5,9800	251	4	1	SI_1
F	8/8	8/8/8	154	−40	7,9593	172	4	1	SI_1
F	4/7	4/7/7	150	−25	3,9742	116	8	1	SI_1
F	4/5	4/5/5	333	45	3,9851	202	6	1	SI_1
F	7/7	7/7/7	333	43	6,9909	661	2	1	(SI_2)
F	6/6	6/6/6	141	−43	5,9819	277	4	1	(SI_2)
F	6/7	6/8/8	141	−61	5,9909	551	3	1	SI_1
F	5/5	5/5/5	132	−52	4,9790	191	5	1	SI_1
F	5/7	7/10/10	7	58	6,9468	113	6	1	α

Table 1 (Continued)

Site	Loc.	X	Y	Dip	d	a
52	Torre Argentina	8 26 16	40 19 23	10N180?–220	a1	1
53	Bosa	8 27 30	40 19 23	~0	b1b2	1
91	Bosa	8 28 34	40 17 46	~0	a1	1
97	Banari	8 37 36	40 34 24	~0	a1	1
131	Banari	8 41 15	40 31 00	–	a1b3	1 1
132	Romana	8 35 48	40 29 33	–	a1	1
133	Banari	8 36 22	40 32 10	5N180	a1b1	1
134	Romana	8 37 02	40 25 50	–	a1	1
135	Romana	8 40 25	40 28 20	10N20	a1b2	1
55	Alghero	8 19 23	40 32 32	–	b3b4	2 1 1
106	Valverde	8 23 21	40 33 44	–	b3b4	1 1
68	Carbonia	8 30 53	39 08 08	Variable	a1	1
69	Perdaxius	8 37 22	39 07 25	–	a1	1
70	Perdaxius	8 41 03	39 08 13	–	b3b4	2 3? 1 1
71	Siliqua	8 49 08	39 15 52	–	a1	1
72	Villamassargia	8 40 22	39 15 36	–	b1b2	1
75	Perdaxius	8 35 43	39 09 51	–	b1b2	1
16	Sinis	8 26 08	39 54 30	–	a1b2	1
49	Sindia	8 34 56	40 18 06	~0	a1	1

In the andesites the measurement of slope was generally impossible. Nevertheless the scatter does not seem to be very much greater than that for the ignimbrites, the slope of which is known. For the latter the directions are coherent and hence the scatter can only be explained by secular variation of anomalous field directions during a reversal. Sites 1, 2, 7, 8 as well as some other sites investigated by de Jong et al. (1973) show the same directions grouping around N 280°–290° C which relate probably to the same layer. This group of directions is removed from the mean direction which is about N 330. Thus, the ignimbrites which cooled rather quickly, probably took on an anomalous field direction. This is probably also the case for some andesites like sites 33, 66, 5, 34.

A preliminary interpretation based on 55 sites was given by Edel and Lörtscher (1978). Their conclusion was as follows. In the lower andesitic and ignimbritic series (SA1, SI1), the NW directions dominate. In the upper andesite

Site	Loc.		X	Y	Dip		d		a
F	4/4	6/6/6	343 ? 346	64 ? 68	5,9955	1117	2	1	(SI_2)
F	4/6	6/6/11	338	58	5,9825	287	4	1	(SI_2)
F	4/4	4/4/4	340	63	3,9982	1686	2	1	(SI_2)
F	7/8	7/8/8	359	52	6,9803	305	3	1	(SI_1)
F	1/3	2/6/6	159	−35					SA_1
C	2/3	4/6	160	−35					
F	3/3	6/6/6	160	−56	5,9916	594	3	1	SA_3
F	4/4	4/4/4	328	48	3,9997	14235	1	1	SI_2
F	4/4	4/4/4	342	55	3,9994	5256	1	1	SI_2
F	4/4	4/4/4	457	58	3,9027	31	17	1	τ_3
F	4/5	7/9/10	323	65	6,9118	68	7	2	π
F	4/5	6/10/10	139	−40	5,8688	38	11		
C	5/5	8/10	140	−60			7	1	
F	5/7	8/10/13	116	−21	7,8122	37	9		π
C	6/7	10/13	147	−38			10	1	
F	7/7	8/9/9	26	36	7,8349	42	9	1	τ
F	6/6	9/9/9	179	−47	8,9515	164	4	1	α
F	4/8	7/10/17	325	52	6,7259	22	13	2	α
F	3/8	3/10/17	354	51	2,9757	82	14		
F	1/8	2/2/17	115	−55					
C	7/8	13/17	120	−60			10	1	
F	6/7	6/8/8	75	−55	5,9798	248	4	1	α
F	5/5	10/10/10	333	31	9,9378	145	4	1	α
F	5/5	7/7/7	130	−59	6,9520	125	5	1	α
F	5/6	5/6/6	198	−48	4,9907	430	5	1	β
F	4/4	4/4/4	4	56	3,9973	1132	3	1	β

series SA2, NW in addition to N directions were obtained. In the upper ignimbritic series (SI2, $\tau 2$) de Jong et al. (1973) and coulon et al. (1974) obtained a clear N direction (Fig. 9d). These results in comparison with petrographic data and some radiometric ages, are in favour of a rotation of Sardinia after 17 MY (Bellon et al., 1978).

Our new results generally agree with the first interpretation. But some contradictions appear. So, for some upper and lower ignimbrites we measured respectively NW and N directions. This means, if we did not measure an anomalous field direction, that, either our model does not fit, or the stratigraphy of the geologists is wrong. Before giving a definitive interpretation we await a new set of radiometric ages. The potassium-argon method, applied to individual minerals of our palaeomagnetic samples, will allow us hopefully to reach definite conclusions.

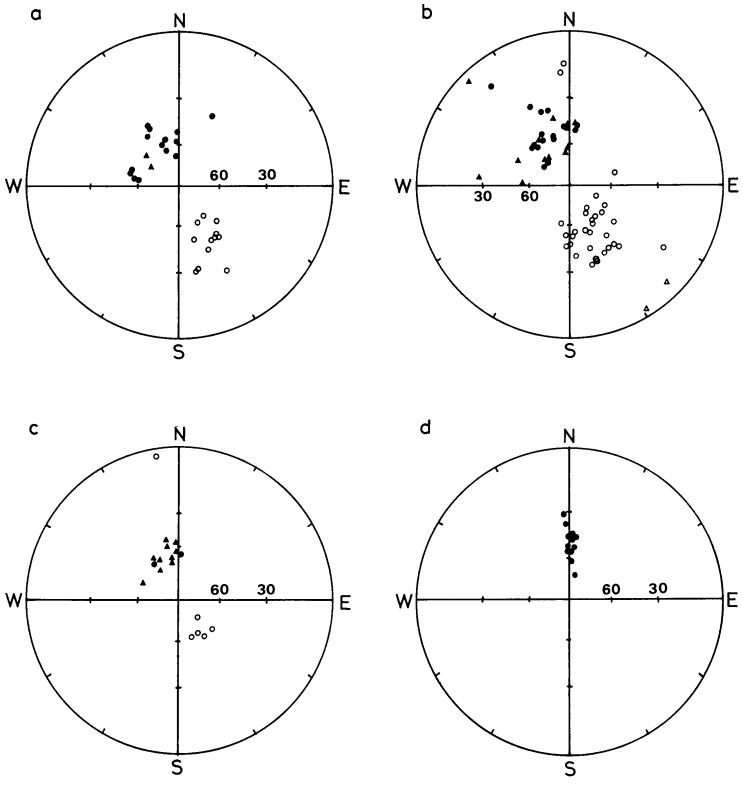

Fig. 9. Projection of the site mean directions in the ignimbrites (**a**), andesites (**b**) and tuffites (**c**) of the calc-alkaline Tertiary volcanics. Primary magnetizations (●) and secondary magnetizations (▲). Upper ignimbritic serie by de Jong et al. (1973) and Coulon et al. (1974) (**d**)

8. Conclusions

In the present paper we have described the different magnetic parameters as a function of the pertrographic nature of the calc-alkaline volcanics. Thermal treatment shows that most calc-alkaline volcanics underwent regional hydrothermal alteration. This results in the presence of secondary magnetizations, the importance of which vary with the petrography. They are very strong in the most tuffites, generally important in the andesites and negligible in the ignimbrites. Thus the palaeomagnetic study necessitates very detailed demagnetizations, especially with regard to the type of magnetization which is present. The directions of characteristic magnetization in the ignimbrites, which show no significant secondary magnetizations and for which the tectonic correction has been done, reveal significant secular variations and anomalous field directions during cooling of the lavas. Field reversals are numerous during Tertiary, and the anomalous directions of magnetization may have been induced during such reversal.

Except for the upper ignimbritic series SI2, the directions are generally NW, scattered around the mean direction $D=332$, $I=52$ with $N=79$, $k=22$, $\alpha_{95}=3°$. Soon, new radiometric ages of our samples will allow us to interpret the palaeomagnetic data from a geodynamic point of view.

Acknowledgments. I am indebted to Professor L. Thaler of the Montpellier University and Professor G. Pecorini of the Cagliari University who improved our contact with the Geology of Sardinia. A. Lörtscher's assistance in field work was very helpful. Professor A. Roche, Dr. M. Westphal, and Dr. R. Montigny kindly read the manuscript and gave constructive advice. The help of Dr. D. Bamford of the Karlsruhe University is gratefully acknowledged for correcting the English text.

This work has been supported by the Institut National d'Astronomie et de Géophysique (A.T.P. Méditerranée Occidentale et A.T.P. Géodynamique).

References

Ade-Hall, J.M.: The magnetic properties of some submarine oceanic lavas. Geophys. J. R. Astron. Soc. **9**, 85–92, 1964

Ade-Hall, J.M., Palmer, H.C., Hubbard, T.P.: The magnetic and opaque petrological response of basalts to regional hydrothermal alteration. Geophys. J. R. Astron. Soc. **24**, 137–174, 1971

Artzt, C.: Réalisation d'une balance thermomagnétique à translation. Application à l'étude des roches. Dipl. Ing. Géophys. 83, Strasbourg I, 1972

Baque, L.: L'association andésitique cénozoique du Logudoro et du Bosano (Sardaigne Nord-Occidentale), au sein de l'ensemble du volcanisme andésitique calco-alcalin de l'île. Thèse 3e Cycle, Aix-Marseille III, 193 pp. 1974

Bellon, H., Coulon, C., Edel, J.B.: Le déplacement de la Sardaigne. Synthèse des données géochronologiques, magmatiques et paléomagnétiques. Bull. Soc. Géol. France 7, t. XIX, n° **4**, 825–831, 1977

Bobier, C.: la signification de l'aimantation rémanente des laves de la série. 'des ignimbrites inférieures'. Conséquences pour l'étude de la rotation du bloc corso-sarde durant le Tertiaire. In: Paleogeografia del Terziaro sardo nell-ambito del Mediterraneo occidentale suppl. ai "Rendiconti del Seminario delle Faculta di Scienze dell' Universita de Cagliari" 35–56, 1974

Bobier, C., Coulon, C.: Résultats préliminaires d'une étude paléomagnétique des formations volcaniques tertiaires et quaternaires du Logudoro (Sardaigne septentrionale). C.R. Acad. Sci. (Paris) **270**, 1434–1437, 1970

Coulon, C.: Le volcanisme calco-alcalin cenozoïque de Sardaigne (Italie). Pétrographie, Géochimie et genèse des laves andésitiques et des ignimbrites. Signification géodynamique. Thèse, 287 pp., Aix-Marseille III, 1977

Coulon, C., Demant, A., Bobier, C.: Contribution du paléomagnétisme à l'étude des séries volcaniques cenozoïques et quaternaires de Sardaigne nord-occidentale. Tectonophysics **22**, 59–82, 1974

Edel, J.B., Lörtscher, A.: Paléomagnétisme du volcanisme tertiaire de Sardaigne. Nouveaux résultats et synthèse. Bull. Soc. Géol. France 7, t. XIX, n° **4**, 815–824, 1977

Halls, H.C.: A least square method to find a remanence direction from converging circles. Geophys. J. Roy. Astron. Soc. **45**, 297–304, 1976

Jong, K.A. De., Manzoni, M., Stavenga, T., Dijk, F. Van, Voo, R. Van der, Zijderveld, J.D.A.: Paleomagnetic evidence for rotation of Sardinia during Early Miocene. Nature **243**, 281–283, 1973

Jong, K.A. De, Manzoni, M., Zijderveld, J.D.A.: Paleomagnetism of the Alghero trachyandesites. Nature **224**, 67–69, 1969

Lörtscher, A.: Etude paléomagnétique des formations volcaniques tertiaires de Sardaigne septentrionale. Régions de Castelsardo et d'Oschiri. Dipl. Ing. Géophys. 138 pp., Strasbourg, 1976

Manzoni, M.: Un interpretazione dei dati paleomagnetici del Terziario dell Sardegna ed alcuni nuovi risultati. In: Paleogeografia del Terziario sardo nell'ambito del Mediterraneo occidentale suppl. ai "Rendiconti del Seminario della Faculta di Science del' Universita di Cagliari" 283–295, 1974

Manzoni, M.: Paleomagnetic data from Tertiary volcanics of the Campidano and associated grabens, Sardinia. Earth. Planet. Sci. Lett. **27**, 275–282, 1975

Readman, P.W., O'Reilly, W.: The synthesis and inversion of non stochiometric titanomagnetites. Phys. Earth Planet. Inter. **4**, 121–128, 1970

Wasilewski, P.: Magnetization of oceanic basalts. J. Geomagn. Geoelectr. **20**, 129–154, 1968

Received August 10, 1978; Revised Version December 27, 1978
Accepted February 22, 1979

J. Geophys. 45, 281–298, 1979

Journal of Geophysics

Analysis of an Eastward Electrojet by Means of Upward Continuation of Ground-Based Magnetometer Data

U. Mersmann, W. Baumjohann, F. Küppers, and K. Lange

Institut für Geophysik der Universität Münster,
Gievenbecker Weg 61, D-4400 Münster, Federal Republic of Germany

Abstract. On October 26, 1975, data from two parallel meridian chains of densely spaced magnetometers in Northern Scandinavia indicated the presence of an evening sector eastward electrojet which between 1606 and 1710 UT was two-dimensional. By separating the relevant components of the magnetic disturbance fields into internal and external parts, and by subsequent upward continuation (towards the source) of the external horizontal component, equivalent height-integrated ionospheric current densities were derived as a function of latitude and time. Whereas the demarcation line between the eastward and westward ionospheric electrojet currents remained stationary, the sharp southern border of the eastward electrojet moved towards the south with a speed of about 50 ms^{-1}, possibly indicating an earthward movement of the inner edge of the magnetospheric plasma sheet. The maximum eastward height-integrated current density was of the order of 0.5 Am^{-1}, the corresponding large-scale field-aligned current density has been estimated to have been of the order of 1.0 μAm^{-2}. After 1630 UT there was evidence for a superposed stationary small-scale structure (wavelength of the order of 250 km) in the eastward flow, which would imply a pair of local field-aligned current sheets possibly related to an auroral arc.

Key words: Magnetic variations – Scandinavian magnetometer array – Field separation – Upward continuation of external fields – Eastward auroral electrojet – Field-aligned currents.

Introduction

It is well known that during periods of enhanced magnetospheric activity an eastward electrojet flows in the dark postnoon and evening sector along the southern part of the auroral oval (Kamide and Fukushima, 1972; Rostoker, 1972) simultaneously with a more poleward situated westward electrojet, which

0340-062X/79/0045/0281/$03.60

penetrates from the midnight into the evening sector during periods of substorm activity (Rostoker and Kisabeth, 1973; Rostoker et al., 1975). The eastward electrojet flows in a conductivity channel generated mainly by diffuse and relatively uniform precipitation (Wallis et al., 1976) of inner plasmasheet particles (Lui et al., 1977). It is driven by a northward electric field, which has been observed by means of satellites (e.g. Maynard, 1974), rockets (e.g., Evans et al., 1977) and the Chatanika-radar (e.g., Banks et al., 1973). Field-aligned currents appear to flow upward in the poleward and downward in the equatorward half of the eastward electrojet region (Rostoker et al., 1975). Therefore it may be assumed that the eastward electrojet mainly consists of a relatively uniform – if compared with the substorm westward electrojet – Hall current (Wescott et al., 1969; Brekke et al., 1974; Baumjohann et al., 1978).

Besides these large-scale features, small-scale phenomena have also been observed in the eastward electrojet region most of which are related to auroral arcs. Wallis et al. (1976) and Wallis (1976) observed auroral arcs embedded in the region of diffuse aurora. Lui et al. (1977) reported highly structured and intense electron precipitation causing discrete auroras sometimes embedded in the diffuse precipitation aurora region and Mende and Eather (1976) found dynamic structures in the soft and mainly diffuse electron precipitation. Iijima and Potemra (1978) observed fine scale structures in the evening sector field-aligned currents during active periods when the westward electrojet had intruded into the evening sector. Armstrong et al. (1975) and Kamide and Rostoker (1977) pointed out that small-scale structures in the field-aligned current flow observed by the TRIAD satellite were related to discrete arcs in the poleward half of the eastward electrojet region. Casserly and Cloutier (1975) found a small-scale field-aligned current sheet pair near an auroral arc in the positive bay region. Maynard et al. (1977) and Evans et al. (1977) reported a decrease of the northward electric field in the eastward electrojet region when their rocket flew over an auroral arc. Beaujardiere et al. (1977) observed southward electric fields in evening arcs, which were embedded in an ambient northward electric field, using data from the incoherent scatter radar at Chatanika.

At the present we have tried to apply the method of field continuation towards the source to ground-based magnetic observations of an eastward electrojet. This method is well-known in applied geophysics (see e.g., Grant and West, 1965) and has been already used by McNish (1938) in order to estimate possible heights of auroral zone ionospheric currents. These results were much limited by the large mutual distances and the irregular distribution of magnetic observation stations. Against this we were able to base our investigation on two parallel, closely neighbouring profiles which were rather evenly and densely occupied by magnetometers.

As compared to methods where, in the course of interpolation, model ionospheric or magnetospheric current systems are adjusted to ground-based magnetic observations by trial and error or some inversion techniques, the method of upward continuation presents a rather direct way by which at least equivalent height-integrated ionospheric current densities can be derived. It was the main purpose of the present study to examine this method in practice for a two-dimensional case in which variability transverse to the profiles of observations

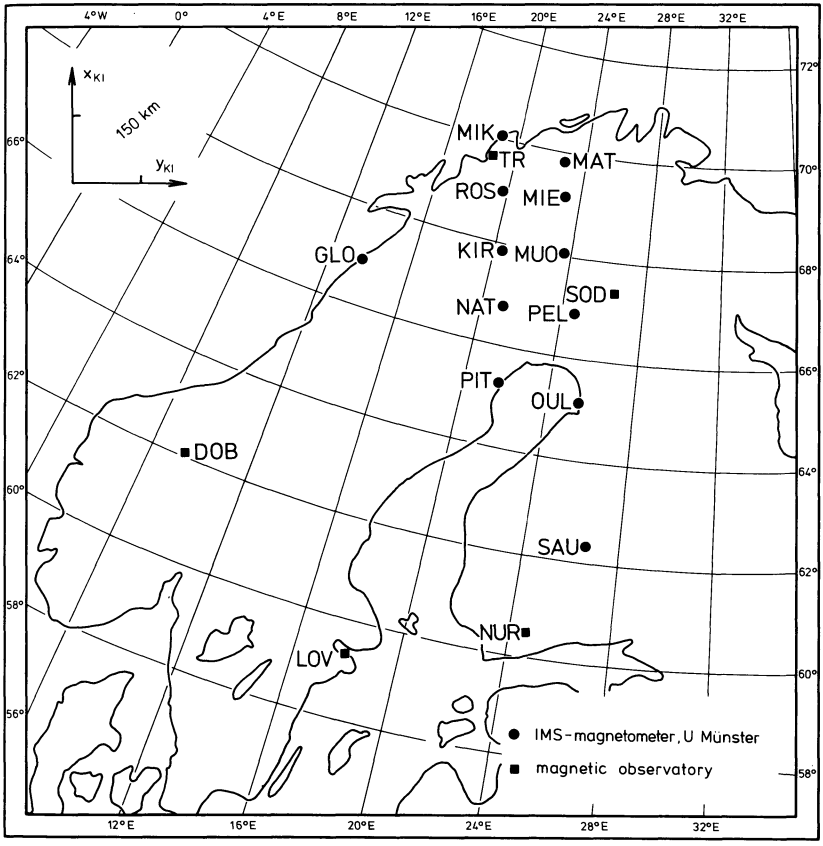

Fig. 1. Locations of magnetic stations used in this study. Within the *upper left corner* the Kiruna system (see text) is indicated, besides its origin which is at Kiruna (*KIR*)

might be neglected, and accordingly a two-dimensional algorithm could be applied.

Instrumentation

During the International Magnetospheric Study (IMS) the University of Münster is operating an array of magnetometers of an improved Gough-Reitzel type (Gough and Reitzel, 1967; Küppers and Post, 1979) in Scandinavia (Küppers et al., 1979). In 1975 13 of these magnetometers, on two nearly parallel profiles aligned along geomagnetic meridians with a spacing of 100–150 km in northern Scandinavia, were already recording. Also an additional one was operating at the western coast of northern Norway. Data from 12 of these stations, as shown in Fig. 1, were available for October 1975 and have been used together with data from the magnetic observatories shown in the figure and from the two observatories Bear Island (BJO, 74.5°N, 19.0°E) and Ny Alesund (NAL, 78.9°N, 11.9°E), which are located further to the north.

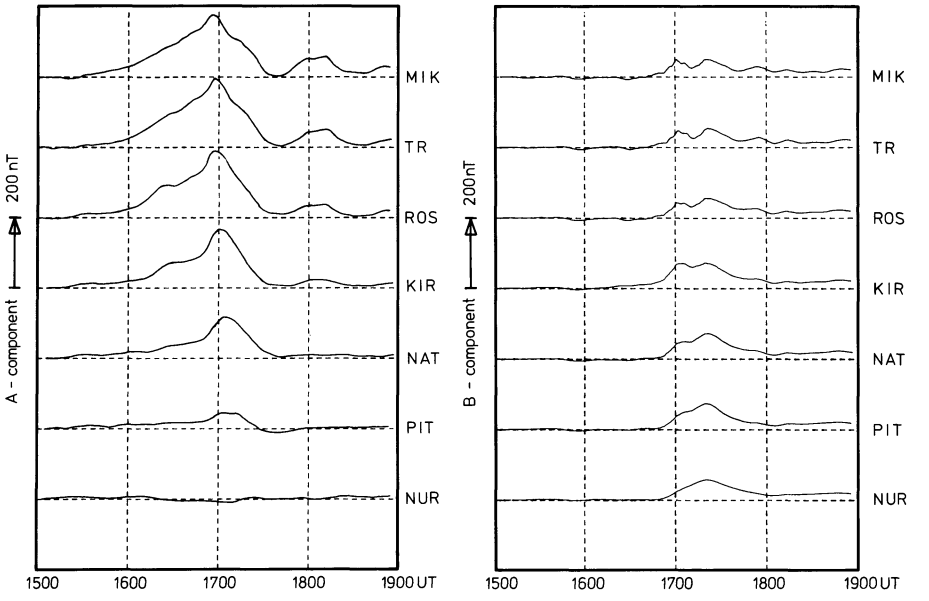

Fig. 2. Magnetograms of lowpass-filtered *A*- and *B*-components for the western profile of magnetometers (see Fig. 1), on October 26, 1975. The *A*- and *B*-components are defined parallel to the x_{KI}- and y_{KI}-axis, respectively (cf. Fig. 1)

The coordinate system indicated in the upper left corner of Fig. 1 has been introduced by Küppers et al. (1979) and named the Kiruna system. It is a Cartesian system obtained by a stereographic projection of the globe onto a tangential plane centered at Kiruna, Sweden (67.8° N, 20.4° E). Cartesian coordinates are very suitable for analysing magnetic field data by means of potential theory methods as applied in this paper. The y_{KI}-axis of the system has been chosen as the tangent to the projection of the ϕ_c (KIR) = 64.8° line with ϕ_c being the revised corrected geomagnetic latitude as given by Gustafsson (1970). The x_{KI}-axis is perpendicular to the y_{KI}-axis and is directed approximately 12° west of geographic north at Kiruna, where the system has its origin ($x_{KI} = y_{KI} = 0$).

General Character of the Magnetic Variations Observed

On October 26, 1975, a positive bay of about 200 *nT* was observed between 1500 and 1800 UT (1730–2130 MLT) in the Scandinavian sector at a time of weak magnetospheric activity ($Kp = 3$). Variations of the magnetic components *H*, *D*, and *Z* relative to the quiet day level were lowpass-filtered with a simple moving average filter to remove small-scale magnetic variations with periods less than 5 min, which were superimposed on the positive bay signature. The filtered variations were then mapped into the Cartesian Kiruna system.

In Fig. 2 the magnetograms for the lowpass-filtered *A*-components (magnetic deflection parallel to the x_{KI}-axis) and *B*-components (magnetic deflection paral-

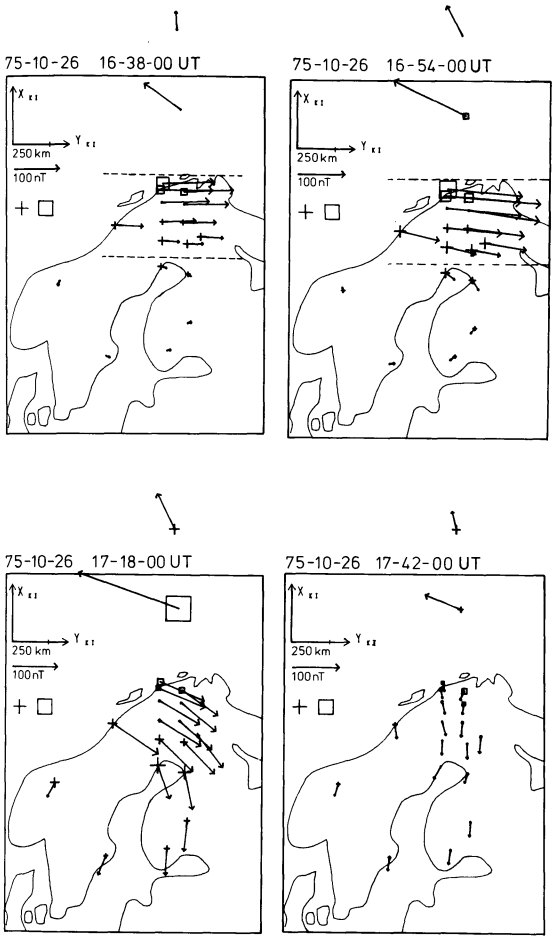

Fig. 3. Equivalent current arrows (in nT) on the earth's surface for 4 instances of time. The current arrows have their origin at the station, where the corresponding magnetic disturbances have been recorded. Squares and crosses denote negative and positive Z-components, respectively. The *dashed lines in the upper two panels* give the borders of the main two-dimensional equivalent eastward flow

lel γ_{KI}) observed on the western profile of stations are illustrated. Figure 3 shows the equivalent current vectors on the earth's surface at four different times. The equivalent current vector is obtained from the measured horizontal magnetic disturbance vector by rotating the latter vector 90° clockwise, as viewed from above.

Apparently the positive A-perturbation (indicating an eastward electrojet) commences for all stations in northern Scandinavia around 1520 UT. The magnitude increases slowly until 1700 UT, when it reaches its peak value with the largest A-values about 100 km south of the northern coast of Norway (stations ROS and MIE). Note that this maximum occurs later at the more southern

and also (not shown in Fig. 2) at the more western stations. This southwestern expansion of the eastward electrojet has also been observed by Kamide and Fukushima (1972). At about 1650 UT the B-perturbation changes from zero to positive, indicating a southward component of the equivalent current flow. From 1650 UT onwards the B-components increase, with their maximum occurring at about 1720 UT while the A-components slowly decrease. This gives rise to a southward turning of the equivalent current flow as seen in the lower two diagrams of Fig. 3.

The small values of B, and the similarity in the A-variations observed at equivalent stations of both profiles, infer that the main part of the current system is rather two-dimensional until 1710 UT. This is supported by the equivalent current vectors plotted in the upper two diagrams of Fig. 3.

Finally it should be noted that the magnetic signatures seen more to the north at BJO show a westward electrojet during the whole interval. This jet penetrated into the evening sector due to substorm activity around midnight (Rostoker and Kisabeth, 1973; Rostoker et al., 1975; Iijima and Potemra, 1978). Magnetograms of Siberian observatories give clear indications of an increase in westward electrojet activity during the interval studied. Especially Cape Chelyuskin showed clear signatures of a substorm onset (cf. Untiedt et al., 1978) by a strong and abrupt decrease in H together with a sudden increase in D when it was located just around magnetic midnight (at about 1645 UT). The northernmost station NAL showed rather northward directed equivalent currents during the whole interval, which seem to be related to polar cap effects (Wallis et al., 1976). Current directions at both stations (BJO and NAL) are not exactly antiparallel to the eastward electrojet flow. This fact together with the rather large spacing made a quantitative analysis of the northern part of the current system impossible. Accordingly, all results for the westward electrojet shown in the next sections should be taken more qualitatively than quantitatively.

Equivalent Height Integrated Ionospheric Current Density Profiles Calculated Via Field Separation and Upward Continuation

For a two-dimensional analysis of the equivalent current system between 1606 and 1710 UT it was necessary to construct latitude profiles of the horizontal and vertical magnetic components perpendicular to the main current direction. Therefore, separately for each instance of time, both spatial (x_{KI}, y_{KI}) and magnetic horizontal (A, B) coordinate axes of the Kiruna system have been rotated by the average of the local angles $\alpha_i(t) = \tan^{-1}[B_i(t)/A_i(t)]$ given by stations under the main current flow (e.g., stations between the two dashed lines in the upper two diagrams of Fig. 3). This minimized the variations in the horizontal component parallel to the jet and yielded the new horizontal magnetic component V, along the new u_{KI}-axis, perpendicular to the eastward electrojet. In the upper part of Fig. 4, latitude profiles constructed by cubic spline interpolation of the V- and Z-components along the u_{KI}-axis for the magnetic field observed on the western profile at 1638 UT are illustrated. Also shown is the magnetic component parallel to the main current direction (W, dotted line

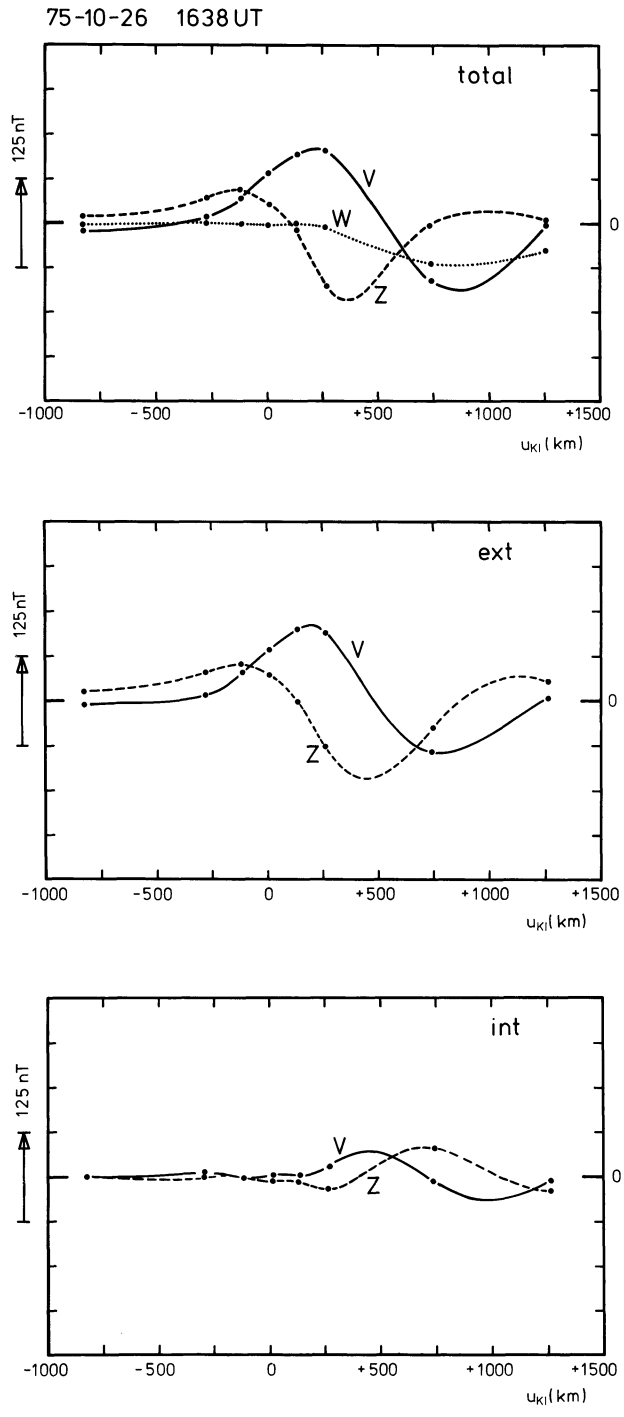

Fig. 4. Latitude profiles of observed (*upper diagram*), external (*middle diagram*) and internal (*lower diagram*) magnetic field components for the western chain at 1638 UT. The solid line gives the horizontal *V*-component (perpendicular to the main current flow), the *dashed line* represents the vertical *Z*-component and the *dotted line* in the upper diagram shows the horizontal magnetic component perpendicular to *V* and parallel to the main current flow (*W*). The big dots denote the position of the stations

in the upper diagram). It can be seen that the variations of this component are essentially zero over the Scandinavian mainland. The latitude profiles constructed with stations on the eastern chain are in excellent agreement and support very strongly the idea that a two-dimensional analysis is possible for this time interval, if one keeps in mind that any results for the westward electrojet indicated by the two northern stations are quite ambiguous because of the deviating current direction and the great spacing between these stations.

Since the magnetic field observed on the ground is a superposition of the ionospheric-magnetospheric source field and the field of the currents induced in the ground, it appeared to be necessary to separate the magnetic horizontal component V and the vertical component Z into inner and outer parts. For a two-dimensional case in a Cartesian coordinate system this can be achieved by means of the Hilbert transform (Kertz, 1954; Siebert and Kertz, 1957; Weaver, 1964). With the Kertz operator K defined by:

$$KF(u_{\mathrm{KI}}) = \frac{1}{\pi} \int_{-\infty}^{+\infty} \frac{F(\hat{u}_{\mathrm{KI}})}{u_{\mathrm{KI}} - \hat{u}_{\mathrm{KI}}} d\hat{u}_{\mathrm{KI}}$$

one gets the following relations for the internal and external parts of the magnetic field on the earth's surface:

$$\begin{aligned}
V_e(u_{\mathrm{KI}}) &= \tfrac{1}{2}[V(u_{\mathrm{KI}}) + KZ(u_{\mathrm{KI}})] \\
V_i(u_{\mathrm{KI}}) &= \tfrac{1}{2}[V(u_{\mathrm{KI}}) - KZ(u_{\mathrm{KI}})] \\
Z_e(u_{\mathrm{KI}}) &= \tfrac{1}{2}[Z(u_{\mathrm{KI}}) - KV(u_{\mathrm{KI}})] \\
Z_i(u_{\mathrm{KI}}) &= \tfrac{1}{2}[Z(u_{\mathrm{KI}}) + KV(u_{\mathrm{KI}})].
\end{aligned}$$

Since the integral has to be calculated from $-\infty$ to $+\infty$ one has to assume extrapolating functions for the V and Z latitude profiles outside the data interval. In the present analysis an exponential trend was matched at the data of the northern and southern limits of the profiles. This trend function slowly decreased to zero with increasing distance from the limits.

The separated fields for 1638 UT are illustrated in Fig. 4, where the middle panel shows the external parts of the magnetic components given in the upper part and the lower diagram gives the internal parts. It is seen quite clearly that the field due to induced currents seems to be rather weak over the Scandinavian mainland ($u_{\mathrm{KI}} < +200$ km) while it appears to increase over the sea. Either the poor two-dimensionality of the westward jet or the good conducting seawater could possibly be responsible for the different positions of extrema respectively zero-crossovers of external and internal parts. For a more detailed discussion of this topic see Küppers et al. (1979).

If the external magnetic horizontal component V_e is assumed to be periodic along the u_{KI}-axis, with $2\pi k_0^{-1}$ defining the basic wavelength (large as compared to the length of our profiles) it may be expanded below the ionosphere according to potential theory into the series:

$$V_e(u_{\mathrm{KI}}, z) = \sum_{n=0}^{\infty} (a_k \cos(k u_{\mathrm{KI}}) + b_k \sin(k u_{\mathrm{KI}})) e^{kz}$$

where $k = nk_0$ denotes the wavenumber and z denotes the height.

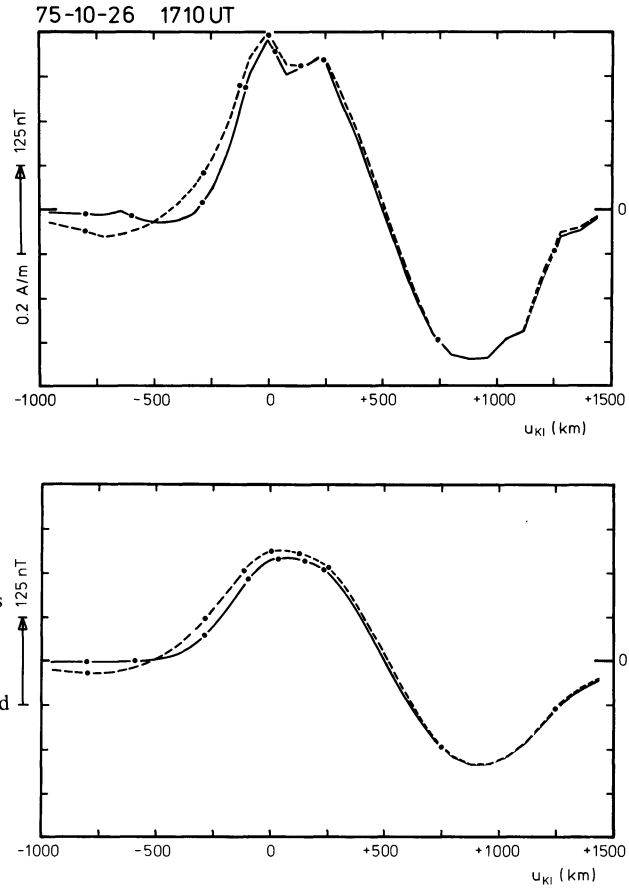

Fig. 5. Latitude profiles of the external horizontal magnetic V component (cf. Fig. 4) for both chains of stations at 1710 UT. The lower diagram gives the components at the earth's surface while the *upper panel* shows the derived V components at 110 km height or the equivalent height-integrated eastward ionospheric current density. The *solid line* is representative for the eastern, the *dashed line* for the western chain of stations and the *dots* denote positions of the stations

Therefore Fourier analysis of the V_e latitude profile on the ground, multiplication of the Fourier coefficients with e^{kh} (h assumed height of ionospheric current layer) and subsequent Fourier synthesis yields the magnetic field just below the ionospheric current layer. We have chosen $h=110$ km according to the observed average height of eastward and westward electrojets (Kamide and Brekke, 1977).

During upward continuation, larger wave-numbers, i.e., very large factors e^{kh} lead to the well-known problem of instability of the method (large short-wavelength oscillations of the continued field). The problem may be solved either by cutting the Fourier spectrum above a certain k-value, or by performing a harmonic analysis and synthesis with sufficiently large spacing Δu_{KI} between neighboured field values instead of the above described Fourier analysis of a continuous function. In our case we proceeded along the second line. We found that with $\Delta u_{KI}=80$ km oscillations of the continued field could be avoided, while the spatial resolution was still sufficient and corresponded to a minimum wavelength of 160 km. As an example of the results, the height-continued V_e-component along both magnetometer profiles at 1710 UT is shown in Fig. 5, together with the V_e (u_{KI}) curves on the ground.

From Biot-Savart's law the following relation can be derived for the current density J_{eq} (in Am^{-1} positive eastwards) of the equivalent height-integrated ionospheric current perpendicular to the u_{KI}-axis generating the magnetic component V_e:

$$J_{eq}(u_{KI}) = \frac{2}{\mu_0} V_e(u_{KI}, h)$$

where it is assumed that V_e is given in T. Accordingly, in Fig. 5 (upper part) the height-continued V_e-component may be considered as a height-integrated current density (c.f., corresponding scale to the left).

As compared to the curves given at ground (lower part of Fig. 5), $V_e(u_{KI})$ at 110 km height (upper part of Fig. 5) is more concentrated and shows larger extremum values, as is to be expected after continuation towards the source. Note, however, that the results for $u_{KI} \geqq +300$ km (i.e., especially for the regime of the westward electrojet) are rather ambiguous, because of the reasons mentioned above. Besides an interesting steepening of the southward flank of the eastward electrojet part of the curves during upward continuation, the appearance of a small scale structure near the V_e maximum is quite conspicuous. It corresponds mainly to a wavelength of nearly 250 km, with the above mentioned factor e^{kh} amounting to about 20. Accordingly, this local structure does not appear as an indentation at ground but only as a slight asymmetry within the curve near its maximum.

Of course, it has to be examined if this small-scale structure is real or if it has been introduced artificially in the course of the different mathematical procedures which have been applied. We exclude the possibility that the structure is due to the above mentioned instability of the continuation method, because the corresponding short-wavelength oscillations disappeared rather uniformly along the whole profile when we enlarged the spacing Δu_{KI} stepwise from 20 to 80 km. Also the special interpolation which has been used seems not to be of importance because we got nearly the same indentation for both our profiles though the distribution of stations is clearly different for them. Furthermore, from our experience in a few other similar cases (as communicated privately to us by König and Sulzbacher) the interesting small scale structures do not always appear. This also seems to exclude the possibility that this irregularity is generated from a conductivity anomaly (coast effect, for example) via a not complete separation of internal and external parts. We therefore conclude that it is justified to assume the physical reality of the discussed small-scale structure.

In order to illustrate the temporal behaviour in Fig. 6, the derived equivalent height-integrated eastward current densities are given for 9 instances of time in the 1606 to 1710 UT interval, for which a two-dimensional analysis is considered valid. Apparently, both eastward and westward flowing currents grow steadily until 1702 UT. The maximum equivalent current densities of the eastward electrojet increase from 0.1 Am^{-1} at 1606 UT up to 0.5 Am^{-1} at 1702 UT and the total equivalent eastward current is also enhanced by a factor of 5 from $4 \cdot 10^4$ A to $2 \cdot 10^5$ A during the same interval. Simultaneously with the

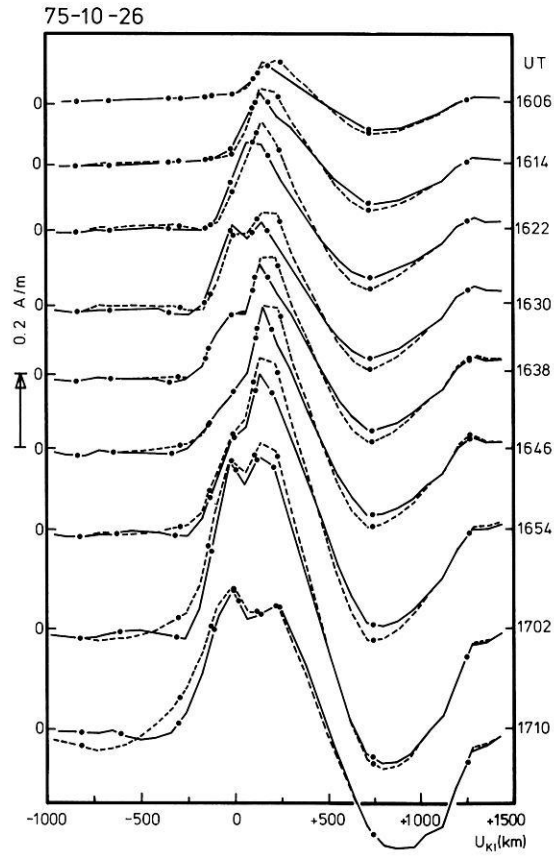

Fig. 6. Latitude profiles of the equivalent height-integrated ionospheric current density for every eighth minute between 1606 and 1710 UT. Otherwise as Fig. 5

growing current amplitude the whole current system broadens. The width of the eastward current system is increased from 500 to 800 km by an equatorward shift of its well-defined southern edge linearly with time (about 50 ms^{-1}), while the demarcation line to the westward flowing current remains stationary at $u_{KI}=500$ km (approximately 69° revised corrected geomagnetic latitude).

Additional to these large-scale features, the above discussed interesting small-scale structure can be seen all the time between 1630 and 1710 UT at a fixed position. It occurs as a local decrease of about 0.1 Am^{-1} near the large-scale current density maximum between $u_{KI}=0$ and 200 km.

Field-Aligned Current Density Profiles

We have also tried to calculate the distribution of field-aligned currents by a method similar to the one used, e.g., by Kamide and Horwitz (1978). The method is based on current continuity:

$$\mathbf{div} \cdot \mathbf{J} = j_{\parallel}$$

and Ohm's law for the ionosphere:

$$\mathbf{J} = \begin{pmatrix} +\Sigma_P & +\Sigma_H \\ -\Sigma_H & +\Sigma_P \end{pmatrix} \cdot \mathbf{E}$$

with $\mathbf{J}$ denoting the horizontal vector of height-integrated ionospheric current density, $j_{\parallel}$ the downward field-aligned current density, Σ_H and Σ_P the height-integrated ionospheric Pedersen- and Hall-conductivity, and $\mathbf{E}$ the horizontal ionospheric electric field (assuming the magnetic field directed vertically downward for high latitudes). If we interpret our equivalent height-integrated ionospheric current density J_{eq} as a Hall-current caused by a pure north-south electric field (e.g., Wescott et al., 1969; Brekke et al., 1974; Zmuda and Armstrong, 1974) we may estimate the downward field-aligned current density by:

$$j_{\parallel}(u_{KI}) = \frac{\partial}{\partial u_{KI}} \left[\frac{\Sigma_P}{\Sigma_H}(u_{KI}) J_{eq}(u_{KI}) \right].$$

The variability of the ratio Σ_H/Σ_P along our profiles and with time is not known. Though results from the Chatanika-radar (see, e.g., Brekke et al., 1974; Horwitz et al., 1978) show that this ratio may vary appreciably with time especially within the regime of the westward electrojet, where it may be as large as 4, a constant value of 2 may be a not too unrealistic estimate for our case of an eastward electrojet (see Brekke et al., 1974; Wedde et al., 1977). With this assumption we get:

$$j_{\parallel}(u_{KI}) = \frac{1}{2} \frac{\partial}{\partial u_{KI}} J_{eq}(u_{KI}).$$

The results of the corresponding calculations are shown in Fig. 7. It shows that the large-scale field-aligned current distribution exhibits downward current flow over a width of 250–500 km in the equatorward half of the eastward electrojet region with current density maxima ranging from $0.4 \cdot 10^{-6}$ to $1.2 \cdot 10^{-6}$ Am^{-2} between 1606 and 1710 UT. The region of field-aligned current flow out of the ionosphere stretches from the poleward half of the eastward electrojet region into the region of the westward electrojet and broadens from 500 to 650 km during the interval studied while the current density maxima increase from 0.3 to $1.0 \cdot 10^{-6}$ Am^{-2}. There is also a poleward region of inflowing field-aligned currents.

The local decrease near the maximum of J_{eq} (cf. Fig. 6) gives rise to a local pair of field-aligned currents of less than 100 km width each (corresponding to the maximum spatial resolution of our analysis). These sheets have maximum current densities of $0.8 \cdot 10^{-6}$ Am^{-2} and $4 \cdot 10^{-2}$ Am^{-1}, respectively, at 1702 UT.

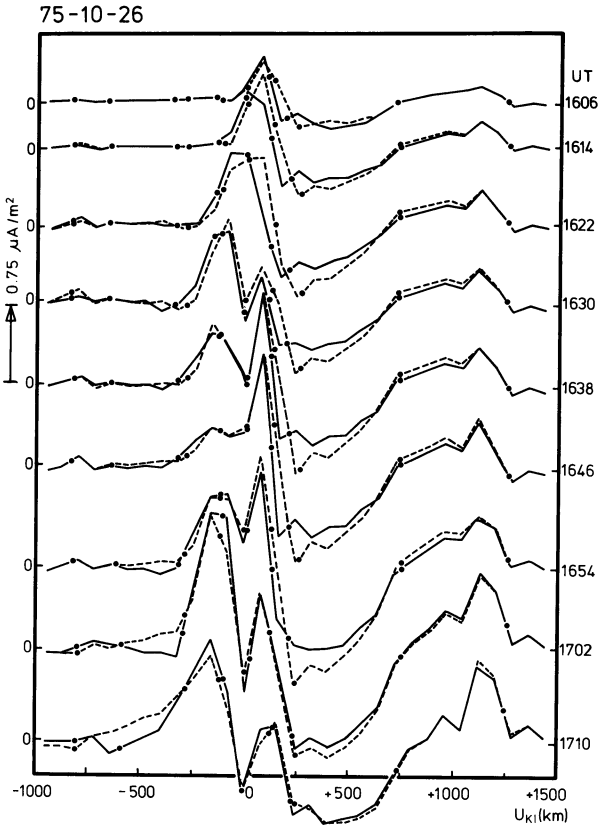

Fig. 7. Latitude profiles of the field-aligned current density derived by differentiating the profiles of Fig. 6. Positive values denote downward currents and vice versa. Otherwise as Fig.. 5

Discussion

The distribution of equivalent height-integrated ionospheric currents and its temporal development derived in this study is in agreement with the results of Kamide and Fukushima (1972) and also consistent with the idea of intrusion of the substorm intensified westward electrojet as introduced by Rostoker and Kisabeth (1973). Wallis et al. (1976) have found a close correlation between the equatorward boundaries of eastward electrojet and diffuse aurora, which Lui et al. (1977) described as the optical image of the inner plasmasheet in the polar ionosphere. Therefore we may relate the equatorward shift of the sharp southern eastward electrojet boundary (see Fig. 6) to an earthward shift of the inner edge of the plasmasheet with increasing activity, which also Winningham et al. (1975) found using Isis observations.

In order to relate the equivalent eastward current to the real ionospheric currents, we have compared the ratio of maximum equivalent height-integrated

eastward current density and maximum northward magnetic variation on the ground with the results of Kamide and Brekke (1975), who compared ionospheric east-west current densities observed by the Chatanika radar with *H*-variations observed at College. We have found good agreement between our ratio (about $2.7 \cdot 10^{-3}$ $Am^{-1}nT^{-1}$) and the ratio which they found for two cases when the center of a slightly stronger current than ours was situated near the Chatanika radar facility. Taking into account that Chatanika observations regularly give a nearly pure northward directed field in the eastward electrojet region (e.g., Wedde et al., 1977; Horwitz et al., 1978) the above mentioned comparison seems to indicate that our technique yields equivalent eastward ionospheric current densities very near to the real eastward Hall-current density when applied to the eastward electrojet. This is consistent with the results of Baumjohann et al. (1978) who found by comparing ground-based magnetometer array data with spatial radar observations that for the eastward electrojet ground-based magnetometers see mainly the effect of the Hall-current flow and magnetic effects of field-aligned and Pedersen-currents cancel each other (Fukushima, 1976).

The large scale configuration of the field-aligned currents observed by us around 1900 MLT is in good agreement with the TRIAD-observations of Iijima and Potemra (1976; 1978) for the same MLT sector and the result of Rostoker et al. (1975). These authors show that field-aligned currents flow downward above both the southern half of the eastward electrojet and the northern half of the westward electrojet region with upward flow in the middle between these two regions. Our field-aligned current densities of about 10^{-6} Am^{-2} are well in the range given by more direct measurements (e.g., Zmuda and Armstrong, 1974; Sugiura and Potemra, 1976) and come very near to the values given by Iijima and Potemra (1978) for their region 1 and 2 currents in this local time sector for disturbed periods. The calculated width of the field-aligned current region (about 1600 km) is greater than that given by Iijima and Potemra (1978) for a substorm expansion phase (about 1000 km) but agrees well with the results of Rostoker et al. (1975).

A really new result found from our present analysis seems to be the small-scale decrease in equivalent eastward ionospheric current density near its maximum. Structures like this have not been reported so far by other authors who used ground-based magnetometer data to model the ionospheric current flow. This is at least partly due to the method of analysis used by these authors, since inverse modelling as used e.g. by Scrase (1967), Czechowsky (1971), and Oldenburg (1976; 1978) needs a forward model of the current density distribution with as few parameters as possible (mostly parabolic or triangular distributions) or a rather smooth latitudinal function to obtain meaningful results.

The local decrease of about 0.1 Am^{-1} (Fig. 6) near the maximum eastward ionospheric current density implies a pair of field-aligned currents of about $4 \cdot 10^{-2}$ Am^{-1} flowing upward in the equatorward and downward on the poleward side of this small-scale structure. Since we have related the equivalent eastward current to a Hall current driven by a pure northward convection electric field, the small-scale field-aligned current pair must have a magnetospheric source. An ionospheric source would require a physically unreasonable decrease in conductivity between the two field-aligned currents to explain the

decrease in eastward current flow (Boström, 1964) and also would yield sheet currents of maximum 10^{-2} Am^{-1} only after Mallinckrodt and Carlson (1978) for polarization electric fields of about 20 mVm^{-1} as given, e.g., by Beaujardiere et al. (1977) for auroral acrs in the evening sector.

We have the strong feeling that the local current sheet pair may be related to an auroral arc. Unfortunately no all-sky camera data was available to prove this, but broad beam riometer recordings made at Tromsø (Stauning and Christensen, 1977) show at least weak precipitation of 10–20 keV electrons in the region of the small-scale structure around 1700 UT when the strongest local sheet currents are observed. This precipitation of energetic electrons is often related to discrete aurora (Wallis, 1976; Evans et al., 1977; Carlson and Kelley, 1977; Lui et al., 1977).

Additional evidence is given by relating our observations to the results of other authors (already reviewed in the introduction to this paper) who observed small-scale structures mostly related to auroral arcs in the eastward electrojet region. The reader may easily see that their observations of structured electron precipitation (Lui et al., 1977; Mende and Eather, 1976), local field-aligned current sheet pairs (Armstrong et al., 1975; Casserly and Cloutier, 1975; Kamide and Rostoker, 1977; Iijima and Potemra, 1978) and southward or strongly decreased northward electric field in or near auroral arcs (Maynard et al., 1977; Evans et al., 1977; Beaujardiere et al., 1977) fit reasonably well to our observations.

We have also compared our results qualitatively with the model of Sato (1978) for quiet auroral arcs, who showed that for an ambient pure northward electric field auroral arcs can develop due to a feedback instability in the coupled ionosphere-magnetosphere system with a local upward current south and a downward sheet current north of the arc, like in our case. He also predicts an arc-associated westward flow of current which should be rather weak if the electric field is only north-south directed, consistent with our observations.

Conclusions and Summary

In the present paper, for the case of an eastward electrojet, we have demonstrated the usefulness of the method of upward continuation (towards the source) for analyzing auroral zone groundbased magnetic observations. This method gives in a rather direct way – as compared to modelling techniques – the density-distribution of the at least equivalent height-integrated ionospheric current. Furthermore, it seems to be capable to reveal rather clearly small-scale (down to 200 km wavelength) structures within the larger scale current flow. Finally, in the present case it allowed for a rather sharp definition of the southward border of the eastward electrojet, this border possibly being related to the inner edge of the magnetospheric plasma sheet.

For the special event which we investigated the more detailed main results have been:

1. Between 1606 and 1702 UT only a two-dimensional analysis was possible both the total value and the maximum density of the eastward flowing height-

integrated equivalent ionospheric current increased by a factor of 5, namely from $4 \cdot 10^4$ to $2 \cdot 10^5$ A, and from 0.1 to 0.5 Am^{-1}, respectively. The demarcation line between the equivalent ionospheric eastward and westward currents remained stationary over this time interval, whereas the well-defined southern border of the eastward current moved towards the south with an average speed of about 50 ms^{-1}, possibly indicating a corresponding movement of the inner edge of the plasma sheet.

2. Under the assumption that the derived equivalent ionospheric current was a pure Hall current, and that the ratio Σ_H/Σ_P was equal to 2 all the time and at all places, the maximum density of the downflowing field-aligned current corresponding to the large-scale eastward electrojet above its southern half was estimated to increase from 0.4 to 1.2 μAm^{-2} over the time interval mentioned. Simultaneously, the broad distribution of upflowing current adjacent to the north showed maximum densities growing from 0.3 to 1.0 μAm^{-2}.

3. A local decrease in eastward electrojet current density probably has been found near its maximum. This implies a local pair (less than 100 km width each) of down- and upflowing field-aligned current sheets with a maximum current density of $0.8 \cdot 10^{-6}$ Am^{-2} and $4 \cdot 10^{-2}$ Am^{-1}, respectively, inside the large-scale region of downflowing current. Evidence has been given that this small-scale structure may possibly be related to a quiet auroral arc.

Acknowledgements. We are greatly indebted to the members of the magnetometer group at the University of Münster, who all were involved collecting the data. We thank especially Professor J. Untiedt for his support during all stages of this work and Dr. A.G. Jones for useful comments on an earlier version of this manuscript. We would like to thank also Drs. Ch. Sucksdorff (Helsinki), S. Berger (Tromsø), F. Eleman (Stockholm), and E. Gjoen (Bergen), who supplied us with the additional magnetic data used in this study. The magnetic observations were performed in cooperation and with much help from the Geophysical Observatory of the Finnish Academy of Sciences and Letters at Sodankylä (Dr. E. Kataja), the Finnish Meteorological Institute at Helsinki (Dr. C. Sucksdorff), the Department of Plasma Physics of the Royal Institute of Technology at Stockholm (Dr. R. Boström, now at Uppsala), the Kiruna Geophysical Institute (Dr. G. Gustafsson), and the Auroral Observatory at Tromsø (Mr. St. Berger). They have been supported financially by grants of the Deutsche Forschungsgemeinschaft. The critical comments and suggestions of two unknown referees have been highly appreciated.

References

Armstrong, J.C., Akasofu, S.-I., Rostoker, G.: A comparison of satellite observations of Birkeland currents with ground observations of visible aurora and ionospheric currents. J. Geophys. Res. **80**, 575–586, 1975

Banks, P.M., Doupnik, J.R., Akasofu, S.-I.: Electric field observations by incoherent scatter radar in the auroral zone. J. Geophys. Res. **78**, 6607–6622, 1973

Baumjohann, W., Greenwald, R.A., Küppers, F.: Joint magnetometer array and radar backscatter observations of auroral currents in Northern Scandinavia. J. Geophys. **44**, 373–383, 1978

Beaujardiere, O. de la, Vondrak, R., Baron, M.: Radar observations of electric fields and currents associated with auroral arcs. J. Geophys. Res. **82**, 5051–5062, 1977

Boström, R.: A model of the auroral electrojets. J. Geophys. Res. **69**, 4983–5000, 1964

Brekke, A., Doupnik, J.R., Banks, P.M.: Incoherent scatter measurements of E-region conductivities and currents in the auroral zone. J. Geophys. Res. **79**, 3773–3790, 1974

Carlson, C.W., Kelley, M.C.: Observation and interpretation of particle and electric field measurements inside and adjacent to an active auroral arc. J. Geophys. Res. **82**, 2349–2360, 1977

Casserly, R.T., Cloutier, P.A.: Rocket-based magnetic observations of auroral Birkeland currents in association with a structured auroral arc. J. Geophys. Res. **80**, 2165–2168, 1975

Czechowsky, P.: Calculation of an equivalent current system in the polar E-region. Radio Sci. **6**, 247–253, 1971

Evans, D.S., Maynard, N.C., Trøim, J., Jacobsen, T., Egeland, A.: Auroral electric field and particle comparisons. 2. Electrodynamics of an arc. J. Geophys. Res. **82**, 2235–2249, 1977

Fukushima, N.: Generalized theorem for no ground magnetic effect of vertical currents connected with Pedersen currents in the uniform-conductivity ionosphere. Rep. Ionos. Space Res. Jpn. **30**, 35–40, 1976

Gough, D.I., Reitzel, J.S.: A portable three component magnetic variometer. J. Geomagn. Geoelectr. **19**, 203–215, 1967

Grant, F.S., West, G.F.: Interpretation theory in applied geophysics. New York: McGraw-Hill 1965

Gustafsson, G.: A revised corrected geomagnetic coordinate system. Ark. Geofys. **5**, 595–617, 1970

Horwitz, J.L., Doupnik, J.R., Banks, P.M.: Chatanika radar observations of the latitudinal distributions of auroral zone electric fields, conductivities, and currents. J. Geophys. Res. **83**, 1463–1481, 1978

Iijima, T., Potemra, T.A.: The amplitude distribution of field-aligned currents at northern high latitudes observed by Triad. J. Geophys. Res. **81**, 2165–2174, 1976

Iijima, T., Potemra, T.A.: Large-scale characteristics of field-aligned currents associated with substorms. J. Geophys. Res. **83**, 599–615, 1978

Kamide, Y., Brekke, A.: Auroral electrojet current density deduced from the Chatanika radar and from the Alaska meridian chain of magnetic observatories. J. Geophys. Res. **80**, 587–594, 1975

Kamide, Y., Brekke, A.: Altitude of the eastward and westward auroral electrojets. J. Geophys. Res. **82**, 2851–2853, 1977

Kamide, Y., Fukushima, N.: Positive geomagnetic bays in evening high-latitudes and their possible connection with partial ring current. Rep. Ionos. Space Res. Jpn. **26**, 79–101, 1972

Kamide, Y., Horwitz, J.L.: Chatanika radar observations of ionospheric and field-aligned currents. J. Geophys. Res. **83**, 1063–1070, 1978

Kamide, Y., Rostoker, G.: The spatial relationship of field-aligned currents and auroral electrojets to the distribution of nightside auroras. J. Geophys. Res. **82**, 5589–5608, 1977

Kertz, W.: Modelle für erdmagnetisch induzierte elektrische Ströme im Untergrund. Nachr. Akad. Wiss. Göttingen 1954, Math.-Phys. Kl., 101–110, 1954

Küppers, F., Post, H.: A second generation Gough-Reitzel magnetometer (accepted for publication). J. Geomagn. Geoelectr. 1979

Küppers, F., Untiedt, J., Baumjohann, W., Lange, K., Jones, A.: A two-dimensional magnetometer array for ground-based observations of auroral zone electric currents during the International Magnetospheric Study (IMS). J. Geophys. 1979

Lui, A.T.Y., Venkatesan, D., Anger, C.D., Akasofu, S.-I., Heikkila, W.J., Winningham, J.D., Burrows, J.R.: Simultaneous observations of particle precipitations and auroral emissions by the Isis 2 satellite in the 19–24 MLT sector. J. Geophys. Res. **82**, 2210–2226, 1977

Mallinckrodt, A.J., Carlson, C.W.: Relations between transverse electric fields and the field-aligned currents. J. Geophys. Res. **83**, 1426–1432, 1978

Maynard, N.C.: Electric field measurements across the Harang discontinuity. J. Geophys. Res. **79**, 4620–4631, 1974

Maynard, N.C., Evans, D.S., Maehlum, B., Egeland, A.: Auroral vector electric field and particle comparisons. 1. Premidnight convection topology. J. Geophys. Res. **82**, 2227–2234, 1977

McNish, A.G.: Heights of electric currents near the auroral zone. Terr. Magn. Atmos. Electr. **43**, 67–75, 1938

Mende, S.B., Eather, R.H.: Monochromatic all-sky observations and auroral precipitation patterns. J. Geophys. Res. **81**, 3771–3780, 1976

Oldenburg, D.W.: Ionospheric current structure as determined from groundbased magnetometer data. Geophys. J. **46**, 41–66, 1976

Oldenburg, D.W.: A quantitative technique for modelling ionospheric and magnetospheric current distributions. J. Geophys. Res. **83**, 3320–3326, 1978

Rostoker, G.: Polar magnetic substorms. Rev. Geophys. Space Phys. **10**, 157–211, 1972
Rostoker, G., Armstrong, J.C., Zmuda, A.J.: Field-aligned current flow associated with intrusion of the substorm-intensified westward electrojet into the evening sector. J. Geophys. Res. **80**, 3571–3579, 1975
Rostoker, G., Kisabeth, J.L.: Response of the polar electrojets in the evening sector to polar magnetic substorms. J. Geophys. Res. **78**, 5559–5571, 1973
Sato, T.: A theory of quiet auroral arcs. J. Geophys. Res. **83**, 1042–1048, 1978
Scrase, F.J.: The electric current associated with polar magnetic sub-storms. J. Atmos. Terr. Phys. **29**, 567–579, 1967
Siebert, M., Kertz, W.: Zur Zerlegung eines lokalen erdmagnetischen Feldes in äußeren und inneren Anteil. Nachr. Akad. Wiss. Göttingen 1957, Math.-Phys. Kl., 87–112, 1957
Stauning, P., Christensen, B.: Compilation of Ionlab riometer data for IMS-Workshop in Hankasalmi. Ionlab Rep. R41, Lyngby (Denmark), 1977
Sugiura, M., Potemra, T.A.: Net field-aligned currents observed by Triad. J. Geophys. Res. **81**, 2155–2164, 1976
Untiedt, J., Pellinen, R., Küppers, F., Opgenoorth, H.J., Pelster, W.D., Baumjohann, W., Ranta, H., Kangas, J., Czechowsky, P., Heikkila, W.J.: Observations of the initial development of an auroral and magnetic substorm at magnetic midnight. J. Geophys. **45**, 41–65, 1978
Wallis, D.D.: Comparison of auroral electrojets and the visible aurora. In: Magnetospheric particles and fields, B.M. McCormack, ed., pp. 247–255. Dordrecht: D. Reidel 1976
Wallis, D.D., Anger, C.D., Rostoker, G.: The spatial relationship of auroral electrojets and visible aurora in the evening sector. J. Geophys. Res. **81**, 2857–2869, 1976
Weaver, J.T.: On the separation of local geomagnetic fields into external and internal parts. Z. Geophys. **30**, 29–36, 1964
Wedde, T., Doupnik, J.R., Banks, P.M.: Chatanika observations of the latitudinal structure of electric fields and particle precipitation on November 21, 1975. J. Geophys. Res. **82**, 2743–2751, 1977
Wescott, E.M., Stolarik, J.D., Heppner, J.P.: Electric fields in the vicinity of auroral forms from motions of barium vapor releases. J. Geophys. Res. **74**, 3469–3487, 1969
Winningham, J.D., Yasuhara, F., Akasofu, S.-I., Heikkila, W.J.: The latitudinal morphology of 10-eV to 10-keV electron fluxes during magnetically quiet and disturbed times in the 2100–0300 MLT sector. J. Geophys. Res. **80**, 3148–3171, 1975
Zmuda, A.J., Armstrong, J.C.: The diurnal flow pattern of field-aligned currents. J. Geophys. Res. **79**, 4611–4619, 1974

Received January 11, 1979; Revised Version April 3, 1979; Accepted April 4, 1979

J. Geophys. 45, 299–317, 1979

Journal of Geophysics

Non-Linear Rheology and Return Flow in the Mantle

W.R. Jacoby[1] and G. Ranalli[2]

[1] Institut für Meterologie und Geophysik der Universität, Feldbergstr. 47, D-6000 Frankfurt 1, Federal Republic of Germany
[2] Department of Geology, Carleton University Ottawa, Canada

Abstract. A simple model of mantle return flow in response to lithospheric plate motions is developed. Such a model is realistic if the buoyancy forces are concentrated in the plates. One-dimensionality is chosen as a simplification to study effects of mantle rheology in as much isolation as possible. Rheology is modelled as a combination of dislocation creep, diffusion creep and fluid phase transport; parameters are those appropriate for olivine. We have varied temperature, grain size, influence of partial melt, diffusivity and activation energy, grain deformation versus grain boundary sliding dominated creep, and surface plate velocity. A peculiar feature of non-linear rheology is the existence of low-stress high-viscosity regions, which, however, are of little dynamic importance because deformation there is very small. The main results are (1) that the model does not predict an excessive pressure gradient to be required by the return flow (which would be evident in a rise of the sea floor and strong increase in free air gravity anomalies toward the trenches); (2) that no excessive shear stresses at the plate bottom are predicted (which might result in observable heat flow effects and intra-plate seismicity and would require implausibly great driving forces at the plate ends); (3) that the model predicts the return flow to extend into the deeper mantle; this follows, however, from the simplifying assumption of olivine rheology below 400 km depth and would then argue for rather high temperatures, small grain sizes, possibly important fluid phase transport, and small activation volume. Recent work on the variation of activation volume with pressure and phase changes suggests a rather 'soft' lower mantle and thus supports the notion of 'deep' return flow. In interpreting the results one must, of course, keep in mind that the model is a purely mechanical one with a predetermined temperature profile (varied within plausible limits) and that the physics of the thermodynamic aspects of the flow problem is ignored.

Key words: Rheology of earth's mantle – Plate sections – Model of mantle flow.

0340-062X/79/0045/0299/$03.80

Introduction

The present state of ignorance about plate dynamics requires model studies of mantle flow. One problem is that of the return flow: if a rigid surface plate moves in one direction the material below must flow back to conserve mass; in this model the plate moves against resistance from the return flow and drives it. The forces driving the plate, and the opposite model where the plate is carried passively or driven against some other resistance by the deep mantle flow, are not the subject of this paper.

In former studies (Schubert and Turcotte, 1972; Jacoby, 1978) depth-dependent Newtonian viscosity was assumed, but it is probably more realistic for the polycrystalline mantle to have non-Newtonian rheology (Stocker and Ashby, 1973). In order to isolate the effects of different rheologies it seems sensible, as done in the above studies, to model the problem in its simplest, i.e., one-dimensional and steady-state form; all quantities vary only with depth and the full circulation is ignored as though a 'cell' is infinite horizontally. The method of solution for non-linear rheology is an iterative one using the direct linear solution given by Jacoby (1978). Stresses and strain rates are found by successive adjustments and as one of the results one obtains the effective viscosity as their ratio. This viscosity is an integral part of the model and will not be appropriate to situations where additional strains are superimposed.

As will be discussed below, the non-linear creep of mantle material is strongly sensitive to temperature (among other parameters) so that shear heating will influence the flow. We have chosen to ignore this thermo-dynamic aspect of the problem in order to keep the model very simple; it is thus a purely mechanical one with predetermined temperature-depth profiles, varied within plausible limits. Schubert and Turcotte (1972), Froidevaux and Schubert (1975), Schubert et al. (1976), Froidevaux et al. (1977), Schubert et al. (1978), and Yuen et al. (1978) have treated the flow problem in a fuller way by including the shear heating and thus solving for temperature beside the flow velocity. As mentioned at the outset, the first of these papers assumed Newtonian viscosity; the later ones assumed non-linear dislocation creep but did not include diffusion creep and fluid phase transport because these would presumably be of little influence. In the simpler of their models the asthenosphere was assumed to be simply a layer of shear (not return) flow; the most complex model (Schubert et al., 1978; Yuen et al., 1978) additionally included partial return flow and vertical flow from below in variable proportions, buoyant forces, and heat advection. This is physically more complete than our model, but also more complex. Furthermore, there is still the unknown distribution of additional heat sources (other than dissipation) such that the complete thermodynamic solution of the flow problem remains open to ad hoc assumptions. We thus present our simple model as an instructive exercise in the study of the effects of various rheologies on the mantle return flow in a purely mechanical sense.

The method of solution and our assumptions, in particular those with respect to rheology, will be presented first. Then the results will be presented and discussed in terms of the geophysical constraints and consequences on gravity, sea floor topography, heat flow, plate kinematics, and stress in the lithosphere.

Method of Solution

In the one-dimensional steady-state return flow model (Jacoby, 1978) all quantities vary only with depth, z, and the horizontal (x) flow is driven entirely by the negative horizontal pressure (p) gradient balancing the resulting vertical gradient of the horizontal shear stress (τ)

$$\frac{\partial p}{\partial x}=\frac{\partial \tau}{\partial z}. \tag{1}$$

Effects of the rising and falling flow and of sphericity are neglected; gravity has no influence. The net transport through a vertical section is assumed to be zero. The surface velocity is imposed on the model and the bottom is held fixed at an arbitrary depth, for which we have usually chosen 2,000 km.

If the viscosity is Newtonian,

$$\tau=\eta\frac{du}{dz} \tag{2}$$

and Eq. (1) can be solved if $\partial p/\partial x$ is an integrable function of z, e.g., $\partial p/\partial x=A$. For stepwise constant $\eta(z)=\eta_i$ for $z_i<z\leqq z_{i+1}$:

$$\tau=A z+\eta_i B_i \quad \text{and} \quad \eta_i B_i=B \tag{3}$$

B is the shear stress at the bottom of the surface plate. The flow velocity u becomes

$$u=\frac{A}{\eta_i}\frac{z^2}{2}+\frac{B}{\eta_i}z+C_i. \tag{4}$$

Assuming continuous velocity and shear stress we can compute C_i. The solution is linear in surface velocity u_l.

If power law creep is assumed, $\tau^n=\beta\frac{du}{dz}$, where β is a PT-dependent parameter and n is a constant PT-independent exponent. Integration gives:

$$\tau=A z+\beta_i^{1/n}B_i=A z+B; \qquad u=\frac{(A z+B)^{n+1}}{A\beta_i(n+1)}+C_i. \tag{5}$$

For large n the velocity-depth profile approaches the cornered one of ideal plasticity. The problem is no longer linear in the surface velocity u_l.

If diffusion *and* dislocation creep govern the effective viscosity, its stress dependence $\eta(\tau)$ is such that no simple analytical solution can be found. A convenient way to solve this non-linear problem is iteration of the linear solutions by progressively adjusting the effective viscosities on the basis of the stresses found in the previous steps. One starts with an arbitrary initial viscosity $\eta_0(z)$ and has found the correct viscosity when successive solutions no longer differ significantly. In this scheme the initial assumption $\eta_0(z)$ may be important for rapid convergence; we found it best to compute $\eta_0(z)$ with the assumed stress-dependence $\eta(\tau)$ and an anticipated stress distribution $\tau(z)$

Convergence was tested by the squared stress change integrated over the whole depth range and normalized with respect to the previous total stress integral:

$$\frac{\int_0^{z_m} \Delta\tau^2\, dz}{\int_0^{z_m} \tau^2\, dz} = \frac{\Delta A^2 z_m^2/3 + \Delta A\, \Delta B z_m + \Delta B^2}{A^2 z_m^2/3 + AB z_m + B^2} < \varepsilon. \tag{6}$$

The convergence was sometimes very slow if the solutions oscillated between two extremes: zero stress → high viscosity and, in turn, high stress → very low viscosity; once the solution approached the final one, convergence became rapid.

Rheology of the Upper Mantle

The effective viscosity used in the above procedure is the ratio of stress and strain rate and cannot be defined without discussion of the creep mechanisms. Experimental results on rock deformation (Carter, 1976), observation of flow textures in rocks of mantle origin (Nicolas, 1976), and theories of solid state creep (Weertman, 1970), show that dislocation creep, which leads to a power-law dependence of strain rate upon stress, is widespread, and may be predominant, in the upper mantle. Glacio-isostatic data can be fitted by the assumption of linear viscosity (Walcott, 1973) and equally well by a power-law model (Post and Griggs, 1973). If a liquid phase is present, diffusional flow through the liquid may become possible (Stocker and Ashby, 1973). Thus as a first approximation there are three creep mechanisms of possible relevance to polycrystals under upper mantle conditions: (i) diffusion creep, governed by the migration of vacancies through the grains (Nabarro-Herring creep) or along grain boundaries (Coble creep), which results in linear viscosity; (ii) dislocation creep, governed by dislocation climb and glide, which results in power-law creep; and (iii) fluid phase transport creep, when diffusion through the liquid (partial melt in the case of the asthenosphere) becomes predominant: it also results in linear viscosity. The results on strain rates and effective viscosities obtained by using the rheological parameters of olivine apply to the upper mantle only, and if extrapolated to the lower mantle must be treated with caution, since olivine goes through a series of phase changes in the mesosphere.

The equations govering the three types of creep can be written down as follows (Stocker and Ashby, 1973):

$$\text{Dislocation creep: } \dot{\varepsilon} = \frac{(3^{1/2})^{n+1}}{2} A \frac{D\mu b}{kT} \left(\frac{\sigma}{\mu}\right)^n \tag{7}$$

$$\text{Diffusion creep: } \dot{\varepsilon} = 21 \frac{D_e \Omega \mu}{kTd^2} \left(\frac{\sigma}{\mu}\right) \tag{8}$$

$$\text{Fluid phase transport: } \dot{\varepsilon} = 21 \frac{D_f \Omega \mu}{kTd^2} \left(\frac{\sigma}{\mu}\right) \tag{9}$$

where $\dot{\varepsilon}$ = shear strain rate; σ = shear stress;
D, D_e, D_f = diffusion coefficients;
A, n = Dorn's parameters; μ = rigidity; b = Burgers' vector; Ω = atomic volume;
k = Boltzmann's constant; T = absolute temperature; d = grain size.

The temperature and pressure dependence of the diffusion coefficient in dislocation creep is

$$D = D_0 \exp\left(-\frac{Q + pV}{RT}\right) \tag{10}$$

where Q = activation energy; V = activation volume; p = pressure; and R = gas constant. Activation energy and volume are those appropriate for lattice diffusion.

In diffusion creep, the diffusion coefficient is given by

$$D_e = D_V + \frac{\pi \delta}{d} D_B \tag{11}$$

where D_V and D_B are the diffusion coefficients for lattice and grain-boundary diffusion, respectively; δ = grain-boundary width; and d = grain size. The PT-dependence of D_V is assumed identical to (10); so is the form of the PT-dependence of D_B, but with activation energy about 1/3 less than the activation energy for lattice diffusion. The diffusion coefficient when fluid phase transport is present is given by

$$D_F = D_V + \frac{\pi \delta}{d} \cdot D_B + f \cdot C_L \cdot D_L \tag{12}$$

where f = volume fraction of the liquid phase; C_L = solubility of the diffusing species in the liquid; and $D_L = kT/8\eta_L \Omega^{1/3}$ is the diffusion coefficient in the liquid (η_L is the liquid viscosity).

In Eqs. (7), (8), and (9) the numerical constants are such that the invariant form of the creep laws is satisfied; $\dot{\varepsilon}$ and σ must be interpreted as shear strain rate and shear stress. If grain boundary sliding with diffusional accommodation is predominant over grain shape changes, the strain rate increases approximately sevenfold. This type of creep has been called 'superplastic' creep (Ashby and Verrall, 1973).

We approximate the upper mantle as a pure olivine layer (Fo_{90-95}). Table 1 lists the values of the rheological parameters adopted in this paper for dislocation and diffusion creep.

In the case of fluid phase transport, the estimation of rheological parameters is at least one order of magnitude less reliable than in solid phase creep. The liquid fraction, on the basis of seismological evidence (Anderson and Sammis, 1970), is taken to be of the order of 0.01. The diffusion coefficient in the liquid depends critically on the viscosity of the melt, and thus on the activation energy for viscous flow:

$$D_L = \frac{kT}{8\eta_L \Omega^{1/3}}, \quad \eta_L = A_\eta \exp\left(\frac{E_\eta}{RT}\right). \tag{13}$$

Table 1. Rheological parameters for olivine

	Parameter	Value	References
Dorn's parameter	A	0.7	[1]
Dorn's parameter	n	3.0	[1], [2], [4]
Burgers' vector	b	$6.98 \cdot 10^{-10}$ m	[1], [3]
pre-exponential diffusivity	D_0	10^{-1} m^2 s^{-1}	[3]
activation energy	Q	$5.4 \cdot 10^5$ J mol^{-1}	[1], [3]
activation volume	V	$1.1 \cdot 10^{-5}$ m^3 mol^{-1}	[1], [2]
atomic volume	Ω	$1.15 \cdot 10^{-29}$ m^3	[1], [3]
grain size	d	$10^{-4} - 10^{-2}$ m	[5]
grain boundary width	δ	$1.4 \cdot 10^{-9}$ m	[1]

[1] Stocker and Ashby, 1973; [2] Kirby and Raleigh, 1973; [3] Twiss, 1976; [4] Carter, 1976; [5] Nicolas, 1976

Experimental results (Murase and McBirney, 1973, Kushiro et al., 1976) suggest $E_\eta \approx 2 \cdot 10^5 J \cdot \text{mol}^{-1}$ and $A_\eta \approx 10^{-6}$ Pa · s. The resulting viscosities in the asthenosphere, however, would be too low by about two orders of magnitude. It should be kept in mind that electroviscous effects may be important, by which the apparent viscosity of a polar liquid in a very thin channel is much larger than that of the bulk liquid. Furthermore grain boundary wetting may be incomplete and not all liquid channels may be interconnected. Therefore D_L [Eqs. (12) and (13)] has been calculated by taking $A_\eta = 10^{-4}$ Pa · s, but in view of the above effects, this is likely to give an upper limit for the influence of partial melting and the influence on the long term rheology of the asthenosphere may well be zero. Finally, the PT-dependence of the rigidity is taken as

$$\mu = \mu_0 \left[1 + \frac{1}{\mu_0}\frac{\partial \mu}{\partial T}(T - T_0) + \frac{1}{\mu_0}\frac{\partial \mu}{\partial p}(p - p_0)\right] \tag{14}$$

where (Stocker and Ashby, 1973):

$$\mu_0 = 7.9 \cdot 10^{10} \text{ Pa}; \quad \frac{1}{\mu_0}\frac{\partial \mu}{\partial T} = -1.36 \cdot 10^{-4} K^{-1} (T \geqq 500 K);$$
$$\frac{1}{\mu_0}\frac{\partial \mu}{\partial p} = 2.25 \cdot 10^{-11} \text{ Pa}^{-1}.$$

This is probably accurate in the upper mantle, but there are discrepancies with the seismically determined rigidity in the lower mantle.

Summarizing Eqs. (7) to (14) and taking into account that in the present return flow problem $\dot{\varepsilon} = \frac{1}{2}\frac{du}{dz}$, we write

$$\eta = 1/\{C_1 \varphi_1(T,p) \cdot \tau^{n-1} + C_2 \varphi_2(T,p) + C_3 \varphi_3(T,p,f)\} \tag{15}$$

with

$$\left.\begin{aligned} &C_1 = 3^{\frac{n+1}{2}} A D_0 b/\mu_0^{n-1}; \\ &\varphi_1 = \exp\left(-\frac{Q+pV}{RT}\right) \Big/ \left\{ kT\left[1+\frac{1}{\mu_0}\frac{\partial\mu}{\partial T}(T-T_0)+\frac{1}{\mu_0}\frac{\partial\mu}{\partial p}(p-p_0)\right]^{n-1}\right\} \end{aligned}\right\}$$

for dislocation creep;

$$\left.\begin{aligned} &C_2 = \alpha D_0 \Omega/d^2; \quad \varphi_2 = \exp\left(-\frac{Q+pV}{RT}\right)\left[1+\frac{\pi\delta}{d}\exp\left(\frac{Q/3}{RT}\right)\right] \Big/ kT \end{aligned}\right\} \quad (16)$$

for diffusion creep; and

$$C_3 = \frac{\alpha}{8} C_L \Omega^{2/3}/(A_\eta d^2); \quad \varphi_3 = f(z)\cdot\exp\left(-\frac{E_\eta}{RT}\right)$$

for fluid phase transport; when the equations are written in terms of u, the constant α is 42 if grain shape change dominates and 294 if grain boundary sliding dominates.

As in other studies (Stocker and Ashby, 1973; Kirby and Raleigh, 1973; Carter, 1976; Twiss, 1976; Durham and Goetze, 1977; Ashby and Verrall, 1977) the complex viscosity law (15) chosen is illustrated by 'deformation maps', showing the stress-temperature fields at various pressures (depths) in which one creep mechanism is predominant; a more detailed discussion is given elsewhere (Ranalli, 1978). The results are presented as a function of temperature; it is then possible to choose the temperature range appropriate for given depths and regions. (Alternatively, deformation maps may be computed as function of depth). Five examples are shown in Fig. 1a–e). The parameters assumed in each case are shown on the diagram. Curves of constant strain rates have been computed for $\dot{\varepsilon}$ from 10^{-16} to $10^{-11}\,s^{-1}$, which should encompass most situations of geodynamic significance. Curves of constant effective viscosity have been computed for $\eta = 10^{16}, 10^{18}, \ldots, 10^{26}$ poise (10 poise = 1 Pa · s).

Figures 1a and b depict the situation within the lithosphere. Effective viscosities are larger than 10^{24} poise for realistic T and σ. It is interesting to note that at lower temperatures linear creep appears to be predominant: purely diffusive flow is sometimes termed 'presseure solution' by geologists, and direct observation of metamorphic rocks shows textures attributable to it (Elliott, 1973). Diffusion-type flow at lower temperatures is also greatly enhanced by the presence of water (Rutter, 1976). Figures 1c and d illustrate a possible situation in the asthenosphere. For grain sizes of 0.1 cm and about 1% partial melt, the asthenosphere behaves linearly at stresses of a few bars or less; dislocation creep is still predominant at higher stresses. If the grain size is larger and the melt fraction smaller, dislocation creep is predominant at all stresses above a few tenths of a bar. Strain rates and effective viscosities are as inferred from tectonic and glacio-isostatic processes. Figure 1e shows the conditions prevailing below the asthenosphere. The main result is that, below the asthenosphere, dislocation creep is predominant at all stresses above a few tenths of a bar.

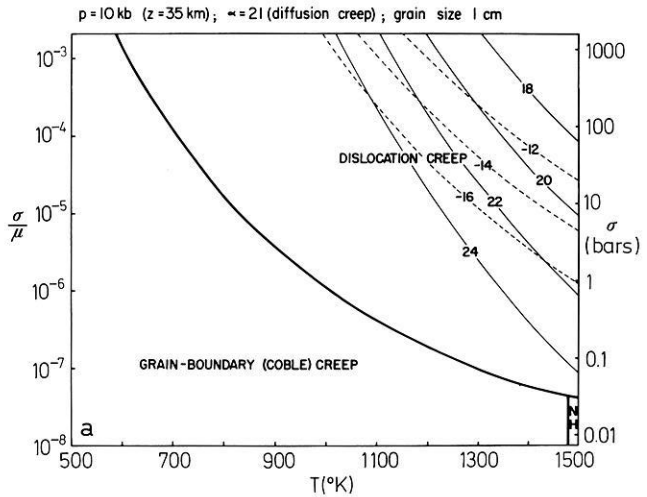
p = 10 kb (z = 35 km) ; ∝ = 21 (diffusion creep) ; grain size 1 cm
DISLOCATION CREEP
GRAIN-BOUNDARY (COBLE) CREEP
a
T(°K)
σ (bars)

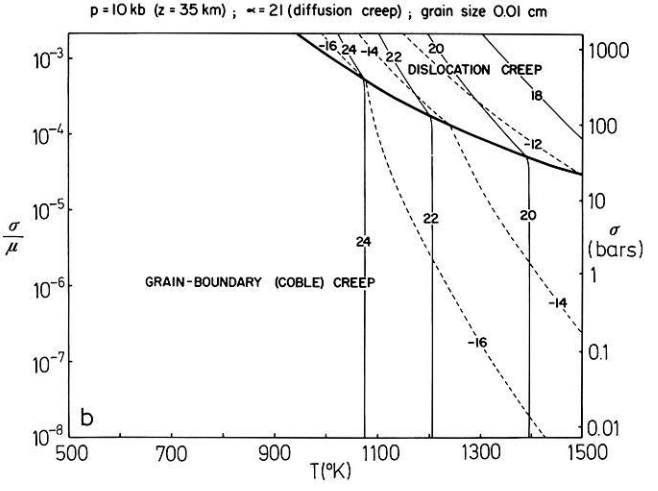
p = 10 kb (z = 35 km) ; ∝ = 21 (diffusion creep) ; grain size 0.01 cm
DISLOCATION CREEP
GRAIN-BOUNDARY (COBLE) CREEP
b
T(°K)
σ (bars)

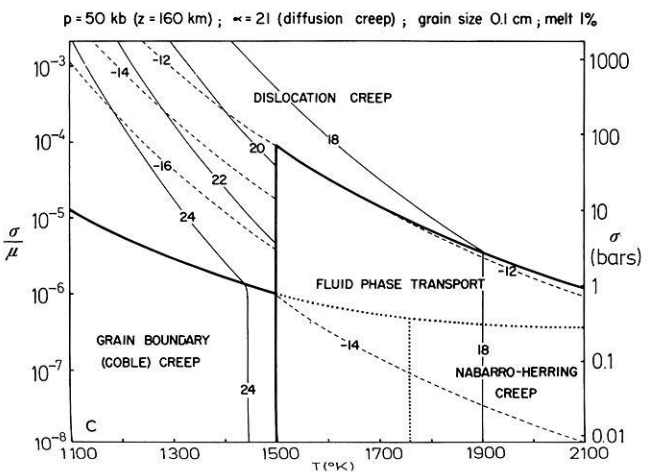
p = 50 kb (z = 160 km) ; ∝ = 21 (diffusion creep) ; grain size 0.1 cm ; melt 1%
DISLOCATION CREEP
FLUID PHASE TRANSPORT
GRAIN BOUNDARY (COBLE) CREEP
NABARRO-HERRING CREEP
c
σ (bars)

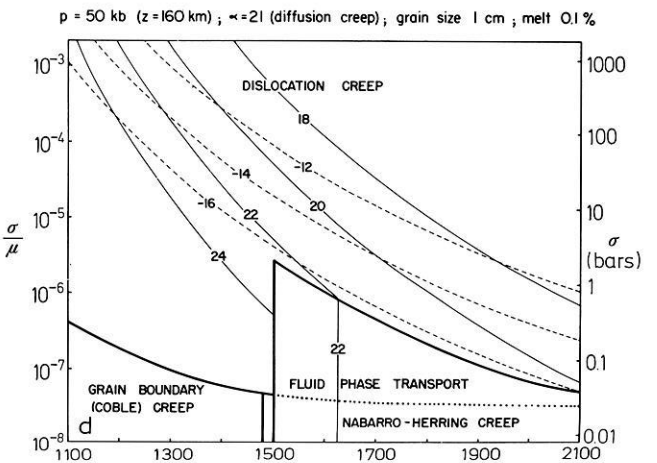
p = 50 kb (z = 160 km) ; ∝ = 21 (diffusion creep) ; grain size 1 cm ; melt 0.1 %
DISLOCATION CREEP
GRAIN BOUNDARY (COBLE) CREEP
FLUID PHASE TRANSPORT
NABARRO-HERRING CREEP
d
σ (bars)

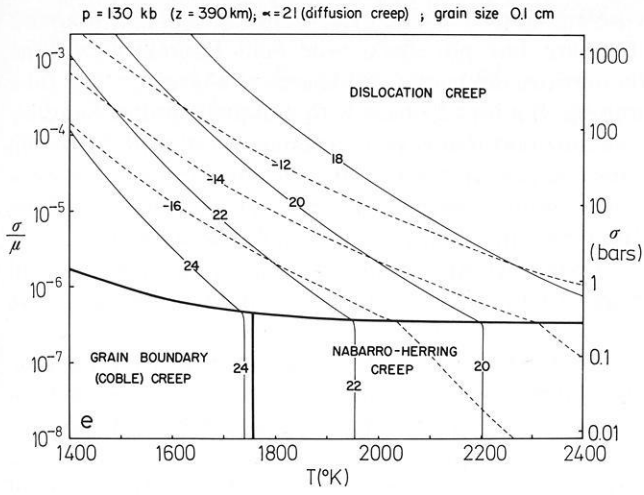

Fig. 1a–e. Deformation maps: *thick continuous lines:* deformation field boundaries; *thin continuous lines:* effective viscosities (as powers of ten); *dashed lines:* strain rates (also as powers of ten). **a** for $z = 35$ km, $d = 1$ cm; **b** $z = 35$ km, $d = 0{,}01$ cm; **c** $z = 160$ km, $d = 0.1$ cm, and 1% partial melting (*the dotted lines* represent the extensions of dislocation diffusion fields if fluid phase transport were absent); **d** $z = 160$ km, $d = 1$ cm, partial melting 0.1%; **e** $z = 390$ km, $d = 0.1$ cm

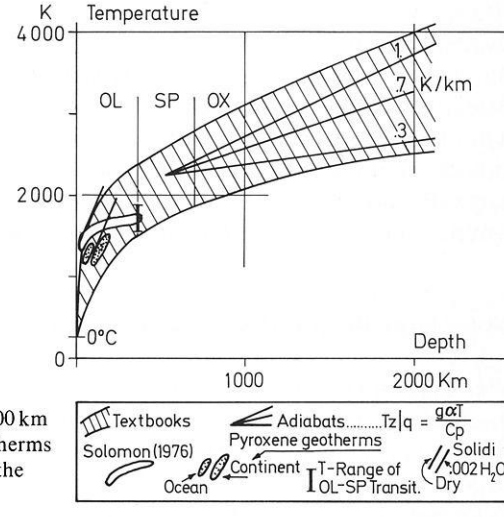

Fig. 2. Temperature range in the mantle to 2,000 km depth; for references see Solomon (1976). Geotherms assumed in model computations are shown in the following figures

In summary, the effective viscosity law we assume has the following main features. In the absence of partial melting, dislocation creep is predominant at high stresses and diffusion creep at small stresses. Superplasticity increases the temperature-dependent transition stress by a factor less than three. An increase in grain size by one order of magnitude decreases the transition stress by approximately the same amount. Within the diffusion creep field an increase in

grain size favours Nabarro-Herring over Coble creep; the latter is predominant at lower temperatures. Pressure has no effect over field boundaries, if the pressure-dependence of the various diffusion coefficients is the same; we take this as a simplifying assumption. If a liquid phase with complete grain-boundary wetting is present, fluid phase transport is always predominant over diffusion creep within the linear field; if, however, electroviscous phenomena were more important in the asthenosphere than assumed here, it may have no relevance at all for mantle rheology (naturally excluding situations in which the melt fraction is much larger than 0.01). Fluid phase transport raises the transition stress between non-linear and linear creep, but at high stresses dislocation creep is always predominant.

As Fig. 1 demonstrates temperature is one of the most critical parameters; the return flow profiles will depend very strongly on the geotherms chosen. Since temperature in the earth is poorly known we have assumed a whole range of geotherms, shown in Figure 2. The upper mantle temperatures are constrained by geophysical and geological observations (Solomon, 1976), but the range of possible lower mantle temperatures is wide. It is often assumed that, because of steady-state convection, the temperature in the deeper mantle is slightly super-adiabatic; the adiabatic gradient is given by $g \alpha T/c_p \approx 0.3 - 0.6\,\mathrm{K/km}$ (gravity $g \approx 10\,\mathrm{m/s^2}$; thermal volume expansion $\alpha \approx 1 - 2 \cdot 10^{-5}\,\mathrm{K^{-1}}$; heat capacity $c_p \approx 800\,\mathrm{J/kg \cdot K}$; absolute temperature $T \approx 2000\,\mathrm{K}$); for the Rayleigh number to be at least critical ($\mathrm{Ra_c} \approx 2{,}000$), only a very small quantity has to be added: $(\mathrm{Ra_c} \cdot \kappa \nu)/(\alpha g d^4) \approx 10^{-2}\,\mathrm{K/km}$ (thermal diffusivity $\kappa \approx 1.5 \cdot 10^{-4}\,\mathrm{m^2/s}$, kinematic viscosity $\nu \approx 10^{17}\,\mathrm{m^2/s}$, depth of convecting layer $d \approx 2{,}000\,\mathrm{km}$). The assumption of internal convection, superimposed on the return flow, is however, self-defeating for our model with non-linear rheology, since the additional strains will alter the effective viscosity. The one-dimensional return flow model clearly cannot simulate realistic mantle flow; what we want to do is to investigate how a mantle of 'realistic' rheology reacts to such a simple model. The geotherms assumed in each of the models presented below are given on the diagrams.

Non-Linear Return Flow Models: Results

We shall first discuss the influence of temperature on the return flow by assuming a set of geotherms within the range of Fig. 2. Other parameters also varied within plausible limits will be discussed subsequently; these involve the pre-exponential diffusivity D_0 and the activation energy Q; the constant α for grain deformation and grain boundary sliding dominated creep, and the influence of partial melt. All models were computed for three grain sizes $d = 1$, 3, 10 mm and three surface plate velocities $u_l = 1$, 3, 10 cm/a. The power of the dislocation creep term has always been assumed $n = 3$. The results are presented in the form of depth profiles (Fig. 3–6) of horizontal flow velocity $u(z)$ and effective viscosity $\eta(z)$ together with the assumed geotherms $T(z)$. Other important parameters assumed fixed are shown on the lower lefthand side of the diagrams. Also given, at the bottom, are the computed pressure gradient A or its equivalent gravity

gradient in mgal/10,000 km and the shear stress B at the bottom of the model surface plate.

Figure 3 compares five geotherms with lower-mantle gradients of 0.5, 0.6, 0.75, 0.9, and 1 K/km; surface velocity is 3 cm/a, grain sizes are 1, 3, and 10 mm. As the temperature gradient is raised, the effective viscosities and stresses generally become smaller and the return flow occurs at greater depth (260 to 540 km) and broadens (with decreasing amplitude). In no model is the return flow concentrated in the asthenosphere of minimum viscosity ($2 \cdot 10^{19}$ Pa·s between 150 and 250 km depth in all models). In all model situations the viscosity minimum is caused by the dominance of temperature over pressure and dislocation creep is more important than diffusion creep. Below the asthenosphere lies a region of maximum return flow and small stresses; diffusion creep dominates below a few tenths of a bar. For small grain sizes ($\lesssim 1$ mm) viscosity remains nearly constant at $< 10^{21}$ Pa·s over several hundred kilometers in all models (over 500 km for $u_l = 1$ cm/a and $dT/dz = 1$ K/km). For grain sizes $d > 1$ mm (see e.g., $d = 10$ mm in Fig. 3) viscosity rises to a maximum in the shear-free fiber but the width of the zone of dominant superplastic diffusion creep (i.e., maximum diffusion creep in the absence of melt) narrows as grain size and surface velocity increase; and the maximum viscosity grows as d^2. Although effective viscosity is so different, the return flow profiles $u(z)$ are hardly affected by grain size, except for slight squaring for large d. At greater depths dislocation creep takes over again and in all models with large (small) grain size the effective viscosity goes to a second minimum (remains rather constant) near 10^{21} Pa·s before pressure makes it rise. Deeper down, this rise is nearly linear with depth for log viscosity; its magnitude is strongly dependent on the temperature gradient leading to many orders of magnitude viscosity difference at 2,000 km ($\sim 10^{29}$ Pa·s for 0.5 K/km versus $\sim 10^{22}$ Pa·s for 1 K/km). Accordingly, the depth extent of the return flow varies from model to model by a factor of 2. This result is hardly affected by difference in stress level for different surface velocities. The peculiar feature of two low viscosity channels may be typical of non-linear flow where temperature and stress are important at different depths.

If the viscosity-temperature relationship found for the deeper mantle appears unrealistic and lower viscosities are to be obtained with the low temperature gradients (e.g., 0.5 K/km), it should be noted that olivine parameters are not appropriate for the deep mantle. The simplest escape from the dilemma would be an activation volume decreasing with depth (e.g., about 30% at 2,000 km). This is indeed likely (O'Connell, 1977; Sammis et al., 1978).

Shear stress B (Fig. 3, bottom) at the plate bottom varies approximately as the inverse of the lower-mantle temperature gradient. Its depth variation is linear (for 0.5 K/km from $+7$ to -50 bar at 2,000 km; for 1 K/km from $+3$ to -8 bar; surface velocity $u_l = 3$ cm/a and all grain sizes considered). Thus even in the most unfavorable case of very high viscosities in the lower mantle the stresses are not excessive. The horizontal pressure gradient A inherent in the return flow model can be roughly transformed into a gravity gradient in the direction of motion across a moving plate (Schubert and Turcotte, 1972; Jacoby, 1978). The computed results are given on Fig. 3, bottom ($A \rightarrow \Delta g$) in

mgal/10,000 km and should be compared to the crude figure of 30 mgal/10,000 km across the Pacific plate, found by Woollard (1975). By this criterion nearly all models fail; only the model with a temperature gradient of 1 K/km gives acceptable gravity gradients of 15, 23, and 34 mgal/10,000 km for surface velocities of 1, 3, and 10 cm/a, respectively. These results are insensitive to grain size. The deep-mantle viscosities of the other models are too large for the return flow model to work. As discussed above, these models would, however, also work if activation volume decreases with depth.

It would be interesting to compare 'oceanic' and 'continental' geotherms. An illustration of the effects is given in Fig. 4. We have assumed two geotherms differing by 250 K at 150 km depth; the difference decreases linearly to zero at 50 and 1,000 km. Such a choice may be more in line with Jordan's (1975) arguments for considerable temperature differences to great depths, than with Solomon (1976) and Duschenes and Solomon (1977). If the difference between oceanic and continental geotherms disappears at shallower depths than in our models the effects will be smaller than discussed here. The two models differ clearly in the depth of the return flow and in the effective viscosities at depths shallower than 1,000 km. At 'asthenospheric' levels the viscosity difference is more than an order of magnitude. For large grain sizes the effective viscosities near the maximum return flow are always relatively large. Below 1,000 km depth the 'oceanic' viscosities are slightly greater than the 'continental' ones because of the smaller stresses if the same plate velocity is assumed. But a 10 cm/a oceanic plate leads to the same effective viscosity as a 1 cm/a continental one. While the 'oceanic' stresses near the surface are only a few bars, and depend slightly on grain size, 'continental' stresses are between 4 and 10b for 1 to 10 cm/a surface velocity independent from grain size. The gravity gradients computed are smaller than 30 mgal/10,000 km for all 'oceanic' models but exceed this value for the 10 cm/a 'continental' one.

Fig. 3. Effect of temperature (T) gradient in lower mantle on return flow (u) and effective viscosity (η); thick curves for grain size $d=1$ mm, thin lines for $d=10$ mm. Other parameters as listed; *GBS:* indicates grain boundary sliding diffusion creep; *ST10 etc:* indicate that the small pre-exponential diffusivity D_0 of Table 1 has been used together with geotherm no. *T10*, etc. For discussion, particularly of results *A*, *B (bottom)*, see text

Fig. 4. Effect of continental versus oceanic geotherm (T) on return flow (u) and effective viscosity (η), Bands marked by dots *(oceanic)* and by short lines *(continental)* indicate whole range of solutions for varying grain size $d=1$ to 10 mm and lithospheric velocity $u_l=1$ to 10 cm/a. Other parameters as listed. *GBS*, *ST6*, *ST7:* see caption of Fig. 3

Fig. 5. Effect of lithospheric velocity u_l (1, 3, 10 cm/a) on return flow (u) and effective viscosity (η) for given geotherm (T), grain size $d=1$ to 10 mm *(dotted band of solutions)*, negligible melt influence and power $n=3$ of power law; *ST10*, *GBS:* see caption of Fig. 3

Fig. 6. Effect of melt (M) on return flow (u) and viscosity (η); geotherm (T), lithospheric velocity u_l, grain size d, and power assumed as shown. For discussion of parameter as well as of results see text. *GBS*, *ST10:* see caption of Fig. 3

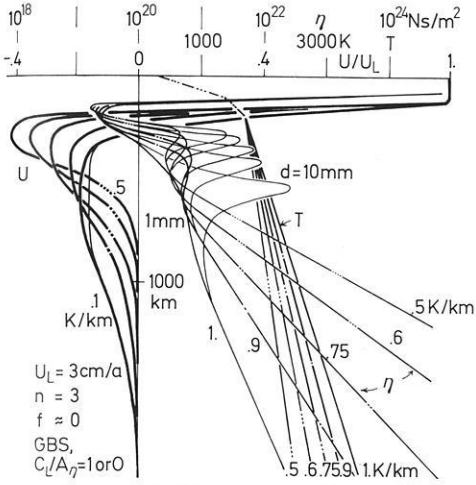

T_z	A→Δg	B	
.5K/km	120 mgal/10000 km	7 bar	ST 11
.6	83	6	ST 13
.75	60	5	ST 12
.9	38	4	ST 10
1.	23	3	ST 9

3

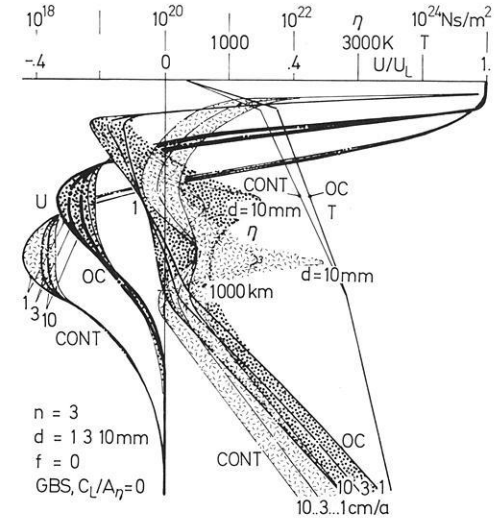

U$_L$	A—Δg	B		
10cm/a	16-17	45mgal/10000km 2.3-2.7	9bar	OC ST 7
3	10-12	28 1.4-1.8	6	CONT ST 6
1	5-8	20 .6-1.2	4	
OC: 1-10 mm		CONT OC: 1-10 mm		CONT

4

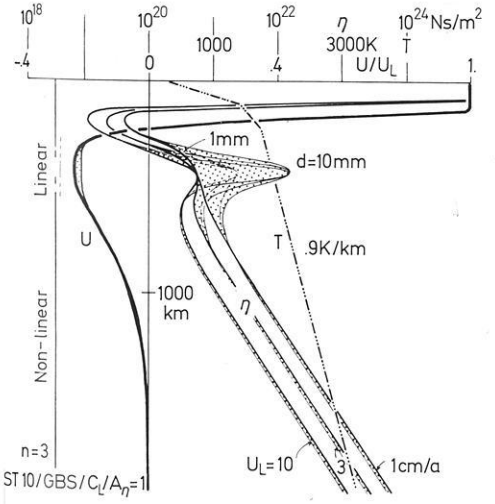

U$_L$	A→Δg	B
1cm/a	27mgal/10000km	2,5 bar
3	38	4
10	58	6

5

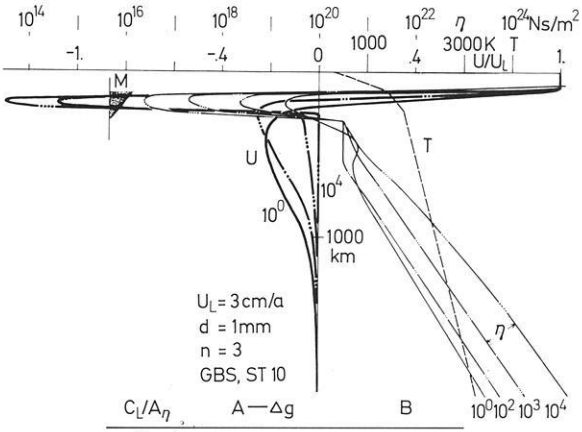

C$_L$/A$_\eta$	A—Δg	B
10^0(Pa·s)$^-$	39 mgal/10000 km	3.7 bar
10^2	22	1.2
10^3	11	.5
10^4	1.4	.1

6

The influence of surface velocity u_l is illustrated by Fig. 5. Where dislocation creep is dominant the logarithmic viscosity-depth profiles are simply shifted, i.e., the viscosities are decreased by a constant factor, if the surface velocity is increased (1/6 or 1/7 for 10-fold increase of u_l) because the stresses are increased (by a factor of 2 or 3). Where diffusion creep dominates (for small grain sizes near the return flow maximum) the effective viscosities become nearly independent from u_l (but grow with grainsize d squared). The influence of plate velocity on the shape of the return flow profiles is hardly noticeable, but the pressure (A) and gravity (Δg) gradients increase [by a factor of (only) 2 for u_l changing from 1 to 10 cm/a].

The effect of grain size has already been discussed in connection with Figs. 3–5. Viscosity is affected only where the stress level is a fraction of a bar. The other parameters as the flow profile, shear stress, and pressure gradient are only slightly affected in our models. Grain sizes would have to be one or two orders of magnitude smaller than 1 mm for diffusion creep to become dominant everywhere and to affect the whole model results.

So far diffusional superplasticity (grain boundary sliding accommodated diffusion creep) was assumed. Had we assumed grain deformation dominated Nabarro-Herring and Coble creep, the influence of diffusion creep on the total deformation would be even smaller than found. The results would hardly change. In a test computation none of the quantities computed changed by more than 10%, except in the case with the smallest stresses ($u_l = 1$ cm/a, $d = 1$ mm and 'hot oceanic' mantle) where superplasticity leads to nearly 50% reduction of stresses and pressure gradient over Nabarro-Herring and Coble creep.

An attempt to estimate the influence of partial melting in the asthenosphere is presented in Fig. 6. It is widely believed that incipient melting occurs there if a fraction of one precent of H_2O is present, because temperature probably exceeds the wet solidus of peridotite (e.g., Solomon, 1976). For some of the geotherms discussed above, we have computed models with a melt fraction $f(z)$ of 1% at 100 km depth decreasing to zero at 250 km; we have assumed the poorly known ratio C_L/A_η (determining the importance of fluid phase transport in Eqs. (12), (13), and (16) to take on the values 0 (no importance), 1, 10, 10^2, 10^3 (preferred value, see above), 10^4, and 10^5 $(\mathrm{Pa}\cdot\mathrm{s})^{-1}$ (value expected from bulk viscosity of basic melts).

The computed flow profile $u(z)$ and viscosity $\eta(z)$ are presented in Fig. 6 for the geotherm, surface velocity, and grain size as indicated. As expected, the presence of melt in the asthenosphere by lowering its effective viscosity facilitates the return flow by requiring a lower pressure gradient. If, however, $C_L/A_\eta \leqq 1$ $(\mathrm{Pa}\cdot\mathrm{s})^{-1}$, 1% of melt has no noticable effect. From $C_L/A_\eta = 1$ to 100, 1,000, 10,000 ... $(\mathrm{Pa}\cdot\mathrm{s})^{-1}$ the effective viscosity in the layer with about 1% melt is decreased by 1, 2, 3, ... orders of magnitude, the stresses are lowered, and the return flow maximum is shifted upward into the layer with melt. It becomes the channel of dominant return flow for C_L/A_η between 100 and 1,000 $(\mathrm{Pa}\cdot\mathrm{s})^{-1}$ and carries the total return flow for $C_L/A_\eta \geqq 10{,}000$ $(\mathrm{Pa}\cdot\mathrm{s})^{-1}$. Because of the stress reduction the effective viscosity rises in the lower mantle until linear diffusion creep dominates at all depths. The gravity gradients drop from

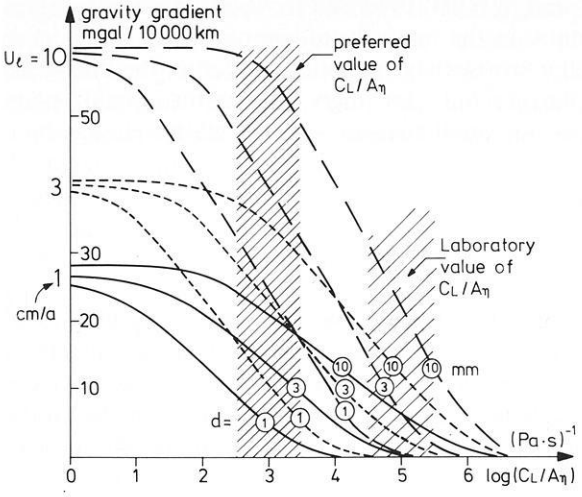

Fig. 7. Influence of 1 % melt on pressure gradient shown by equivalent gravity gradient of return flow as a function of fluid phase transport parameter C_L/A_η *(Kabscissa)*, surface plate velocity u_l *(parameter shown on lefthand side)*, and grain size *(parameter shown by circled numbers at each curve)*. The upper turning region of each curve marks the beginning of melt influence; the lower turning region marks that of total dominance of flow system by melt in asthenosphere

38 mgal/10,000 km (no melt) to essentially zero. The values of C_L/A_η where the effects of fluid phase transport first become noticeable and where the return flow becomes confined to the channel depend on grain size, and, to a minor degree, on plate velocity and temperature. This is illustrated in Fig. 7 by the gravity gradients Δg/10,000 km for all models computed with the same geotherm as that of Fig. 6, but varying u_l and d. The individual Δg-curves are asymptotic to the value appropriate to no melt for small C_L/A_η, then turn down to turn again approaching zero asymptotically for large C_L/A_η. The two turning regions indicate the beginning of melt effects and the beginning of their total dominance. Beyond, viscosity continues to decrease in the channel but the return flow profile is no longer affected. The 'turning regions' of C_L/A_η are proportional to d^2 for constant u_l and they increase as u_l for large d but are hardly affected by u_l for small d. It turns out that the preferred C_L/A_η value of $10^3\,(\mathrm{Pa}\cdot\mathrm{s})^{-1}$ lies in the region of important but not total melt influence. It depends on too many factors for an evaluation to be possible at present, but since our model probably gives an upper limit, we feel safe to suggest that a dominant influence of 1 % melt on the return flow is unlikely but that it could be of some importance for small grain sizes and plate velocities.

Finally we want to discuss whether or not the uncertainty of diffusivity D_0 and activation energy Q is critical to our model. We computed a number of models with both the values given in Table 1 and the ones given by Stocker and

Ashby (1973): $D_0 = 120\,m^2/s$ and $Q = 6.4 \cdot 10^5\,J\,mol^{-1}$; both pairs of values reasonably fit the laboratory data. In the majority of computations the Stocker and Ashby values lead to smaller stresses and pressure gradients; the difference was, however, not very significant; only for high temperature, small plate velocity and small grain size, i.e., for small stresses was the relative change by a factor of 1/5 or so.

Discussion

Although we cannot simulate realistic mantle flow with the one-dimensional model, we have been able to study the influence of rheological parameters of olivine, grain size, melt fraction, temperature, stress, and plate velocity. The results are more directly applicable to large plates than to small ones; but if the model works with an infinite plate it is likely to work with a finite one too (see Davies, 1977a and b).

In an earlier study of the return flow model (Jacoby, 1978) it had been shown that the model is not in conflict with geophysical observations as gravity, sea floor topography, heat flow, and lithospheric stress, if plausible mantle viscosities are assumed which are based on glacio-isostatic rebound data (e.g. Walcott, 1973; Post and Griggs, 1973; Brennen, 1974; Peltier, 1974; Cathles, 1975; Peltier and Andrews, 1976; Peltier et al., 1978). Another result had been that the return flow may well extend to great depths in the mantle (Jacoby, 1978; see also Davies, 1977 a and b).

The main conclusions of the present study largely agree with those of the earler one. If non-linear olivine rheology is assumed the return flow model works equally and the return flow is likely to extend to depths well below the asthenosphere. In other words, olivine rheology in connection with plausible assumptions on temperature and grain size leads to similar effective viscosities in the return flow model as those found from glacial rebound (similar strain rates). This is opposite to what was found for exclusive diffusion creep rheology by Schubert and Turcotte (1972) who thence suggested that dislocation creep ougth to be considered. The suggestion is borne out by the present models in which dislocation creep was generally dominant over diffusion creep, and also by the models of Froidevaux and Schubert (1975), Schubert et al. (1976), Froidevaux et al. (1977), Schubert et al. (1978), and Yuen et al. (1978), who assumed only dislocation creep of olivine. An interesting result of the two last papers mentioned was that under many circumstances the pressure gradient of the return flow is rather constant with depth; we mention in passing that this is an a posteriori justification for our arbitrary choice of this asssumption.

Results obtained for the deep mantle must be regarded with special caution since the rheological parameters of olivine assumed are not likely to be correct there. If they are correct, our model results favour a high temperature gradient (order 1 K/km), very small grain size (<0.1 mm), and/or important fluid phase transport in the asthenosphere. Alternatively a decrease of the activation volume (describing the pressure influence on the creep) with depth is suggested; this is

supported by the work of O'Connell (1977) and Sammis et al. (1977). Some of their estimates give such a strong decrease of the activation volume that temperature gradients as low as 0.3 K/km would still lead to acceptably low viscosities (and plausible return flow solutions). If these estimates are correct, our model results lead us to speculate that the return flow may extend deep into the lower mantle with the asthenosphere being essentially a "decoupling" layer of shear flow, in line with Davies' (1977a) conclusions.

Some of the particular features of non-Newtonian rheology deserve a little more discussion. One obvious effect is that stresses and pressure gradients are not linear with plate velocity. If grain size is greater than 1 mm we can expect these quantities to grow by a factor of only 2 to 3 when plate velocity increases from 1 to 10 cm/a. Gravity gradients and lithospheric stress should thus not strongly depend on plate velocity. Shear heating, not included in our model, would weaken this dependency further. The model implies stresses of the order of a few hundred bars in the lithosphere, because the surface plate must be driven from its ends (ridge, trench) to balance and maintain the shear stress B at its bottom; an oceanic plate 100 km thick and 10,000 km long would suffer a maximum (compressive or tensile) stress of $100 \cdot B$ and B was usually of the order of a few bars. The shear stress under continental plates is greater than under oceanic ones, if our assumptions concerning the geotherms are not grossly wrong. Considering the uncertainties, we estimate the difference to be roughly by a factor three. The maximum (compressive or tensile) stress for a continental plate 3,000 km long would thus be of the same order of magnitude as that in an oceanic plate 10,000 km long.

Regions of low-stress high viscosity are characteristic of non-linear viscosity. The important point is that this is dynamically irrelevant. In the low-stress regions there is so little deformation that further reduction because of non-linearity makes little difference in the flow distribution. In large regions with intermediate stress the effective viscosity does not vary very much; the assumption of Newtonion viscosity will thus not lead to gross errors. In small regions, however, of high stress, e.g., in descending slabs, non-Newtonian rheology may be critical to the solutions (Schmeling and Jacoby, in preparation). Superposition of additional strains (not considered in our model) will generally tend to 'soften' the mantle.

The major unknowns in modelling mantle dynamics are temperature, grain size, activation volume, and the physics of fluid phase transport. The return flow is facilitated by high temperature, small grain size, small activation volume, and fluid phase transport, or a combination of these. Jumps in activation energy and activation volume may be important too; they should be taken into account in future models.

Acknowledgements. Computing facilities of Carleton University were used for this study. The financial support (including that for the stay at Carleton University of one of us – W.R.J.) by the National Research Council of Canada (grant number A7971 to G.R.) and Deutsche Forschungsgemeinschaft (grants Ja 258/1, 3, 6) is gratefully acknowledged. The comments of one of the anonymous referees were very useful.

References

Anderson, D.L., Sammis, C.: Partial melting in the upper mantle. Phys. Earth Planet. Inter. **3**, 41–50, 1970

Ashby, M.F., Verrall, R.A.: Diffusion-accommodated flow and superplasticity. Acta Metall. **21**, 149–163, 1973

Ashby, M.F., Verrall, R.A.: Micromechanisms of deformation and fracture, and their relevance to the rheology of the upper mantle. Philos. Trans. R. Soc. London, Ser. A: **288**, 59–95, 1977

Brennen, C.: Isostatic recovery and the strain rate dependent viscosity of the earth's mantle. J. Geophys. Res. **79**, 3993–4001, 1974

Carter, N.L.: Steady-state flow of rocks. Rev. Geophys. Space Phys. **14**, 301–360, 1976

Cathles, III, L.M.: The viscosity of the earth's mantle. Princton, N.J.: Princton Univ. Press, 386 pp., 1975

Davies, G.F.: Whole mantle convection and plate tectonics. Geophys. J. R. Astron. Soc. **49**, 459–486, 1977a

Davies, G.F.: Viscous mantle flow under moving lithospheric plates and under subduction zones. Geophys. J. R. Astron. Soc., **49**, 557–563, 1977b

Durham, W.B., Goetze, C.: Plastic flow of oriented single crystals of olivine. J. Geophys. Res. **82**, 5737–5753, 1977

Duschenes, J.D., Solomon, S.C.: Shear wave travel time residuals from oceanic earthquakes and the evolution of the oceanic lithosphere. J. Geophys. Res. **82**, 1985–2000, 1977

Elliott, D.: Diffusion flow laws in metamorphic rocks. Bull. Geol. Soc. Am. **84**, 2645–2664, 1973

Froidevaux, C., Schubert, G.: Plate motion and structure of the continental asthenosphere: a realistic model of the upper mantle. J. Geophys. Res. **80**, 2553–2564, 1975

Froidevaux, C., Schubert, G., Yuen, D.A.: Thermal and mechanical structure of the upper mantle: a comparison between continental and oceanic models. Tectonophysics **37**, 233–246, 1977

Goetze, C.: A brief summary of our present-day understanding of the effect of volatiles and partial melt of the upper mantle. In: High Pressure Research Applications in Geophysics, M. Manghnani and S. Akimoto (eds.), pp. 3–23. New York: Academic Press 1977

Jacoby, W.R.: One-dimensional modelling of mantle flow. Pure Appl. Geophys. **116**, 1231–1249, 1978

Jordan, T.H.: The continental tectosphere. Rev. Geophys. Space Phys. **13**, 1–12, 1975

Kirby, S.H., Raleigh, C.B.: Mechanisms of high-temperature, solid-state flow in minerals and ceramics and their bearing on the creep behaviour of the mantle. Tectonophysics **19**, 165–194, 1973

Kushiro, I., Yoder, H.S. Jr., Mysen, B.O.: Viscosities of basalt and andesite melts at high pressures. J. Geophys. Res. **81**, 6351–6356, 1976

Murase, T., McBirney, A.R.: Properties of some common igneous rocks and their melts at high temperatures. Bull. Geol. Soc. Am. **84**, 3563–3592, 1973

Nicolas, A.: Flow in upper mantle rocks: some geophysical and geodynamical consequences. Tectonophysics **32**, 93–106, 1976

O'Connell, R.J.: On the scale of mantle convection. Tectonophysics **38**, 119–136, 1977

Peltier, W.R.: The impulse response of a Maxwell earth. Rev. Geophys. Space Phys. **12**, 649–669, 1974

Peltier, W.R., Andrews, J.T.: Glacial-isostatic adjustment – I. The forward problem. Geophys. J. Roy. Astron. Soc. **46**, 605–646, 1976

Peltier, W.R., Farrell, W.E., Clark, J.A.: Glacial isostasy and relative sea level: a global finite element model. Tectonophysics **50**, 81–110, 1978

Post, R.L., Griggs, D.T.: The earth's mantle: evidence for non-Newtonian flow. Science **181**, 1242–1244, 1973

Ranalli, G.: Regional models of the steady-state rheology of the upper mantle. In: Earth rheology, isostasy and eustasy, N.A. Mörner (ed.) New York: Wiley 1978 (in press)

Rutter, E.H.: The kinetics of rock deformation by pressure solution. Philos. Trans. R. Soc. London, Ser. A.: **283**, 203–219, 1976

Sammis, C.G., Smith, J.C., Schubert, G., Yuen, D.A.: Viscosity-depth profile of the earth's mantle: effects of polymorphic phase transitions. J. Geophys. Res. **82**, 3747–3761, 1977

Schubert, G., Turcotte, D.L.: One-dimensional model of shallow convection. J. Geophys. Res. **77**, 945–951, 1972

Schubert, G., Froidevaux, C., Yuen, D.A.: Oceanic lithosphere and asthenosphere: thermal and mechanical structure. J. Geophys. Res. **81**, 3525–3540, 1976

Schubert, G., Yuen, D.A., Froidevaux, C., Fleitout, L., Souriau, M.: Mantle circulation with partial shallow return flow: effects on stresses in oceanic plates and topography of the sea floor. J. Geophys. Res. **83**, 745–758, 1978

Solomon, S.C.: Geophysical constraints on radial and lateral temperature variations in the upper mantle. Am. Mineral. **61**, 788–803, 1976

Stocker, R.L., Ashby, M.F.: On the rheology of the upper mantle. Rev. Geophys. Space Phys. **11**, 391–426, 1973

Twiss, R.J.: Structural superplastic creep and linear viscosity in the earth's mantle. Earth Planet. Sci Lett. **33**, 86–100, 1976

Walcott, R.I.: Structure of the earth from glacio-isostatic rebound. Ann. Rev. Earth Planet. Sci. **1**, 15–37, 1973

Weertman, J.: The creep strength of the earth's mantle. Rev. Geophys. Space Phys. **8**, 145–168, 1970

Woollard, G.P.: The interrelationship of crustal and upper mantle parameter values in the Pacific. Rev. Geophys. Space Physics **13**, 87–137, 1975

Yuen, D.A., Tovish, A., Schubert, G.: Shear flow beneath oceanic plates: local nonsimilarity boundary layers for olivine rheology. J. Geophys. Res. **83**, 759–765, 1978

Received November 29, 1978; Revised Version February 14, 1979
Accepted February 22, 1979

J. Geophys. 45, 319–327, 1979

Journal of Geophysics

Crustal and Upper Mantle Structure Beneath the Apennines Region as Inferred From the Study of Rayleigh Waves*

G. Calcagnile and G.F. Panza

Istituto di Geodesia e Geofisica, Università di Bari, I-70100 Bari, Italy

Abstract. Rayleigh wave phase velocities were obtained in the period range 12.5–83.3 s using the almost linear array of long period seismic stations installed at Bari (BAI), Grosseto (GSO), Bologna (BOL) and Torino (TNO).

The Hedgehog inversion gives a crustal thickness in the range 25–37 km.

The presence of a low-velocity layer in the crust is allowed, while low-velocity material within a few kilometers of the Moho is required. The shear-wave velocities below 60 km are rather higher than usual channel values. If crustal thicknesses of the order of 37 km are rejected as suggested by other geophysical data then the low-velocity layer in the crust is required in order to satisfy the observed dispersion relation.

Key words: Rayleigh waves – Crust – Upper mantle – Italy.

Introduction

Among other benefits to be derived from such investigations, the study of the upper mantle structure under Italy and the regions adjoining it is important for deriving an understanding of the stress history of interactions at the boundary between the European and African plates. But more interesting in this investigation is the study of crustal properties, in view of the possibility to determine the distribution versus depth of *S*-wave velocity, which gives information about the presence or not of partial melting in crustal layers. The detection of extended areas with soft crustal layers is indeed relevant for the understanding of the crustal deformation, mainly in mountaineous regions. These informations cannot be obtained from the study of body waves because of the non-uniqueness in the inversion to models with a low-velocity zone unless travel-times for reflected waves or for those of a deep seismic source are available (Gerver and Markusevitch, 1966).

* Publ. No 104 of P.F. Geodinamica-CNR-Roma

0340-062X/79/0045/0319/$01.80

Further interest for such research is represented by the relevant differences in the models of the Apennines region constructed up to now. Caloi (1957, 1958), using earthquake travel-times, has indicated that the North-Central Apennines have a crustal thickness of about 45 km. Close to this result is the value found by Caputo et al. (1976) using surface waves at periods larger than 23 s and an oversimplified crustal model. Much to the south, Colombi et al. (1973) have found a crustal thickness of the order of 35 to 45 km under the westernmost part of the Apennines, thinning to the east, by refraction methods. Based on sketchy information, Giese and Morelli (1973, 1975) have attributed a crustal thickness to this region of 25 to 30 km. More recently Nolet et al. (1978) have found a crustal thickness of 35 km, essentially based on single station group velocity data and over paths east of the area sampled by our data. The consideration of the geological frame (e.g. Elter et al., 1975) makes the difference in location of the aforementioned profiles significant, thus we don't feel confident in combining these two data sets to reduce the possible range of solutions in the inversion process.

Data

The results reported here are obtained from the processing of seismograms recorded for an earthquake which occurred on April 4, 1975, at 38.1 N, 22.0 E, origin time 05:16:16.2, $M_b = 5.4$, focal depth = 53 km.

We have used recordings of fundamental mode Rayleigh waves made on the vertical component long-period seismographs (WWSSN equivalent) installed at Bari (BAI), Bologna (BOL), Grosseto (GSO) and Torino (TNO) (Fig. 1) as part of the Italian Long Period Seismographic Network. The station coordinates are given in Table 1, as well as the ones for Aquila (AQU).

The records were analyzed by a standard time-windowing and frequency-filtering technique (e.g. Pilant and Knopoff, 1964; Biswas and Knopoff, 1974; Panza, 1976).

The station spacing is too short to provide any possible resolution of the structure underneath any subregion spanned by a station pair. The overall span of the array means that the data for all four stations are best used in a joint array-processing analysis. This means that we shall only be able to determine the 'average' dispersion characteristics for the entire region and hence, after inversion, obtain an 'average' structural cross-section for the entire region.

To calculate the 'average' phase velocity without bias toward the phase data for any particular subset of stations we fit a phase versus distance diagram at a given period by a linear regression. Examples of these plots are given for two periods in Fig. 2. The phase slownesses are the slopes of the phase-distance curves. The results are given in Table 2 for selected multiples of the folding frequency.

Figure 3 gives a comparison of the data with dispersion values available for Italy (Caputo et al., 1976; Calcagnile et al., 1979). Significant differences can be observed at periods larger than 50 s, reasonably reflecting the presence of large lateral variations also in the upper mantle in the Italian region.

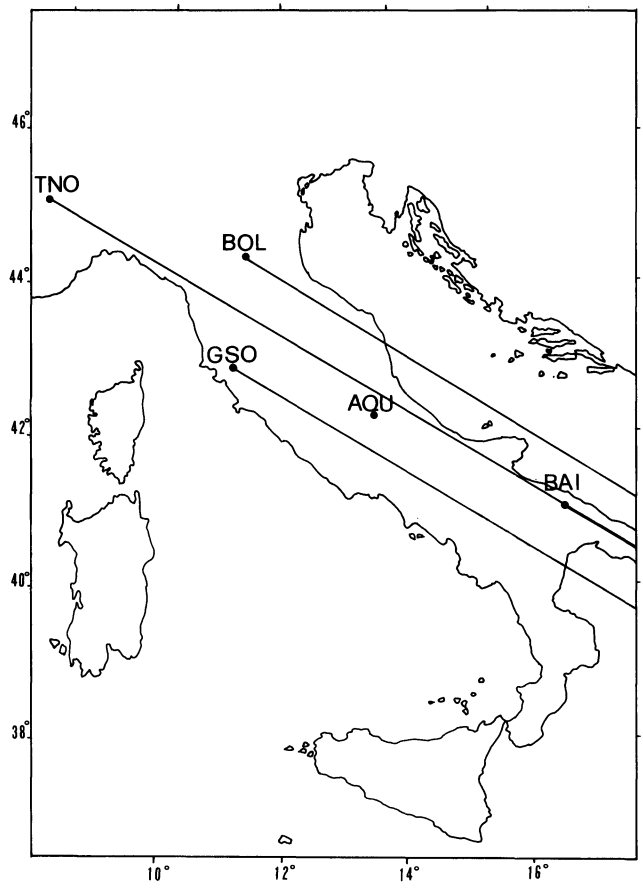

Fig. 1. Wave paths to the stations used in the determination of Rayleigh wave dispersion

Table 1. Seismic stations

L'Aquila	(AQU)	42°21′14.0″N	13°24′11.0″E
Bari	(BAI)	40°52′40.0″N	17°12′13.0″E
Bologna	(BOL)	44°29′12.0″N	11°19′44.4″E
Grosseto	(GSO)	42°45′08.1″N	11°06′58.6″E
Torino	(TNO)	45°03′31.5″N	07°41′49.0″E

Table 2. Phase velocities used in the inversion

Period (s)	Phase velocity (km/s)	Error ε (km/s)
83.3	4.03	0.07
62.5	4.00	0.05
50.0	3.91	0.05
41.7	3.81	0.05
31.3	3.64	0.05
25.0	3.51	0.05
17.9	3.11	0.05
12.5	2.84	0.07

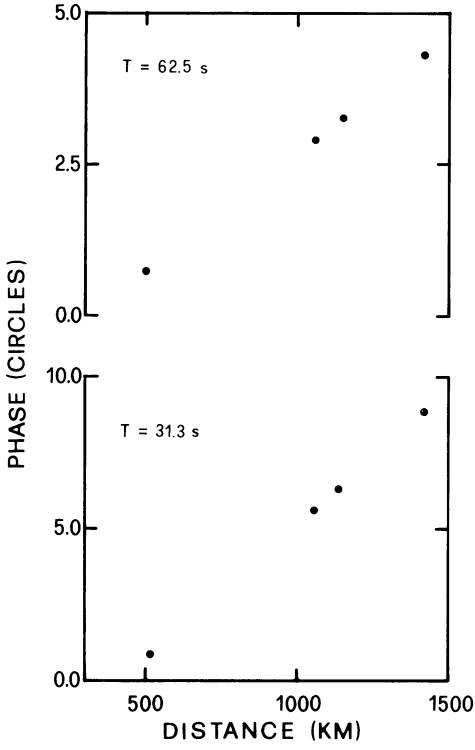

Fig. 2. Examples of plots of phase versus epicentral distance used to determine the average phase velocity. At each period phases are referred to an arbitrary integer

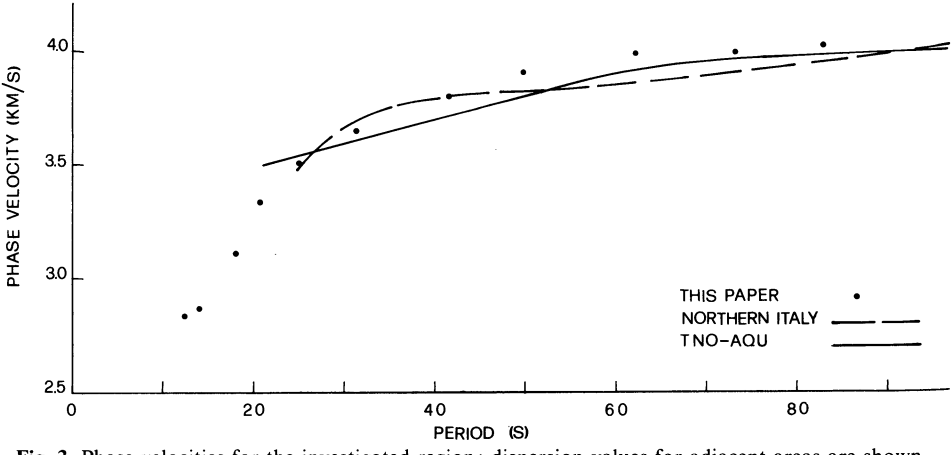

Fig. 3. Phase velocities for the investigated region; dispersion values for adjacent areas are shown for comparison; TNO-AQU from Caputo et al. (1976), Northern Italy from Calcagnile et al. (1979)

Dispersion values analogous to those given in this paper have been obtained by Biswas and Knopoff (1974) in the Colorado plateau region.

Inversion

As indicated, the small spacing between stations prevents us from dividing the span of the array into smaller regions. Accordingly, to invert the dispersion results, we assume that a homogeneous horizontally layered structure underlies the region from Bari to Torino. The assumption of a layered model does not imply a commitment on our part to the presence of sharp discontinuities in properties; they simply point toward a rapid change in the gradient of elastic parameters. The inversion method applied is the well-known Hedgehog procedure. In the inversion, if the difference between computed and observed phase velocities exceeded the limit $\pm\varepsilon$ (see Table 2) at any individual period, the model was rejected. Models which pass these tests were further tested to determine whether the root-mean-square (rms) deviation σ was appropriately small. All models with $\sigma \leqq 0.03$ km/s were finally accepted. These estimates of error are suggested by the scatter of the data in the phase versus distance diagrams.

The cross-section used in the inversion is listed in Table 3. Six model parameters were allowed to vary, namely the thickness of the middle and lower crustal layers and their shear-wave velocity, the thickness and the shear-wave velocity of the lid. Furthermore we tested five values for the upper asthenosphere shear

Table 3. Cross-section used in the inversion

Layer thickness (km)	β (km/s)	α (km/s)	ρ (km/s)	
5.0	1.90	3.50	2.00	sediments
10.0	3.10	5.50	2.50	upper crust
P4	P1	6.10	2.75	middle crust
P4	P2	6.90	3.00	lower crust
P5	P3	8.10	3.45	lid
303-2·P4-P5	P6	8.20	3.50	upper asthenosphere
∞	4.85	8.60	3.65	

Confidence limits $\sigma = 0.03$ km/s, single point rejection if $|\Delta c| > \varepsilon$ (see Table 2)

Parameter	Range and step	Starting value	Grid variable x_n
P1 (km/s)	2.7 (0.2) 3.9	3.5	$-4 \div +2$
P2 (km/s)	3.1 (0.2) 4.1	3.9	$-4 \div +1$
P3 (km/s)	4.2 (0.1) 4.8	4.3	$-1 \div +5$
P4 (km)	5 (2) 15	9	$-2 \div +3$
P5 (km)	15 (20) 75	35	$-1 \div +2$
P6 (km/s)	4.3 (0.1) 4.7	4.4	$-1 \div +3$

Table 4

Solution number	Middle crust (P1/P4)	Lower crust (P6/P4)	Lid (P3/P5)	r.m.s. σ
(a) Upper asthenosphere P6 = 4.50 km/s				
1	3.3/11	3.9/11	4.3/35	0.028
2	3.5/11	3.7/11	4.3/35	0.023
3	3.3/9	3.7/9	4.2/35	0.024
4	3.3/9	3.7/9	4.3/55	0.026
5	3.3/11	3.9/11	4.3/55	0.029
6	3.5/11	3.7/11	4.3/55	0.027
7	3.3/11	4.1/11	4.2/35	0.023
8	3.3/11	4.1/11	4.3/55	0.027
9	3.5/11	3.7/11	4.4/55	0.026
10	3.5/13	4.1/13	4.3/35	0.023
11	3.5/13	3.9/13	4.4/35	0.025
12	3.5/13	3.9/13	4.3/55	0.029
13	3.5/13	4.1/13	4.2/35	0.029
14	3.5/13	3.9/13	4.4/55	0.022
15	3.5/13	4.1/13	4.2/15	0.030
16	3.5/9	3.5/9	4.2/35	0.022
17	3.5/9	3.5/9	4.3/55	0.023
18	3.3/9	3.5/9	4.3/55	0.028
19	3.5/11	3.7/11	4.4/75	0.024
20	3.5/13	3.9/13	4.4/75	0.024
21	3.5/15	4.1/15	4.4/15	0.027
22	3.5/15	4.1/15	4.5/35	0.028
23	3.5/15	4.1/15	4.5/15	0.030
24	3.5/15	4.1/15	4.5/55	0.028
25	3.5/15	4.1/15	4.5/75	0.028
26	3.5/9	3.3/9	4.3/35	0.028
27	3.7/9	3.3/9	4.3/55	0.027
28	3.3/7	3.3/7	4.2/55	0.027
29	3.5/7	3.1/7	4.2/35	0.026
30	3.7/9	3.1/9	4.4/55	0.027
31	3.5/7	3.1/7	4.2/55	0.027
32	3.7/9	3.1/9	4.4/75	0.024
33	3.5/7	3.1/7	4.3/75	0.028
(b) Upper asthenosphere P6 = 4.60 km/s				
	3.3/9	3.7/9	4.3/75	0.030
	3.5/9	3.5/9	4.3/75	0.028
	3.3/11	4.1/11	4.4/75	0.030
	3.5/13	4.1/13	4.5/55	0.030
	3.5/13	3.9/13	4.5/75	0.028
(c) Upper asthenosphere P6 = 4.40 km/s				
	3.5/15	4.1/15	4.5/75	0.030

velocity obtaining solutions indicating its range of variability. The allowed range of variation for these parameters are given in the lower part of Table 3.

The constant values in the crustal model are suggested by results of DSS and indirectly relevant gravity data (e.g., Giese and Morelli, 1975). Small differences from the constant values in density and *P*-wave velocity are not expected

to have a significant influence on the result of the inversion presented in Table 4. Reasonable changes in the first 15 km of the crust do not affect significantly the inversion result. This is not a surprising result if variational parameters in this layer and the error allowed at short periods are considered. Thirty-three successful solutions x_n were obtained, values of x_n are listed as well as the values of the rms deviation between the model curve and the observations over the eight selected periods. The test on the upper asthenosphere shear velocity indicates that its range is limited to values in the range 4.4–4.6 km/s.

Owing to the period range we are dealing with our major concern is the estimate of average crustal properties. It must be mentioned here that, since from the record of station TNO it has been possible to obtain reliable phases only for periods larger than 25 s, the crustal models we will describe are mostly proper for the area covered by the tripartite array BAI-BOL-GSO, to which an average Moho depth less than about 31 km might be assigned according to independent geophysical results (e.g., Giese and Morelli, 1975). Our data are consistent with a crustal thickness in the range 28–37 km. A 'crustal' thickness up to 45 km is compatible with the data but since average Moho depths of 41–45 km are not realistic according to the geophysical results in the area and since the larger crustal thickness requires shear wave velocities for the lower crust which seem too high (3.9–4.1 km/s) we think that solutions n. 10-11-12-13-14-15-20, having an apparent crustal thickness of 41 km, actually correspond to models with total crustal thickness equal to 28 km, and solutions n. 21-22-23-24-25, with apparent crustal thickness of 45 km, give models with a crust of 30 km. Namely they indicate actually the presence of a transition zone rather than an abrupt jump in velocity to the underlying 'soft' mantle with a shear-wave velocity in the range 4.2–4.5 km/s. These crusts overlie mantle material characterized by strong positive velocity gradients. Thus on the basis of dispersion data only we cannot distinguish between crustal models containing or not a significant layer of what is usually called 'gabbro'. If we exclude crustal thicknesses larger than 33 km, i.e., if we exclude a Moho depth equal to 37 km or larger, as suggested by independent geophysical data (e.g., Giese and Morelli, 1975), then only crustal models where the 'gabbro' layer is practically absent are possible, except for solutions 3 and 4. Furthermore the presence of negative gradients in the velocity-depth function is allowed with a velocity contrast as high as 0.6 km/s. The absence of a clearcut 'gabbro' layer is in agreement with the model given by Giese and Morelli (1975) for the Northern Apennines and is also substantiated by the structure proposed by Colombi et al. (1973) for the southernmost part of the area. On the other hand the velocity inversion given by Giese and Morelli (1975) in the aforementioned model around 25 km, is not clearly substantiated by experimental evidence as travel-time for reflected waves or for those of a deep seismic source (Gerver and Markusevitch, 1966), while surface waves data have allowed the determination of a set of models, wherein shear-wave velocity in the low-velocity zone can be in the range 3.1–3.3 km/s, which corresponds to compressional-wave velocity in the range 5.4–5.7 km/s, if the standard relation $v_p = \sqrt{3}\, v_s$ is used. The origin of crustal low-velocity zone is not yet clearly understood, however the low-velocity values in the lower crust may indicate partial melting perhaps in combination with the presence of dehydration water.

Being aware of the fact that we cannot exclude the presence of very thin veneers with high velocity just below the Moho, on the base of our data we can state that the sub-Moho material is characterized by low velocities, never exceeding 4.4 km/s, and that below it the velocity increases with depth or is constant, being in the range 4.4–4.6 km/s.

Conclusions

The crustal structure of the Apennines region, as inferred from Rayleigh wave dispersion measurements, is in good agreement with the model given by Giese and Morelli (1975). More detail is given about the possible low-velocity zone at a depth of about 25 km, which is characterized by *S*-wave velocities in the range 3.1–3.3 km/s. If the presence of a soft layer in the crust at a depth of about 25 km is accepted, in agreement with DSS and surface wave data, then this depth can be considered as the upper limit for the focal depth of crustal shocks in the Apennines. The maximum crustal thickness consistent with the data is 37 km; all crustal models exclude the presence of crustal doubling as suggested for the Northern Apennines by Morelli et al. (1977). At the most *S*-wave velocities in the range 3.9–4.1 km/s can be considered strong indicators of the presence of some kind of transition zone, instead of the usual rapid change in elastic properties associated with the Moho discontinuity. The *S*-wave velocity in the sub-Moho material never exceeds 4.4 km/s and this is in agreement with the low P_n velocities given by Giese and Morelli (1975).

Caputo et al. (1976) from the study of the path TNO-AQU where not able to resolve between two groups of models, one with relatively low-velocity material just below the Moho, the other with a high velocity lid of thickness 30–40 km overlying a very low-velocity channel. On the basis of our results and DSS data this ambiguity seems to be resolved, and the first group of models seems to be more appropriate for the Apennines region.

The presence of high-velocity material, about 4.5 km/s, starting at depths as low as 60 km may be interpreted as evidence of a possible downbuckling process of the high-velocity lid in this region.

References

Biswas, N.N., Knopoff, L.: Structure of the upper mantle under the United States from the dispersion of Rayleigh waves. Geophys. J. R. Astron. Soc. **36**, 515–539, 1974

Calcagnile, G., Panza, G.F., Knopoff, L.: Upper mantle structure of North-Central Italy from the dispersion of Rayleigh waves. Tectonophysics **56**, 1979

Caloi, P.: Caratteristiche della crosta terrestre dalle Alpi agli Appennini. Ann. Geofis. **10**, 189–192, 1957

Caloi, P.: La crosta terrestre dagli Appennini all'Atlantico, ricostruita sulla base dei rilievi sismici. Ann. Geofis. **11**, 249–264, 1958

Caputo, M., Knopoff, L., Mantovani, E., Mueller, St., Panza, G.F.: Rayleigh wave phase velocities and upper mantle structure in the Apennines. Ann. Geofis. **29**, 199–214, 1976

Colombi, B., Giese, P., Luongo, G., Morelli, C., Riuscetti, M., Scarascia, S., Schutte, K.G., Strowald, J., De Visintini, G.: Preliminary report on the seismic refraction profile Gargano-Salerno-Palermo-Pantelleria (1971). Boll. Geof. Teor. Appl. **15**, 225–254, 1973

Elter, P., Giglia, G., Tongiorgi, M., Trevisan, L.: Tensional and compressional areas in the recent (Tortonian to present) evolution of the Northern Apennines. Boll. Geof. Teor. Appl. **17**, 3–18, 1975

Gerver, M.L., Markusevitch, V.M.: Determination of a seismic wave velocity from travel-time curve. Geophys. J. R. Astron. Soc. **11**, 165–173, 1966

Giese, P., Morelli, C.: Structural map of the Moho. In: Structural Model of Italy, Sheet South 2, CNR Rome, 1973

Giese, P., Morelli, C.: Crustal structure in Italy. Quaderni de 'La Ricerca Scientifica', CNR-Roma, **90**, 453–489, 1975

Morelli, C., Giese, P., Hirn, A., Colombi, B., Eva, C., Guerra, I., Letz, H., Nicolic, R., Reichert, C., Scarascia, S., Wigger, P.: Seismic investigations of crustal and upper mantle structure of the northern Apennines and Corsica. In: Structural history or of the Mediterranean basin, B. Biju-Duval and L. Montadert, eds., pp. 281–286. Paris: Technip 1977

Nolet, G., Panza, G.F., Wortel, R.: An averaged model for the Adriatic subplate. Pure Appl. Geophys. **116**, 1284–1294, 1978

Panza, G.F.: Phase velocity determination of fundamental Love and Rayleigh waves. Pure Appl. Geophys. **114**, 753–763, 1976

Pilant, W.L., Knopoff, L.: Observations of multiple seismic events. Bull. Seism. Soc. Am. **54**, 19–39, 1964

Received May 16, 1978; Revised Version January 15, 1979,
April 20, 1979; Accepted May 10, 1979

J. Geophys. 45, 329–336, 1979

Journal of Geophysics

On the Coastal Effect on Geoelectrical Soundings

E. Mundry and P. Worzyk

Niedersächsisches Landesamt für Bodenforschung, Alfred-Bentz-Haus, Postfach 510153, D-3000 Hannover 51, Federal Republic of Germany

Abstract. To estimate the influence of the ocean on a geoelectrical sounding carried out on land near the coast, a model is chosen consisting of a perfectly conducting, infinitely thin, half-infinite sheet lying on the surface of a homogeneous earth. Model curves of the apparent resistivity are given for measurements made parallel or perpendicular to the edge of the sheet. From these model curves it is possible to derive apparent resistivity curves for other configurations of the current and potential electrodes.

As an example, we have considered a geoelectrical sounding made with large electrode separation in Southern Africa. For a homogeneous half-space, the maximum deviation of the apparent resistivity from the resistivity of the half-space is of the order of about 15% for the applied maximum electrode spacing of 1,250 km due to the effect of the Indian Ocean. Therefore it may be concluded that the measured sharp minimum of the apparent resistivity curve (ρ_a) is not produced by the ocean. If the measured ρ_a-curve is accordingly corrected for the coastal effect it yields nearly the same conductivity model as before.

Key words: Apparent resistivity – Effect of ocean – Conducting half-infinite sheet.

1. Introduction

Blohm et al. (1977) have reported on results of geoelectrical depth soundings carried out in Southern Africa from 1973 to 1975. The measurements were made using a Schlumberger configuration with electrode spacings up to 1,250 km. The array was nearly parallel to the Indian Ocean at an average distance of about 350 km from it. Therefore, the question may be asked to what extent the data could have been affected by the highly conductive salt water of the ocean. (Sea water has a resistivity of about 0.2 Ohm · m as compared with up to 100,000 Ohm · m of the South-African rocks at shallow depth.) The mean depth of the

0340-062X/79/0045/0329/$01.60

ocean (about 3 km) was very small compared with the distances of the electrodes from the coast as well as from each other. Accordingly, an infinitely thin, half-infinite sheet with vanishing resistivity at the boundary of a half-space may serve as a model of the ocean in order to estimate the possible effect on the sounding curve.

Such a simple model may also be used to estimate the effect of the sea water on soundings carried out immediately near the coast. Additionally, this model may be helpful for the interpretation of soundings made near the edge of shallow highly conductive deposits of large lateral extent.

Grant and West (1965) have quoted a paper by Sommerfeld (1897), in which the potential of a point source is derived for the case of an infinitely conducting half-plane embedded in a uniform space. Sommerfeld's formula was later corrected by Carslaw (1899). By means of this formula, corresponding Schlumberger sounding apparent resistivities may be derived from the gradients of the potential, especially from gradients parallel or perpendicular to the edge of a semi-infinite sheet lying at the earth's surface.

2. Theory

Within a uniform space with resistivity ρ_1, Sommerfeld (1897) assumes a half-infinite thin sheet with no resistivity which coincides with the half-plane $z=0$, $x \geqq 0$ in Cartesian coordinates. A point source A with current I is located at $A(x', y', z')$; the point P where the potential is measured is assumed to have the coordinates $P(x, y, z)$. If cylindrical coordinates (r, φ, y) are introduced so that the axis of the cylinder coincides with the edge of the sheet which is described by $\varphi=0$, then

$$\begin{aligned} x &= r \cdot \cos\varphi \\ y &= y \\ z &= r \cdot \sin\varphi. \end{aligned} \tag{1}$$

Now, the potential V may be written as

$$V=\frac{I\rho_1}{2\pi^2} \cdot \left[\frac{1}{R} \cdot \arctan\left(\frac{\sigma+\tau}{\sigma-\tau}\right)^{1/2} - \frac{1}{R'} \arctan\left(\frac{\sigma+\tau'}{\sigma-\tau'}\right)^{1/2}\right]. \tag{2}$$

This formula is derived by conformal mapping of the half-infinite plane onto an infinite plane applying additionally the method of images in a space of two revolutions. The following definitions are used:

$$R=[r^2+r'^2-2rr'\cos(\varphi-\varphi')+(y-y')^2]^{1/2} \tag{3a}$$

$$\tau=\cos\frac{\varphi-\varphi'}{2} \tag{3b}$$

$$\sigma=\left[\frac{(r+r')^2+(y-y')^2}{4rr'}\right]^{1/2}. \tag{3c}$$

The quantities R' and τ' are obtained from (3a) and (3b), respectively, by inserting $-\varphi'$ in place of φ'.

In our case the half-plane is assumed at the earth's surface $z=0$, for $x \geqq 0$ ($\varphi=0$), and the source A and the point of measurement P are also located at the earth's surface with $x<0$, i.e.

$$\varphi=\varphi'=\pi. \tag{4}$$

If a half-space rather than uniform space is considered, one has only to multiply the potential by a factor of two. Since $r=-x$, $r'=-x'$, $\tau=1$, $\tau'=-1$, $R=R'$, using definitions (3c) and the addition theorem for the arctan function, Eq. (2) takes the simple form

$$V=\frac{I\rho_1}{\pi^2}\cdot\frac{1}{R}\cdot\arctan u, \tag{5}$$

where

$$u=2(xx')^{1/2}/R \tag{5a}$$

and

$$R=[(x-x')^2+(y-y')^2]^{1/2}. \tag{5b}$$

If the point of measurement P approaches the source, one obtains

$$V\to V_0=\frac{I\rho_1}{2\pi}\cdot\frac{1}{R} \quad (P\to A), \tag{6}$$

which is the potential of a point source at the boundary of a half-space without any disturbing bodies. If P approaches the edge of the sheet, we get

$$V\to 0 \quad (x\to 0). \tag{7}$$

To obtain the gradient of the potential V at the point P in any direction s defined by the angle ψ with respect to the x-axis, we have to calculate the derivatives with respect to x and y:

$$\frac{\partial V}{\partial s}=\frac{\partial V}{\partial x}\cdot\cos\psi+\frac{\partial V}{\partial y}\cdot\sin\psi. \tag{8}$$

The apparent resistivity $\rho_a^{(s)}$ may be defined for a measurement of the gradient in the s-direction by

$$\rho_a^{(s)}=\rho_1\cdot\frac{\partial V/\partial s}{\partial V_0/\partial s}. \tag{8a}$$

Especially for a measurement perpendicular or parallel to the edge of the sheet, one obtains:

$$\frac{\rho_a^{(x)}}{\rho_1}=\frac{\partial V/\partial x}{\partial V_0/\partial x}=\frac{2}{\pi}\left[\arctan u+\frac{u^2(x-x')-2x'}{(x-x')\,u(1+u^2)}\right] \tag{9}$$

(perpendicular to the edge),

$$\frac{\rho_a^{(y)}}{\rho_1}=\frac{\partial V/\partial y}{\partial V_0/\partial y}=\frac{2}{\pi}\left[\arctan u+\frac{u}{1+u}\right] \tag{10}$$

(parallel to the edge).

3. Results

3.1. Model Curves of the Apparent Resistivity

From expressions (9) and (10) it is possible to calculate model curves of the apparent resistivity for a single electrode A (measurement of the gradient) by setting $y'=0$ and expressing all geometric quantities in terms of the distance D from the source A to the edge of the conducting sheet. The distance between the electrode A and the measuring point (center of MN in Fig. 1) is designated by d; in practice the gradient of the potential is obtained from the difference of the potentials between the potential electrodes M and N when placed close together.

Depending upon the position of the potential electrodes M and N, as shown in Fig. 1 (inset), three types of apparent resistivity curves will result. For example, when M and N are situated between electrode A and edge of the sheet ($d=x-x'$), we obtain the apparent resistivity curve (a) shown in Fig. 1. Similarly, when A lies between MN and the sheet, curve (b) results, and when MN is moved parallel to the edge, curve (c) will be obtained.

The gradient $\partial V/\partial s$ of the potential – and therefore the apparent resistivity according to (8a) – in the case of two electrodes A (with current I) and B (with current $-I$) can be obtained by superposition of the gradients for the case of a single current electrode A. Especially for a Schlumberger configuration (with potential electrodes M and N in the middle between A and B) with the electrode separation $L=\overline{AB}$ being perpendicular to the edge of the sheet and with the distance l from the midpoint of the electrode configuration to the edge of the conducting sheet, the following formula may be used:

$$\rho_a=\left(\frac{L/2}{l-L/2}\right)^2\cdot\rho_a^{(x+)}\left[\frac{L/2}{l-L/2}\right]+\left(\frac{L/2}{l+L/2}\right)^2\rho_a^{(x-)}\left[\frac{L/2}{l+L/2}\right], \tag{11}$$

where the arguments of $\rho_a^{(x+)}$ and $\rho_a^{(x-)}$ denote the abscissa of the curves (a) and (b) in Fig. 1. In case of a Schlumberger configuration parallel to the edge of the sheet (with two electrodes A and B) we obtain the same apparent resistivity curve as shown in curve (c), Fig. 1, for a single electrode A, with $d=L/2$ and D = distance of A and B from the edge. In our example, this case is of special interest. It may be concluded from curve (c) that the deviation of $\rho_a^{(y)}$ from ρ_1 is less than 3% for $d/D<0.85$. As d/D approaches infinity ($u\to 0$), the following expression for $\rho_a^{(y)}$ with a maximum error of 3% may be used:

$$\rho_a^{(y)}\approx\rho_1\cdot\frac{8}{\pi(d/D)}\qquad(d/D>9.4). \tag{12}$$

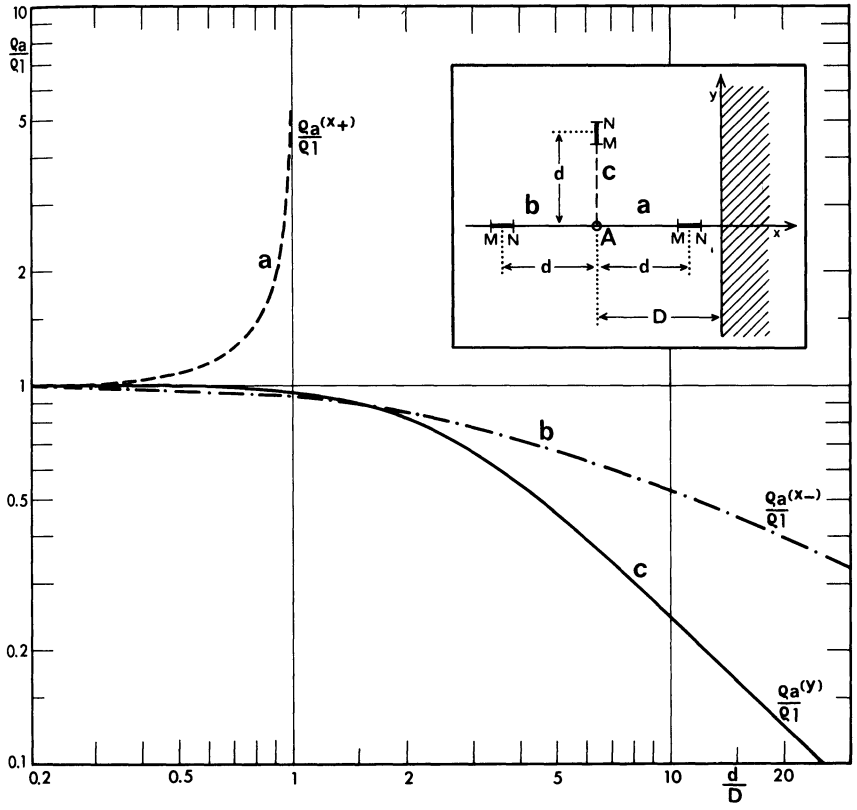

Fig. 1. Apparent resistivity (ρ_a) model curves for a single current electrode A and an infinitely thin perfectly conducting half-infinite sheet (hatched) situated on top of a homogeneous halfspace of resistivity ρ_1. Three different cases are shown for different positions (cf. inset) of the closely spaced potential electrodes M and N

Thus for large values of d/D, the apparent resistivity curve plotted on a logarithmic scale is a straight line with a slope of $-45°$.

3.2. Comparison With a Lateral Discontinuity of Resistivity

For measurements near a lateral change of resistivity, the question arises to what extent a finite thickness of a layer of high conductivity at the boundary of a half-space for $x>0$ may influence a sounding curve within the region $x<0$. For example, is it possible to obtain within a given accuracy of the measurements the model curve (c) for a sheet-like body with a finite or an infinite thickness? The extreme case of an infinite thickness of the layer with resistivity ρ_2 may be treated in the following simple manner, which allows a useful comparison with the model consisting of an infinitely thin sheet as treated in Sect. (3.1).

The model consists of a quarter-space $z>0$, $x<0$ with resistivity ρ_1 and a quarter-space $z>0$, $x>0$ with resistivity ρ_2. The potential V at the earth's surface in case of a point source $A(x', y', 0)$ in medium 1 as given in Van Nostrand and Cook (1966) is:

$$V=\frac{I\rho_1}{2\pi}\{[(x-x')^2+(y-y')^2]^{-1/2}+k[(x+x')^2+(y-y')^2]^{-1/2}\} \tag{13}$$

where $k=(\rho_2-\rho_1)/(\rho_2+\rho_1)$ is the reflection coefficient. The apparent resistivities, which correspond to curves (a)–(c) in Fig. 1 are now

$$\frac{\rho_a^{(x\pm)}}{\rho_1}=1\mp k\left(\frac{d/D}{2\mp d/D}\right)^2, \tag{14a, b}$$

$$\frac{\rho_a^{(y)}}{\rho_1}=1+k\left(\frac{d/D}{\sqrt{4+(d/D)^2}}\right)^3. \tag{14c}$$

By comparing formulas (10) and (14c), we find that for $d/D<3$, the apparent resistivity values from (10) are nearly equal (with 3% difference) to the apparent resistivity values of (14c) for the case when $\rho_2/\rho_1=0.3$. On the other hand, for $\rho_2=0$ ($k=-1$) we get from (14c):

$$\rho_a^{(y)}\to\rho_1\frac{6}{(d/D)^2}\quad(d/D\to\infty), \tag{15}$$

e.g. the corresponding curve has a slope of $-63.4°$ if plotted on a logarithmic scale. Furthermore, for a gradient measurement perpendicular to the boundary of this contact model, we have for $\rho_2=0$ about the same $\rho_a^{(x+)}$-values for $d/D<0.85$ as before. For larger values ($d/D\to1$), in the case of a conducting sheet, the apparent resistivity values rise to infinity, whereas in the case of the contact model, these values reach $2\cdot\rho_1$. Thus a distinction between both models is possible only for measurements made immediately near the edge of a layer of high conductivity.

3.3. Results and Conclusions for Measurements Made in Southern Africa

For further interpretation of measurements made in Southern Africa (Blohm et al., 1977) it should be helpful to simulate the distribution of the equipotential lines at the earth's surface as disturbed by the ocean. Therefore, two current electrodes A and B with current I and $-I$ respectively, are placed parallel to the edge of the sheet at a distance D and the equipotential lines calculated from Eq. (5) are shown in Fig. 2. $D=350$ km and $\overline{AB}=1{,}250$ km have been chosen according to the case of the maximum electrode distance applied (Blohm et al., 1977). As may be seen in Fig. 2, the potential lines are disturbed considerably only immediately near the coast line.

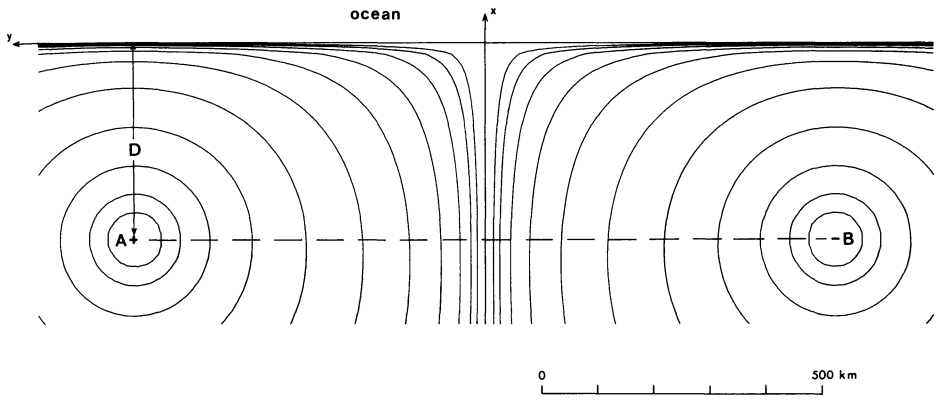

Fig. 2. Equipotential lines on the earth's surface $z=0$ for two electrodes A and B near an infinitely thin and infinitely conducting sheet ($x>0$) over a homogeneous half-space. The geometrical configuration corresponds to $\overline{AB}=1{,}250$ km and distance $D=350$ km [approximate model of an electrical sounding made in Southern Africa near the Indian Ocean (Blohm et al. 1977)]

For the mentioned maximum electrode spacing we have a ratio $d/D \approx 1.8$, and from curve (c) in Fig. 1 follows $\rho_a^{(y)}/\rho_1 \approx 0.85$. This means that the measured apparent resistivity is about 15% smaller due to the influence of the ocean if homogeneous space below the surface is assumed. The sharp minimum of the sounding curve was measured at half an electrode spacing of about 100 km (see Fig. 3), that means at a ratio $d/D \approx 0.3$. As curve (c) in Fig. 1 shows, nearly no influence of the ocean is to be seen at this ratio ($\rho_a \approx \rho_1$). Therefore, the apparently indicated well conducting layer at a depth of about 30 km cannot be due to the influence of the ocean.

Even for larger electrode spacings the effect of the ocean on the sounding curve remains so small that it should be permitted to correct the ρ_a-values in a first approximation according to the model of a perfectly conducting, infinitely thin sheet lying on the surface $x>0$ of a homogeneous earth. A better correction would be obtained by taking a layered model below the ocean similar to that on land, but in this case an analytic solution does not seem to be possible. For the largest five electrode spacings from curve (c) in Fig. 1 the corresponding ratio $F=\rho_a/\rho_1$ is taken and the measured ρ_a-values are multiplied by $1/F$. The measured and corrected ρ_a-values of the geoelectrical sounding (Blohm et al., 1977) are shown in Fig. 3 and the results of the interpretation assuming a horizontally layered model are given below:

Best Model for Measured ρ_a-Values

Resistivity	100,000	5,000	50	7,800	1 Ωm
Depth	0	2.5	30.5	35.5	150 km

Best Model for Corrected ρ_a-Values (for the influence of ocean)

Resistivity	100,000	5,000	50	9,250	1 Ωm
Depth	0	2.5	30.5	35.5	170 km

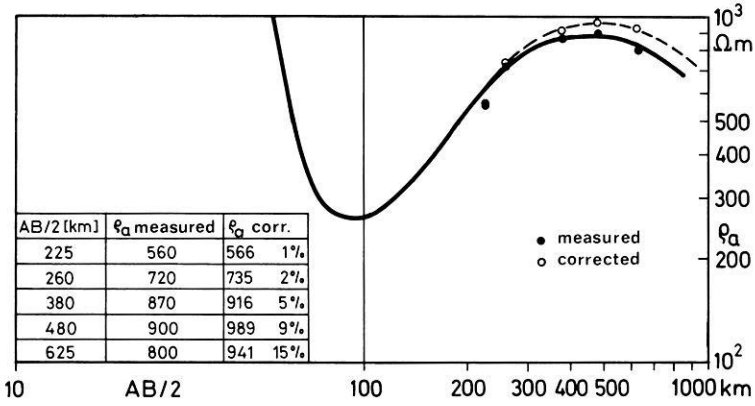

AB/2 [km]	ϱ_a measured	ϱ_a corr.
225	560	566 1%
260	720	735 2%
380	870	916 5%
480	900	989 9%
625	800	941 15%

Fig. 3. Part (large electrode spacings *AB* only) of the geoelectrical sounding curve from measurements in Southern Africa (see Blohm et al., 1977). Due to the influence of the Indian Ocean the last five ρ_a-values have been corrected according to the thin sheet model as explained in the text

It may be seen from a comparison of these results that the resistivity and the depth of the next to last layer increase from 7,800 Ωm to 9,250 Ωm and from 150 km to 170 km, respectively.

References

Blohm, E.K., Worzyk, P., Scriba, H.: Geoelectrical Deep Soundings in Southern Africa Using the Cabora Bassa Power Line. J. Geophys. **43**, 665–679, 1977

Carslaw, H.S.: Some Multiform Solutions of the Potential Differential Equations of Physical Mathematics and their Applications. Proc. London Math. Soc. **30**, 121–163, 1899

Grant, F.S., West, G.F.: Interpretation Theory in Applied Geophysics. New York etc.: McGraw-Hill Book Company 1965

Nostrand, R.G. van, Cook, K.L.: Interpretation of Resistivity Data. Washington: U.S. Government Printing Office 1966

Sommerfeld, A.: Über verzweigte Potentiale im Raum. Proc. London Math. Soc. **28**, 395–429, 1897

Received November 9, 1977; Revised Version March 26, 1979; Accepted March 30, 1979

J. Geophys. 45, 337–340, 1979

Journal of Geophysics

Short Communications

Observations of sPn From Swabian Alb Earthquakes at the GRF Array

R. Kind

Seismologisches Zentralobservatorium, Krankenhausstr. 1–3, D-8520 Erlangen, Federal Republic of Germany

Key words: Swabian Alb earthquakes – Observations of sPn – Theoretical seismograms.

A number of the largest earthquakes from the Swabian Alb recorded at the Gräfenberg array have been examined (the geographic coordinates of the main station GRF are 49.69° N and 11.22° E; see Harjes and Seidl (1978) for a description of the array). The interest was concentrated at the time window between the first onset Pn and Pg. In Fig. 1 are shown GRF records proportional to ground displacement of five events which have indications for a second arrival between Pn and Pg. The parameters for these five events are given in Table 1. The amplitudes of Pg in Fig. 1 are clipped only for the plotting purpose. The seismograms in Fig. 1 are plotted in form of seismogram sections, as it is common in explosion seismology. Only for this purpose, the known epicenter of the large earthquake of September 3, 1978, is adopted for all earthquakes. The phase between Pn and Pg, labeled sPn, is clearly visible for the largest events, and it is getting weaker for smaller events. The magnitude 4.1 event at September 3, 1978, at 08:10 and a few more smaller events have also been examined without success, in order to detect this phase. The reason for that was an unfavorable signal to noise ratio. However, it seems possible that more sophisticated data processing methods lead to better results. The time difference sPn-Pn is about 2.6 s for the events 2 and 3, and it is about 1.0 s for the remaining three events. This variation of the sPn-Pn times rules out the possibility that structural effects have caused the phase labeled sPn. Another possibility is, that a second shock is responsible for this phase. In order to check the sPn hypothesis, theoretical seismograms have been computed using the buried source version of Fuchs' reflectivity method by Kind (1978) and Kind (1979). The ray path of Pn and sPn is demonstrated in Fig. 2. In Fig. 3 are shown sections of theoretical seismograms for several possible source orientations (Götz Schneider, personal communication). The used crustal model is a simplified version of model I by Aichele (1976), derived from explosion seismol-

0340-062X/79/0045/0337/$01.00

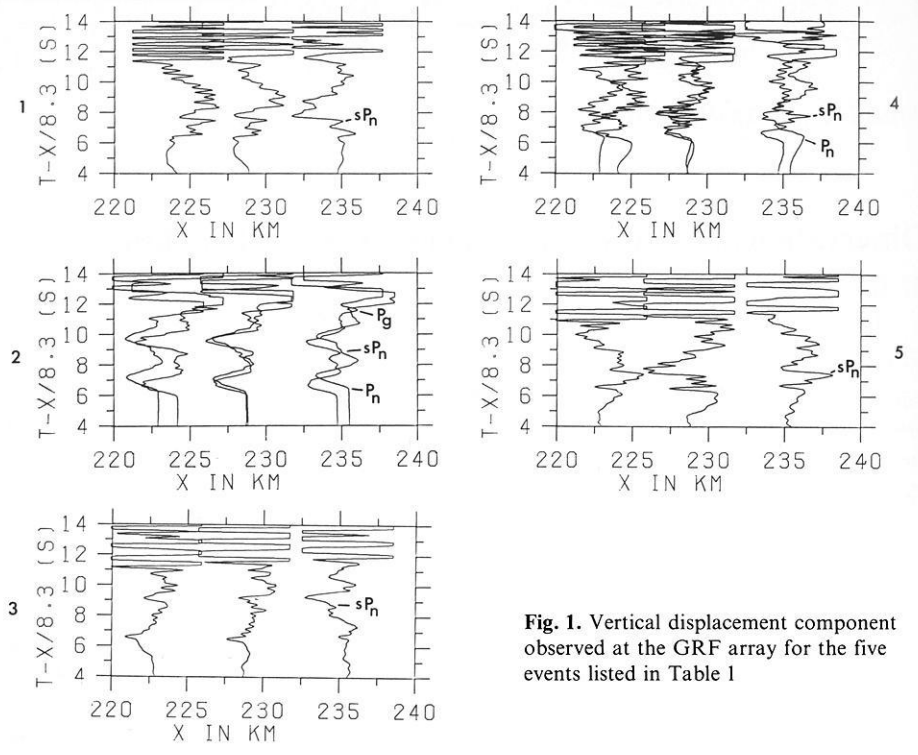

Fig. 1. Vertical displacement component observed at the GRF array for the five events listed in Table 1

Table 1

Event	Date	Pn time at GRF	Magnitude (GRF)	Filter	Subarray
1	16. January 1978	143147.7	4.6	HP	A
2	03. September 1978	050904.7	5.9	BB	A+B
3	03. September 1978	053452.5	4.3	HP	B
4	03. September 1978	100316.6	4.7	BB	A+B
5	19. September 1978	235421.4	4.1	HP	B

Parameters of the Swabian Alb events used. HP = simulated records of a 2 s displacement proportional seismometer, BB = broad band displacement proportional. The three stations 1, 2, and 3 of the subarrays A and B are used

ogy for an area about 70 km west of GRF. The observed Pg-Pn times are about 1 s larger than the ones taken from the theoretical section. Because this point is not relevant for the present purpose, it will not be pursued further. The time difference sPn-Pn in the theoretical Section 1 in Fig. 3 is about 1 s, very similar to the observed values for the events 1, 4, and 5. This leads to a focal depth of about 2.5 km. The source orientation is typical for Swabian Alb events (strike slip, strike of the fault plane N 15° E, dip 80° W). Theoretical

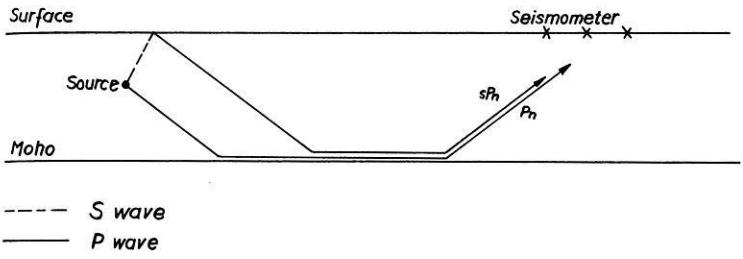

Fig. 2. Ray path of Pn and sPn

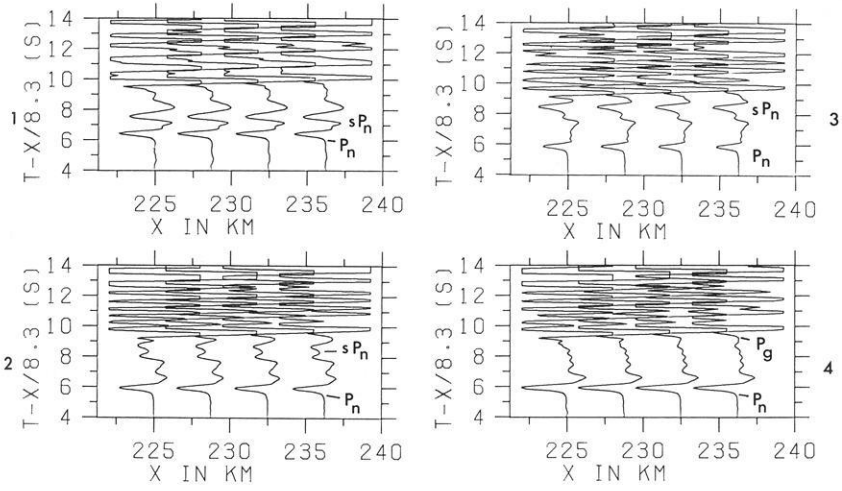

Fig. 3. Theoretical seismograms for comparison with the data shown in Fig. 1. Section 1: $h=2.5$, $\lambda=0$, $\delta=80$. Section 2: $h=6.5$, $\lambda=0$, $\delta=80$. Section 3: $h=6.5$, $\lambda=-10$, $\delta=80$. Section 4: $h=6.5$, $\lambda=0$, $\delta=60$. With h=source depth in km, λ=slip vector down negative in degrees, δ=dip of the fault plane to the west in degrees. The strike of the fault plane was N 15° E in all sections

seismograms for the same source orientation, but with a source depth of 6.5 km are plotted in section 2, Fig. 3. The amplitudes of sPn are clearly smaller than the amplitudes of Pn. There is another phase about 1 s in front of sPn. This is a phase very similar to sPn, but reflected from an assumed first order discontinuity between the sediments and the basement instead at the free surface. In Sect. 3, Fig. 3 has sPn about the same amplitudes, as it is observed. The phase about 1 s in front of sPn is very much reduced in its amplitudes. The first order discontinuity between sediments and basement was replaced by a gradient zone in this section. The dip of the fault was assumed 80° W, and the slip vector was assumed to have a dip of 10° down. The time difference sPn-Pn is about 2.6 s, like for the observed events 2 and 3. In Sect. 4, Fig. 3 are shown theoretical seismograms for another possible source orientation: pure strike slip and fault dip 60° W. However, in this section is no sPn visible. This source orientation can therefore probably be excluded, which narrows the error bounds

of the fault plane solution. In conclusion it has been shown that the GRF records of some of the largest Swabian Alb earthquakes have a clear additional arrival between Pn and Pg. It can be said, that the inpretation of this arrival as sPn is at least for the large earthquake (event 2) in good agreement with focal parameters determined by traditional methods. For another earthquake (event 5) is the focal depth 4–5 km, according to a referee's comment, whereas 2.5 km result from the present study. This disagreement requires further studies of several kinds of data.

Acknowledgements. This research was supported by the Deutsche Forschungsgemeinschaft. I wish to thank Dieter Seidl for using his filter programs, for discussions and for reading the manuscript, and Götz Schneider for discussions.

References

Aichele, H.: Interpretation refraktionsseismischer Messungen im Gebiet des Fränkisch-Schwäbischen Jura. Dissertation. Stuttgart: Universität 1976

Harjes, H.-P., Seidl, D.: Digital recording and analysis of broad-band seismic data at the Gräfenberg (GRF)-array. J. Geophys. **44**, 511–523, 1978

Kind, R.: The reflectivity method for a burried source. J. Geophys. **44**, 603–612, 1978

Kind, R.: Extensions of the reflectivity method. J. Geophys. **45** (in press, 1979)

Received March 16, 1979; Revised Version May 16, 1979;
Accepted May 22, 1979

J. Geophys. 45, 341–342, 1979

Journal of Geophysics

Macroseismic Intensity Map of Austria for the Swabian Alb Earthquake of September 3, 1978

J. Drimmel, E. Fiegweil, and G. Lukeschitz

Zentralanstalt für Meteorologie und Geodynamik, Hohe Warte 38, A-1190 Wien, Austria

Key words: Swabian Alb earthquake – Macroseismic observations in Austria.

The strong tectonic earthquake of September 3, 1978, at 05 h 08.5 m UTC, in the region of the western Swabian Alb (Albstadt, Baden-Württemberg, F.R.G.) was widely felt in Austria, too. However, with $I_o = \text{VIII}°$ MSK (according to USGS) and $M_s = 5.3$ (the arithmetical mean of eleven MLH, MLV and M-values published by CSEM) it was evidently weaker than the earthquake of November 16, 1911, in the same area.

On September 3 and 4, 1978, the 'Österreichischer Erdbebendienst' (Austrian Earthquake Service) propagated by means of broadcasting and newspapers an appeal, asking people for reports how they perceived the earthquake. Many persons reacted spontaneously. In order to increase the number of reports, 649 inquiries were sent to police stations, post offices, and schools. Finally, 377 reports from 179 places in Austria (besides 8 reports from abroad) as well as 539 negative reports could be used in working out the macroseismic map. The classification of the reports was made according to the macroseismic scale of Medvedev-Sponheuer-Kárník, 1964.

As Fig. 1. (solid isolines) shows, in Austria a maximum intensity of 5° MSK was reached in the northwest of Vorarlberg. The 3° isoseismal, being practically the limit of perceptibility, was in an epicentral distance of at least 350 km (Kötschach-Mauthen in Carinthia) and 550 km at the utmost (Vienna). – In Austria, 48,000 square km (about 58% of the whole territory) were shaken with an intensity of at least 3° MSK, 9,600 sq. km with at least 4° MSK, and 450 sq. km with at least 5° MSK. There were no damages in Austria. Accordingly, the effects of this earthquake were clearly inferior to those of November 16, 1911, event (cf. Fig. 1, dashed isolines); this time, in the west of Austria the intensity was about one degree MSK lower, corresponding to an earthquake magnitude being about 0.7 units smaller. – Remarkable in both cases is a better perceptibility of the earthquakes north of the main line of the Alps than south of it.

0340-062X/79/0045/0341/$01.00

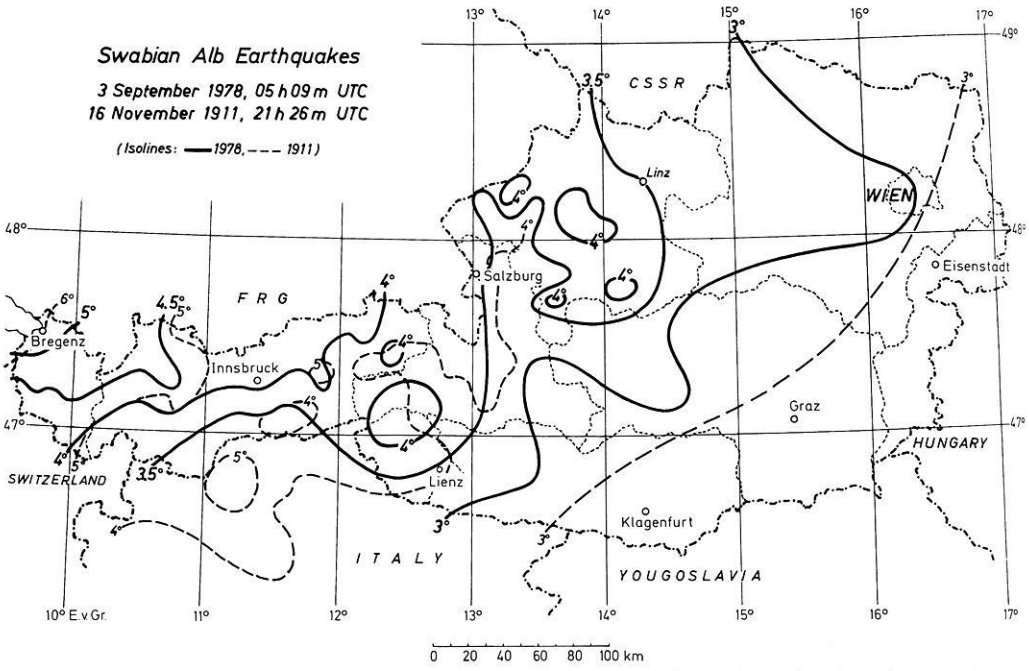

Fig. 1. Macroseismic intensity map of Austria for the Swabian Alb earthquake of September 3, 1978 (*solid isolines*) and of November 16, 1911 (*dashed isolines*). The isoseismals were drawn on ground of unpublished macroseismic data of the Austrian Earthquake Service

References

Centre Seismologique Europeo-Mediterraneen Strasbourg: Determination hypocentrale No. 3/9/78, October 19, 1978

U.S. Department of the Interior, Geological Survey: Provisional hypocenters No. 23P-78, September 12, 1978

Received January 17, 1979; Revised Version March 23, 1979; Accepted May 10, 1979

J. Geophys. 45, 343–347, 1979

Journal of Geophysics

Das Schwerefeld im Bereich der Nordfriesischen Inseln und des benachbarten Festlands

S. Plaumann

Niedersächsisches Landesamt für Bodenforschung, Postfach 510153, D-3000 Hannover 51, Federal Republic of Germany

The Gravity Field of the North Frisian Islands and the Adjacent Mainland

Key words: Gravity map – Sylt anomaly – Precambrian massif.

Einleitung

Durch Zusammenfassung gravimetrischer Daten verschiedener Herkunft ist eine geschlossene Schwerekarte des deutsch-dänischen Grenzbereiches im nordwestlichen Schleswig-Holstein hergestellt worden.

Eine gravimetrische Vermessung Schleswig-Holsteins – ohne die Nordfriesischen Inseln bis auf Nordstand – besteht seit der geophysikalischen Reichsaufnahme. 1965 hat Saxov die Ergebnisse dänischer Schweremessungen in Südjütland veröffentlicht. Vom Niedersächsischen Landesamt für Bodenforschung, Hannover (unveröff. Bericht 1977) ist schließlich eine gravimetrische Regionalvermessung auf den Nordfriesischen Inseln durchgeführt worden.

Alle Einzelvermessungen sind jetzt zusammengefaßt worden und haben zu der Schwerekarte Abb. 1 geführt. Diese Arbeit ist sehr erleichtert worden durch neuzeitliche Schwerenetze, welche Länder und Kontinente überspannen und die Umrechnung verschiedener Daten in ein einheitliches System ermöglichen.

Grundlagen für einen einheitlichen Bezug der verschiedenen Schweredaten

Ein nationales Schwerebezugssystem ist in der Bundesrepublik Deutschland durch das Deutsche Schweregrundnetz von 1962 (DSGN-62) gegeben, dessen Aufbau am übersichtlichsten bei Marzahn (1959) beschrieben ist. Die Regional-

0340-062X/79/0045/0343/$01.00

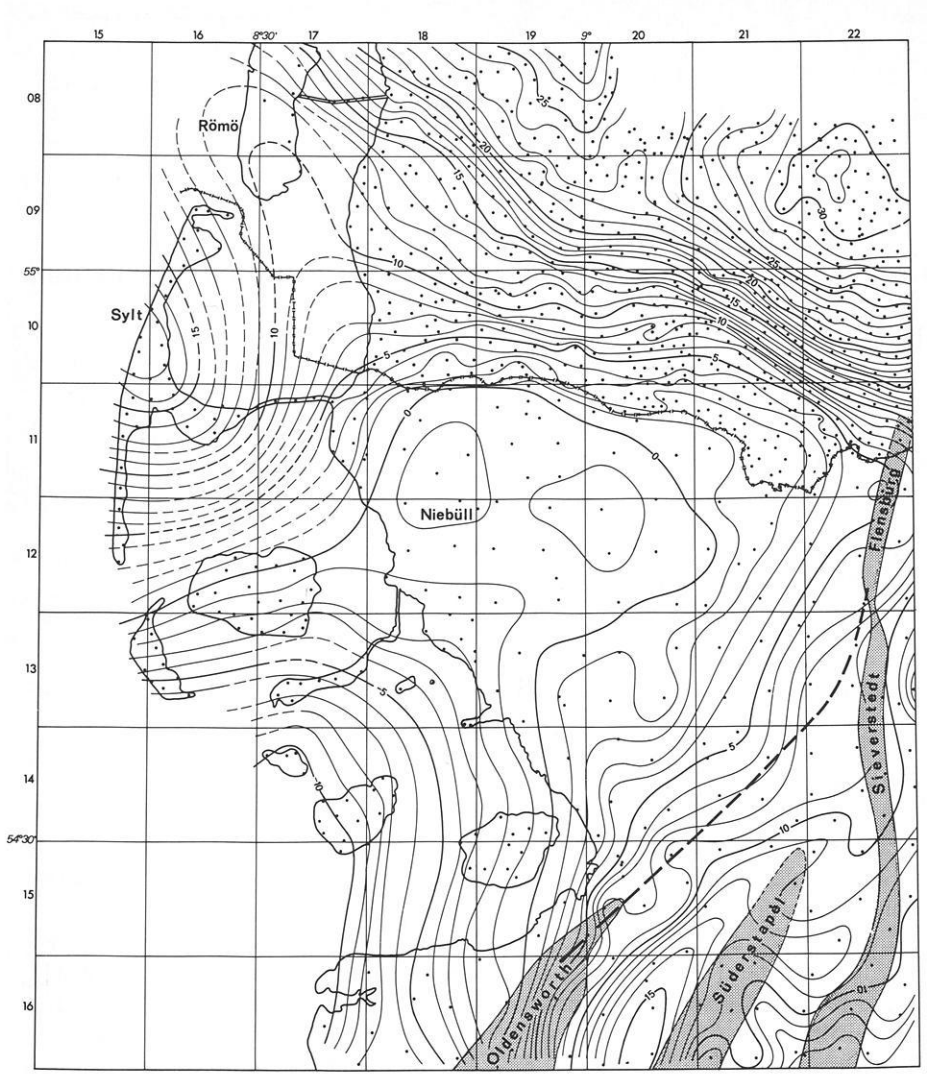

Abb. 1. Schwerekarte (Bougueranomalien in mgal; 1 mgal $= 10^{-5}$ ms^{-2}) der Nordfriesischen Inseln und des benachbarten dänischen und deutschen Festlands. Die Rasterflächen im unteren Bereich der Abbildung geben die Lage einiger Salzstrukturen an. Die Zahlen am Rande zwischen den Angaben für Breite und Länge entsprechen den amtlichen Nummern der Topographischen Karte 1:25000

vermessung der Nordfriesischen Inseln ist an die Punkte Westerland 1015/1A, Hörnum 1215/1A, Niebüll 1219/8B und Treia 1421/7B des DSGN-62 angeschlossen.

Die geophysikalische Reichsaufnahme hat ein eigenes Netz von Basispunkten, sogenannter Bezugspunkte, verwendet. Eine große Anzahl dieser Bezugspunkte ist bald nach der Erstellung des DSGN-62 mit jeweils nahegelegenen Punkten dieses Netzes direkt verbunden worden (Plaumann, unveröff. Bericht

Tabelle 1. Schwerewerte dänischer Basispunkte in Süd-Jütland

Basispunkt	Schwerewert bei Saxov (1965)	Schwerewert im IGSN-71	Differenz
Christiansfeld	981 574,32	981 559,42	−14,90 mgal
Hoptrup	981 565,52	981 550,65	−14,87
Søgaard	981 529,53	981 514,63	−14,90
Krusaa	981 505,02	981 490,14	−14,88

des Nieders. Landesamtes für Bodenforschung, 1961). Hiermit war dann eine genauere Umrechnung der Reichsaufnahmedaten in das System des DSGN-62 möglich, als wenn man lediglich den beiden Netzen gemeinsamen westdeutschen Hauptpendelpunkt Bad Harzburg verwendet hätte (der Grund liegt in der geringeren Genauigkeit der früheren Messungen und der damit verbundenen geringeren Stabilität größerer Netze).

Eine Verbindung der deutschen mit den dänischen Messungen ist über das International Gravity Standardization Net 1971 (IGSN-71, Morelli et al., 1974) möglich. Nach Saxov (1965) sind die Messungen in Südjütland auf ein Netz von 11 Basisstationen bezogen. Von diesen sind nun vier Stationen gleichzeitig Punkte des IGSN-71. Die Schwerewerte sind in Tabelle 1 gegenübergestellt.

Mit einer Subtraktion von 14,89 mgal, dem Mittelwert der Differenzen, sind hiernach die bei Saxov (1965) angegebenen Schwerewerte in das IGSN-71 überführt worden.

Die zunächst im System DSGN-62 erhaltenen Schwerewerte der Regionalvermessung auf den Nordfriesischen Inseln und der Reichsaufnahme in Schleswig-Holstein wurden ebenfalls in IGSN-71-Werte umgerechnet; dies geschah mit Hilfe einer bei Doergé u.a. (1977) angegebenen Transformation.

Reduktion der Schwerewerte

An den Schwerewerten g wurden, nachdem sie sämtlich im System IGSN-71 vorlagen, folgende Reduktionen angebracht:

Die Höhenreduktion auf das Niveau NN mit der Stationshöhe h und dem gravimetrischen Höhenfaktor

$$(0{,}3086–0{,}04191 \cdot D);$$

für die Dichte D wurde hierin der Wert 1,90 $g \cdot cm^{-3}$ eingesetzt.

Die Normalschwere wurde nach der Schwereformel 1967

$$\gamma = 978031{,}85 \cdot (1 + 0{,}00578895 \cdot \sin^2\varphi + 0{,}000023462 \cdot \sin^4\varphi)$$

φ = geographische Breite

für das Geodetic Reference System 1967 berechnet.

Die Berechnung von Geländekorrekturen war nur bei wenigen, exponiert auf Dünen, Warften oder Dämmen gelegenen Punkten erforderlich; der größte Wert betrug dabei 0,15 mgal.

Mit diesen Reduktionen und Korrekturen ergeben sich die in Abb. 1 dargestellten Bougueranomalien.

Kurze Diskussion der Schwerekarte

Die Mitte der Schwerekarte wird von einem ausgedehnten Minimum eingenommen, das die Nordfriesischen Inseln mit Ausnahme von Sylt sowie das nordöstlich angrenzende Festland um Niebüll herum bis zur deutsch-dänischen Grenze bedeckt (das Zentrum des Minimums ist nicht erfaßt, es muß südwestlich der Inseln auf dem Nordseeschelf gesucht werden). Dem Aufbau des Untergrundes nach handelt es sich um den Bereich der westschleswigschen Scholle, welcher sich nach Südosten die mittelholsteinische Scholle anschließt (Hecht u.a., 1955; Weber, 1957). Die Grenze zwischen beiden Schollen ist in der Schwerekarte als eine vom Salzstock Oldensworth zum Salzstock Flensburg verlaufende Linie eingetragen. Sie wurde aus Kehrer und Andres (1953) übertragen, welche sie als ‚westholsteinischen Abbruch' bezeichnet und vorläufig dorthin verlegt haben, ‚wo die Korrelation markanter Reflexionshorizonte unmöglich wird'. Sie soll hier nur ein grober Anhaltspunkt sein. Gripp (1964) z.B. gibt dieser Schollengrenze insbesondere im mittleren Bereich einen etwas anderen Verlauf, nämlich über die Westflanken der Salzstöcke Oldensworth, Süderstapel und Sievershorst hinweg; das braucht hier jedoch nicht weiter verfolgt zu werden.

Die Lage der Salzstöcke in Abb. 1 wurde aus Jaritz (1973) übertragen.

Während die mittelholsteinische Scholle durch das Vorhandensein langgestreckter Salzaufbrüche und damit verbundener großer Mächtigkeitsschwankungen im Perm und in der Trias charakterisiert ist, zeichnet sich die westschleswigsche Scholle durch eine flache, nahezu konkordante und kaum gestörte Lagerung der sedimentären Schichten seit dem Perm aus. Diesem unterschiedlichen Aufbau des Untergrundes entspricht das Schwerebild. Einem kleinräumigen Wechsel lokaler Anomalien im Bereich der mittelholsteinischen Scholle steht der weitgehend glatte Isolinienverlauf bei dem weitgespannten Schwereminimum über der westschleswigschen Scholle gegenüber.

Wenig nördlich der deutsch-dänischen Grenze beginnt ein starker Anstieg der Bougueranomaliewerte. Er markiert gravimetrisch den nördlichen Grenzbereich der westschleswigschen Scholle. Die enge Isolinienscharung bildet die S- oder SW-Flanke des Ringkjöbing-Fünen-Schwerehochs, einer prägnanten Schwereanomalie über einer Hochlage von praepalaeozoischem Grundgebirge (Hinz u.a., 1967). Der Zone der starken Schweregradienten vorgelagert und von dieser durch ein über die Südspitze vom Römö verlaufendes Minimum getrennt ist das neu aufgefundene Schwerehoch von Sylt. Diese bemerkenswerte Schwereanomalie konnte jedoch nur in ihrem Randbereich erfaßt werden. Die Isolinien sind nach Westen offen. Ihr Verlauf bleibt insgesamt etwas unsicher, doch ist im Mittelteil der Insel eine Achsenrichtung SE-NW ziemlich gut belegt. Diese Achsenrichtung trifft nach Nordwesten zu in etwa 25 km Entfernung auf ein Schweremaximum, das dort durch eine bei etwa 8°05′ östlicher Länge in Nord-Süd-Richtung verlaufende seegravimetrische Meßlinie belegt ist (Fleischer, 1963). Eine Verbindung beider Maxima ist vielleicht naheliegend, aber nicht völlig sicher.

Seit langem (Reich, 1928) ist auch eine magnetische Anomalie von Sylt bekannt. Die Korrelation beider Anomalien ist so gut, daß hier der Fall vorzuliegen scheint, daß magnetische Anomalie und Schwereanomalie denselben Stör-

körper haben. Reich schließt die ΔZ-Isanomalen im Westen, doch ist das nicht hinreichend belegt. Es besteht auch für die magnetische Anomalie die Möglichkeit, daß ihr Zentrum nordwestlich von Sylt liegt und daß nur ihr Südost-Ende erfaßt wurde – wie bei der Schwereanomalie.

Die magnetische Anomalie von Sylt ist seit ihrem Bekanntwerden als geophysikalisches Abbild eines ‚Massivs' angesehen worden. Bei diesem und anderen ‚Massiven', die bogenartig von Jütland und Schleswig-Holstein nach Südosten bzw. Osten die Ostsee umgeben, kann es sich (Lotze, 1971) um präkambrische Körper des fennoskandischen Kristallins handeln.

Die Sylter Schwereanomalie läßt sich z.Zt. noch nicht quantitativ interpretieren, da sie nur gerade eben angeschnitten wurde. So kann auch zwischen den beiden hauptsächlich in Betracht kommenden Möglichkeiten, einer Intrusion vermutlich basischen Gesteins in das Grundgebirge und einer horstartigen Heraushebung des Grundgebirges analog dem Ringkjöbing-Fünen-Hoch, vorerst nicht sicher unterschieden werden.

Literatur

Doergé, W., Reinhard, E., Boedecker, G.: Das ‚International Gravity Standardization Net 1971 (IGSN 71)' in der Bundesrepublik Deutschland. – Dt. Geod. Komm., Bayer. Akad. Wiss., Reihe B, Nr. 225, München 1977

Fleischer, U.: Surface ship gravity measurements in the North Sea. – Geophys. Prospecting **11**, 535–549, 1963

Gripp, K.: Erdgeschichte von Schleswig-Holstein. Neumünster: Wachholtz 1964

Hecht, F., Helms, H. v., Kehrer, W.: Reflection seismic exploration of Schleswig-Holstein, Germany, and its geological interpretation by well data. Proc. Fourth World Petr. Congr., Sect. I, 715–730, Rom: Colombo 1955

Hinz, K., Plaumann, S., Stein, A.: Geophysikalische Untersuchungen im Raum des Ringkjöbing-Fünen-Hochs. – Papers presented at the 9th Assembly of the European Seismological Commission 1.–7.8.1966 in Copenhagen, 285–292; H. Jensen, ed. Copenhagen: Akademisk Verlag 1967

Jaritz, W.: Zur Entstehung der Salzstrukturen Nordwestdeutschlands. – Geol. Jb., Reihe A, Nr. 10, Hannover 1973

Kehrer, W., Andres, J.: Ergebnisse neuerer geophysikalischer Untersuchungen im nördlichen Schleswig-Holstein und Versuche ihrer geologischen Deutung. – N. Jb. Geol. Paläontol., Abh. **97**, 79–89, 1953

Lotze, F.: Dorn-Lotze: Geologie Mitteleuropas. 4. Auflage. – Stuttgart 1971

Marzahn, K.: Ausgleichung des Deutschen Schweregrundnetzes (Gravimeter- und Pendelmessungen). – Dt. Geod. Komm., Bayer. Akad. Wiss., Reihe B, Nr. 54, München 1959

Morelli, C., Gantar, C., Honkasalo, T., McConnel, R.K., Tanner, J.G., Szabo, B., Uotila, U., Whalen, C.T.: The International Gravity Standardization Net 1971 (IGSN 71). – Publ. Spec. No. 4, International Association of Geodesy, Paris 1974

Reich, H.: Zur Frage der regionalen magnetischen Anomalien Deutschlands, insbesondere derjenigen Norddeutschlands. – Z. Geophys. **4**, 84–102, 1928

Saxov, S.: Some Gravity Measurements in Sønderjylland. – Geodaetisk Inst. Skrifter 3, Raekke Bind XXXVI, København 1965

Weber, H.: Der geologische Bau des Untergrundes von Schleswig-Holstein und seine Erdöllagerstätten. – Kiel: Geolog. Landesamt Schleswig-Holstein 1957

Eingegangen am 6. Februar 1979; Revidierte Fassung 27. März 1979;
Angenommen am 29. März 1979

J. Geophys. 45, 349–352, 1979

Journal of Geophysics

Letter to the Editor

Probable Relations Between Seismic Anisotropy and a Fine Structure of the Lithosphere

R.O. Meissner and E.R. Flüh

Institut für Geophysik, Neue Universität, Physikzentrum, D-2300 Kiel, Federal Republic of Germany

Key words: Lithspheric Fine Structure – Seismic Anisotropy.

P-wave anisotropy in horizontal directions has been observed in various parts of the world in the upper mantle, for instance in some regions of the Pacific Ocean (Hess, 1964; Morris et al., 1969; Raitt et al., 1969; Shimamura and Asada, 1978) and in some continental areas (Nevskiy et al., 1974; Bamford, 1977; Hirn, 1977). The observations on continents are not yet substantiated by the same amount of data and by the same level of confidence as are the oceanic ones. From laboratory data peridotitic and metamorphic rocks are known to exhibit a strong seismic anisotropy (Peselnick et al. 1974; Kern and Fakhimi, 1975; Meissner and Fakhimi, 1977; Kern, 1978) which has been attributed to the preferred lattice orientation of olivine in peridotites, the main rock type of the upper mantle. In fact, the preferred orientation of olivine seems to be the main reason for the observed large anisotropy in oceanic areas.

Parallel to the observations of anisotropy, mostly performed on medium range deep seismic sounding (=DSS) profiles, of 200 to 300 km in length, some so called 'Lithospheric profiles' of more than 500 km in length have been observed in oceanic and continental regions (Hirn et al., 1973; Bamford et al., 1976; Orcutt and Dorman, 1977; Nagumo et al., 1978; among others). Unfortunately, only very few lithospheric profiles exist so far, and none of them are crossing each other. From measurements along lithospheric profiles various interpreters derive a fine structure of *P*-wave velocity for the upper mantle. This is an alteration of layers of high and low velocities ($\Delta v \approx 0.5$ km/s) showing individual thicknesses of some tens of kilometers. In some cases, such a fine structure can be followed over adjacent and very long parts of a profile (Hirn et al., 1973). Recently such a fine structure has been derived for the western part of the Pacific based on surface wave studies and long range profiles (Nagumo et al., 1978). Independently, anisotropy has been observed in the same region along normal DSS-profiles (Shimamura and Asada, 1978). It seems possible, hence, that lithospheric fine structure is mainly an effect of a crystallographic

0340–062X/79/0045/0349/$01.00

anisotropy and not related to a fine structure in density and composition. Some arguments for this hypothesis can be summarized as follows:

(i) The range of anisotropy values from 7.4 to 8.7 km/s as derived from laboratory measurements as well as from field experiments in the Pacific (Raitt et al., 1969) is only slightly larger than that of the reported fine structure of the upper mantle.

(ii) Although up to now no intersecting lithospheric profiles (>500 km in length) exist which could definitely prove or disprove the existence of an azimuthal (and hence anisotropically generated) fine structure, there are two regions where anisotropy (along several crustal profiles with different azimuths) and fine structure (along one lithospheric profile) do co-exist. These observations are from the Western Pacific region, as mentioned before, and from parts of France (Hirn et al., 1973; Hirn, 1977). No other areas are known to us where both kinds of observations exist, i.e., several crustal profiles with different azimuths and a lithospheric profile. In the southern and southwestern part of Germany, where Bamford (1977) reported an anisotropy which is however much debated, a fine structure for a large area was reported based on body waves from earthquakes (Baer et al., 1979) providing another, though weaker, indication for a correlation of fine structure and anisotropy.

(iii) If the reported fine structure in *P*-velocity would be caused by a related density structure, for instance by the correlation of Woollard (1959), densities as low as $\rho=3.3$ g/cm^3 ($v_p=7.8$ km/s) would underly layers of $\rho=3.5$ g/cm^3 ($v_p=8.4$ km/s) in some places. Large areas would be unstable. Calculations indicate that such a layering would be very short-lived, especially near the oceanic ridges where new lithosphere is created and viscosities are near 10^{17} poise (Vetter and Meissner, 1977). Even if viscosity were 10^{19} poise and the density differences only 0.01 g/cm^3 a spherical inhomogeneity of 30 km radius would need less than 100,000 years to intrude the denser layer. (From a set of master curves, using Maxwell rheology, Inst. f. Geophys., Kiel, unpubl.). As the oceanic lithosphere is definitely created at oceanic ridges in a high temperature and low viscosity environment, the assumption of a density structure in the oceanic upper mantle which corresponds to the *P*-velocity structure seems impossible from genetic and stability reasons.

(iv) The assumption that the velocity structure represents different layers with different anisotropy, caused by a preferred orientation of olivine crystals in peridotite, seems plausible from genetic reasons: During the generation of new oceanic lithosphere at the oceanic ridges, which is certainly a high temperature process, a preferred orientation of olivine crystals is easily obtained due to stress fields. Such a process of creating an anisotropy by weak or medium stresses and elevated temperatures is much debated. Plastic flow and/or recrystallization may be involved in these processes (Francis, 1969; Ave'Lallemant and Carter, 1970).

Various stresses have to be considered for creating a preferred orientation of olivine crystals near ridges: The largest stresses seem to originate from bending of flow lines. Due to Francis (1969), *a*-axes of olivines adjust to flow lines. Other stresses, such as those of thermal origin, overburden pressure, and perhaps solidification stresses seem to play an additional role. All stresses may really

be different at different depth levels due to flow inhomogeneities and discontinuous flow patterns. Later tectonic events such as the origin of fracture zones, dyke injections, re-heating and plastic flow may destroy (or raise) the anisotropy. However, basically anisotropy – like magnetization – is assumed to be 'frozen in' during the period of bending and cooling near the ridges. According to possible differences in stress at different depth levels, also the anisotropy may be depth-dependent, i.e., show a layered structure. In general, of course, *a*-axes of olivines and the direction of maximum P_n-velocity should be directed perpendicular to the ridges, as found for the uppermost part of the mantle in many marine in situ-experiments. The greater the depth down from the *M*-discontinuity, the smaller is the bending stress, the longer the cooling time, and the greater the possibility of a contribution of other stresses. A density layering would certainly not be created during a gravitational differentiation of oceanic lithosphere at ridges.

All four points mentioned above might well explain a correlation between anisotropy and fine structure under oceans and continents. Points (iii) and (iv), which primarily seem to explain anisotropy and fine structure in the *oceanic* lithosphere, might well be extended to continental areas if one assumes a general underplating of oceanic lithosphere below continents, which was especially strong and shallow in the Precambrian (Meissner, 1979). Old continental shields, on the other hand, have often undergone various orogenic cycles with a re-heating and metamorphism, increasing the probability of destroying large scale uniform orientation of olivines in peridotitic layers. Additionally, shear stresses acting on the base of the continental lithosphere as suggested by Fuchs, 1977, may generate a new orientation of the olivine crystals and thereby of maximum velocity orientation. Long range (lithospheric) observations of different orientations are required in suspected areas to establish a solid basis for the suggested relation between anisotropy and fine structure. They should show, then, an azimuthal variation of the fine structure.

Acknowledgements. We thank H. Kern for critically reading the mansucript. Our ideas evolved from studies within a marine seismic project, supported by the Deutsche Forschungsgemeinschaft (Me 335/41). Publication No. 180 from Institut für Geophysik, Kiel

References

Ave'Lallemant, H.G., Carter, N.L.: Syntectonic recrystallization of olivine and modes of flow in the upper mantle. Bull. Geol. Soc. Am. **81**, 2203–2220, 1970

Baer, M., Müller, St., Mayer Rosa, D.: Laufzeitkurven von *P*-Wellen für Entfernungen von 2°–25° in Europa, Abstr., 39. Jahrestagung der DGG, Kiel 1979, p. 72, 1979

Bamford, D.: P_n-velocity anisotropy in a continental upper mantle. Geophys. J. R. Astron. Soc. **49**, 29–48, 1977

Bamford, D., Faber, S., Jacob, B., Kaminski, W., Nun, K., Prodehl, C., Fuchs, K., King, R., Willmore, P.: A lithospheric seismic profile in Britain – I. Preliminary results. Geophys. J. R. Astron. Soc. **44**, 145–160, 1976

Francis, T.J.G.: Generation of seismic anisotropy in the upper mantle along the mid-oceanic ridges. Nature **221**, 162–165, 1969

Fuchs, K.: Seismic anisotropy of the subcrustal lithosphere as evidence for dynamical processes in the upper mantle; Geophys. J. R. Astron. Soc. **49**, 167–179, 1977

Hess, H.H.: Seismic anisotropy of the uppermost mantle under oceans. Nature **203**, 629–631, 1964

Hirn, A.: Ansiotropy in the continental upper mantle: possible evidence from explosion seismology. Geophys. J. R. Astron. Soc. **49**, 49–58, 1977

Hirn, A., Steinmetz, L., Fuchs, K.: Long range profiles in western Europe: II. Fine structure of the lower lithosphere in France (southern Bretagne). Z. Geophys. **39**, 363–384, 1973

Kern, H.: The effect of high temperature and high confining pressure on compressional wave velocities in quartzbearing and quartz-free igneous and metamorphic rocks. Tectonophysics **44**, 185–203, 1978

Kern, H., Fakhimi, M.: Effect of fabric anisotropy on compressional-wave propagation in various metamorphic rocks for the range 20°–700° C at 2 kbars. Tectonophysics **28**, 227–244, 1975

Meissner, R.: Fennoscandia – a short outline of its geodynamical development. Geophys. J. (in press, 1979)

Meissner, R., Fakhimi, M.: Seismic anisotropy as measured under high-pressure, high-temperature conditions. Geophys. J. R. Astron. Soc. **49**, 133–143, 1977

Morris, G.B., Raitt, R.W., Shor, G.G.: Velocity anisotropy and delay time maps of the mantle near Hawaii. J. Geophys. Res. **74**, 4300–4316, 1969

Nagumo, S., Ouchi, T., Kasahara, J., Koresawa, S., Tomoda, Y., Kobayashi, K., Furumoto, A., Odegard, M., Sutton, G.: Sub-Moho seismic profile in the Mariana Basin by OBS long range explosion. Abstr. EOS **59**, 1133, 1978

Nevskiy, M.V., Epinatjeva, A.M., Volosow, S.G.: The investigation of the seismic anisotropy of the crystalline basement. Dokl. Akad. Nauk. SSSR, **218** (No. 5), 1974

Peselnick, L., Nicolas, A., Stevenson, P.R.: Velocity anisotropy in a mantle peridotite from the Ivrea-zone: application to upper-mantle anisotropy. J. Geophys. Res. **79**, 1175–1182, 1974

Raitt, R.W., Shor, G.G., Francis, T.J., Morris, G.B.: Anisotropy of the Pacific upper mantle. J. Geophys. Res. **74**, 3095–3109, 1969

Shimamura, H., Asada, T.: Evidence for the probable existence of anisotropy extending over the entire depth of the oceanic lithosphere. Abstr. EOS **59**, 1133, 1978

Vetter, U., Meissner, R.: Creep in Geodynamic Processes. Tectonophysics **42**, 37–54, 1977

Woollard, G.P.: Crustal structure from gravity and seimic measurements. J. Geophys. Res. **64**, 1521–1544, 1959

Received February 20, 1979; Revised Version May 11, 1979; Accepted May 22, 1979

J. Geophys. 45, 353, 1979

Journal of Geophysics

Book Reviews

A.E. Ringwood: Composition and Petrology of the Earth's Mantle. New York: Mc Graw-Hill 1975. 618 Seiten, 153 Abbildungen, 70 Tabellen. US $ 29.95.

Der Verfasser des vorliegenden Buches hat durch seine umfangreiche Forschungstätigkeit auf dem Gebiet der experimentellen Petrologie und der Geochemie unser gegenwärtiges Bild von der Zusammensetzung des Erdinnern zu einem erheblichen Teil mitgeprägt und ist damit in besonderer Weise geeignet, den Versuch einer Synthese der bisherigen Ergebnisse und Erkenntnisse zu wagen.

Das Buch ist in zwei Hauptteile gegliedert: Teil 1 (8 Kapitel) befaßt sich mit der Erdkruste und dem Oberen Erdmantel, während in Teil 2 (7 Kapitel) der tiefere Erdmantel behandelt wird. Ein abschließendes Kapitel enthält einige Folgerungen und Spekulationen bezüglich Entstehung und Evolution der Erde.

Insgesamt fällt auf, daß die Behandlung des Stoffes in großem Umfang von den Arbeiten und Meinungen des Verfassers bestimmt ist und im wesentlichen eine Zusammenstellung und Synthese der eigenen Arbeiten darstellt. Dies ist zwar verständlich, im Hinblick auf die zahlreichen noch existierenden Kontroversen auf diesem sich rasch entwickelnden Forschungsgebiet hätte man sich aber eine stärkere Berücksichtigung der Arbeiten anderer Gruppen und Schulen gewünscht.

So erfolgt die Diskussion im wesentlichen unter dem Konzept des Ringwoodschen Pyrolit-Modells, ohne daß der Verfasser näher auf durchaus vorhandene Kritik an diesem Konzept eingeht.

Auf der anderen Seite erreicht der Verfasser mit dieser Beschränkung eine bewundernswerte Geschlossenheit der Darstellung seiner Synthese. Besonders lesenswert sind dabei auch die Abschnitte, in denen die geophysikalischen Randbedingungen für die petrologisch-chemische Zusammensetzung behandelt werden, z.B. Kap. 9.

Das Buch enthält eine Fülle von Informationen und Ideen, die den Leser zu eigenen Überlegungen und Folgerungen anregen können. Es wendet sich jedoch im wesentlichen an Geowissenschaftler, die auf Grund von Vorkenntnissen über die Komplexität des Themas die oft recht kategorischen Folgerungen des Autors entsprechend einordnen und werten können. Insofern ist das Buch kein Lehrbuch im üblichen Sinn, das verschiedene Meinungen objektiv nebeneinanderstellt.

Trotz aller Einschränkungen kann das Buch allen an diesem aktuellen Problem Interessierten empfohlen werden, gibt es doch einen umfassenden und exemplarischen Einblick in die Arbeits- und Denkweise der experimentellen Petrologie und ihrer Verknüpfung mit den Nachbarwissenschaften.

H. Burkhardt, Clausthal

J. Geophys. 45, 355–372, 1979

Journal of Geophysics

Reinterpretation of a Deep-Seismic-Sounding Profile on the Ukrainian Shield*

M. Jentsch

Geophysikalisches Institut der Universität Karlsruhe,
Hertzstr. 16, D-7500 Karlsruhe 21, Federal Republic of Germany

Abstract. A single deep-seismic-sounding profile from the Ukrainian shield has been reinterpreted. The spacing of geophone traces in the original data was 100 m. The data are presented with 200 m, 1 km and 3 km distance between traces to allow a comparison with the type of explosion seismic data common in Western Europe and North America. Different possible correlations are presented and discussed. The DSS data have been interpreted using conventional techniques for laterally homogeneous models, i.e., traveltime modelling and synthetic seismograms. No decision can be made over the possible existence of a low velocity zone in the middle or lower crust. Two one-dimensional velocity-depth functions are derived. They include a high-velocity layer beneath the crust-mantle boundary, introduced to explain strong amplitudes at rather short shotpoint distances. These results are compared with earlier interpretations of this profile.

Key words: Deep-seismic-sounding – Traveltimes – Synthetic seismograms – Correlation.

Introduction

The Ukrainian shield is bordered by the Dnjepr-Donetz-Depression in the north and the Crimean Highlands and the Black-Sea-Depression in the south. It forms the core of the ancient East-European Platform where mountain systems existed in the early Proterozoic. The roots of these mountains are still present today and form a crust of 30–60 km thickness (Sollogub et al., 1973a).

To obtain a better understanding of the area a number of seismic measurements were undertaken during the last decade (Sollogub et al., 1973b). From the *Deep-Seismic-Sounding* (DSS) profile No. 10, situated on the extreme eastern part of the shield, the first 135 km of observations from shotpoint 0.0 (Fig. 1)

* Contribution no. 157, Geophysical Institute, University of Karlsruhe. – This paper was presented at the CCSS-workshop on comparative interpretation of explosion seismic data in Karlsruhe in August 1977

0340-062X/79/0045/0355/$03.60

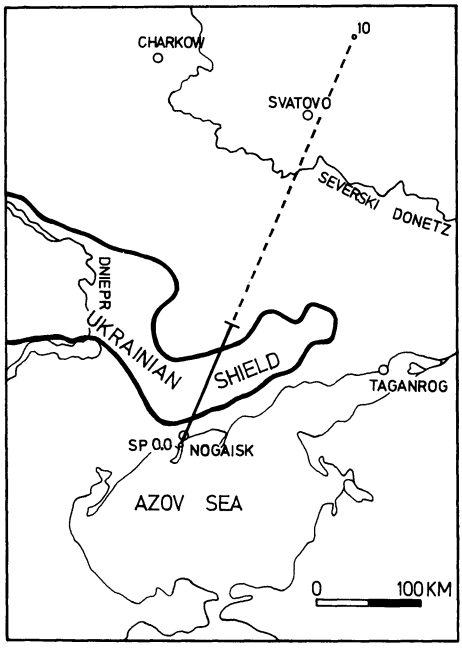

Fig. 1. Position of the USSR national profile No. 10 Nogaisk-Svatovo. *Solid line*: part of profile No. 10 covered by shot 0.0. *Stippled line*: part of profile No. 10 not available in this interpretation

are reinterpreted in this paper. The technique of DSS was developed during the 1950's and 60's from seismic prospecting methods used in the USSR (Kosminskaya, 1971). Since high frequencies and seismometer spacing of 100–200 m are used, correlations can be made quite easily and many seismic phases can be identified on typical DSS-record sections, many of them with only limited horizontal persistence. The published interpretations of profile No. 10 were presented in 2-dimensional cross-sections with contours of iso-velocity. In this paper conventional one-dimensional methods based on assumptions of lateral homogeneity have been applied to the DSS-data. These methods were developed for the interpretation of explosion seismic data with a mean seismometer spacing of 3–5 km. To illustrate the difference between the very close and wider spaced data and the resulting effects on correlation and information content record sections were plotted with different spacing of traces. Another purpose of this work was to show to what extent it might be useful to use amplitudes in a high frequency crustal study.

A comparison between the two-dimensional interpretations of Pavlenkova (1971) and Pavlenkova and Smelyanskaya (1970) and the joint traveltime and amplitude interpretation described in this paper indicates that the main features of the crustal structure appear in both types of models although a lot of information was missing for the interpretation presented here, e.g., reversed profiles, exact position of the shotpoint, setting of instruments etc.

The Data

The data available were photographic copies of the original recordings (Fig. 2). On every trace the shotpoint-receiver distance was indicated together with time

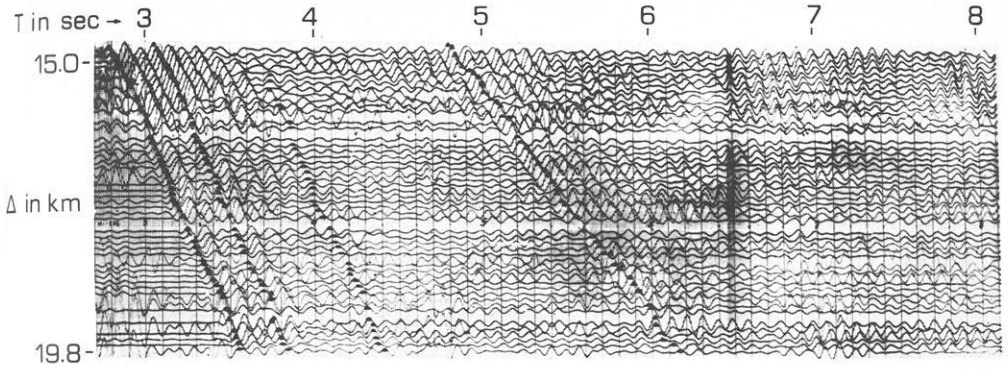

Fig. 2. Photographic copy of the original data. Distance Δ in Kilometer, time in seconds from the shot instant

marks in seconds counted from the shot instant. The smallest distance was 14.8 km, the largest 134.8 km. From 14.8 to 99.8 km the available recording time on average was 8.0 s, from 99.8 km on up to 22.0 s.

The records were obtained as follows (Sollogub and Chekunov, 1972): low frequency apparatus SSR-30/60-KMgW and magnetic tape recording units 'Poisk48' were used together with seismographs Spen 1 (natural frequency 10–11 Hz) and NS-3 (natural frequency about 4 Hz, manufacturer unknown, perhaps home made). One recording unit consisted of a central unit and a 5.2 km long cable with vertical geophones placed every 100 m. According to the information available, usually 2 such spreads were used together, occasionally 3–4 in areas of difficult access thus allowing the recording of a total spread length of 10.4 and 20.8 km respectively. The recorded frequency band was fairly narrow with a dominant frequency of 10 Hz.

Shots were fired in boreholes 25 to 30 m deep. For longer recording distances 500–700 kg, or under unfavourable conditions 1.0–1.5 tons of explosives were used. In general not more than 50 kg TNT or 150–200 kg gunpowder were fired in one borehole. For bigger shots a cluster of boreholes was used. Shotpoint 0.0 was situated near Nogaisk on the southern boundary of the Ukrainian shield. The first 70 km of the profile crossed an Archean acidic complex. From 70 to 90 km distance migmatites, injected gneisses and contaminated granites were crossed. The rest of the profile was situated in Oligocene and Miocene formations.

To facilitate processing and presentation in reduced-time-record sections the data were digitized on a digitizing table. To reduce work only every other trace was digitized. If traces could not be followed over their full length due either to bad photographic exposure or to instrumental failures, they were omitted. Thus the average spacing on the record sections presented here is 200 m (Fig. 3). Because of failures in the original data – bad exposure, changes in time scale – together with mechanical errors associated with hand digitizing, an error of up to 0.1 s over the full length of a trace resulted.

Because the maximum recording distance was 135 km, mainly reflected and refracted waves from the crust and the crust-mantle boundary could be expected.

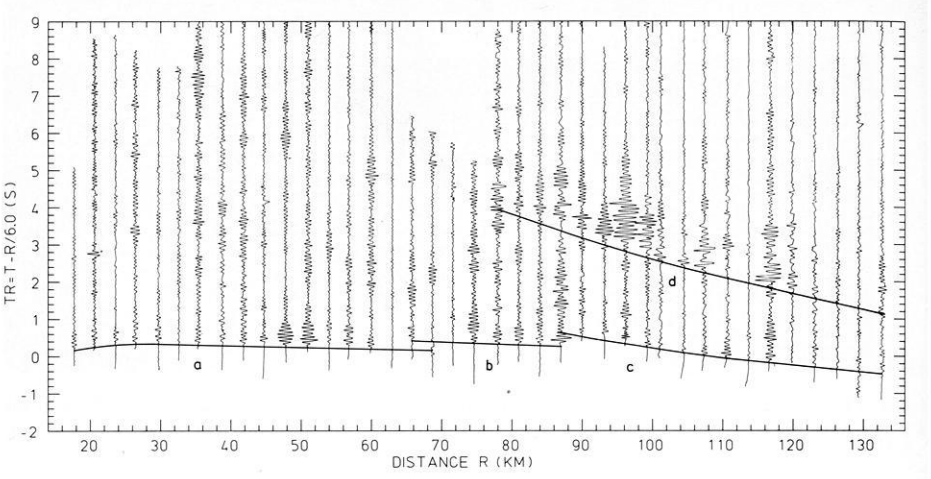

Fig. 4. Record section with mean spacing of 3 km. *a*, *b*, *c*: different branches of P_g-waves, penetrating into the basement. *d*: reflections from the crust mantle boundary ($P_M P$)

Therefore, a reduction velocity of 6.0 km/s has been chosen as this represents a good approximation for the mean crustal velocity (Fig. 3).

Correlation of Phases

In Figs. 4–6 record sections are presented with respectively 3.0, 1.0, and 0.2 km spacing between traces. Figure 4, which corresponds in observation density to record sections usually obtained in explosion seismic studies in western countries, shows a relatively simple wave-field consisting of two main phases: first arrivals that result from waves penetrating into the basement, henceforth referred to as P_g, and strong later arrivals between 75 and 135 km distance, produced by reflected waves from the Mohorovičić-discontinuity ($P_M P$). In a record section like this the first arrivals would probably be correlated in three branches as indicated in Fig. 4. Because there appear no correlatable phases between these three branches and $P_M P$ (though there are pulses of strong energy), no structure in the middle crust can be modelled.

Looking at Fig. 5, a different picture arises: a rather inhomogeneous wave-field now appears between $P_M P$ and P_g (still broken up into three parts). Fairly strong amplitudes can be followed over longer distances, interrupted only by small gaps. Relying on these data alone, one could be tempted to correlate phases over those gaps, since one could argue that these are simply due to local amplitude minima resulting, for example, from destructive interferences or high attenuation along the wave path. This is often done on wider spaced data where phases are connected over large gaps and assumed to be continuous (Fig. 5). This correlation suggests the existence of a reflector of considerable lateral extent in the middle crust.

Figure 6, however, reveals a still more complicated wave field in which seismic energy can be correlated only over short distances between P_g and

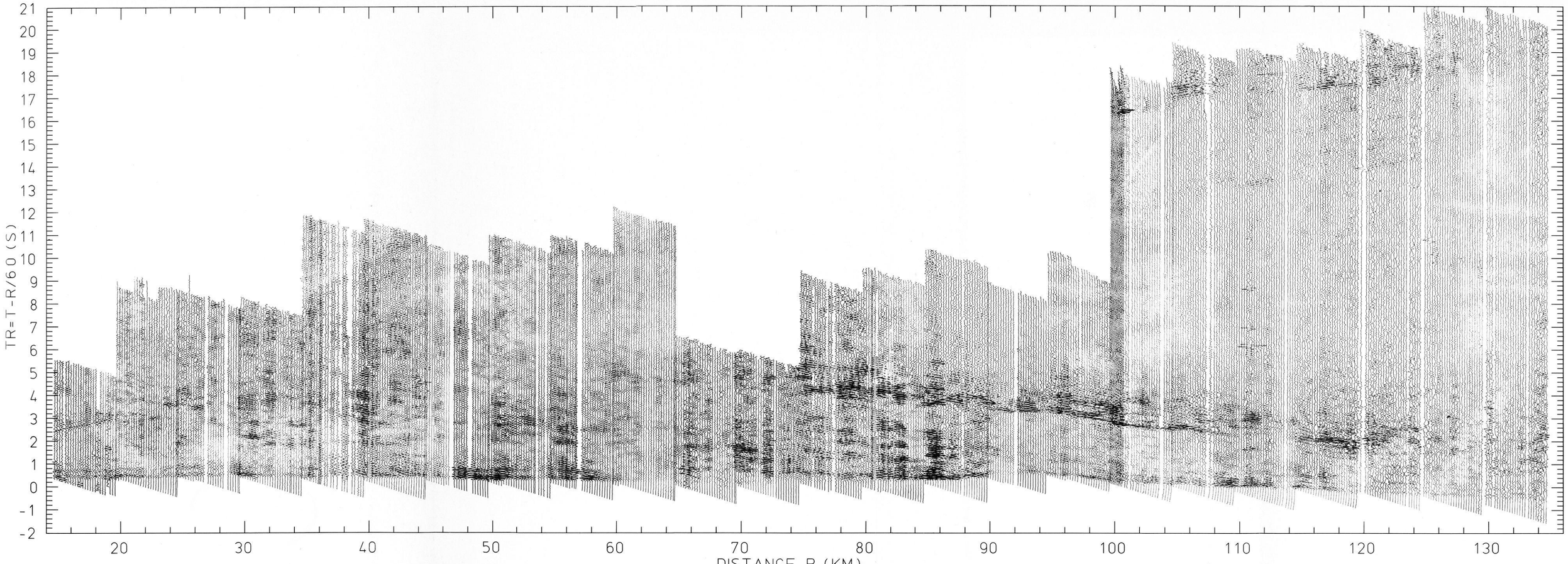

Fig. 3. Record section after handdigitizing in reduced time scale. Reduction velocity 6 km/s, mean spacing of traces 200 m

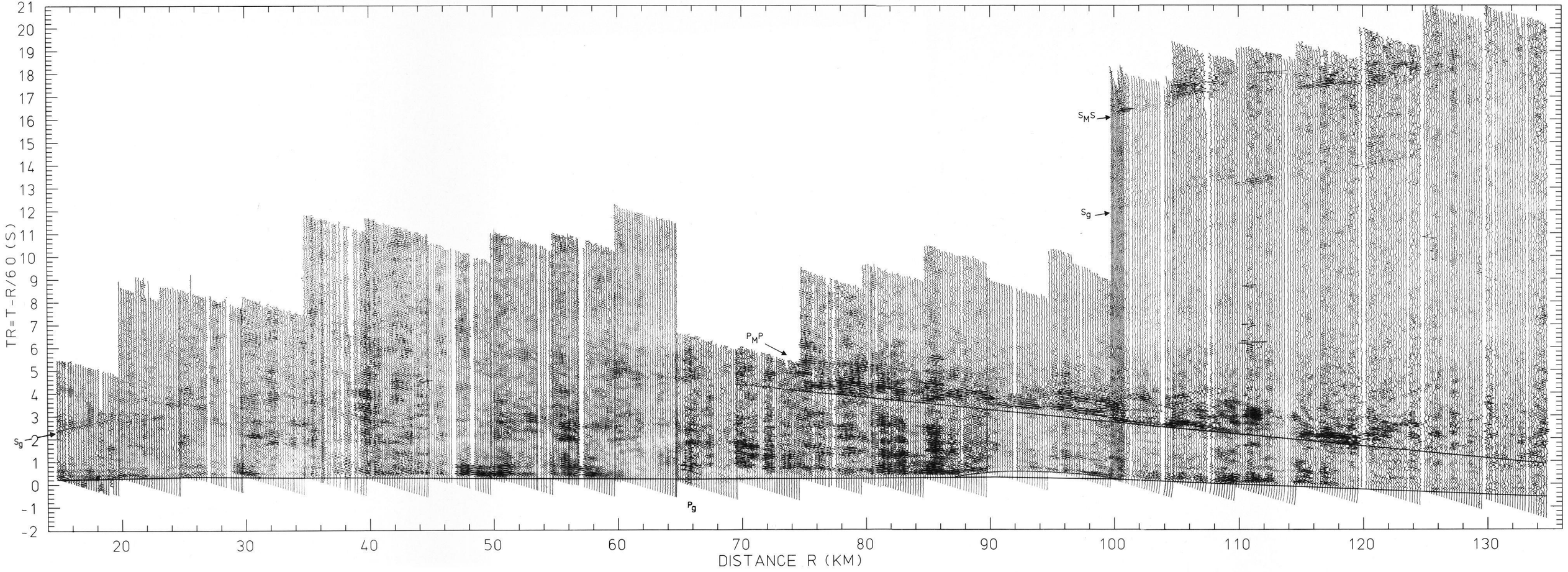

Fig. 7. Complete record section (see Fig. 3) with correlations as used for the interpretation (*solid lines*). The corresponding *S*-waves are indicated by *arrows*

$P_M P$. Such arrivals could arise from lateral inhomogeneities that are able to focus energy into certain distance ranges, and may be only of limited lateral extent. Because first arrivals appear in the gaps between 60 and 70, and 90 and 92 km distance, which led to the division into three branches in Figs. 4 and 5, P_g is correlated now as one continuous branch. These arrivals can be identified quite clearly, although the amplitudes are rather small.

The fine structure between P_g and $P_M P$ just described cannot be interpreted with the methods available, and it must be questioned of any presently available method, including two dimensional modelling would be capable of modelling structures that could be responsible for such wave patterns. Thus only the main traveltime branches have been used for the interpretation (Fig. 7).

Interpretation

Modelling was done in the following way: first traveltimes that were identified from the correlations made on the digitized record sections were read from the original data. These were then fitted by theoretical traveltime branches calculated from velocity-depth functions by trial and error. The best fitting models were then used to calculate synthetic seismograms with the reflectivity method (Fuchs, 1968; Fuchs and Müller, 1971; Müller and Kind, 1976). The computed amplitude ratios $P_g/P_M P$ were compared to the observed ratios. If no satisfying fit within the range of scatter between the observed and synthetic amplitude ratios could be obtained, the whole procedure was repeated. Amplitudes were measured from peak to peak at the maximum in a time window of 0.5 s after the respective arrival time. The distance of critical reflection of the phase $P_M P$ has been assumed to be around 75 km distance from the shotpoint since large amplitudes are observed slightly beyond this range as one would expect for the critical distance.

Two models were derived (Figs. 8a and 9a). The velocity-depth functions are listed in the appendix. Both velocity-depth functions start with 5.5 km/s

Fig. 5. Record section with mean spacing of 1 km. Branches *a, b, c, d* as in Fig. 3. Note the appearance of travel-time branches between 1 and 4s reduced time indicating structure in the middle crust

Fig. 6. Record section with mean spacing of 200 m. P_g now appears as one continuous branch. Traveltime branches between 1 and 4s reduced time now only have small horizontal persistence. *Dotted line* between 88 and 100 km corresponds to delays due to the deposits in a small sedimentary basin

Fig. 8. **a** Velocity depth function of model P2. **b** traveltimes as calculated from model P2 (*solid lines*). Small crosses indicate observed arrivals. **c** synthetic seismograms as calculated from model P2; *M* multiple reflections from the upper crust; *N* numerical effects not corresponding to real phases. **d** amplitude ratios $P_g/P_M P$. Squares and *solid line*: theoretical values as measured from 8c; *triangles*: observed ratios of peak to peak amplitudes measured at the maximum in a 0.5 s time window

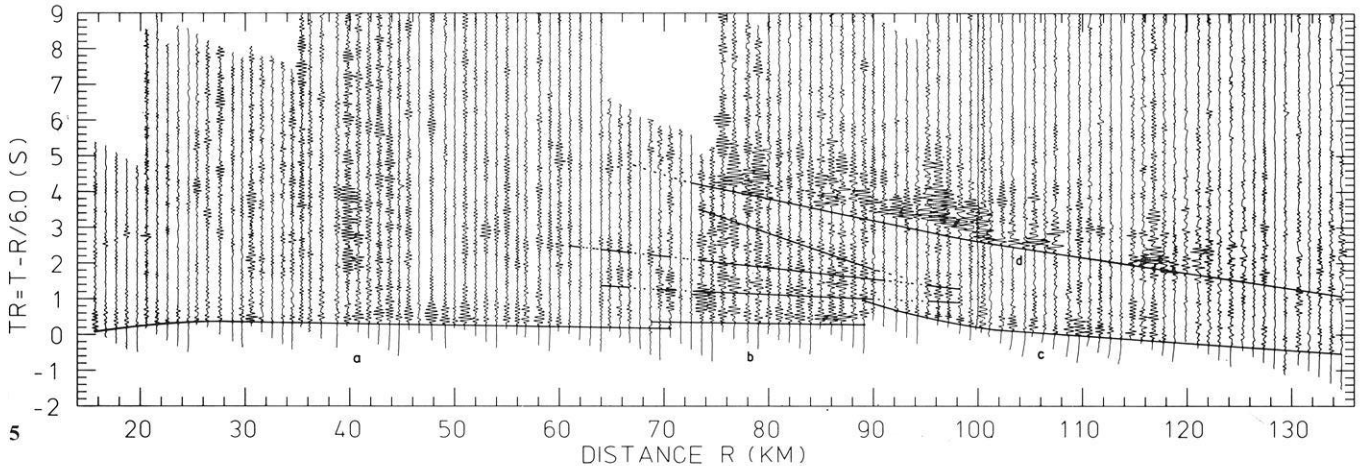

5

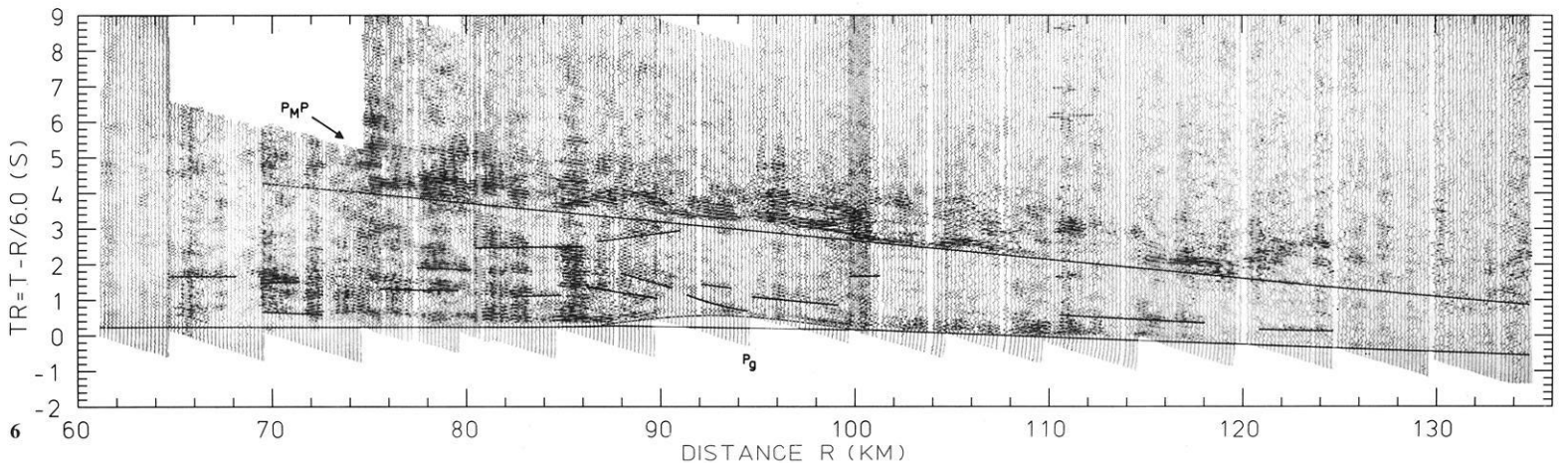

6

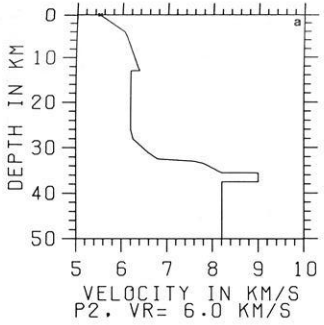
a
DEPTH IN KM
0
10
20
30
40
50
5
6
7
8
9
10
VELOCITY IN KM/S
P2. VR= 6.0 KM/S

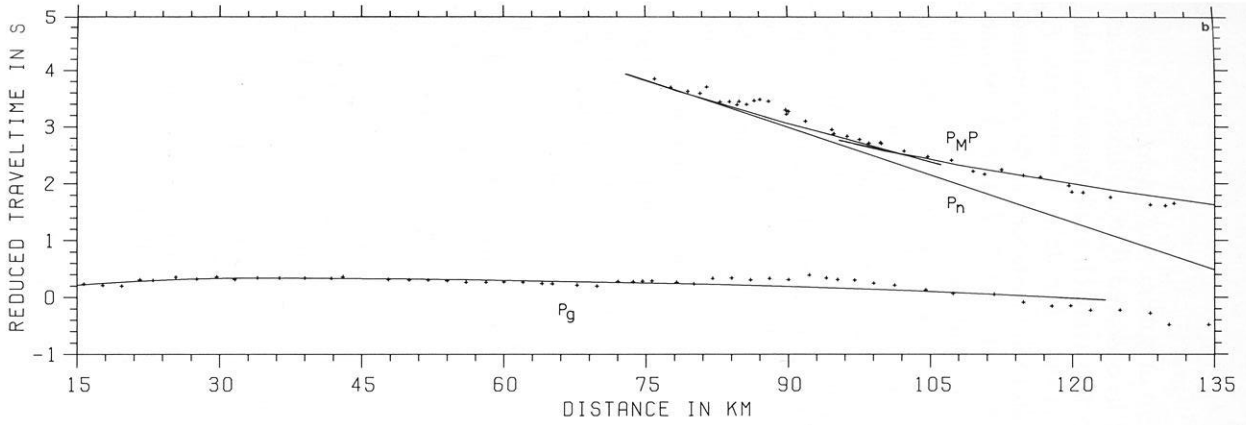
b
REDUCED TRAVELTIME IN S
5
4
3
2
1
0
-1
P_MP
P_n
P_g
15
30
45
60
75
90
105
120
135
DISTANCE IN KM

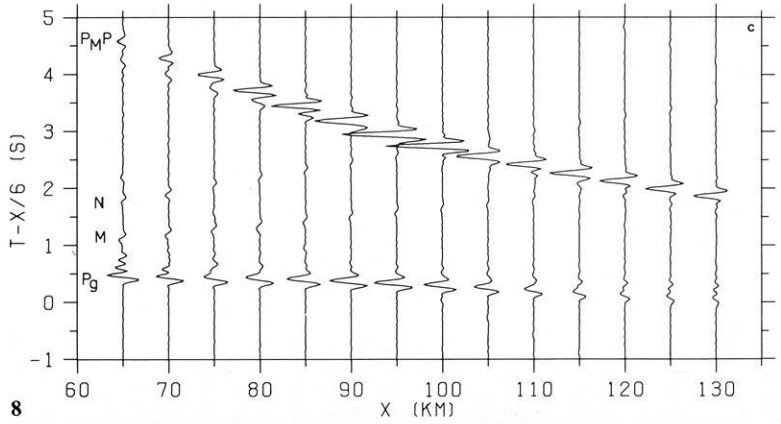
c
T-X/6 (S)
5
4
3
2
1
0
-1
P_MP
N
M
P_g
60
70
80
90
100
110
120
130
X (KM)

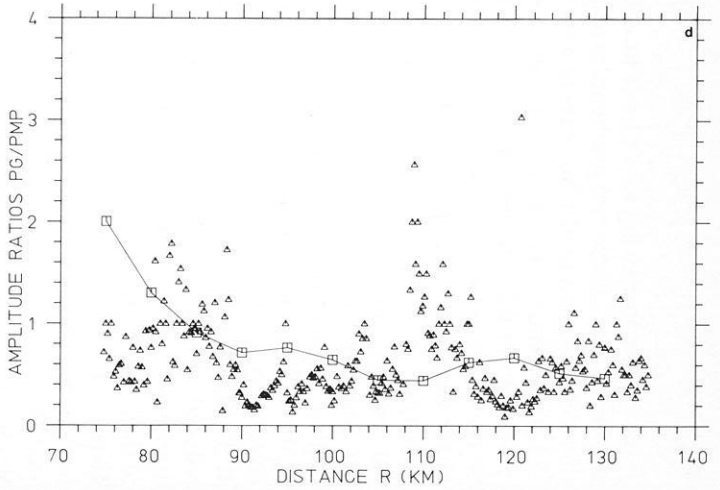
d
AMPLITUDE RATIOS PG/PMP
4
3
2
1
0
70
80
90
100
110
120
130
140
DISTANCE R (KM)

at the surface increasing to 6.1 km/s at a depth of 5.0 km and reaching 6.4 km/s at 13 km depth. These two gradients explain the observed P_g traveltimes reasonably well (Fig. 8b and 9b). Since there were no data available at distances less than 15 km, 5.5 km/s was taken as the surface velocity. The delay of observed P_g traveltimes of 0.2 s between 85 and 100 km shotpoint distance can be explained by the lower velocities in a small sedimentary basin. As $P_M P$ arrivals beyond 75 km were considered as overcritical two major problems arose: first the rather high apparent velocities of 8.8 km/s measured in the critical distance range and the resulting curvature of the $P_M P$ branch had to be explained, and secondly the amplitude ratios $P_g/P_M P$ had to be interpreted. This could be done by finding a model that produced small P_g amplitudes and large $P_m P$ amplitudes at the same time. Although the data contain no evidence for a low-velocity layer, in model P2 a small velocity decrease (6.4–6.2 km/s) was introduced at 13 km depth extending to 29.6 km so as to enable P_g amplitudes to be reduced to match the observed ratios $P_g/P_M P$ (Figs. 8c and d). This could not be done at will (for example by decreasing the depth of the upper boundary of the low-velocity layer) because there are significant P_g arrivals beyond 100 km distance in the observations that cannot be ignored. Thus $P_M P$ amplitudes had to be modelled large enough. One possibility to do so and at the same time to explain the curvature of the $P_M P$-traveltime branch would have been simply to increase the upper mantle velocity. This velocity could in principle be checked by the P_n arrivals. Unfortunately, the observation range of 135 km on this profile was not long enough to observe P_n as first arrival. Second arrivals within the observation range that could be identified as P_n (for example by being tangential to $P_M P$ or having a high velocity) were also not observed. Thus an explanation had to be found for the large amplitudes and the curvature of the $P_M P$-traveltime branch that would not result in a headwave with strong second arrivals tangential to $P_M P$ or with a correspondingly high velocity in the synthetic seismograms. This problem was solved by introducing a thin layer of high velocity immediately beneath the Moho (Fuchs and Schulz, 1976). The thickness of this layer has been chosen to be one wavelength. Other thicknesses were tried, but no significant changes in amplitudes arose. The thickness of one wavelength is sufficient to suppress P_n in the synthetic seismograms in agreement with the observations.

The Moho itself was modelled as a broad transition zone at which the velocity increases from 6.4 to 8.2 km/s. This was suggested by the absence of PS/SP converted waves in the observations at about twice the reduced $P_M P$-arrival times where one would expect such waves (Fig. 7). A first order discontinuity could also explain the observed traveltimes of $P_M P$ but at the same time would produce such conversions with considerable amplitudes whereas a transition zone suppresses them (Fuchs, 1975). Although the upper boundary of the high-velocity layer is a first order discontinuity no PS conversions arise, because the velocity contrast with respect to the overlying layer (0.8 km/s) is not strong enough. A 2 km/s contrast would have been necessary to produce PS conversions (Fuchs, 1975).

Thus a fit of the observed amplitude ratios was obtained within the range of scatter (Fig. 8d). Only beyond 120 km distance the computed ratios are too low because of the shadow zone resulting from the crustal low-velocity

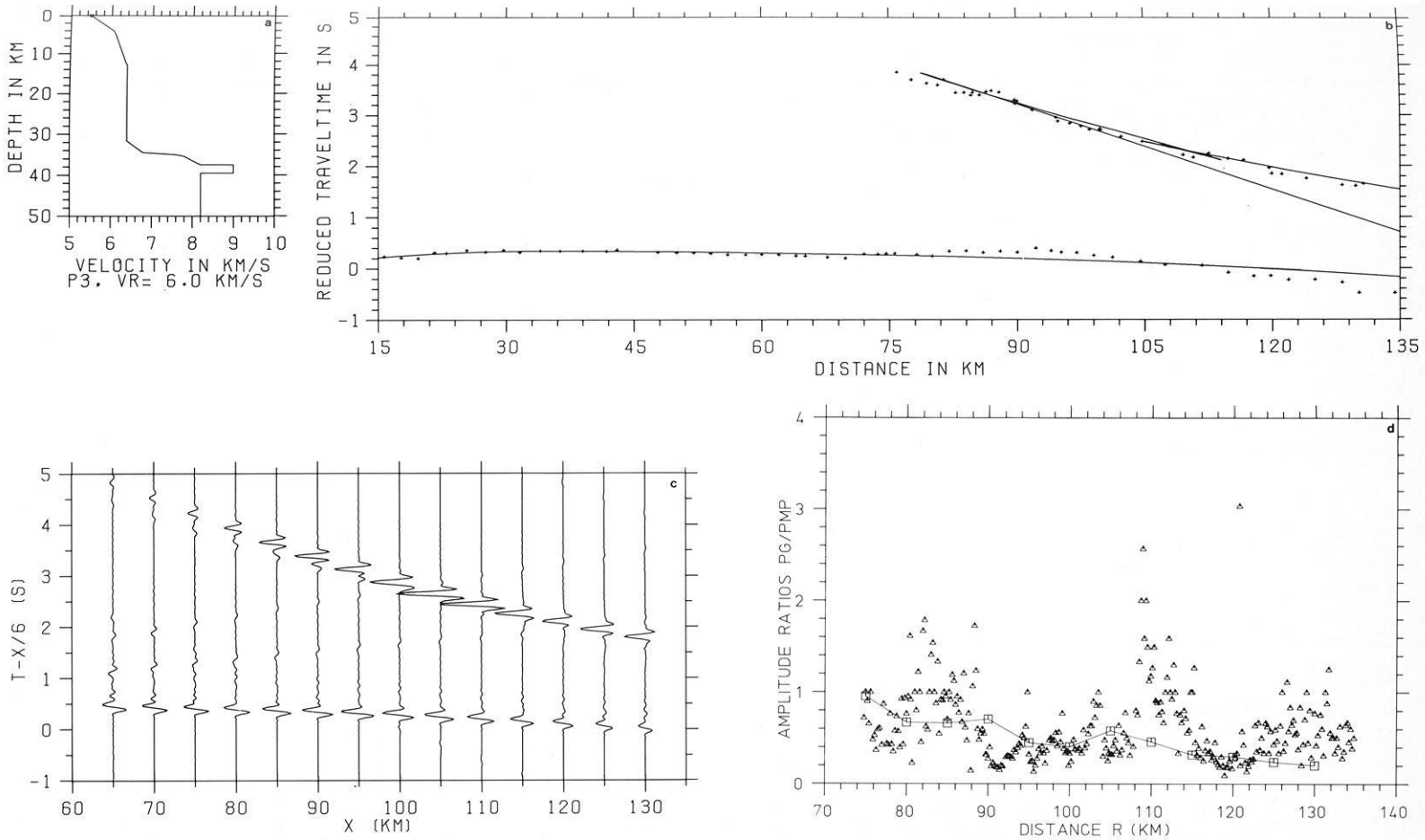

Fig. 9a–d. Same as Fig. 8, now for model P3

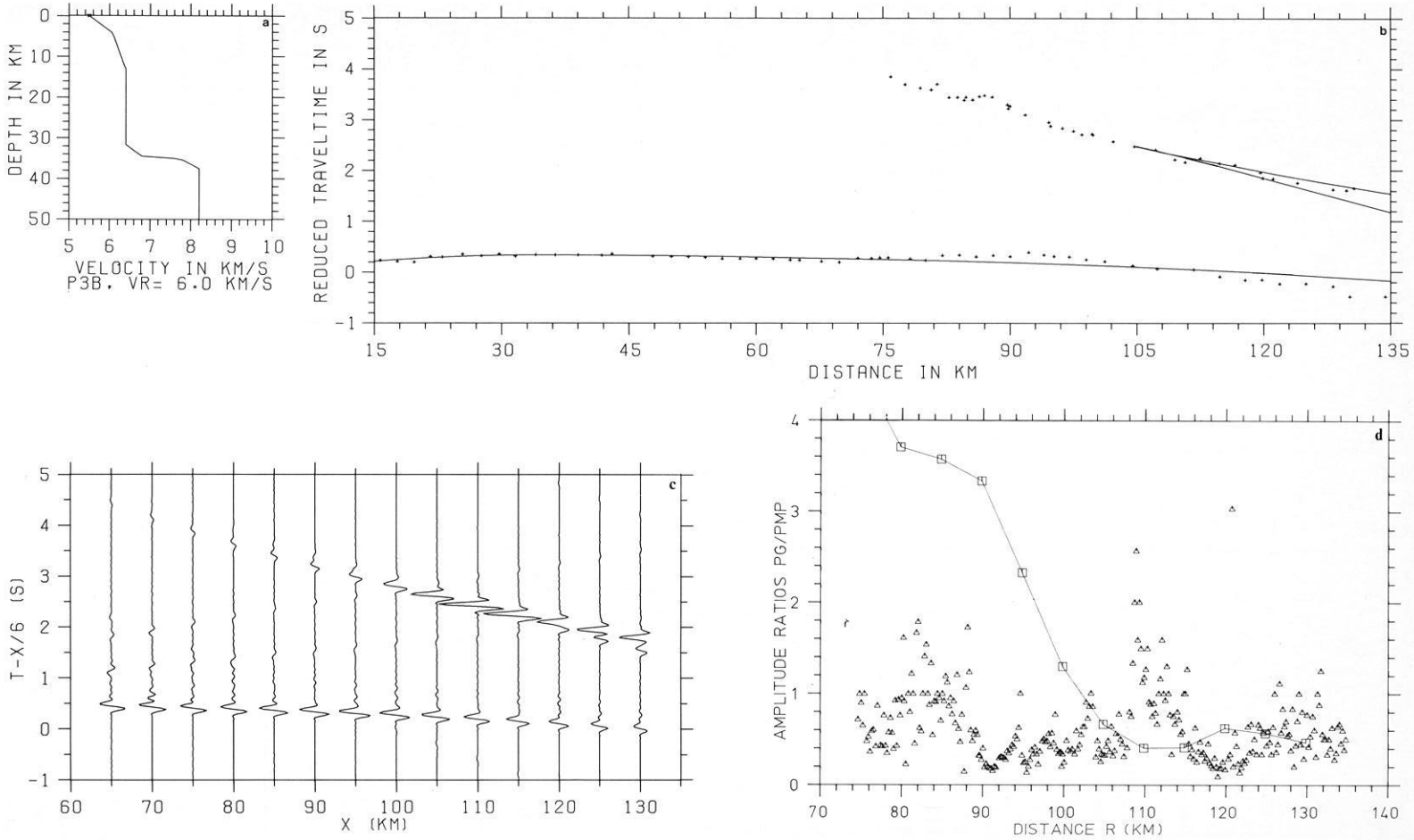

Fig. 10a–d. Same as Fig. 8, now for model P3B. Note the fast drop of amplitudes in the critical distance range between 100 and 105 km due to omitting the high velocity layer

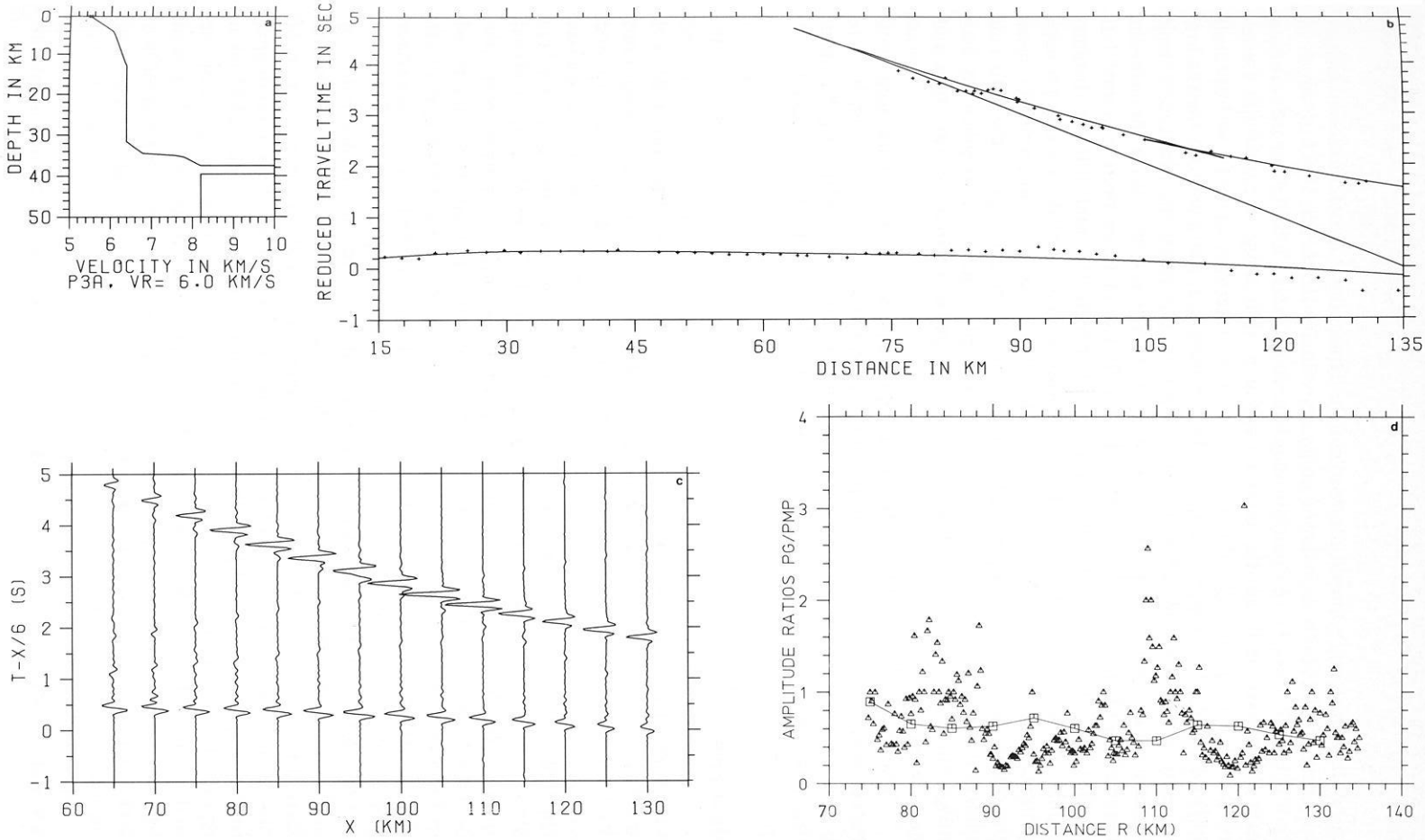

Fig. 11a–d. Same as Fig. 8, now for model P3A showing the effect of an extreme high velocity (10 km/s right beneath the crust mantle boundary)

zone that reduces P_g amplitudes too much. Thus, this zone of reduced velocity has been replaced by a layer of constant velocity down to 31.6 km depth in model P3 (Fig. 9a). Here P_g amplitudes between 70 and 100 km increase resulting in a slightly worse fit of the observed ratios in that range. Because the scatter of the data is quite high, this fit may also be tolerated. The fit is improved beyond 100 km because P_g amplitudes become stronger there without the shadow zone caused by the low-velocity layer (Fig. 9c). The fit of the observed traveltimes became slightly worse because of the 6.4 km/s velocity. With the gradient reaching 6.7 km/s at 18 km depth a better fit would have been obtained but at the same time too large P_g amplitudes between 100 and 120 km distance would have resulted. Therefore, 6.4 km/s must be considered as a compromise between the two solutions. As there is no delay due to a low-velocity layer the depth of the Moho transition increases by 2 km. In Fig. 10 the effect of omitting the high-velocity layer is demonstrated. Figure 11a–d gives an idea how a maximum velocity of 10 km/s would change the theoretical traveltime and amplitude curves.

Other possibilities like a stack of thin lamina or a low-velocity zone with higher velocity contrast at the upper boundary, situated at greater depth, were not able to explain the amplitude ratios and the curvature of the $P_M P$ branch in the critical region with 'normal' sub-Moho velocities of 8.0–8.2 km/s.

Discussion

At this point the question must be raised as to what extent the models derived in this paper resemble the real structure of the earth. Already the correlations shown in Figs. 4–7 reflect the problems one has to face in interpreting refraction seismic data. Apart from the fact that picking of secondary onsets and phases depends highly on the observer's opinion, even with narrow spaced data where one might think that waves correlate automatically the large number of short-running phases reflected from the middle crust is hard to interpret with the methods available today. The methods used for this interpretation are based on the assumption that the earth consists of homogeneous horizontal layers of large extent. If one considers the highly disturbed and heterogeneous surface geology one must allow for similar structures in the deeper parts of the crust so that flat layering over large distances will be a strong simplification of reality. Where energy is correlatable over large distances, however, such a lateral continuity seems to in fact be present underground, and an interpretation of these phases like the one presented here seems to be justified. The velocity-depth functions of models P2 and P3 between 13 km and, respectively, 29.6 and 31.6 km depth (Figs. 8 and 9), will be too simple to reflect the true structure of the earth in these depths. The velocity-depth function above 13 km depth has been derived from the assumption that P_g is a continuous branch, as described earlier. Slight changes could arise if one preferred the first arrivals to be split into more than one traveltime branch.

The range of possible models that satisfy the data excludes the possibility of a sharp discontinuity at the crust-mantle boundary and indicates a smooth

transition zone. If one would be more inclined to omit the high velocity layer by defining the critical point at larger distances (beyond 110 km) one could explain the traveltimes with 'normal' Moho velocities around 8.0 km/s but would then have to face the facts that the large amplitudes around 75 km distance could not be explained.

Because the use of amplitudes had a major influence on the models presented here, the question arises as to whether this is really justified. With the use of amplitude ratios one would expect a reduction of the scatter that usually is imposed on the normal amplitude-distance graphs, because the effects of surface geology near the shotpoint and the receivers will be eliminated. In Figs. 8d–11d, however, still much scatter appears, so that the theoretical curves only represent one possibility within a whole family of solutions. This is mainly due to the sensitivity of the high frequency signals of this set of data to horizontal and vertical inhomogeneities within the crust. Thus, it must be questioned as to whether amplitude information can really improve results gained from traveltimes in such high-frequency studies. The two main points affected by the consideration of amplitudes in models P2 and P3 are the following:

Firstly, the 6.4 km/s velocity at 13 km depth would have been increased to 6.7 km/s at 18 km depth, which would explain the observed traveltimes beyond 110 km distance much better and would possibly represent a better estimate for a velocity in such depths in a stable shield area (Berry and Fuchs, 1973; Hirschleber et al., 1975). The only reason why it has been omitted was that the synthetic $P_g/P_M P$ ratios computed from it would not fit the observed ones. Secondly, the maximum velocity of 9 km/s immediately beneath the Moho would have been replaced by normal values of maximum 8.2–8.3 km/s which still would explain $P_M P$ traveltimes, but would lead to smaller amplitudes at distances less than 80 km – thus the introduction of the high velocity layer was necessary.

In comparison with the interpretations of profile 10 of Pavlenkova and Smelyanskaya (1970) and Pavlenkova (1971) the following differences and similarities can be stated: two different models, one with and one without a low-velocity zone (Figs. 12a and b) have been obtained. The P_g traveltime branch that was correlated as one continuous curve here has been broken up into several branches (Pavlenkova, 1973) which leads to two main reflectors in the two-dimensional models between 10 and 20 km depth, whereas a rather smooth gradient without a distinct reflector appears in the models P2 and P3 (Figs. 8a and 9a) down to 13 km depth (these models would correspond to a depth section at about 60 km distance in Fig. 12). The phases of short horizontal persistence that appear between 1 and 4 s reduced time in the record sections (Fig. 6) have been interpreted in terms of small and sometimes steeply inclined reflectors in the middle crust (10–25 km depth) in the earlier published interpretations (Fig.12) whereas no attempt has been made in the present paper to find explanations for those phases because the analysis methods were not suitable to do so. One has to ask, whether such a complicated wavefield which definitely indicates a very complicated crustal structure can really be interpreted with presently available techniques even if more data of the same quality as the ones presented here were available. From the data available here it was not

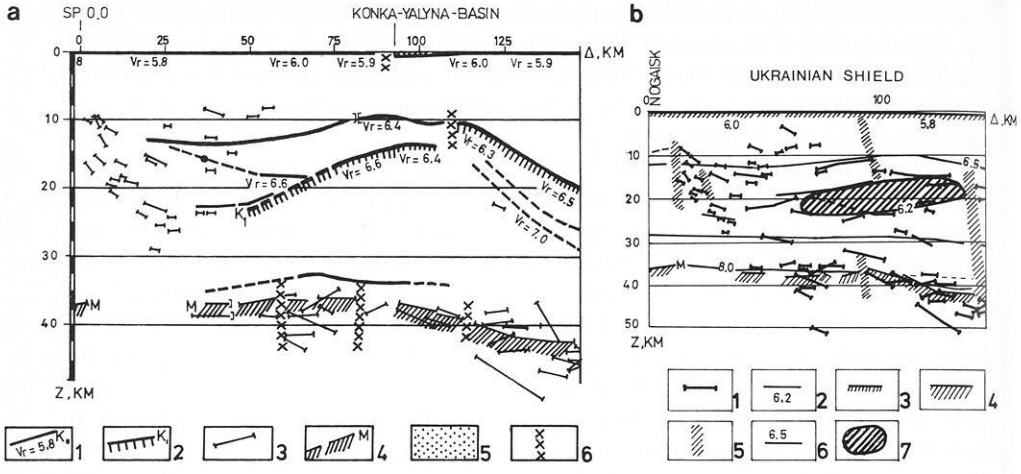

Fig. 12a and b. Different interpretations of the part of profile 10 covered by shot 0.0. **a**: crystalline basement surface with velocities in km/s; 2: Conrad surface; 3: reflectors; 4: Moho; 5: sedimentary layer; 6: disjunctive dislocations. (Modified from Sollogub and Chekunov, 1972) **b**: 1: reflectors; 2: refractors with boundary velocities in km/s; 3: crystalline basement surface; 4: Moho; 5: deep reaching faults; 6: lines of iso velocity; 7: low velocity zone; (modified from Pavlenkova, 1973)

possible to decide if a low velocity layer is really present on this part of the Ukrainian shield. Also the earlier published interpretations allow for the two possibilities (Alekseev et al., 1973). The crust-mantle boundary as a horizontally and vertically heterogeneous zone with a system of criss-crossing, inclined reflectors and refractors has been derived from the complicated wavefield of the $P_M P$-reflection (Fig. 7) by Pavlenkova and Smelyanskaya (1970). Since the phases appear in a complicated but somewhat regular pattern with large amplitudes and show up on reversed and overlapping profiles also, they are assumed to originate from the same depth range. The possibility that the heterogeneous structure of the overlying crust is responsible for this $P_M P$-pattern was ruled out by the argument that other phases do not show similar features as the $P_M P$ reflections. This may be a bit too rigorous, though, because from the wavefield between P_g and $P_M P$ (Fig. 6) which also shows a somewhat regular pattern with pulses of high energy and from similar detailed studies (Healy, 1971) one has to ask why mid-crustal structure should have no effect on waves reflected from the base of the crust.

The transition zone at the Moho as presented in this paper has been derived from the absence of PS-SP converted waves. The maximum velocity is 8.2 km/s and is reached at approximately the same depth as the 8.0 km/s velocity in Fig. 12a and b. In summary the models P2 and P3 show the same main structures as the two-dimensional solutions of Fig. 12 with the exception of the high velocity layer which has to be treated with caution anyway, because it is based on amplitude data alone.

As a result it seems sensible to record at station intervals of 100–200 m only if a great many overlapping, crossing and reversed profiles are measured

so that a better control over the crustal structure is obtained, and if much more sophisticated methods can be developed to handle such data. With high quality data and some care applied to the correlations a station spacing of 1–2 km seems to be sufficient to achieve reasonable results.

Acknowledgements. I am indebted to Professor Dr. K. Fuchs for making this work possible and for stimulating discussions. My special thanks go to Dr. Kind who was always there for discussions, advice and help. The data was kindly provided by Drs. Sologub and Pavlenkova. Drs. C. Prodehl, G. Müller, and D. Bamford critically read the manuscript. The calculations were performed at the Rechenzentrum der Universität Karlsruhe and on the RAYTHEON 500 of the Geophysical Institute Karlsruhe.

Appendix

Model P2		Model P3	
z (km)	v_p (km/s)	z (km)	v_p (km/s)
0.0	5.5	0.0	5.5
4.0	6.0	4.0	6.0
5.0	6.1	5.0	6.1
12.0	6.3	12.0	6.3
13.0	6.4	13.0	6.4
13.0	6.2	31.6	6.4
26.0	6.2	33.0	6.6
29.6	6.4	34.5	6.8
31.0	6.6	35.0	7.6
32.5	6.8	35.4	7.8
33.0	7.6	37.5	8.2
33.4	7.8	37.5	9.0
35.5	8.2	39.5	9.0
35.5	9.0	39.5	8.2
37.5	9.0		
37.5	8.2		

Model P3A like P3, maximum velocity at the high velocity layer is 10 km/s
Model P3B like P3 up to 37.5 km depth, then halfspace with velocity 8.2 km/s

References

Alekseev, A.S., Belonosova, A.V., Burmakov, I.A., Krasnopevtseva, G.V., Matveeva, N.N., Nersessov, G.L., Pavlenkova, N.I., Romanov, V.G., Ryaboi, V.Z.: Seismic studies of low-velocity layers within the crust and upper mantle on the territory of the USSR. Tectonophysics **20**, 47–56, 1973

Berry, M.J., Fuchs, K.: Crustal structure of the superior and Greenville provinces of the northeastern Canadian Shield. Bull. Seismol. Soc. Am. **63**, 1393–1432, 1973

Fuchs, K.: Das Reflexions- und Transmissionsvermögen eines geschichteten Mediums mit beliebiger Tiefenverteilung der elastischen Moduln und der Dichte für schrägen Einfall ebener Wellen. J. Geophys. **34**, 389–413, 1968

Fuchs, K.: Synthetic seismograms of Ps-reflections from transition zones computed with the reflectivity method. J. Geophys. **43**, 445–462, 1975

Fuchs, K., Müller, G.: Computation of synthetic seismograms with the reflectivity method and comparison with observations. Geophys. J. R. Astron. Soc. **23**, 417–433, 1971

Fuchs, K., Schulz, K.: Tunneling of low frequency waves through the subcrustal lithosphere. J. Geophys. **42**, 175–190, 1976

Healy, J.H.: A comment on the evidence for a worldwide zone of low seismic velocity at shallow depths in the earth's crust. In: The structure and physical properties of the earth's crust, Geophysical Monograph 14, Heacock (ed.), pp. 35–40. Washington, D.C.: American Geophysical Union 1971

Hirschleber, H.B., Lund, C.-E., Meissner, R., Vogel, A., Weinrebe, W.: Seismic investigations along the Scandinavian 'Blue Road' traverse. J. Geophys. **41**, 135–148, 1975

Kosminskaya, I.P.: Deep seismic sounding of the earth's crust and upper mantle. Special report, Consultants Bureau, London 1971

Müller, G., Kind, R.: Observed and computed seismograms for the whole earth. Geophys. J.R. Astron. Soc. **44**, 699–716, 1976

Pavlenkova, N.I.: Methods and some results of velocity-cross-section determination for the earth's crust in the Ukraine, I and II. Geofiz. Sb. **39**, 12–22 and **42**, 46–55, 1971

Pavlenkova, N.I.: Elastische Wellen und Modelle der Erdkruste (in Russian). Kiev, 1973

Pavlenkova, N.I., Smelyanskaya, T.V.: The nature of the group of reflected waves from the base of the earth's crust. Izv., Physics of the solid earth 10–18, 1970

Sollogub, V.B., Chekunov, A.V.: The results of DSS measurements in the Ukrainian Soviet Socialist Republic. In: The crustal structure of Central and Southeastern Europe based on the results of explosion seismology, Hungarian Geophysical Institut 'Roland Eötvös', Geophysical Transactions, Special Edition. Budapest: Muszaki Könyokiado 44–68, 1972

Sollogub, V.B., Litvinenko, I.V., Chekunov, A.V., Ankudinov, S.A., Ivanov, A.A., Kalyuzhnáya, L.T., Kokorina, L.K., Tripolsky, A.A.: New DSS-data on the crustal structure of the Baltic and Ukrainian Shields. Tectonophysics **20**, 67–84, 1973a

Sollogub, V.B., Prosen, D., Dachev, C., Petkov, I., Velchev, T., Andonova, E., Mihailov, S., Mituch, E., Posgay, K., Militzer, H., Knothe, C., Uchman, I., Constantinescu, P., Cornea, I., Subbotin, S.I., Chekunov, A.V., Garkalenko, I.A., Khain, V.E., Slavin, V.I., Beranek, B., Weiss, J., Hridlička, A., Dudek, A., Zounkova, M., Suk, M., Feifar, M., Milovanović, B., Roksandić, M.: Crustal structure of central and southeastern Europe by data of explosion seismology. Tectonophysics **20**, 1–33, 1973b

Received June 30, 1978; Revised Version March 10, 1979; Accepted May 9, 1979

J. Geophys. 45, 373–380, 1979

Journal of Geophysics

Extensions of the Reflectivity Method

R. Kind

Seismologisches Zentralobservatorium, Krankenhausstr. 1–3, D-8520 Erlangen, Federal Republic of Germany

Abstract. The reflectivity method for the computation of theoretical seismograms is extended to include a dislocation point source of arbitrary orientation buried in a layered medium. The second extension is a change in the numerical integration over the circular frequency in order to avoid time aliasing effects.

Key words: Theoretical seismograms – Dislocation point source – Aliasing.

Introduction

The reflectivity method for the computation of theoretical seismograms by Fuchs and Müller (1971) was extended by Kind (1978) to include some types of buried sources, using an analytical development by Harkrider (1964, 1970). The original version by Fuchs and Müller (1971) was extended by Kind and Müller (1975) to include a double couple source. In the following the buried source version will be extended for the case of a buried dislocation point source of arbitrary orientation, using an analytical description of such a source by Harkrider (1976).

In the original version of the reflectivity method the integration over the circular frequency ω was carried out using Fast Fourier Transform methods and equidistant ω spacing. This leads to time aliasing problems for cases in which a seismic phase extends over a longer time duration than the corresponding time window. A solution of this problem is in many cases to increase the length of the time window, but in some cases this is beyond the capacity of the available computer.

The same problem occurs in the wavenumber integration. But this part of the problem was solved by Fuchs (1968). He has carried out the integration over the angle of incidence, instead over the wavenumber k. An equivalent method would be to integrate over the slowness. This change of the variable of integration causes the disappearance of aliasing effects in a certain distance window. Starting from this point, attempts have been made to reduce time aliasing effects as well.

0340-062X/79/0045/0373/$01.60

Displacements and Stresses for a General Source in a Homogeneous Medium

Following Harkrider (1964) we have the following radial and azimuthal dependence for the P-wave potential integrand $\varphi_i(r,\theta,z,k)$ and the S-wave potential integrand $\psi_i(r,\theta,z,k)$ of the source. The index i indicates summation over a number of terms. The symbols for the integration over the wavenumber k are omitted.

$$\begin{aligned}\varphi_i(r,\theta,z,k)&=\varphi_i(z)\,J_i(kr)\,\Lambda_i(\theta)\\ \psi_i(r,\theta,z,k)&=\psi_i(z)\,J_i(kr)\,\Lambda_i(\theta)\end{aligned}\tag{1}$$

where (r,θ,z) is a cylindrical coordinate system, $J_i(kr)$ is the Bessel function of order i, $\varphi_i(z)$ and $\psi_i(z)$ depend on z only and $\Lambda_i(\theta)$ describes the dependence on θ. From the relation between displacement and potential we obtain for the radial and vertical displacement integrand in the farfield

$$\begin{aligned}u_i(r,\theta,z,k)&=\frac{1}{k}\frac{\dot{u}_i}{c}(z)\frac{dJ_i(kr)}{dkr}\Lambda_i(\theta)\\ w_i(r,\theta,z,k)&=-\frac{j}{k}\frac{\dot{w}_i}{c}(z)\,J_i(kr)\,\Lambda_i(\theta)\end{aligned}\tag{2}$$

with

$$\begin{aligned}\frac{\dot{u}_i}{c}(z)&=k^2\left[\varphi_i(z)+\frac{d\psi_i(z)}{dz}\right]\\ \frac{\dot{w}_i}{c}(z)&=jk\left[\frac{d\varphi_i(z)}{dz}+\frac{d^2\psi_i(z)}{dz^2}+k_\beta^2\psi_i(z)\right]\end{aligned}\tag{3}$$

and $k_\beta=\omega/\beta$, where ω is the circular frequency and β the shear velocity, j is the imaginary unit.

Since the source will be described by a discontinuity of the dislocation-stress vector, we also need expressions for the stress P_{zz} normal, and P_{rz} radial tangential to the z-plane. From the relation between stress and potential we obtain

$$\begin{aligned}P_{i_{zz}}(r,\theta,z,k)&=\sigma_i(z)\,J_i(kr)\,\Lambda_i(\theta)\\ P_{i_{rz}}(r,\theta,z,k)&=j\tau_i(z)\frac{dJ_i(kr)}{dr}\Lambda_i(\theta)\end{aligned}\tag{4}$$

with

$$\begin{aligned}\sigma_i(z)&=2\mu\left[\frac{d^2\varphi_i(z)}{dz^2}+\frac{d^3\psi_i(z)}{dz^3}+k_\beta^3\frac{d\psi_i(z)}{dz}\right]-\lambda k_\alpha^2\varphi_i(z)\\ \tau_i(z)&=-jk\mu\left[2\frac{d\varphi_i(z)}{dz}+2\frac{d^2\psi_i(z)}{dz^2}+k_\beta^2\psi_i(z)\right]\end{aligned}\tag{5}$$

where λ and μ are Lame's constants, $k_\alpha=\omega/\alpha$ with the P-velocity α.

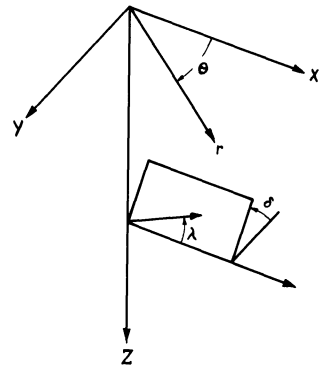

Fig. 1. Geometry of a dislocation source. θ: angle between strike of the fault and observer; δ: dip angle of fault; λ slip direction

The Dislocation Source in a Homogeneous Medium

The geometry of the fault is given in Fig. 1. The *P*- and *S*-wave potentials of this fault, Φ and Ψ, are given by Harkrider (1976) as follows

$$\Phi = \frac{\overline{M}(\omega)}{4\pi\rho\omega^2} \sum_{i=0}^{2} \Lambda_i \int_0^\infty A_i F_\alpha J_i(kr)\, dk$$

$$\Psi = \frac{\overline{M}(\omega)}{4\pi\rho\omega^2} \sum_{i=0}^{2} \Lambda_i \int_0^\infty B_i F_\beta J_i(kr)\, dk \tag{6}$$

with the spectral moment $\overline{M}(\omega)$, the density ρ and

$$\Lambda_0 = \tfrac{1}{2} \sin\lambda \sin 2\delta$$

$$\Lambda_1 = \cos\lambda \cos\delta \cos\theta - \sin\lambda \cos 2\delta \sin\theta$$

$$\Lambda_2 = \tfrac{1}{2} \sin\lambda \sin 2\delta \cos 2\theta + \cos\lambda \sin\delta \sin 2\theta \tag{7}$$

and

$$A_0 = k^2 + 2\nu_\alpha^2, \quad A_1 = -2\varepsilon k \nu_\alpha, \quad A_2 = k^2$$

$$B_0 = 3\varepsilon\nu_\beta, \quad B_1 = (k_\beta^2 - 2k^2)/k, \quad B_2 = \varepsilon\nu_\beta \tag{8}$$

with $\varepsilon = \text{sign}(z-h)$

$$\nu_v = [k^2 - k_v^2]^{1/2} \qquad k > k_v$$

$$\nu_v = -j[k_v^2 - k^2]^{1/2} \qquad k < k_v$$

and $v = \alpha, \beta$; source depth h, and

$$F_v = k \exp(-\nu_v |z-h|)/\nu_v$$

Comparing (1) and (6) one obtains

$$\varphi_i(z) = \frac{\overline{M}(\omega)}{4\pi\rho\omega^2} A_i F_\alpha$$

$$\psi_i(z) = \frac{\overline{M}(\omega)}{4\pi\rho\omega^2} B_i F_\beta. \tag{9}$$

From (3), (5), and (9) follows

$$\begin{aligned}
\frac{\dot{u}_i^{\pm}}{c}(z) &= Rk^2[A_i k/v_\alpha \mp B_i k] \\
\frac{\dot{w}_i^{\pm}}{c}(z) &= Rjk[\mp A_i k + B_i k^3/v_\beta] \\
\sigma_i^{\pm}(z) &= R[A_i k/v_\alpha(2\mu v_\alpha^2 - \lambda k_\alpha^2) \mp 2\mu B_i k^3] \\
\tau_i^{\pm}(z) &= -Rjk\mu[\mp 2A_i k + B_i k/v_\beta(k^2 + v_\beta^2)]
\end{aligned} \tag{10}$$

with $R = \overline{M}(\omega)/(4\pi\rho\omega^2)$.

The plus and minus sign indicate $z > h$ and $z < h$, respectively. The exponential term is omitted in (10).

Denoting $(\Delta_{i_1}, \Delta_{i_2}, \Delta_{i_3}, \Delta_{i_4})$ the discontinuity of the displacement-stress vector at $z = h$, then we have

$$\begin{pmatrix} \Delta i_1 \\ \Delta i_2 \\ \Delta i_3 \\ \Delta i_4 \end{pmatrix} = \begin{pmatrix} \dot{u}_i/c(z)^+ \\ \dot{w}_i/c(z)^+ \\ \sigma_i(z)^+ \\ \tau_i(z)^+ \end{pmatrix} - \begin{pmatrix} \dot{u}_i/c(z)^- \\ \dot{w}_i/c(z)^- \\ \sigma_i(z)^- \\ \tau_i(z)^- \end{pmatrix} \tag{11}$$

from (11), (10), and (8) follows for $i = o$

$$\begin{pmatrix} \Delta_{0_1} \\ \Delta_{0_2} \\ \Delta_{0_3} \\ \Delta_{0_4} \end{pmatrix} = \begin{pmatrix} 0 \\ 4Rjk^2k_\alpha^2 \\ 0 \\ 2Rjk_\mu^2(3k_\beta^2 - 4k_\alpha^2) \end{pmatrix} \tag{12}$$

for $i = 1$

$$\begin{pmatrix} \Delta_{1_1} \\ \Delta_{1_2} \\ \Delta_{1_3} \\ \Delta_{1_4} \end{pmatrix} = \begin{pmatrix} -Rk^2k_\beta^2 \\ 0 \\ 0 \\ 0 \end{pmatrix} \tag{13}$$

and for $i = 2$

$$\begin{pmatrix} \Delta_{2_1} \\ \Delta_{2_2} \\ \Delta_{2_3} \\ \Delta_{2_4} \end{pmatrix} = \begin{pmatrix} 0 \\ 0 \\ 0 \\ 2Rjk^2\mu k_\beta^2 \end{pmatrix} \tag{14}$$

Displacements at the Free Surface Due to a Dislocation Source Buried in a Layered Medium

The Fourier transformed displacement components are obtained from (2)

$$\bar{u}(r,\theta,z)=\int_0^\infty \frac{1}{k}\sum_{i=0}^{2}\frac{\dot{u}_i}{c}(z)\frac{dJ_i(kr)}{dkr}\Lambda_i(\theta)\,dk$$

$$\bar{w}(r,\theta,z)=-\int_0^\infty \frac{j}{k}\sum_{i=0}^{2}\frac{\dot{w}_i}{c}(z)\,J_i(kr)\,\Lambda_i(\theta)\,dk. \tag{15}$$

In order to obtain the displacements at the free surface, we replace in (15) the displacement integrands at the depth z in the full space by $\dot{u}_i/c(0)$ and $\dot{w}_i/c(0)$ at the free surface with the source buried in the layered medium. The displacement integrands at the free surface are obtained from

$$R_{11}\frac{\dot{u}_i}{c}(0)=(R^h_{11}R^h_{12}R^h_{13}R^h_{15}R^h_{16})\begin{pmatrix}-A_{22} & A_{12} & 0 & 0\\ -A_{32} & 0 & A_{12} & 0\\ -A_{42} & -A_{32} & A_{22} & A_{12}\\ 0 & -A_{42} & 0 & A_{22}\\ 0 & 0 & -A_{42} & A_{32}\end{pmatrix}\begin{pmatrix}\Delta_{i_1}\\ \Delta_{i_2}\\ \Delta_{i_3}\\ \Delta_{i_4}\end{pmatrix}$$

$$-R_{11}\frac{\dot{w}_i}{c}(0)=(R^h_{11}R^h_{12}R^h_{13}R^h_{15}R^h_{16})\begin{pmatrix}-A_{21} & A_{11} & 0 & 0\\ -A_{31} & 0 & A_{11} & 0\\ -A_{41} & -A_{31} & A_{21} & A_{11}\\ 0 & -A_{41} & 0 & A_{21}\\ 0 & 0 & -A_{41} & A_{31}\end{pmatrix}\begin{pmatrix}\Delta_{i_1}\\ \Delta_{i_2}\\ \Delta_{i_3}\\ \Delta_{i_4}\end{pmatrix} \tag{16}$$

Equation (16) are due to Kind (1978). The R^h_{st} are Dunkin's (1965) delta matrix elements of the J matrix, where J is the product Haskell matrix of the halfspace and all layers up to the source. R_{11} is the Rayleigh function of the complete model. The matrix A is the product of the Haskell layer matrices above the source. From (15) one obtains in time domain, applying (16)

$$u(r,\theta,t)=\int_{-\infty}^{+\infty}\int_0^\infty \frac{K_u(w,k)}{k}\exp(-j(kr-\omega t))\,dk\,d\omega$$

$$w(r,\theta,t)=\int_{-\infty}^{+\infty}\int_0^\infty \frac{-jK_w(\omega,k)}{k}\exp(-j(kr-wt))\,dk\,dw \tag{17}$$

with

$$K_u(\omega,k)=\frac{\exp(\pi/4)}{\sqrt{2\pi kr}}\left[-j\Lambda_0(\theta)\frac{\dot{u}_0}{c}(0)+\Lambda_1(\theta)\frac{\dot{u}_1}{c}(0)+j\Lambda_2(\theta)\frac{\dot{u}_2}{c}(0)\right]$$

$$K_w(\omega,k)=\frac{\exp(\pi/4)}{\sqrt{2\pi kr}}\left[\Lambda_0(\theta)\frac{\dot{w}_0}{c}(0)+j\Lambda_1(\theta)\frac{\dot{w}_1}{c}(0)-\Lambda_2(\theta)\frac{\dot{w}_2}{c}(0)\right]$$

where the asymptotic approximation of the Bessel functions for large arguments in positive direction of propagation is used. Equation (17) may be considered as a double Fourier-transformation from the (ω,k)-domain to the (r,t)-domain.

The Numerical Integration

The numerical integration of (17) seems simple. Fast Fourier Transform programs could be applied successively for the integration over k and ω. The

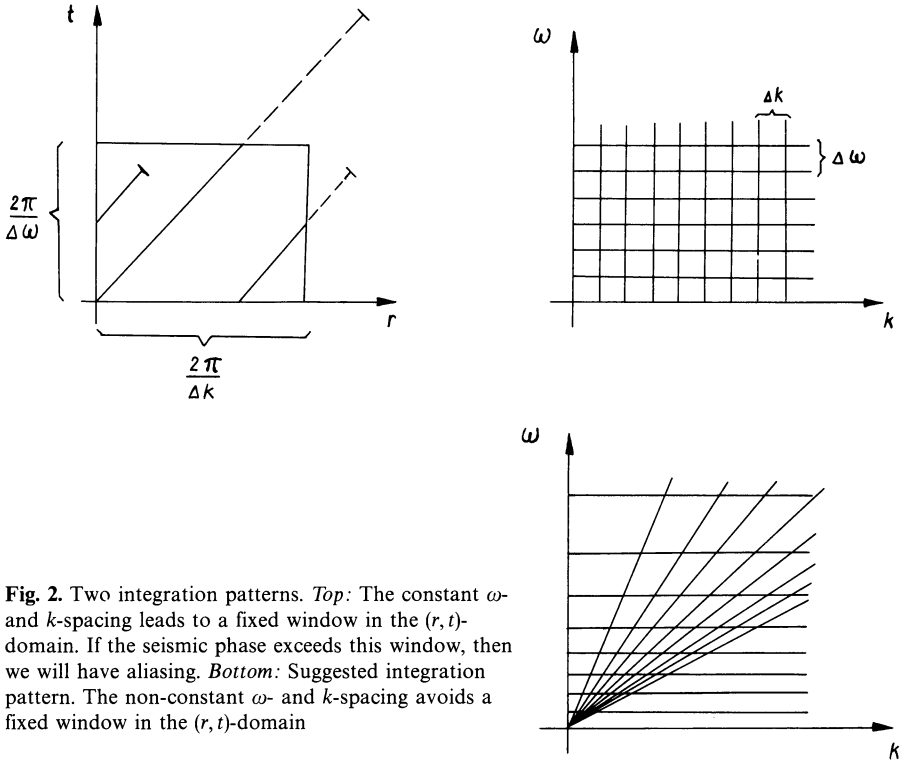

Fig. 2. Two integration patterns. *Top:* The constant ω- and k-spacing leads to a fixed window in the (r,t)-domain. If the seismic phase exceeds this window, then we will have aliasing. *Bottom:* Suggested integration pattern. The non-constant ω- and k-spacing avoids a fixed window in the (r,t)-domain

integrand could be set zero for $k<0$. The spacing in the (ω,k)-domain determines the window in the (r,t)-domain, and the Nyquist (ω,k)-values determine the spacing in the (r,t)-domain. However, this works only if aliasing problems can be disregarded. This is illustrated in Fig. 2. If the spacing in the (ω,k)-domain is not close enough, so that a seismic phase reaches the boundaries of the according window in the (r,t)-domain, then we will have aliasing. Fuchs (1968) has introduced a method to avoid aliasing in the distance domain. He has carried out the integration over the angle of incidence intead over k. This subdivides the (ω,k)-domain in a manner, which is shown in the lower part of Fig. 2. There it may be seen, that the k-spacing is not longer constant. On the other hand, Fuchs (1968) was still using a constant ω-spacing.

The general problem is, how the (ω,k)-plane may be sampled in order to reduce aliasing effects in the (r,t)-plane. A very similar problem appears in the design of arrays (Haubrich, 1968). There one is searching the best pattern for a fixed number of instruments in the two dimensional r-domain, in order to minimize aliasing (side lobes) in the two dimensional k-domain. Aliasing effects are reduced in this case by using nonequal spacing. This method is adopted for the present problem. A disadvantage of this integration method over non-equidistant intervals is however, that Fast Fourier methods cannot be used any more in the usual way. One from many possible patterns for the non-constant ω-spacing is indicated in the lower part of Fig. 2. We have for small frequencies a small ω-

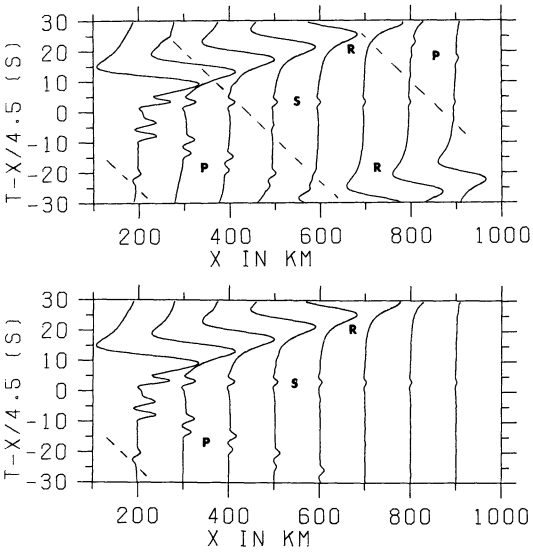

Fig. 3. Theoretical seismograms for two different ω-integration methods: *Top:* constant ω-spacing. *Bottom:* Variable ω-spacing. The source is a single vertical force at 30 km depth in a halfspace. The *dashed line* indicates a numerical phase connected with the limit of the k-integration. All phases due to aliasing have disappeared in the bottom case. R: Rayleigh wave; P: P-wave; S: S-wave

spacing (or a large time window), and for large frequencies a large ω-spacing (or a small time window). Such a pattern may be obtained using the following recursive equation:

$$\omega_{i+1}=\omega_i+2\pi/\left[T+a\cdot 2\pi/\left(\omega_i+\frac{2\pi}{T}\right)\right] \quad \text{for } i=0\ldots n \tag{18}$$

with the starting value $\omega_0=0$, when T is the desired duration of the seismogram, and with $a>0$. The first non-zero ω-value is $\omega_1=2\pi/(T+a\cdot T)$, for high frequencies approaches the ω-increment $2\pi/T$. The value ω_n is the desired largest circular frequency.

An example of the new ω-integration is shown in Fig. 3. The horizontal radial component is shown in this figure, observed at the free surface due to a single vertical force at 30 km depth in a homogeneous halfspace. The P-velocity in the halfspace is 6 km/s and the S-velocity is 4.5 km/s. Numerical examples of multilayered models and dislocation point sources may be found in Kind (1978; 1979). The results of the integration with a constant ω-spacing is shown on top of the figure. The Rayleigh wave and the P-wave reach the boundaries of the time window and are continued at the other side o the time window. At the bottom of Fig. 3 are shown the same seismograms for an ω-integration with non-constant ω-spacing. The value a in (18) was 4.5. All phases caused by aliasing have disappeared. The integration time only, was about eight times larger in the bottom case, about 50 % more frequencies have been computed. It must be kept in mind, that the integration time is only a small percentage of the total computer time, if the model consists of many layers. More computer time can be saved if more storage is available. In practical cases the disadvantage of the longer computer time may be reduced because of the possibility to compute

now very short time windows only. The variable ω-spacing integration was carried out using the trapezoidal rule.

Conclusions

The extension of the reflectivity method for a buried dislocation point source allows now to interpret farfield earthquake records. The changed ω-integration makes it now possible to compute only short time windows, even if the seismogram has a very long duration.

Acknowledgement. This research was supported by the Deutsche Forschungsgemeinschaft. I wish to thank Gerhard Müller for reading the manuscript and Paul Richards for discussions.

References

Dunkin, J.W.: Computation of modal solution in layered media at high frequencies. Bull. Seismol. Soc. Am. **55**, 335–358, 1965

Fuchs, K.: The reflection of spherical waves from transition zones with arbitrary depth-dependent elastic moduli and density. J. Phys. Earth **16** (Special Issue), 27–41, 1968

Fuchs, K., Müller, G.: Computation of synthetic seismograms with the reflectivity method and Comparison with observations. Geophys. J. R. Astron. Soc. **23**, 417–433, 1971

Harkrider, D.G.: Surface waves in multilayered elastic media, 1. Rayleigh and love waves from buried sources in a multilayered elastic half space. Bull. Seismol. Soc. Am. **54**, 627–679, 1964

Harkrider, D.G.: Surface waves in multilayered elastic media, Part II. Higher modes spectra and spectral ratios from point sources in plane layered earth models. Bull. Seismol. Soc. Am. **60**, 1937–1987, 1970

Harkrider, D.G.: Potentials and displacements from two theoretical seismic sources. Geophys. J. R. Astron. Soc. **47**, 97–133, 1976

Haubrich, R.A.: Array design. Bull. Seismol. Soc. Am. **58**, 977–991, 1968

Kind, R., Müller, G.: Computation of SV waves in realistic earthmodels. J. Geophys. **41**, 149–172, 1975

Kind, R.: The reflectivity method for a buried source. J. Geophys. **44**, 603–612, 1978

Kind, R.: Observations of sPn from Swabian Alb earthquakes at the GRF Array. J. Geophys. (in press, 1979)

Received February 8, 1979; Revised Version May 29, 1979; Accepted May 29, 1979

J. Geophys. 45, 381–390, 1979

Journal of Geophysics

Ray Amplitudes of Compressional, Shear, and Converted Seismic Body Waves in 3D Laterally Inhomogeneous Media With Curved Interfaces

I. Pšenčík

Geophysical Institute, Czechosl. Acad. Sci. Boční II, 141 31 Praha 4 – Spořilov, Czechoslovakia

Abstract. A compact formula for the leading term of the ray series for the displacement vector of an arbitrary compressional, shear or converted multiply reflected wave in an inhomogeneous medium with curved interfaces is derived. The components of the vector are expressed with respect to a special system of three mutually perpendicular unit vectors moving along the investigated ray. A method of determination of these vectors at any point of the ray is suggested.

Key words: Leading term of the ray series – Compressional, shear, and converted multiply reflected waves – Laterally inhomogeneous media with curved interfaces.

1. Introduction

It is well-known from the study of propagation of high frequency waves or discontinuities in laterally inhomogeneous isotropic media that there are two wave fronts which propagate independently. One of them corresponds to the compressional (P) wave, the other to the shear (S) wave.

The complex-valued leading term of the ray series for the displacement vector of the P wave, $\vec{\mathbf{U}}_P$, is tangent to the ray (i.e., both real-valued vectors forming real and imaginary parts of $\vec{\mathbf{U}}_P$ are tangent to the ray) and can be expressed as follows (Červený et al., 1977, p. 23)

$$\vec{\mathbf{U}}_P = U_P F(t-\tau_P)\vec{\mathbf{t}}. \tag{1}$$

Complex quantity U_P is usually called the principal component of the P wave in the zero approximation of the ray theory. Complex function F describes in a certain sense the form of the signal of the investigated wave, t is the time, $\vec{\mathbf{t}}$ denotes a unit vector tangent to the ray, τ_P is the phase function (eikonal) of the P wave. Function τ_P is a solution of the eikonal equation $(\nabla\tau_P)^2 = \alpha^{-2}$, where $\alpha(x_i)$ is the P wave velocity.

0340-062X/79/0045/0381/$02.00

The complex-valued leading term of the ray series for the displacement vector of the S wave, $\vec{\mathbf{U}}_S$, lies in the plane perpendicular to the ray (both the real-valued vectors forming $\vec{\mathbf{U}}_S$ can have different directions in this case). Usually, vector $\vec{\mathbf{U}}_S$ is expressed in terms of the principal components U_{Sn} and U_{Sb} in the zero approximation of the ray theory. The components U_{Sn} and U_{Sb} are taken with respect to the vectors of unit normal $\vec{\mathbf{n}}$ and binormal $\vec{\mathbf{b}}$ to the ray (Červený et al., 1977, p. 23):

$$\vec{\mathbf{U}}_S = (U_{Sn}\vec{\mathbf{n}} + U_{Sb}\vec{\mathbf{b}})\, F(t-\tau_S). \tag{2}$$

Here τ_S is the eikonal of the S wave, $(\nabla\tau_S)^2 = \beta^{-2}$, where $\beta(x_i)$ is the S wave velocity.

The formulae for the determination of the components of the leading term of the ray series for a displacement vector along a ray in a 3D continuous inhomogeneous medium as well as formulae determining the behaviour of these components at an interface in the medium are presented in Sect. (2). The determination of the leading term at any point of an arbitrary multiply reflected wave can then be performed by successively applying the formulae of Sect. (2), following the ray from one interface to another. It would be more desirable, however, to have a compact formula for this purpose. Compact formulae are known for some special types of waves, such as pure P waves in 3D media or P-SV waves in 2D media (Červený et al., 1977, pp. 36–39). An alternative compact formula for the determination of the leading term of a general multiply reflected wave is suggested in Sect. (3). In Sect. (2) it is shown that it is useful to express the components of the leading term of the ray series for a displacement vector with respect to a special system of three mutually perpendicular unit vectors moving along the ray. A method of determining these vectors at any point of the ray is suggested in Sect. (4).

2. Formulae for a Successive Determination of the Leading Term of the Ray Series

In an inhomogeneous isotropic medium the principal components U_P, U_{Sn}, U_{Sb} can be given by the following expressions

$$\begin{aligned} U_P &= (\alpha\rho J)^{-1/2}\, \Psi_P(\gamma_1,\gamma_2), \\ U_{Sn} &= (\beta\rho J)^{-1/2}[\Psi_{Sn}(\gamma_1,\gamma_2)\cos\Theta + \Psi_{Sb}(\gamma_1,\gamma_2)\sin\Theta], \\ U_{Sb} &= (\beta\rho J)^{-1/2}[-\Psi_{Sn}(\gamma_1,\gamma_2)\sin\Theta + \Psi_{Sb}(\gamma_1,\gamma_2)\cos\Theta]. \end{aligned} \tag{3}$$

In (3) symbol J denotes a measure of the cross-sectional area of the ray tube, γ_1, γ_2 are ray parameters, ρ denotes density. Functions Ψ_P, Ψ_{Sn}, Ψ_{Sb} are arbitrary functions of γ_1 and γ_2, being constant along the whole ray. Quantity Θ is given by the formula

$$\Theta = \int_{\tau_0}^{\tau} \beta T d\xi, \tag{4}$$

where T denotes the torsion of the ray (for details see Červený et al., 1977, p. 23).

It follows from (3) that the components U_{Sn} and U_{Sb} are mutually coupled unless $T=0$. It also follows from (3) that as the wave progresses, vector $\vec{\mathbf{U}}_S$ rotates in the plane perpendicular to the ray with respect to vectors $\vec{\mathbf{n}}$ and $\vec{\mathbf{b}}$. The velocity of the rotation is $d\Theta/d\tau=\beta T$.

To determine the vector $\vec{\mathbf{U}}_S$ at an arbitrary point of a ray, it is necessary to know the unit vectors of the normal and binormal to the ray. They could be determined from Frenet's formulae, which, however, represent an additional system of differential equations to be solved. Moreover, it is necessary to know the torsion and curvature of the ray at any of its points. This can be connected with certain difficulties, e.g. in models containing both homogeneous and inhomogeneous regions (see Červený et al., 1977, pp. 89–90). To avoid these difficulties, the following procedure is suggested.

In the plane perpendicular to the ray, let us introduce two mutually perpendicular unit vectors $\vec{\mathbf{e}}_1, \vec{\mathbf{e}}_2$ on the ray (see Fig. 1) by the following relations

$$d\vec{\mathbf{e}}_1/d\tau=-vK\cos\vartheta\,\vec{\mathbf{t}}, \qquad d\vec{\mathbf{e}}_2/d\tau=-vK\sin\vartheta\,\vec{\mathbf{t}}, \tag{5}$$

where K denotes the curvature of the ray and v is the velocity, $v=\alpha$ along the rays of the P wave, $v=\beta$ along the rays of the S wave. The angle ϑ is given by the formula

$$\vartheta=\int_{\tau_0}^{\tau} v\,T\,d\xi+\vartheta_0, \tag{6}$$

thus

$$\vartheta=\Theta+\vartheta_0. \tag{6'}$$

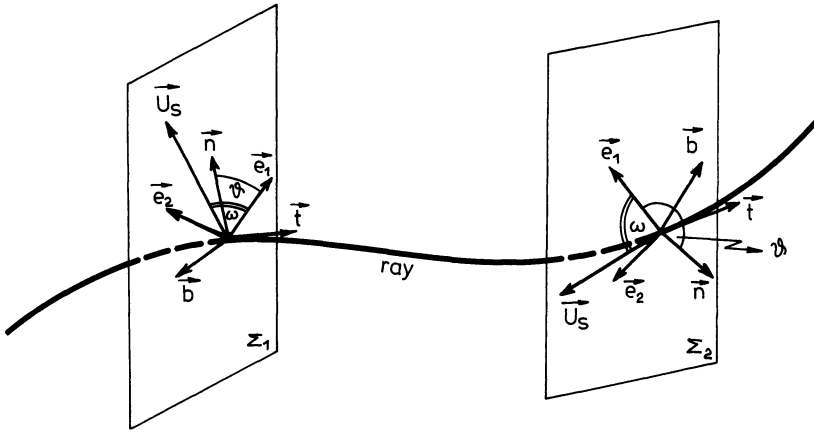

Fig. 1. Introduction of vectors $\vec{\mathbf{e}}_1, \vec{\mathbf{e}}_2$ in a plane perpendicular to the ray. Unit vector $\vec{\mathbf{t}}$, tangent to the ray, and vectors $\vec{\mathbf{e}}_1$, $\vec{\mathbf{e}}_2$ form a right-handed system of orthonormal vectors. As the wave progresses, the vector $\mathbf{U}_S$ rotates in the plane perpendicular to the ray with respect to normal $\vec{\mathbf{n}}$ and binormal $\vec{\mathbf{b}}$, see Σ_1 and Σ_2. The vector $\vec{\mathbf{U}}_S$, however, does not rotate with respect to vectors $\vec{\mathbf{e}}_1, \vec{\mathbf{e}}_2$, the angle ω is constant along the ray. For details see text

The vectors $\vec{e}_1$, $\vec{e}_2$ change according to relations (5) along the ray. The initial orientation of the vectors $\vec{e}_1$, $\vec{e}_2$ (for $\tau=\tau_0$) in the plane perpendicular to the ray can be chosen arbitrarily by a choice of the additive constant ϑ_0.

Using Frenet's formulae, we easily obtain

$$\vec{e}_1=\vec{n}\cos\vartheta-\vec{b}\sin\vartheta, \qquad \vec{e}_2=\vec{n}\sin\vartheta+\vec{b}\cos\vartheta. \tag{7}$$

It follows from (7) that in the plane perpendicular to the ray, vectors $\vec{e}_1$, $\vec{e}_2$ rotate with respect to vectors $\vec{n}$ and $\vec{b}$ as the wave progresses. The velocity of the rotation is $d\vartheta/d\tau=vT$. Thus, in the case of an S wave, the velocity of the rotation of vectors $\vec{e}_1, \vec{e}_2$ is the same as the velocity of the rotation of the vector $\vec{U}_S$. It means that vector $\vec{U}_S$ does not rotate with respect to vectors $\vec{e}_1$, $\vec{e}_2$, see Fig. 1. Therefore it seems quite natural to express the vector $\vec{U}_S$ with respect to vectors $\vec{e}_1$, $\vec{e}_2$ (instead of $\vec{n}$ and $\vec{b}$)

$$\vec{U}_S=(U_{S1}\vec{e}_1+U_{S2}\vec{e}_2)F(t-\tau_S). \tag{8}$$

Comparing (2) and (8) and taking into account the formulae (7), we obtain

$$U_{S1}=U_{Sn}\cos\vartheta-U_{Sb}\sin\vartheta, \qquad U_{S2}=U_{Sn}\sin\vartheta+U_{Sb}\cos\vartheta. \tag{9}$$

Let us further denote

$$\Psi_{S1}(\gamma_1,\gamma_2)=\Psi_{Sn}\cos\vartheta_0-\Psi_{Sb}\sin\vartheta_0, \qquad \Psi_{S2}(\gamma_1,\gamma_2)=\Psi_{Sn}\sin\vartheta_0+\Psi_{Sb}\cos\vartheta_0. \tag{10}$$

After substituting (3) into (9) and taking into account (10), we arrive at final formulae

$$U_{S1}=(\beta\rho J)^{-1/2}\Psi_{S1}(\gamma_1,\gamma_2), \qquad U_{S2}=(\beta\rho J)^{-1/2}\Psi_{S2}(\gamma_1,\gamma_2). \tag{11}$$

Thus, in the medium without interfaces, components U_{S1} and U_{S2} are not coupled to each other and they both change along the ray in the same way. However, this will not hold true after a reflection (transmission) at an interface.

To determine the vector $\vec{U}_S$ at an arbitrary point of a ray, vectors $\vec{e}_1$, $\vec{e}_2$ must be known at this point. If Eqs. (5) or (7) are used for this purpose then the above mentioned difficulties connected with the determination of vectors $\vec{n}$ and $\vec{b}$ arise again. Fortunately, the vectors $\vec{e}_1$, $\vec{e}_2$ can be determined without knowledge of vectors $\vec{n}$ and $\vec{b}$, as it is shown in Sect. (4).

If there are curved interfaces of the first order in the medium, the leading term of the ray series changes discontinuously across them. This discontinuity can be expressed by introducing the reflection (transmission) coefficients. In the zero approximation of the ray theory, the process of reflection (transmission) at a curved interface can be investigated locally as a reflection (transmission) of a plane wave at a plane interface. Therefore it is convenient to introduce the SV and the SH components of the leading term of the ray series for the S wave in the vicinity of the point of incidence. We shall denote these components by U_{SV} and U_{SH}. At the point of incidence the vector $\vec{U}_S$ can then be expressed as $\vec{U}_S=U_{SV}\vec{e}_{SV}+U_{SH}\vec{e}_{SH}$. Here $\vec{e}_{SV}$ and $\vec{e}_{SH}$ are two mutually perpendicular unit vectors both perpendicular to the ray. Vector

$\vec{\mathbf{e}}_{SV}$ lies in the plane of incidence, i.e., in the plane determined by the normal to the interface and the tangent to the ray at the point of incidence. Vector $\vec{\mathbf{e}}_{SH}$ is perpendicular to this plane. Vectors $\vec{\mathbf{t}}, \vec{\mathbf{e}}_{SH}, \vec{\mathbf{e}}_{SV}$ form a right-handed system.

When a P or SV wave impinges at an interface, only P and SV reflected and transmitted waves are generated, when an SH wave impinges at an interface, only SH reflected and transmitted waves are generated. Thus, there are five reflection and five transmission coefficients of the types: R_{PP}, R_{PSV}, R_{SVP}, R_{SVSV}, R_{SHSH}.

If we denote any of the components U_P, U_{SV}, U_{SH} corresponding to the incident wave at the point of incidence by U^I and any component of a reflected (transmitted) wave at the same point by U^R, we can write

$$U^R = U^I \cdot R, \tag{12}$$

where R is the appropriate coefficient of reflection (transmission).

In the case of pure P waves, the component U_P determined from (3) can be immediately substituted in formula (12). Thus, without difficulties, it is possible to get a well-known compact formula for an unconverted multiply reflected wave [see (19)].

The situation becomes more complicated when there is at least one element of the ray along which the wave propagates as an S wave. Then, before applying formula (12) at the point of incidence, it is necessary to transform components U_{S1}, U_{S2} (or U_{Sn}, U_{Sb}) into U_{SH} and U_{SV} components. Then it is possible to apply (12) and to use U_{SH}, U_{SV} as U_{S1}, U_{S2} on the reflected (transmitted) ray at the point of incidence or return to components U_{Sn}, U_{Sb}. It is evident that it is not straightforward to get a compact formula for the leading term of the ray series for a displacement vector of a multiply reflected converted wave similar to that for pure P waves. Therefore it has often been proposed to determine the components of this vector following the ray from one interface to another, successively applying relations (3) [or (11)] and (12). An alternative compact formula for the determination of the leading term of the ray series for a displacement vector of a general multiply reflected wave is suggested in the next section.

3. Compact Formulae for the Determination of the Leading Term of the Ray Series

Let us introduce a vector $\vec{\mathbf{U}}^T = (U_P, U_{S1}, U_{S2})$, where the superscript T stands for transpose. For a P wave only the first component of the vector $\vec{\mathbf{U}}^T$ is non-zero, for an S wave the second and third components are non-zero, U_P being zero. Let us further introduce the vector $\vec{\mathbf{\Psi}}^T = (\Psi_P, \Psi_{S1}, \Psi_{S2})$ which has similar properties to those of the vector $\vec{\mathbf{U}}^T$. Then, the first Eq. in (3) and Eq. (11) can be rewritten as follows

$$\vec{\mathbf{U}} = (v \rho J)^{-1/2} \vec{\mathbf{\Psi}}(\gamma_1, \gamma_2), \tag{13}$$

where $v = \alpha$ along the rays of the P wave ($U_{S1} = U_{S2} = \Psi_{S1} = \Psi_{S2} = 0$) or $v = \beta$

along the rays of the S wave ($U_P = \Psi_P = 0$). Relation (12) can be also expressed in terms of the vector $\vec{\mathbf{U}}$. It is

$$\vec{\mathbf{U}}^n = P^{mn}\,\vec{\mathbf{U}}^m. \tag{14}$$

Index m corresponds to the incident wave: $m=1$ for the incident P wave, $m=-1$ for the incident S wave. Index n corresponds to the generated wave: $n=1$ for the generated P wave, $n=-1$ for the generated S wave. The values -1 and 1 were chosen in accordance with the numerical code of waves suggested in Červený et al. (1977), pp. 88–89. The 3×3 matrix P^{mn} has the following form

$$P^{mn} = \begin{pmatrix} R_{PP}\,\delta_{1m}\delta_{1n} & R_{SVP}\,\delta_{-1m}\delta_{1n}\sin\Omega & R_{SVP}\,d_{-1m}\delta_{1n}\cos\Omega \\ 0 & R_{SHSH}\,\delta_{-1m}\delta_{-1n}\cos\Omega & -R_{SHSH}\,\delta_{-1m}\delta_{-1n}\sin\Omega \\ R_{PSV}\,\delta_{1m}\delta_{-1n} & R_{SVSV}\,\delta_{-1m}\delta_{-1n}\sin\Omega & R_{SVSV}\,\delta_{-1m}\delta_{-1n}\cos\Omega \end{pmatrix}. \tag{15}$$

Here R_{PP}, R_{PSV}, R_{SVP}, R_{SVSV}, R_{SHSH} are standard coefficients of reflection (transmission), see (12), δ_{ij} is Kronecker's symbol, Ω is the angle by which it is necessary to rotate vectors $\tilde{\mathbf{e}}_1$, $\tilde{\mathbf{e}}_2$ at the point of incidence to make them coincide with the vectors $\tilde{\mathbf{e}}_{SH}$, $\tilde{\mathbf{e}}_{SV}$, respectively, see Sect. (4), formula (26). The matrix P^{mn} includes both the transformation of the components of the leading term U_P, U_{S1}, U_{S2} into U_P, U_{SH}, U_{SV} and the coefficients of reflection (transmission) at an interface.

Now it is not difficult to combine relations (13) and (14) and to write a compact formula for a general converted multiply reflected wave at a point M on the ray

$$\vec{\mathbf{U}}(M) = [v(M)\,\rho(M)\,J(M)]^{-1/2} \prod_{j=1}^{N} \left\{ \left[\frac{\rho'(O_j)\,v'(O_j)\,J'(O_j)}{\rho(O_j)\,v(O_j)\,J(O_j)} \right]^{1/2} P^{mn}(O_j) \right\} \vec{\Psi}. \tag{16}$$

The terms $[(\rho' v' J')/(\rho v J)]^{1/2}$ are introduced to compensate the discontinuities of the function $(\rho v J)^{-1/2}$ at interfaces. N is the number of reflections and transmissions along the ray, O_j is the j-th point of incidence of the ray at an interface. The primed (unprimed) quantities are taken on that side of an interface where the generated (incident) wave propagates. For $m=-1$, $v=\beta$, $m=1$ implies $v=\alpha$. The same holds for a generated wave.

For a point source with the directional characteristics $\tilde{\mathbf{g}}^T(\varphi_o, \delta_o) = (g_P, g_{S1}, g_{S2})$, formula (16) can be rewritten into the form

$$\vec{\mathbf{U}}(M) = \frac{1}{L(M)} \left[\frac{\rho_o v_o}{\rho(M)\,v(M)} \right]^{1/2} \prod_{j=1}^{N} \left\{ \left[\frac{\rho'(O_j)\,v'(O_j)}{\rho(O_j)\,v(O_j)} \right]^{1/2} P^{mn}(O_j) \right\} \tilde{\mathbf{g}}(\varphi_o, \delta_o), \tag{17}$$

where $L(M) = \left(\frac{J(M)}{\sin\delta_o} \right)^{1/2} \prod_{j=1}^{N} \left[\frac{J(O_j)}{J'(O_j)} \right]^{1/2}$, see Červený et al. (1977), p. 38. The symbols φ_o, δ_o denote two take off angles of the ray under consideration at the source.

For an unconverted S wave we can again use formulae (16) and (17). The individual quantities can be however, simplified to have the following meaning:

$$\vec{\mathbf{U}}^T=(U_{S1}, U_{S2}), \qquad \vec{\boldsymbol{\Psi}}^T=(\Psi_{S1}, \Psi_{S2}), \qquad \vec{\mathbf{g}}^T=(g_{S1}, g_{S2}),$$

$$P=\begin{pmatrix} R_{SHSH}\cos\Omega & -R_{SHSH}\sin\Omega \\ R_{SVSV}\sin\Omega & R_{SVSV}\cos\Omega \end{pmatrix}. \tag{18}$$

For an unconverted P wave formula (16) reduces to the wellknown formula (Červený et al., 1977, p. 38)

$$U_P=(\alpha\rho J)^{-1/2}\prod_{j=1}^{N}\left\{R_j\left[\frac{\rho'(O_j)\,\alpha'(O_j)\,J'(O_j)}{\rho(O_j)\,\alpha(O_j)\,J(O_j)}\right]^{1/2}\right\}\Psi_P(\gamma_1,\gamma_2). \tag{19}$$

In (19) R_j denotes the appropriate reflection (transmission) coefficient at the j-th point of incidence O_j.

4. Determination of the Vectors $\vec{\mathbf{t}}$, $\vec{\mathbf{e}}_1$, $\vec{\mathbf{e}}_2$

To determine the vector $\vec{\mathbf{U}}$ at an arbitrary point of a ray, it is necessary to know the vectors $\vec{\mathbf{t}}$, $\vec{\mathbf{e}}_1$, $\vec{\mathbf{e}}_2$ at any point of the ray. Let us note that the knowledge of these vectors is not necessary only for the determination of the vector $\vec{\mathbf{U}}$. The vectors $\vec{\mathbf{t}}$, $\vec{\mathbf{e}}_1$, $\vec{\mathbf{e}}_2$ may also play an important role in some methods of computation of geometrical spreading (Červený et al., 1977; Popov and Pšenčík, 1978a; Popov and Pšenčík, 1978b; Červený and Pšenčík, 1979; Hubral, 1979). Thus, once determined, the vectors $\vec{\mathbf{t}}$, $\vec{\mathbf{e}}_1$, $\vec{\mathbf{e}}_2$ can serve two purposes: to determine the geometrical spreading and to determine the components of the vector $\vec{\mathbf{U}}$ along the ray.

The vectors $\vec{\mathbf{t}}$, $\vec{\mathbf{e}}_1$, $\vec{\mathbf{e}}_2$ can be determined in various ways depending on the form of the ray-tracing system used for the computation of rays. Here, the following ray-tracing system will be considered (Červený et al., 1977, p. 58)

$$dx_i/d\tau=v^2 p_i, \qquad dp_i/d\tau=-v^{-1} v_i. \tag{20}$$

In (20), p_i are the components of the slowness vector $\nabla\tau$, $v_i=\partial v/\partial x_i$, $i=1,2,3$.

The determination of the vector $\vec{\mathbf{t}}$ is straightforward,

$$\vec{\mathbf{t}}=(v p_1, v p_2, v p_3). \tag{21}$$

The vectors $\vec{\mathbf{e}}_1, \vec{\mathbf{e}}_2$ can be determined in the following way. At an arbitrary point of the ray, let us define two mutually perpendicular unit vectors

$$\vec{\mathbf{i}}_1=(vD^{-1} p_1\ p_3, vD^{-1} p_2 p_3, -vD), \qquad \vec{\mathbf{i}}_2=(-D^{-1} p_2, D^{-1} p_1, 0) \tag{22}$$

where $D=(p_1^2+p_2^2)^{1/2}$. Vectors $\vec{\mathbf{i}}_1, \vec{\mathbf{i}}_2$ lie in the plane perpendicular to the ray, see Fig. 2. Vector $\vec{\mathbf{i}}_1$ is always lying in the vertical plane containing the tangent to the ray $\vec{\mathbf{t}}$, vector $\vec{\mathbf{i}}_2$ is always horizontal. The vectors $\vec{\mathbf{t}}$, $\vec{\mathbf{i}}_1$, $\vec{\mathbf{i}}_2$ form a right-handed

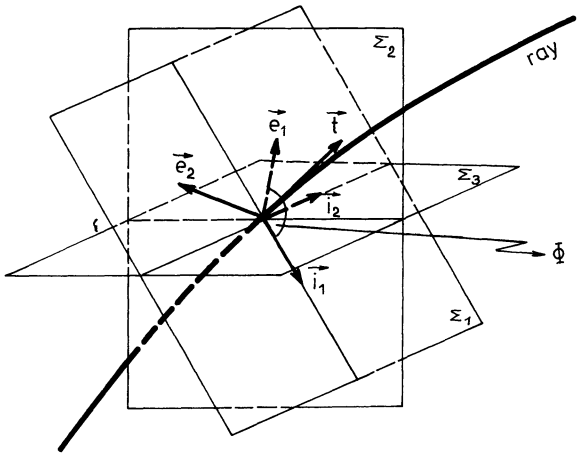

Fig. 2. Introduction of auxiliary vectors $\vec{i}_1, \vec{i}_2$ in the plane Σ_1 perpendicular to the ray. Vector $\vec{i}_1$ lies along the intersection of the plane Σ_1 and vertical plane Σ_2 containing the tangent to the ray $\vec{t}$. Vector $\vec{i}_2$ lies along the intersection of plane Σ_1 and horizontal Σ_3. Vectors $\vec{t}$, $\vec{i}_1$, $\vec{i}_2$ form an orthonormal right-handed system. For details see text

system. When the components of the slowness vector p_i are known the vectors $\vec{t}$, $\vec{i}_1$, $\vec{i}_2$ can be simply determined. Let us note that $\vec{i}_1$, $\vec{i}_2$ cannot be determined from (22) in the case of the ray parallel with the z-axis, i.e., for $p_1 = p_2 = 0$. In such a case, the vectors $\vec{i}_1$, $\vec{i}_2$ can be defined in another way, e.g., as follows

$$\vec{i}_1 = (-v\bar{D}, v\bar{D}^{-1} p_1 p_2, v\bar{D}^{-1} p_1 p_3), \qquad \vec{i}_2 = (0, -\bar{D}^{-1} p_3, \bar{D}^{-1} p_2), \tag{22'}$$

where $\bar{D} = (p_2^2 + p_3^2)^{1/2}$.

Since the vectors $\vec{e}_1, \vec{e}_2$ also lie in the plane perpendicular to the ray, it is possible to express them as follows (see Fig. 2)

$$\vec{e}_1 = \vec{i}_1 \cos\Phi - \vec{i}_2 \sin\Phi, \qquad \vec{e}_2 = \vec{i}_1 \sin\Phi + \vec{i}_2 \cos\Phi. \tag{23}$$

As it was shown above, the vectors $\vec{i}_1, \vec{i}_2$ can be simply determined, thus the problem of the determination of the vectors $\vec{e}$, $\vec{e}_2$ reduces to the problem of the determination of the angle Φ.

Taking into account that the relations

$$vK\cos\vartheta = -(\nabla v \cdot \vec{e}_1), \qquad vK\sin\vartheta = -(\nabla v \cdot \vec{e}_2)$$

hold identically along the considered ray [Popov and Pšenčík, 1978a, Eq. (3.18)], Eq. (5) can be rewritten as follows

$$d\vec{e}_i/d\tau = (\nabla v \cdot \vec{e}_i)\vec{t}, \qquad i = 1, 2.$$

Then, differentiating the first equation in (23) with respect to τ and taking into account the new form of Eq. (5), we obtain

$$(d\vec{\mathbf{i}}_1/d\tau)\cos\Phi-\vec{\mathbf{i}}_1\sin\Phi(d\Phi/d\tau)$$
$$-(d\vec{\mathbf{i}}_2/d\tau)\sin\Phi-\vec{\mathbf{i}}_2\cos\Phi(d\Phi/d\tau)=(\nabla v\cdot\vec{\mathbf{e}}_1)\vec{\mathbf{t}}.$$

Considering, e.g., the z-component of this vectorial equation, after some manipulation using relations (20)–(23), we get

$$d\Phi/d\tau=p_3(p_1^2+p_2^2)^{-1}(v_1p_2-v_2p_1). \tag{24}$$

Let us mention that a similar expression for Φ was obtained by Popov and Pšenčík (1978b). They, however, used the ray-tracing system in which the polar angles φ and δ were used instead of p_1, p_2, p_3.

At each point of incidence O_j of a ray at an interface the vectors $\vec{\mathbf{e}}_1$, $\vec{\mathbf{e}}_2$ must be rotated by an angle Ω_j to make them coincide with vectors $\vec{\mathbf{e}}_{SH}$, $\vec{\mathbf{e}}_{SV}$, respectively. Let us denote the corresponding value of the angle Φ, which includes Ω_j, by $\Phi(O_j)$. After reflection (transmission) the vectors $\vec{\mathbf{e}}_{SH}$, $\vec{\mathbf{e}}_{SV}$ as well as $\vec{\mathbf{i}}_1$, $\vec{\mathbf{i}}_2$ transform into vectors $\vec{\mathbf{e}}'_{SH}$, $\vec{\mathbf{e}}'_{SV}$, $\vec{\mathbf{i}}'_1$, $\vec{\mathbf{i}}'_2$ corresponding to the reflected (transmitted) ray at the point of incidence O_j, and it holds $\vec{\mathbf{e}}'_{SH}=\vec{\mathbf{e}}_{SH}$. Let us choose the vectors $\vec{\mathbf{e}}'_1$, $\vec{\mathbf{e}}'_2$ corresponding to the reflected (transmitted) ray at the point of incidence as follows, $\vec{\mathbf{e}}'_1=\vec{\mathbf{e}}_{SH}$, $\vec{\mathbf{e}}'_2=\vec{\mathbf{e}}'_{SV}$. It corresponds to the choice of U_{SH}, U_{SV} components as U_{S1} U_{S2} [Sect. (2)] at the point of reflection (transmission). Then, it follows from (23) that the angle Φ changes discontinuously across the interface, from the value $\Phi(O_j)$ to a value $\Phi'(O_j)$. Let us denote the difference between these values by Ω'_j, $\Omega'_j=\Phi'(O_j)-\Phi(O_j)$.

If we take into account all the above facts, we can integrate (24) to yield

$$\Phi(\tau)=\int_{\tau_0}^{\tau}p_3(p_1^2+p_2^2)^{-1}(v_1p_2-v_2p_1)\,d\xi+\sum_{j=1}^{N}(\Omega_j+\Omega'_j)+\Phi(\tau_o). \tag{25}$$

The angle Ω_j is determined by the relations

$$\cos\Omega_j=[\vec{\mathbf{e}}_{SH}(O_j)\cdot\vec{\mathbf{e}}_1(O_j)],\qquad \sin\Omega_j=-[\vec{\mathbf{e}}_{SH}(O_j)\cdot\vec{\mathbf{e}}_2(O_j)]. \tag{26}$$

The angle Ω'_j is determined by the relations

$$\cos\Omega'_j=(\vec{\mathbf{e}}_{SH}\cdot\vec{\mathbf{i}}'_1)\cos\Phi(O_j)-(\vec{\mathbf{e}}_{SH}\cdot\vec{\mathbf{i}}'_2)\sin\Phi(O_j),$$
$$\sin\Omega'_j=-(\vec{\mathbf{e}}_{SH}\cdot\vec{\mathbf{i}}'_1)\sin\Phi(O_j)-(\vec{\mathbf{e}}_{SH}\cdot\vec{\mathbf{i}}'_2)\cos\Phi(O_j), \tag{27}$$

where, as above, the symbol $\Phi(O_j)$ denotes the value of the angle Φ corresponding to the vectors $\vec{\mathbf{e}}_{SH}(O_j)$, $\vec{\mathbf{e}}_{SV}(O_j)$ (i.e., the angle which includes only Ω_j, not Ω'_j). The additive constant $\Phi(\tau_0)$ in (25) can be determined from the following relations

$$\cos\Phi(\tau_o)=[\vec{\mathbf{e}}_1(\tau_0)\cdot\vec{\mathbf{i}}_1(\tau_0)],\qquad \sin\Phi(\tau_o)=-[\vec{\mathbf{e}}_1(\tau_o)\cdot\vec{\mathbf{i}}_2(\tau_0)]. \tag{28}$$

Let us emphasize again that the orientation of vectors $\vec{\mathbf{e}}_1(\tau_o)$, $\vec{\mathbf{e}}_2(\tau_o)$ can be chosen arbitrarily, see (6′), (7) and the joined discussion.

Thus, formulae (21)–(28) make possible the unique determination of the vectors $\vec{\mathbf{t}}$, $\vec{\mathbf{e}}_1$, $\vec{\mathbf{e}}_2$ at an arbitrary point of a multiply reflected wave.

Acknowledgements. This research was stimulated by discussions with Dr. V. Červený, Charles University, Prague and Dr. M.M. Popov, Academy of Sciences of the USSR, Leningrad. The author wishes to thank both of them for many valuable comments. The author is also grateful to Dr. P. Hubral, Bundesanstalt für Geowissenschaften und Rohstoffe, Hannover for making available the manuscript of his paper prior to its publication.

References

Červený, V., Molotkov, I.A., Pšenčík, I.: Ray method in seismology. Prague: Charles University Press 1977

Červený, V., Pšenčík, I.: Ray amplitudes of seismic body waves in laterally inhomogeneous media. Geophys. J. **57**, 91–106, 1979

Hubral, P.: A wave front curvature approach to computing ray amplitudes in inhomogeneous media with curved interfaces. Stud. Geophys. Geod. **23**, 131–137, 1979

Popov, M.M., Pšenčik, I.: Ray amplitudes in inhomogeneous media with curved interfaces. Geofys. Sb. Vol. 24, pp. 111–129. Praha: Academia 1978a

Popov, M.M., Pšenčik, I.: Computation of ray amplitudes in homogeneous media with curved interfaces. Stud. Geophys. Geod. **22**, 248–258, 1978b

Received September 12, 1978; Revised Version March 21, 1979; Accepted May 28, 1979

J. Geophys. 45, 391–407, 1979

Journal of Geophysics

Spectral Analysis of Pc3 and Pc4 Pulsations With Regard to the Dayside Plasmapause Position

M. Palandt

Institut für Geophysik der Universität Göttingen, Herzberger Landstraße 180, D-3400 Göttingen, Federal Republic of Germany

Abstract. Based on the observational data obtained simultaneously at 12 stations (most of them along a north-south profile crossing the projection of the plasmapause), the characteristics of pc3–4 pulsations are investigated. Data analysis of selected pulsation events reveals that the power spectra are influenced especially by the magnetic activity and by the positions of the auroral belts and the plasmapause. A shift of power density is observed in H between adjacent spectral bands near the plasmapause position which could be estimated at any time of day by the method of Orr and Webb.

For low magnetic activity ($Kp < 1o$) spectral bands corresponding to periods of $T = 25$–60s are observed. Of these, the shorter period pulsations dominate outside the estimated plasmapause position, the longer period dominate inside. At $Kp > 2o$ the contrary is observed: spectral bands centered on $T = 50$–60s occur predominantly at the southern stations (Wingst, Enköping) whereas spectral bands corresponding to periods of $T = 70$–150s -with pc3 usually superposed on pc4 – are observed at the north of the profile with an amplitude maximum between 65° and 67° geomagnetic latitude. At moderate magnetic activity ($Kp \sim 2o$) a minimum in the distribution of spectral amplitudes appears with adjacent maxima at 62° and 65° geomagnetic latitude.

The polarization properties of the magnetic disturbance vector, projected on the *H-D* plane, are very complex; sometimes the sense of polarization does not change along the profile at all and in other cases there are several reversals of the rotational sense. Some events showing reversals in the region of the plasmapause agree with results of pulsation theories.

Key words: Pc3 and pc4 pulsations – Spectral amplitude distribution – Polarization properties – Dayside plasmapause position.

Introduction

At 11 European observatories between the auroral zone and Italy pulsations are recorded by induction-type variometers described by Voelker (1963). Al-

0340-062X/79/0045/0391/$03.40

Table 1. List of observatories (O) and recording sites with tape equipment (T) and film equipment (F) during 1970 and 1971 in Scandinavia

Abbreviations	Station	Type	Geograph. Coordin.		Geomagn. Coordin. (centered dipole 1945 model)		*L*-value
			Lat.	Long.	Lat.	Long.	
HEI	Heiss	O	80.70	58.00	71.37	156.33	14.28
TR	Tromsø	O	69.68	19.00	67.14	116.80	6.30
REP	Repparfjord	T	70.37	24.50	66.77	121.81	6.42
ABI	Abisko	T	68.35	18.50	66.02	114.96	5.69
KI	Kiruna	O	67.80	20.40	65.24	115.56	5.41
ÅLL	Ålloluokta	F	67.08	19.50	64.78	114.05	5.18
POR	Porjus	F	66.97	19.85	64.61	114.21	5.13
MES	Messaure	T	66.65	20.53	64.21	114.44	5.01
ARJ	Arjeplog	F	66.00	17.90	64.11	111.58	4.85
SO	Sodankylä	O	67.38	26.58	63.79	120.00	5.10
MAL	Malå	F	65.22	18.83	63.24	111.58	4.57
LYC	Lycksele	T(F)	64.62	18.73	62.71	110.90	4.40
ÅSE	Åsele	F	64.18	17.33	62.59	109.31	4.31
JUN	Junsele	F	63.72	16.87	62.25	108.47	4.21
HAM	Hammarstrand	T(F)	63.12	16.45	61.80	107.58	4.06
FRN	Fränsta	F	62.45	16.08	61.26	106.68	3.90
DEL	Delsbo	T(F)	61.80	16.57	60.57	106.56	3.74
EDS	Edsbyn	F	61.37	15.82	60.32	105.55	3.66
SVJ	Svärdsjö	F	60.80	15.88	59.78	105.15	3.55
GAR	Garpenberg	T	60.30	16.22	59.26	105.05	3.45
ENK	Enköping	O	59.50	17.28	58.31	105.42	3.29
WN	Wingst	O	53.75	9.07	54.46	94.47	2.54

though five of these stations (Reykjavik, Tromsø, Kiruna, Sodankylä, and Enköping) are in Scandinavia, in the analysis of the data as well as in the interpretation of the results the station distribution is not entirely satisfactory. In particular, the distance between Enköping and Kiruna is too large to correlate pulsation events at the northern stations with those in Enköping. And Sodankylä, Tromsø and Reykjavik are at such different longitudes that it is difficult to decide whether the observed properties depend on latitude or longitude.

The aim of this experiment was to investigate the distribution of geomagnetic pulsations on a north-south profile by means of closely spaced mobile stations, and to study how this distribution can be interpreted to reveal some properties of the magnetosphere. Therefore, during August and September 1970 and from May to October 1971 a chain of six field operating pulsation stations was installed on a profile between the North Cape and Stockholm. The magnetic field measurements were made at 16 different sites to supplement the 5 existing instruments with similar characteristics working at Scandinavian observatories. Table 1 lists the names, the geographic and geomagnetic coordinates and the corresponding *L*-values of the stations used. Figure 1 shows the distribution of the stations along the profile. Wingst and Sodankylä are far from the profile on either side.

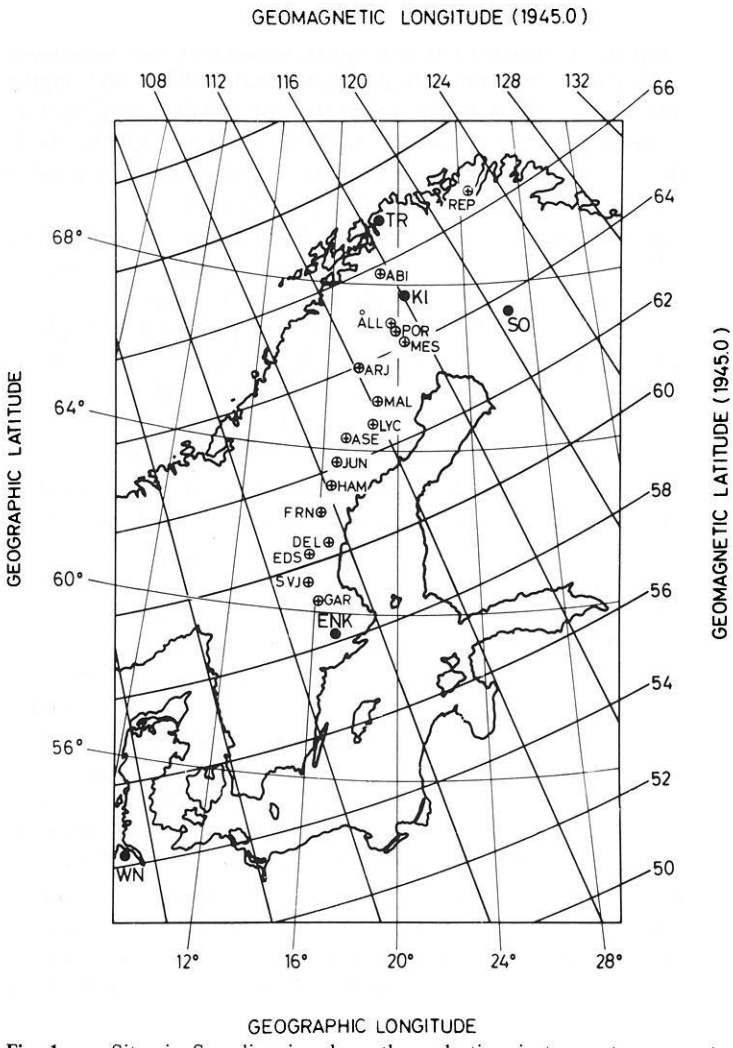

Fig. 1. ⊕: Sites in Scandinavia where the pulsation instruments were set up during 1970 and 1971. ●: Observatories in Scandinavia and Northern Germany (WN) with Grenet type pulsation systems whose records were used in data analysis. (Heiss in USSR is located outside this area)

The (1945) coordinates used in this study differ only slightly from more recent representations (1965) of the dipol field. The difference to the (1945) coordinates is nearly the same (−0.1°, 0.5°) for all stations listed in Table 1.

Experiment and Data Analysis

The measurements were carried out in three stages. During the first period the instruments, with average spacings of 100 km, recorded between the North Cape (Repparfjord) and Lycksele. Then a longer profile was installed between

Abisko and Fränsta. The distance between the working stations in this case was about 200 km. Finally, in order to reveal more details of the behaviour of the pulsations in the transition zone from the midlatitudes to the higher latitudes, measurements were made between Lycksele and Enköping again with shorter spacings of about 80 km. Altogether the portable systems and the observatories (including Heiss, the northernmost Soviet station, which is located far from the profile) yielded simultaneous data from 12 stations.

Each pulsation system consists of three Grenet Variometers recording the magnetic components *H*, *D*, and *Z*. At the observatories the variometer signals are recorded optically by galvanometers on photo sensitive paper. In order to improve the sensitivity, three mobile field systems were provided with photo electric amplifiers consisting of galvanometers and differential photo resistors. For three further portable systems the output voltages (approximately 10μV/nT) were directly amplified by DC amplifiers and then recorded by slow speed FM-tape recorders (15/320 ips) which allowed 10 days continuous recording. The amplitude responses of *H*, *D* and *Z* components at all stations differ only by constant calibration factors. The phase responses are similar at all stations.

The magnetic activity was generally low during the period of measurement. The Kp indices ranged from Kp=0 to 6 with a maximum of occurrence frequency between Kp=1+ and 2+.

In order to establish the spectral behaviour of the pc3 and pc4 between auroral and mid-latitudes and to study the properties of the pc3–4 frequency bands near the plasmapause, power density spectral analysis was used in which both the autocovariance functions and the power spectra were calculated. Cross-spectral analysis was utilized to determine phase differences between similar components at different stations and between components at the same location. Moreover, wave hodograms as well as the Multiple-Filter-Method (Dziewonski et al., 1969) were used to study the characteristics of the wave polarization. The amplitudes and phase differences are presented in a frequency-time diagram, so the sense of polarization and the orientation of the wave ellipses can be evaluated for any frequency band of interest and for any time interval of the record being examined. The determinations of the polarization quantities were generally made within those intervals (mostly 3–4 min) of the record where the maximum amplitudes of the pulsation event occurred.

Spectral Properties of Pc3, 4 Events

An event occuring during a period of moderate magnetic activity (Kp=2o) is shown in Fig. 2. The *H* and *D* component field data were plotted from top to bottom in order of decreasing geomagnetic latitude. The calibration factor at WN and ENK is represented by the longer bar at the right hand side of the plots, and the shorter bar for the other stations. Each bar equals 3nT. The high coherencies, especially between *D* components of different stations, are remarkable. At WN and ENK the dominant period of the *H* component ($T \sim 40$s) is shorter than at the northern stations ($T > 60$s), where, in

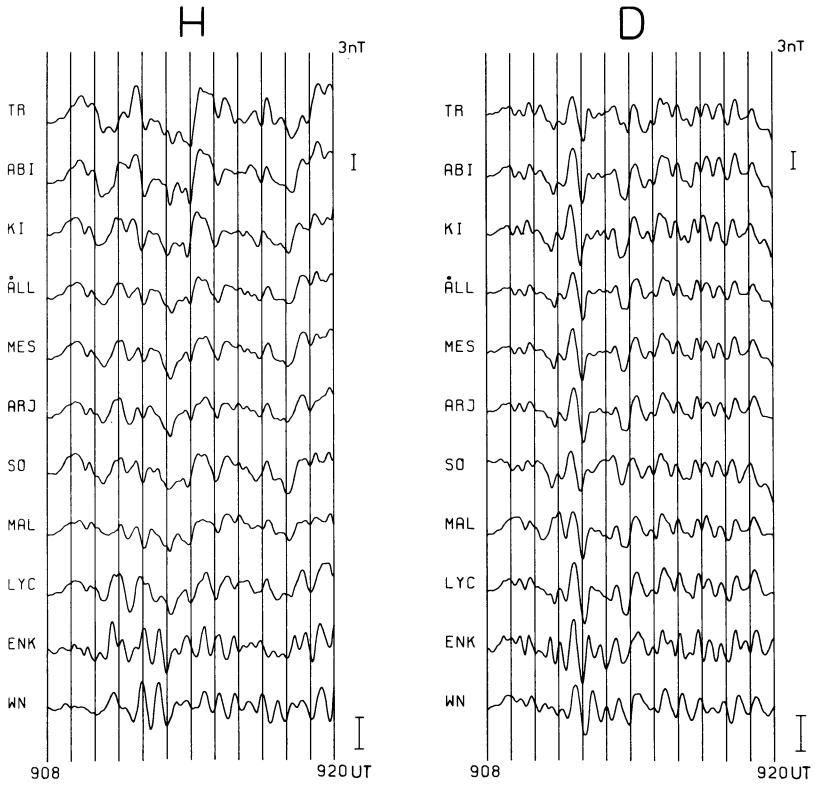

Fig. 2. Example of a pulsation event on June 3, 1971, at Kp=2o. The calibration factor at WN and ENK is represented by the longer bar at the right hand side of the plots, and the shorter bar for the other stations. Each bar equals 3nT

the interval 9.16–9.17 h UT, note that pc3 ($T \sim 20$s) are superposed on pc4, especially at MAL, SO, ARJ, MES, and ÅLL. The spectral behaviour of this event is shown in Fig. 3. In the following the spectral range corresponding to periods greater than $T = 150$s is not referred to, due to poor spectral resolution. The spectra of H show that at WN and ENK the dominant spectral peak is centered on $T = 38$s. This peak is significant at the higher latitude stations, too, but with somewhat less power between LYC and KI. The adjacent peak centered on $T = 55$s is also consistent along the profile. At WN the period is shorter ($T = 50$s). Perhaps this is due to the fact that WN is far from the profile. The power of this spectral band increases strongly from ENK to LYC, has a minimum between MAL and ÅLL and reaches the maximum power again at KI, ABI and TR. Significant peaks with high power centered on $T \sim 150$s appear only at the northern stations, especially at ABI and TR. Also the pc3 spectral range centered on $T \sim 25$s occurs predominantly at those stations situated north of ENK.

In *D* all spectral peaks show a remarkable consistency along the profile. The dominant peaks are centered on $T = 86$s, $T = 55$s, $T = 38$s and $T = 24$s. The

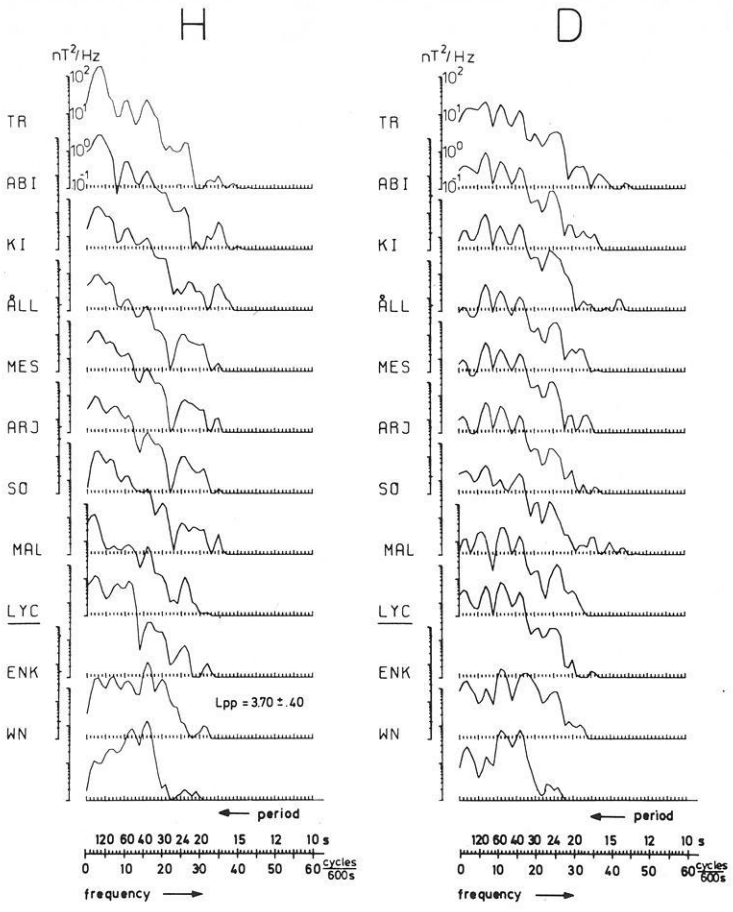

Fig. 3. Power spectra of the pulsation event plotted in Fig. 2. The *underlined symbol* of the station LYC at the left hand side of the spectra indicate that this station corresponds to the region of the plasmapause which has been estimated by the method of Orr and Webb (1975)

peak centered on $T=86$s does not appear in H, i.e., the longer period frequency range of D is different from H, but the power of this spectral band increases strongly from ENK to LYC and has its maximum power at the stations north of LYC.

Another example of a pulsation event at Kp=3+ is shown in Fig. 4, and its power spectra are represented in Fig. 5. Again D is very consistent for all significant spectral bands along the profile. The dominant peaks of D are centered on $T=60$s, $T=33$s, and $T=23$s. The pc3 range on $T=23$s appears to be significant at those stations which are north of ENK. The maximum peaks at WN and ENK are centered on $T=60$s, at LYC on $T=50$s, at SO on $T=86$s, at ARJ on $T=50$s and at MES, ÅLL, KI, ABI, and TR again on $T=86$s. It is obvious from these spectra that the dominant periods of the

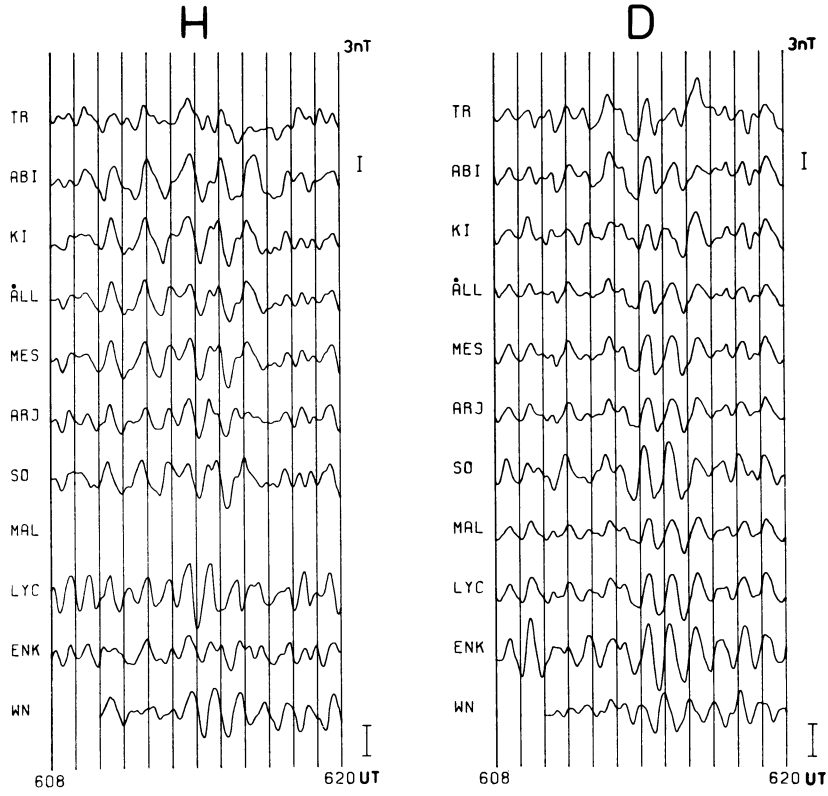

Fig. 4. Example of a pulsation event on June 4, 1971, at Kp=3+

pulsation change between LYC and MES, i.e., a distinct shift of spectral power density appears in this region.

Figure 6 shows the power spectra of a pulsation event under quiet magnetic conditions (Kp=1−). In *D* there is only one dominant frequency band, centered on $T=46$s. The same period is seen in *H* at WN, ENK, LYC, and MAL. A shift of power density between spectral bands centered on $T=46$s and $T=35$s is observed at SO, ARJ, MES, and ÅLL. At the northernmost stations KI and TR only the peak centered on $T=35$s appears.

The pulsation event in Fig. 7 (Kp=4o) is typical of the strong attenuation of the amplitudes at higher Kp values when going along the profile from north to south. The maximum amplitudes with values up to 30nT are limited to a range in latitude near the auroral belts. Moreover this event shows in H an obvious increase of period with increasing latitude.

It is important to know if the region where the sudden shift of pulsation event spectral maximum is observed correlates with the position of the plasmapause. For this purpose the method of Orr and Webb (1975) was used to estimate the statistical plasmapause position, using their equation $L=6.52-1.44\mathrm{Kp}+0.18\mathrm{Kp}^2$ with Kp in the range 0–4. This is in accordance with

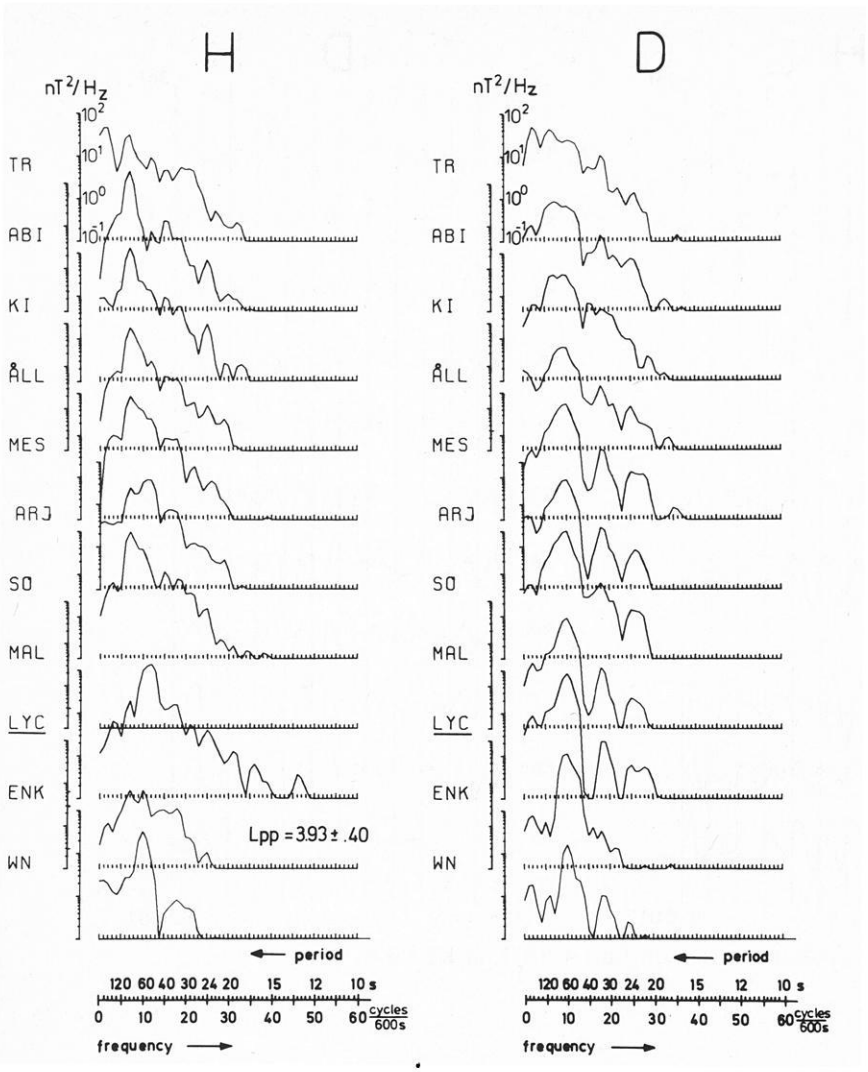

Fig. 5. Power spectra of the pulsation event plotted in Fig. 4

data from OGO-5 (Chappel, et al., 1970). For their fit of formula to data the rms residual of 0.4 is interpreted as equivalent scatter of ± 0.4 earth radii in the equatorial plane of the estimated position of the plasmapause. The underlined symbols of the stations at the left hand side of the power spectra in Fig. 3, 5, and 6 indicate that these stations correspond to the region of the estimated plasmapause. This procedure, estimating the plasmapause position and comparing its L-value with the corresponding L-values of the stations along the profile, was performed for each wave event being analyzed. It was found that under quiet magnetic conditions ($Kp \leqq 1+$) only one or two dominant frequency bands appear in the spectra. The corresponding periods range from $T = 25$s to 60s. A systematic increase of period with increasing latitude is not seen. However, tracing the projection of the statistical plasmapause position onto the earth surface a shift of power density is observed between adjacent spectral bands in its region of influence. The shorter period (25s–40s) occurs

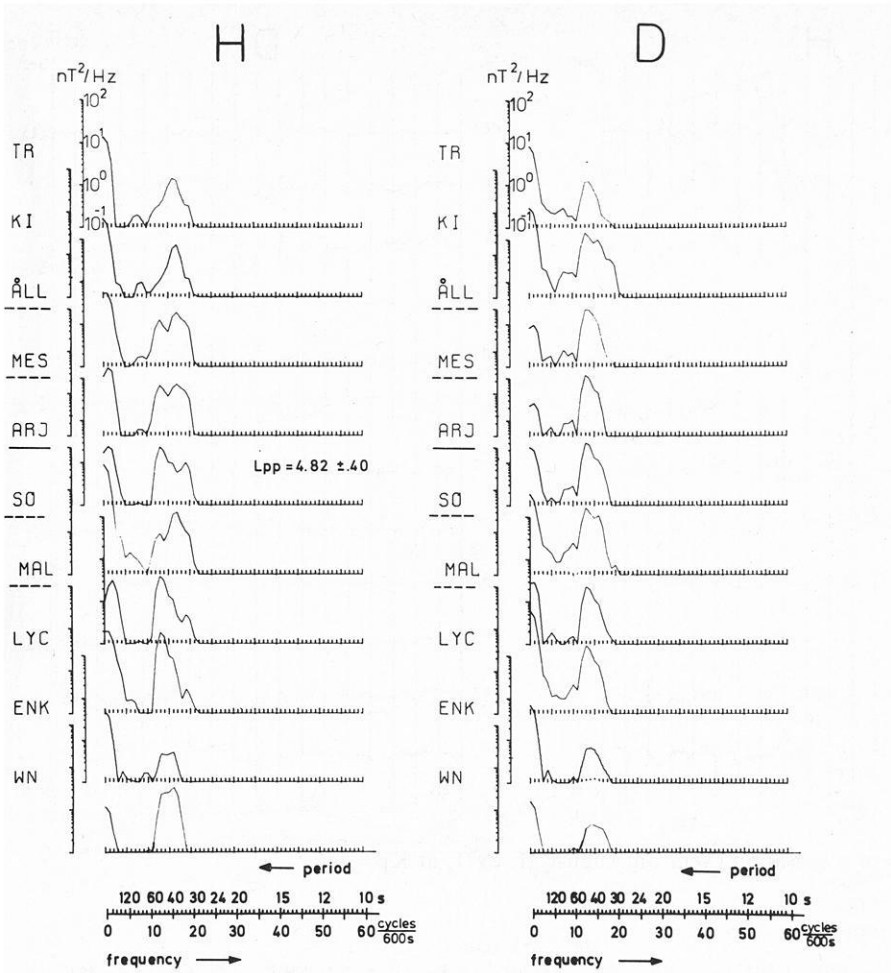

Fig. 6. Power spectra of a pulsation event under quiet magnetic conditions on June 19, 1971, Kp = 1−. The stations *MAL, SO, ARJ, MES,* and *ÅLL* correspond to the estimated plasmapause $L_{pp} = 4.82 \pm 0.4$, as indicated by the *underlined symbols*

outside and the longer period (40s–60s) inside the plasmapause. This behaviour is mostly observed in H. Similar results have been found by Lanzerotti et al. (1974; 1976) at somewhat different spectral bands. They reported that the latitude of the *H*-component peak power in the 15 to 27mHz band (37s–67s) is generally higher than the latitude of the H-component peak power in the 10 to 15kHz band (67s–100s).

In the Scandinavian data when the magnetic activity increases the number of significant frequency bands grows too, and the mean power shifts to the longer period pc4 range; e.g., for the range $2o \leqq Kp \leqq 3+$ the main power is found in spectral bands corresponding to periods from $T = 50$s to 90s. The shorter period bands ($T = 50$s to 60s) dominate at the southern stations, especially at WN and ENK. In the region where the profile is crossing the projection of the plasmapause position, a clear discontinuity is observed in the spectral behaviour of *H*: Outside the plasmapause the main power is concentrated in the lower frequency bands corresponding to periods of $T = 80$s–90s and ampli-

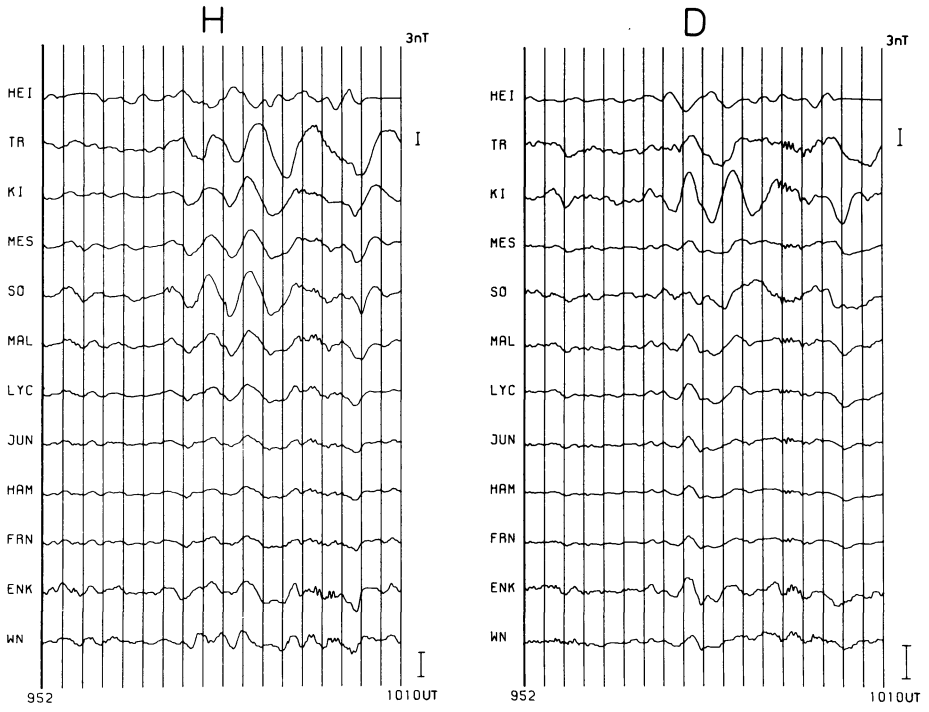

Fig. 7. Example of a pulsation event on August 31, 1971, at Kp=4o

tudes of about 10nT; the power inside the plasmapause is concentrated in the higher frequency range centered on $T=50$s–60s.

The spectral range centered around $T=150$s reveals high peaks of power in H at the northern stations TR, ABI, and KI if the Kp index is $\geqq 4$o. These peaks do not appear at the southern stations because of the strong attenuation of the amplitudes in southward direction. The demarcation line is at about 62° geomagnetic latitude. Toward HEI, the northernmost Soviet station, which is located far from the profile and probably outside the range of closed magnetic lines, the power is strongly attenuated, too. The peaks in the pc3 range centered on $T=25$s occur predominantly outside the estimated plasmapause position and there the spectral power decreases exponentially from the lower frequency pc4 domain to the higher frequency pc3 domain. The pc3 spectra show no latitude dependence of period; this is consistent with the results of Kopytenko et al. (1975).

The spectra of D generally have a more regular behaviour than those of H. In particular the midfrequencies of the main power peaks in D do not change along the profile.

A more detailed examination of the spectral peaks reveals that the longer period pc4's ($T=80$s–150s) have their maximum power between 65° and 67° geomagnetic latitude, when Kp is $\geqq 3+$. Up to 62° the distribution of spectral

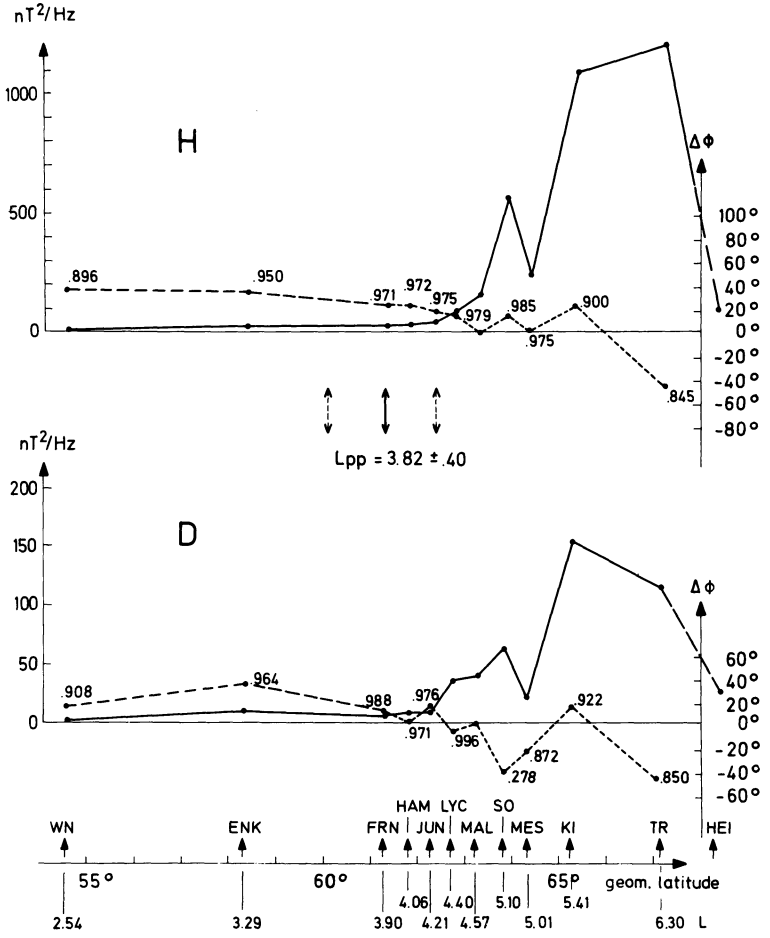

Fig. 8. Spectral amplitude distribution for the frequency band of 4/600 cycles/$s = 6.67$ mHz. The pulsation event is shown in Fig. 7. Also shown are the phase difference (*interrupted lines*) and coherency with respect to the reference at *MAL*. For this example the plasmapause is estimated to be $L_{pp} = 3.80 \pm 0.4$ and is indicated by arrows in the middle of the figure

amplitudes is nearly constant and generally does not exceed values of $10 nT^2/Hz$. From 64° to 65° an increase of power density is observed sometimes up to $1000 nT^2/Hz$ and more. It seems that the latitude gradient of power is a sensitive function of magnetic disturbance. The same conclusion is given with regard to the 2 to 5mHz band (200s–500s) in the study of pc3, 4 and pc5 pulsations, presented by Lanzerotti et al. (1976). Moreover they found that the latitude gradients of the power levels change with local time and from day to day within their latitude range of observation ($L = 3.2$–4.4), and, with only minor exceptions, the maximum power levels occur at the highest latitudes of observation (Girardville $L = 4.4$ corresponds to Lycksele $L = 4.4$) for essentially all local times and all days. In the region of maximum power the power in *D* is normally

two to five times lower than in H in the Scandinavian data. The maximum in H of the shorter period pc4's ($T=45$s to 60s) is located inside the plasmapause, south of 60° to 62° geomagnetic latitude; the corresponding maximum in D is found between 65° and 67°.

Figure 8 is a typical example of spectral amplitude distribution for longer pc4's when Kp is $\geqq 4o$. The pulsation event is shown in Fig. 7. Also shown are the phase difference $\Delta\phi=\phi$ (MAL) $-\phi$ (station) and coherency with respect to the reference at MAL. A positive phase difference means the signal arrives later at MAL than at the station. The plasmapause is estimated to be $L=3.8\pm0.4$ and is indicated by arrows in the middle of Fig. 8. The phase differences vary smoothly in H, and also in D except in the region of increasing power. The coherencies are high, nearly reaching 1 in most cases, except at SO. Notice also that the H and D amplitudes at SO deviate from the general profile distribution. Since this station lies well off the profile meridian the deviation of coherency and amplitude may reflect a longitudinal dependence.

Those events occurring during moderate magnetic activity (Kp $\sim$ 2) often have a minimum in the amplitude distribution. The adjacent maxima are located at $\sim 62°$ and 65°, respectively. An example showing this behaviour is given in Fig. 9. The wave trains corresponding to this example are shown in Fig. 2. The minimum in H amplitude is quite clear, and there is also a definite minimum in D. But, unlike the previous case for Kp $=4o$, the station SO is an exception from the profile distribution only in D, not in H.

Polarization Properties of Pc3, 4 Events

The wave polarization of about forty significant frequency bands (evaluated from fifteen pulsation events) centered on periods ranging from $T=25$s to 150s have been investigated. The shorter period range is discussed first, the longer second, for events occurring at more disturbed magnetic activity (Kp $\geqq 3o$).

It was found that the wave ellipses for the shorter period range ($T=25$s–55s) have predominantly LH (left hand) polarization in the morning, i.e., the disturbance vector rotates anticlockwise viewed in the direction of a line of force, whereas the ellipses for events occurring between 11.00 and 15.00 h LT often show reversals (1) in the south of the profile, (2) between 65° and 67° geomagnetic latitude and (3) sometimes at stations at the plasmapause position. For these reversals the change can be either LH to RH (right hand) or RH to LH, varying from event to event.

In the lower frequency range of period $T=70$s–150s the ellipses have predominantly RH polarization for events around local noon (10.30–15.00 h LT), but for morning events the polarization changes several times along the profile. In some cases the magnetic disturbance vector of morning events of longer period pc4's is LH north of the line of maximum amplitude (65°–67°) and RH south of it. In other cases the reverse behaviour is observed as was also found by Samson and Rostoker (1972) for pc4 and pc5 pulsations; there is RH polarization north and LH south of a demarcation line characterized by maximum amplitudes and linear polarization. The events being investigated

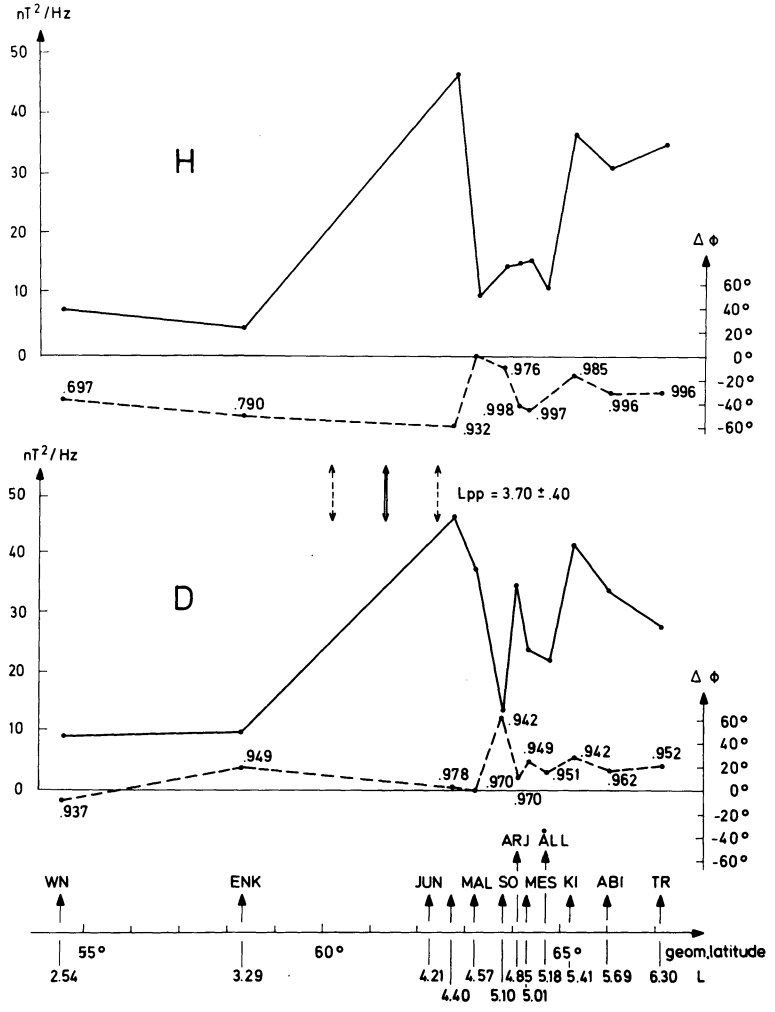

Fig. 9. Spectral amplitude distribution, phase difference and coherency for the frequency band at 10/600 cycles/s = 16.67 mHz with respect to the reference at *MAL*. The corresponding pulsation event and the power spectra are shown in Figs. 2 and 3, respectively

in this study show that the major axis of the polarization ellipses are preferentially oriented in the NE-direction.

Figure 10 shows some examples of the latitudinal distribution of polarization ellipses in the *H-D* plane. These ellipses have been evaluated from five wave events which occurred on different days and under low to moderate magnetic activity ($1- \leqq Kp \leqq 2+$). Station, geomagnetic latitude and *L*-value are given along the right hand side of the diagram. The polarization has been evaluated for the bands whose periods are noted at the top of each column. For each event the time (LT), Kp index and the projection of the estimated plasmapause

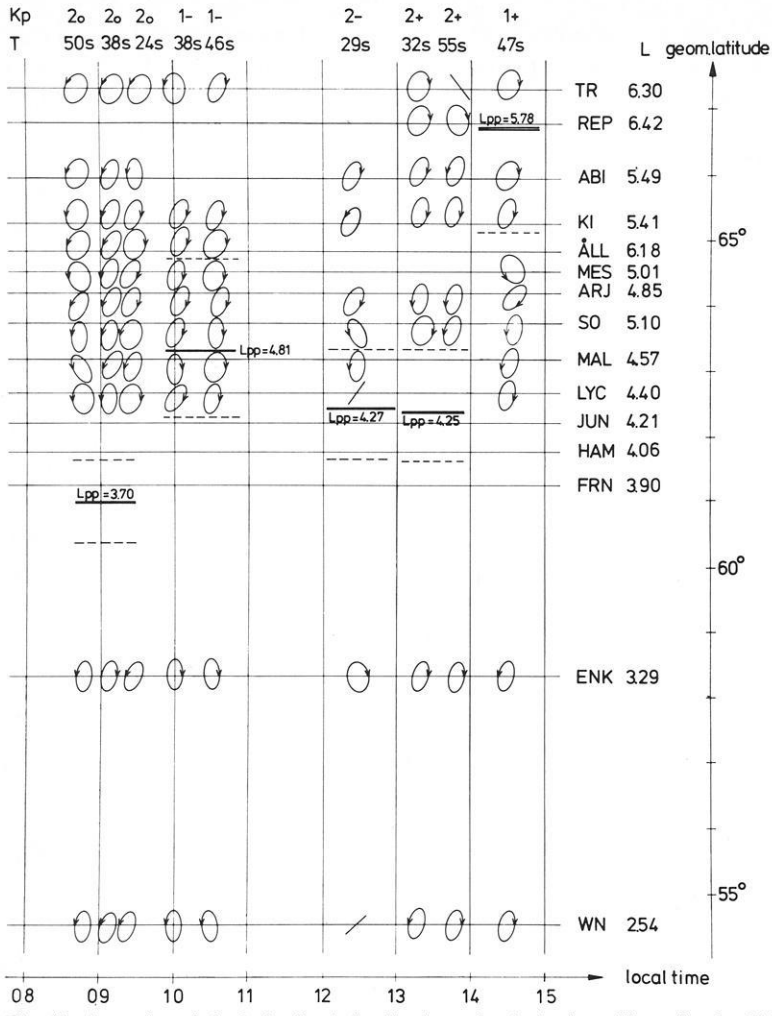

Fig. 10. Examples of the latitudinal distribution of polarization ellipses in the *H-D* plane. Further details of this figure are described in the text

position, indicated by the dashed lines, are given. For the earlier of the two morning events (9.00 h LT) – the corresponding wave train is seen in Fig. 2. – the polarization is predominantly LH in the longer period bands of $T=50$s and $T=38$s, but variable for the short period band $T=24$s. The polarization of the 10.00 h LT event is RH north of WN ($T=38$s and 46s at Kp$=1-$). The behaviour of polarization for events from 12.00 to 15.00 h LT is more complicated. For example, for the event at 14.30 h LT there occur 6 polarization reversals, and 3 for the event at 12.30 h LT (6th column of Fig. 10). One of the reversals in the former event occurs in the estimated plasmapause position, and, although no reversals occur in the plasmapause position in the latter event, there is a change of major axis orientation.

Summary and Discussion

In summary several points can be made about the analysis of amplitude spectra and of polarization of the magnetic disturbance vector. The latitude dependence of D and H spectra is complex. For this study the following points are noted.

1. There are a few cases in this study of more disturbed magnetic activity for which the dependence at latitude $>63°$ to 70° is similar to that observed by Voelker (1963) at midlatitude observatories Fürstenfeldbruck, Göttingen, and Wingst. And the few pse's (pulsation single effects, which occur predominantly in connection with sudden impulses and storm sudden commencements) observed in this study confirm earlier investigations of Hillebrand et al. (1973). These results do not, however, favor conclusively one theory over another.

2. For low activity, $Kp<2$, the present results are similar to those of Lanzerotti et al. (1974; 1976). Stations with dominant peaks at pc4 frequency tend to be at lower latitude than stations with dominant pc3 frequency peaks (Lanzerotti's data is for northern latitude stations with $L=3.2$–4.4).

3. At higher activity, $Kp\geqq 2o$, however, the opposite effect is observed. The shorter period bands ($T=50$s–60s) dominate in spectra from southern stations of the profile, while the longer period bands ($T=70$s–150s) dominate at the higher latitude stations.

4. In both cases (2) and (3) the transition between high and low latitude behaviour occurs at the estimated plasmapause position, and is especially clear in H spectra.

The latitude dependence of polarization is also complex, and the sense of polarization is found to depend on frequency and time of day, too. Thus, in this study (1) there is a tendency for LH polarization in the morning at higher frequencies ($T=25$s–55s) with reversals of polarization sense at lower frequencies ($T=70$s–150s), and (2) there is a tendency for RH around noon (10.30–15.00 h LT) at lower frequency, but no clear pattern at the higher frequencies.

This may be compared with the polarization characteristics observed by Lanzerotti et al. (1976).

(1) In the 2 to 5mHz band (200s–500s) all stations ($L=3.2$–4.4) exhibited similar characteristics on day to day basis, as well as on the average over several days. There was RH polarization between 12.00 and 18.00 h LT, and LH otherwise, and near local noon the major axis of polarization switched from NW-SE to NE-SW.

(2) In the 10 to 15mHz band (66.7s–100s) the same tendency for reversal of polarization and change of axis direction at local noon was found only in the average.

(3) In the 15 to 27mHz band (37s to 66.7s) the polarization character varied with latitude. From 12.00 to 18.00 h LT RH polarization was observed, and LH otherwise, but whereas this was observed on a day to day basis for $L=3.2$–3.5 it was found only in the average for $L=4.0$ –4.4.

A few fundamental results from current theoretical work with resonance models of pulsations can now be compared with observational results.

(1) Southwood (1974a and b) and Chen and Hasegawa (1974) showed that (a) the sense of polarization changes across the resonant region, (b) the polarization is linear at the resonant field line, and (c) the major axis does not switch across the resonant region.

(2) Lanzerotti et al. (1974) used a specific model of plasmapause-type density distribution, and considered the polarization characteristics at latitudes away from the resonant region. At these latitudes they showed that the major axis direction can also switch.

(3) Hughes and Southwood (1976a and b) have extensively studied the ionospheric modification of pulsation. They found that the atmosphere and ionosphere alter the magnetospheric signal so as to smooth the amplitude and phase variation at ground level. They conclude that because of this smoothing polarization reversals may not be observed, and they suggest that disagreements of observational results with theoretical results may be explained by observing that the magnetosphere NS-field and EW-field at ground level show a relatively larger peak at resonance than is indicated by the models the authors used.

Although some observations of the present studies of Scandinavian data tend to fit the resonance models others do not, as, especially, the polarization ellipses which are more variable then would be expected. Some of the disagreement may be due to the ionospheric modification suggested by Hughes and Southwood (1976a and b). Future work with magnetometer networks and synchronous data from satellites will tell us more about the excitation and propagation of magnetohydrodynamic waves. These topics are under active investigation in the international magnetospheric study (IMS) project at present.

Acknowledgements. I acknowledge the cooperative assistance of the Scandinavian observatories during the field work in Scandinavia. This work is part of a project sponsored by the 'Deutsche Forschungsgemeinschaft'. The numerical calculations were carried out on the computer of the Gesellschaft für wissenschaftliche Datenverarbeitung, GWD, Göttingen. I thank Dr. M. Richards, Professor Dr. M. Siebert and Dr. H. Voelker for many profitable discussions and for their assistance in evaluating this paper.

References

Chappel, C.R., Harris, K.K., Sharp, G.W.: A study of the influence of magnetic activity on the location of the plasmapause as measured by OGO 5. J. Geophys. Res. **75**, 50–56, 1970

Chen, L., Hasegawa, A.: A theory of long period magnetic pulsations. J. Geophys. Res. **79**, 1024–1032, 1974

Dziewonski, A., Block, S., Landisman, M.: A technique for the analysis of transient seismic signals. Bull. Seismol. Soc. Am. **59**, 427–444, 1969

Hillebrand, O., Palandt, M., Voelker, H.: Beobachtungen und erste Auswertung von erdmagnetischen Pulsationen nahe der Polarlichtzone im Zusammenhang mit dem Auftreten von si's und ssc's. Kleinheubacher Berichte, Nr. **16**, 411–419, 1973

Hughes, W.J., Southwood, D.J.: The screening of micropulsation signals by the atmosphere and ionosphere. J. Geophys. Res. **81**, 3234–3240, 1976a

Hughes, W.J., Southwood, D.J.: An illustration of modification of geomagnetic pulsation structure by the ionosphere. J. Geophys. Res. **81**, 3241–3247, 1976b

Kopytenko, Yu,A., Raspopov, O.M., Dmitrieva, L.A.: The behaviour of the geomagnetic pulsations near the boundary of the plasmasphere. Planet. Space Sci. **33**, 1195–1203, 1975

Lanzerotti, L.J., Fukunishi, H., Chen, L.: ULF pulsation evidence of the plasmapause. 3. Interpreta-

tion of polarization and spectral amplitude studies of pc3 and pc4 pulsations near $L=4$. J. Geophys. Res. **79**, 4648–4653, 1974

Lanzerotti, L.J., Maclennan, C.G., Fukunishi, H.: ULF geomagnetic power near $L=4$, 5. Cross power spectral studies of geomagnetic variations 2–27 mHz in conjugate areas. J. Geophys. Res. **81**, 3299–3315, 1976

Orr, D., Webb, D.C.: Statistical studies of geomagnetic pulsations with periods between 10 and 70s and their relationship to the plasmapause region. Planet. Space Sci. **23**, 1169–1178, 1975

Samson, J.C., Rostoker, G.: Latitude dependent characteristics of high latitude pc4 and pc5 micropulsations. J. Geophys. Res. **77**, 6133–6144, 1972

Southwood, D.J.: Some features of field line resonances in the magnetosphere. Planet. Space Sci. **22**, 483–491, 1974a

Southwood, D.J.: Recent studies in micropulsation theory. Space Sci. Rev. **16**, 413–425, 1974b

Voelker, H.: Zur Breitenabhängigkeit erdmagnetischer Pulsationen. Mitteilungen aus dem Max-Planck-Inst. für Aeron. Nr. 11, 1963

Received October 15, 1977; Revised Version March 26, 1979; Accepted June 1, 1979

J. Geophys. 45, 409–416, 1979

Journal of Geophysics

A Theoretical Investigation of the Dipole- and Unipole-Resistivity Methods for Geoelectrical Prospecting in Marine Areas

J. Sebulke and W. Hildebrandt

Institut für Angewandte Geophysik, Petrologie und Lagerstättenforschung
der Technischen Universität Berlin, Straße des 17. Juni 135, EB 15, 1000 Berlin 12

Abstract. The apparent resistivity of a dipole-dipole and a unipole-configuration has been calculated based on the potential of a buried electrode. The model calculations indicate that the thickness of seafloor sediments can be determined with good accuracy; however, the results cannot be expected better than by application of the two-electrode configurations, which were described in previous papers (Sebulke, 1973; 1978).

Key words: Marine geoelectrical sounding – Dipole- and unipole-resistivity measurements – Computed apparent resistivity.

1. Introduction

Within the last seven years investigations of the resistivity method for use in marine areas have been carried out at the department of Applied Geophysics (Institut of Applied Geophysics, Petrology, Economic and Mining Geology) at the Technical University of Berlin. In different papers (Sebulke, 1973; Bischoff and Sebulke, 1976) special configurations for marine resistivity measurements have been suggested. Results of field measurements with different two-electrode configurations have been published (e.g., Bischoff, 1978).

The present article (being based on a diploma thesis by Hildebrandt, 1976) discusses the possibility of using dipole-dipole and unipole measuring arrays in marine resistivity prospecting. The aim of the theoretical investigations is to find out, if the two examined configurations have any advantages in comparison to the two-electrode configurations.

2. Theoretical Foundation

The potential of a buried physical electrical dipole is deducible when using the potential of a buried electrical point-source. The considered model is the horizontally stratified three-layered-earth with homogenous and isotropic re-

0340-062X/79/0045/0409/$01.60

sistivities. The potential of a buried electrical point source is well known (Therekin, 1962; Alfano, 1962; Merkel, 1971). It can be calculated by the complementary solution of the Laplace's equation in cylindrical coordinates (Stefanesco et al., 1930) and by the application of the boundary conditions of the stationary electrical field applied to the generally formulated potentials.

The following form of the potentials was introduced by Sebulke (1973; 1978).

$$V_p = V(r, z)$$
$$= q_j \left(A_j + C_j \int_0^\infty \frac{\sum_i g_i e^{-2\lambda b_i}}{1 - k_1 e^{-2\lambda h_1} - k_2 e^{-2\lambda h_2} + k_1 k_2 e^{-2\lambda(h_2 - h_1)}} J_0(\lambda r)\, d\lambda \right). \quad (1)$$

where

j = index of the layer where the point source is situated

$$q_j = \frac{\rho_j \cdot I}{4\pi}. \quad (2)$$

A_j = term, which describes the primary potential

C_j = factor, which depends on the layer where the source and testpoint are placed

g_i = coefficients of numerator polynomal of the Kernel function, they depend on the position of current and potential electrodes in the different layers

$J_0(\lambda r)$ = Bessel function of zero order

λ = constant from the separation of the Laplace's equation

h_n = depth of the lower boundary of layer n

r = horizontal distance between the point source and the test point

$k_n = \frac{\rho_{n+1} - \rho_n}{\rho_{n+1} + \rho_n}$ resistivity contrast.

The fully written formulas will be found in the appendix.

The improper integral in Eq. (1) can be easy transformed into infinite convergent series by means of the Weber-Lipschitz formula. The potential of an inclined dipole (Fig. 1) can be derived from the point electrode potential as follows:

$$V_D = -\left(\frac{\partial V_p}{\partial r} L \cos\alpha + \frac{\partial V_p}{\partial z} L \sin\alpha \right) = -\operatorname{grad} V_p \cdot \vec{L} \quad (3)$$

where $E_1 E_2 = L$ = length of the inclined current dipole and α = inclination of the current dipole.

The test point is situated in a vertical plane across the physical current dipole.

For a dipole-dipole configuration as presented in Fig. 1 the apparent resistivity is (horizontal measuring dipol):

$$\rho_s = K \left(-\frac{\partial V_D}{\partial r} \right) \frac{1}{I} \quad (4)$$

with

K = configuration factor

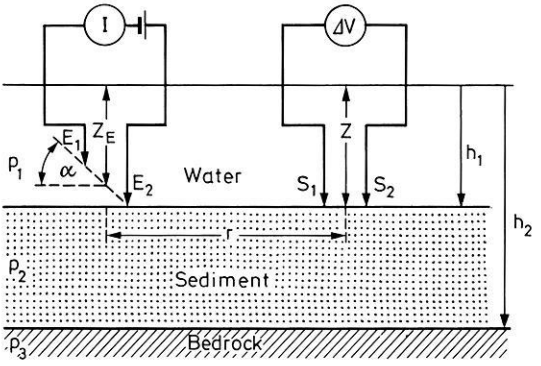

Fig. 1. The dipole-dipole configuration for use in marine resistivity sounding and the assumed model of the ground (Both dipoles in a joint vertical plane). Z_E: depth of the current dipole; Z: depth of the measuring dipole in the halfspace; E_1, E_2: electrodes of the current dipole; S_1, S_2: electrodes of the potential dipole

and

$S_1 S_2 = 1 =$ length of the measuring dipole.

The condition must hold, that the length of the both dipoles is very small in comparision to the distance r. For the special case in which the current electrodes and the two potential probes are placed either on the bottom of the sea or both in the sediment we can use for further computations the potential of a point electrode and a test point located in layer 2 (A 4). We get the following expression for the apparent resistivity:

$$\rho_s = \rho_2 K_D^* \left[\frac{1}{r} \cos\alpha \int_0^\infty (e^{-\lambda(z_E - z)} + \Theta_2(\lambda) e^{-\lambda z} + \Psi_2(\lambda) e^{+\lambda z}) \lambda J_1(\lambda r) \, d\lambda \right.$$
$$- \cos\alpha \int_0^\infty (e^{-\lambda(z_E - z)} + \Theta_2(\lambda) e^{-\lambda z} + \Psi_2(\lambda) e^{+\lambda z}) \lambda^2 J_0(\lambda r) \, d\lambda$$
$$\left. - \sin\alpha \int_0^\infty (e^{-\lambda(z_E - z)} - \Theta_2(\lambda) e^{-\lambda z} + \Psi_2(\lambda) e^{+\lambda z}) \lambda^2 J_1(\lambda r) \, d\lambda \right] \tag{5}$$

with

$$K_D^* = \frac{[r^2 + (z_E - z)^2]^{5/2} [r^2 + (z_E + z)^2]^{5/2}}{3r[r^2 + (z_E + z)^2]^{5/2} [r \cdot \cos\alpha - (z_E - z)\sin\alpha] - [r^2 + (z_E - z)^2]}$$
$$\times [r^2 + (z_E + z)^2]^{5/2} \cos\alpha + 3r[r^2 + (z_E - z)^2]^{5/2} [r\cos\alpha - (z_E + z)\sin\alpha]$$
$$- [r^2 + (z_E - z)^2]^{5/2} [r^2 + (z_E + z)^2] \cos\alpha \tag{6}$$

and

$$\Theta_2(\lambda) = \frac{e^{-\lambda z_E} - k_1 e^{-\lambda(z_E - 2h_1)} + k_2 e^{-\lambda(2h_2 - z_E)} - k_1 k_2 e^{-\lambda(2h_2 - 2h_1 - z_E)}}{1 - k_1 e^{-2\lambda h_1} - k_2 e^{-2\lambda h_2} + k_1 k_2 e^{-2\lambda(h_2 - h_1)}} \tag{7}$$

$$\Psi_2(\lambda) = \frac{k_2 [e^{-\lambda(2h_2 - z_E)} + e^{-\lambda(2h_2 + z_E)}] - k_1 k_2 [e^{-\lambda(2h_2 + 2h_1 - z_E)} + e^{-\lambda(2h_2 - 2h_1 + z_E)}]}{1 - k_1 e^{-2\lambda h_1} - k_2 e^{-2\lambda h_2} + k_1 k_2 e^{-2\lambda(h_2 - h_1)}}. \tag{8}$$

$\Theta_2(\lambda)$, $\Psi_2(\lambda)$ = Kernel functions for the three layer case

$J_1(\lambda)$ = Bessel function of the first order.

The symbols of the parameters are the same as previously used by Flathe (1955).

3. Results of the Calculations for Dipole-Measurements

A large number of model graphs obtained with a FORTRAN IV computer program (Hildebrandt, 1976) were examined upon the possibility to determine the sediment's thickness. Some of them will be presented here.

Figure 2a and b show the results of model calculations for two different inclinations of the current dipole. The resistivity ratios are based on results from field measurements in the Mediterranean (Bischoff and Sebulke, 1976).

The graphs show that different thicknesses of the sediment can be resolved with a good accuracy but there is no improvement upon the results of the formerly published two-electrode configurations. Figure 3 shows calculations for the symmetrical two-electrode configuration derived for the same model as before.

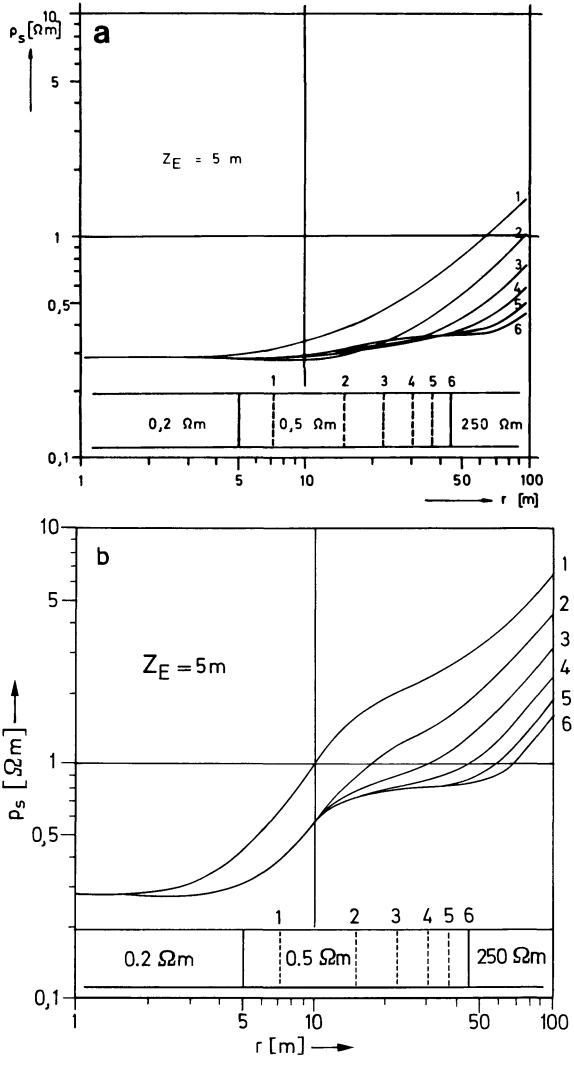

Fig. 2a and b. Computed apparent resistivity for the dipole-dipole configuration for various thicknesses of the sediment layer
a Inclination of the current-dipole $\alpha = 0°$
b Inclination of the current-dipole $\alpha = 120°$
(current- and potential-electrodes on the seafloor, $Z_E = Z = h_1 = 5$ m, the resistivities and thicknesses of the layers are demonstrated in the logarithmic sectional drawing)

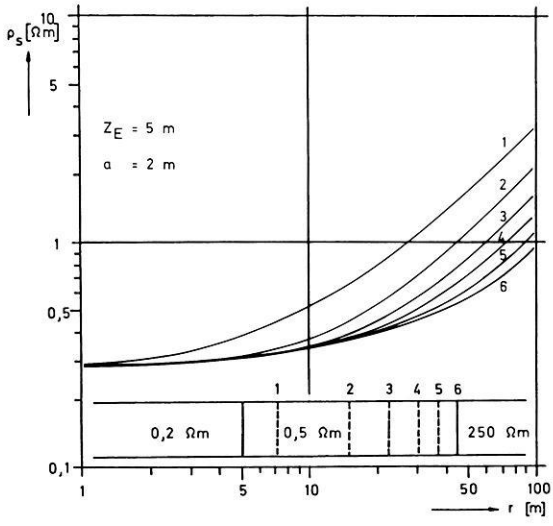

Fig. 3. Computed apparent resistivity for the symmetrical two-electrode configuration for various thicknesses of the sediment layer (current- and potential-electrodes on the seafloor, $Z_E = Z = h_1 = 5$ m)

4. Results for the Unipole-Configuration

The unipole-configuration is shown in Fig. 4. Two electrodes with the same polarity generate the electrical field. The potential difference is measured with one probe against a physical infinite located point.

The corresponding formula for the apparent resistivity of this configuration can be deduced from the point-electrode-potential (1). If the current-electrodes and the potential-electrode are situated all in the first sediment layer the apparent resistivity will be calculated using formula (A 4).

$$\rho_s = \rho_2 K_u^* \int_0^\infty [e^{\pm\lambda(z_E - z)} + \Theta_2(\lambda)\, e^{-\lambda z} + \Psi_2(\lambda)\, e^{+\lambda z}]\, [J_0(\lambda r) + J_0(\lambda 2r)]\, d\lambda. \qquad (9)$$

The reduced configuration factor K_u^* depends only on the geometrical position of the electrodes in this three-point-configuration and is defined as:

$$K_u^* = \frac{1}{[r^2 + (z_E - z)^2]^{-1/2} + [r^2 + (z_E + z)^2]^{-1/2} + [4r^2 + (z_E - z)^2]^{-1/2} + [4r^2 + (z_E + z)^2]^{-1/2}}$$

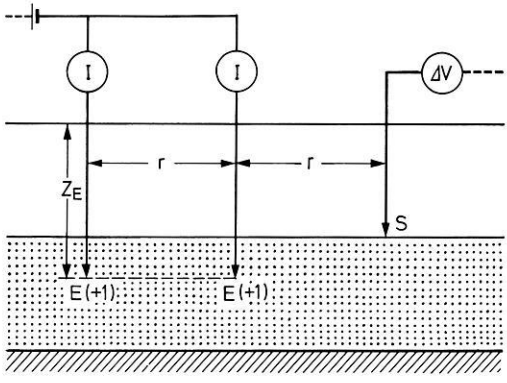

Fig. 4. The unipole-configuration for use in marine resistivity sounding

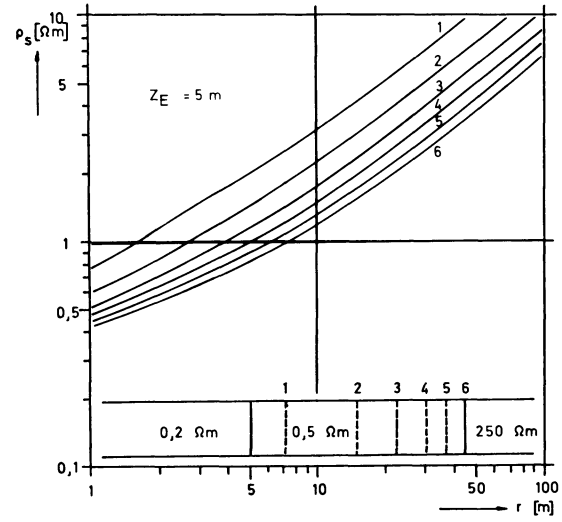

Fig. 5. Computed apparent resistivity for the unipole configuration for various thicknesses of the sediment layer (current- and potential-electrodes on the seafloor, $Z_E = Z = h_1 = 5$ m)

$\Theta_2(\lambda)$ and $\Psi_2(\lambda)$ are the same Kernel functions for the three-layer-case as given before (7), (8).

One example of calculated apparent resistivities for the described unipol configuration is shown in Fig. 5. The model is the same as that of the dipole-computation in Fig. 2. It is obvious that the differences between the curves for various thicknesses of the second layer (sediment) are sufficient to determine that thickness with a good accuracy (until a thickness of about 30 m); however, the resolving power is not better than that for the two-electrode configuration (s. Fig. 3) and the dipole-dipole configuration (s. Fig. 2).

5. Conclusion

Several model calculations have been done to compute the apparent resistivity of the here described dipole-dipole configuration and the unipole array. Some of the results are presented in this paper. It may be concluded that both examined configurations could be used for marine geoelectrical prospecting.

Practical measurements with different two-electrode configurations have been carried out in the Mediterranean and in the North Sea. A digital measuring system was used. The current electrodes and the electrodes for the determination of the potential differences are connected at a towed multiple conductor cable, which is layed out on the seafloor. The potential electrodes are scanned by an automatic scanner and the data are recorded computer compatible on a digital cassette recorder. The potential differences measured with such an array are very small. Using a dipole-dipole configuration the potential differences will become smaller than the one hundredth part of that obtainable with a two-electrode configuration. Using a unipole configuration it is necessary to bring a second potential electrode to a physical infinit point. Because the dipole-dipole and unipole configurations cannot be expected better results in

resolving the thickness of the sediment layers than the two-electrode configurations, which moreover have some advantages in measuring techniques, practical measurements with the both presented configurations have not been excuted and have not been projected in the future.

Acknowledgement. The valuable suggestions of three unknown referees are gratefully acknowledged.

Appendix

Potentials of buried point sources and test points in different layers:

1. Potential-Electrode in Layer 1

1.1. Current-Electrode in Layer 1:

$$V(r,z)=q_1\left[\frac{1}{(r^2+(z-z_E)^2)^{1/2}}+\frac{1}{(r^2+(z+z_E)^2)^{1/2}}\right.$$
$$+\int_0^\infty \frac{k_1(e^{-\lambda(2h_1-z_E)}+e^{-\lambda(2h_1+z_E)})+k_2(e^{-\lambda(2h_2-z_E)}+e^{-\lambda(2h_2+z_E)})}{1-k_1e^{-2\lambda h_1}-k_2e^{-2\lambda h_2}+k_1k_2e^{-2\lambda(h_2-h_1)}}$$
$$\left.\cdot(e^{-\lambda z}+e^{\lambda z})\,J_0(\lambda r)\,d\lambda\right]. \tag{A1}$$

1.2. Current Electrode in Layer 2:

$$V(r,z)=q_2(1-k_1)\int_0^\infty \frac{(e^{-\lambda z_E}+k_2e^{-\lambda(2h_2-z_E)})(e^{-\lambda z}+e^{\lambda z})}{1-k_1e^{-2\lambda h_1}-k_2e^{-2\lambda h_2}+k_1k_2e^{-2\lambda(h_2-h_1)}}J_0(\lambda r)\,d\lambda. \tag{A2}$$

1.3. Current Electrode in Layer 3:

$$V(r,z)=q_3(1-k_1)(1-k_2)$$
$$\cdot\int_0^\infty \frac{e^{-\lambda z_E}(e^{-\lambda z}+e^{\lambda z})}{1-k_1e^{-2\lambda h_1}-k_2e^{-2\lambda h_2}+k_1k_2e^{-2\lambda(h_2-h_1)}}J_0(\lambda r)\,d\lambda. \tag{A3}$$

2. Potential- and Current-Electrode in Layer 2

$$V(r,z)=q_2\left(\frac{1}{[r^2+(z-z_E)^2]^{1/2}}\right.$$
$$+\int_0^\infty \frac{[e^{-\lambda z_E}-k_1e^{-\lambda(z_E-2h_1)}+k_1e^{-\lambda(2h_2-z_E)}-k_1k_2e^{-\lambda(2h_2-h_1-z_E)}]e^{-\lambda z}}{1-k_1e^{-2\lambda h_1}-k_2e^{-2\lambda h_2}+k_1k_2e^{-2\lambda(h_2-h_1)}}$$
$$\left.+\frac{+[k_2(e^{-(2h_2-z_E)}+e^{-(2h_2+z_E)})-k_1k_2(e^{-(2h_2+2h_1-z_E)}+e^{-\lambda(2h_2-2h_1+z_E)})]e^{+\lambda z}}{}\right)J_0(\lambda r)\,d\lambda). \tag{A4}$$

3. Potential- and Current-Electrode in Layer 3

$$V(r,z)=q_3\left[\frac{1}{[r^2+(z-z_E)^2]^{1/2}}\right.$$
$$\left.+\int_0^\infty \frac{(e^{-\lambda z_E}-k_1e^{-\lambda(z_E-2h_1)}-k_2e^{-\lambda(z_E-2h_2)}+k_1k_2e^{-\lambda(2h_1+z_E-2h_2)})e^{-\lambda z}}{1-k_1e^{-2\lambda h_1}-k_2e^{-2\lambda h_2}+k_1k_2e^{-2\lambda(h_2-h_1)}}J_0(\lambda r)\,d\lambda\right]. \tag{A5}$$

References

Alfano, L.: Geoelectrical prospecting with underground electrodes. Geophys. Prospect. **10**, 290–303, 1962

Bischoff, J.: Die Anwendung geoelektrischer Widerstandsmethoden im marinen Bereich. Dissertationsschrift D 83. Berlin: Technische Universität 1978

Bischoff, J.; Sebulke, J.: Geoelektrische Widerstandsverfahren zur Prospektion im marinen Bereich. Kongreßberichtswerk Bd. 2. Interocean 1976, 1081–1090, 1976

Flathe, H.: A practical method of calculation geoelectrical model graphs for horizontal stratified media. Geophys. Prospect. **3**, 268–294, 1955

Hildebrandt, W.: Modifizierung unterschiedlicher Konfigurationen bekannter Widerstandsverfahren für den Einsatz im marinen Bereich zur Erhöhung der Interpretationsgenauigkeit. Diplomarbeit. Berlin: Technische Universität 1976

Merkel, R.H.: Resistivity analysis for plane-layer-half-space models with buried current sources. Geophys. Prospect. **19**, 626–639, 1971

Sebulke, J.: Entwicklung und Untersuchung einer Widerstandsmethodik zur geoelektrischen Prospektion im marinen Bereich. Dissertationsschrift D83. Berlin: Technische Universität 1973

Sebulke, J.: The theoretical investigation of resistivity methods for geoelectrical prospecting in marine areas. J. Geophys. **44**, 245–255, 1978

Stefanesco, S.; Schlumberger, C.; Schlumberger, M.: Sur la distribution électrique potentielle autour d'une prise de terre ponctuelle dans un terrain á chouches horizontales, homogénes et isotropes. J. Phys. Rad. **1**, 132–140, 1930

Terekhin, E.I.: Theoretical bases of electrical probing with an apparatus immersed in water. In: Applied Geophysics USSR, N. Rast, ed.: pp. 169–195. Oxford: Pergamon Press 1962

Received July 4, 1978; Revised Version May 22, 1979;
Accepted May 25, 1979

J. Geophys. 45, 417–432, 1979

Journal of Geophysics

Paleomagnetism and Rock Magnetism of the Pliocene Rhyolite at San Vincenzo, Tuscany, Italy*

W. Lowrie[1] and W. Alvarez[2]

[1] Institut für Geophysik, ETH Hönggerberg, CH-8093 Zürich, Switzerland
[2] Department of Geology and Geophysics, University of California, Berkeley, California 94720, USA

Abstract. A paleomagnetic study of the Pliocene rhyolite near San Vincenzo, Italy, indicates that the counter-clockwise rotation of the Italian peninsula was complete by 4.7 m.y.B.P. Studies of IRM acquisition, low-temperature behavior, and AF demagnetization of both NRM and IRM show that the remanence is carried by very fine-grained magnetite, in the single domain, and possibly pseudo-single domain size range. All 10 sites are reversely magnetized, with an over-all mean direction of $D=160°$, $I=-45°$, $\alpha_{95}=6.6°$. This direction is 21° away from the reverse of the present axial dipole field direction. Part of the discrepancy may originate from incomplete averaging of the magnetic field, but it is likely that tectonic rotations are also involved. There are significant deviations of both declination and inclination, so the result cannot be explained by rotation of the peninsula about a vertical axis. No sedimentary rocks are exposed, so we cannot make a standard bedding correction, but a correction can be made by assuming that cooling joints in the rhyolite formed with a near-vertical orientation. When their common intersection line is restored to vertical, the inverse of the present axial dipole direction falls within the circle of confidence of the corrected mean direction for the rhyolite.

Key words: Paleomagnetism – Rock magnetism – Italy – Pliocene rhyolite.

Introduction

Paleomagnetic studies of the Jurassic, Cretaceous, and Paleocene sedimentary rocks of the Umbrian sequence of northern Peninsular Italy have consistently shown remanent declinations in the northwest quadrant (Lowrie and Alvarez, 1974; 1975; 1977b; Channell and Tarling, 1975; Klootwijk and VandenBerg, 1975; VandenBerg et al., 1978; Roggenthen and Napoleone, 1977; Alvarez and Lowrie, 1978; Channell et al., 1978). These results have generally been inter-

* Institut für Geophysik, ETH Zürich, Contribution Nr. 243

0340-062X/79/0045/0417/$03.20

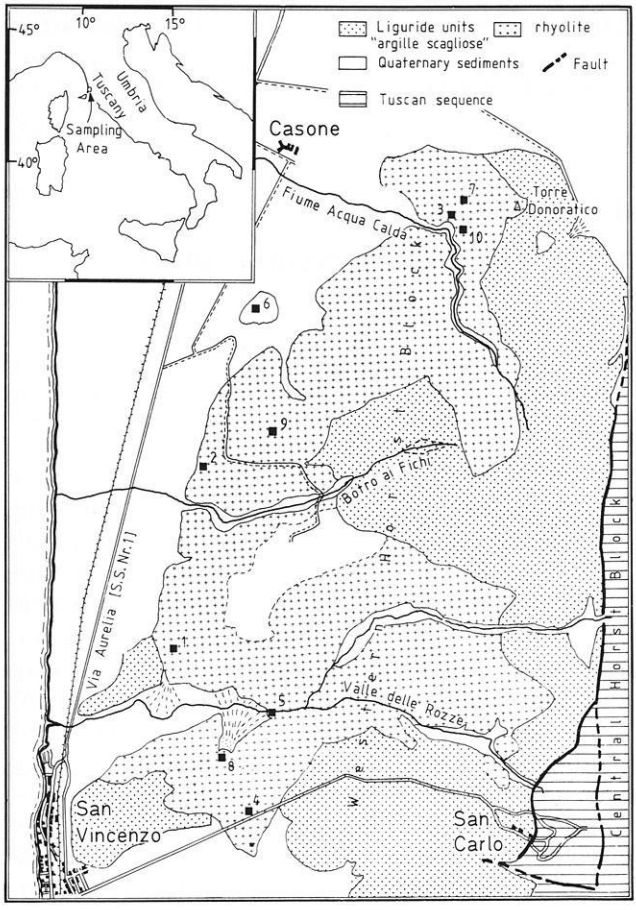

Fig. 1. Map showing the simplified geology of the sampling area (Giannini, 1955) and the locations of the ten paleomagnetic sites

preted as indicative of a counter-clockwise rotation of the Italian Peninsula. However, to accommodate the shortening represented by the folds of the Umbrian Apennines, the Umbrian sedimentary sequence is almost certainly detached at the level of the Triassic evaporites (Martinis and Pieri, 1964), so it is impossible to determine directly the rotational history of the basement, which does not outcrop. A further complication is the arcuate curvature of the Umbrian fold belt, which is reflected in the pattern of paleomagnetic declination (Channell, 1976; Channell et al., 1978).

Study of the thick stratigraphic sections at Gubbio and Moria (Lowrie and Alvarez, 1977a and b; Alvarez and Lowrie, 1978; VandenBerg et al., 1978) shows that some of the counter-clockwise rotation of the Umbrian sequence took place during the Cretaceous, but that further rotation must have occurred at some time after the Middle Eocene.

This Cretaceous rotation has been variously interpreted. Lowrie and Alvarez (1975) associated it with the rotation of the Italian peninsula on a microplate independently of Europe and Africa. Channell and Tarling (1975) disregarded Umbrian data as irrelevant to the rotation of Italy on the grounds that the Umbrian sequence is allochthonous. VandenBerg et al. (1978) disputed this assumption and interpreted Umbrian data in terms of rotation of the Italian peninsula with the African plate.

The subsequent, post-Middle-Eocene rotation of Italy has been attributed by VandenBerg (1979) to continent-continent collision between the Adriatic promontory of the African plate (Channell and Horvath, 1976) and the Balkan-Rhodope-Turkey continental block. Unfortunately, in Umbria the soft shales that continue the section upward cannot be sampled readily for paleomagnetic investigation.

Suitable Oligocene and Miocene rocks have not been located, but in the hope of placing an upper limit on the time of rotation, we have studied the paleomagnetism of the Pliocene rhyolite of San Vincenzo. This locality on the west coast of Italy, about 40 km south of Pisa, is almost opposite the isle of Elba and about 100 km west of the outcrop area of the Umbrian sequence (Fig. 1).

Geologic Setting

Tectonics of Tuscany

Orogenic activity in the Northern Apennines began in the Late Oligocene. The locus of most intense compressional deformation has shifted progressively from west to east, and orogenic activity probably continues at the present time near the Adriatic coast. As the locus of deformation shifted, compression was followed in a particular area by extensional tectonics. As a result our area of interest, on the Tuscan coast, was undergoing normal faulting during the Late Miocene and Pliocene, while the Umbrian area was still being folded. This phenomenon has been discussed by Elter et al. (1975).

In coastal Tuscany, Upper Miocene and Pliocene sediments are found in small basins interrupted by horsts in which the older, deformed rocks are exposed. Two major groupings of deformed rocks are recognized throughout coastal Tuscany. The lower unit is the Tuscan sequence, which closely resembles the Umbrian sequence farther east. The Tuscan sequence, like the Umbrian sequence, was deposited on Italian continental crust during the Mesozoic and Early Tertiary; it is now folded, detached from the underlying basement, and has been thrust a moderate distance – perhaps a few tens of kilometers – to the east. Tectonically overlying the Tuscan sequence are ophiolites and deep-water oceanic sedimentary rocks ranging from kilometer-scale slabs down to chaotic melange units. These 'Liguride units' are generally interpreted as having originated in the Mesozoic-Early Tertiary Tethyan Ocean, to the west of the Italian continent. During the Apennine orogeny the Tethys was consumed, and the Liguride units were transported 100 km or more toward the east.

From late Pliocene time to the present, coastal Tuscany has been rising relative to sea level. As a result, the horst blocks, which formerly were islands, have gradually been incorporated into the Italian mainland. The process is clear from the present morphology. Islands not yet joined to the mainland form the Tuscan Archipelago (Elba, Giglio, Mentecristo, etc.). Blocks recently joined are linked to the mainland by tombolo sand spits (Monte Argentario) or low sandy areas (Piombino). Blocks incorporated still earlier form the characteristic patchy, irregular mountains of coastal Tuscany. One of these small mountain groups is the Monti di Campiglia; the rhyolite of San Vincenzo occupies its western side, facing the sea (Fig. 1).

Local Geology

Giannini (1955) has made a detailed study of the Monti di Campiglia. Structurally the mountain group is a compound horst. The central block, tapering northward, is the highest. It exposes mainly the lower part of the sequence (Jurassic): only in the southernmost part are remnants of the Liguride units preserved ('argille e calcari'). A small body of granite and several quartz porphyry dikes cut the Tuscan sequence limestones. In the eastern block, the upper part of the Tuscan sequence (Cretaceous-Lower Tertiary) is exposed, with a more extensive cover of Liguride allochthon.

The western block shows only a small exposure of Tuscan sequence, adjacent to its fault contact with the higher central block. This is covered by Liguride allochthon, which forms the surface of about half of the western block. In 1955 the Liguride ensemble had not yet been subdivided, and Giannini mapped all of this material as *argille scagliose* (scaly clays). In more recent map compilations (Bortolloti et al., 1970; Giannini et al., 1971) this material is assigned to two different units. In the western half of the western block, the Liguride units are covered by the Pliocene rhyolite of San Vincenzo.

The San Vincenzo Rhyolite

Two young magmatic provinces are recognized in the northern Apennines (Marinelli and Mittempergher, 1966; Marinelli, 1967; Bortolotti and Passerini, 1970). The Tuscan Province includes a number of small bodies of granitic intrusive rocks and acid volcanics, and has yielded age dates ranging from 7 to 0.43 m.y. (Barberi et al., 1971). The much larger volcanic districts of the Latian Province are dominantly of potassic trachyte composition and are almost entirely younger than 1 m.y. (Locardi et al., 1975; Alvarez, 1975).

The volcanic rocks, dikes, and pluton of the Monti di Campiglia are part of the Tuscan Province. Their petrography and chemistry have been studied by Barberi et al. (1967), who conclude that all three types were derived from an anatectic magma of quartz-monzonite composition. Depending on the classification scheme, the volcanic rocks of San Vincenzo would be considered either rhyolites or quartz latites.

Borsi et al. (1967) have reported the following K/Ar age determinations on rocks from the Monti di Campiglia:

Granite: 5.7 ± 0.16 m.y. (orthoclase),
Granitic porphyry: 4.3 ± 0.13 m.y. (whole rock),
Pegmatitic vein: 5.0 ± 0.15 m.y. (phlogopite),
San Vincenzo volcanite: 4.7 ± 0.14 m.y. (biotite).

Barberi et al. (1967, p. 679) point out that the 4.3 m.y. date is from a metasomatically altered dike, and therefore gives only a minimum age for the time of emplacement.

The San Vincenzo rhyolite covers several square kilometers, but much of this is brushy country with poor outcrop; the best exposures are in quarries. Access is further hampered by the fact that the woods are on private farms and hunting estates, stocked with wild boar. We were able to find 10 sites with fairly large outcrops in quarries, road cuts and a stream bed (Fig. 1) and at these we drilled 100 samples for rock-magnetic and paleomagnetic evaluation. Because of the thick Quaternary sedimentary overburden and absence of underlying, overlying or interbedded sediments, local tectonic correction at each site was not possible.

The most striking feature of the rhyolite in outcrop is a layering or pseudostratification marked by planes of flattened vesicles with a centimeter-scale spacing (Fig. 2). We interpret the layering as marking planes of concentrated simple shear strain during flow of the rhyolite. This is supported by (1) the elongation of the vesicles, (2) the presence in some places (e.g., site CM-2) of microbrecciated zones along the planes of pseudostratification and (3) the occasional presence of inclusions which have clearly been rolled. In small outcrops the layering generally shows a uniform orientation, but its attitude varies considerably form place to place, and in some of the larger quarry faces it is strikingly folded (Fig. 2).

The layering may be marking the forms of lava domes, and the presence of such domes is reported by Micheluccini (1964) and by Barberi et al. (1967). However, on the basis of our admittedly brief examination, we would interpret the layering as levels of vesicles that formed on surfaces of high simple shear strain as the viscous lava flowed, and which were deformed as the flowing

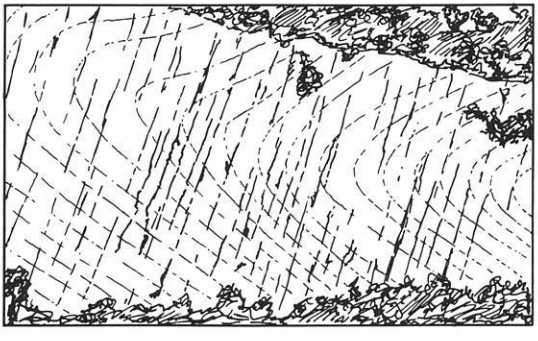

Fig. 2. Exposed face of the rhyolite in the abandoned quarry of site 3 (drawn from a photograph, looking NE). The curved flow lines are formed by layers of vesicles; the steep joint surfaces are tilted at a small angle from the vertical. The face is about 10–15 m high

continued. In this interpretation the large recumbent folds (Fig. 2) would have formed where the more viscous, frontal part of the flow was over-ridden and turned under as the rest of the flow continued to move.

Cooling joints are well developed in some exposures, for example locality CM-3, where they cut across the layering on both limbs of a recumbent fold of the layering (Fig. 2). As discussed below, the cooling joints are important, in that they provided us with a way of making a tectonic correction to our paleomagnetic data.

Rock Magnetism

Optical examination of polished sections was not particularly helpful in identifying the carrier of magnetization in the rock. The only opaque minerals observed were fairly coarse ilmenites and occasionally hematite. The nature and concentration of the visible grains can not account for the strong, stable magnetic character of the samples, which must be attributed therefore to very fine, sub-microscopic grain sizes. The magnetic mineralogy was investigated further by studying the acquisition of isothermal remanent magnetization (IRM), low-temperature behavior, and the alternating field (AF) demagnetization characteristics of IRM and the natural remanent magnetization (NRM).

IRM Acquisition

Selected samples from each site were progressively given IRM in ever-increasing magnetizing fields until saturation IRM was reached. The behavior of all the samples was remarkably similar, and their IRM acquisition curves fell between the two extreme cases illustrated in Fig. 3a. Between 85 and 95% of saturation IRM was reached in magnetizing fields of less than 0.2 T (2 kOe), and saturation was reached between 0.35 and 0.45 T (3.5 to 4.5 kOe). There were no indications of the presence of higher coercivity magnetic minerals. It therefore appears unlikely that the few coarse hematite grains observed optically can contribute appreciably to the natural remanence. The magnetic mineralogy is characterized by moderate coercivity carriers of remanence.

Low Temperature Studies

Nagata et al. (1964) have shown that it is possible to identify the magnetic minerals in a rock by observing the occurrence of low-temperature magnetic transitions during thermal cycling between liquid nitrogen temperature ($-196°$ C) and room temperature.

The sample was given an IRM in 1 Tesla at room temperature. Using a device described by Heiniger and Heller (1976) which allows continual monitoring of all three components of a remanence during thermal cycling, the magnetization was observed during cooling to $-196°$ C, and partial rewarming to

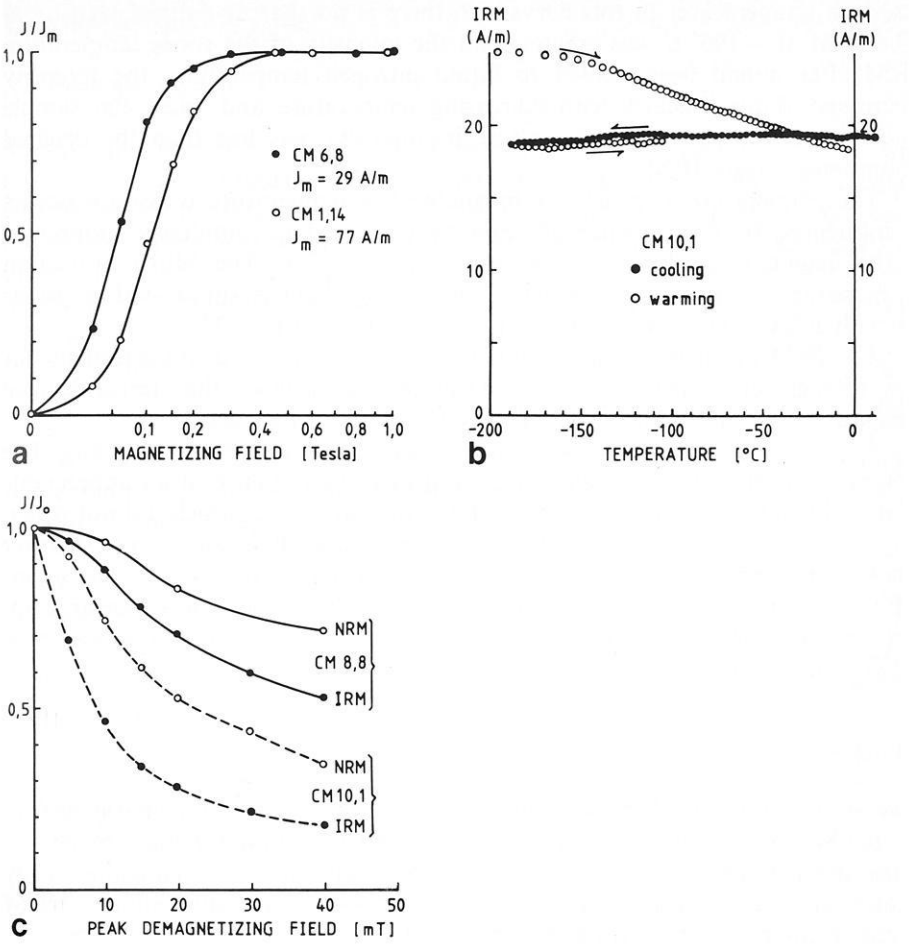

Fig. 3. a Acquisition of isothermal remanent magnetization (J), normalized in terms of the saturation *IRM* (J_m), for two representative samples. **b** Low temperature thermal cycling of *IRM*. *Solid points* represent intensities measured during cooling of room temperature *IRM*. *Open points* are values observed during rewarming of this *IRM*, and also during warming of an *IRM* given at low temperature (−196° C). **c** Normalized AF demagnetization curves for natural remanent magnetization (*NRM*) and isothermal remanent magnetization (*IRM*), showing the dominance of very fine grained carriers of remanence

about −105° C (Fig. 3b). Any component of the room temperature IRM carried by pure hematite would be lost at the Morin transition at about −20° C, and in coarse-grained magnetite a further change in magnetization should be observed at the magnetocrystalline anisotropy transition point (about −150° C for pure magnetite). Neither of these sharp transitions was observed; there was negligible change of remanence during cooling, or during rewarming to −105° C.

The sample was given a new IRM in an applied field of 1 T at liquid nitrogen temperature and the magnetization was monitored during re-warming

to room temperature. In this curve also there is no sharply defined transition. The IRM at $-196°$ C was greater than the intensity of the room temperature IRM after it had been cooled to liquid nitrogen temperature, the intensity decreased almost linearly with increasing temperature and when the sample had warmed up to room temperature its intensity was less than the original room temperature IRM.

The temperature at which the magnetite low-temperature transition occurs is influenced by the presence of impurity ions, and is completely suppressed if the magnetite grains are in the single domain size. The Morin transition in hematite is not greatly sensitive to particle size, but is suppressed in grains finer than 0.01 μm, or when the titanium content exceeds 0.3%.

The IRM acquisition curves and the absence of a Morin transition in our low temperature experiments are interpreted as evidence that ferromagnetic hematite is not an important magnetic constituent of the rock.

The room temperature IRM is unaffected by low temperature cycling. The absence of a magnetite transition argues against the presence of an appreciable multidomain fraction, in sympathy with the optical studies which did not reveal any visible magnetite grains. The low temperature IRM was much stronger than room temperature IRM; the difference is probably due to ultra-fine grains which are single domain at low temperature, and which become superparamagnetic on warming up to room temperature, causing a loss of low-temperature IRM in the process.

Domain State Test

Lowrie and Fuller (1971) pointed out that the AF demagnetization characteristics of thermo-remanent magnetization (TRM) and IRM in multidomain magnetite were distinctively different from those in single domain magnetite. They suggested a simple test by means of which the domain state of the NRM carrier in an igneous rock (in which the NRM was a TRM) could be determined. This is, that single domain TRM is more resistant than IRM to AF demagnetization, and multi-domain TRM is less resistant than IRM. This test becomes less clear-cut when a mixture of single and multidomain grains are present, and it is not clear how effective it is for pseudo-single domain grains.

AF demagnetization curves of representative specimens of the San Vincenzo rhyolite show that the NRM is clearly more resistant than IRM to this form of demagnetization (Fig. 3c). The NRM is therefore dominated by single domain carriers of remanence.

Summary of Rock Magnetism

The rock magnetic studies show that the magnetic mineralogy is dominated by a single phase, consisting of magnetite in very fine, sub-microscopic grain sizes, probably in the very stable single domain range. It is also possible that some of these grains extend into the pseudo-single domain range, which might account for the slight losses of remanence during the low temperature cycling.

Paleomagnetism

AF Demagnetization

The average intensity of the NRM of the San Vincenzo rhyolite was 0.72 A/m (7.2×10^{-4} G). The remanences were uniformly stable, with quite high median destructive fields averaging almost 40 *mT* (400 Oe.). One specimen from each of the 100 samples was progressively demagnetized in alternating magnetic fields up to at least 80 *mT*. Vector diagrams (Fig. 4) were used to determine the inclination and declination of the characteristic remanent magnetization (ChRM).

All samples were reversely magnetized. A slight instability was remarked during the initial cleaning steps, accompanied in a few samples by a slight increase in intensity as a low coercivity normal component was removed. Beyond about 15 *mT* all samples possessed very good directional stability, with a single stable component of remanence defined by straight lines to the origin for both inclination and declination.

Thermal Demagnetization

A number of specimens were thermally demagnetized using either the conventional, progressive (stepwise) technique, or a continuous observation technique.

Stepwise thermal demagnetization (Fig. 5a) showed negligible change of NRM intensity or direction below 200° C. A single component of magnetization, leading linearly to the origin in both inclination and declination parts of the vector diagram, characterized the temperature range from 400° to 580° C. A small component remaining at 580° C was completely eliminated by heating to 600° C, and probably represents a small error in temperature calibration. The blocking temperature spectrum is clearly dominated by the high temperature component between 400° and 600° C (Fig. 5a).

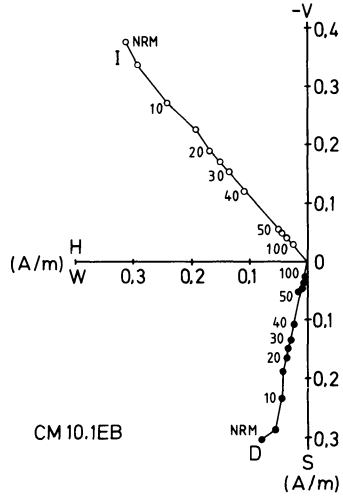

Fig. 4. Vector diagram illustrating the behavior of *NRM* during AF demagnetization. *Open points* are defined by the vertically upwards *(V)* and horizontal *(H)* components, and illustrate the variations of inclination. *Solid points* define south *(S)* and west *(W)* components and illustrate the variations of declination

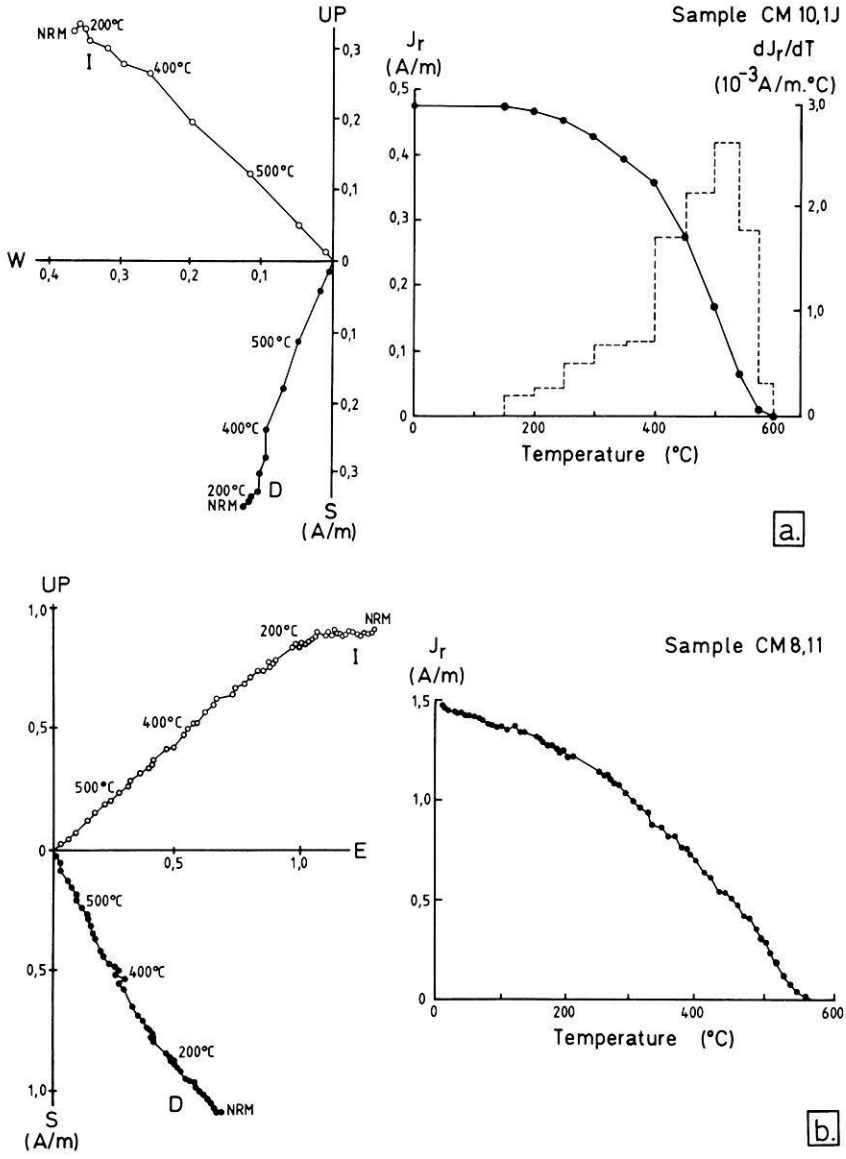

Fig. 5. a Step-wise thermal demagnetization of *NRM* (J_r). The dashed histogram is obtained by differentiating the intensity decay curve, and represents the blocking temperature spectrum. **b** Continuous thermal demagnetization of *NRM*. As in the stepwise example, the remanence above 400° C consists of a single stable component. Vector diagrams: as in Fig. 4

The continuous thermal demagnetization method (Heiniger and Heller, 1976) enables the determination of all three components of remanence at any temperature during heating up to the Curie temperature. An almost continuous record of the intensity and direction of the remanence is obtained. The method has the disadvantage that both decay of spontaneous magnetization and thermal

unblocking of remanence are observed as a joint effect, but an advantage is that mineralogical changes can be recognized. The technique can be a powerful tool for unravelling the magnetic composition of complex rocks in which metastable magnetic minerals are present (see Heller, 1978).

The continuous demagnetization curves (Fig. 5b) are very similar to the progressive demagnetization curves, and indicate that no marked mineralogical change occurs during heating. The slight change of direction below 200° C is exaggerated by the accompanying reduction of spontaneous magnetization, there is again a slightly unsettled component between 200° and 400° C, and from 400° C until the magnetization disappears at about 560° C there is a single stable component of magnetization.

Characteristic Remanent Magnetization (ChRM)

The remanent magnetizations have a single, stable component after demagnetizing in fields above 20 mT or in temperatures above 400° C. The directions of this ChRM component were averaged using Fisher statistics for all sites. The site mean directions are given in Table 1 and Fig. 6a.

The data are extremely tightly clustered at each site, and the 10 site mean directions are also closely grouped. The overall mean direction for the formation has declination 160°, inclination −45°, and the circle of 95% confidence of this mean has radius 6.6°.

The negative polarity found in these rocks agrees well with that expected for their radiometric age of 4.7 m.y. On the geomagnetic reversal time scale (LaBrecque et al., 1977) this is appropriate to the reversed polarity zone near to the base of the Gilbert reversed chron. The direction expected for this age should not be very different from the reversed direction of the present axial dipole field, with declination 180° and inclination −62°. The observed formation mean direction is 21° away from the expected direction.

Determination of the Tectonic Correction

The absence of stratified rocks in association with the rhyolite prevented us from making a standard bedding correction, but the presence of cooling joints in the rhyolite suggested that we might correct for post-eruption tilting by restoring the joint-bounded columns to a vertical orientation. We recognize that not all cooling joints are vertical when formed, but the consistency of orientation of the columns throughout the rhyolite mass makes an original vertical orientation quite likely.

The available number, degree of exposure and quality of the joint surfaces were variable. At each of the four quarry sites we measured the orientations of 20 cooling joint surfaces (Fig. 7a). A great circle (the π-plane) was fitted to the set of poles at each site using the method given by Ramsay (1967). The pole of the π-plane (D_p, I_p) and the angular standard deviation of the measured poles from the best-fitting π-plane (δ) were computed. The degree

Table 1.

Site number	Number of samples	k	Declination	Inclination	α_{95}
1	14	369	154	−48	2.1
2	9	948	165	−42	1.7
3	8	1383	171	−55	1.5
4	7	424	159	−40	2.9
5	5[a]	680	137	−43	2.9
6	8	1022	156	−35	1.7
7	10	102	173	−49	4.8
8	11	240	156	−41	3.0
9	10	609	148	−42	2.0
10	15	678	184	−45	1.5
Site mean	10	54	160	−45	6.6

[a] Three samples rejected from unsafe (displaced) outcrop in stream bed

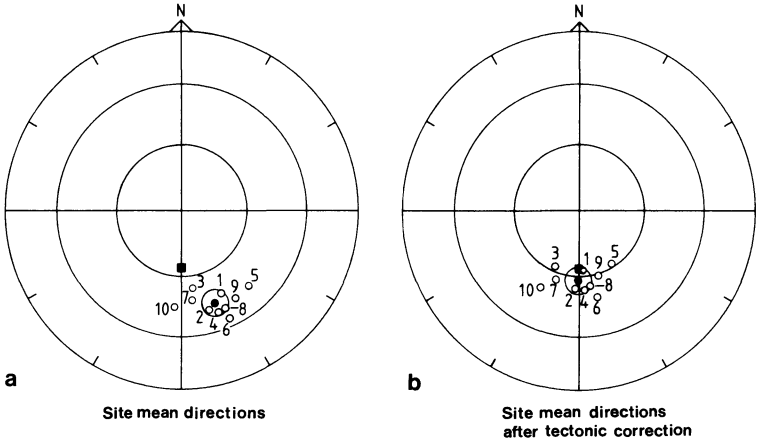

Fig. 6. a Stereographic projection of the site mean directions of the characteristic remanence (ChRM). *Solid square:* direction of reversed axial dipole field. *Small circle:* circle of 95% confidence of the overall mean direction *(solid circle)*. **b** The directions of **a** after making a tectonic correction by rotating the pole of the π-plane (Fig. 7b) to the vertical

of fit was good at all sites (δ less than 10°), and the poles of the π-planes were very similar. Differences between the poles could be due to local differences in tilt from site to site. However, we were able to determine a π-plane pole at only four of the ten sites, and this did not allow us to make individual tectonic corrections at each site.

Instead, we note that the differences between the π-plane poles are small, and combine the 80 measured poles to columnar joint surfaces at all four sites to obtain a single π-plane (Fig. 7b). The pole of this plane has azimuth 300° and inclination of 70°. The tectonic correction for all paleomagnetic sites consists of restoring this pole, which corresponds to the mean intersection line of the

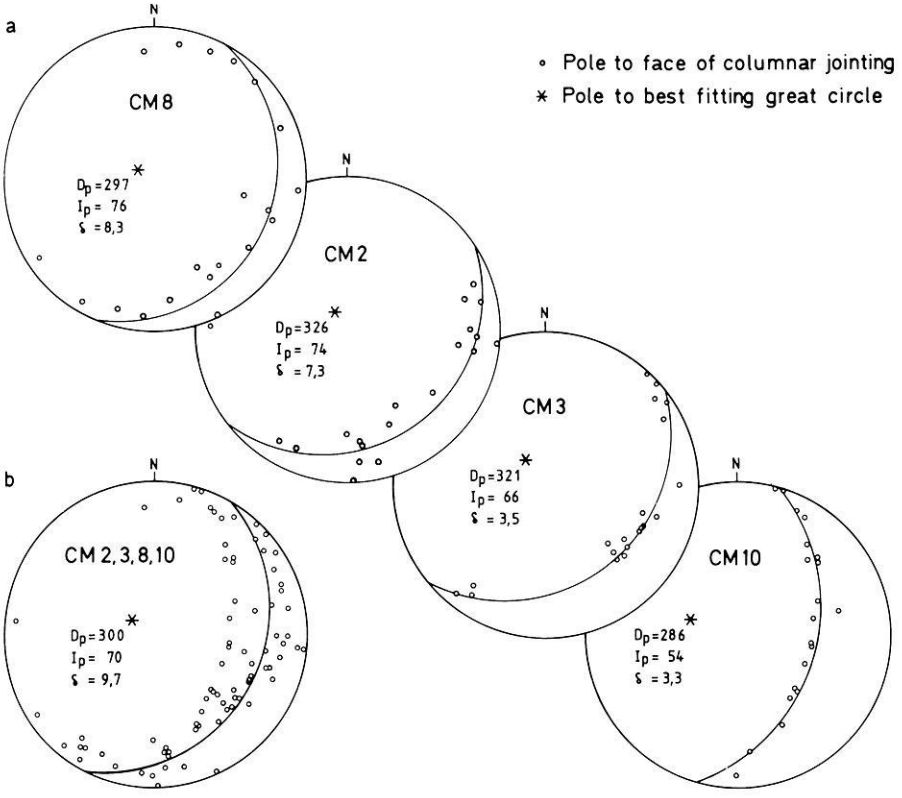

Fig. 7. a At sites 2, 3, 8, and 10 in active or abandoned quarries, the poles to 20 measured joint surfaces form a girdle. The best fitting great circle (π-plane) has its pole at (D_p, I_p); the goodness of fit is expressed by the average angular deviation from the π-plane (δ). **b** The combined data (80 poles) from all 4 sites define a π-plane whose pole has azimuth 300° and inclination 70° to the horizontal

joints, to the vertical. When this is done, the mean paleomagnetic direction has declination 179°, inclination −58°, and the reversed axial dipole direction falls within the circle of confidence of the corrected mean (Fig. 6b).

VGP Positions and Dispersion

The normal paleomagnetic pole position calculated from the uncorrected formation mean direction lies at 67°N 242°E and the principal axes of the oval of 95% confidence are $\delta p = 5.2°$, $\delta m = 8.3°$. The corresponding pole position for the tectonically corrected formation mean is 84°N 240°E ($\delta p = 7.2°$, $\delta m = 9.7°$).

If the virtual geomagnetic pole positions (VGP) computed from the uncorrected mean direction of each site are averaged they give a pole position at 67°N 241°E, and the circle of 95% confidence has radius $\alpha_{95} = 7.7°$. The corresponding

pole position for tectonically corrected data is 84°N 246°E ($\alpha_{95}=7.7°$). The angular dispersion of this distribution (given by $\alpha=81/\sqrt{k}$, where k is the best estimate of Fisher's precision parameter) was found to be 12.8°.

Models of the secular variation of the geomagnetic field (Cox, 1970) recognize two contributions to the angular dispersion of VGP. The first of these is wobble of the geomagnetic dipole about its mean (axial) position; this effect has an amplitude of about 11° and is independent of the latitude of the observation. The second contribution derives from secular variation of the non-dipole field and is latitude-dependent (Creer, 1962). For the latitude of our sampling sites (43.1°N) the non-dipole contribution to the angular dispersion of VGP ought to amount to about 10.8°. The observed dispersion in our study is slightly too high to be accounted for by the nondipole field alone. If dipole wobble is incorporated with non-dipole effects secular variation models *C* and *D* (Cox, 1970) predict a dispersion of 16.0° to 16.4°, considerably larger than that observed.

Discussion

The San Vincenzo rhyolite has a single, stable component of natural remanent magnetization. Magnetic mineralogy studies indicate that the NRM is probably carried by single domain or pseudo single domain magnetite. The remanence is probably original; there are no rock magnetic indications that it has been altered since formation of the lava.

Although the polarity of NRM corresponds to expectation for the appropriate position in the Gilbert reversed chron at the base of the Pliocene, the uncorrected mean direction has an inclination that is lower than expected, and a declination that is rotated by 20° in a counterclockwise sense.

The observed VGP dispersion is indicative of incomplete averaging of secular variation effects. This thick lava would not cool rapidly except at its surface; it evidently took long enough passing through the broad range of blocking temperatures (Fig. 5a) to record a variety of total field directions. The observed VGP dispersion is large enough to account for averaging of the non-dipole field but not of the total field. It is probable that at least part of the 21° discrepancy between the observed formation mean direction and the reversed axial dipole field direction can be accounted for in this way. However, part must also derive from other causes, probably tectonic in origin.

Examination of the local tectonic situation indicated that some compensation for possible rotation about a horizontal axis would be necessary. The only geological indicator that could be used was an internal structural feature of the lava, the attitude of cooling joint surfaces. By measuring the poles to these joint planes, and determining the pole to their π-planes, an overall tectonic correction for the region was obtained, assuming that the joints were vertical when formed.

On application of the tectonic correction the mean direction was found to be not significantly different from that of the expected reversed field. Therefore, any rotation of the northern part of the Italian peninsula, as proposed

by VandenBerg (1979) for the Late Tertiary, was completed by the time of formation of the San Vincenzo rhyolite, 4.7 m.y. ago, in the earliest Pliocene.

Acknowledgements. We thank Professor Enzo Giannini for an introduction to the San Vincenzo area, and Marcia Lowrie for significant contributions to sample measurement and manuscript preparation. Constructive criticism of the manuscript was received from Dr. R. Kligfield and Dr. F. Heller. This research was partially supported by NSF grants GA-39151 and EAR-76-03272.

References

Alvarez, W.: The Pleistocene volcanoes north of Rome. In: Geology of Italy, C. Squyres, ed.: pp. 355–377. Earth Sci. Soc. Libyan Arab Rep. 1975

Alvarez, W., Lowrie, W.: Upper Cretaceous magnetic stratigraphy at Moria (Umbrian Apennines, Italy): confirmation of the Gubbio section. Geophys. J. R. Astron. Soc. **54**, 1–17, 1978

Barberi, F., Innocenti, F., Mazzuoli, R.: Contributo alla conoscenza chimico-petrografica e magmatologica delle rocce intrusive, vulcaniche e filoniane del Campigliese (Toscana). Mem. Soc. Geol. Ital. **6**, 643–681, 1967

Barberi, F., Innocenti, F., Ricci, C.A.: La Toscana meridionale – Il magmatismo. Rend. Soc. Ital. Mineral. Petrol. **27**, Fascicolo Speciale, 169–210, 1971

Borsi, S., Ferrara, G., Tongiorgio, E.: Determinazione con il metodo del K/Ar delle età delle rocce magmatiche della Toscana. Boll. Soc. Geol. Ital. **86**, 403–410, 1967

Bortolotti, V., Passerini, P.: Development of the Northern Appenines geosyncline – Magmatic activity. Sediment. Geol. **4**, 599–624, 1970

Bortolotti, V., Sagri, M., Abbate, E., Passerini, P.: Geological map of the Northern Apennines and adjoining areas, 1:500,000, 1969 Sediment. Geol. **4**, No. 3–4, 1970

Channell, J.E.T.: Umbrian palaeomagnetism and the concept of the African Adriatic promontory. Mem. Soc. Geol. Ital. **15**, 119–128, 1976

Channell, J.E.T., Horvath, F.: The African/Adriatic promontory as a palaeogeographic premise for Alpine orogeny and plate movements in the Carpatho-Balkan region. Tectonophysics **35**, 71–101, 1976

Channell, J.E.T., Lowrie, W., Medizza, F., Alvarez, W.: Palaeomagnetism and tectonics in Umbria, Italy. Earth Planet. Sci. Lett. **39**, 199–210, 1978

Channell, J.E.T., Tarling, D.H.: Palaeomagnetism and the rotation of Italy. Earth Planet. Sci. Lett. **25**, 177–188, 1975

Cox, A.: Latitude dependence of the angular dispersion of the geomagnetic field. Geophys. J. R. Astron. Soc. **20**, 253–269, 1970

Creer, K.M.: The dispersion of the geomagnetic field due to secular variation and its determination for remote times from paleomagnetic data. J. Geophys. Res. **67**, 3461–3476, 1962

Elter, P., Giglia, G., Tongiorgi, M., Trevisan, L.: Tensional and compressional areas in the recent (Tortonian to present) evolution of the Northern Apennines. Boll. Geofis. Teor. Appl. **17**, 3–18, 1975

Giannini, E.: Geologia dei Monti di Campiglia Marittima (Livorno). Boll. Soc. Geol. Ital. **24**, 1–78, 1955

Giannini, E., Lazzarotto, A., Signorini, R.: Carta geologica della Toscana meridionale, 1:200,000, 1971. Rend. Soc. Ital. Mineral. Petrol. **27**, Fascicolo speciale, 1971

Heiniger, Ch., Heller, F.: A high temperature vector magnetometer. Geophys. J. R. Astron. Soc. **44**, 281–287, 1976

Heller, F.: Rockmagnetic studies of Upper Jurassic limestones from Southern Germany. J. Geophys. **44**, 525–543, 1978

Klootwijk, C.T., VandenBerg, J.: The rotation of Italy: preliminary palaeomagnetic data from the Umbrian sequence, northern Apennines. Earth Planet. Sci. Lett. **25**, 263–273, 1975

LaBrecque, J.L., Kent, D.V., Cande, S.C.: Revised magnetic polarity time scale for Late Cretaceous and Cenozoic time. Geology **5**, 330–335, 1977

Locardi, E., Funiciello, R., Lombardi, G., Parotto, M.: The main volcanic groups of Latium (Italy). Rome: Guidebook for the International Colloquium of Planetary Geology 32 p. 1975

Lowrie, W., Alvarez, W.: Rotation of the Italian peninsula. Nature **251**, 285–288, 1974
Lowrie, W., Alvarez, W.: Paleomagnetic evidence for rotation of the Italian peninsula. J. Geophys. Res. **80**, 1579–1592, 1975
Lowrie, W., Alvarez, W.: Upper Cretaceous-Paleocene magnetic stratigraphy at Gubbio, Italy, III: Upper Cretaceous magnetic stratigraphy. Geol. Soc. Am. Bull. **88**, 374–377, 1977a
Lowrie, W., Alvarez, W.: Late Cretaceous geomagnetic polarity sequence: detailed rock- and palaeomagnetic studies of the Scaglia Rossa limestone at Gubbio, Italy. Geophys. J. R. Astron. Soc. **51**, 561–581, 1977b
Lowrie, W., Fuller, M.D.: On the alternating field demagnetization characteristics of multidomain thermoremanent magnetization in magnetite. J. Geophys. Res. **76**, 6339–6349, 1971
Marinelli, G.: Genèse des magmas du volcanisme plio-quaternaire des Apennins. Geol. Rundschau **57**, 127–141, 1967
Marinelli, G., Mittempergher, M.: On the genesis of some magmas of typical Mediterranean (Potassic) suite. Bull. Volcanol. **29**, 113–140, 1966
Martinis, B., Pieri, M.: Alcune notizie sulla formazione evaporitica del Triassico superiore nell'Italia centrale e meridionale. Mem. Soc. Geol. Ital. **4**, 523–579, 1964
Micheluccini, M.: Studio chimico-petrografico delle vulcaniti del Campigliese. University Pisa; Thesis-Lauria (Geology) 44 p., 1964
Nagata, T., Kobayashi, K., Fuller, M.D.: Identification of magnetite and hematite in rocks by magnetic observation at low temperature. J. Geophys. Res. **69**, 2111–2120, 1964
Ramsay, J.G.: Folding and fracturing of rocks. 568 p. New York: McGraw Hill 1967.
Roggenthen, W., Napoleone, G.: Upper Cretaceous-Paleocene magnetic stratigraphy at Gubbio, Italy, IV: Upper Maastrichtian-Paleocene magnetic stratigraphy. Geol. Soc. Am. Bull, **88**, 378–382, 1977
VandenBerg, J.: Paleomagnetism and the changing configuration of the western Mediterranean area in the Mesozoic and early Cenozoic eras. Geol. Ultriectina (Holland) No. **20**, 179 pp. 1979
VandenBerg, J., Klootwijk, C.T., Wonders, A.A.H.: Late Mesozoic and Cenozoic movements of the Italian peninsula: further paleomagnetic data from the Umbrian sequence. Geol. Soc. Am. Bull. **89**, 133–150, 1978

Received May 8, 1979; Revised Version June 19, 1979;
Accepted June 19, 1979

J. Geophys. 45, 433–446, 1979

Journal of Geophysics

On the Presence of Titanomagnetite in Basalts

C. Radhakrishnamurty[1], E.R. Deutsch[2], and G.S. Murthy[2]

[1] Tata Institute of Fundamental Research, Bombay 5, India
[2] Geomagnetic Research Laboratory, Physics Department, Memorial University of Newfoundland, St. John's, Canada

Abstract. Observed magnetic properties such as the apparent Curie point of magnetite occurring in association with titanium in basalts are usually explained on a titanomagnetite solid-solution model. A possible alternative is to invoke grain size effects, for example if very fine, stable single-domain (SD) particles of *magnetite* become superparamagnetic on heating to temperatures several hundred degrees below the Curie point of magnetite. It is shown that measurement of the magnetic hysteresis at different field strengths and temperatures may enable one to distinguish between these alternatives. Moreover, magnetic properties due to multi-domain (MD) magnetite in rocks should be distinguishable from those due to MD titanomagnetite, for example in measurements of the temperature dependence of low-field susceptibility. Extensive studies carried out with these techniques on basalts from different continents and oceans showed surprisingly that a magnetic behaviour attributable to 'true' titanomagnetite was very rare in the continental samples. In only one case of a young (< 30,000 years old) marine pillow basalt were the properties of the dominant magnetic mineral found to be compatible with SD *titanomagnetite*. These results can be interpreted in terms of a possible compositional instability of original titanomagnetites with time and of associated changes in the effective grain size and magnetic properties of basalts.

Key words: Titanomagnetites – Magnetic domain state – Magnetic granulometry – Basalts – Curie points.

1. Introduction

From studies on synthetic samples, it has long been known (e.g., Chevallier et al., 1955; Uyeda, 1958) that iron-titanium oxides form series of solid solutions of which titanomagnetite (TM) has the most important direct bearing on the understanding of the magnetic properties of basalt. The magnetic properties of oxidized or cation-deficient titanomagnetites, sometimes called titano-

0340-062X/79/0045/0433/$02.80

maghemites (TMh), have been studied, also on synthetic samples, as a function of Ti content and degree of oxidation (e.g. Readman and O'Reilly, 1972).

Serious difficulties may be encountered in applying these solid-solution properties based on synthetics to actual rocks. For example, Mössbauer studies by Jensen and Shive (1973) of magnetite-rich ($x \leqq 0.20$) synthetic TM have suggested that most of the titanium resides in submicroscopic clusters of Ti-rich material surrounded by nearly pure magnetite, and that the size and composition of these clusters may be affected by the method of sample preparation. Also, attempts by several workers (Ade-Hall, 1964; Smith, 1967; Creer, 1971) to correlate the Curie points (T_c) of basalts determined by experiment with those calculated from chemical composition of the magnetic minerals have revealed large discrepancies. For one particular synthetic TM of composition 0.6 $Fe_2TiO_4 \cdot 0.4\ Fe_3O_4$ (hereafter called TM60) a scatter of 70° C in T_c data of different workers was reported (Hauptman, 1974). Even when only one magnetic mineral is present, such uncertainties could result from grain-size effects (Radhakrishnamurty et al., 1972); thus if the magnetite or TM occurs as very fine particles dispersed in the basalt, the loss of ferromagnetic properties observed at a relatively low temperature may be partly or entirely due to thermal agitation, as distinct from the disappearance of spontaneous magnetization. Then T_c is an apparent Curie point rather than the true Curie point corresponding to some TM mineral composition.

In this paper we propose a few criteria for distinguishing the presence of 'true' (solid-solution) TM from magnetite in titaniferous basalts, and we show from measurements on nearly 400 continental and oceanic basalts that cases of magnetic behaviour which can be attributed unquestionably to the presence of true TM were virtually absent. Unfortunately, this very fact makes it difficult to provide an adequate experimental test of the above-mentioned criteria, which therefore remain somewhat speculative.

2. Curie Points in Basalts

The Curie point is one of the important parameters for ferromagnetic materials and it can be determined to a very high degree of accuracy in the case of pure metals like iron, cobalt and nickel, or of stoichiometric compounds such as magnetite. For magnetic alloys it may not be possible to measure T_c as accurately, because minor variations in synthesising conditions could cause variations in observed T_c values of a few degrees between different samples. In the case of rocks containing magnetic minerals having a broad blocking temperature spectrum, the measurement of T_c may be subject to greater errors. Sometimes the procedure of heating rocks to determine the Curie points of the minerals in them will cause progressive and irreversible changes whereby any values experimentally obtainable may have an ambiguous relationship to the original minerals.

The two most common methods for the determination of T_c are (i) measurement of temperature dependence of saturation magnetization (J_s) or maximum

undersaturated magnetic moment (M) of the sample in fields of a few thousand oersteds, referred to as the $J_s - T$ *or* $M - T$ method, and (ii) study of thermal variation of susceptibility (k) measured in low fields and termed the $k - T$ method. In the $J_s - T$ or $M - T$ method a signal proportional to J_s which decreases with increasing T for a given material is measured, for example in Curie point balances. In the $k - T$ method the measurement involves a signal that sometimes increases with T and attains a peak value just below T_c because of the Hopkinson (1889) effect. Only the $J_s - T$ ($M - T$) methods will generally ensure that the Curie points measured are representative of the medium to high coercive force (H_c) fraction. However, $k - T$ curves can be highly diagnostic of the properties especially of soft components. Since basalts commonly exhibit a broad H_c spectrum of magnetite or TM, the most effective procedure for obtaining the Curie points of two or more components present in a sample is to employ high-field and low-field measurements (including those of hysteresis) jointly. Successful combined applications of these methods to mixed-component basalts have been reported (Radhakrishnamurty and Deutsch, 1974; Deutsch and Pätzold, 1976; Murthy et al., 1976).

3. Effects of Oxidation and Grain Size on Curie Point

In view of the widespread occurrence of a mineral with composition around TM60 in marine basalts, its magnetic properties have special significance for understanding marine magnetic anomalies. It is also important to know how TM60 alters and what the alteration products are, for a proper interpretation of magnetic anomalies associated with somewhat weathered rocks. In the work of Ozima et al. (1968) and Ozima and Larson (1970) it is implied that TM and TMh are distinguishable by heating. From studies of synthetic samples they conclude that heating stoichiometric TM's to 600° C in either air or vacuum tends to produce nearly reversible $J_s - T$ curves, whereas in the case of TMh such heating produced a sharp irreversible increase of both J_s and T_c. Although these authors showed that this criterion worked in some marine basalts, it is doubtful whether it applies to all basalts, especially when the moisture and gas content of different samples could vary widely.

It is, in any case, a widely observed fact (Wilson and Smith, 1968; Ozima and Larson, 1970) that the thermomagnetic curves of many basalts are highly irreversible, often with T_c increasing to 580° C or higher temperatures upon heating. Such behaviour is consistent with relatively unoxidized magnetite or TM becoming (more) cation-deficient to produce CD magnetite, TMh or maghemite as the case may be.

When a magnetic material can be obtained in bulk form and remains unchanged on heating, its T_c can be determined accurately. This is the case even when large multidomain (MD) grains of such a sample are dispersed in a non-magnetic matrix. However, if the grains are very fine single-domains (SD), then thermal disordering might have caused the blocking temperatures (T_b) to be substantially lower than T_c; in that case, measurement of magnetization of the grains at temperatures much higher than T_b may be difficult and

hence determining T_c may involve some uncertainty. That grain-size effects can be important is underlined in an extreme example: Sato et al. (1971) report that the apparent magnetization of 150 Å and 100 Å grains of manganese ferrite and $Mn_{0.6}Co_{0.4}Fe_2O_4$, respectively, was zero in both cases even in an applied field of 9.2 Koe when measured at room temperature where these materials are ferrimagnetic in bulk.

In the case of magnetite, Feitknecht and Gallagher (1970) postulated that heating to 200° to 300° C provokes ferrous ion migration and this mechanism causes oxidation of small grains to maghemite. One consequence of this cation migration in magnetite on heating is that, whereas it may interfere with magnetization measurements on fine grains at high temperature, it will have negligible effect in large grains and hence should not impede a precise determination of T_c based on large grains. A far-reaching implication of this phenomenon is that it establishes a measurable criterion for distinguishing MD magnetite from MD titanomagnetite dispersed in rocks (see below). Another important aspect of heating magnetite grains is that a protective coating of hematite may form on the surface of the grains and complete conversion to hematite is prevented even by prolonged heating in air. This mechanism could account for the observation that some basalts are affected very little in their magnetic properties even after being heated in air at 100° C for 24 h (Radhakrishnamurty and Sahasrabudhe, 1965).

The above features need careful consideration, and grain size as well as oxidation effects on the observed magnetic properties of basalts have to be recognized before these can be interpreted in terms of TM or TMh solid solution models.

4. Criteria for Distinguishing MD Magnetite From MD Titanomagnetite

In Fig. 1, a $k-T$ curve characteristic of large MD grains of magnetite (Radhakrishnamurty and Deutsch, 1974) is compared with that inferred for a titano-

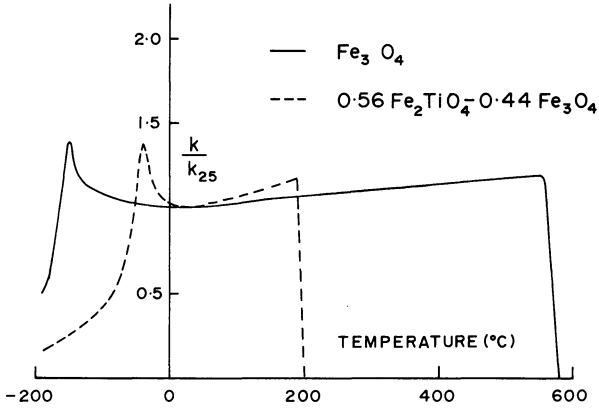

Fig. 1. Thermal variation of susceptibility for large multidomain grains (schematic). The magnetite curve is a composite based on experimental results from magnetite ore and very old basalts. The titanomagnetite curve is constructed from data available in the literature

magnetite of composition 0.56 $Fe_2TiO_4 \cdot 0.44$ Fe_3O_4 ('TM56'). The magnetite curve (solid) is based on combined experimental observations on magnetite ore and on very old basalts. The curve is nearly or (as depicted) entirely reversible and shows an abrupt drop of k at the Curie point of magnetite and a sharp peak near the isotropic point ($-155°$C) that would be suppressed in SD magnetite owing to the predominance of shape anisotropy over other forms of anisotropy. Also, with SD grains, the curve may be more highly irreversible and its high-temperature portion should be less blocky. The 'magnetite' curve is almost identical to that obtained (Murthy et al., 1976) on a sample of young (9 m.y.) peridotite from Leg 37 of the Deep Sea Drilling Project, which exhibited MD characteristics in a Lowrie-Fuller test and could therefore be regarded as material in a 'true' multi-domain rather than pseudo single-domain (PSD) state (Johnson et al., 1975).

The $k-T$ curve for TM56 (dashed line) is constructed from magnetic data available for it in the literature and by making use of the analogy it bears to magnetite. Our reason for depicting here an inferred rather than experimental curve is simply that curves of this type based on synthetic MD titanomagnetite, as distinct from magnetite, apparently have never been reported in the literature. A possible cause of this lack of data is suggested by the results of some recent experiments we undertook using coarse, single-phased synthetic TM's, in which the samples failed to show obvious MD properties. That the dashed curve nevertheless conforms to a realistic expectation for natural rock is clear from the known properties of the MD state and from the measured variation of isotropic and Curie points in titanomagnetite. Thus Syono and Ishikawa (1964) obtained a set of isotropic temperatures on homogeneous TM crystals grown in the laboratory, including a value of about $-40°$ C for TM56. Curie point values of TM56 or of material close to this composition quoted by different workers (see Hauptman, 1974) vary over a range of about 50° C and for the present purpose T_c is taken as 200° C. By further extrapolation, one could expect similar curves for other members of the TM series with k-peaks at their respective isotropic points, though in TMh the transition is probably absent (see 'Discussion'). Because of the expected appearance of such peaks in the curves of TM56 and similar material, it is again implicit that they apply only to a truly multi-domain state.

It follows that, *in the multi-domain state only,* variations of (i) T_c and (ii) the isotropic point observed in $k-T$ curves can serve as two criteria for distinguishing magnetite from titanomagnetite in rocks. Widely different intermediate members of the TM series, if they occur as MD's, could be similarly distinguished from one another. Single-domain criteria are discussed later.

5. Results of Measurements

In a study at the Tata Institute and Memorial University, several hundred basalt samples from different parts of the world were subjected to measurements of thermomagnetic and hysteresis properties.

The $k-T$ curves were obtained on standard cylindrical specimens of about 20 g, heated and cooled in air in the temperature range $-196°$C to 650°C, and the signal noted at regular intervals. Using the equipment described earlier (Radhakrishnamurty and Likhite, 1970; Pätzold, 1972), the procedure was to measure k first in the range $-196°$C to 20°C during the natural heating of samples after immersion in liquid nitrogen. Between 20° and 650°C both heating and cooling curves are traced at rates of 6–10°C per minute, then the -196

to 20° C measurement is repeated so that each 'cooling' curve actually consists of cooling and heating sections coinciding at 20° C. Since in this way the heating rate is not controlled between −196° and 20° C, some rocks, especially among those with low (≦300° C) apparent Curie points, were treated more rigorously below 20° C so as to produce both cooling and heating curves, each kind with rate-control. The technique is standard, using a furnace and cool N_2 gas under regulated pressure down to −180° C, whereby cooling or heating can be slowed as desired so as to equalize temperatures over the specimen volume. This was important near the isotropic point of magnetite (−155° C) or titanomagnetite where, in the $k-T$ curves, the susceptibility peak characteristic of MD material (Fig. 1) might be suppressed by the presence of significant thermal gradients within the specimen. Careful application of these procedures has satisfied us that, in all cases where diagnostic features such as transition peaks were not observed, their absence is due to other than experimental causes.

Rayleigh loops (hysteresis in 10 oe) and high-field (1500 oe) hysteresis at 25° C and −196° C for all the samples were also observed, using instruments

Table 1. Prominent magnetic state of some submarine and continental basalts samples. None of the samples indicated a magnetic behaviour unambiguously attributable to a titanomagnetite. Most of the samples are mixtures of two or three states, but a sample is placed under the inferred most prominent state of the mixture. MD: multi-domain, SD: single-domain, SP: superparamagnetic and CD: (strongly) cation-deficient state of magnetite grains. In some cases (e.g. Refs. A,B), column 3 cites fewer samples than were reported in the original study, after omitting those whose magnetic state could not be clearly established

Formation or source	Age	Number of samples (+) or sites (@)	Prominent magnetic state				Ref.
			MD	SD	SP	CD	
1	2	3	4	5	6	7	8
Leg 34, DSDP	15, 30, and 40 m.y.	37+	–	6	31	–	A
Leg 37, DSDP	3.5, 10, and 13 m.y.	18+	1	9	1	7	B
Columbia River basalts	Miocene	8+	–	2	6	–	C
Western Iceland basalts	12 m.y.	29+	–	11	10	8	D
Northern Ireland basalts	Tertiary	26+	–	3	15	8	D
Hungary basalts	Tertiary	6+	–	1	4	1	D
Mull dykes	Tertiary	16@	–	6	9	1	D
Mull and Skye basalts	Tertiary	82+	6	24	35	17	D
Dykes, England and Wales	Tertiary	11+	–	3	4	4	D
Deccan traps	60 to 65 m.y.	36@	–	3	12	21	C
Hungary basalts	Cretaceous	6+	–	3	2	1	D
Rajmahal traps	Cretaceous	17@	–	11	4	2	C
Scotland basalts	Carboniferous	24+	5	7	–	12	D
Newfoundland ophiolites	Ordovician	56+	31	1	23	1	C
Bijiwar traps	Precambrian	6@	5	–	–	1	D
Cuddapah traps	Precambrian	15@	14	–	–	1	C
Basic dykes, India	Precambrian	6@	6	–	–	–	C

A: Deutsch and Pätzold (1976)
B: Murthy, Deutsch, and Pätzold (1976)
C: Radhakrishnamurty and Deutsch (1974)
D: Radhakrishnamurty, Raja, Likhite, and Sahasrabudhe (1972)

and procedures given in earlier papers (Likhite and Radhakrishnamurty, 1966; Radhakrishnamurty, Likhite and Sastry, 1971). M−T curves were obtained on powders heated in a vertical Curie point balance in air at 1300 oe (Deutsch and Pätzold, 1976), as a supplementary study.

A striking result of these measurements, using the criteria proposed above, is that not a single $k-T$ curve that could be attributed to large MD grains of titanomagnetite was found. Instead almost all old (Precambrian) basalts and some younger ones showed characteristic MD curves with Curie points and isotropic points of magnetite (Fig. 1, solid curve). A summary of available results showing the inferred domain states in these basalts is given in Table 1. These results suggest that large TM grains behaving magnetically as multi-domains occur very rarely in basalts.

Next, a detailed study was made of two marine basalt samples dredged from the Mid-Atlantic Ridge 45° N and kindly provided to us by Dr. J.M. Hall of Dalhousie University along with photomicrographs of their polished surfaces (Fig. 2). Figure 2a is that of sample HU56-3-20 taken from a pillow basalt of age less than 30,000 years (reported age $12{,}000 \pm 18{,}000$ years; Aumento, 1969) and Fig. 2b is for a sample, HU74-003-6-1, believed to have come from the interior of a flow whose age may be a few million years. Both the photographs were taken at $\times 900$ in oil. The opaque grains in both the samples have compositions around that of TM60 (J.M. Hall, private communication, 1974).

In Fig. 3 the $k-T$ curves and Rayleigh loops of the two samples are given. It is interesting to note that, while the $k-T$ curves are similar in the 20°–600° C range, HU74-003 shows a Rayleigh loop (Fig. 3d) and the other sample (Fig. 3c) does not.

Figure 4 shows the high-field hysteresis loops of the samples both at 25° C and −196° C. Sample HU56-3 is weak and hence parameters like coercive force (H_c) and relative remanence (ratio of remanent to maximum intensity, J_r/J_m) obtainable from the hysteresis loops are approximate. However, it is clear that the loop characters of the two samples are distinctly different from

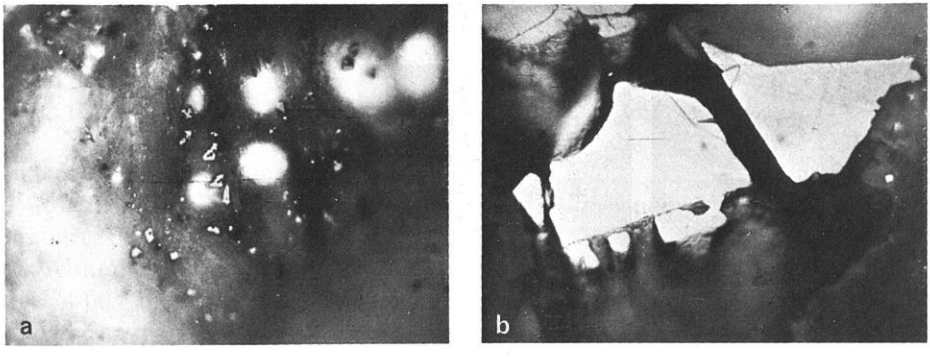

Fig. 2a and b. Photomicrographs of polished surfaces of two optical marine basalt samples, taken at $\times 900$ in oil. (*a*) is for a pillow basalt, HU56-3-20 and (*b*) for HU74-003-1, a fragment believed to have come from the interior of a flow. The samples and photomicrographs were provided by Dr. J.M. Hall of Dalhousie University

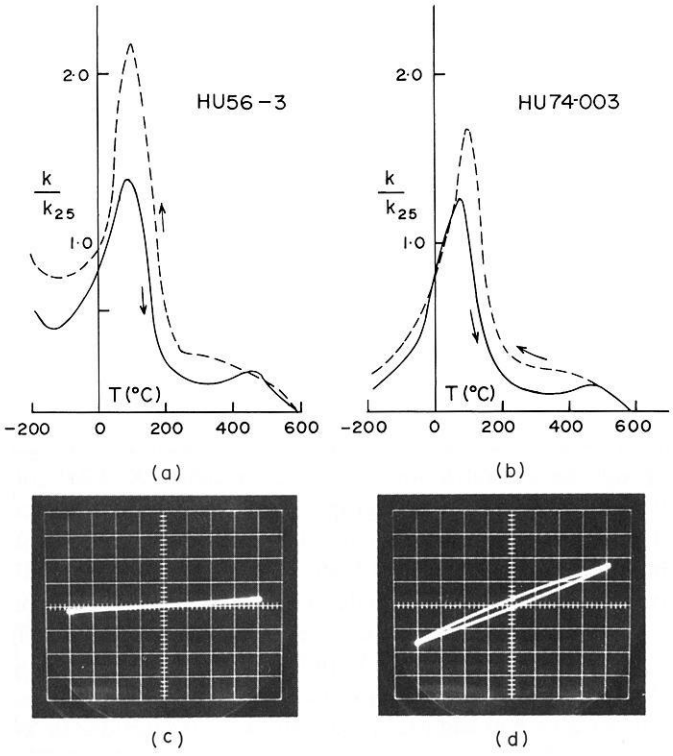

Fig. 3a–d. $k-T$ curves and Rayleigh loops for the two samples of Fig. 2. Rayleigh loops were obtained from (*c*) 11.2 g of HU56-3-20 and (*d*) 13.9 g of HU74-003-6-1. Scales for (*c*) and (*d*) are the same: X-axis, one small division = 0.5 oe; Y-axis, one small division = 0.013 emu

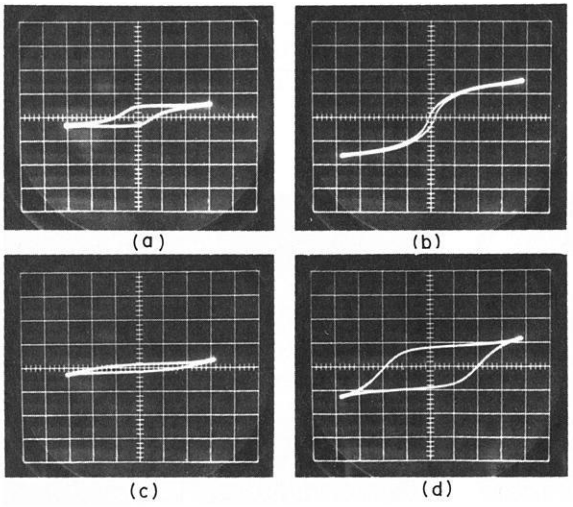

Fig. 4a–d. High-field hysteresis loops for the samples whose Rayleigh loops are given in Fig. 3. (**a**) and (**c**) are for HU56-3 at 25°C and −196°C respectively; (**b**) and (**d**) are for HU74-003 at the two temperatures. Scale (same for all loops): X-axis, one small division = 75 oe; Y-axis, one small division = 1.17 emu. The distortion at some of the loop extremities is due to instrumental noise superimposed on a weak signal

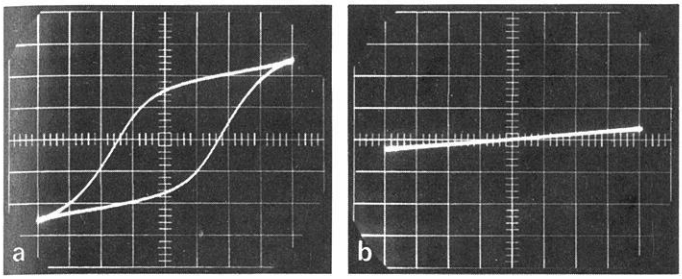

Fig. 5a and b. Medium-field (400 oe) hysteresis loops for a large disc of sample HU56-3. (**a**) is at 25°C and (**b**) is at −196°C. Scale: X-axis, one small division=20 oe; Y-axis, arbitrary

one another at 25° C (Fig. 4a and 4b), though both show a considerable increase in H_c at −196° C (Fig. 4c and d). The J_r/J_m value for HU56-3 is more than 0.5 at 25° C (Fig. 4a), which may imply a substantial contribution from magnetocrystalline and/or stress-induced anisotropy of the grains. To show this feature clearly, medium-field (400 oe) hysteresis loops, for which a larger sample and higher instrument sensitivity could be used, are given in Fig. 5. The J_r/J_m value is a little over 0.6 for this sample even in a field of 400 oe at 25° C (Fig. 5a). The sample has a coercive force of more than 700 oe at −196° C (Fig. 4c) and hence an observable hysteresis could not be excited in 400 oe (Fig. 5b); no minor loop is seen since the differential susceptibility is small even in low fields. On the other hand, J_r/J_m for HU74-003 is about 0.2 at 25° C (Fig. 4b) and 0.7 at −196° C (Fig. 4d) and the respective H_c values are 50 oe and 675 oe.

6. Criteria for Distinguishing SD Titanomagnetite From Hyperfine Magnetite

The characteristic features of HU74-003, namely a $k-T$ curve with spectacular 'Hopkinson' peak and a tail, a Rayleigh loop at 25° C, and having the high-field hysteresis parameters quoted above, are compatible with the presence of fine, predominantly superparamagnetic (SP) interacting particles (Radhakrishnamurty et al., 1971) that become stable SD on cooling to low temperatures. In a study of 46 basalt cores recovered by the Deep Sea Drilling Project (Leg 34) from the Nazca Plate (Deutsch and Pätzold, 1976) about two-thirds were found to have properties such as these, termed 'type 1', as did also a single core out of 46 available from DSDP Leg 37 in the North Atlantic (Murthy et al., 1976). In most of these type 1 samples, the $k-T$ and hysteresis parameters are virtually identical to those of HU74-003.

Although above 0° C the $k-T$ curves of HU56-3 are similar to those of HU74-003, the hysteresis properties are quite different. The properties of HU56-3 may be explained by postulating the presence of SD grains of composition like TM60, for in such a material the contribution to hysteresis properties from magnetocrystalline anisotropy (K_1, K_2), and especially from stress-induced anisotropy (K_σ), can exceed that due to uniaxial shape anisotropy of the grains

because of the low saturation intensity. For comparison, J_s decreases from 93 emu/g for magnetite to about 24 emu/g for TM60; the corresponding decrease of K_1 is slightly less, from -1.4×10^5 to about -0.4×10^5 erg/cm^3, whereas K_σ increases from about $+0.6\times10^5$ ergs/cm^3 for magnetite to about 2.2×10^5 ergs/cm^3 for TM60 (all values at 17° C, taken or extrapolated from Y. Syono, quoted by Nagata, 1965). Hence K_σ/J_s for TM60 is roughly 15 times as large as the same ratio for magnetite.

The above composition-dependent properties can explain the observed large values of J_r/J_m and H_c and the absence of a Rayleigh loop in sample HU56-3 if its composition were that of a high-Ti titanomagnetite. On the other hand, the observed hysteresis parameters are incompatible with a very-fine particle explanation based on magnetite, where one would expect to observe small hysteresis parameters and an open Rayleigh loop. It seems reasonable that the converse argument applies to sample HU74-003. Then the $k-T$ curve for HU56-3 above room temperature may be explained as being due to SD titanomagnetite particles, indicating a T_c of about 200° C which would correspond to a composition a little closer to magnetite than TM60. We can offer no clear explanation for the minima in k near -150° C for sample HU56-3. Some changes have taken place on heating the two samples as revealed by comparing the heating and the cooling curves. HU56-3 showed a thin Rayleigh loop after cooling, which can be attributed to some 'SP' particle formation. The susceptibility of both samples had increased after cooling, but the $k-T$ curves corresponding to their virgin and heated states are similar in trend.

These results suggest two criteria for distinguishing stable-SD titanomagnetite from extremely fine-grained ('SP'-sized) magnetite in rocks where in either case the true or apparent Curie point is less than that of magnetite. *Criterion 1:* At a temperature just below the blocking temperature range as indicated for example by $k-T$ curves, the sample probably is an SD titanomagnetite if hysteresis experiments show that J_r/J_s is large ($\geqq 0.5$) and the coercive force also is large (several hundred oersteds). *Criterion 2:* SD titanomagnetite, like SD magnetite, does not show low-field hysteresis (a Rayleigh loop). Conversely, magnetite (or TM) in a predominantly SP state is indicated if the high-field hysteresis is small (Criterion 1) and if a Rayleigh loop is observed (Criterion 2). Let us now re-formulate the two criteria proposed earlier. *Criterion 3:* A sample is MD titanomagnetite rather than MD magnetite if its $k-T$ characteristics are of 'multi-domain' type and T_c is less than for magnetite. *Criterion 4:* MD titanomagnetite is indicated if the isotropic point, as shown for example in $k-T$ curves, differs from that of magnetite. Conversely, a sample having multi-domain characteristics is magnetite rather than titanomagnetite if its Curie point is close to 578°C (Criterion 3) and its isotropic point is close to -155°C (Criterion 4).

According to Ade-Hall, Johnson and Ryall (1976) most of the DSDP Leg34 samples identified as 'type 1' by Deutsch and Pätzold (1976) contain magnetic grains of composition around TM60, a deduction based on J_s-T curves and chemical analysis of the magnetic grains using the electron microprobe. However, Ade-Hall, Johnson and Ryall (1976) designated some samples as TM's and others as TMhs using the Ozima, Ozima and Kaneoka reversibility criterion.

They also report that a sharply defined T_c was absent even though a nitrogen atmosphere was used for getting the $J_s - T$ curves for the samples. This was also generally observed from $M - T$ curves obtained in air by Deutsch and Pätzold (1976). Ade-Hall et al. (1976) further found a factor of 20 variation in k values when they expected a factor of three among the samples on the basis of grain-size effects and mineral abundance. For all the observed discrepancies cation-deficiency of the TMs, attributed to low-temperature oxidation, was proposed as the main reason.

It should be noted, however, that discussions involving cation-deficiency in the deep-sea basalts, whether of low- or high-temperature origin, are relevant only to samples having T_c values generally above 175°–225° C (Johnson and Hall, 1978). For example, in the study of DSDP Leg 37 basalts (Table 1), all but two of the samples exhibited 'type 2' behaviour attributed to single-domain particles of magnetite or titanomagnetite, which in some cases appeared to be moderately to strongly cation-deficient ('type 2b'; Murthy et al., 1976). On the other hand, the 'type 1' basalts forming the majority of samples in the Nazca Plate study (Leg 34, Table 1) yielded T_c values exclusively below 200° C, along with more or less reversible $k - T$ and $M - T$ curves (Deutsch and Pätzold, 1976). This agrees with thermomagnetic results for other Nazca Plate samples of composition close to TM60 (Ade-Hall et al., 1976; Johnson and Hall, 1978). In each case the carrier is an unoxidized spinel of stoichiometric titanomagnetite (Johnson and Hall, 1978) or magnetite (Deutsch and Pätzold, 1976). Hence, in the type 1 basalts at least, there are no considerations of serious cation-deficiency to complicate the interpretation here presented: namely that low observed T_c values may represent a grain-size effect in hyperfine magnetite, as distinct from a 'true' Curie point in titanomagnetite.

7. Discussion

The main points of observation may be summarized as follows:

(i) Although chemical compositions close to high-Ti titanomagnetite (e.g., TM60) commonly occur in basalts, the magnetic properties vary widely even between samples of similar composition.

(ii) Magnetic behaviour that could be attributed to large MD grains of true titanomagnetite has not been found among the samples so far studied by us.

(iii) Only one sample (HU56-3), from a submarine pillow basalt less than 30,000 years old, has been shown to have properties expected of TM60-like material.

(iv) Many marine basalt samples show the magnetic behaviour attributable to fine single-domain including SP particles, and this feature has been observed even when the physical grain-size of the iron oxide minerals was large enough to form multi-domains.

(v) Samples with sharply indicated Curie points are uncommon, except in some old basalts containing MD magnetite.

The above points seem to suggest that some mechanism or mechanisms operated on the grains of previously TM60-like material in the marine basalts which fundamentally altered their magnetic behaviour. One possible way of explaining the above features is to hypothesize the formation of homogeneous grains of TM60 when the lavas were extruded, and subsequent subdivision into SD and SP particle sizes insofar as the magnetic behaviour is concerned. If the TMs are unstable, time alone can change their magnetic behaviour, with other physical and/or chemical processes speeding up the alteration. Since, in this presumed subdivided condition, our observations indicate mostly properties attributable to pure or nearly pure magnetite, it may be postulated that most of the titanium is able to exsolve submicroscopically in some form or other from the original TM, given enough time. What we regard as single-domain behaviour due to TM could be inferred in only one sample less than 30,000 years old, compared with 93 other marine basalts (HU74-003 plus 46 samples each from Legs 34 and 37), all but one of which are also of single-domain nature but are much older (3 to 20 m.y.). Therefore it is possible that the compositional stability of true titanomagnetites may be limited to time periods of less than a million years. For the present this hypothesis must remain somewhat speculative.

The lack of observed cases of multi-domain TM may imply that, even if large titanomagnetite grains had been common at the time the basalts originated, they were not homogeneous enough in terms of their magnetism to show MD behaviour, probably because of defects, strains or impurities in the grains.

Alternatively, if one considers that all cases of a sharp drop in $J_s - T$ or $k - T$ curves represent an approach to the true Curie point of a TM phase, then the different hysteresis properties found for such samples may have to be attributed to some unknown magnetic properties of these phases. Although the isotropic points of all the members of the TM series are not yet known, from the few available it seems reasonable to assume (e.g. data by Syono and Ishikawa, 1964) that transition points exist up to TM60 or TM70. Since maghemite has no low-temperature transition like that of magnetite, it may not be unreasonable to assume TMhs also to be without transitions. As for highly-cation-deficient titanomagnetites, they may have peculiar magnetic properties like those reported for cation-deficient magnetite (Radhakrishnamurty et al., 1971). However, most of the marine basalts studied by Deutsch and Pätzold (1976) and Murthy et al. (1976) indirectly showed low-temperature transitions in terms of an increase in H_c and J_r/J_m values at $-196°$C compared to their respective values at 20° C; it is therefore difficult to see how they could be strongly cation-deficient TM as was deduced by Johnson and Hall (1978).

Finally, it might be argued that the presence, typical in oceanic basalts, of minor cation impurities (Al, Mg, Mn) in titanomagnetite may have affected the magnetic properties of our samples sufficiently to cause a misdiagnosis of the domain state. By this argument, the presence of such impurities in multi-domain grains conceivably could have suppressed the isotropic peak seen otherwise in the $k - T$ curves of 'pure' samples; then, assuming that some samples identified by us as single-domained actually have an MD structure, this could explain our failure to identify such MD's. This possibility is difficult to assess, in view of the nearly complete absence of relevant

experimental data. The effect of minor cations on the isotropic points of titanomagnetite such as TM60 does not appear to have been studied, as distinct from their effect on other magnetic properties of sea-floor basalts (Petersen et al., 1979). A total Al+Mg+Mn contribution of about 2% by weight in TM60 is characteristic, for example in Nazca Plate basalts (Bunch and Laborde, 1976), which applies to the samples measured by Deutsch and Pätzold (1976). As we have pointed out, however, most of these samples do show indirectly the low-temperature transition in (titano) magnetite, and we argue therefore that the presence of the minor impurities is unlikely to have had a critical effect on those magnetic properties measured by us that relate to domain structure.

Unfortunately, the hysteresis properties of TMs and TMhs have not been studied and recorded systematically by workers who synthesised them for comparison with the properties of marine basalts. Nevertheless, to ignore the hysteresis and susceptibility properties of basalts, especially when they strongly indicate the presence of SP and/or SD particles, in preference to the results of optical and chemical studies, may lead to error in inferring their magnetic state.

In support of the view that even large ferromagnetic grains may be effectively subdivided in terms of their magnetic properties, Jacobs and Bean (1963) recorded: '... an interesting example has been recently described in a mixed cobalt-zinc ferrite by Booth and Crangle (1962). Superparamagnetic behaviour was observed despite the fact that the material was in bulk, essentially single phase, polycrystalline form'. Thus it seems reasonable to propose that magnetic behaviour expected from effective SD/SP particles occurs in apparently large magnetite or titanomagnetite grains in marine basalts, which could then account for the observed magnetic properties of the iron oxide grains.

Acknowledgements. We are grateful to Dr. J.M. Hall of Dalhousie University for providing the marine basalt samples HU56-3 and HU74-003 and their photomicrographs. We were greatly assisted by critical comments on the manuscript received from Dr. M.E. Evans, the late Dr. Pullaiah Guntur and Dr. N. Petersen. The research at Memorial University of Newfoundland was supported by Grants A-1946 to E.R. Deutsch and A-8707 to G.S. Murthy, from the National Research Council of Canada.

References

Ade-Hall, J.M.: Electron probe micronanalyser analysis of basaltic titanomagnetites and their significance to rock magnetism. Geophys. J. R. Astron. Soc. **8**, 301–312, 1964

Ade-Hall, J.M., Johnson, H.P., Ryall, P.J.C.: Rock magnetism of basalts, Leg 34. In: Initial Reports of the Deep Sea Drilling Project, Vol. 34, S.R. Hart and R.S. Yeats, eds.: pp. 459–468. Washington, DC: U.S. Government Printing Office, 1976

Aumento, F.: The Mid-Atlantic Ridge near 45° N. V. Fission track and ferro-manganese chronology. Can. J. Earth Sci. **6**, 1431–1440, 1969

Booth, J.G., Crangle, J.: Magnetic properties of mixed ferrites; I. Behaviour near the Curie point. II. Superparamagnetism and exchange anisotropy in a Cobalt-Zinc ferrite. Proc. Phys. Soc. London **79**, 1271–1281, 1962

Bunch, T.E., Laborde, R.: Mineralogy and compositions of selected basalts from DSDP Leg 34. In: Initial Reports of the Deep Sea Drilling Project, vol 34, S.R. Hart and R.S. Yeats, eds.: pp. 263–275. D C: U.S. Government Printing Office, Washington 1976

Chevallier, R., Bolfa, J., Mathieu, S.: Titanomagnétites et ilménites ferromagnétiques. Bull. Soc. Fr. Minéral. Cristallogr. **78**, 307, 1955

Creer, K.M.: Geophysical interpretation of remanent magnetization in oxidized basalts. Z. Geophys. **37**, 383–407, 1971

Deutsch, E.R., Pätzold, R.R.: Magnetism of basalt cores from the Nazca Plate and implications for magnetic anomaly interpretation. J. Geophys. Res. **81**, 4188–4198, 1976

Feitknecht, W., Gallagher, K.G.: Mechanism for the oxidation of magnetite. Nature **228**, 548–549, 1970

Hauptman, Z.: High temperature oxidation, range of non-stoichiometry and Curie point variation of cation-deficient titanomagneite $Fe_{2.4}\ Ti_{0.6}O_{4+}$. Geophys. J. R. Astron. Soc. **38**, 29–47, 1974

Hopkinson, J.: Magnetic and other physical properties of iron at a high temperature. Philos. Trans. R. Soc. Lond. [Ser. A] **180**, 443, 1889

Jacobs, I.S., Bean, C.P.: Fine particles, thin films and exchange anisotropy (effects of finite dimensions and interfaces on the basic properties of ferromagnetics). pp. 271–350 Magnetism III, New York: Academic Press, 1963

Jensen, S.D., Shive, P.N.: Cation distribution in sintered titano-magnetites. J. Geophys. Res. **78**, 8474–8480, 1973

Johnson, H.P., Hall, J.M.: A detailed rock magnetic and opaque mineralogy study of the basalts from the Nazca Plate. Geophys. J. R. Astron. Soc. **52**, 45–64, 1978

Johnson, H.P., Lowrie, W., Kent, D.V.: Stability of anhysteretic remanent magnetization in fine and coarse magnetite and maghemite particles. Geophys. J. R. Astron. Soc. **41**, 1–10, 1975

Likhite, S.D., Radhakrishnamurty, C.: Initial susceptibility and constricted Rayleigh loops of some basalts. Curr. Sci. **35**, 534–536, 1966

Murthy, G.S., Deutsch, E.R., Pätzold, R.R.: Inferences on the magnetic domain state of Leg 37 basalts. J. Geophys. Res. **81**, 4199–4206, 1976

Nagata, T.: Low temperature characteristics of rock magnetism. J. Geomag. Geoelec. **17**, 315–324, 1965

Ozima, M., Larson, E.E.: Low and high temperature oxidation of titanomagnetite in relation to irreversible changes in the magnetic properties of submarine basalts. J. Geophys. Res. **75**, 1003–1017, 1970

Ozima, M. Ozima, M. Kaneoka, I.: Potassium-argon ages and magnetic properties of some dredged submarine basalts and their geophysical implications. J. Geophys. Res. **73**, 711–723, 1968

Pätzold, R.R.: High temperature magnetic susceptibility bridge. M.Sc. thesis, Memorial University of Newfoundland, 1972

Petersen, N., Eisenach, P., Bleil, U.: Low temperature alteration of the magnetic minerals in ocean floor basalts. Maurice Ewing Series, vol. 1, M. Talwani and W.C. Pitman III, eds. Washington, D.C.: Am. Geophys. Union (in press, 1979)

Radhakrishnamurty, C., Deutsch, E.R.: Magnetic techniques for ascertaining the nature of iron oxide grains in basalts. J. Geophys. **40**, 453–465, 1974

Radhakrishnamurty, C., Likhite, S.D.: Hopkinson effect, blocking temperature and Curie point in basalts. Earth Planet. Sci. Lett. **7**, 389–396, 1970

Radhakrishnamurty, C., Likhite, S.D., Raja, P.K.S., Sahasrabudhe, P.W.: Magnetic grains in Bombay columnar basalts. Nature Phys. Sci. **235**, 33–35, 1971

Radhakrishnamurty, C., Likhite, S.D., Sastry, N.P.: Low temperature magnetic hysteresis of fine particle aggregates ocurring in some natural samples. Philos. Mag. **23**, 503–507, 1971

Radhakrishnamurty, C., Raja, P.K.S., Likhite, S.D., Sahasrabudhe, P.W.: Problems concerning the magnetic behaviour and determination of Curie points of certain basalts. Pure Appl. Geophys. **93**, 129–140, 1972

Radhakrishnamurty, C., Sahasrabudhe, P.W.: Magnetic hysteresis of heat treated basalts. Curr. Sci. **34**, 474–476, 1965

Readman, P.W., O'Reilly, W.: Magnetic properties of oxidized (cation-deficient) titanomagnetites $(Fe, Ti, \blacksquare)_3O_4$. J. Geomag. Geoelec. **24**, 69–90, 1972

Sato, T., Kuroda, C., Saito, M.: Preparation and magnetic characteristics of ultra-fine spinel ferrites. Ferrites: Proc. International Conference, July 1970, Japan, Univ. Park Press, pp. 72–74, 1971

Smith, P.J.: Electron probe microanalysis of optically homogeneous titanomagnetites and ferrian ilmenites of paleomagnetic significance. J. Geophys. Res. **72**, 5087–5100, 1967

Syono, Y., Ishikawa, Y.: Magnetocrystalline anisotropy and magnetostriction of $xFe_2TiO_4 \cdot (1-x)Fe_3O_4$ $(x > 0.5)$. J. Phys. Soc. Japan **19**, 1752–1753, 1964

Uyeda, S.: Thermo-remanent magnetism as a medium of paleomagnetism, with special reference to reverse thermo-remanent magnetism. Japan. J. Geophys. **2**, 1–123, 1958

Wilson, R.L., Smith, P.J.: The nature of secondary natural magnetizations in some igneous and baked rocks. J. Geomag. Geoelec. **20**, 367–380, 1968

Received May 10, 1977; Revised Version October 12, 1978 and March 20, 1979;
Accepted May 26, 1979

J. Geophys. 45, 447–450, 1979

Journal of Geophysics

Short Communication

Palaeomagnetism of Permo-Triassic Red Sandstones From the Northern Calcareous Alps

H. Soffel

Institut für Allgemeine und Angewandte Geophysik, Theresienstrasse 41,
Universität München, D-8000 München 2, Federal Republic of Germany

Key words: Northern Calcareous Alps – Permo-Triassic sandstones.

1. Introduction

It is generally agreed (Gwinner, 1971) that the Northern Calcareous Alps (together with the Northern Grauwackenzone) rest allochthonously on top of a Penninic basement and have been transported into their present position from the South after Upper Eocene. Their complicated structure is characterized by a series of nappes of various lateral extensions and thicknesses. A sketch map of the Western part of the Northern Calcareous Alps (Fig. 1) shows the main nappes (after Gwinner, 1971).

Earlier palaeomagnetic measurements on rocks from the Northern Calcareous Alps gave contradictory results. Hargraves and Fischer (1959) studied Liassic red limestones and radiolarites near Lofer (Lo) and deduced a slight (20°) clockwise rotation with respect to Central Europe. A much larger clockwise rotation (40°) was concluded by Mauritsch and Frisch (1978) from the study of Upper Jurassic red limestones of the Osterhorngruppe (Os). However, an anticlockwise rotation (60°) was deduced by Soffel (1975) from the palaeomagnetism of Upper Permian to Lower Triassic effusives in Vorarlberg (Vo). None of these data seem to have a general validity for a rotation of the Northern Calcareous Alps as a whole during their transport by gravity gliding.

Along the southern margin of some of the nappes, Permo-Triassic (Skythian) red sandstones are exposed which are in some places in an undisturbed tectonic context with overlying Triassic limestones and dolomites. Several localities of these brown to violet coloured fine grained sandstones have been sampled. (In: Innsbruck, Rumer Spitze, 1 site, 10 samples; Wö: Hopfgarten near Wörgl, 5 sites, 36 samples; Le: Leogang near Saalfeld, 4 sites, 29 samples.) All localities and their corresponding position within the different nappes are shown in Fig. 1.

0340-062X/79/0045/0447/$01.00

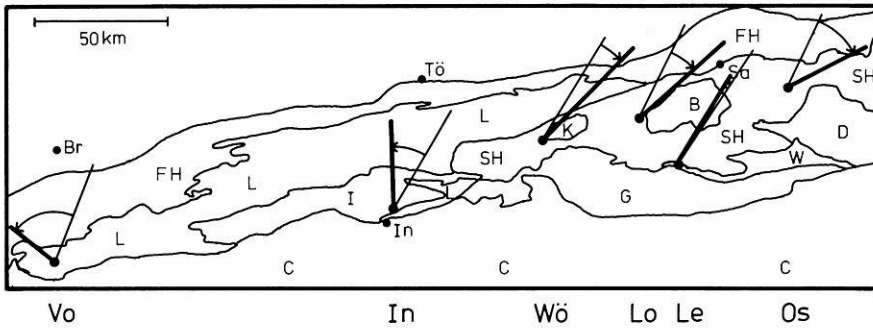

Fig. 1. Western part of the Northern Calcareous Alps. *L* Lechtaldecke; *I* Inntaldecke; *SH* Staufen-Höllengebirgsdecke; *K* Kaiserdecke; *B* Berchtesgadener Schubmasse; *W* Werfener Schuppenzone; *D* Dachsteindecke; *G* Grauwackenzone; *FH* Flysch, Helvetikum; *C* Kristallin, Schieferhülle. *Br* Bregenz; *Tö* Bad Tölz; *Sa* Salzburg. For sampling localities see text. Measured remanence directions (*thick*) and reference directions with regard to Central Europe (*thin lines*). *Arrows* indicate rotation.

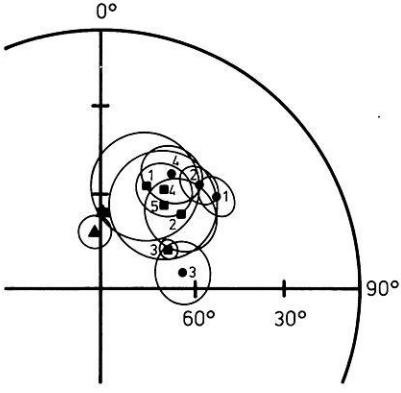

Fig. 2. NRM directions in equal area projection. *Star:* present geomagnetic field direction. *Triangle:* site In. *Squares:* sites Wö. *Dots:* sites Le

2. Palaeomagnetic Results

Figure 2 shows the NRM directions, all being normal. For meaning of the symbols see legend. With exception of site In, all directions differ significantly from the present local geomagnetic field direction (star). AF demagnetization up to 2,000 Oe and thermal demagnetization up to 650° C revealed the presence of two antiparallel remanence components in all three localities: a reversed component which could be destroyed with AF fields up to 100 Oe and thermal treatment up to 300° C, and a normal component stable up to 2,000 Oe and thermal treatment up to 560° C. At higher temperatures the directions scattered randomly and revealed no indication of a consistent component with higher blocking temperatures. Largest precision parameter was obtained for thermal demagnetization at 300° C.

Figure 3a and b show the site mean and locality mean directions after thermal cleaning and tectonic correction in equal area projection. For details see legend. The locality means are as follows: In: $N=10$, $R=9.82$, $D=359.0°$,

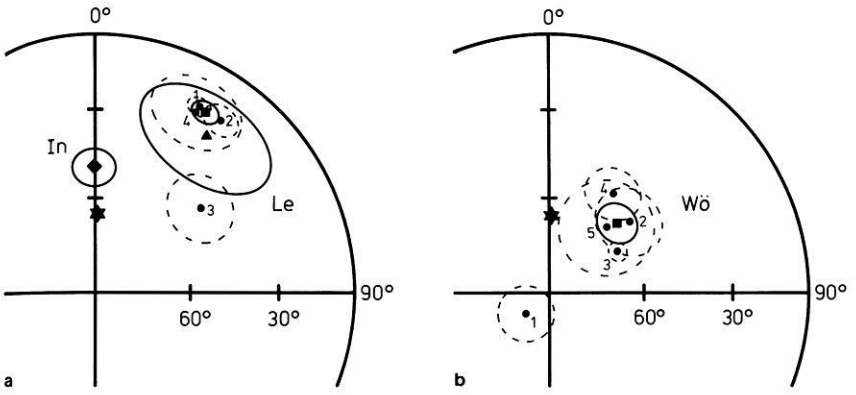

Fig. 3a and b. RM directions after thermal cleaning with 300° C and tectonic correction. *Star:* present geomagnetic field direction. **a** *Diamond:* site In. *Square:* sites Le, 3 closely grouped. *Triangle:* sites Le, all. **b** *Square:* sites Wö, 4 closely grouped

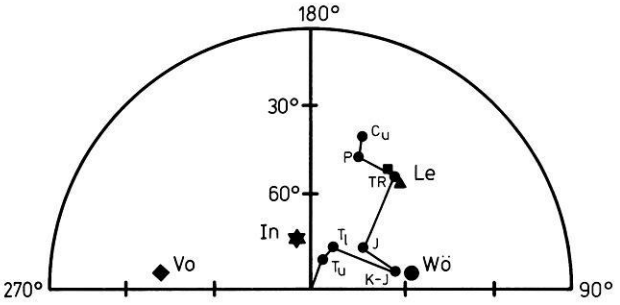

Fig. 4. Pole positions and part of European polar wander path. For details see text. *Diamond:* Vorarlberg after Soffel (1975); *Star:* Innsbruck; *Square:* Leogang, 3 closely grouped sites; *Triangle:* Leogang, all sites. *Full circle:* Wörgl

$I=49.9°$, $k=50.1$, $\alpha_{95}=6.3°$; Wö: $N=4$, $R=3.97$, $D=44.3°$, $I=59.2°$, $k=102.7$, $\alpha_{95}=6.9°$ (omitting site 1 because of uncertain tectonic position); Le: $N=3$, $R=2.995$, $D=31.5°$, $I=19.6°$, $k=414.8$, $\alpha_{95}=4.0°$ (omitting site 3 because of too large deviation from the remaining group). The corresponding pole positions are: In: 194.5° E, 73.4° N; Wö: 98.9° E, 57.6° N; Le: 147.0° E, 44.1° N. The mean geographic coordinates are 12° C, 47.5° N, however the exact coordinates were used for the computation of the pole positions. They are shown in Fig. 4 together with a part of the European polar wander path after McElhinny (1973). The Jurassic pole is from Heller (1977), the Lower Cretaceous-Upper Jurassic pole was taken from Schweitzer (1975).

3. Discussion and Conclusions

The presence of two almost exactly antiparallel remanence components (with fortunately not too much overlapping coercivity and blocking temperature spec-

tra) indicates a complicated magnetization history of these sandstones. The too steep inclinations for rocks of Early Triassic age (except for site Le) suggests a later overprint, perhaps during Upper Cretaceous or Lower to Middle Tertiary (early stage of the alpine orogeny). On the other hand, the presence of a third magnetization component with shallover inlination could not be found during the demagnetization experiments. From polished section studies the carrier of remanence seems to be detrital magnetite to some degree oxidized to hematite. From the petrology of the rocks there is no evidence for major mineralogical changes or reheating. The exact age of remanence of sites In and Wö remains therefore uncertain. Only the Leogang sandstones have a pole position which agrees with the Triassic pole for Central Europe indicating no rotation during the transport. Supposing an at least pre-Oligocene age of remanence of the two other sandstone sites, a slight clockwise rotation (15°) must be assumed for the Wörgl and a small anticlockwise rotation (20°) for the Innsbruck sandstones. The amounts of rotation are indicated in Fig. 1, where the corresponding rotations from Vorarlberg (Vo), Lofer (Lo) and Osterhorngruppe (Os) are also shown. The pattern of rotations (anticlockwise in the West, clockwise in the East) does in my view not reflect any bending of the Northern Calcareous Alps. Unless more data from the whole extend of the Northern Calcareous Alps are available I tend to regard the observed rotations as local effects which may be typical for a specific nappe or a part of it. They seem to reflect the sense and amount of relative rotation of the different units during their post Eocene northward transport by gravity gliding.

Acknowledgement. Dr. H. Bögel (Munich) and Dr. R. Brandner (Innsbruck) are kindly acknowledged for their advice and help during the collection of the samples. Thanks are also due to N. Grohmann, Dr. A Schult, Professor Dr. G. Angenheister and Dr. N. Petersen for many interesting discussions and to the Deutsche Forschungsgemeinschaft for the financial support.

References

Gwinner, M.P.: Geologie der Alpen. p. 237ff. Stuttgart: E. Schweizerbart'sche Verlagsbuchhandlung, 1971

Hargraves, R.B., Fischer, A.G.: Remanent magnetism in jurassic red limestones and radiolarites from the Alps. Geophys. J. R. Astron. Soc. **2**, 34–41, 1959

Heller, F.: Palaeomagnetism of upper jurassic limestones from Southern Germany. J. Geophys. **42**, 475–488, 1977

Mauritsch, H.J., Frisch, W.: Palaeomagnetic data from the central part of the Northern Calcareous Alps, Austria. J. Geophys. **44**, 623–637, 1978

McElhinny, M.W.: Palaeomagnetism and Plate Tectonics. p. 206. Cambridge: University Press 1973

Schweitzer, Ch.: Vergleich mehrerer Methoden zur Bestimmung der Intensität des Erdmagnetfeldes an rezenten Laven und ihre Anwendung auf mesozoische und palaozoische magmatische Gesteine. Universität München: Dissertation 1975

Soffel, H.: The Palaeomagnetism of the Permian Effusives near St. Anton, Vorarlberg (Austria) and the Anticlockwise Rotation of the Northern Calcareous Alps through 60°. Neues Jahrb. Geol. Palaeontol. Monatsh. **6**, 375–384, 1975

Received May 2, 1978; Revised Version April 5, 1979;
Accepted June 19, 1979